

UNIVERSITY OF BIRMINGHAM

DINUCLEAR LANTHANIDE(III) COMPLEXES FOR LIGHT EMITTING SURFACES AND PLASMONIC NANOMATERIALS

by

ELENA DEL GIORGIO

A thesis submitted to the University of Birmingham for the degree of

DOCTOR OF PHILOSOPHY

School of Chemistry

College of Engineering and Physical Sciences

University of Birmingham

August 2023

UNIVERSITY OF
BIRMINGHAM

University of Birmingham Research Archive

e-theses repository

This unpublished thesis/dissertation is copyright of the author and/or third parties. The intellectual property rights of the author or third parties in respect of this work are as defined by The Copyright Designs and Patents Act 1988 or as modified by any successor legislation.

Any use made of information contained in this thesis/dissertation must be in accordance with that legislation and must be properly acknowledged. Further distribution or reproduction in any format is prohibited without the permission of the copyright holder.

Abstract

Lanthanide(III) luminescence is extremely valuable for the development of optical devices. The long luminescence lifetimes, high photostability and narrow and characteristic emission peaks of lanthanides(III) are accompanied by low molar absorption coefficients, demanding sensitisation from light harvesting units *via* the antenna effect. In addition to careful ligand design, nanostructured plasmonic materials can enhance lanthanide(III) luminescence and overcome some of the most common limitations of luminescent materials and particularly near infrared (NIR) emission, such as poor signal to noise ratios and low quantum yields and brightness. Here, we present novel surface active bis β-diketonate lanthanide(III) complexes for the fabrication of visible and NIR emitting materials. The incorporation of thioacetate units in the ligand scaffold enables the complexes to be anchored on metallic substrates. The characteristic visible and NIR luminescence is retained upon coating on gold (Au) surfaces, and the preparation of a handheld sensing device is demonstrated as a response of the Eu(III) surfaces to F^- coordination. Incorporation of the complexes to plasmonic substrates is determined to be an excellent approach for the enhancement of both visible and NIR luminescence. Plasmonic Au (pGold) surfaces, in particular, lead to exceptional resolution and intensity of NIR Nd(III) and Yb(III) emission, driving the progress of lanthanide(III) NIR light to advanced applications. Finally, the complexes are anchored on Au nanoparticles (AuNPs), producing highly emissive H_2O dispersed nanomaterials. An alternative approach for the preparation of surface active bis β-diketonates is demonstrated by coordination of functionalised 1,10-phenanthroline units, also optimising the luminescent output of both the complex in solution and on AuNPs.

Acknowledgments

First of all, I would like to express my sincere gratitude to my supervisors, Prof. Zoe Pikramenou, Prof. Shuang Zhang and Karl Lymer. I am extremely grateful for the guidance and support I have received: thank you for giving me the opportunity to work on such an exciting project and for keeping me motivated throughout the years. I would also like to thank Prof. Mike Hannon and his group for the always helpful input at group meetings, as well as our collaborators at the Department of Physics and Astronomy, University of Birmingham, Dr. Miguel Navarro-Cía, Dr. Angela Demetriadou and Dr. Rohit Chikkaraddy, for their extremely valuable and expert knowledge of plasmonics and metamaterials. Finally, I would like to acknowledge the Defence Science and Technology Laboratory (Dstl) for funding and the Deutscher Akademischer Austauschdienst (DAAD) for the travel grant to fund my stay in Berlin.

During these 3 years of research, I have had the opportunity to work with collaborators at different departments and institutions. At the Bundesanstalt für Materialforschung und -prüfung (BAM) in Berlin, I would like to sincerely thank Dr.-Ing. Vasile-Dan Hodoroaba for providing excellent support and guidance during my stay, as well as Sigrid Benemann for the many SEM images and EDX data, and Jörg Stockmann and Jörg Radnik for the XPS data. I would like to thank Dr. Simon Connell and Dr. Pallavi Kumari at the Department of Physics and Astronomy, University of Leeds, for the AFM imaging during my visit. Thank you to Dr. Sarah Griffin for the XRD analysis of my crystals and for the elucidation of the crystal structures. To Dr. Demie Kepaptsoglou at the SuperSTEM laboratory in Daresbury, for the SuperSTEM studies. I also extend my gratitude to Dr. James Churm at the School of Engineering, University of Birmingham, for the AFM imaging, as well as training and support in the clean room. Thank

you to the technical staff at the University of Birmingham for help and training with instruments. In particular, thank you to Trevor Hardy, Dr. Chris Williams, Dr. Cécile Le Duff, Dr. Ludwig Schneider and Theresa Morris.

I would like to thank all the members of the Pikramenou group, past and present: you've made life in the office and the lab so much better and fun. In particular, a huge thank you to Patricia for being such a great colleague, housemate and friend from the very start, to Asier for being the least boring person I know, to Maria for being an amazing and knowledgeable postdoc, to Grace for teaching me how to really speak English, to Jamie for being a solid bloke and to Kun for always being so positive and kind. A big thank you also to George, because he's a legend, and to all the friends I've found during my time in Birmingham: Gauri, Cam, Demo and Matt, you've made it very hard to leave.

A massive, enormous, gigantic thank you to Sam, for his never ending support, belief in me and positivity.

Grazie a Francesco, Martina e Sofia per le lunghe passeggiate e chiacchierate due volte all'anno che, malgrado gli anni e la distanza, non cambiano mai.
Grazie alla mia famiglia, per essermi stati vicini e avermi sempre ricordato quello che conta. Grazie per essere sempre la mia casa, ovunque io sia.

Table of Contents

Abstract II

Acknowledgments III

Table of Contents V

List of Abbreviations XI

Chapter 1 – General introduction 1

1.1 Principles of lanthanide(III) luminescence and coordination chemistry 1

1.1.1 Introduction to the lanthanides 1

1.1.2 Lanthanide(III) luminescence 2

1.1.3 Luminescent lanthanide(III) coordination compounds 6

1.1.3.1 An overview of common ligand designs and the luminescence of their lanthanide(III) complexes 6

1.1.3.2 Lanthanide(III) β-diketonates 13

1.2 Plasmonic materials 29

1.2.1 Plasmon mediated fluorescence enhancement 31

1.2.2 Plasmonic surfaces as fluorescent sensing platforms 36

1.3 Thesis Outline 42

1.4 References 44

Chapter 2 – Design of surface active dinuclear lanthanide(III) complexes as new luminescent probes 50

2.1 Introduction 50

2.1.1 Lanthanide(III) complexes as optical probes for the detection of analytes 50

2.1.2 Detection of fluoride with luminescent lanthanide(III) complexes 57

2.1.3 Aims of the project 68

2.2 Results and discussion 70

2.2.1 Synthesis of the surface active SAcbisDBM ligand 70

2.2.2 Synthesis and characterisation of Ln_2SAcbisDBM$_3$ complexes 75

2.2.3 Optical properties of Ln_2SAcbisDBM$_3$ complexes 82

2.2.3.1 Luminescence of the visible emitting Eu_2SAcbisDBM$_3$ complex in solution 83

2.2.3.2 Luminescence of the NIR emitting Yb_2SAcbisDBM$_3$ and Nd_2SAcbisDBM$_3$ complexes in solution 87

2.2.4 Detection and coordination of F^- to Eu(III) diketonates complexes 90
2.3 Conclusions and future studies 99
2.4 References 101
2.5 Appendix I 104
2.5.1 Materials and methods 104
2.5.2 Synthetic procedures 106
2.5.2.1 Synthesis of 3,3'-(5-bromo-1,3-phenylene)bis(1-phenylpropane-1,3-dione) (3) 106
2.5.2.2 Synthesis of 1,1'-(5-((trimethylsilyl)ethynyl)-1,3-phenylene)bis(3-hydroxy-3-phenylprop-2-en-1-one) (4) 107
2.5.2.3 Synthesis of 1,1'-(5-ethynyl-1,3-phenylene)bis(3-hydroxy-3-phenylprop-2-en-1-one) (5) 108
2.5.2.4 Synthesis of S-(3-(4-(3,5-bis(3-hydroxy-3-phenylacryloyl)phenyl)-1H-1,2,3-triazol-1-yl)propyl) ethanethioate (SAcbisDBM) 109
2.5.2.5 Synthesis of Ln_2SAcbisDBM$_3$ (Ln=Eu(III), Gd(III), Nd(III), Yb(III)) 110
2.5.2.6 Synthesis of 1,3-bis(3-phenyl-3-oxopropanoyl)benzene (bisDBM)[1] 112
2.5.2.7 Synthesis of Ln_2bisDBM$_3$ (Ln=Eu(III), Yb(III), Nd(III))[45] 113
2.5.3 Anion coordination procedures 114
2.5.3.1 Testing with F^- (NaF) 114
2.5.3.2 Testing with F^- (TBAF) 114
2.5.3.3 Testing with Br^- (TBAB) 115
2.5.4 Characterisation data 115
2.5.4.1 3,3'-(5-bromo-1,3-phenylene)bis(1-phenylpropane-1,3-dione) (3) 115
2.5.4.2 1,1'-(5-((trimethylsilyl)ethynyl)-1,3-phenylene)bis(3-hydroxy-3-phenylprop-2-en-1-one) (4) 119
2.5.4.3 1,1'-(5-ethynyl-1,3-phenylene)bis(3-hydroxy-3-phenylprop-2-en-1-one) (5) 123
2.5.4.4 S-(3-(4-(3,5-bis(3-hydroxy-3-phenylacryloyl)phenyl)-1H-1,2,3-triazol-1-yl)propyl) ethanethioate (SAcbisDBM) 126
2.5.4.5 Eu_2SAcbisDBM$_3$ 130
2.5.4.6 Yb_2SAcbisDBM$_3$ 132
2.5.4.7 Nd_2SAcbisDBM$_3$ 134
2.5.4.8 Gd_2SAcbisDBM$_3$ 137
2.5.5 Additional photophysical data 138

2.5.5.1 Steady state excitation and emission data 138
2.5.5.2 Time resolved data 143
2.5.6 Crystal structures data 155
Chapter 3 – Plasmonic enhancement of visible and NIR lanthanide(III) emission on nanostructured surfaces 160
3.1 Introduction 160
3.1.1 Lanthanide(III) complexes on Au surfaces 160
3.1.2 Plasmonic enhancement of lanthanide(III) luminescence 164
3.1.2.1 Plasmon enhanced upconversion luminescence 164
3.1.2.2 Plasmon enhanced emission of lanthanide(III) molecular complexes 167
3.1.3 Introduction to polyaniline (PANI) 176
3.1.3.1 PANI, lanthanides(III) and their assemblies 177
3.1.4 Aims of the project 179
3.2 Results and discussion 181
3.2.1 Visible and NIR luminescent dip coated Ln_2SAcbisDBM$_3$@Au surfaces 181
3.2.2 F^- sensing with Eu_2SAcbisDBM$_3$@Au surfaces 189
3.2.3 Spin coating as a robust coating method for Au surfaces 194
3.2.4 Characterisation and modelling of plasmonic Au (pGold) surfaces 198
3.2.5 Effect of pGold surfaces on lanthanide(III) luminescence 203
3.2.5.1 Visible Eu_2SAcbisDBM$_3$ luminescence 203
3.2.5.2 NIR Yb_2SAcbisDBM$_3$ and Nd_2SAcbisDBM$_3$ luminescence 207
3.2.5.3 Further studies on SP_Eu_2SAcbisDBM$_3$@pGold: epifluorescence microscopy and SERS 209
3.2.6 Preparation of Ag nanoislands (AgNIs) surfaces 214
3.2.7 Effect of Ag nanostructured surfaces (AgNIs) on lanthanide(III) luminescence and comparison with pGold 216
3.2.8 Polymer assisted deposition of Ln_2bisDBM$_3$ complexes on Au surfaces 220
3.2.8.1 Evaluation of the supramolecular assembly of Ln_2bisDBM$_3$ and PANI 220
3.2.8.2 Luminescence of Au surfaces coated with Ln_2bisDBM$_3$ complexes and PANI 224
3.2.8.3 Morphology and characterisation of the surfaces 227
3.3 Conclusions and future studies 233
3.4 References 237

3.5 Appendix II 242
3.5.1 Materials and methods 242
3.5.1.1 Fabrication 242
3.5.1.2 Characterisation 242
3.5.2 Cleaning of surfaces 244
3.5.3 Coating of surfaces 245
3.5.4 Fluoride sensing 247
3.5.5 Preparation of AgNIs surfaces 248
3.5.6 Addition of PANI to Eu_2bisDBM$_3$ for UV-Vis absorption spectroscopy 249
3.5.7 Additional photophysical data 250
3.5.7.1 Steady state excitation and emission data 250
3.5.7.2 Time resolved data 260
3.5.8 Additional imaging data 272
3.5.9 XPS data 278
3.5.10 Additional simulations of pGold 280
3.5.11 Addition Raman data and assignments 280
Chapter 4 – Lanthanide(III) coated luminescent Au nanoparticles (AuNPs) 281
4.1 Introduction 281
4.1.1 General principles of AuNPs 281
4.1.1.1 The fabrication of AuNPs 281
4.1.1.2 The optical properties of AuNPs 283
4.1.1.3 The functionalisation of AuNPs 285
4.1.2 The functionalisation of AuNPs with luminescent lanthanide(III) complexes 287
4.1.3 Aims of the project 295
4.2 Results and Discussion 297
4.2.1 Preparation, optimisation and luminescence of Eu_2SAcbisDBM$_3$ coated AuNP14 297
4.2.1.1 Direct coating of AuNPs: Eu_2SAcbisDBM$_3$@AuNP14 297
4.2.1.2 Coating and characterisation of Zonyl FSA stabilised AuNPs: Eu_2SAcbisDBM$_3$●Z@AuNP14 299
4.2.1.3 Visible luminescence of Eu_2SAcbisDBM$_3$●Z@AuNP14 305
4.2.2 Effect of AuNP size on Eu_2SAcbisDBM$_3$ luminescence and NIR emitting Ln_2SAcbisDBM$_3$●Z@AuNPs (Ln(III)=Yb(III), Nd(III)) 307

4.2.3 Design and preparation of bright surface active $Eu_2bisDBM_3$_$PhenSS_2$ and $Eu_2bisDBM_3$_$PhenSS_2$●Z@AuNP14 315
4.2.3.1 Synthesis and characterisation of PhenSS 315
4.2.3.2 Spectroscopic studies on the coordination of PhenSS to $Eu_2bisDBM_3$ 317
4.2.3.3 Preparation of $Eu_2bisDBM_3$_$PhenSS_2$●Z@AuNP14 and comparisons with $Eu_2SAcbisDBM_3$●Z@AuNP14 321
4.2.3.4 Luminescence properties of $Eu_2bisDBM_3$_$PhenSS_2$●Z@AuNP14 324
4.3 Conclusions and future studies 327
4.4 References 329
4.5 Appendix III 334
4.5.1 Materials and methods 334
4.5.2 Synthetic procedures 336
4.5.2.1 Synthesis of 5-(1,2-dithiolan-3-yl)-N-(1,10-phenanthrolin-5-yl)pentanamide (PhenSS) 336
4.5.2.2 Synthesis of AuNP14 337
4.5.2.3 Synthesis of AuNP25, AuNP50 and AuNP100 337
4.5.3 PhenSS coordination studies 339
4.5.3.1 Addition of PhenSS to $Eu_2bisDBM_3$ for spectroscopic studies 339
4.5.3.2 Preparation of $Eu_2bisDBM_3$_$PhenSS_2$ for coating on Z@AuNP14 339
4.5.4 Coating procedures 339
4.5.4.1 Coating of AuNP14 and AuNP50 with Zonyl FSA: Z@AuNP14-50 339
4.5.4.2 Coating of AuNP100 with Zonyl FSA: Z@AuNP100 340
4.5.4.3 Coating of Z@AuNP14, Z@AuNP50 and Z@AuNP100 with $Ln_2SAcbisDBM_3$: $Ln_2SAcbisDBM_3$●Z@AuNP14-50-100 340
4.5.4.4 Coating of Z@AuNP14 with $Eu_2bisDBM_3$_$PhenSS_2$: $Eu_2bisDBM_3$_$PhenSS_2$ ●Z@AuNP14 340
4.5.5 Correction of emission spectra by absorbance loss 341
4.5.6 Calculation of concentration of AuNPs from UV-Vis absorption spectra 341
4.5.7 ICP-MS experiments 342
4.5.7.1 Preparation of samples and calibration 342
4.5.7.2 Calculations of AuNP concentration and number of complex molecules per AuNP 342
4.5.8 Size distributions of AuNPs 343
4.5.9 UV-Vis data 354

4.5.10 Epsilon curves....360
4.5.11 Additional photophysical data....362
4.5.11.1 Steady state excitation and emission data....362
4.5.11.2 Time resolved data....366
4.5.12 Additional characterisation data of PhenSS....372
4.5.13 ICP-MS data....375
Chapter 5 – General conclusions and future studies....377

List of Abbreviations

ADP: Adenosine Diphosphate

AFM: Atomic Force Microscopy

AIE: Aggregation Induced Emission

AMP: Adenosine Monophosphate

APTES: (3-Aminopropyl)triethoxysilane

ATP: Adenosine Triphosphate

BODIPY: 4,4-Difluoro-4-bora-3a,4a-diaza-s-indacene#

CCDC: Cambridge Crystallographic Data Centre

CD: Circular Dichroism

CPL: Circularly Polarised Luminescence

COSY: Correlated Spectroscopy

CT: Charge Transfer

CuAAC: Copper-Catalysed Azide Alkyne Cycloaddition

DBM: Dibenzoylmethane

DLS: Dynamic Light Scattering

DMAP: 4-Dimethylaminopyridine

DMF: N,N-Dimethylformamide

DMSO: Dimethyl Sulfoxide

DO2A: 1,4,7,10-Tetraazacyclododecane-1,7-diacetic acid

DO3A: 1,4,7,10-Tetraazacyclododecane-1,4,7-triacetic acid

DOTA: 1,4,7,10-Tetraaza-cyclododecane-*N,N′,N″,N‴*-tetraacetic acid

DTPA: Diethylentriaminepentaacetic

EB: Emeraldine Base

ED: Electric Dipole

EDCI: 1-Ethyl-3-(3-dimethylaminopropyl)carbodiimide

EDX: Energy Dispersive X-Ray

EELS: Electron Energy Loss Spectroscopy

EM: Electromagnetic

ES: Emeraldine Salt

ESI-MS: Electrospray Ionisation Mass Spectrometry

ET: Energy Transfer

EtOH: Ethanol

FLIM: Fluorescence Lifetime Imaging

FRET: Förster Resonance Energy Transfer

FWHM: Full Width Half Maximum

HAADF: High-Angle Annular Dark-Field Imaging

HMBC: Heteronuclear Multiple Bond Correlation

HOBT : Hydroxybenzotriazole

HOPO: 1-Hydroxy-pyridin-2-one

HSQC: Heteronuclear Single Quantum Coherence

ICP-MS: Inductively Coupled Plasma Mass Spectrometry

ILCT: Intra-Ligand Charge Transfer

IR: Infrared

ISC: Intersystem Crossing

LB: Leucoemeraldine Base

L-LSPR: Longitudinal Localised Surface Plasmon Resonance

LMCT: Ligand to Metal Charge Transfer

Ln/Ln(III): Lanthanide(III)

LOD: Limit of Detection

LSP: Localised Surface Plasmon

LSPR: Localised Surface Plasmon Resonance

MALDI-TOF: Matrix Assisted Laser Desorption Ionization – Time of Flight

MD: Magnetic Dipole

MeOH: Methanol

MLCT: Metal to Ligand Charge Transfer

MOF: Metal-Organic Framework

MRI: Magnetic Resonance Imaging

Nd-YAG: Neodymium-doped Yttrium Aluminium Garnet

NGAL: Neutrophil Gelatinase-Associated Lipocalin

NIR: Near Infrared

NMR: Nuclear Magnetic Resonance

NOTA: 1,4,7-Triazacyclononane-N,N’,N’’-triacetic acid

NP: Nanoparticle

NPoM: Nanoparticle-on-Mirror

NR: Nanorod

NTRs: Nitroreductases

OD: Optical Density

OLED: Organic Light-Emitting Diode

PANI: Polyaniline

PB: Pernigraniline Base

PBS: Phosphate-buffered saline

PDMS: Polydimethylsiloxane

PET: Photoinduced Electron Transfer

PMMA: Polymethyl Methacrylate

POEGMA: Poly[oligo(ethylene glycol) methyl ether methacrylate]

RGB: Red Green Blue

ROI: Region of Interest

SEM: Scanning Electron Microscopy

SERS: Surface Enhanced Raman Scattering

SPR: Surface Plasmon Resonance

STEM: Scanning Transmission Electron Microscopy

TATB: 4,4',4''-s-triazine-2,4,6-triyltribenzoate

TBAB: Tetrabutylammonium Bromide

TBAF: Tetrabutylammonium Fluoride

TEM: Transmission Electron Microscopy

THF: Tetrahydrofuran

T-LSPR: Transversal Localised Surface Plasmon Resonance

TMS: Trimethylsilane

TRIS: Trisaminomethane

UCL: Upconversion Luminescence

UCNC: Upconversion Nanocrystal

UCNP: Upconversion Nanoparticle

UV: Ultra Violet

Vis: Visible

WHO: World Health Organization

XPS: X-Ray Photoelectron Spectroscopy

Chapter 1 – General introduction

1.1 Principles of lanthanide(III) luminescence and coordination chemistry

1.1.1 Introduction to the lanthanides

Located in the f block of the periodic table, the lanthanide series includes the metal elements from La (Z=57) to Lu (Z=71, Figure 1.1). Often described as "rare earths", these elements are anything but rare, with even the scarcest lanthanides (i.e. Tm and Lu, 0.5 ppm and 0.8 ppm in the Earth's crust, respectively) being more abundant than Ag and Pt.[1] Their separation, however, is extremely challenging, as lanthanides share very similar physical and chemical properties.[2] Despite this, lanthanides have found widespread applications in our everyday lives, mostly due to their exceptional optical and magnetic properties. Some of the most essential uses of lanthanides are in telecommunications and lasers (e.g. Er or Nd in neodymium-doped yttrium aluminium garnet, i.e. Nd:YAG lasers), as magnetic resonance imaging (MRI) contrast agents (Gd, e.g. Magnevist and Artirem), security tags (e.g. Eu in Euro banknotes), permanent magnets (e.g. Nd, Dy) and phosphors (e.g. Eu, Tb).[3-9]

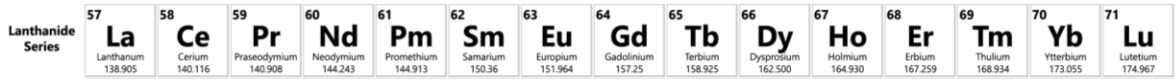


Figure 1.1 – The lanthanide series in the periodic table of the elements. The image was taken from [10].

Lanthanides are mostly found in the (III) oxidation state and, along the series, the 4*f* orbitals are gradually filled to give the [Xe]4f^n (n=0-14) electronic configuration for the trivalent

cations. 4*f* orbitals considerably penetrate the Xe core and are shielded by 5*s* and 5*d* orbitals, so that they do not actively participate in bonding or overlap with the orbitals of other atoms.[1, 11] As a consequence, the spectroscopic and magnetic properties of lanthanides are essentially unaffected by their environment.

Lanthanides(III) can form stable salts and complexes with a range of elements and molecules. Due to their hard Lewis acidity, these metals prefer hard donors such as oxygen, nitrogen and fluoride, while their large ionic radii (from 0.86 Å for Lu(III), to 1.03 Å for La(III)) can accommodate high coordination numbers (≈8-9, in solution). Unlike d-block metals, the coordination number and geometry of lanthanides(III) are determined by the ligands, and not by the metal itself. This is due to the bonding with lanthanides(III) being primarily ionic, so that steric factors from the ligand profoundly affect their coordination chemistry.[1, 11]

1.1.2 Lanthanide(III) luminescence

The luminescence of lanthanides(III) arises from *f-f* transitions and spans the ultra violet (UV) (Gd(III)), visible (Dy(III), Tb(III), Eu(III) and Sm(III), among others) and near infrared (NIR, including Nd(III), Er(III) and Yb(III)) regions of the electromagnetic spectrum.[12]

Despite the different emission ranges, all lanthanides(III) display some very characteristic features and their electronic levels can be described by the Russel-Saunders terms $^{(2S+1)}L_J$, where (2S+1) represents the spin multiplicity, L the quantum number for the total orbital angular momentum and J the spin orbit coupling. Splitting of the electronic levels (Figure 1.2) is caused by two main contributions: the inter-electron repulsion of 4*f* electrons to give the terms (e.g. ^5D and ^7F for Eu(III), in the order of 10^4 cm^{-1}) and spin orbit coupling to give J levels (e.g. J=0-6 for Eu(III), in the order of 10^3 cm^{-1}). Further splitting is afforded by crystal field

perturbations in the presence of a ligand and lead to Stark levels (m_J, splitting in the order of 10^2 cm^{-1}), which can be observed as a fine spectral structure.[12, 13]

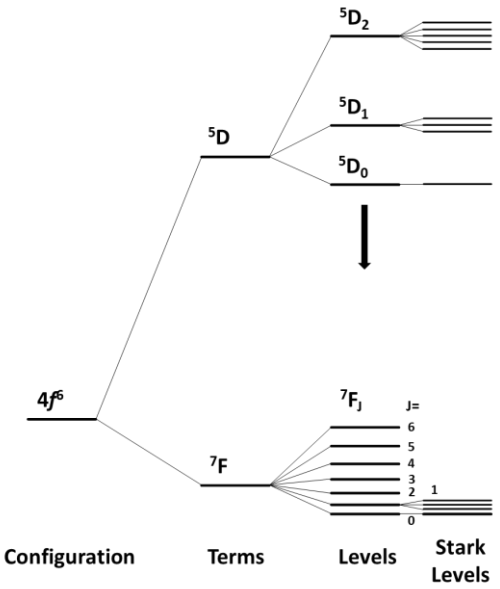


Figure 1.2 – Partial energy diagram of Eu(III) displaying the splitting of electronic levels into terms, levels and Stark levels by inter-electron repulsions, spin orbit coupling and crystal field, respectively.

The shielding of the 4*f* orbitals results in well defined energy levels, unperturbed by the ligand field, with fingerprint emission wavelengths and narrow peaks (full width half maximum, i.e. FWHM≈10 nm). This is in sharp contrast to organic dyes where, upon excitation, the configuration of the excited state is altered and broad emission bands are recorded.[14, 15]

f-f transitions are formally forbidden by the Laporte selection rule, which states that for electric dipole transitions to be allowed, a change in parity has to be present. This rule strictly applies to truly centrosymmetric systems. In most complexes, however, the rule is relaxed due to a degree of parity mixing permitted by the ligand field and vibronic coupling, making *f-f* transitions partially allowed, albeit very weak. As a result, lanthanides(III) display long luminescence lifetimes (µs-ms range), but also very low molar absorption coefficients (**ε**=1-10 M^{-1} cm^{-1}), so that in most practical applications, the power required for direct excitation would

be prohibitive.[12] To circumvent this limitation, lanthanide(III) luminescence can be sensitised *via* the antenna effect. The antenna effect was first reported by Weissman in 1942 and relies on the energy transfer from a light harvesting unit (the antenna) to the excited states of the lanthanide(III) to enhance the brightness of the complex.[16, 17] In a simplified system (Figure 1.3) and considering an organic chromophore as sensitiser, absorption of light by the antenna leads to excitation from the ground (S_0) to the excited singlet state (S_1). This is followed by intersystem crossing (ISC) to the triplet state (T_1), promoted by the presence of the lanthanide(III) (i.e. heavy atom effect), and then energy transfer (ET) to the accepting states of the lanthanide(III).[18] Due to the considerable wavelength separation between ligand absorption and lanthanide(III) emission, sensitised lanthanide(III) complexes display large ligand-induced Stokes' shifts.[4]

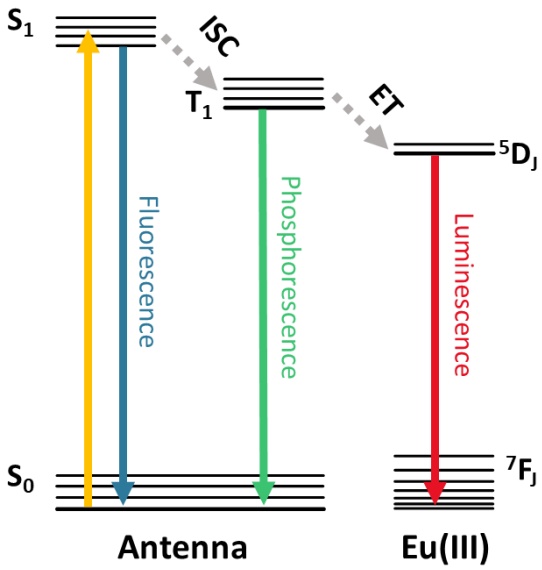


Figure 1.3 – Sketch of the antenna effect for the sensitisation of Eu(III). ISC = Intersystem crossing, ET = Energy transfer.

Selection of an antenna with a suitable T_1 state for the chosen lanthanide(III) is essential for the preparation of efficiently sensitised complexes. A delicate balance is in place: a triplet state

energy that is too close to the one of the excited states of the lanthanide(III) leads to back energy transfer and results in limited quantum yields, while too big of an energy gap results in ineffective energy transfer and prevalence of the antenna fluorescence. It is estimated that an energy gap of 2,500-3,000 cm^{-1} is optimal for the efficient energy transfer to the lanthanide(III).[18] The overall observed quantum yield of a lanthanide(III) complex (**Φ** in Equation 1.1) upon indirect excitation (i.e. with an antenna) can thus be described as:

$$\Phi = \eta_{\text{Sens.}} \Phi_{\text{Ln}} \quad Equation\ 1.1$$

Where $\boldsymbol{\eta_{Sens.}}$ is the sensitisation efficiency of the antenna and $\boldsymbol{\Phi_{Ln}}$ the intrinsic quantum yield of the lanthanide(III) upon direct excitation.[14] $\boldsymbol{\eta_{Sens.}}$ mostly concerns the photophysical properties of the antenna to optimise the ISC and ET processes. The intrinsic quantum yield of the lanthanide(III) ($\boldsymbol{\Phi_{Ln}}$), however, solely concerns the non-radiative processes that can deactivate the metal excited states. The primary quenching mechanism is by means of vibrational energy transfer to high energy oscillators, such as O-H, N-H and, in part, C-H.[19] This mechanism is particularly detrimental for NIR emitting lanthanides(III), due to the smaller energy gap between their emitting and ground states which match , and careful ligand design is essential to minimise the presence of such oscillators in the first and second coordination sphere.[14, 20] Furthermore, particularly relevant for Eu(III), photo-induced electron transfer mechanisms caused by ligand to metal charge transfer (LMCT) states can also lead to quenching and have to be considered. From these considerations, $\boldsymbol{\Phi_{Ln}}$ can be described as the ratio between the observed luminescence lifetime ($\boldsymbol{\tau_{Obs.}}$), thus including the deactivation processes, and the radiative lifetime ($\boldsymbol{\tau_{Rad.}}$), in absence of any quenching mechanism:[4]

$$\Phi_{\text{Ln}} = \frac{\tau_{\text{Obs.}}}{\tau_{\text{Rad.}}} \quad Equation\ 1.2$$

1.1.3 Luminescent lanthanide(III) coordination compounds

1.1.3.1 An overview of common ligand designs and the luminescence of their lanthanide(III) complexes

Due to the primarily ionic character of lanthanide(III)-ligand interactions, the formation and stability of lanthanide(III) complexes merely depend on the properties of the ligand, including the affinity and number of available donor atoms. When considering luminescence based applications, minimisation of vibronic quenching by filling of the coordination sphere allows for the optimisation of the intrinsic quantum yield of the metal.[14] The choice of a suitable antenna with an appropriate triplet state energy for efficient energy transfer to the selected ion, as well as high **ε** (>10,000 M^{-1} cm^{-1}), leads to improved $\eta_{Sens.}$ and brightness (**B**) of the complex, respectively, as described in Equations 1.1 and 1.3.[15]

$$B = \varepsilon \Phi \quad Equation\ 1.3$$

Depending on the design and structure of the ligand, light harvesting units can be incorporated as either appended groups or as a chelating antennae (Figure 1.4, **b** and **c**, respectively).

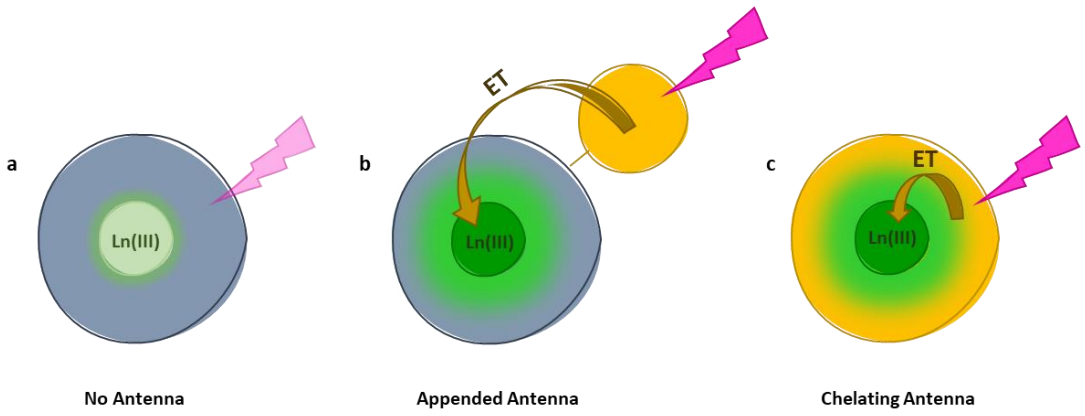


Figure 1.4 – Sketches of systems where the ligand scaffold does not include an antenna (**a**), resulting in poor light absorption and weak emission, or includes either an appended (**b**) or chelating (**c**) antenna. The ligand is represented by the grey (**a**, **b**) circle around the lanthanide centre (Ln(III), green circle). The appended antenna (**b**) is depicted as a linked yellow circle and the chelating antenna (**c**) as the yellow circle around the lanthanide(III).

For pendant antennae in particular, in addition to the parameters listed above, the distance (*r*) between the antenna and the metal ion governs the resulting ET efficiencies. Indeed, energy transfer can occur through either Förster or Dexter mechanisms, with the first relying on dipole-dipole coupling and having a distance dependence of $1/r^6$ (i.e. 5 Å<*r*<20 Å), and the second being a double electron transfer, stemming from orbital overlap with an efficiency of $1/e^r$ (i.e. *r*<10 Å).[15] Decreasing *r* by introduction of shorter linker lengths or allowing for antenna coordination to the metal has been shown to improve the ET efficiencies of the complex by either optimised Förster energy transfer or, more likely, by undergoing of a Dexter mechanism.[15, 18] The pendant antenna approach is particularly relevant for polyaminocarboxylate ligands, due to the lack of light harvesting units in their ligand scaffold. This class of ligands includes the macrocyclic 1,4,7,10-tetraaza-cyclododecane-*N,N′,N″,N‴*-tetraacetic acid (**DOTA**), 1,4,7-triazacyclononane-N,N′,N″-triacetic acid (**NOTA**) and open chain diethylentriaminepentaacetic acid (**DTPA**, Figure 1.5).[21] Organic chromophores based on polyaromatic or heterocyclic scaffolds (e.g. quinolines, acridones, coumarins and azaxanthones, Figure 1.5) have been traditionally conjugated to these chelates to produce sensitised visible (e.g. Tb(III), Sm(III), Eu(III)) and NIR (e.g. Yb(III), Nd(III), Er(III)) luminescence.[15, 22] Importantly, their complexes display high thermodynamic stabilities (LogK>10 M^{-1}), with the high preorganisation and rigidity of **DOTA** also affording impressive kinetical inertness (i.e. decomplexation $k_{obs}<10^{-5}$ s^{-1} at pH 1). This is essential for applications where the disassociation and release of free ions must be avoided (e.g. as MRI contrast agents), but it can also allow for the formation of multimetallic architectures where, due to their stability, the single complexes are treated as molecular building blocks.[7, 23, 24]

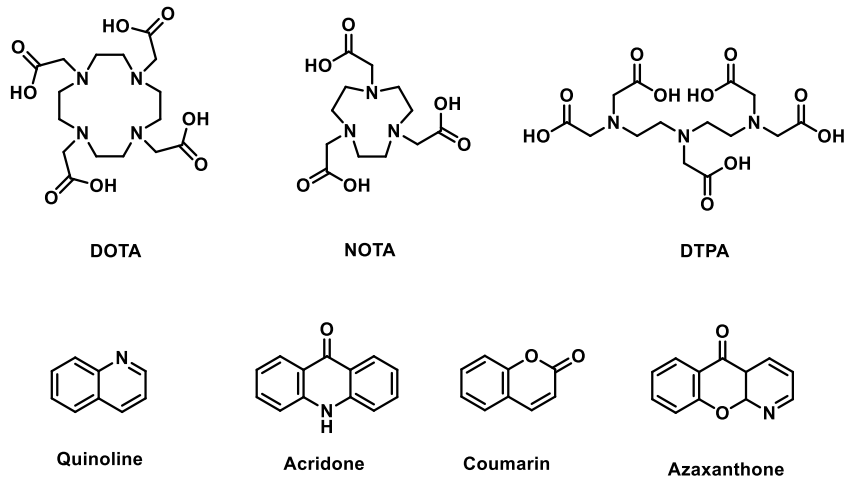


Figure 1.5 – Chemical structures of ligands **DOTA**, **NOTA** and **DTPA**, as well as examples of popular pendant antennae.

Parker and co-workers have conducted extensive work on the preparation of bright lanthanide(III) complexes for bioimaging purposes.[25] The group has reported a series of Eu(III) probes based on the 1,4,7-triazacyclononane scaffold appended with substituted tris-pyridine carboxylate or phosphinate antennae with excitation in the 330-360 nm range (Figure 1.6). The complexes have exhibited impressive quantum yields and brightness in MeOH, up to 55% and 25,000, respectively. These have been attributed to the nine-coordinated state of the metal, the high **ε** of the alkoxyphenylethynyl charge-transfer sensitising units and the reduction of deactivation pathways afforded by the high rigidity of the complexes, particularly in the presence of phosphinate units.[26, 27]

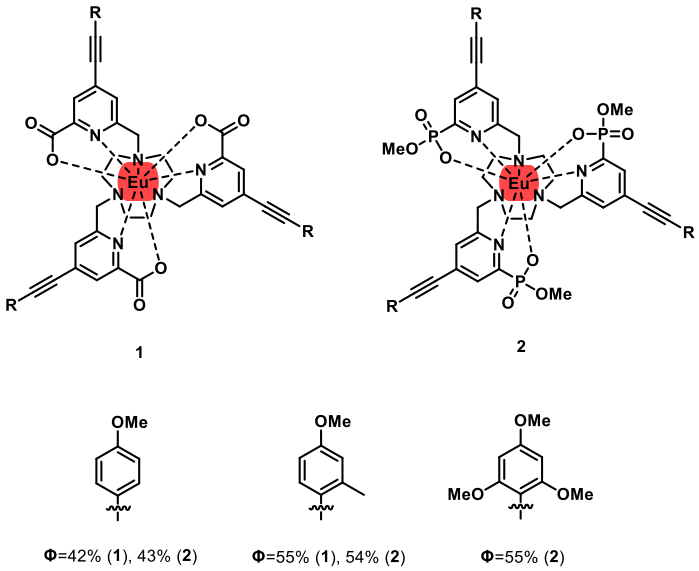


Figure 1.6 – Chemical structures of some of the Eu(III) complexes reported by Parker and co-workers. Only the substituents affording the more emissive complexes are reported. The overall quantum yields (**Φ**) are reported in MeOH.[26, 27]

In the context of bioimaging, the preparation of lanthanide(III) probes with visible light excitation is desirable. This is due to the reduced phototoxicity of longer excitation wavelengths, as well as the wider availability of e.g. 405 nm lasers in commercial fluorescence microscopes.[22] In a recent example by Sørensen and co-workers, the introduction of a methoxy group at the *para* position to the bridging sulfur of the 1-azathioxanthone pendant antenna (**4**) has provided a red shift in the absorption maximum, from 382 nm (**3**) to 403 nm. Indeed, an improved brightness for complex **4** was recorded upon excitation at 405 nm in phosphate-buffered saline (PBS) (42 versus 26 for **3**) and cell imaging could be conducted with both probes upon excitation at 405 nm.[28]

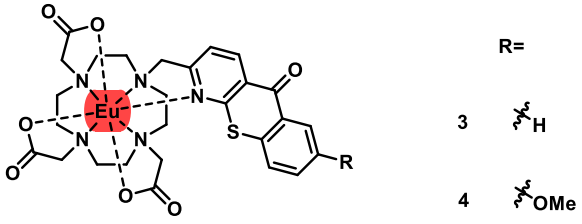


Figure 1.7 – Chemical structures of the Eu(III) complexes reported by Sørensen and co-workers.[28]

In the designs described until now, the primary ligand scaffold, and not the pendant antenna, is responsible for the complexation of the metal. With chelating antennae, however, the light harvesting unit covers the dual role of sensitising lanthanide(III) luminescence and filling the coordination sphere of the ion to produce chelated complexes.

In this class of ligands, we find the 1-hydroxy-pyridin-2-one (HOPO) based chelates developed by the Raymond group, with the octadentate derivative **5** depicted in Figure 1.8.[29] Ligand **5** is composed of four HOPO units anchored *via* amide bonds on a spermine backbone, producing monoanionic and fully coordinated species upon complexation of the hard oxygen donors (pink, Figure 1.8) with the lanthanide(III). Interestingly, upon *in situ* complexation in trisaminomethane (TRIS) buffer, the authors report the identification of a kinetic isomer (**Φ**=14.0% for Eu(III), 0.39% for Sm(III)) and its conversion to a more emissive thermodynamic isomer (**Φ**=15.6% for Eu(III), 0.41% for Sm(III)) after 10 minutes. Evaluation of the luminescence lifetime and magnetic circular dichroism data indicated that the rearrangement of the complex afforded improved shielding from quenching oscillators, justifying the observed difference in luminescence quantum yields.[29]

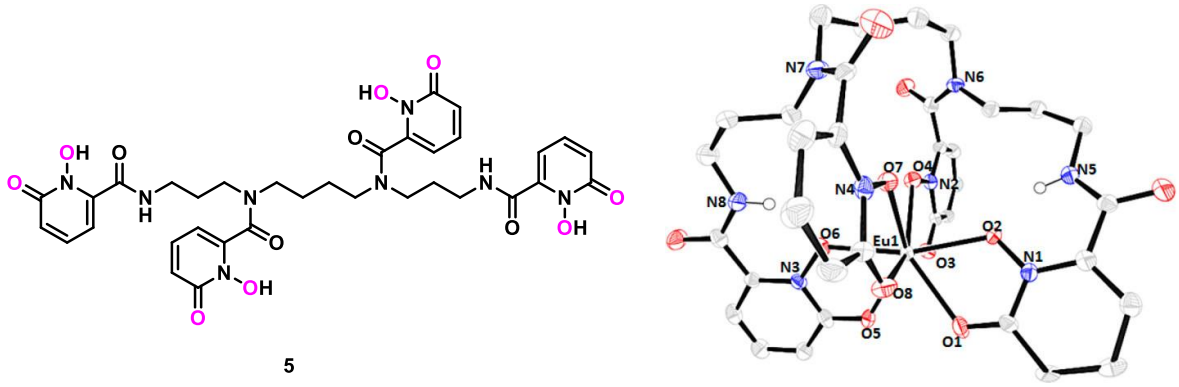
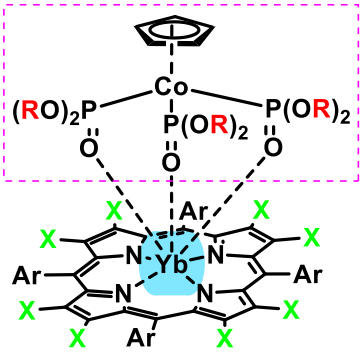


Figure 1.8 – Chemical structure of ligand **5** and the crystal structure of its respective monoanionic Eu(III) complex. Highlighted in pink are the ligand atoms that coordinate to the Eu(III) ion. The image of the crystal structure was taken from [29].

The substitution with C-F or C-D bonds in the ligand scaffold is a common approach to prevent the vibronic quenching from C-H oscillators. This is of particular relevance in the NIR, where the proximity of such bonds is especially detrimental for e.g. Nd(III) and Yb(III) ions.[30] NIR emission is extremely advantageous in both telecommunications and bioimaging applications, due to the presence of transparency windows for silica in optical fibres (1320-1550 nm) and biological tissues (700-1100 nm).[31] Furthermore, longer signal transmission and a lower amount of endogenous emission from biological matrices occur at such long wavelengths, allowing for reduced background fluorescence and better signal to noise ratios.[32]

Zhang and co-workers have investigated the effect of fluorination and deuteration on Yb(III) porphyrinate complexes capped with a tripodal Kläui ligand (pink dashed box in complexes **6**-**8**, Figure 1.9).[33, 34] Upon excitation at the Soret band of the phorphyrinate antenna (i.e. 425 nm), the authors report that substitution with C-D bonds at the Kläui ligand (red "R", Figure 1.9) considerably increased the luminescence quantum yield of the complex (5-fold compared to the non-deuterated **7** in CH_2Cl_2). Additionally, substitution with either C-F or C-D oscillators at the β position of the phorphyrinate antenna (green "X", Figure 1.9) produced higher quantum yields (**Φ**=25%) for the former (**6**), while a considerably smaller value of 15% was recorded for the C-D substituted complex (**8**). This was attributed to the lower vibration energy of C-F oscillators (≈1,200 cm^{-1} versus ≈2,300 cm^{-1} for C-D) and confirmed by the exceptional intrinsic quantum yield of Yb(III) (**Φ_{Yb}**=75%) as well as the long luminescence lifetimes in either CH_2Cl_2 or CD_2Cl_2 (285 μs and 714 μs, respectively, with overall **Φ**=63% in the deuterated solvent).[33]



6 R=CD_3, X=F, Ar=C_6F_5
7 R=CH_3, X=F, Ar=C_6F_5
8 R=CD_3, X=D, Ar=C_6F_5

Figure 1.9 – Chemical structure of the sandwich complexes **6**-**8** proposed by Zhang and co-workers. The pink dashed box indicates the Kläui ligand.[33]

Pikramenou and co-workers have investigated the effect of fluorination of imidodiphosphinate ligands on both visible and NIR lanthanide(III) luminescence. This class of ligands provides bidentate coordination through the phosphinate oxygens and forms six-coordinated complexes with 12 sensitising units around the metal.[35, 36] As expected, full fluorination of the ligand (**10**, Figure 1.10) afforded an enormous increase in the luminescence lifetimes of the respective NIR emitting complexes (Ln=Yb(III), Nd(III), Er(III)). Considering the values in the solid state, the Yb(III) complex of **10** displayed a monoexponential decay of 582 μs, while its non-fluorinated counterpart (**9**) exhibited a decay of only 17.8 μs, consistent with the presence of detrimental C-H oscillators in proximity of the metal. The trend was consistent along the NIR series, with the Er(III) and Nd(III) complexes displaying 137- and 38-fold increases in luminescence lifetimes upon ligand fluorination. Interestingly, despite the confirmed presence of sensitisation pathways, very low quantum yields (**Φ**=0.1%) were observed for visible emitting complexes of **10** in CH_3CN (Ln=Eu(III), Tb(III), Dy(III)). This was a significant decrease from the ones of the respective non-fluorinated complexes of ligand **11** (1.3 % and 19 % for Ln=Eu(III) and Tb(III), respectively) and was ascribed to the presence of a low energy π–σ*

state, caused by the extensive fluorination of the ligand and quenching visible luminescence.[35, 36]

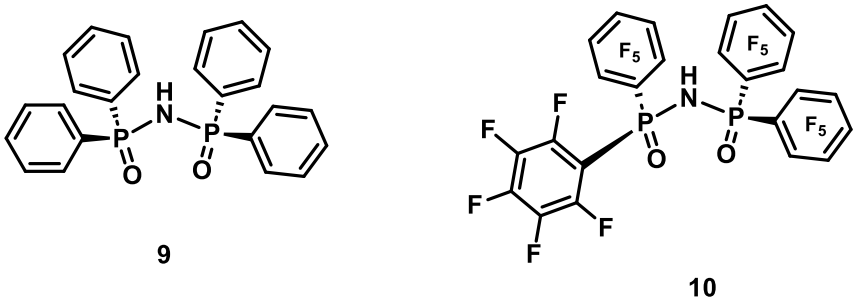


Figure 1.10 – Chemical structures of the imidodiphosphinate ligands presented by Pikramenou and co-workers.[35, 36]

1.1.3.2 Lanthanide(III) β-diketonates

In addition to the designs described in section 1.3.1, an extremely important class of ligands is the one of β-diketones. Despite their lower kinetic stability in solution compared to e.g. DOTA complexes, lanthanide(III) β-diketonates have received widespread attention. Due to their facile synthesis and functionalisation, along with high sensitisation efficiencies and luminescence outputs, these complexes are extremely valuable in the fields of luminescent materials and optoelectronic devices, as well as magnetic materials and NMR shift reagents.[37-39]

The general scaffold of β-diketones is based on the one of their simplest precursor, acetylacetone (**11**, Figure 1.11), where two carbonyl units are separated by an α-carbon and can undergo keto-enol tautomerism.[40] The high acidity of the α-proton (pKa=9 for **11**), compared to the one of the respective simple ketone (pKa=20), allows for ready deprotonation in the presence of relatively weak bases such as triethylamine and NaOH.[41] Deprotonation is further favoured by the presence of electron withdrawing groups, such as -CF_3 groups.[40] The

resulting negative charge is delocalised and six-membered chelate rings are easily formed by coordination with lanthanide(III) ions to produce triple or quadruple stranded complexes, with the metal in a six or eight coordination state, respectively (Figure 1.11 for quadruple stranded **12**).

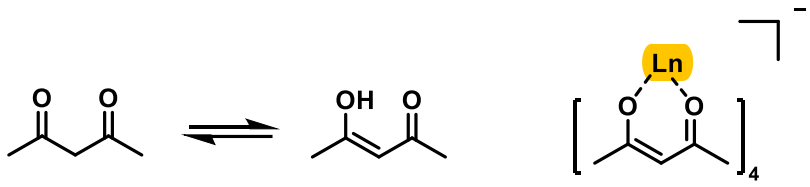


Figure 1.11 – Chemical structure of the acetylacetone ligand (**11**) displaying keto-enol tautomerism, as well as the formation of a six-membered chelate ring in a quadruple stranded Ln(III) complex (**12**).

The nature of the substituents on the β-diketone can strongly influence the overall photophysical properties of the complex. Increasing the degree of π-conjugation lowers the energy of the triplet state, exemplified by the trend observed from the aliphatic acetylacetone **11** (T_1=25,310 cm^{-1}) to the aromatic substituted dibenzoylmethane ligand (**13**, Figure 1.12, T_1=19,169 cm^{-1}).[39, 40] This affects the sensitisation of the selected lanthanide(III), where aromatic β-diketones can effectively transfer energy to Eu(III) (with the $^5D_0$ state lying at 17,277 cm^{-1}) but not to Tb(III), due to the higher energy of its excited $^5D_4$ state (i.e. 20,545 cm^{-1}).[12, 39, 40]

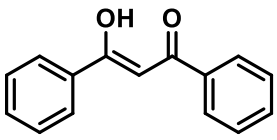


Figure 1.12 – Chemical structure of the dibenzoylmethane ligand **13**.

Unless synthesised in completely anhydrous conditions, the coordination sphere of neutral six-coordinated complexes is filled by H_2O molecules. To exclude quenching by O-H oscillators, a popular strategy is the exchange with ancillary ligands to optimise the intrinsic quantum yield of the complexes. The most common ancillary ligands are neutral Lewis bases bearing either nitrogen or oxygen donors, including 1,10-phenanthroline and 2,2'-bipyridine, but also triphenylphosphine oxide and pyridine N-oxide scaffolds (Figure 1.13).[42, 43]

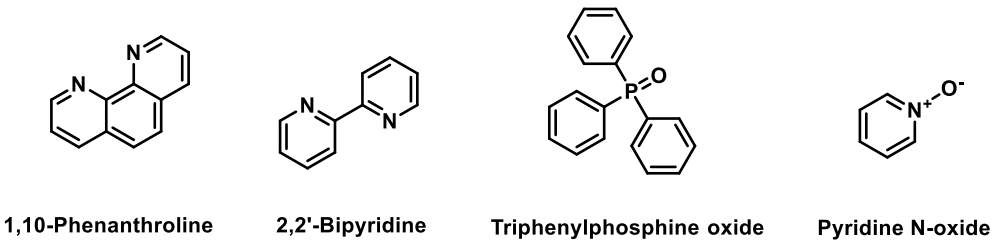
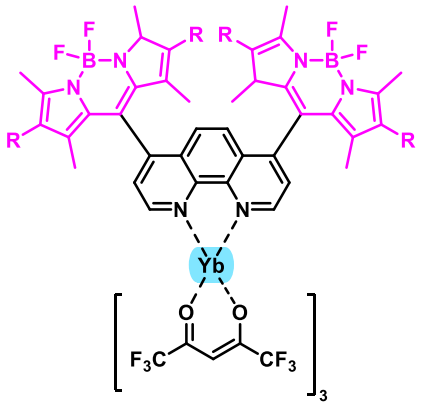


Figure 1.13 – Chemical structures of the ancillary 1,10-phenanthroline, 2,2'-bipyridine, triphenylphosphine oxide and pyridine N-oxide ligands.

In addition to filling the coordination sphere of the metal, ancillary ligands can also serve as light harvesting units, providing an additional sensitisation pathway to the one of the β-diketonate ligands. Kukoyi *et al.* have modified the ancillary 1,10-phenanthroline ligand to include two 4,4-difluoro-4-bora-3a,4a-diaza-s-indacene (BODIPY) derivatives for the long wavelength sensitisation of the β-diketonate Yb(III) complex (pink units in **14** and **15**, Figure 1.14).[44] Compared to visible emitting lanthanides(III), the lower energy of the accepting excited states of NIR emitting Yb(III) and Nd(III), among others, allow for visible light excitation.[14, 32] This is particularly relevant for bioimaging applications, where UV light is damaging to the biological sample.[22] Here, formation of **15** by addition of the ancillary ligand to the triple stranded β-diketonate complex was monitored by titration experiments. An increase in Yb(III) emission was observed upon excitation at 545 nm (i.e. at the ancillary ligand absorption wavelength), reaching a maximum at a molar ratio of 1 and thus confirming the

expected 1:1 binding. Due to the energy transfer to Yb(III), the fluorescence arising from the ancillary ligand was reduced by 95% and 15% (**14** and **15**, respectively). Interestingly, isoabsorptive solutions of **14** and **15** produced identical emission intensities, indicating that ligand **15** did not lead to higher sensitisation efficiencies, as originally postulated on the basis of the heavy atom effect of iodine.[44]



14 R=H
15 R=I

Figure 1.14 – Chemical structure of the complexes **14** and **15** proposed by Kukoyi *et al.*.[44]

Khan *et al.* have reported the inclusion of the bis(2-(diphenylphosphino)phenyl)ether oxide) ancillary ligand (pink in Figure 1.15) to triple stranded fluorinated Eu(III) complexes **16** and **17**.[45] The presence of a terminal naphthyl group in the β-diketone unit of **17** resulted in a 22 nm red shift of the absorption band-edge of the ligand (404 nm), compared to the phenyl substituted **16** (382 nm), and ascribed to the increased conjugation. The ancillary ligand provided excellent sensitisation upon excitation in the 380-390 nm range ($\eta_{Sens.}$= 92% and 96% for **16** and **17**, respectively). The authors reported an enhancement of Eu(III) emission provided by the large bite angle of the ancillary ligand, which could force a significant distortion to the geometry of the complex and thus increase the asymmetry around the Eu(III) centre. The complexes displayed impressive quantum yields (80% and 79% in CH_2Cl_2,

respectively) and were incorporated as emitting layers of an electroluminescent device, producing one of the best performing Eu(III) based organic light-emitting diodes (OLEDs).[45]

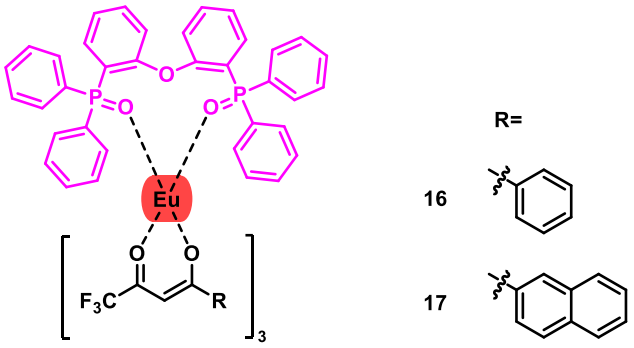


Figure 1.15 – Chemical structure of the complexes **16** and **17** proposed by Khan *et al.*.[45]

The addition of a second binding pocket to the ligand scaffold of β-diketones allows for the coordination of two lanthanide(III) ions, producing dinuclear complexes with novel photophysical properties and architectures.[46] Some representative examples are reported below.

Considering the dibenzoylmethane ligand **13**, Pikramenou and co-workers have presented a dinuclear derivative (**18**, Figure 1.16) where the β-diketone units are separated by a 1,3-phenylene spacer. The ligand was employed for the formation of either triple or quadruple stranded complexes (**19**, **20**, Figure 1.16), depending on the selected ligand to Ln(III) ratio (3:2 and 4:2, respectively).[47] Well resolved visible (Eu(III), Sm(III)) and NIR (Nd(III)) luminescence was observed upon excitation of **19** at 350 nm, with the quantum yield of the Eu(III) derivative being 5% in DMF. The authors report that the C-H oscillators in the ligand scaffold do not significantly quench the excited states of the selected lanthanides(III), a particularly important feature for the design of NIR emitting complexes, and a quantum yield of 0.6% was estimated for the Nd(III) of **19** derivative in DMSOd_6. Importantly, a 11-fold increase in emission intensity was observed for the dinuclear Sm(III) complex **19** compared to its isoabsorptive mononuclear

counterpart (**21**), indicating that the bis β-diketonate ligand could produce higher emitting complexes.[47]

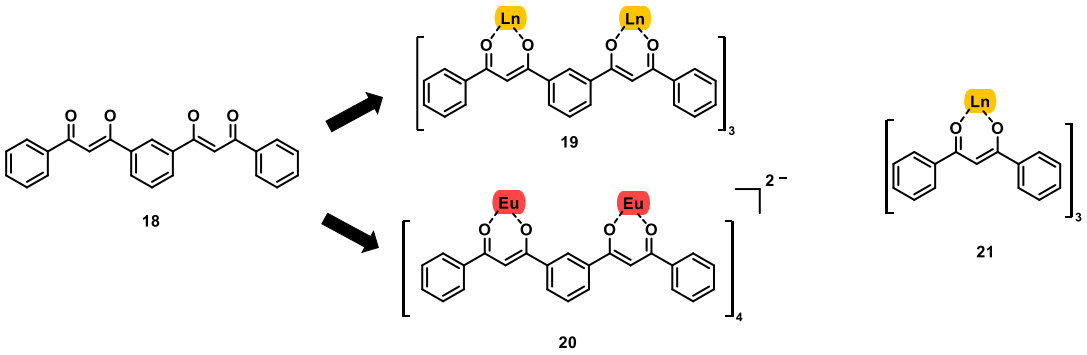


Figure 1.16 – Chemical structures of the bis β-diketone ligand **18**, the respective triple (**19**, Ln=Eu(III), Nd(III), Sm(III)) and quadruple (**20**) stranded dinuclear complexes reported by Pikramenou and co-workers and the mononuclear complex **21** (Ln=Eu(III), Sm(III), Nd(III), Yb(III)). The counterion of **20** is the piperidinium cation.[47]

Ligand **18** was also employed by the group for the formation of dinuclear luminescent racks (**23**, Figure 1.17).[48] This was achieved by the heteroligand self-assembly of both **18** and the DTPA derivative **22** with Eu(III). Here, ligand **22** wrapped around the Eu(III) ion, leaving an unfilled coordination sphere for the coordination of **18** to a total of two complexes. Importantly, the phenylene spacer in the bis β-diketonate ligand (blue in Figure 1.17) acted as rigid unit, thus driving the formation of the desired rack architecture.[48]

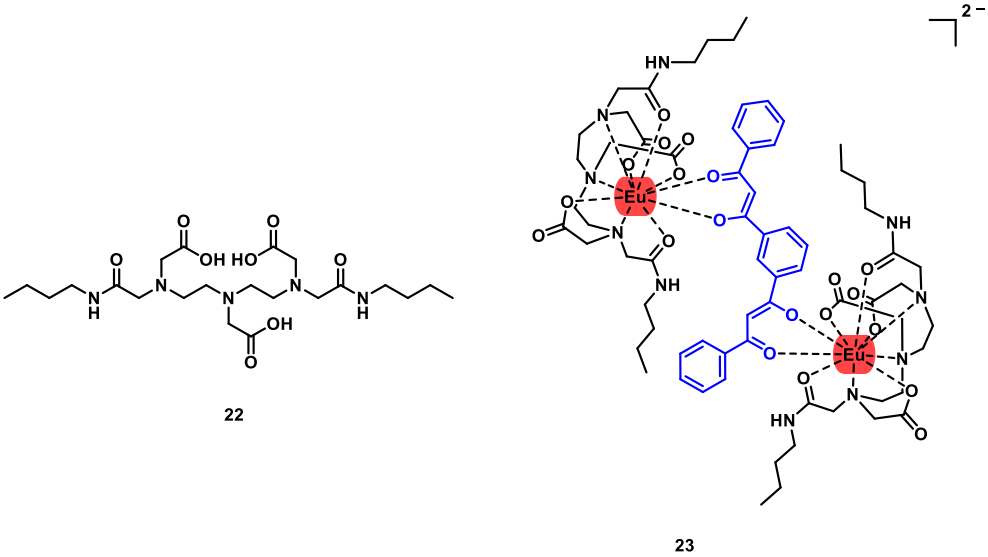
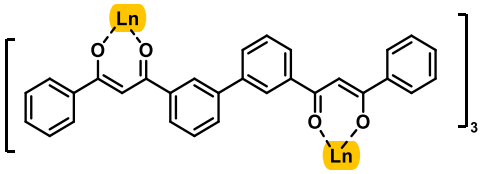


Figure 1.17 – Chemical structures of DTPA derivative **22** and the dinuclear rack assemblies **23** reported by Pikramenou and co-workers.[48]

The higher emission intensity of dinuclear bis β-diketonates compared to mononuclear complexes has also been observed in an example by Li *et al.*.[49] Here, another dinuclear dibenzoyl scaffold was presented (**24**), which included a biphenylyl group as spacer between β-diketone units, instead of the 1,3-phenylene of **19**. The authors report a 1.8- and 2.4-fold increase in emission intensity for the dinuclear Nd(III) and Yb(III) complexes, respectively, compared to the mononuclear derivatives, as well as a modest increase in quantum yield for Eu(III) complex **24** (from 1.1%, **21** to 1.8%, **24**). The effect was ascribed to the higher rigidity of the bis β-diketonate structure, which can limit thermal vibrations and reduce the associated deactivation pathways, affording a higher luminescence output.[49]

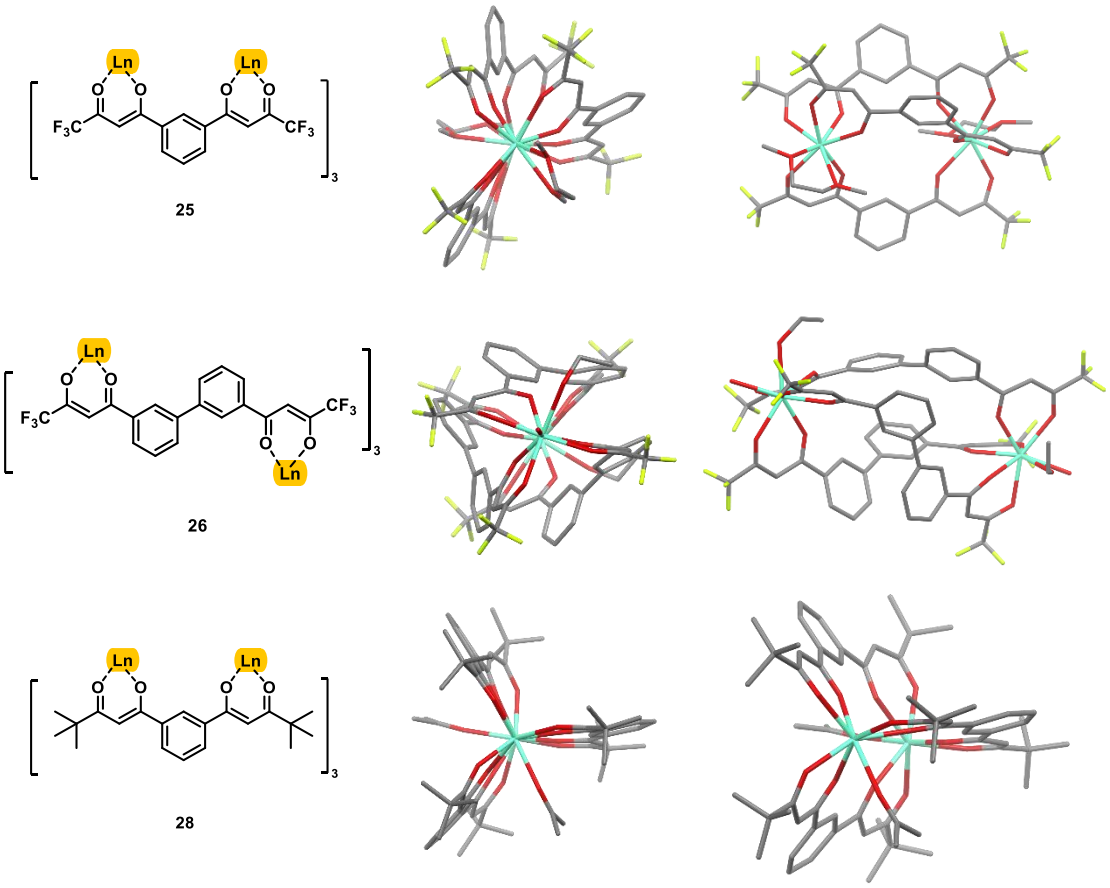


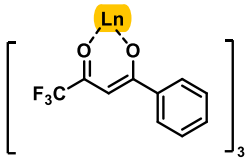
24

Figure 1.18 – Chemical structure of complex **24** reported by Li *et al.* (Ln(III)=Eu(III), Yb(III), Nd(III)).[49]

Sun and co-workers and Li and co-workers have prepared fluorinated bis β-diketonate complexes **25** and **26**, respectively (Figure 1.19). The inclusion of -CF_3 groups was aimed to improve the solubility of the complexes in organic solvents, as well as to limit the presence of C-H oscillators in the scaffold .[50-52] Eu(III) complexes **25** and **26** respectively displayed a 1.7- and 1.3-fold increase in emission compared to the mononuclear **27** in CH_3CN. For **25**, a similar trend was also observed for the NIR emitting Nd(III) and Yb(III) derivatives (2.5- and 1.6-fold, respectively). A quantum yield of 13% was reported for the Eu(III) derivative **25** in the solid state, which could be further enhanced by introduction of either 1,10-phenanthroline (**Φ**=65%) or 2,2'-bipyridine (**Φ**=55%) ancillary ligands to exclude quenching solvent

molecules.[50] Similarly, the introduction of 1,10-phenanthroline or 2,2'-bipyridine ligands to the Eu(III) complex **26** afforded a significant increase (from 26% to 39% and 47%, respectively).[52] The crystal structures of both complex **25** and **26** displayed helical conformations (Figure 1.19), with each Ln(III) atoms in the eight coordination state: six oxygens from the bis β-diketonate ligands and two oxygens from either dimethoxy ethane (**25**) or EtOH and H_2O (**26**).[50-52] Interestingly, in a later report, Clegg and co-workers reported the crystal structure of another bis β-diketonate derivative, **28**, found in the seven-coordinate state with either acetone or DMF coordinating. Independently from the lanthanide(III) selected, the complexes displayed a mesocate structure, with one of the ligands in an "untwisted", almost opposite, conformation (Figure 1.19).[53]

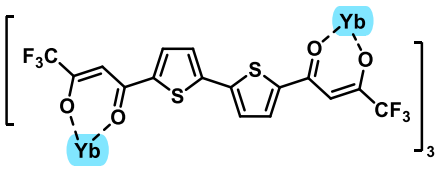




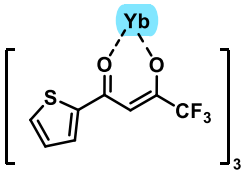
27

Figure 1.19 – Chemical structures with respective crystal structures of complexes **25**, **26** and **28** reported by Sun and co-workers (**25**), Li and co-workers (**26**) and Clegg and co-workers (**28**). Chemical structure of complex **27**. Ln(III)=Eu(III), Yb(III), Nd(III).[50-53] The crystal structures reproduced here are all of the Eu(III) derivatives and have been obtained from Cambridge Crystallographic Data Centre (CCDC), deposition numbers: 886032 (**25**), 833523 (**26**) and 1979094 (**28**). The elements colours are as follows: grey – Carbon, acid green – Fluorine, red – Oxygen and aqua – Europium.

The impact of the triple stranded helical conformation of bis β-diketonates on Yb(III) emission has been investigated by Li *et al.*.[54] In their work, two thenoyltrifluoroacetone units (**30**) were conjugated at the 5,5'- position of the thiophene ring to produce triple stranded complex **29** with the coordination sphere filled by two DMSO molecules per Yb(III) atom. In addition to higher emission intensities (10-fold), justified by the higher tension and reduced thermal quenching, the dinuclear Yb(III) complex **29** also possessed higher solvent shielding abilities. This was assessed by monitoring the luminescence response in DMSO and upon addition of H_2O. Whereas **30** suffered an 83% decrease in the presence of 10% in volume of H_2O, complex **29** only exhibited a 58% decrease in luminescence. This was described as a consequence of the better encapsulation of Yb(III) ions in the triple stranded dinuclear complex, thus shielding the metal from O-H oscillators in a more effective manner.[54]



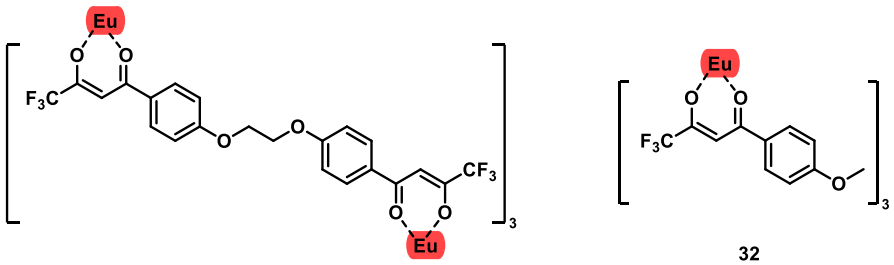
29



30

Figure 1.20 – Chemical structures of Yb(III) complexes **29** and **30** reported by Li *et al.*.[54]

Despite most studies reporting enhanced photophysical properties for dinuclear β-diketonates, Zhu *et al.* have presented an exception.[55] In their work, the authors prepared both mono- and dinuclear triple stranded Eu(III) complexes **31** and **32** and compared their quantum yields and luminescence lifetimes in the solid state. Surprisingly, lower values were observed for the dinuclear complex **31** (25% and 536 μs, respectively) than for **32** (38% and 623 μs, respectively). The authors concluded that the worse luminescence performance of **31** was due to the extensive intermolecular π-π stacking observed in the crystal structure of the complex, which was instead absent for the mononuclear derivative **32**. Such π-π interactions would lower the energy of the excited states of the ligand, promoting back energy transfer from the Eu(III) centre.[55]

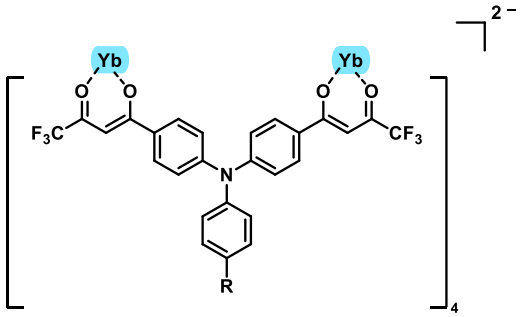


31 32

Figure 1.21 – Chemical structures of Eu(III) complexes **31** and **32** reported by Zhu *et al.*.[55]

The examples presented up to now highlight the close relationship between structure and conformation of the complex and resulting photophysical properties. In addition to possessing high quantum yields, an important parameter for the assessment of luminescent complexes is the excitation wavelength. Whereas the excitation wavelengths of most β-diketonate complexes lie in the 300-400 nm range, the coupling of two thiophene units in **29** (Figure 1.20) afforded a significant shift in absorption maximum to cover the 420-480 nm wavelength range.[54] An alternative approach is based on the design of ligands with low lying intra-ligand

charge transfer (ILCT) states. Zhang *et al.* have presented two quadruple stranded bis β-diketonate complexes, **33** and **34**, which display NIR Yb(III) luminescence upon excitation at visible wavelengths.[56] The ligand scaffold was based on two fluorinated β-diketones separated by a triphenylamine central unit. The formation of low energy intra-ligand charge transfer (ILCT) states was driven by a "push-pull" mechanism between the donor triphenylamine and electron withdrawing CF_3 groups. Importantly, introduction of the strong electron donor N,N-dimethyl in the triphenylamine unit (**34**, Figure 1.22) afforded a 100 nm red shift in absorption edge, from 450 nm to 560 nm, as well as a small increase in quantum yield from 1.1% to 1.5% in CH_3CN.[56]



33 R=H
34 R=N(CH$_3$)$_2$

Figure 1.22 – Chemical structures of Yb(III) complexes **33** and **34** reported by Zhang *et al.*. The counterion is the triethylammonium cation.[56]

Yin *et al.* have reported the preparation of triple stranded Eu(III) complex **35** for the detection of Cu(II) ions.[57] Interestingly, the presence and π-π interactions of 2,2'-bipyridine units in the bis β-diketonate ligand scaffold prevented the expected helical conformation, promoting instead a quasi-lantern structure (Figure 1.23). The resulting cavity allowed for coordination of Cu(II) to 2,2'-bipyridine units, quenching Eu(III) luminescence by modification, and thus mismatch, of the triplet state energy of the ligand *via* LMCT and metal to ligand charge transfer (MLCT) states. Importantly, no change in the luminescence lifetime of the complex was

observed, which indicated that Cu(II) coordination at the 2,2'-bipyridine sites would not affect the coordination of the ligand to Eu(III).[57]

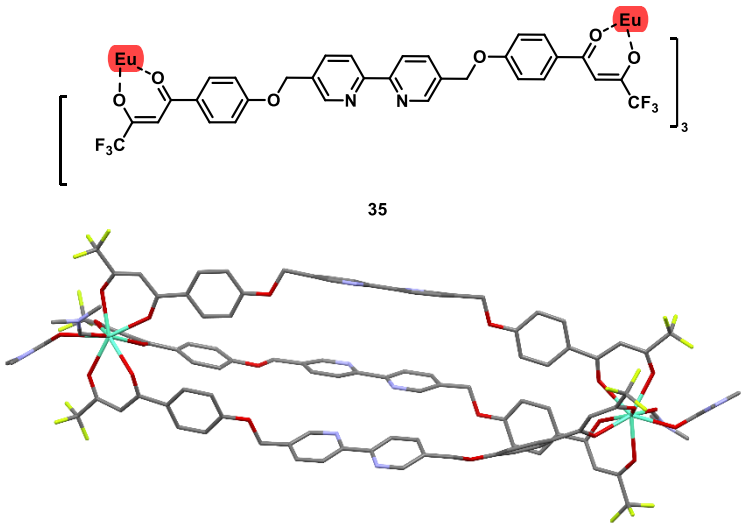


Figure 1.23 – Chemical structure and respective crystal structure of Eu(III) complex **35** reported by Yin *et al.*.[57] The crystal structure reproduced here has been obtained from Cambridge Crystallographic Data Centre (CCDC), deposition number 2251298. The elements colours are as follows: grey – Carbon, acid green – Fluorine, red – Oxygen, lilac – Nitrogen and aqua – Europium.

In the context of functional bis β-diketonate complexes, Li and co-workers have presented a Eu(III) complex **36** (1.24) for the improvement of photocyclization quantum yields of diarylethenes.[58] The authors report that complexation with Eu(III) to form the quadruple stranded complex enforces the antiparallel conformation of the ligand, which, in turn, is associated with higher photocyclization efficiencies. This is confirmed by UV-Vis spectroscopy, where a double photocyclization quantum yield ($\Phi_{o\text{-}c}$=40%) compared to the free ligand ($\Phi_{o\text{-}c}$=18%) is observed. Furthermore, the process could also be monitored with luminescence spectroscopy, where a significant decrease in Eu(III) emission was recorded upon irradiation with UV light (i.e. 365 nm), associated with the conversion from the open to closed form of the diarylethene unit (quantum yields from 7% to 0.7% in MeOH:$CHCl_3$ 1:1, respectively). It was experimentally determined that the closed ring form had a triplet state energy of 14,728 cm^{-1}, lower than the one of the open ring form and the $^5D_0$ excited state of Eu(III) (20,833 cm^{-}

[1] and 17,500 cm^{-1}, respectively), thus disrupting energy transfer processes from ligand to metal centre. Importantly, the luminescence of the complex was completely reinstated upon irradiation with visible light (i.e. 526 nm) to produce the sensitising open ring form of the ligand.[58]

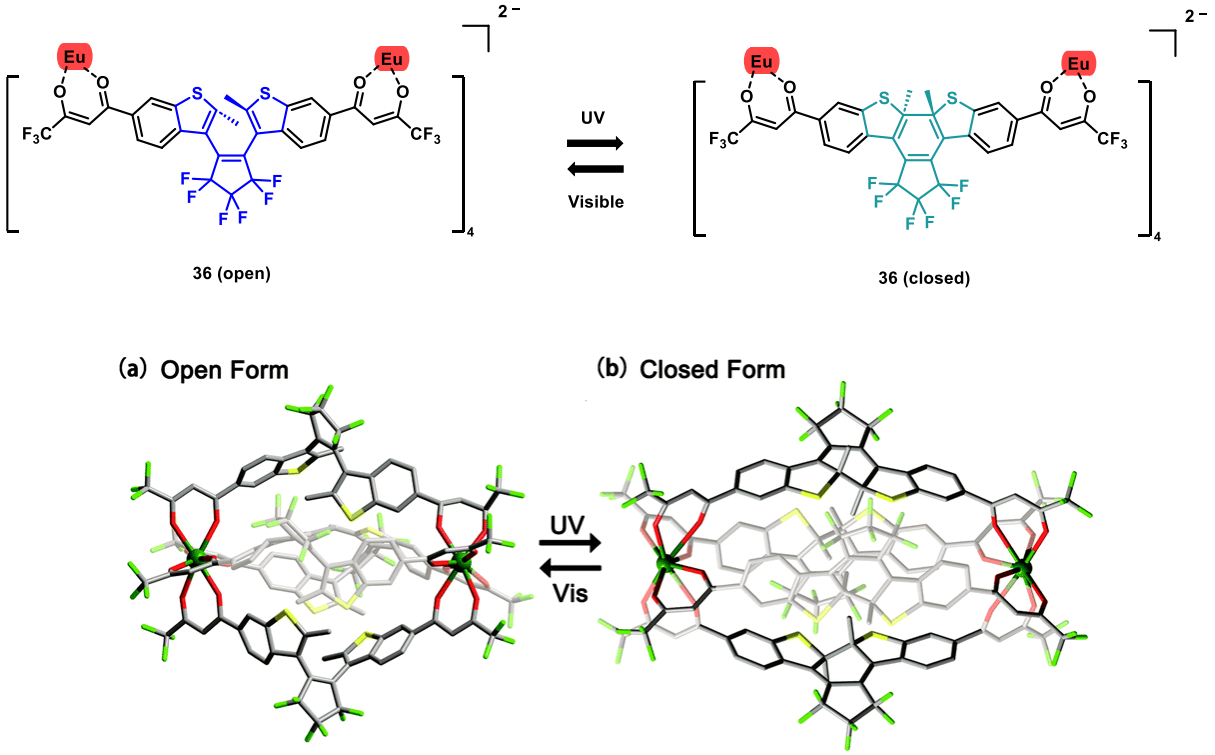
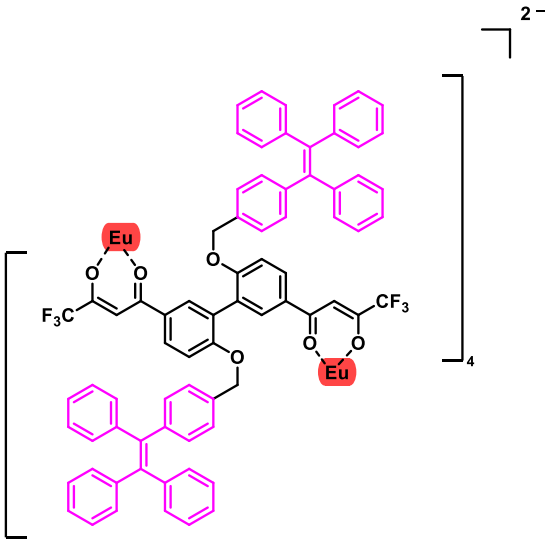


Figure 1.24 – Chemical structures of the open and closed forms of complex **36** reported by Li and co-workers.[58] Below each structure, the molecular mechanic models of the complexes. The image was taken from [58].

Lanthanides(III) have particular significance in the fabrication of luminescent displays due to their high colour purity and characteristic narrow emission lines. Li and co-workers have presented a quadruple stranded bis β-diketonate Eu(III) complex **37** for the preparation of white light emitting materials (Figure 1.25).[59] The design was based on the presence of tetraphenylethylene units, whose aggregation induced emission (AIE) at ≈480 nm could combine with red Eu(III) emission to produce white light. The AIE properties of the ligand were preserved upon helicate formation with Eu(III) and white light emission with high overall

quantum yield (49%) was observed in the solid state. The complex was also doped in a trihydroxymethylpropyl trimethylacrylate film, where the level of doping (0.1% to 10% in weight) could tune the resulting colour purity of the material (from 2.6% to 64.8%). An overall quantum yield of 16.9% was measured, while partial energy transfer to the metal centre allowed for a Eu(III) centred quantum yield of 7.8% to be recorded.[59]



37

Figure 1.25 – Chemical structure of complex **37** reported by Li and co-workers.[59]

The helicity and inherent chirality of some lanthanide(III) bis β-diketonates has received attention for the development of chiroptical materials which can display circularly polarised luminescence (CPL). The formation of enantiomerically pure complexes, however, is often challenging, as the complexes are commonly prepared as racemic mixtures. One strategy for the preparation of enantiopure complexes has been exemplified by the groups of Frölich and Pikramenou, where a (*R*,*R'*)-tartaric acid unit was incorporated as chiral element to the bis β-diketone ligand scaffold (**38**-**40**, Figure 1.26).[60] Enantiomerically pure triple or quadruple stranded lanthanide(III) complexes were thus prepared, displaying well resolved luminescence

for all ions selected (i.e. Eu(III) and Tb(III)) and, particularly, with complex **40** due to improved energy transfer efficiencies from the *p*-bromophenyl units.[60] In a similar approach, Zhou *et al.* have employed the chiral (*R*/*S*)-1,2-propanediol as spacer between the β-diketonate units in complex **41**, affording quadruple stranded *ΔΔ* or *ΛΛ* complexes with high quantum yields (68% in THF) and moderate luminescent dissymmetry factors (g_{lum}=|0.146|).[61] Due to the opposite chiralities, the complexes also possessed mirror-image CPL and circular dichroism (CD) spectra, which further confirmed the preservation of the stereochemical properties of the ligands upon complexation.[61]

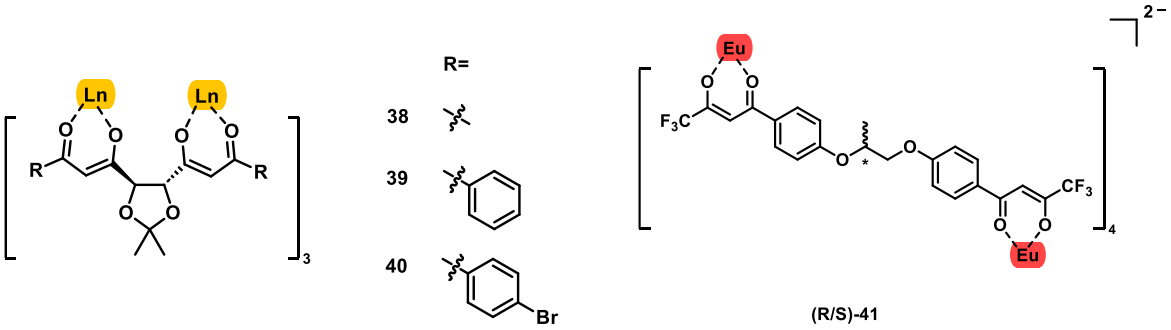
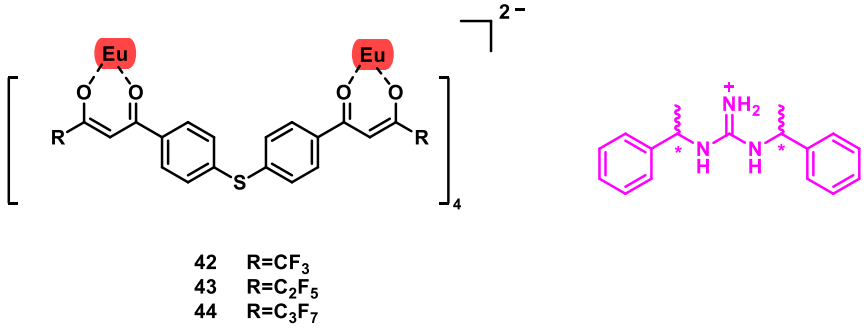


Figure 1.26 – Chemical structures of complexes **38**-**40** reported by the groups of Frölich and Pikramenou and the pair of quadruple stranded complexes **41** reported by Zhou *et al.*.[60, 61] The counterion of **41** is the trimethylammonium cation. Ln(III)=Eu(III), Ho(III), Er(III), Tb(III), Dy(III), Yb(III), Nd(III).

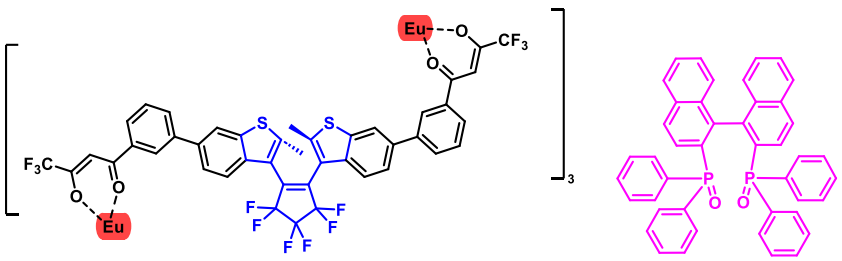
Li and co-workers have presented the deracemization of Eu(III) complexes **42**-**44** by addition of a chiral guanidine counterion.[62] It was found that the *S* and *R* enantiomers of the guanidine salt (pink, Figure 1.27) would drive the racemic equilibrium towards *ΔΔ* or *ΛΛ* configurations, respectively. This was ascribed to the formation of a hydrogen network between the N-H groups of guanidine and the oxygens and fluorines of the bis β-diketonate. High quantum yields were observed for the complexes in CH_3Cl (10% CH_3CN, 42-54%) and, importantly, good g_{lum} in the |0.137–0.266| range were recorded, indicating the successful stereoselective recognition and chirality induction with the selected ion pairs.[62]



42 R=CF_3
43 R=C_2F_5
44 R=C_3F_7

Figure 1.27 – Chemical structures of complexes **42**-**44** reported by Li and co-workers. In pink it is represented the structure of the guanidium counterion.[62]

The preparation of enantiopure complexes was also induced by the presence of chiral ancillary ligands.[63] This was reported, for example, by introduction of either *R* or *S* bis(diphenylphosphoryl)-1,10-binaphthyl (**46**) ligands to fill the coordination sphere of the triple stranded Eu(III) complex **45** (Figure 1.28).[64] As for **42**-**44**, the complexes displayed mirror-image CPL and CD spectra, confirming transfer of chirality from the ancillary ligand to the complexes. Furthermore, the introduction of a photoswitchable diarylethene unit in the bis β-diketonate scaffold afforded additional functionality to the complex. The photocyclization of the ligand could be monitored as a variation in the chiroptical properties of the complex, which was further demonstrated in a logic gate circuit with either UV (275 nm) or visible (526 nm) light irradiation as stimuli and four total outputs (i.e. CPL, luminescence and CD spectra and g_{lum} values).[64]



45 46

Figure 1.28 – Chemical structures of complex **45** and ancillary ligand **46** reported by Li and co-workers.[64]

1.2 Plasmonic materials

The incorporation of molecules and fluorophores to a solid substrate is an attractive approach to fabricate devices, imparting new physical and chemical properties to the material. Metallic surfaces are popular substrates for the covalent attachment of molecules due to the strong affinity of sulfur and, partly, amino and carboxylate groups, for soft metals such as gold, silver and platinum, among others.[65, 66] The development of luminescent materials, however, is often hindered by the low quantum yields and signal to noise ratios of the emitting components. In the context of sensing platforms, this limits the sensitivity of the systems, thus requiring highly specialised equipment.[67, 68] To overcome this limitation, new dyes and approaches to increase quantum yields have been reported over the years.[69] Nanostructured plasmonic materials, in particular, can enhance the luminescence of traditional fluorophores, such as organic dyes (e.g. Alexa Fluor, IRDye, among others), even by several orders of magnitude, thus maximising the signal to noise ratio and lowering the detection limit of fluorescent sensing platforms to femto- and picomolar levels.[67, 68, 70, 71]

Such an effect is ascribed to the unique interaction of plasmonic nanostructures with light. Their nanoscale nature allows for the polarisation of conductive electrons by the incident electric field, generating localised surface plasmons (LSPs, Figure 1.29) and the respective localised surface plasmon resonances (LSPRs).[72]

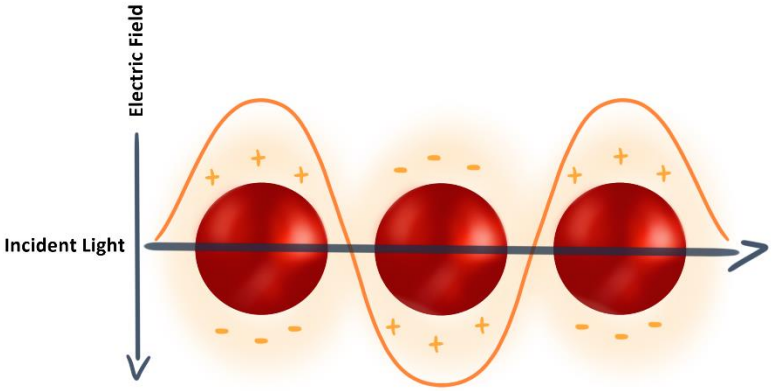


Figure 1.29 – Sketch of the LSPR of plasmonic nanoparticles.

Furthermore, the incident electromagnetic (EM) field can be confined and amplified at the surface of nanostructures, greatly enhancing optical and chemical processes.[73-76] Gold (Au) and, in part, silver (Ag) are some of the most popular elements for the fabrication of nanostructures due to their well-known chemistry, ease of functionalisation, high plasmon quality factors and plasmon resonances spanning the visible and NIR regions.[77] These nanomaterials can be dispersed in a medium (e.g. as nanoparticles, NPs) or assembled as arrays or films on surfaces, strongly influencing their plasmonic behaviour and thus enhancement capabilities.[72, 78, 79]

Additionally, the enhancement is not limited to fluorescence, and Surface Enhanced Raman Scattering (SERS) has found widespread use for the increase of inelastic Raman scattering signals (Figure 1.30).[80-82] By coupling fluorescence and SERS readouts to Localised Surface Plasmon Resonance (LSPR) monitoring, plasmonic materials offer a multimodal approach for the ultrasensitive detection of relevant analytes and biomarkers, thus constituting an extremely attractive choice for the development of sensing platforms (Figure 1.30).[80, 83-85]

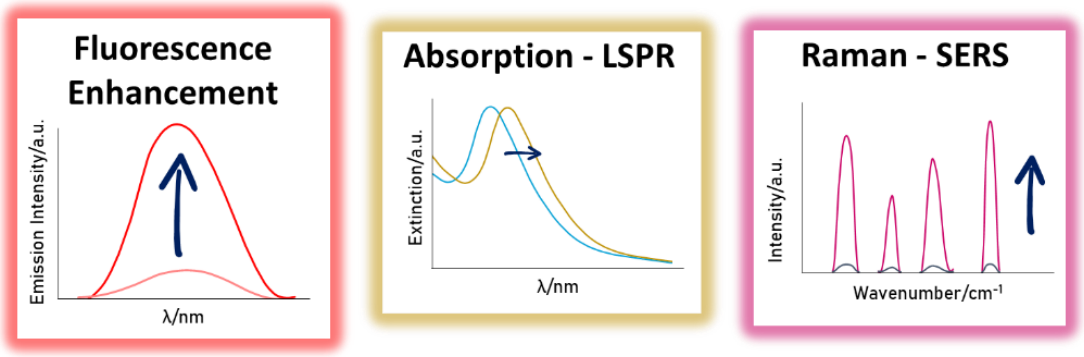


Figure 1.30 – Sketch of the possible readouts with plasmonic systems.

1.2.1 Plasmon mediated fluorescence enhancement

Focusing on the enhancement of fluorescence, a great number of systems incorporating fluorophores, organic dyes in particular, to plasmonic substrates have been reported.[77, 79, 85-91] Generally, the choice of shape, size and composition of a plasmonic nanostructure is based on both the photophysical properties of the emitter and the application.[67]

Compared to a fluorophore in free space, plasmonic nanostructures alter the EM field experienced by the emitter. Consequently, three processes are generally recognised, depending on the spectral overlap between the plasmon modes of the plasmonic material and the photophysical processes of the fluorophore, as well as the separation distance between nanostructure and emitter.[71, 92] At short distances (< 5 nm), Förster Resonance Energy Transfer (FRET)-like processes are typically predominant, with both quenching and enhancement taking place upon spectral overlap with the absorption spectrum of the emitter (Figure 1.31, **a**). The enhancement process is ascribed to the presence of amplified local fields in proximity to the nanostructure, leading to enhanced excitation rates and consequent greater brightness, allowing for reduced background and decreased excitation intensity.[93, 94] Beyond the FRET region, significant fluorescence enhancements can be observed upon overlap with the

emission spectrum of the emitter (Figure 1.31, **b**). Here, the amplification of the spontaneous emission of the fluorophore *via* Purcell effect is accompanied by an increase in the radiative decay rate (γ_{Rad}). The Purcell enhancement factor (**F**) can be correlated to the intrinsic properties of the plasmonic material and described as follows:

$$\gamma_{Tot} = \gamma_{Rad} + \gamma_{NRad} \qquad Equation\ 1.4$$

$$F = \frac{\gamma_{Tot}}{\gamma_{Tot(0)}} = \frac{3}{4\pi^2}\left(\frac{Q}{V_{Mode}}\right)\left(\frac{\lambda}{n}\right)^3 \qquad Equation\ 1.5$$

where γ_{Tot} is described in Equation 1.4, with γ_{NRad} being the non radiative decay. γ_{Tot} and $\gamma_{Tot(0)}$ are the total decay rates of the emitter in presence and absence of a plasmonic nanostructure, respectively, **Q** is the quality factor of the plasmonic material, V_{Mode} is the volume of the plasmon mode, **λ** is the emission wavelength and **n** the refractive index of the medium.[95, 96] Importantly, the increase in radiative decay rate strongly reduces the photobleaching of organic dyes by limiting the probability of occurrence of photothermal reactions, justifying the higher photostability of dyes coupled to plasmonic materials and overcoming one of the main drawbacks of this class of emitters.[97]

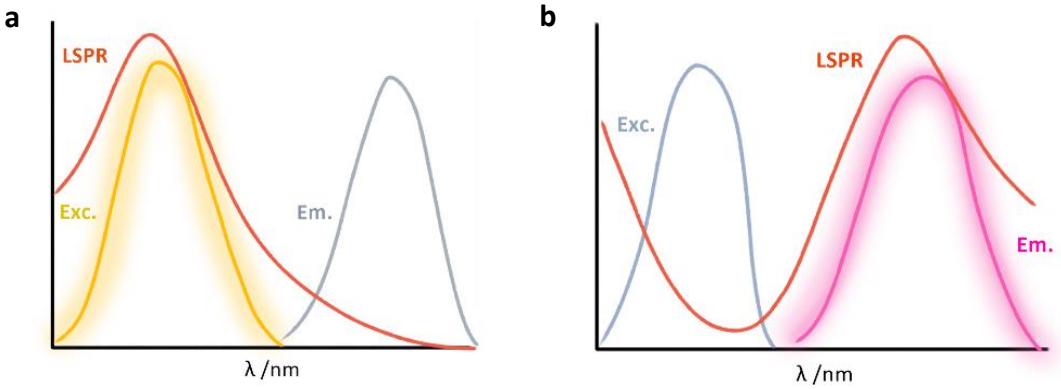
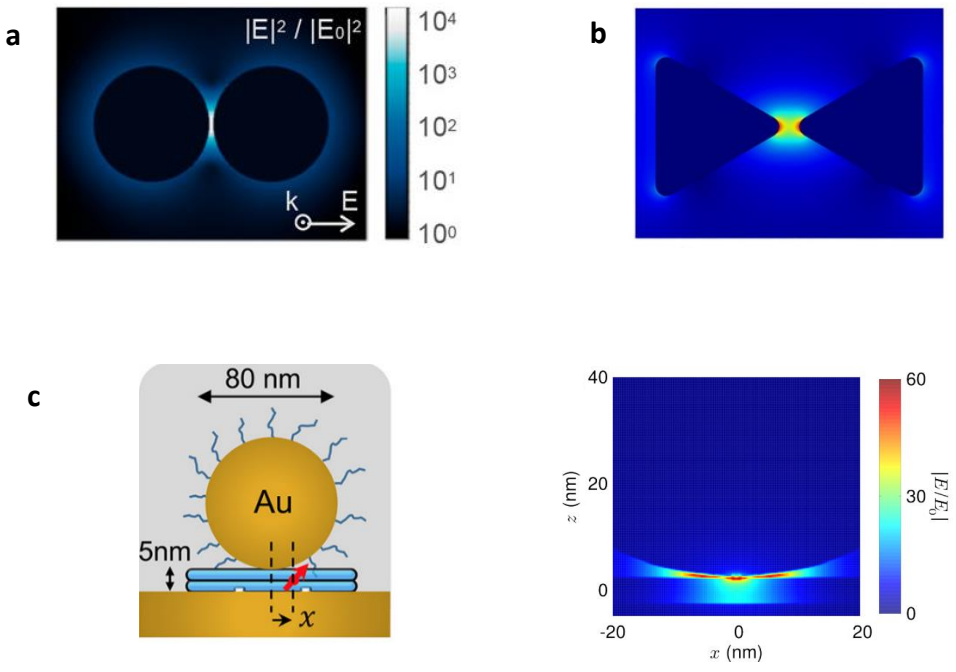


Figure 1.31 – Sketches of the spectral requirements for either excitation (**a**) or emission (i.e. Purcell, **b**) enhancements. In the first case, the LSPR of the plasmonic material is represented in red and the excitation spectrum of the emitter in yellow. In the second case, the LSPR is again red, while the enhanced emission is in pink. The y axes of the sketched spectra represent both extinction and emission intensity (a.u.).

Due to the small Stokes shift of organic dyes, the overlap of the plasmon modes with both absorption and emission spectra is often possible. In these cases the enhancement arises from a combination of both processes, and is thus approximated as follows:

$$\gamma_{Em}=\gamma_{Exc}\cdot\Phi=\gamma_{Exc}\cdot\left(\frac{\gamma_{Rad}}{\gamma_{Tot}}\right) \quad Equation\ 1.6$$

where, γ_{Rad} and γ_{Tot} are the radiative and total decay rates (Purcell) and γ_{Exc} the excitation rate of the emitter.[90, 98-101] To further maximise the enhancement, fluorophores can be placed in the gaps between nanostructures as the EM field confinement is highest when two or more nanostructures are in proximity to each other (within the field decay distance, i.e. ≈20-30 nm).[102-105] In these conditions, the near field coupling of nanostructures leads to hybridised plasmon modes and affords even larger amplifications of the confined EM field (from 10 for a spherical NP to 10^4 for an array of NPs) and the formation of so called "hot spots" (Figure 1.32 **a**).[103, 104, 106, 107] In addition to the coupling of neighbouring NPs, such EM field enhancements have been observed with Nanoparticle-on-Mirror (NPoM) and 3D tapered designs (Figures 1.32 **b**-**d**).[100, 108-111]



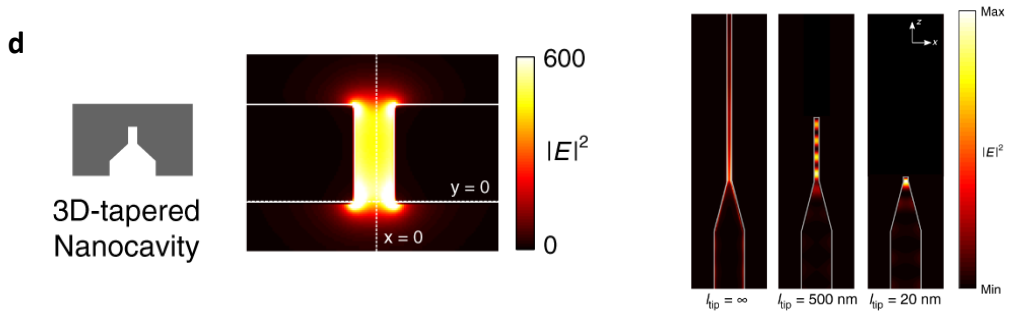


Figure 1.32 – **a**, **b** Electric field enhancement of coupling AuNPs (80 nm) and bowties The images were taken from [112] and [108], respectively. **c** Sketch of the NPoM system (left) with the respective electric field intensity as seen perpendicularly to the substrate (right). Both images were taken from [100]. **d** Intensity of the EM field in a 3D tapered nanocavity as seen perpendicularly (left) and from the top (right). The image was taken from [109].

When nanomaterials are dispersed in a medium, the distances between nanostructures are dictated by diffusion and the formation of well-defined gaps is complex.[113] If grown or deposited on flat substrates, however, nanostructures can be arranged in patterns of controlled distances. In addition to top down approaches such as lithography, the advance of reliable bottom-up fabrication methods has provided efficient and economic alternatives, often allowing for the large-scale preparation of plasmonic surfaces.[78, 114-116]

In an example by Flauraud *et al.*, an enhancement factor of 15,000 was achieved by the inclusion of crystal violet in the nanogap (10 nm) of two Au half spheres (80 nm, Figure 1.33) fabricated by a lithographic top down method. Here, the inclusion of the nanoantenna dimers in a "nanobox" drives the exclusion of emitters diffusing away from the hot spot and allowing for a more accurate and clear analysis of the enhancement. The precise fabrication of the nanoantenna to fully expose the hot spot at the top of the dimer, as well as the presence of both excitation and Purcell effects are believed to contribute to such high enhancement factors.[117]

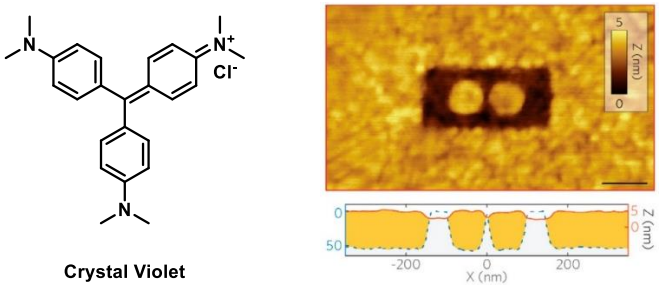


Figure 1.33 – AFM image of the Au nanodimers (half spheres) in a nanobox (darker rectangular area). The scale bar is 100 nm. The image was taken from [117].

The anisotropic shape of nanorods (NRs) allows for the presence of both longitudinal (L-LSPR) and transversal (T-LSPR) modes, whose frequencies can be tuned in the biological relevant NIR window by variation of the aspect ratio of the NR. Furthermore, improved fluorescence enhancements to spherical NPs can be obtained in the near-field of the NR tip.[98] Trofymchuk *et al.* have recently reported the control of AuNR orientation to obtain tip-to-tip dimers with gap sizes of 11 nm. DNA origami is a popular method to assemble nanostructures and obtain well defined arrays and hot spots.[102, 107, 118, 119] Here, DNA origami nanopillars were used not only to anchor the AuNRs (67×20 nm) in the tip-to-tip orientation, but also to place the fluorescent dye (Cy7) specifically at the hot spot, leading to fluorescence intensities up to 1600-fold higher than the nanopillar without the AuNR dimer.[120]

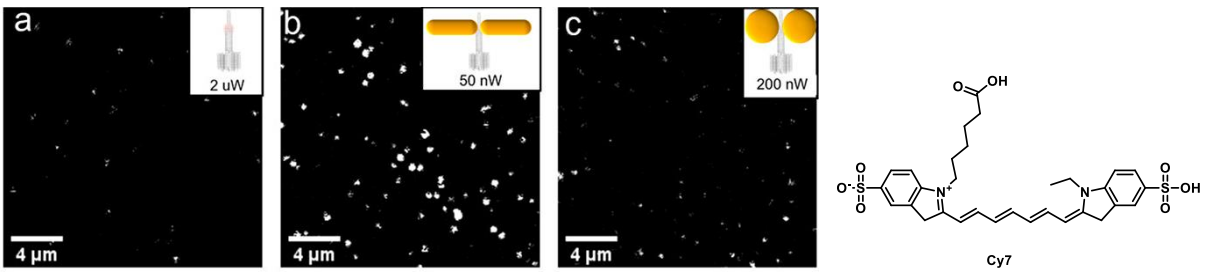


Figure 1.34 – Confocal images of Cy7 immobilised on the DNA origami nanopillar alone (**a**), in the gap between two AuNRs (**b**) and in the gap between two AuNPs (40 nm, **c**). The laser power used to obtain the images is reported in the inset. All images were taken from [120].

Finally, Baumberg and co-workers have reported extreme enhancement factors, in the order of 10^8, upon two-photon excitation of $RuBpy_3$ in the nanogaps of a NPoM design.[121] The dye molecules were assembled as a monolayer in the 1 nm nanocavity created by AuNPs (80 nm) and an Au mirror (Figure 1.35, **a**). Importantly, the lifetime of $RuBpy_3$ decreased from 520±10 ns (as a solution) to 0.2±0.1 ns in the NPoM nanocavity, indicating a Purcell factor of 2600 (Equation 1.5). However, the measurement of such small lifetimes is limited by the instrument response and, by finite-difference time domain simulations, the authors report an actual Purcell factor of 10^6 with a lifetime of 500 fs for $RuBpy_3$.[121]

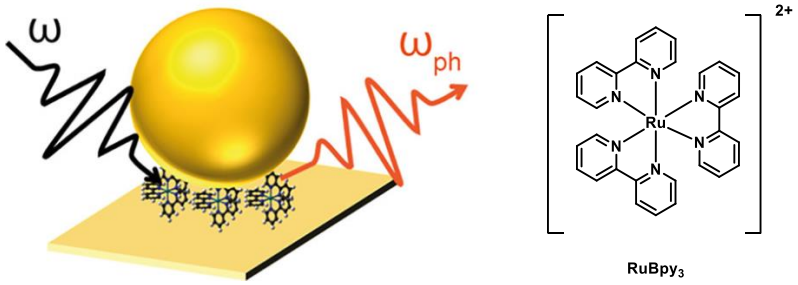


Figure 1.35 – Sketch of the NPoM design employed by Baumberg and co-workers. The image was taken from [121].

1.2.2 Plasmonic surfaces as fluorescent sensing platforms

The hot-spots approach has been incorporated to fluorescence based diagnostic platforms, allowing for the detection of a variety of biomarkers and analytes at ultra-low concentrations (pM-fM).[77, 85-88, 122] In this context, one must consider parameters such as stability, versatility and ease of handling and preparation of both substrates and materials, in addition to a significant fluorescence enhancement.

Mikkelsen and co-workers have recently presented a sandwich immunoassay (Figure 1.36, **a**) relying on the enhanced electromagnetic field in the nanocavity between Ag nanocubes (100

nm) and an Au film.[77] The fluorescence of an Alexa 647 label dye is thus enhanced by a factor of 151 compared to the glass control, improving the limit of detection (LOD) by 14-fold and making the recognition of a cardiac biomarker (B-type natriuretic peptide) feasible with an inexpensive point-of-care detector. Here, a polymer brush (i.e. Poly[oligo(ethylene glycol) methyl ether methacrylate], POEGMA, Figure 1.36, **a**) grown on a Au film is used both as a spacer (from 5 nm to 20 nm) and to immobilise the capture antibody by non contact inkjet printing. The Ag nanocubes are introduced on the Alexa 647 labelled detection antibody *via* a secondary antibody, producing a highly intense fluorescent readout upon detection of the antigen (Figure 1.36, **b**).[77]

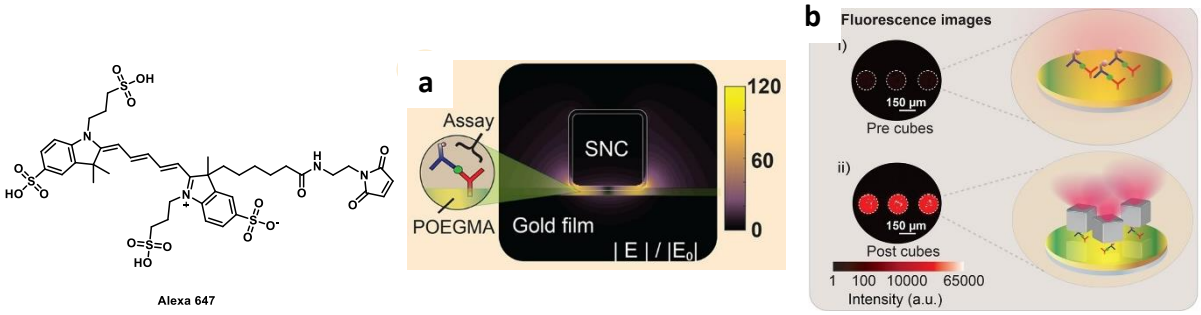


Figure 1.36 – **a** Sketch of the sandwich assay approach developed by Mikkelsen and co-workers. The electric field enhancement ($|E|/|E_0|$) is simulated, showing the maximum enhancement in the gap between the Au film and the Ag nanocube (SNC). The image was taken from [77]. **b** Fluorescence images of the sandwich assay in the presence (top, pre cubes) and absence (bottom, post cubes) of the enhancing Ag nanocubes. The image was taken from [77].

In an example by Minopoli *et al.*, AuNP arrays (50 nm diameter, 20 nm interparticle distance) fabricated by block copolymer micelle nanolithography were employed for the amplification of the fluorescence signal of Cy5 in a Malaria immunosensor.[123] The detection of the Malaria biomarker *Plasmodium Falciparum* Lactate Dehydrogenase (*Pf*LDH) in whole blood was carried out by photochemically immobilising the detection antibody on AuNPs *via* cysteine units and translating the recognition event with the Cy5 labelled *Pf*LDH-specific aptamer in a sandwich

approach (Figure 1.37, **a**). The overlap of the extinction spectrum of the AuNP array with both excitation and emission spectra of Cy5 (Figure 1.37, **b**) leads to enhancement factors up to $7x10^4$, lowering by several orders of magnitude the limit of detection (fM concentrations) compared to commercial diagnostic kits (Figure 1.37, **c**).[123]

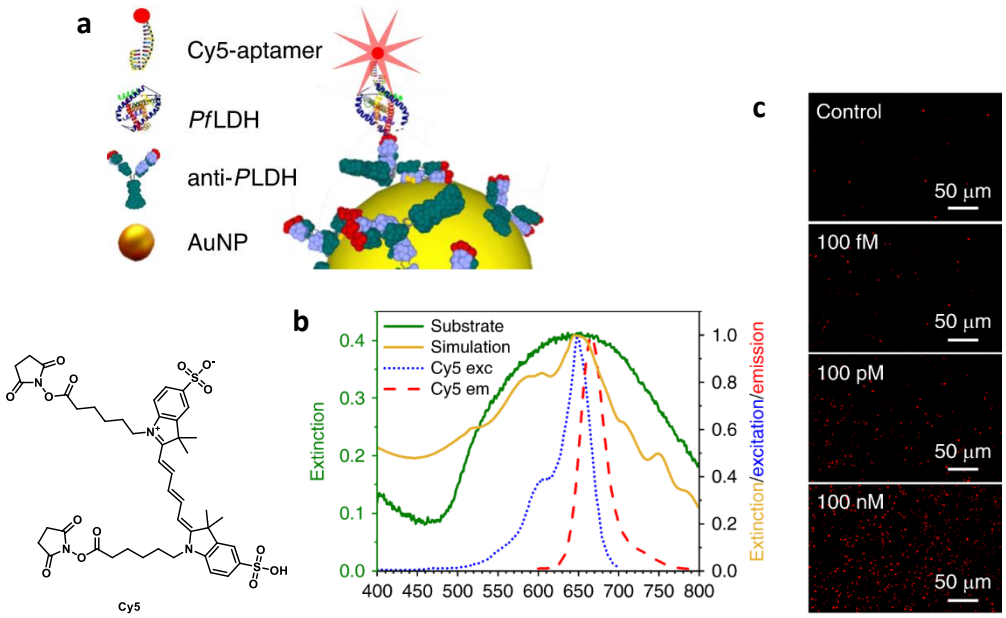


Figure 1.37 – **a** Sketch of the assay developed by Minopoli *et al.* on AuNP arrays (50 nm, interparticle distance of 20 nm). The image was taken from [123]. **b** Extinction (green and yellow), emission (red) and excitation (blue) spectra of the substrate prepared by Minopoli *et al.*. The image was taken from [123]. **c** Fluorescence images of the system for different concentrations of *Pf*LDH spiked in whole blood. The image was taken from [123].

An interesting approach has been presented by Luan *et al.*, where plasmonic nanostructures are adsorbed in a flexible elastomeric polydimethylsiloxane (PDMS) patch which can be placed on top of existing fluorescence immunoassays (Figure 1.38 **a**), thus improving their signal to noise ratios without changing the existing methodologies. The overlap between the LSPR and the emission spectra of the dye was tailored by changing the nature or size of the nanostructure in the patch. Among others, the authors report the enhancement of the fluorescence signals of either IRDye680 or IRDye800 in two immunoassays for the detection of early stage biomarker for acute kidney injury (kidney injury molecule-1, KIM-1, or neutrophil

gelatinase-associated lipocalin, NGAL, respectively). The plasmonic patch included AuNRs of either 112x54 nm size and LSPR at 670 nm or 63x18 nm size and LSPR at 760 nm, overlapping with the spectra of IRDye680 and IRDye800 (≈700 nm and 800 nm), respectively. Fluorescence enhancements up to 100-fold are reported and, importantly, the LODs of the assays are reduced by 280- and 100-fold for KIM-1 and NGAL, respectively, compared to the unenhanced platform (Figure 1.38, **b**).

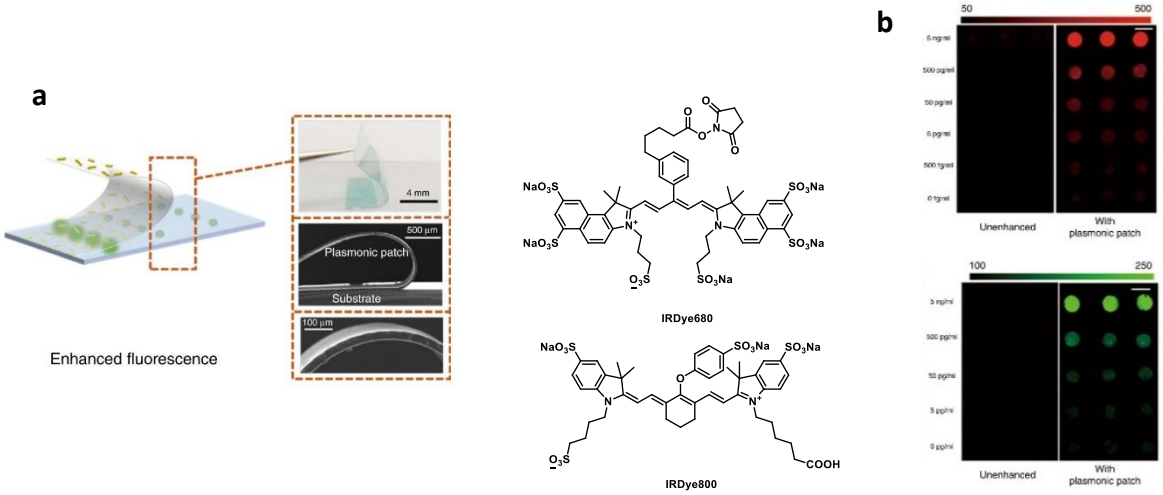


Figure 1.38 – **a** Sketch of the plasmonic patch developed by Luan *et al.*. The image was taken from [124]. **b** Fluorescence images of the immunoassays for the detection of KIM-1 (top) and NGAL (bottom) at different concentrations and either in the absence (left) or presence (right) of the enhancing plasmonic patch. The dyes used in the assays are IrDye680 and IrDye800, respectively. The image was taken from [124].

In the context of versatility, the enhancement of emitters at multiple wavelength ranges is highly desirable. Compared to accurate arrays or monodispersed NPs, disordered arrangements of nanostructures on a surface lead to a multitude of plasmon modes.[125] The resulting broad extinction allows for the overlap with the photophysical processes of a wider range of emitters, thus advancing the versatility of the plasmonic substrates. Nanostructured Au surfaces such as pGold (Figure 1.39 **b**) have shown significant potential for the

enhancement of both visible and NIR fluorescence due to the overlap with the broad extinction (>500 nm) of the plasmonic material (Figure 1.39, **a**).[126, 127]

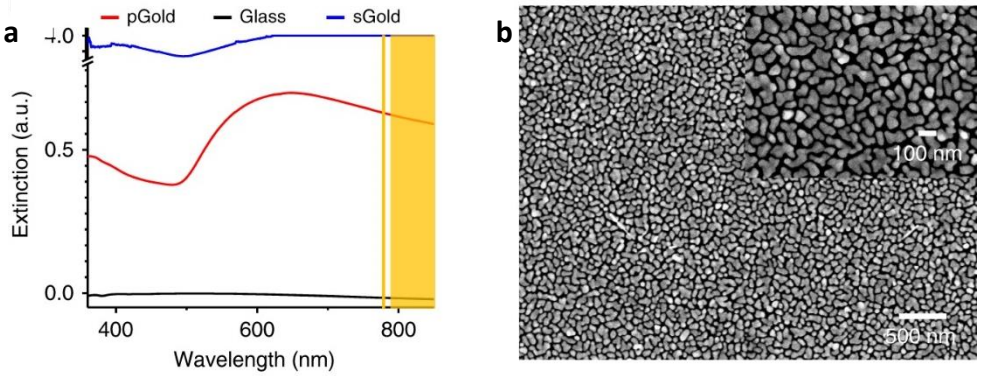


Figure 1.39 – **a** Extinction spectra of pGold, glass and sputtered Au. The image has been taken from [126]. **b** SEM image of pGold. The image has been taken from [126].

pGold has been used in the preparation of imaging substrates, enhancing the fluorescence of a wide range of available organic dyes (i.e. Cy3, Cy5, IRDye680 and IRDye800). Whereas modest enhancement factors (≈3-fold) were observed for Cy3 and Cy5 dyes, due to the limited overlap between their excitation/emission (568 nm and 667 nm) and the plasmon modes of pGold, enhancement factors up to 30-fold were recorded for the IRDye680 and IRDye800 dyes emitting above 700 nm (λ_{em}: ≈700 nm and 800 nm, respectively). The plasmonic enhancement allowed for the multicolour cell imaging with NIR emitting dyes, which could not be achieved on a simple glass substrate (Figure 1.40).

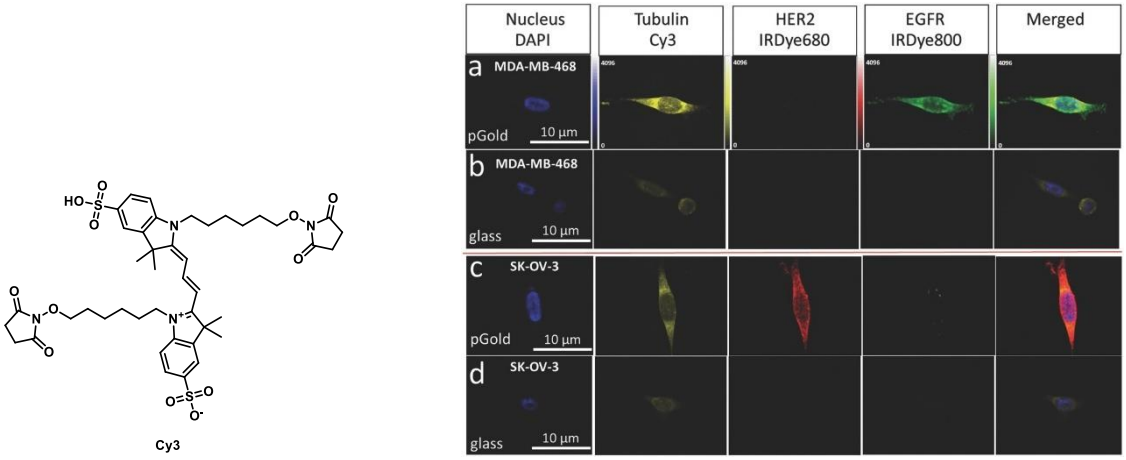


Figure 1.40 – Multicolour fluorescence images of two cell lines either on a glass slide (control) or on pGold, showing the fluorescence enhancement in the NIR region (IRDye680, IRDye800), in particular. The image was taken from [127].

pGold has also been used in the development of ultra-sensitive assays for the detection of, among others, myocardial infarction (Figures 1.41, **a** and **b**), type 1 diabetes and Zika virus biomarkers. [126 87, 125-128] For the detection of cardiac Troponin I (cTnI), a sandwich assay was developed, where the capture antibody was printed on the pGold substrate and the fluorescence readout was obtained upon recognition of cTnI by the IRDye800 labelled detection antibody (Figure 1.41, **a**). Compared to the glass and sputtered Au (sGold) controls, limits of detection and quantification as low as 0.0100 and 0.0157 ng mL^{-1}, respectively, could be obtained, surpassing the ones of the current standard method for cardiac Troponin I detection (i.e. chemiluminescence immunoassay, 0.0152 and 0.0208 ng mL^{-1}, respectively).[126]

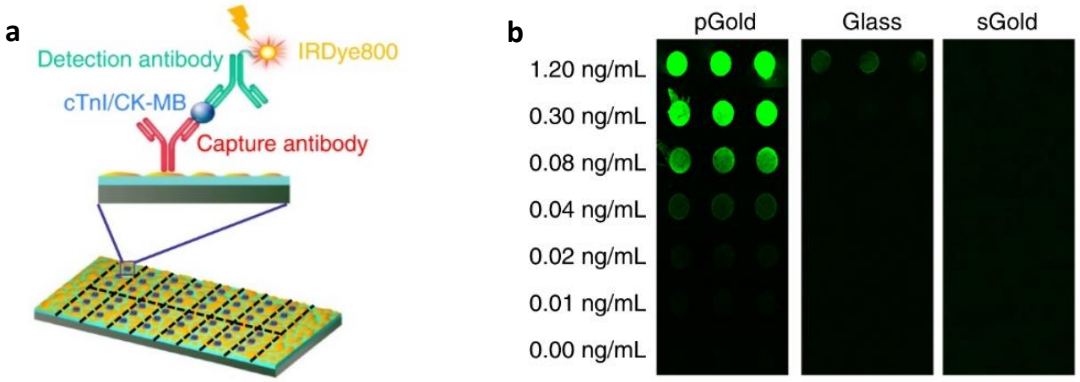


Figure 1.41 – **a** Illustration of the sandwich assay on pGold for the detection of cardiac Troponin I (cTnI), a serum biomarker for myocardial infarction, with IRDye800. The image was taken from [126]. **b** Fluorescence mapping for the detection of cTnI with the developed sandwich assay on either pGold, glass and sputtered Au (sGold). The image was taken from [126].

1.3 Thesis Outline

In this thesis, a novel surface active bis β-diketone ligand and its respective dinuclear lanthanide(III) complexes are designed, synthesized and characterised. The complexes are employed for the fabrication of luminescent Au surfaces and Au nanoparticles (AuNPs). Furthermore, the plasmonic enhancement of both visible and NIR lanthanide(III) luminescence is assessed by incorporation of the prepared complexes to pGold and Ag nanoislands (AgNIs) surfaces.

Chapter 2 concerns the synthesis of the novel surface active bis β-diketone ligand and respective complexes. Here, in addition to the characterisation and assessment of the luminescent properties of the complexes, the crystal structure of the Yb(III) derivative is included and discussed. The respective Eu(III) complex is investigated as a luminescent probe for the detection of anions, and the response towards F^- coordination is evaluated for the development of a handheld sensing platform on Au surfaces.

Chapter 3 includes the coating of the prepared surface active complexes on Au surfaces, the characterisation of the materials and the assessment of their luminescent response to F^- concentration. The complexes are also incorporated to plasmonic pGold and AgNIs surfaces and the enhancement of both visible and NIR luminescence is assessed. Finally, an alternative approach for the preparation of luminescent surfaces is briefly described, focusing on the polyaniline assisted deposition of unfunctionalized lanthanide(III) bis β-diketonates.

Chapter 4 concerns the preparation of luminescent AuNPs dispersed in H_2O by anchoring of the prepared surface active lanthanide(III) bis β-diketonates. The visible and NIR luminescence of the coated nanoparticles is assessed and correlated to the size and optical properties of the nanomaterials. Finally, a surface active 1,10-phenanthroline ancillary ligand is prepared and coordinated to unfunctionalized lanthanide(III) bis β-diketonates. The complexes are anchored on Au nanoparticles and their optimised luminescence properties are investigated.

Each research chapter contains a brief literature review to introduce the context of the discussed research. This is followed by an outline of the aims of the chapter and the results and discussion section. Conclusions and outlook of each project are included at the end of each research chapter, as well as an appendix detailing the experimental procedures and materials used in the chapter and additional characterisation data. Finally, a brief section outlining the general conclusions and future studies is included at the end of the thesis.

1.4 References

1. S. Cotton, in *Lanthanide and Actinide Chemistry*, 2006, pp. 1-7.
2. T. Cheisson and E. J. Schelter, *Science*, 2019, **363**, 489-493.
3. R. D. Teo, J. Termini and H. B. Gray, *Journal of Medicinal Chemistry*, 2016, **59**, 6012-6024.
4. J. C. Bunzli and C. Piguet, *Chemical Society Reviews*, 2005, **34**, 1048-1077.
5. S. V. Eliseeva and J.-C. G. Bünzli, *New Journal of Chemistry*, 2011, **35**, 1165-1176.
6. A. Abdollahi, H. Roghani-Mamaqani, B. Razavi and M. Salami-Kalajahi, *ACS Nano*, 2020, **14**, 14417-14492.
7. G. J. Stasiuk and N. J. Long, *Chemical Communications*, 2013, **49**, 2732-2746.
8. L. E. MacKenzie and R. Pal, *Nature Reviews Chemistry*, 2021, **5**, 109-124.
9. G. Tessitore, G. A. Mandl, S. L. Maurizio, M. Kaur and J. A. Capobianco, *RSC Advances*, 2023, **13**, 17787-17811.
10. https://sciencenotes.org/periodic-table-2017-edition-black-white/.
11. D. G. Karraker, *Journal of Chemical Education*, 1970, **47**, 424.
12. J.-C. G. Bünzli and S. V. Eliseeva, in *Lanthanide Luminescence: Photophysical, Analytical and Biological Aspects*, eds. P. Hänninen and H. Härmä, Springer Berlin Heidelberg, Berlin, Heidelberg, 2011, 1-45.
13. K. Binnemans, *Coordination Chemistry Reviews*, 2015, **295**, 1-45.
14. J.-C. G. Bünzli, *Coordination Chemistry Reviews*, 2015, **293-294**, 19-47.
15. M. C. Heffern, L. M. Matosziuk and T. J. Meade, *Chemical Reviews*, 2014, **114**, 4496-4539.
16. S. I. Weissman, *The Journal of Chemical Physics*, 1942, **10**, 214-217.
17. G. A. Crosby, R. E. Whan and R. M. Alire, *The Journal of Chemical Physics*, 1961, **34**, 743-748.
18. L. Armelao, S. Quici, F. Barigelletti, G. Accorsi, G. Bottaro, M. Cavazzini and E. Tondello, *Coordination Chemistry Reviews*, 2010, **254**, 487-505.
19. J. H. S. K. Monteiro, *Molecules*, 2020, **25**, 2089.
20. G. Mancino, A. J. Ferguson, A. Beeby, N. J. Long and T. S. Jones, *Journal of the American Chemical Society*, 2005, **127**, 524-525.
21. J.-C. G. Bünzli, *Journal of Coordination Chemistry*, 2014, **67**, 3706-3733.
22. A. J. Amoroso and S. J. A. Pope, *Chemical Society Reviews*, 2015, **44**, 4723-4742.
23. T. J. Sørensen and S. Faulkner, *Accounts of Chemical Research*, 2018, **51**, 2493-2501.
24. J. Wahsner, E. M. Gale, A. Rodriguez-Rodriguez and P. Caravan, *Chemical Reviews*, 2019, **119**, 957-1057.
25. S. J. Butler, L. Lamarque, R. Pal and D. Parker, *Chemical Science*, 2014, **5**, 1750-1756.
26. M. Soulié, F. Latzko, E. Bourrier, V. Placide, S. J. Butler, R. Pal, J. W. Walton, P. L. Baldeck , B. Le Guennic, C. Andraud, J. M. Zwier, L. Lamarque, D. Parker and O. Maury, *Chemistry – A European Journal*, 2014, **20**, 8636-8646.
27. A. T. Frawley, Holly V. Linford, M. Starck, R. Pal and D. Parker, *Chemical Science*, 2018, **9**, 1042-1049.
28. L. Gundorff Nielsen, A. K. Ravnsborg Hansen, P. Stachelek, R. Pal and T. Just Sørensen, *European Journal of Inorganic Chemistry*, 2023, **24**, e202300245.

29. L. J. Daumann, D. S. Tatum, B. E. R. Snyder, C. Ni, G.-l. Law, E. I. Solomon and K. N. Raymond, *Journal of the American Chemical Society*, 2015, **137**, 2816-2819.
30. G.-Q. Jin, Y. Ning, J.-X. Geng, Z.-F. Jiang, Y. Wang and J.-L. Zhang, *Inorganic Chemistry Frontiers*, 2020, **7**, 289-299.
31. S. V. Eliseeva and J.-C. G. Bünzli, *Chemical Society Reviews*, 2010, **39**, 189-227.
32. Y. Ning, M. Zhu and J.-L. Zhang, *Coordination Chemistry Reviews*, 2019, **399**, 213028.
33. J.-Y. Hu, Y. Ning, Y.-S. Meng, J. Zhang, Z.-Y. Wu, S. Gao and J.-L. Zhang, *Chemical Science*, 2017, **8**, 2702-2709.
34. Y. Ning, S. Cheng, J.-X. Wang, Y.-W. Liu, W. Feng, F. Li and J.-L. Zhang, *Chemical Science*, 2019, **10**, 4227-4235.
35. P. B. Glover, A. P. Bassett, P. Nockemann, B. M. Kariuki, R. Van Deun and Z. Pikramenou, *Chemistry – A European Journal*, 2007, **13**, 6308-6320.
36. A. P. Bassett, R. Van Deun, P. Nockemann, P. B. Glover, B. M. Kariuki, K. Van Hecke, L. Van Meervelt and Z. Pikramenou, *Inorganic Chemistry*, 2005, **44**, 6140-6142.
37. J. K. Clegg, F. Li and L. F. Lindoy, *Coordination Chemistry Reviews*, 2022, **455**, 214355.
38. K. Nehra, A. Dalal, A. Hooda, S. Bhagwan, R. K. Saini, B. Mari, S. Kumar and D. Singh, *Journal of Molecular Structure*, 2022, **1249**, 131531.
39. A. Dalal, K. Nehra, A. Hooda, D. Singh, P. Kumar, S. Kumar, R. S. Malik and B. Rathi, *Inorganica Chimica Acta*, 2023, **550**, 121406.
40. K. Binnemans, *Handbook on the Physics and Chemistry of Rare Earths*, 2005, **35**, 107-272.
41. E. K. Amason, M. H. Jones, C. Keuk, G. M. Ferrence, E. E. Joslin and R. E. Bachman, *Polyhedron*, 2021, **201**, 115188.
42. D. Singh, S. Bhagwan, A. Dalal, K. Nehra, R. K. Saini, K. Singh, S. Kumar and I. Singh, *Journal of Luminescence*, 2020, **223**, 117255.
43. R. Ilmi, S. Kansız, N. Dege and M. S. Khan, *Journal of Photochemistry and Photobiology A: Chemistry*, 2019, **377**, 268-281.
44. A. Kukoyi, E. A. Micheli, B. Liu, H. He and P. S. May, *Dalton Transactions*, 2019, **48**, 13880-13887.
45. M. S. Khan, R. Ilmi, W. Sun, J. D. L. Dutra, W. F. Oliveira, L. Zhou, W.-Y. Wong and P. R. Raithby, *Journal of Materials Chemistry C*, 2020, **8**, 5600-5612.
46. X.-Z. Li, C.-B. Tian and Q.-F. Sun, *Chemical Reviews*, 2022, **122**, 6374-6458.
47. A. P. Bassett, S. W. Magennis, P. B. Glover, D. J. Lewis, N. Spencer, S. Parsons, R. M. Williams, L. De Cola and Z. Pikramenou, *Journal of the American Chemical Society*, 2004, **126**, 9413-9424.
48. M. M. Castaño-Briones, A. P. Bassett, L. L. Meason, P. R. Ashton and Z. Pikramenou, *Chemical Communications*, 2004, 2832-2833.
49. H.-F. Li, G.-M. Li, P. Chen, W.-B. Sun and P.-F. Yan, *Spectrochimica Acta Part A: Molecular and Biomolecular Spectroscopy*, 2012, **97**, 197-201.
50. J. Shi, Y. Hou, W. Chu, X. Shi, H. Gu, B. Wang and Z. Sun, *Inorganic Chemistry*, 2013, **52**, 5013-5022.
51. Y. Hou, J. Shi, W. Chu and Z. Sun, *European Journal of Inorganic Chemistry*, 2013, **2013**, 3063-3069.
52. H. F. Li, P. F. Yan, P. Chen, Y. Wang, H. Xu and G. M. Li, *Dalton Transactions*, 2012, **41**, 900-907.

53. A. J. Brock, I. M. Etchells, E. G. Moore and J. K. Clegg, *Dalton Transactions*, 2021, **50**, 4874-4879.
54. B. Li, H. Li, P. Chen, W. Sun, C. Wang, T. Gao and P. Yan, *Physical Chemistry Chemical Physics*, 2015, **17**, 30510-30517.
55. T. Zhu, P. Chen, H. Li, W. Sun, T. Gao and P. Yan, *Physical Chemistry Chemical Physics*, 2015, **17**, 16136-16144.
56. Z. Zhang, Y. Zhou, H. Li, T. Gao and P. Yan, *Dalton Transactions*, 2019, **48**, 4026-4034.
57. F. Yin, Z. Liu, J. Yang, L.-P. Zhou, C.-B. Tian and Q.-F. Sun, *ACS Omega*, 2023, **8**, 24477-24484.
58. Y. Zhang, Y. Zhou, T. Gao, P. Yan and H. Li, *Chemical Communications*, 2020, **56**, 13213-13216.
59. Y. Li, Y. Zhou, Y. Yao, T. Gao, P. Yan and H. Li, *New Journal of Chemistry*, 2021, **45**, 7196-7203.
60. M. Albrecht, S. Schmid, S. Dehn, C. Wickleder, S. Zhang, A. P. Bassett, Z. Pikramenou and R. Fröhlich, *New Journal of Chemistry*, 2007, **31**, 1755-1762.
61. Y. Zhou, Y. Yao, Z. Cheng, T. Gao, H. Li and P. Yan, *Inorganic Chemistry*, 2020, **59**, 12850-12857.
62. Y. Wang, Y. Zhou, Z. Yao, W. Huang, T. Gao, P. Yan and H. Li, *Dalton Transactions*, 2022, **51**, 10973-10982.
63. Z. Yao, Y. Zhou, T. Gao, P. Yan and H. Li, *RSC Advances*, 2021, **11**, 10524-10531.
64. Z. Zhang, Y. Zhou, T. Gao, P. Yan, X. Zou and H. Li, *Dalton Transactions*, 2021, **50**, 4604-4612.
65. C. Vericat, M. E. Vela, G. Benitez, P. Carro and R. C. Salvarezza, *Chemical Society Reviews*, 2010, **39**, 1805-1834.
66. J. C. Love, L. A. Estroff, J. K. Kriebel, R. G. Nuzzo and G. M. Whitesides, *Chemical Reviews*, 2005, **105**, 1103-1170.
67. D. Semeniak, D. F. Cruz, A. Chilkoti and M. H. Mikkelsen, *Advanced Materials*, **35**, 2107986.
68. S. M. Fothergill, C. Joyce and F. Xie, *Nanoscale*, 2018, **10**, 20914-20929.
69. X. Tian, L. C. Murfin, L. Wu, S. E. Lewis and T. D. James, *Chemical Science*, 2021, **12**, 3406-3426.
70. J. Luan, A. Seth, R. Gupta, Z. Wang, P. Rathi, S. Cao, H. Gholami Derami, R. Tang, B. Xu, S. Achilefu, J. J. Morrissey and S. Singamaneni, *Nature Biomedical Engineering*, 2020, **4**, 518-530.
71. A. Minopoli, A. Acunzo, B. Della Ventura and R. Velotta, *Advanced Materials Interfaces*, 2022, **9**, 2101133.
72. V. Amendola, R. Pilot, M. Frasconi, O. M. Maragò and M. A. Iatì, *Journal of Physics: Condensed Matter*, 2017, **29**, 203002.
73. M. A. Fusella, R. Saramak, R. Bushati, V. M. Menon, M. S. Weaver, N. J. Thompson and J. J. Brown, *Nature*, 2020, **585**, 379-382.
74. J. Min, T. Son, J.-S. Hong, P. S. Cheah, A. Wegemann, K. Murlidharan, R. Weissleder, H. Lee and H. Im, *Advanced Biosystems*, 2020, **4**, 2000003.
75. L. Mascaretti, A. Dutta, Š. Kment, V. M. Shalaev, A. Boltasseva, R. Zbořil and A. Naldoni, *Advanced Materials*, 2019, **31**, 1805513.

76. S. Li, P. Miao, Y. Zhang, J. Wu, B. Zhang, Y. Du, X. Han, J. Sun and P. Xu, *Advanced Materials*, 2021, **33**, 2000086.
77. D. F. Cruz, C. M. Fontes, D. Semeniak, J. Huang, A. Hucknall, A. Chilkoti and M. H. Mikkelsen, *Nano Letters*, 2020, **20**, 4330-4336.
78. A. Alvarez-Fernandez, C. Cummins, M. Saba, U. Steiner, G. Fleury, V. Ponsinet and S. Guldin, *Advanced Optical Materials*, 2021, **9**, 2100175.
79. J.-E. Park, J. Kim and J.-M. Nam, *Chemical Science*, 2017, **8**, 4696-4704.
80. J. Langer, D. Jimenez de Aberasturi, J. Aizpurua, R. A. Alvarez-Puebla, B. Auguié, J. J. Baumberg, G. C. Bazan, S. E. J. Bell, A. Boisen, A. G. Brolo, J. Choo, D. Cialla-May, V. Deckert, L. Fabris, K. Faulds, F. J. García de Abajo, R. Goodacre, D. Graham, A. J. Haes, C. L. Haynes, C. Huck, T. Itoh, M. Käll, J. Kneipp, N. A. Kotov, H. Kuang, E. C. Le Ru, H. K. Lee, J.-F. Li, X. Y. Ling, S. A. Maier, T. Mayerhöfer, M. Moskovits, K. Murakoshi, J.-M. Nam, S. Nie, Y. Ozaki, I. Pastoriza-Santos, J. Perez-Juste, J. Popp, A. Pucci, S. Reich, B. Ren, G. C. Schatz, T. Shegai, S. Schlücker, L.-L. Tay, K. G. Thomas, Z.-Q. Tian, R. P. Van Duyne, T. Vo-Dinh, Y. Wang, K. A. Willets, C. Xu, H. Xu, Y. Xu, Y. S. Yamamoto, B. Zhao and L. M. Liz-Marzán, *ACS Nano*, 2020, **14**, 28-117.
81. S. Schlücker, *Angewandte Chemie International Edition*, 2014, **53**, 4756-4795.
82. S. Y. Ding, E. M. You, Z. Q. Tian and M. Moskovits, *Chemical Society Reviews*, 2017, **46**, 4042-4076.
83. C. M. Das, K. V. Kong and K.-T. Yong, *Chemical Communications*, 2022, **58**, 9573-9585.
84. Y. Hang, J. Boryczka and N. Wu, *Chemical Society Reviews*, 2022, **51**, 329-375.
85. X. Wu, C. Hao, J. Kumar, H. Kuang, N. A. Kotov, L. M. Liz-Marzán and C. Xu, *Chemical Society Reviews*, 2018, **47**, 4677-4696.
86. C. Jin, Z. Wu, J. H. Molinski, J. Zhou, Y. Ren and J. X. J. Zhang, *Materials Today Bio*, 2022, **14**, 100263.
87. B. Zhang, R. B. Kumar, H. Dai and B. J. Feldman, *Nature Medicine*, 2014, **20**, 948-953.
88. C. Liang, J. Luan, Z. Wang, Q. Jiang, R. Gupta, S. Cao, K.-K. Liu, J. J. Morrissey, E. D. Kharasch, R. R. Naik and S. Singamaneni, *ACS Applied Materials & Interfaces*, 2021, **13**, 11414-11423.
89. J. Xu, W. Morton, D. Jones, T. A. Tabish, M. P. Ryan and F. Xie, *Applied Physics Reviews*, 2022, **9**, 031406.
90. G. K. Hodgson, N. P. Dogantzis and S. Impellizzeri, *The Journal of Physical Chemistry C*, 2020, **124**, 28298-28305.
91. H. Mishra, B. L. Mali, J. Karolin, A. I. Dragan and C. D. Geddes, *Physical Chemistry Chemical Physics*, 2013, **15**, 19538-19544.
92. J.-F. Li, C.-Y. Li and R. F. Aroca, *Chemical Society Reviews*, 2017, **46**, 3962-3979.
93. Y. Chen, K. Munechika and D. S. Ginger, *Nano Letters*, 2007, **7**, 690-696.
94. M. Li, S. K. Cushing and N. Wu, *Analyst*, 2015, **140**, 386-406.
95. J. Liu, Q. Wang, X. Sang, H. Hu, S. Li, D. Zhang, C. Liu, Q. Wang, B. Zhang, W. Wang and F. Song, *Nanomaterials*, 2021, **11**, 1037.
96. M. Pelton, *Nature Photonics*, 2015, **9**, 427-435.
97. H. Cang, Y. Liu, Y. Wang, X. Yin and X. Zhang, *Nano Letters*, 2013, **13**, 5949-5953.
98. D. Botequim, I. I. R. Silva, S. G. Serra, E. P. Melo, D. M. F. Prazeres, S. M. B. Costa and P. M. R. Paulo, *Nanoscale*, 2020, **12**, 6334-6345.

99. N. Gandra, C. Portz, L. Tian, R. Tang, B. Xu, S. Achilefu and S. Singamaneni, *Angewandte Chemie International Edition*, 2014, **53**, 866-870.
100. N. Kongsuwan, A. Demetriadou, R. Chikkaraddy, F. Benz, V. A. Turek, U. F. Keyser, J. J. Baumberg and O. Hess, *ACS Photonics*, 2018, **5**, 186-191.
101. P. Anger, P. Bharadwaj and L. Novotny, *Physical Review Letters*, 2006, **96**, 113002.
102. V. Glembockyte, L. Grabenhorst, K. Trofymchuk and P. Tinnefeld, *Accounts of Chemical Research*, 2021, **54**, 3338-3348.
103. M. B. Ross, C. A. Mirkin and G. C. Schatz, *The Journal of Physical Chemistry C*, 2016, **120**, 816-830.
104. D. Liu and C. Xue, *Advanced Materials*, 2021, **33**, 2005738.
105. Y. Wy, H. Jung, J. W. Hong and S. W. Han, *Accounts of Chemical Research*, 2022, **55**, 831-843.
106. E. Prodan, C. Radloff, N. J. Halas and P. Nordlander, *Science*, 2003, **302**, 419-422.
107. G. P. Acuna, F. M. Möller, P. Holzmeister, S. Beater, B. Lalkens and P. Tinnefeld, *Science*, 2012, **338**, 506-510.
108. J. Gargiulo, R. Berte, Y. Li, S. A. Maier and E. Cortes, *Accounts of Chemical Research*, 2019, **52**, 2525-2535.
109. S. Kumar, H. Park, H. Cho, R. H. Siddique, V. Narasimhan, D. Yang and H. Choo, *Nature Communications*, 2020, **11**, 2930.
110. J. J. Baumberg, J. Aizpurua, M. H. Mikkelsen and D. R. Smith, *Nature Materials*, 2019, **18**, 668-678.
111. J.-M. Kim, C. Lee, Y. Lee, J. Lee, S.-J. Park, S. Park and J.-M. Nam, *Advanced Materials*, 2021, **33**, 2006966.
112. A. P. Francisco, D. Botequim, D. M. F. Prazeres, V. V. Serra, S. M. B. Costa, C. A. T. Laia and P. M. R. Paulo, *The Journal of Physical Chemistry Letters*, 2019, **10**, 1542-1549.
113. F. Schulz, O. Pavelka, F. Lehmkühler, F. Westermeier, Y. Okamura, N. S. Mueller, S. Reich and H. Lange, *Nature Communications*, 2020, **11**, 3821.
114. J. B. Lee, H. Walker, Y. Li, T. W. Nam, A. Rakovich, R. Sapienza, Y. S. Jung, Y. S. Nam, S. A. Maier and E. Cortés, *ACS Nano*, 2020, **14**, 17693-17703.
115. S. P. Scheeler, S. Mühlig, C. Rockstuhl, S. B. Hasan, S. Ullrich, F. Neubrech, S. Kudera and C. Pacholski, *The Journal of Physical Chemistry C*, 2013, **117**, 18634-18641.
116. H.-H. Hsiao, C. H. Chu and D. P. Tsai, *Small Methods*, 2017, **1**, 1600064.
117. V. Flauraud, R. Regmi, P. M. Winkler, D. T. L. Alexander, H. Rigneault, N. F. van Hulst, M. F. García-Parajo, J. Wenger and J. Brugger, *Nano Letters*, 2017, **17**, 1703-1710.
118. M. Dass, F. N. Gür, K. Kołątaj, M. J. Urban and T. Liedl, *The Journal of Physical Chemistry C*, 2021, **125**, 5969-5981.
119. A. T. M. Yeşilyurt and J.-S. Huang, *Advanced Optical Materials*, 2021, **9**, 2100848.
120. K. Trofymchuk, K. Kołątaj, V. Glembockyte, F. Zhu, G. P. Acuna, T. Liedl and P. Tinnefeld, *ACS Nano*, 2023, **17**, 1327-1334.
121. O. S. Ojambati, R. Chikkaraddy, W. M. Deacon, J. Huang, D. Wright and J. J. Baumberg, *Nano Letters*, 2020, **20**, 4653-4658.
122. S. M. Tabakman, L. Lau, J. T. Robinson, J. Price, S. P. Sherlock, H. Wang, B. Zhang, Z. Chen, S. Tangsombatvisit, J. A. Jarrell, P. J. Utz and H. Dai, *Nature Communications*, 2011, **2**, 466.

123. A. Minopoli, B. Della Ventura, B. Lenyk, F. Gentile, J. A. Tanner, A. Offenhäusser, D. Mayer and R. Velotta, *Nature Communications*, 2020, **11**, 6134.
124. J. Luan, J. J. Morrissey, Z. Wang, H. G. Derami, K.-K. Liu, S. Cao, Q. Jiang, C. Wang, E. D. Kharasch, R. R. Naik and S. Singamaneni, *Light: Science & Applications*, 2018, **7**, 29.
125. B. Liu, Y. Li, H. Wan, L. Wang, W. Xu, S. Zhu, Y. Liang, B. Zhang, J. Lou, H. Dai and K. Qian, *Advanced Functional Materials*, 2016, **26**, 7994-8002.
126. W. Xu, L. Wang, R. Zhang, X. Sun, L. Huang, H. Su, X. Wei, C. C. Chen, J. Lou, H. Dai and K. Qian, *Nat Commun*, 2020, **11**, 1654.
127. B. Koh, X. Li, B. Zhang, B. Yuan, Y. Lin, A. L. Antaris, H. Wan, M. Gong, J. Yang, X. Zhang, Y. Liang and H. Dai, *Small*, 2016, **12**, 457-465.
128. B. Zhang, B. A. Pinsky, J. S. Ananta, S. Zhao, S. Arulkumar, H. Wan, M. K. Sahoo, J. Abeynayake, J. J. Waggoner, C. Hopes, M. Tang and H. Dai, *Nature Medicine*, 2017, **23**, 548-550.

Chapter 2 – Design of surface active dinuclear lanthanide(III) complexes as new luminescent probes

2.1 Introduction

2.1.1 Lanthanide(III) complexes as optical probes for the detection of analytes

The exceptional optical properties of lanthanides(III), coupled to their rich coordination chemistry, offer exciting opportunities for the fabrication of luminescent sensing probes. The development of sensing systems based on lanthanide(III) luminescence has been the focus of extensive research.[1-5] When designing lanthanide(III) probes for detection, the structure of the complex must be tailored to elicit a response in the presence of the analyte. The sensing event can be transduced as variation in lifetime, total or relative emission intensity or, in the case of chiral compounds, circular polarised luminescence.[1] The response may be triggered by either the indirect modulation of the photophysical processes of the complex or the direct coordination of the analyte to the lanthanide(III) ion.[6]

In the first case, the analyte interacts with a component of the complex to give a luminescent readout by modulation of the energy transfer processes (Figure 2.1).

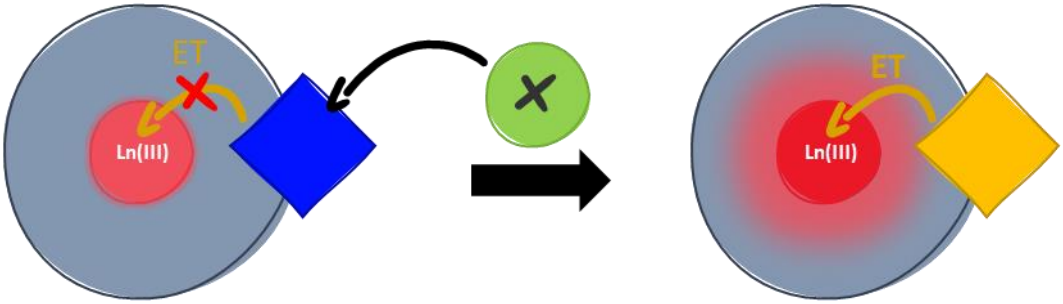


Figure 2.1 – Sketch of the sensing mechanisms by reaction of the analyte (green, "X") with the reacting unit (blue square). Here, a system where the energy transfer (ET) process is reinstated upon reaction with the analyte is depicted and the chemical modification to the reacting unit is displayed as a change in colour from blue to yellow.

The chemical reactivity of the analyte towards specific molecular units can be exploited for the design of activity-based sensing probes. In this context, the ligand scaffold includes a reacting unit, which is either cleaved or chemically modified upon reaction with the analyte, and leading to a modulation of the emission intensity.[6] Brennecke *et al.* have reported the formation of a carbostyril sensitising unit (**1-B**) by reaction of the non-luminescent precursor (**1**) with nitroreductases (NTRs). The consequent luminescence switch-on was used as a sensing readout and the time gated detection of Tb(III) luminescence was performed in live bacteria, where NTR activity could be tracked by fluorescence lifetime imaging (FLIM).[7] With a similar mechanism, Boros and co-workers have proposed a readout based on the modulation of the triplet state energy of the antenna. In the presence of H_2S, the conversion from a nitro (**2**) to an amino (**2-B**) group on the *para*-substituted pyridyl antenna occurs, triggering the energy transfer to Tb(III) due to the now suitable triplet state energy. Interestingly, the resulting luminescence switch-on could be detected using Cherenkov radiation as *in situ* excitation source and with a small animal imager.[8]

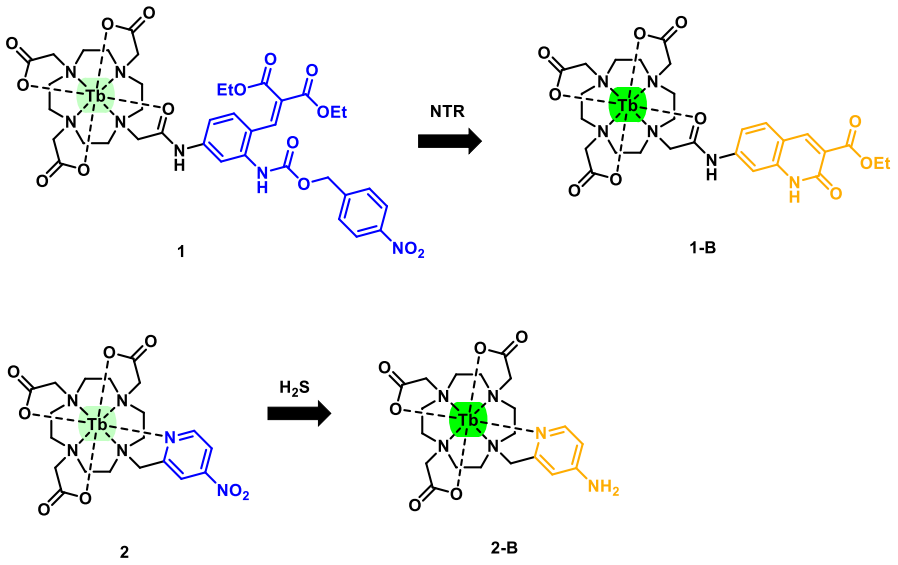


Figure 2.2 – Chemical structures and mechanisms of nitroreductase (NTR, **1**, **1-B**), H_2S (**2**, **2-B**) detection reported by Brennecke *et al.* and Boros and co-workers, respectively.[7, 8]

The detection of CN^- in H_2O *via* a luminescence switch-off mechanism has been shown in an example by Faulkner and co-workers.[9] Here, the luminescence decrease was not accompanied by any variations in either emission profile or lifetime, indicating that the detection solely relies on the interaction of the ligand scaffold, and not the Eu(III) centre, with the analyte. Indeed, the authors report the reaction of CN^- with the carbonyl group of the appended antenna in **3** (Figure 2.3) to form a cyanohydrin in **3-B**, thus disrupting the sensitisation of Eu(III) and leading to the switch-off readout.[9] Similarly, Butler and co-workers report the cleavage of the benzyl boronic acid unit (**4**) by reaction with peroxynitrite ($ONOO^-$), preventing the population of Eu(III) excited states due to the too low triplet state energy of the remaining 8-hydroxyquinolinate unit in **4-B**. The presence of $ONOO^-$ could be monitored in live cells, where time gated detection of luminescence allowed for the exclusion of autofluorescence from the sample.[10]

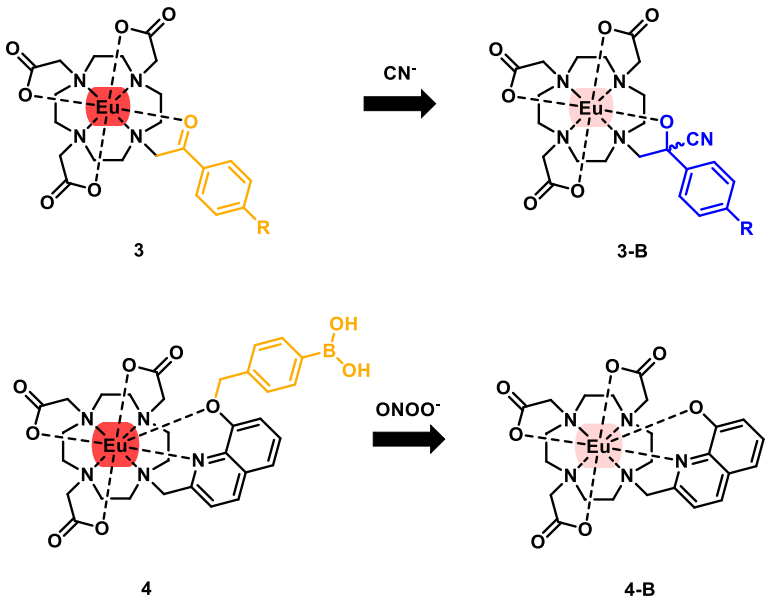


Figure 2.3 – Chemical structures and mechanisms of CN^- (**3**, **3-B,** R = F, Br) and $ONOO^-$ (**4**, **4-B**) detection reported by Faulkner and co-workers and Butler and co-workers, respectively.[9, 10]

In the activity-based approach, the sensing mechanism is non-reversible and so does not allow for the constant monitoring of a system. In the second sensing approach (Figure 2.4), a variation to the coordination sphere of the lanthanide(III) is monitored as a modulation of the relative or total emission intensity and lifetime of the complex. This approach relies on the direct coordination of the analyte to the metal and is thus limited to the sensing of species that have a high affinity for hard Lewis acids. In the presence of the analyte, this can displace either coordinating solvent molecules or labile ligands. The largest effects are recorded when O-H oscillators, such as those of H_2O, are excluded from the coordination sphere. The elimination of non-radiative deactivation pathways leads to an increase in lifetime, while the variation in the nature and polarizability of the coordinating atoms affects the crystal field splitting of lanthanide(III) emission.

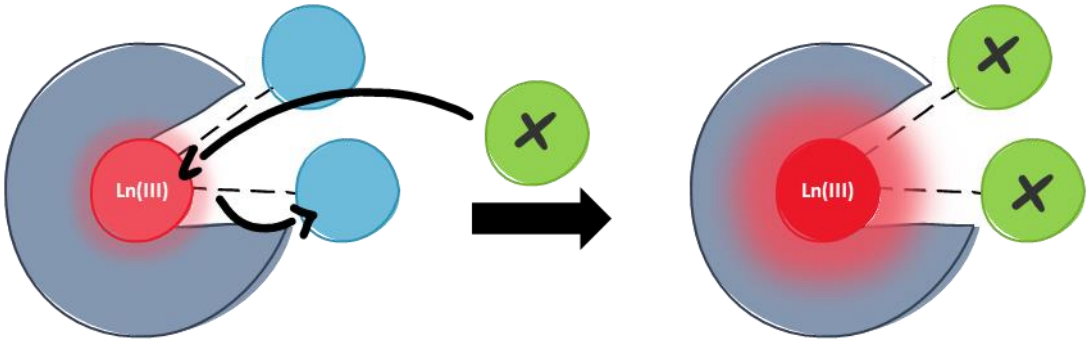


Figure 2.4 – Sketch of the sensing mechanisms based on the coordination of the analyte (green, "X") to the lanthanide(III) (red, Ln(III)) with consequent emission and lifetime modulation. The blue circles on the left represent the coordinating solvent molecules, while the grey unit the ligand.

Compared to the activity based systems reported before, this approach does not require the presence of specific sensing units nor relies on the kinetics of organic reactions. On the other hand, a careful design and knowledge of the structure of the complex is crucial to understand the coordination sphere and the sensing process of the complex.[1] The detection of anions is favoured with this sensing approach, as the negative charge of the analyte strongly favours coordination to the lanthanide(III) centre. A range of probes for the sensing of relevant anions has been reported and some recent examples are described below.

Pierre and co-workers have reported the effect of increasing the number of inner sphere H_2O molecules (q, Figure 2.5) for the sensing of CN^- in aqueous environments. Here, the inclusion of a wider ligand cap (**6**), compared to the scaffold of a simple 1,2-hydroxypyridonate (HOPO, **5**) ligand, accommodates an additional coordinating H_2O molecule. Whereas **5** did not display any sensing capabilities, the modified Eu(III) complex **6** not only allows for the detection of CN^- by displacement of the coordinated H_2O molecules, but also displays selectivity in the presence of other biologically relevant anions.[11] However, in a following study, the group reported that the ligand cap would indeed affect the number of coordinating H_2O molecules of a series of

Eu-HOPO derivatives, but the binding affinity towards anions could not be correlated solely on this parameter.[12]

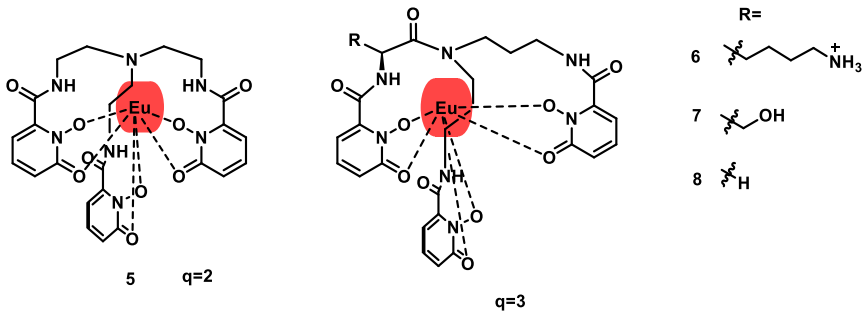


Figure 2.5 – Chemical structures of the Eu(III) complexes reported by Pierre and co-workers for the detection of CN^- (**5**-**6**) and inorganic phosphate (**6**-**8**).[11, 13]

In a different approach, the binding affinity of Eu-HOPO derivatives for inorganic phosphate is tuned by addition of a charged or neutral unit peripheral to the coordination pocket. Here, the inclusion of a positively charged group (**6**, Figure 2.5) or a hydrogen bonding group (**7**) sees an increase of the first association constant by up to 2 orders of magnitude compared to the neutral control complex (**8**), highlighting how careful ligand design can modulate the affinity for the analyte.[13]

In this context, Sørensen and co-workers have recently investigated the effects of both lipophilicity and charge on the binding affinities and sensing performance of Eu-DO2A and -DO3A derivatives (**9** and **10**, **11**, respectively, in Figure 2.6) towards relevant oxyanions in aqueous solutions.[14, 15] Interestingly, the charge of the complex influences the binding affinity but not the selectivity towards mono- or polyanionic species (e.g. L-lactate versus L-malate and citrate, Figure 2.6), indicating that coulombic interactions do not play a role and the residual charge is shifted on the Eu(III) centre, merely strengthening the Eu-anion interaction.[14] However, the authors report that the presence of a lipophilic side chain in the ligand scaffold

(complex **11** versus **10**) improves the binding of all oxyanions selected and a significant increase in selectivity for mono-anionic L-lactate over the trianionic citrate is observed.[15]

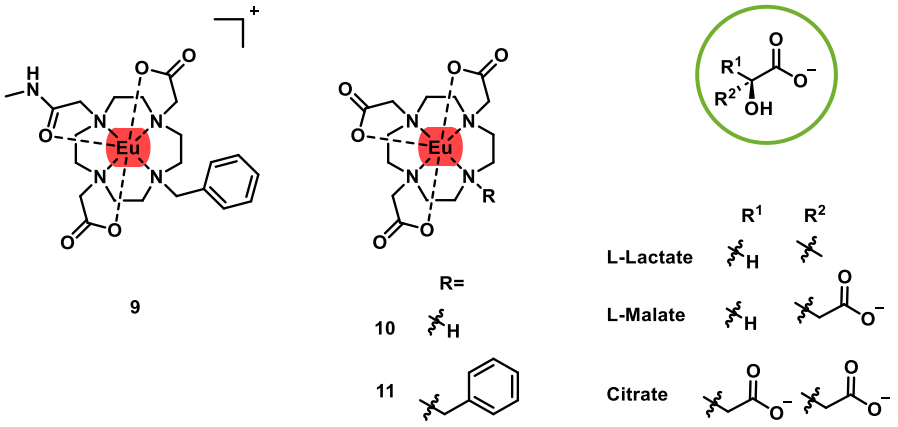


Figure 2.6 – Chemical structures of the Eu(III) complexes reported by Sørensen and co-workers for the detection of oxyanions. Only the oxyanions mentioned here are reported in the green circle.[14, 15]

The selective detection of adenosine monophosphate (AMP) over the respective di- and tri-phosphates (ADP and ATP, respectively) is reportedly challenging. Butler and co-workers have presented a probe scaffold based on a Eu-DO2A derivative (**12** and **13** Figure 2.7).[16] In their work, a 8-(benzyloxy)quinoline pendant unit was introduced for the steric hindering of the axial position in the coordination sphere of Eu(III). As a consequence, only the smaller inorganic phosphate and AMP could access the binding pocket, allowing for the time gated and selective measurement of phosphate in serum (**12**) and the monitoring of AMP production in a simulated biological environment (**13**).[16] An alternative approach has been reported by Sahoo *et al.*, where a dinuclear Eu(III) helicate complex with an unfilled coordination sphere is presented (**14**, Figure 2.7, q=4). Interestingly, the affinity of the complex for AMP over anionic species such as ADP and ATP, among others, was ascribed to the ideal distance between the two Eu(III) centres to allow the bridging of AMP, thus imparting impressive selectivity to the probe.[17]

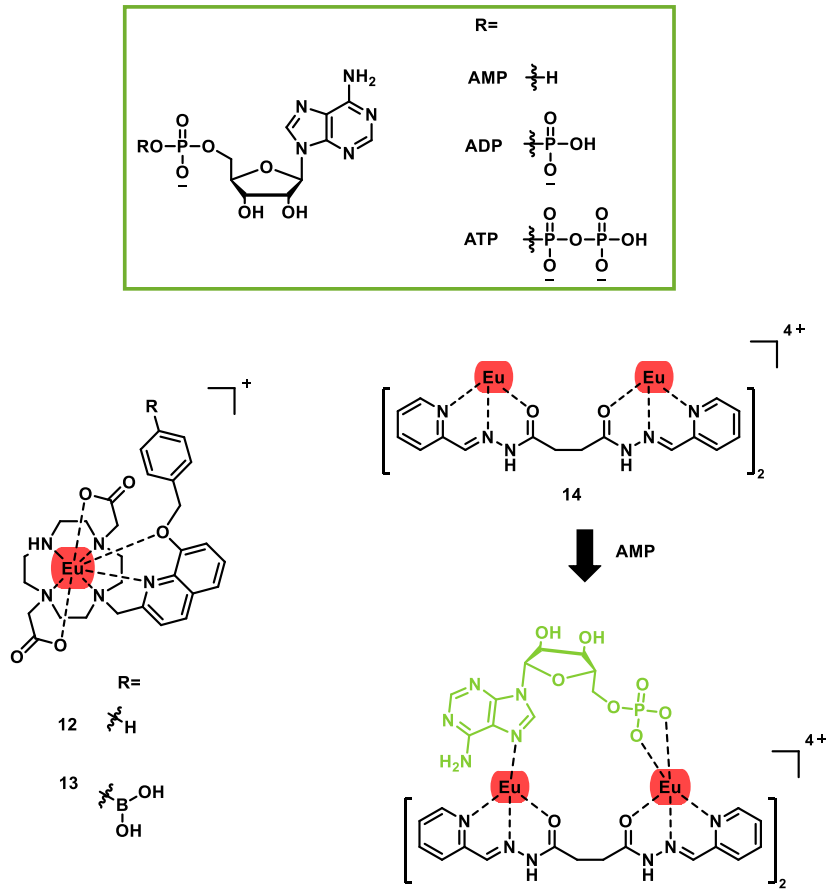


Figure 2.7 – Chemical structures of the Eu(III) complexes reported by Butler and co-workers (**12**, **13**) and Sahoo *et al.* (**14**) for the detection of AMP (chemical structure in green square).[16, 17] The coordination of AMP (green) to **14** is depicted here.[17]

2.1.2 Detection of fluoride with luminescent lanthanide(III) complexes

Fluoride (F^-) is essential for our wellbeing, having important roles in the mineralisation of bones and being commonly added to drinking water. However, high consumptions of F^- can lead to disease (e.g. skeletal fluorosis), with the safe consumption range being 20-210 µM, according to the world health organisation (WHO).[18, 19] For this reason, the detection of F^- is of high interest. Most current sensing approaches are based on either ion chromatography, ion selective electrodes or fluorescent chemosensors, the latter mostly based on organosilicon or boronic acid detection units.[20-22]

F^- anions are small and highly electronegative, with sizes comparable to the ones of OH^- (1.33 Å for both). The coordination of F^- to lanthanides(III) is well known but the development of sensing platforms is often hindered by the high free hydration energies of F^- ($-\Delta G°_{hydr}$=465 kJ mol^{-1}), leading to relatively small binding constants in H_2O (LogK≈3).[23]

Charbonnière and co-workers have reported a series of ligands to improve the affinity of positively charged lanthanide(III) complexes for F^- detection in H_2O by formation of supramolecular assemblies. By monitoring variations in relative intensity of the hypersensitive $^5D_0 \rightarrow {}^7F_2$ transition and luminescence lifetime values (≈2-fold increase) as sensing readouts of Eu(III) complexes **15** and **16** (Figure 2.8), the authors observed higher association constants for the first complex (LogK ≈ 2.9 vs 1.4 for **15** and **16**, respectively).[24, 25] This effect was correlated to the formation of a dimer with F^- bridging two Eu(III) complexes in the solid state, solely observed for complex **15**. This supramolecular assembly was ascribed to the presence of CH···F hydrogen bonding and π-π stacking, both driven by the presence of the pyridyl units in **15**. The observation of the dimer assembly in solution was achieved with complex **17**, where such stabilisation of the assembly was driven by both the single charge to reduce electrostatic repulsions and the NH···O interaction between the two complexes in the dimer.[26] A Logβ≈13.0 was reported, a staggering improvement from the previous examples, as well as a detection limit of 24 nM. This approach has been used for the development of alternative F^- sensing readouts by the group. These include a ratiometric response by means of FRET from Tb(III) to Eu(III) in heterodimers of **17** and the increase in upconversion luminescence of the Er(III) **17** derivative upon formation of the dimeric assembly.[27, 28]

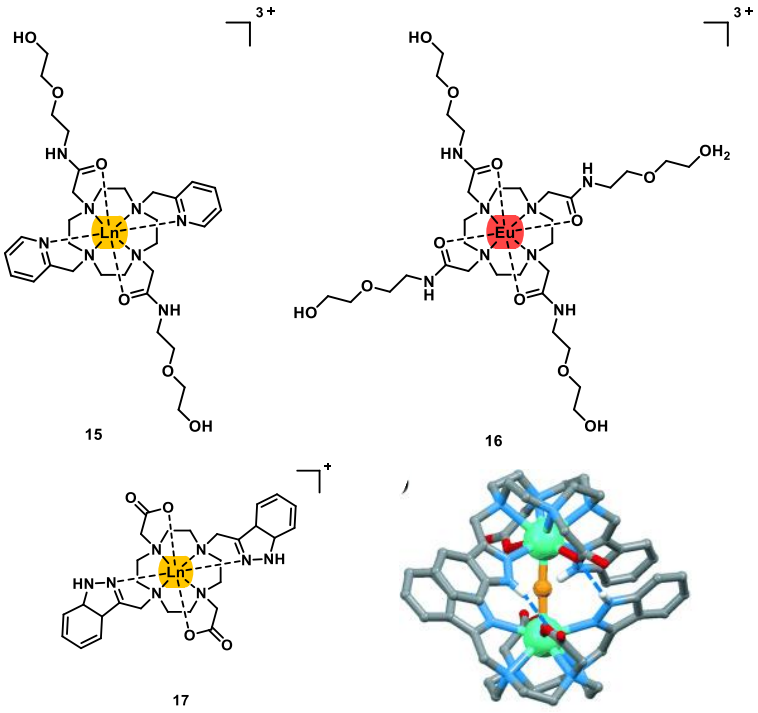


Figure 2.8 – Chemical structures of the complexes reported by Charbonnière and co-workers. (Ln=Eu(III), Tb(III), Er(III)).[24-28] Crystal structure of the dimer formed by two Eu(III) complexes (**17**, Eu(III) is green, oxygen red, nitrogen blue, carbon grey and hydrogen white) bridged by F^- (orange). The image was taken from [26].

Faulkner and co-workers have extensively examined the effects of F^- coordination on the spectroscopic properties of tricationic lanthanide (III) complexes (**18-25**, Figure 2.9).[29-32] F^- coordination by exchange of the single axial H_2O molecule was confirmed by both NMR and luminescence spectroscopies. Indeed, the authors report an increase in the luminescence lifetime of Eu(III) complex **18** (from 0.54 ms to 1.07 ms), as well as significant variations in the profile and relative intensities of the $^5D_0 \rightarrow {}^7F_J$ (ΔJ=1, 4) emission transitions, both associated with F^- coordination. Interestingly, the slow exchange between hydrated and F^- coordinated species of **18** on the NMR timescale allowed for the observation of the sets of peaks for both species. An inversion of the characteristic anisotropic electronic distributions of the paramagnetic metal complexes was also observed which, alongside the decrease in Stark splitting of the $^5D_0 \rightarrow {}^7F_1$ transition, was ascribed to the profound effects of F^- coordination on the local crystal field of the metals.[29, 30] The effect of amide substituents on the association

constants of the complexes was also explored. Although relatively low association constants were observed for all complexes (**18**-**25**, LogK=1.0-1.9), higher affinities could be identified for the complexes bearing electron withdrawing substituents (**23**-**24**) due to the higher residual charge on the lanthanide(III), while substitution of all pendant acetamide groups with picolyl units (**25**) led to considerable improvements in the binding constant (LogK≈5).[31, 32]

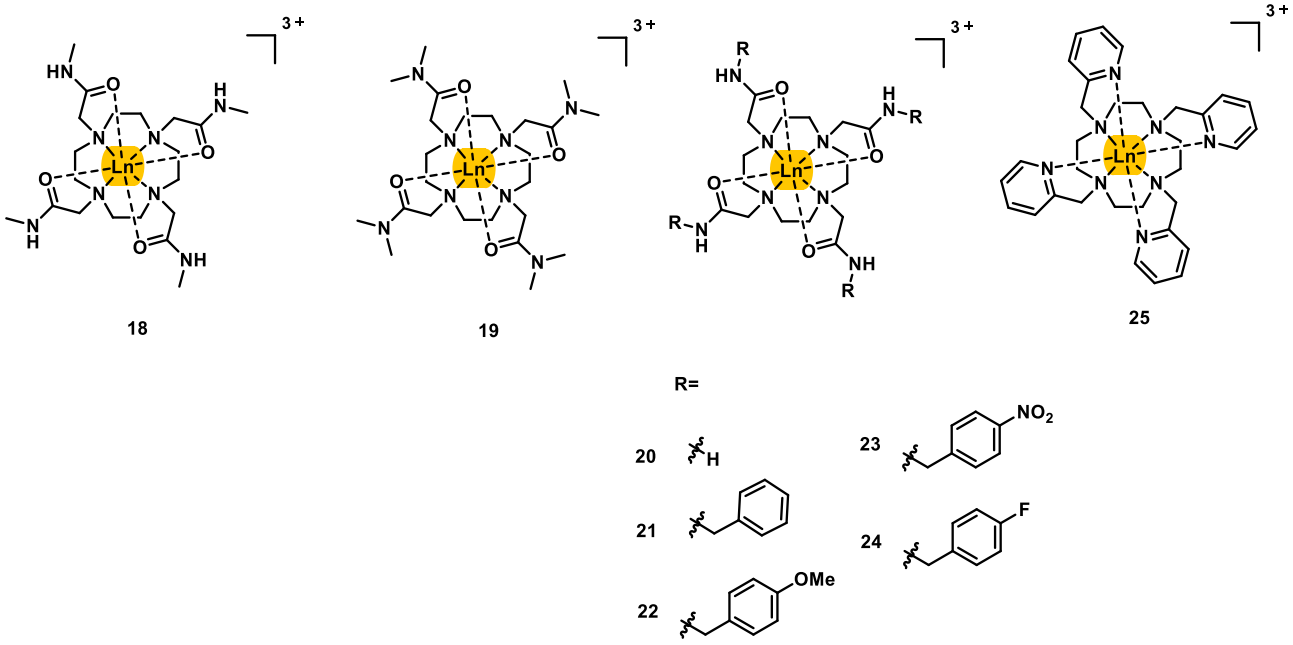


Figure 2.9 – Chemical structures of the complexes reported by Faulkner and co-workers. (Ln=Eu(III), Tb(III), Nd(III), Yb(III), Ce(III), Pr(III), Sm(III)).[29-32]

In a recent example, the group reported neutral dinuclear lanthanide(III) complexes (**26**, **27**, Figure 2.10) for the detection of Cl^- ions in H_2O. Here, F^- coordination was employed to elucidate the binding mechanism, indicating the presence of three separate binding events in both H_2O and MeOH (Figure 2.10): 1. bridging of one F^- between both metal centres (K_1), 2. coordination of one F^- to each lanthanide(III) (K_2) and 3. additional bridging of one F^- to each metal (K_3). A first association constant of $K_1=6x10^5$ M^{-1} was obtained for **26** in deionised H_2O, while a single and considerably smaller constant ($K=693$ M^{-1}) was calculated for the control

mononuclear complex **28**, highlighting the importance of having both metal centres to improve binding.[33]

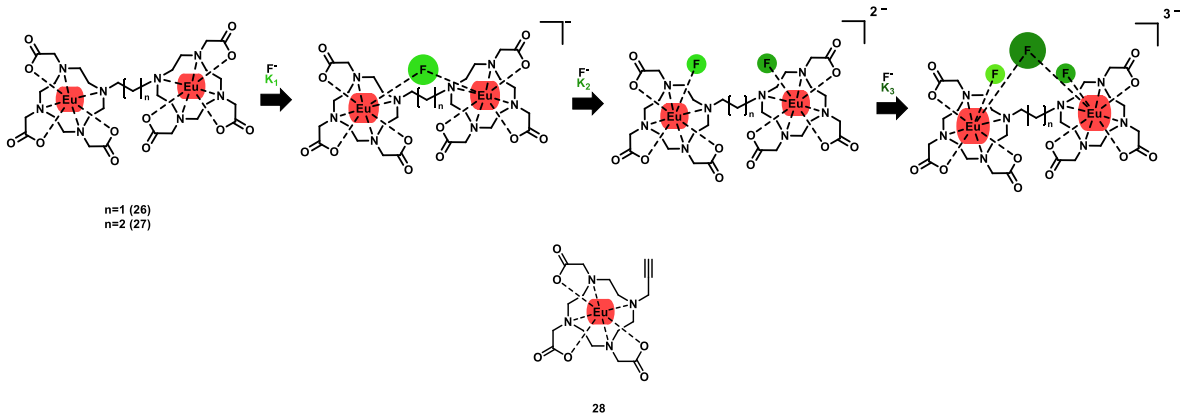


Figure 2.10 – Chemical structures of dinuclear complexes **26**, **27**, as well as control mononuclear complex **28** reported by Faulkner and co-workers with representation of F^- coordination events for **26**/**27**.[33]

In an alternative approach from Beer and co-workers, a Eu(III) [2]rotaxane (**29**, Figure 2.11) was presented for the detection of anions. Here, a topological cavity produced by the interlocked units could be accessed upon removal of the template NO_2^-, offering a binding site for the recognition of anions (i.e. Cl^-, F^-, acetate and NO_2^-). Interestingly, F^- afforded the most intense effects on Eu(III) luminescence, with a decrease in emission signal down to 10% of the initial value, as well as a 2-fold increase in luminescence lifetime and a significant increase in the relative intensity of the hypersensitive $^5D_0 \rightarrow {}^7F_2$ transition. These effects were observed in a 99:1 acetone/H_2O mixture, with tetrabutylammonium fluoride (TBAF) as source of F^-, and ascribed to both the coordination of F^- to the Eu(III) centre, as well as its interaction with the organic moiety to disrupt the energy transfer processes. A $K=2.42 \times 10^5$ M^{-1} was calculated for the [2]rotaxane, while a smaller $K=9.69 \times 10^4$ M^{-1} was obtained for the macrocycle alone (red unit in **29**), indicating the importance of the interlocked architecture for improved binding constants.[34]

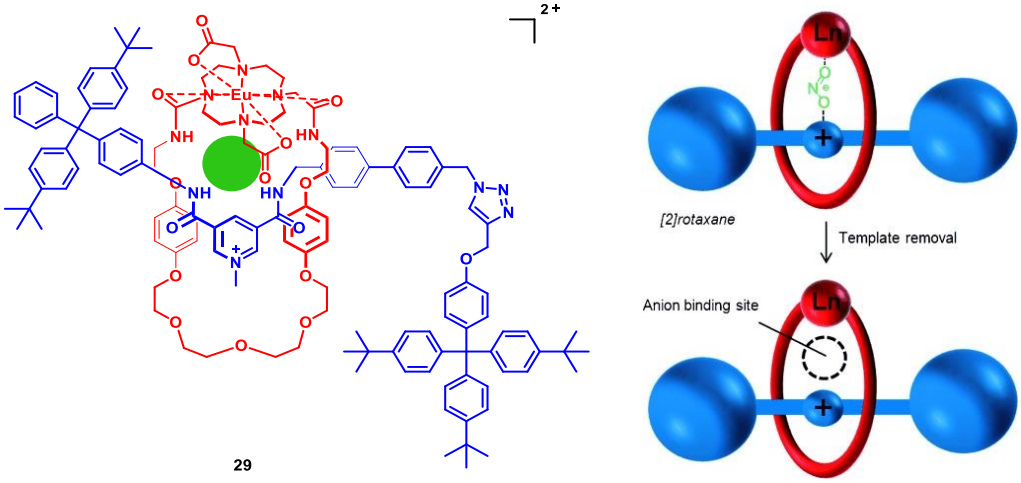
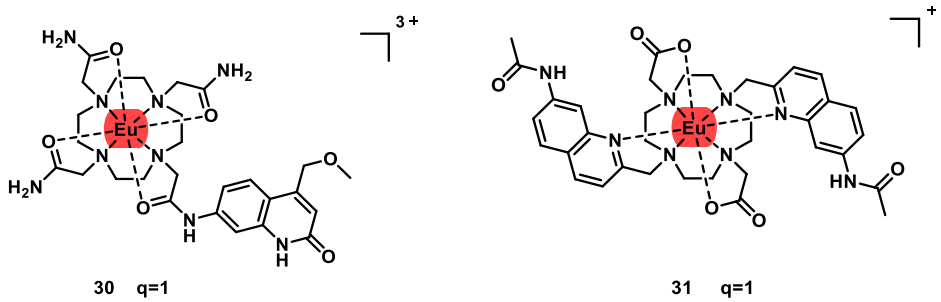


Figure 2.11 – Chemical structure (**29**, left) of the [2]rotaxane reported by Beer and co-workers with sketch (right) of the system for F^- sensing at the topological cavity (green circle in **29**) upon removal of the NO_2^- template. The sketch on the right was taken from [34].

Borbas and co-workers have investigated the luminescence response to F^- of a series of tri- and tetraazamacrocyclic Eu(III) complexes bearing carbostyril antennae.[35] After assessing the effect of the macrocycle size, as well as the secondary or tertiary nature of the amide groups and substituents on the light harvesting unit, the authors report a maximum increase in emission intensity of 25-fold with complex **30** (Figure 2.12). Interestingly, this is attributed not only to the substitution of quenching oscillators by F^-, but also to the stabilisation of the (III) oxidation state against reduction by the photosensitising antenna.[35] Butler has presented a charged Eu(III) complex (**31**, Figure 2.12) for the determination of F^- concentration in drinking water within the relevant WHO recommended range (20-210 µM).[23] Upon addition of F^-, an increase in luminescence lifetime from 0.49 ms to 1.13 ms was recorded, as well as a 9-fold emission increase and variation of the spectral profile, as already observed for other macrocyclic Eu(III) complexes, with an association constant of LogK=4.1. Notably, the probe was selective for F^- even in the presence of relevant competing anions at high concentrations (i.e. Cl^-, HPO_4^{2-}, NO_3^- and SO_4^{2-}, 5 mM), with the quantification of F^- concentrations in drinking water correlating strongly to the values obtained using a fluoride-selective electrode. Such an impressive

performance was ascribed to both the strong affinity of Eu(III) for F^- and the presence of CH···F interactions from the quinoline units to stabilise the assembly. Furthermore, the same Eu(III) complex **31** was employed in a recent example to track the transmembrane transport of F^- into liposomes. [36] In the reported approach, Eu(III) probe **31** was encapsulated in large unilamellar vesicles and a range of synthetic F^- transporters were inserted in the liposomal membrane. As expected, the luminescence readout associated with F^- detection could be recorded only in the presence of the transporters, allowing for the evaluation of their performance. Importantly, the strong fluorescence of the synthetic F^- transporters did not prevent the accurate interpretation of Eu(III) spectra, as the long luminescence lifetimes of Eu(III) allowed for time-gated luminescence measurements, excluding interfering short lived fluorescence.[36]



30 q=1 **31** q=1

Figure 2.12 – Chemical structures of one of the complexes reported by Borbas and co-workers (**30**) and the complex reported by Butler and co-workers (**31**).[35, 36]

The detection of F^- with luminescent lanthanide(III) complexes can also rely on the interaction with the ligand scaffold, thus modulating the energy transfer from the sensitising units to the lanthanide(III), as observed in Section 1.1. Examples of this approach have vastly relied on the interaction with F^- of NH groups or boron containing units. Chen *et al.* have proposed a quadruple stranded tetranuclear lanthanide(III) helicate (**32**), whose chirality and luminescence offer a dual readout for F^- sensing. Indeed, the response to F^- by interaction with the NH groups in the ligand (orange unit, Figure 2.13) can be monitored in either MeOH or

CH_3CN as both a variation in the CD spectra of the La(III) derivative or as an increase in the NIR emission of the respective Nd(III) complex. The authors suggest that the formation of supramolecular assemblies upon binding of F^- contributes to the observed sensing readouts.[37] The interaction of F^- with the imidazole group in the ancillary 1,10-phenanthroline ligand of **33** and **34** leads to a switch-off effect of both Eu(III) and Tb(III) luminescence, respectively in DMSO with TBAF as source of F^-. In this example, the luminescence decrease is ascribed to the decomposition of the complex, confirmed by the reinstated blue fluorescence (450 nm) of the ligand at 5 equivalents of F^- (i.e. 5 µM) due to absence of energy transfer processes.[38]

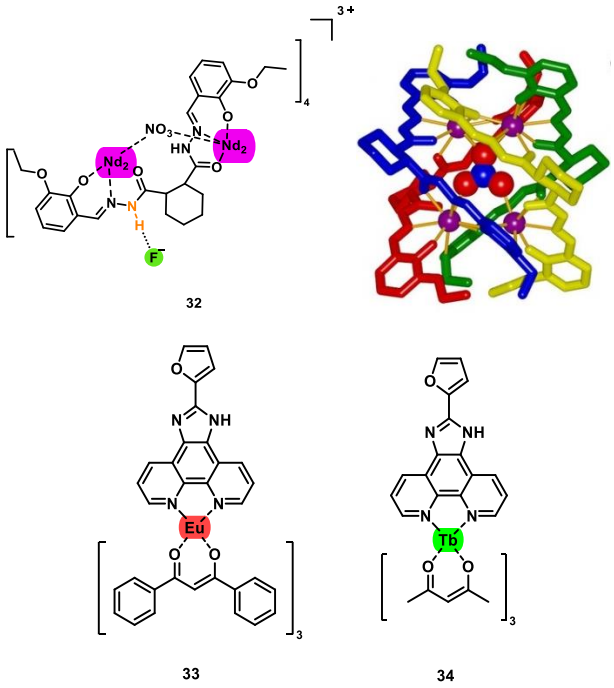


Figure 2.13 – Chemical structure of the Nd(III) derivative of tetranuclear and quadruple stranded complex **32** reported by Chen *et al.* with the respective crystal structure (left).[37] Nd(III) atoms are represented as purple, while the nitrogen and oxygen atoms of the bridging NO_3^- molecule are in blue and red, respectively. The image of the crystal structure was taken from [37]. Chemical structures of complexes **33** and **34** reported by Zheng and co-workers.[38]

Wang and co-workers have investigated the introduction of boron units on Eu(III) and Tb(III) complexes for the development of F^- sensing probes (Figure 2.14).[39, 40] The triarylboryl functionalisation of both β-diketonate and dipicolinic acid ligands produced complexes **35**-**36**

and **37**-**39**, respectively, which could respond to the addition of F^- (as TBAF, in THF) as either an increase or decrease in their luminescence. This was ascribed to the modulation of the triplet state and ILCT energies upon binding of F^- to the boron units, thus tuning the overall emission efficiency of the complexes. The observed association constants were comparable to the ones of other boron based F^- sensors (LogK≈4) and, importantly, upon embedding in polymethyl methacrylate (PMMA) films, complexes **37**-**39** preserved their sensing capabilities.[39, 40]

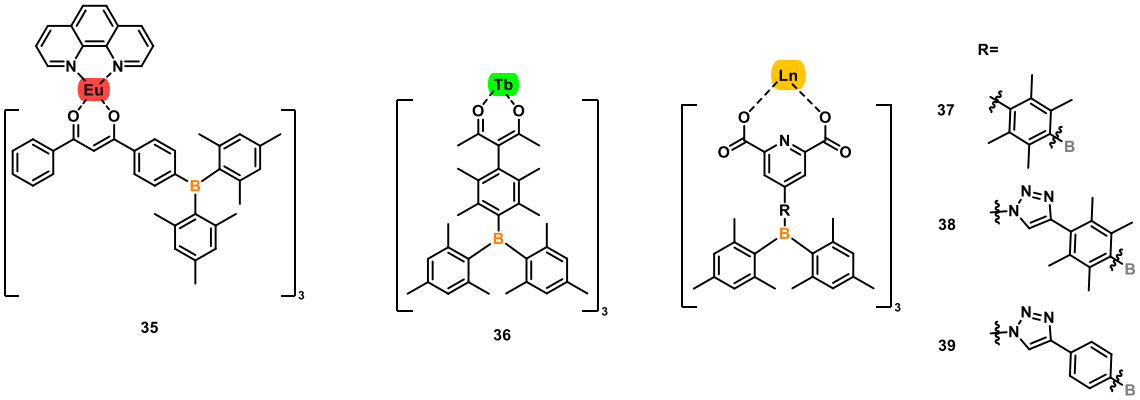
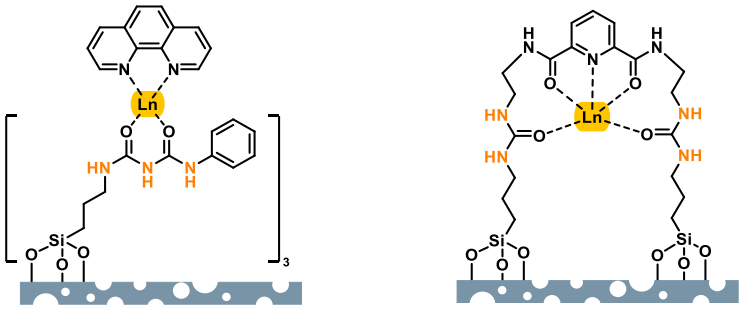


Figure 2.14 – Chemical structures of some of the β-diketonate (**35**-**36**) and dipicolinic acid (**37**-**39**) complexes reported by Wang and co-workers containing boron units (orange) for binding of F^-. Ln=Eu(III), Tb(III).[39, 40]

The incorporation of F^- sensing probes to solid substrates is highly desirable, as such materials offer easier handling, storage and durability. The interaction between F^- and the NH units in the phenylurea derivative of **40** (Figure 2.15) reportedly led to a luminescence switch-off effect (66-fold for Eu(III) and 77-fold for Tb(III)) due to the deactivation of energy transfer processes, which was not observed for other competitive ions (including Cl^-, Br^- and NO_3^-, among others) The complexes were anchored on SiO_2 to obtain a luminescent mesoporous sensing material and the detection was conducted in CH_3CN with TBAF as source of F^-, displaying LODs of 1.3 µM and 6.1 µM for the Eu(III) and Tb(III) derivatives, respectively.[41] An analogous approach was also reported with complex **41** anchored on amorphous and mesoporous SiO_2

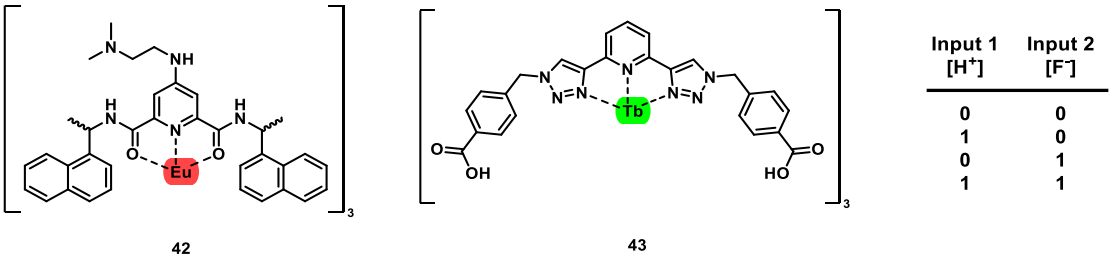
nanoparticles (300 nm). Upon addition of TBAF in DMSO, both systems display deactivation of both Tb(III) and Eu(III) luminescence, attributed to NH···F interactions and quenching of the energy transfer processes, with LODs for Eu(III) and Tb(III) luminescent mesoporous nanoparticles of 25 nM and 34 nM, respectively.[42]



40 41

Figure 2.15 – Chemical structures and sketches of complexes **40** and **41** on mesoporous SiO_2 nanostructures for the detection of F^-. Ln=Eu(III), Tb(III).[41, 42]

Gunnlaugsson and co-workers have reported the fabrication of logic gate mimics responsive to H^+ or F^-. Eu(III) and Tb(III) complexes **42** and **43**, respectively, were embedded in a poly(hydroxyethyl methacrylate-co-methyl methacrylate) matrix and the swelled gels were immersed in solutions of HCl (2 mM) or TBAF (1 mM) in MeOH for 20 minutes before readout. Here, the choice of a 2,3-bis(1,2,3-triazol-4-yl)picolinamide ligand, well known for its strong affinity to F^-, leads to the disassembly of the Tb(III) complex **43** in the presence of F^- to reinstate the ligand fluorescence, with no modulation of the red Eu(III) luminescence of complex **42**. In acidic environments, however, the minimisation of photoinduced electron transfer (PET) processes by the pendant amine in **42** affords enhanced Eu(III) luminescence and a total of four outputs (Figure 2.16) can be recorded with the combined system.[43]



Input 1 [H^+]	Input 2 [F^-]
0	0
1	0
0	1
1	1

Figure 2.16 – Chemical structures of complexes **42** and **43** reported by Gunnlaugsson and co-workers for the detection of H^+ and F^- with luminescent soft materials. The possible combinations of the logic gate mimic are reported in the table on the right.[43]

The incorporation of both Eu(III) and Tb(III) in a metal-organic framework (MOF) for the detection of F^- in drinking water was reported by Zeng *et al.*, affording a ratiometric response that could be detected by monitoring the Red Green Blue (RGB) value with a smartphone camera. The readout is justified as following: coordination of F^- to Eu(III) for increased red emission alongside interaction of F^- with the ligand (4,4',4''-s-triazine-2,4,6-triyltribenzoate, **TATB**, Figure 2.17) to activate back energy transfer processes for Tb(III) and decrease in green Tb(III) luminescence, thus altering the RGB value of the system. Importantly, the LOD was found to be below the maximum F^- limit in drinking water recommended by the Environmental Protection Agency (2.0 ppm).[44]

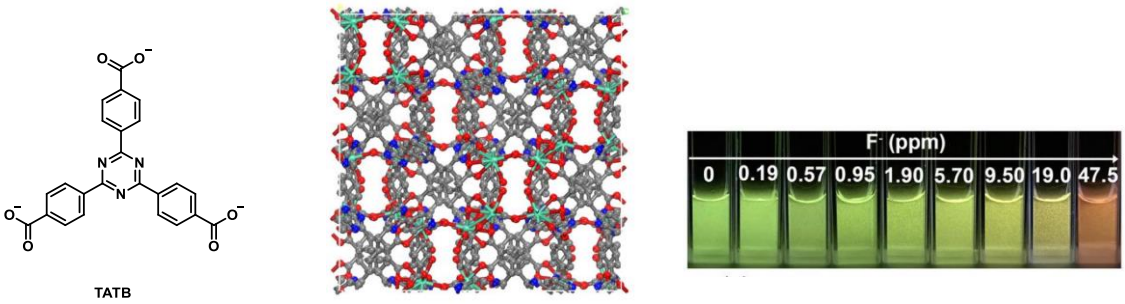
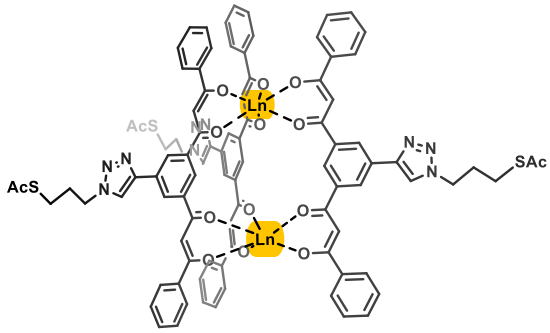


Figure 2.17 – Chemical structure of the trianionic form of the TATB ligand with images of the crystal structure of the Tb(III) MOF (Tb(III) green, oxygen green, nitrogen blue and carbon grey) and of the luminescence of the combined Eu(III)/Tb(III) MOFs upon illumination at 310 nm and at increasing concentrations of F^- in water. Both images were taken from [44].

2.1.3 Aims of the project

In this project, we first design and synthesize a novel dinuclear bis β-diketone ligand (**SAcbisDBM**) alongside its respective triple stranded Eu(III), Gd(III), Yb(III) and Nd(III) complexes (**Ln_2SAcbisDBM$_3$**, Figure 2.18). The **bisDBM** ligand scaffold is selected due to its reported sensitisation of both visible (Eu(III)) and NIR (Nd(III)) luminescence.[45] The inclusion of a thioacetate unit in the **SAcbisDBM** ligand imparts further functionality to the complexes, allowing for the anchoring on the surface of metallic substrates. Here, a spacing unit is included to limit the quenching arising from the metal surface of e.g. Au nanoparticles or surfaces.



Ln_2SAcbisDBM$_3$

Figure 2.18 – Sketch of the tridimensional structure of **Ln_2SAcbisDBM$_3$** complexes. Ln=Eu(III), Gd(III), Yb(III), Nd(III).

Finally, we aim to evaluate **Eu_2SAcbisDBM$_3$** as a luminescent probe. Due to the six-coordination of triple stranded bis β-diketonate complexes, an unfilled coordination sphere is present (q≈3 for **Eu_2bisDBM$_3$**), allowing for exchange and recognition of analytes.[45] We select F^- as representative analyte, due to the strong optical response it has elicited in other unsaturated Eu(III) complexes (section 2.1.2). By comparing the response with the ones of the mononuclear derivative (**EuDBM$_3$**) and the unfunctionalised complex (**Eu_2bisDBM$_3$**, Figure 2.19), we also aim to elucidate the impact of dinuclearity and the presence of a surface active unit on the response to F^- coordination.

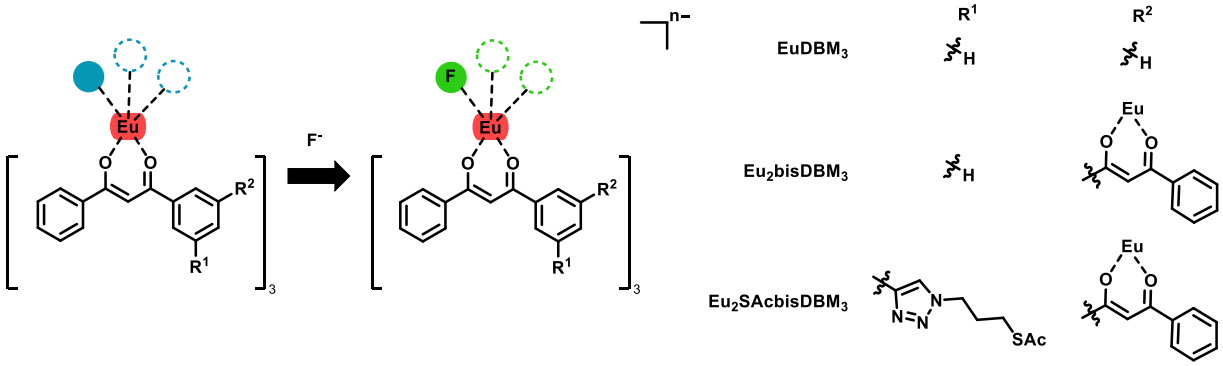


Figure 2.19 – Chemical structures of the mononuclear **EuDBM$_3$** and dinuclear **Eu$_2$bisDBM$_3$** and **Eu$_2$SAcbisDBM$_3$** complexes. The mechanism for F^- detection is depicted as exchange of coordinated H_2O molecules (blue) with F^- (green) to form negatively charged species.

2.2 Results and discussion

2.2.1 Synthesis of the surface active SAcbisDBM ligand

In this work, both the **SAcbisDBM** ligand the previously reported **bisDBM** ligand were synthesised. The synthesis of the novel **SAcbisDBM** ligand is reported here.

The designed **SAcbisDBM** ligand is prepared in a 4-step synthesis (Figure 2.20), relying on the copper-catalysed azide alkyne cycloaddition (CuAAC, i.e. click reaction) between the alkyne **bisDBM** derivative (**5**, Figure 2.20) and the azide of compound **6** to incorporate the surface active unit. Such a synthetic approach is extremely versatile, allowing for the introduction of any unit in a one step reaction without further modification to derivative **4**.

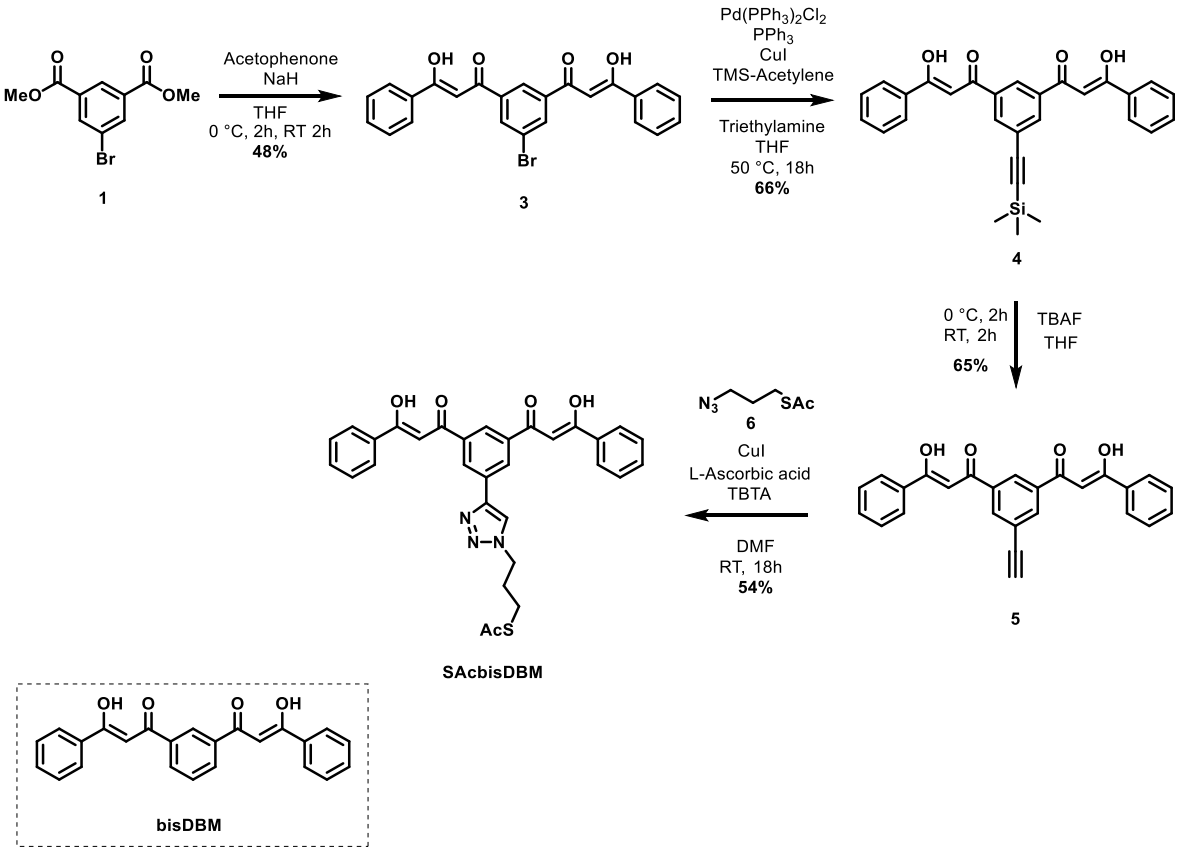


Figure 2.20 – Synthesis route to **SAcbisDBM**. The control ligand **bisDBM** is reported below.

β-Diketones are commonly synthesized *via* Claisen condensation.[46] The α-proton of acetophenone (**2**) is removed by a strong base (i.e. sodium hydride), to give its enolate form and drive the nucleophilic attack on the esters of dimethyl 5-bromoisophthalate (**1**).

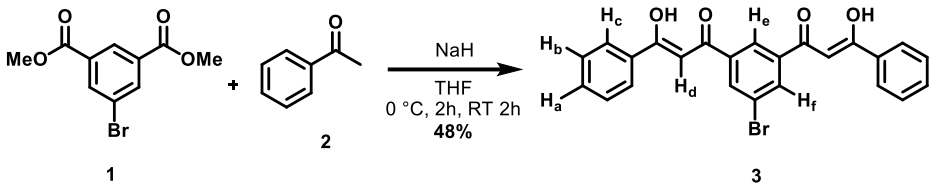


Figure 2.21 – Synthesis of compound **3**.

The synthesis was adapted from the reported procedure for **bisDBM**, increasing both the concentration of **1** in the reaction mixture as well as the equivalents of **2** and NaH to optimise the yield (from 14-17% to 45-50%).[45] Compound **3** was obtained in moderate yields after purification by recrystallisation, and successful formation of the bis β-diketone was established by ^{1}H-NMR spectroscopy. Here, both the presence and integration (2H) of the H_d protons are characteristic of the formation of a bis β-diketone compound (Figure 2.41, Appendix).[45] Furthermore, by comparing the ^{1}H-NMR spectrum of compound **3** with the one of **bisDBM**, we observe significant variations to the chemical shifts of H_e, H_f and H_d protons (-0.1 ppm, +0.09 ppm and -0.05 ppm, with "+" and "-" representing down- and up-field shifts, respectively). The downfield shift of the H_f protons, in particular, is representative: due to the proximity of H_f to the bromo substituent, these protons are the most affected by the deshielding effect given by such an electronegative atom.[47] ESI^{-}-MS shows the correct isotope pattern for a bromo compound (Figure 2.47, Appendix) and further characterisation has been obtained by ^{13}C-NMR, 2D NMR and IR (section 2.5.4.1, Appendix).

Compound **3** is then employed in a Sonogashira reaction for introduction of C-C bonds at the aryl halide site and conversion to the TMS protected alkyne **4**. The coupling is carried out in the typical mild conditions, with palladium and copper catalysts in an anaerobic and dark environment.[48, 49]

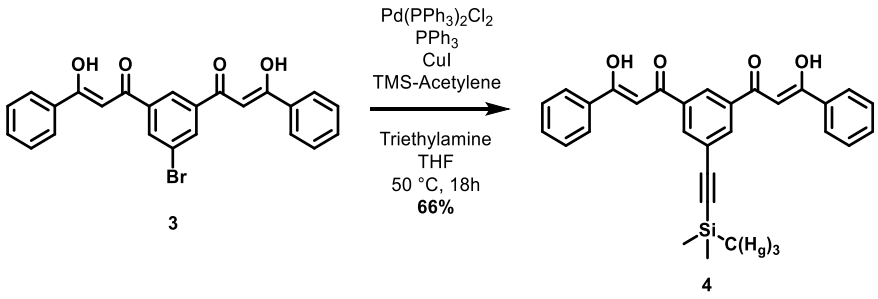
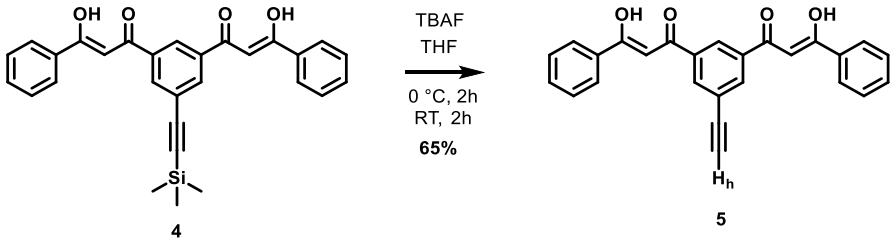


Figure 2.22 – Synthesis of compound **4**.

After purification by column chromatography, compound **4** was isolated in 66% yield. The successful formation of the coupled compound can be monitored by the presence and relative integration (9H) of the H_g protons in the ^{1}H-NMR spectrum. These are found in the upfield region at 0.31 ppm, characteristic of TMS groups, where the strong shielding effect of silicon results in such low chemical shifts. Furthermore, as also seen above, we find that the peaks for the H_e, H_f and H_d protons are shifted, when compared to compound **3** (+0.03 ppm, -0.05 ppm and +0.04 ppm, Figure 2.48, Appendix).[47] The ^{13}C-NMR spectrum of **4** displays the appearance of three new peaks at 103.23 ppm, 96.97 ppm and 0.00 ppm (Figure 2.51, Appendix). By analysis of the respective HSQC and HMBC spectra (Figures 2.53 and 2.54, Appendix), these have been attributed to the two alkyne carbons and the methyl groups in the TMS unit, respectively. Finally, ESI$^-$-MS of **4** lacks the isotope pattern typical of bromo containing molecules such as **3**, and IR spectroscopy displays the presence of a strong peak at

837 cm^{-1}, attributable to the CH_3-Si stretching in compound **4**. The compound has also been characterised by UV-Vis absorption spectroscopy (section 2.5.4.2, Appendix).

Deprotection of the TMS group is carried out by reaction of **4** with TBAF. Silicon is well known for its high affinity to fluoride, with the Si-F bond being more than 1.7 times stronger than the Si-C bond.[50]



4 5

Figure 2.23 – Synthesis of compound **5**.

Successful deprotection can be confirmed by the presence of the alkyne proton H_h at 3.24 ppm and disappearance of the TMS protons in the ^{1}H-NMR spectrum (Figure 2.56, Appendix). This is also confirmed by examination of the ^{13}C-NMR spectrum (Figure 2.57, Appendix), where the C_h peak is observed at 79.39 ppm and the peak for the second alkyne carbon displays a shift from 103.23 ppm in **4** to 82.10 ppm in **5**. Further confirmation of the successful conversion to **5** is also given by IR spectroscopy where, alongside the absence of the CH_3-Si stretching at 837 cm^{-1}, a new band at 3269 cm^{-1} appears, ascribed to the ≡C-H stretching. After purification by column chromatography, compound **5** was obtained in 65% yield and was further characterised by 2D NMR and UV-Vis absorption spectroscopies and ESI^--MS (section 2.5.2.3, Appendix).

To introduce the surface active unit and obtain target ligand **SAcbisDBM**, a click reaction is conducted between the terminal alkyne of **5** and the azide of S-(3-azidopropyl)thioacetate **6**. Excess L-Ascorbic acid is added to the reaction mixture to inhibit the conversion of Cu(I) to

Cu(II), which could coordinate to the hard oxygen atoms of the ligand and lead to more challenging purification steps. After purification by column chromatography, target ligand **SAcbisDBM** is obtained in 54% yield.

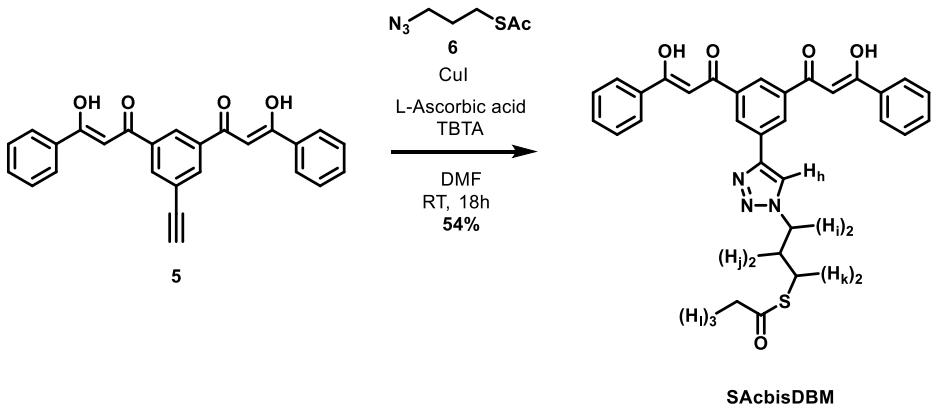


Figure 2.24 – Synthesis of **SAcbisDBM**.

The formation of the product can be established by the absence of the alkyne proton and the presence and matching integration of the propyl chain H_i, H_j and H_k protons in the ^{1}H-NMR spectrum (Figure 2.63, Appendix). The 1,2,3-triazole proton H_h is commonly observed in the aromatic region and, in our case, overlaps with the H_c protons of the **bisDBM** scaffold at 8.07-8.05 ppm. This is inferred from both the integration of the peaks in the ^{1}H-NMR and the presence of a new peak at 120.89 ppm in the ^{13}C-NMR spectrum (Figure 2.64, Appendix). From 2D HSQC spectroscopy (Figure 2.66, Appendix), we find that the peak couples with the ones in the 8.07-8.05 ppm region of the ^{1}H-NMR spectrum. Further proof of the completion of the click reaction is given by IR spectroscopy. The disappearance of the alkyne ≡C-H peak of **5** at 3269 cm^{-1}, the absence of the N_3 peak of **6** at 2092 cm^{-1} and the presence of the thioacetate C=O peak at 1691 cm^{-1} all support the conversion to the **SAcbisDBM** ligand (Figure 2.62, Appendix). Finally, the **SAcbisDBM** ligand absorbs light at the characteristic range for β-diketonates, with a band at 357 nm attributable to the singlet-singlet π→π* absorption. This is identical to the one of the parent scaffold **bisDBM** and the molar absorption coefficient (**ε**)

of **SAcbisDBM** in DMF is equivalent to the one of **bisDBM** (5 x 10^4 M^{-1} cm^{-1} and 4 x 10^4 M^{-1} cm^{-1}, respectively).

2.2.2 Synthesis and characterisation of Ln_2SAcbisDBM$_3$ complexes

The **SAcbisDBM** ligand is employed in the complexation reaction with the trichloride salt of the desired lanthanide(III) to give **Ln_2SAcbisDBM$_3$** complexes. The complexation follows a metathesis reaction mechanism and the typical conditions for β-diketones are employed here.[45, 46] $LnCl_3 \cdot 6H_2O$ and **SAcbisDBM** are reacted in a 2:3 ratio, respectively, and in presence of triethylamine to promote deprotonation of the **SAcbisDBM** ligand and coordination of the lanthanides(III) at the diketonate pockets. The desired **Ln_2SAcbisDBM$_3$** complexes are isolated as pale yellow powders in moderate yields (25-30%, Ln=Eu(III), Yb(III), Nd(III), Gd(III)).

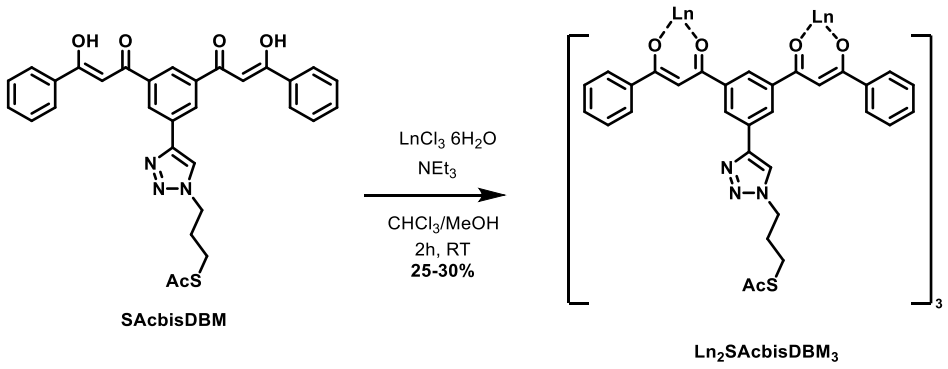


Figure 2.25 – Synthesis of **Ln_2SAcbisDBM$_3$**. Ln=Eu(III), Gd(III), Yb(III), Nd(III).

Considering the Eu(III) derivative, upon complexation a small red shift (2 nm, λ_{max}: 359 nm) is observed in the absorption maximum of the **SAcbisDBM** ligand in DMF, accompanied by a change in the shape of the band (Figure 2.26). This is attributed to the perturbation induced by the coordination to the Eu(III) ions.

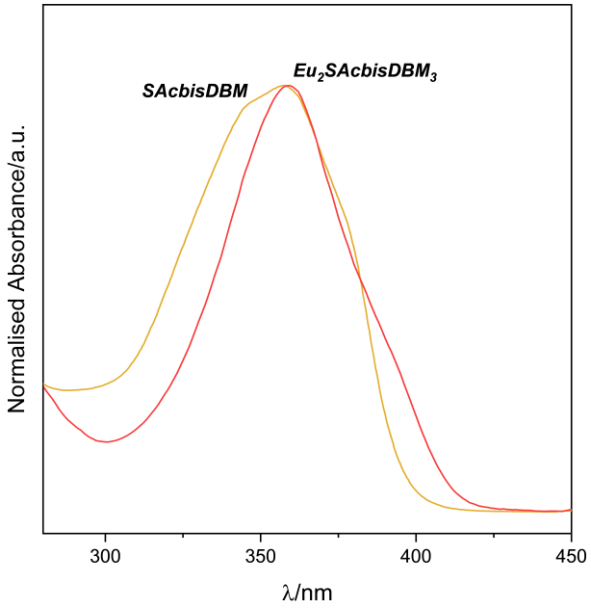


Figure 2.26 – Overlaid and normalised absorption spectra of **SAcbisDBM** (orange) and **Eu_2SAcbisDBM$_3$** (red) in DMF.

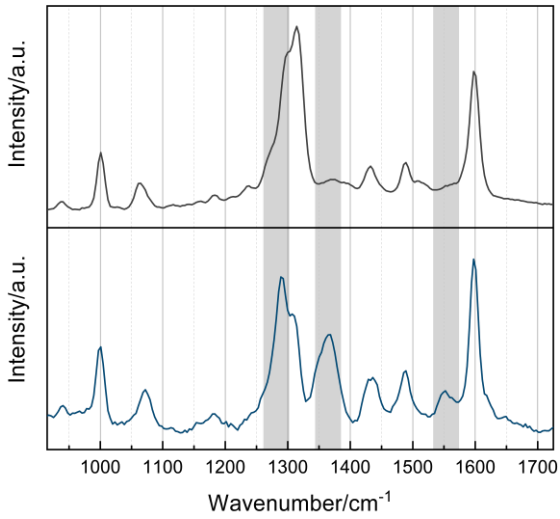
Furthermore, the **ε** of all **Ln_2SAcbisDBM$_3$** derivatives match well with the expected values for triple stranded complexes, i.e. three times the one of the ligand, thus supporting the formation of the complex (Table 2.1 for **Eu_2SAcbisDBM$_3$** and sections 2.5.4.6-8, Appendix). The successful complexation to give triple stranded **Ln_2SAcbisDBM$_3$** complexes is further confirmed by MALDI-TOF, where the expected isotope patterns and m/z values are observed (sections 2.5.4.5-8, Appendix).

	ε/M^{-1} cm^{-1}	
Ln(III)	**Ln_2bisDBM$_3$**	**Ln_2SAcbisDBM$_3$**
-	4 x 10^4*	5 x 10^4
Eu(III)	1.3 x 10^5*	1.5 x 10^5

Table 2.1 – Molar absorption coefficients (**ε**) of **SAcbisDBM** and **Eu_2SAcbisDBM$_3$** in DMF compared to the respective **bisDBM** and **Eu_2bisDBM$_3$** in DMF.
*As reported in [45].

Characterisation of the **Eu_2SAcbisDBM$_3$** complex by Raman spectroscopy is facilitated by comparison with the respective control **Eu_2bisDBM$_3$** complex (Figure 2.27). Most peaks can be

identified in both spectra and are assigned to the modes of the bis β-diketonate unit.[51, 52] However, as highlighted in Figure 2.27, new peaks are observed in the 1250 – 1575 cm^{-1} region of the spectrum of **Eu_2SAcbisDBM$_3$**. These can be assigned to the 1,2,3-triazole ring modes (Table 2.2), which are indicative of the surface active unit, solely present in the **Eu_2SAcbisDBM$_3$** complex.



	Wavenumber/cm^{-1}	
Assignment	**Eu_2bisDBM$_3$**	**Eu_2SAcbisDBM$_3$**
C=O	1598 (vs)	1598 (vs)
Triazole ring **C=C**	-	1551 (m)
Ring stretching	1488 (m)	1488 (m)
Ring stretching	1433 (m)	1435 (m)
Triazole ring **C-N + C-H**	-	1365 (s)
C-H in plane deformation	1313 (vs)	1309 (sh)
Triazole ring **N=N**	-	1291 (vs)
-	1183 (vw)	1181 (w)
C-H ring bending	1065 (m)	1072 (m)
Ring breathing	1000 (s)	1000 (s)
-	938 (vw)	940 (vw)

Figure 2.27 – Stacked Raman spectra of **Eu_2bisDBM$_3$** (top, grey) and **Eu_2SAcbisDBM$_3$** (bottom, blue) as powders. The grey bands highlight the new peaks for the **Eu_2SAcbisDBM$_3$** complex. Laser excitation λ: 633 nm. **Table 2.2** – Peak positions and assignments of the Raman spectra of **Eu_2bisDBM$_3$** and **Eu_2SAcbisDBM$_3$** as powders.

Excluding La(III) and Lu(III), lanthanides(III) have unpaired electrons and are paramagnetic. The paramagnetism has profound effects on the NMR spectra of their complexes, where the ligand protons undergo pseudo-contact shifts with direction and magnitude strictly depending on the ion. In the ^{1}H-NMR spectrum of the control **Eu_2bisDBM$_3$** complex in DMSOd_6, the methine H_d and aromatic H_c protons display the largest upfield shifts, in accordance with their higher proximity to the paramagnetic Eu(III) centre (Figure 2.28). Similar pseudo-contact shifts for the

H_a, H_b, H_c, H_d and H_e protons can be identified in the spectrum of the **Eu_2SAcbisDBM$_3$** complex in DMSOd_6. However, a significant downfield shift (+0.35 ppm) is recorded for the peak attributed to the H_f protons, which is consistent with the presence of different substituents on the central phenylene ring of the ligand (H_g for **Eu_2bisDBM$_3$** versus the surface active unit in **Eu_2SAcbisDBM$_3$**).

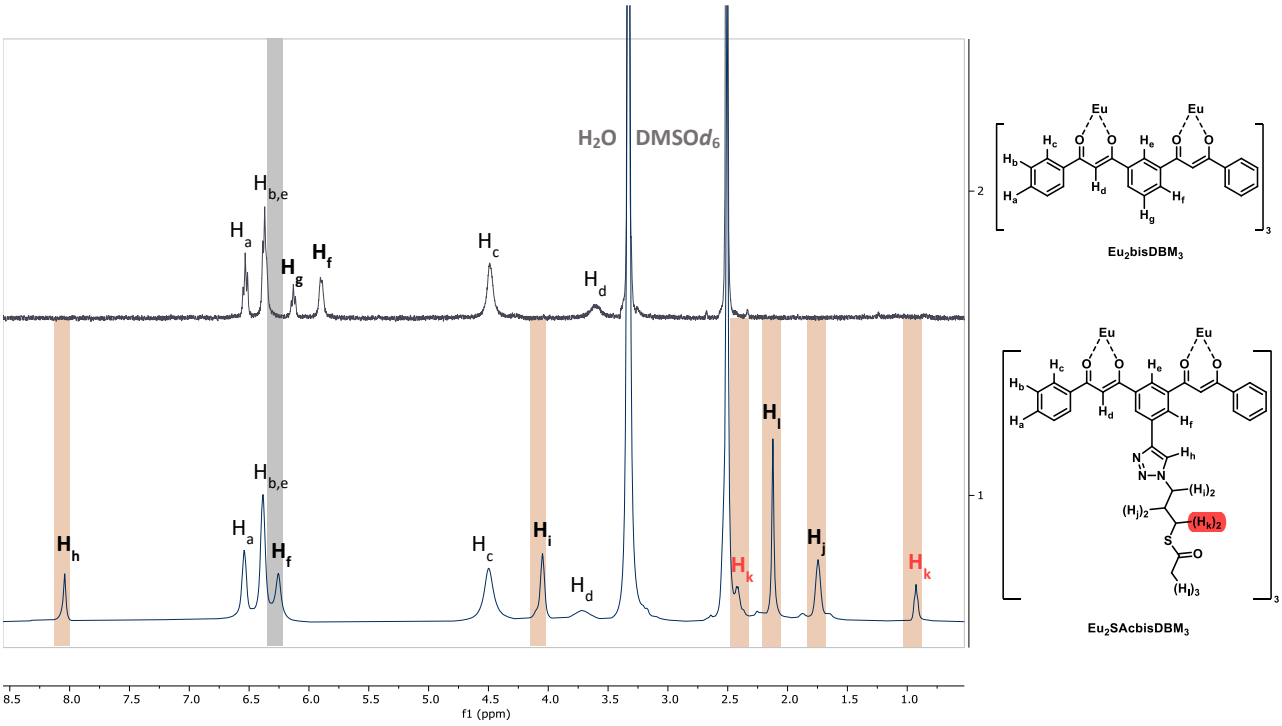
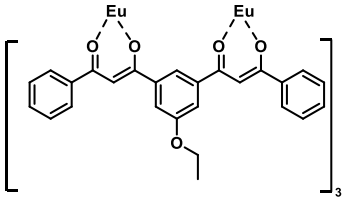


Figure 2.28 – Stacked ^{1}H-NMR spectra (500 MHz, DMSOd_6) of **Eu_2bisDBM$_3$** (top, grey) and **Eu_2SAcbisDBM$_3$** (bottom, blue) with the respective assignments. The proton names (H_x) are as reported in the chemical structures on the right. The grey band illustrate the position and shift of the H_f protons of **Eu_2SAcbisDBM$_3$** compared to **Eu_2bisDBM$_3$**. The orange overlaid bands highlight the new peaks of **Eu_2SAcbisDBM$_3$** arising from the surface active chain. The diastereotopic H_k protons are further highlighted in red.

The peak at 8.04 ppm is assigned to the H_h proton in the 1,2,3-triazole ring and correctly integrates to 3H for the triple stranded complex, while the acetate protons H_l are identified at 2.11 ppm, indicating the stability of the thioacetate unit in the complexation conditions. The propyl chain protons (H_i, H_j, H_k) are observed in the upfield region of the spectrum and are assigned with the aid of the 2D COSY spectrum (Figure 2.71, Appendix). The H_i and H_j peaks

are found at 4.04 ppm and 1.74 ppm, respectively, and their integration matches the expected 6H value each. However, two sets of peaks for the H_k protons are observed at 2.42 ppm and 0.92 ppm, each integrating to 3H. This could not be observed in the ^{1}H-NMR spectrum of the free **SAcbisDBM** ligand and indicates diastereotopicity of the H_k protons of the **Eu_2SAcbisDBM$_3$** complex. This, in turn, is an indication of helicity of the complex in solution. Indeed, in the reported analysis of **Ln_2bisDBM$_3$** complexes, the authors suggested a helical conformation of the complex. Although a crystal structure was not reported, this conclusion was drawn from the ^{1}H-NMR analysis of **8**, a derivative bearing an ethoxy group on the central phenylene ring (Figure 2.29). The splitting of several peaks after addition of Pirkle's reagent was attributed to the chirality of the complex, and thus helicity.[45]



8

Figure 2.29 – Chemical structure of the Eu(III) bis β-diketonate derivative **8** reported by Pikramenou and co-workers.[45]

The ^{1}H-NMR spectra of the **Yb_2SAcbisDBM$_3$** and **Nd_2SAcbisDBM$_3$** complexes were also obtained in DMSOd_6 (Figures 2.75 and 2.80, Appendix). The assignments were confirmed by comparison to the ones of control **Yb_2bisDBM$_3$** and **Nd_2bisDBM$_3$** complexes (Figures 2.74 and 2.79, Appendix) and with the aid of 2D COSY (Figures 2.76 and 2.81, Appendix). Similarly to the **Eu_2SAcbisDBM$_3$** complex, the H_c and H_d peaks for **Yb_2SAcbisDBM$_3$** are observed upfield (4.97 ppm), compared to the H_a, H_c and H_e peaks (7.14-7.05 ppm). The **Nd_2SAcbisDBM$_3$** complex, on the other hand, exhibits an opposite behaviour, with the H_c and H_d protons peaks shifted downfield (12.35 ppm, 11.21 ppm) and the H_a, H_c and H_e in the more upfield region

(8.43 ppm). This is attributed to the orthogonal magnetic anisotropy orientations of Nd(III) compared to Eu(III) and Yb(III) ions (oblate versus prolate, respectively).

Single crystals of **Yb_2SAcbisDBM$_3$** suitable for X-ray analysis were grown in DMSOd_6 and the crystal structure is portrayed in Figure 2.30, **c** and **d**. The crystal structure of the respective unfunctionalised **Yb_2bisDBM$_3$** complex, or any **Ln_2bisDBM$_3$**, has never been reported. Single crystals of **Yb_2bisDBM$_3$** were also grown by the slow evaporation of MeOH in DMF and the crystal structure is displayed in Figure 2.30, **a** and **b**.

Both complexes are seven-coordinate and display a monocapped trigonal prismatic geometry. In addition to the six oxygen atoms of the **SAcbisDBM** (or **bisDBM**) ligands, each Yb(III) atom accommodates one axial DMSO molecule (**Yb_2SAcbisDBM$_3$**) or either a single H_2O or MeOH molecule (**Yb_2bisDBM$_3$**). The crystal structures of both complexes display a distorted helical conformation, where one of the ligands possesses opposite twist. This has been observed in the crystal structures of other seven-coordinate lanthanide(III) bis β-diketonate derivatives (**9**, Figure 2.30). Interestingly, the crystal structures of the respective transition metal **M_2bisDBM$_3$** complexes (with M=Fe(III), Mn(III), V(III) and Ti(III)) do not display any distortion to the helix.[53] This correlation has been observed also with the Fe(III) derivative of **9**, which displays a helical conformation, while all the rare earth derivatives exhibit a seven-coordinated "lantern" mesocate-like structure with one acetone molecule axially coordinating to each ion.[54]

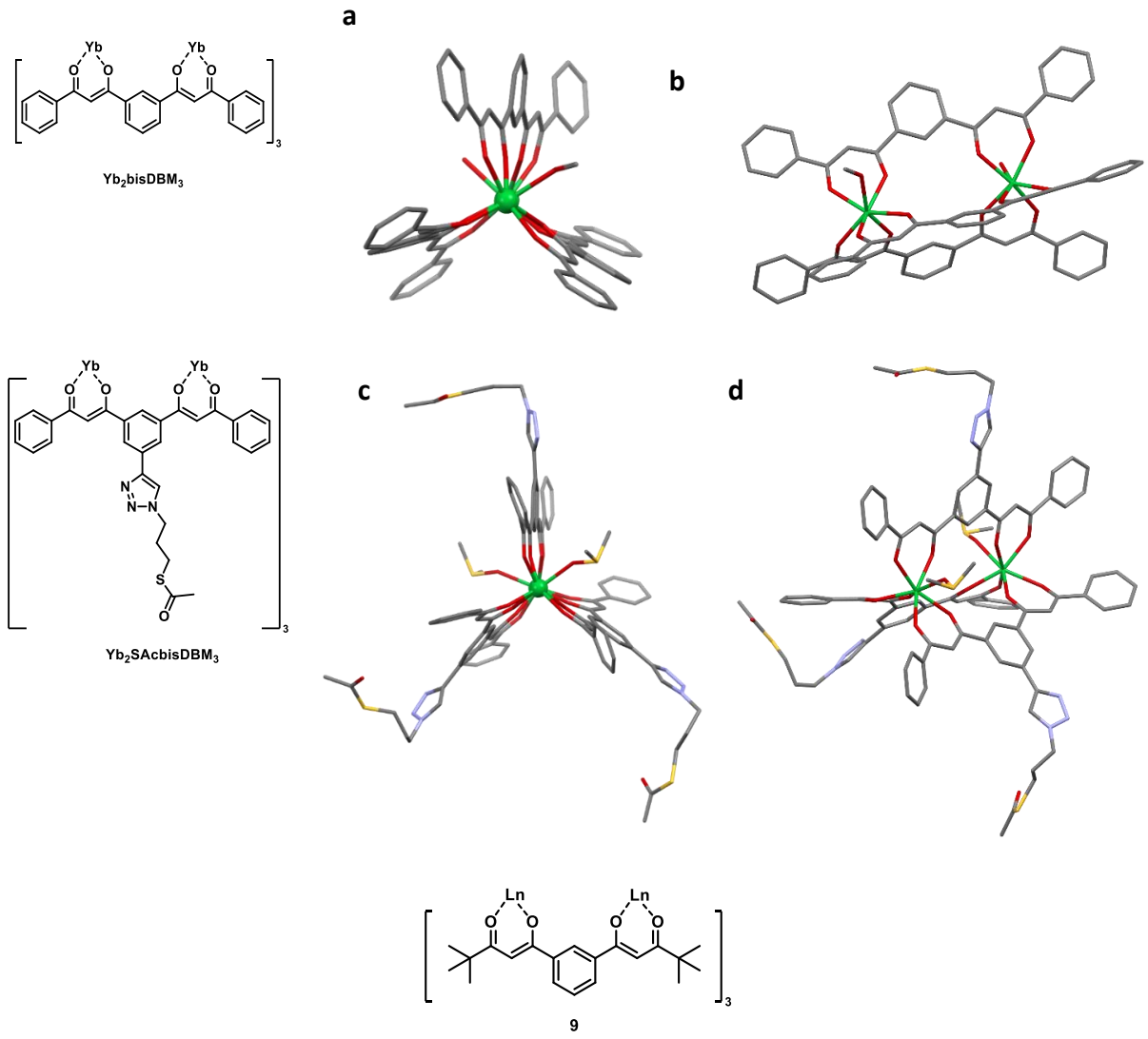


Figure 2.30 – Crystal structures of **Yb_2bisDBM$_3$** (**a**, **b**) and **Yb_2SAcbisDBM$_3$** (**c**, **d**) viewed down the Yb-Yb axis and from the side. These were collected by Dr. Sarah Griffin at the University of Birmingham. The elements colours are as follows: grey – carbon, lilac – nitrogen, yellow – sulphur, red – oxygen and green – ytterbium. For clarity, hydrogen atoms have been omitted. The chemical structure of complex **9** reported by Clegg and co-workers is reported below. Ln=Y(III), Eu(III), Gd(III), Yb(III).[54]

In **Yb_2bisDBM$_3$** and **Yb_2SAcbisDBM$_3$**, the Yb-O distances are ≈2.2 Å for both complexes and the Yb-Yb distance is calculated to be 7.6 Å and 7.5 Å, respectively. This is equivalent to the ones of complex **9** (7.5 Å) but longer than the respective **Fe_2bisDBM$_3$** complex (7.3 Å).[53, 54] The effect is ascribed to the less twisted conformation of the **bisDBM** ligands in the Yb(III) derivative, as well as the larger ionic radius of Yb(III) compared to Fe(III) (0.9 Å and 0.6 Å).[55] Finally, the Yb-S distance in **Yb_2SAcbisDBM$_3$** is calculated to be ≈12 Å for both Yb(III) centres.

2.2.3 Optical properties of Ln_2SAcbisDBM$_3$ complexes

The optical properties of the **Ln_2SAcbisDBM$_3$** complexes were investigated by absorption, time-resolved and steady state spectroscopies.

The phosphorescence of the ligand was recorded by low temperature steady state emission measurements of the **Gd_2SAcbisDBM$_3$** complex (Figure 2.31). The lowest excited energy level of Gd(III), $^6P_{7/2}$, lies at higher energies than most sensitising ligands, thus not allowing for energy transfer. Furthermore, the Gd(III) ion promotes intersystem crossing from the excited singlet state to the excited triplet state *via* heavy atom effect and, by recording the emission at 77 K and in absence of oxygen, the processes that commonly quench phosphorescence are excluded. From the phosphorescence spectrum in Figure 2.31, the energy of the triplet state is calculated to be 20,325 cm^{-1}. This is optimal for energy transfer to Eu(III): according to Latva's rule, the energy gap between the triplet state of the ligand and the emitting $^5D_0$ state (17,220 cm^{-1}) of Eu(III) must be greater 2,500 cm^{-1} to avoid back energy transfer. Here, the energy gap is 3,105 cm^{-1}, thus satisfying the rule. Furthermore, it has been reported that, for β-diketonate Eu(III) complexes, a smaller gap between the triplet state energy and the $^5D_1$ state (19,100 cm^{-1}) of Eu(III) gives better overall quantum yields.[56] Here, there is a small energy gap of 1,225 cm^{-1}, again supporting the suitability of the ligand for Eu(III) sensitisation. In the case of NIR emitting lanthanides(III) such as Yb(III) and Nd(III), their excited states lie in the 10,000-12,000 cm^{-1} range, allowing for energy transfer in this region as well.[57, 58] Finally, the phosphorescence spectrum of **Gd_2SAcbisDBM$_3$** matches well with the one reported for the **Gd_2bisDBM$_3$** complex, suggesting that the 1,2,3-triazole ring and surface active chain do not perturb the triplet state energy of the ligand.[45]

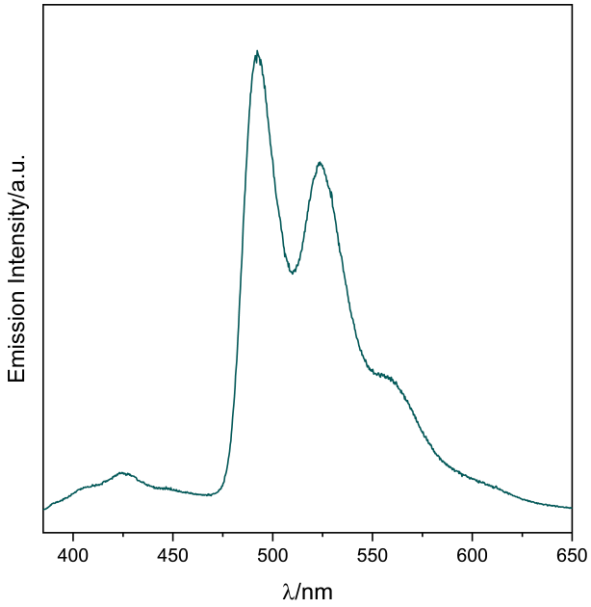


Figure 2.31 – 77 K Phosphorescence spectrum of **Gd_2SAcbisDBM$_3$** in a MeOH:DMF 4:1 glass, λ_{exc}: 368 nm.

2.2.3.1 Luminescence of the visible emitting Eu_2SAcbisDBM$_3$ complex in solution

As for other lanthanides(III), Eu(III) luminescence arises from *f-f* transitions, thus displaying the characteristic qualities of lanthanide emission spectra: narrow and fingerprint like emission peaks and long luminescence lifetimes. Furthermore, Eu(III) transitions are particularly sensitive to crystal field effects and the splitting patterns and relative intensities found in Eu(III) spectra are extremely useful to determine the local environment around the metal, as well as the point group symmetry of the complex.

The excitation spectrum of the **Eu_2SAcbisDBM$_3$** complex in DMF is consistent with the absorption spectrum, displaying a band centred at 360 nm and confirming energy transfer from the **SAcbisDBM** units to the Eu(III) centres (Figure 2.32, **a**).

Focusing on the emission spectrum of the complex (Figure 2.32, **b**), the $^5D_0 \rightarrow {}^7F_J$ (ΔJ=0-4) transitions are observed centred at the following wavelengths: 579 nm, 593 nm, 611 nm, 652 nm and 699 nm, respectively. The $^5D_0 \rightarrow {}^7F_2$ transition is an induced electric dipole transition

and is often described as hypersensitive, due to its intensity being strongly dependent on both the local symmetry and the nature of the coordinating ligands. On the other hand, the magnetic dipole character of the $^5D_0 \rightarrow {}^7F_1$ transition makes its intensity independent of the local environment, hence this transition is commonly used as reference to calibrate the intensities of other transitions.[59] In our case, the $^5D_0 \rightarrow {}^7F_2$ transition dominates the emission spectrum of **Eu_2SAcbisDBM$_3$** in DMF and a $\Delta J=2/\Delta J=1$ ratio of 18 is calculated. This is comparable to the one of other β-diketonate complexes and the effect can be attributed to both the low local symmetry and the high polarizability of the β-diketonate ligands.[46, 59] The $^5D_0 \rightarrow {}^7F_0$ transition is strongly forbidden by the Laporte selection rule in highly symmetric environments, and its presence is indicative of lower symmetries, such as C_{nv}, C_v or C_s point groups. Furthermore, this transition is often employed to determine the number of different species in solution due to the non-degeneracy of the $^7F_0$ level.[59] One peak is to be expected for a single species, while the presence of a shoulder or more peaks suggests multiple species and sites. In the **Eu_2SAcbisDBM$_3$** emission spectrum, only one sharp symmetric peak is found (Figure 2.32, **b**), attributable to the presence of a single species in solution and indicating the equivalency of the two Eu(III) sites in the complex. Finally, the splitting (Stark levels) of the transitions in Eu(III) spectra reflects the point group symmetry of the metal. By following the splitting pattern in the emission spectrum of **Eu_2SAcbisDBM$_3$**, we can observe a C_3 or C_{3v} point group symmetry for the complex, which is expected for triple stranded β-diketonate complexes.[46, 60]

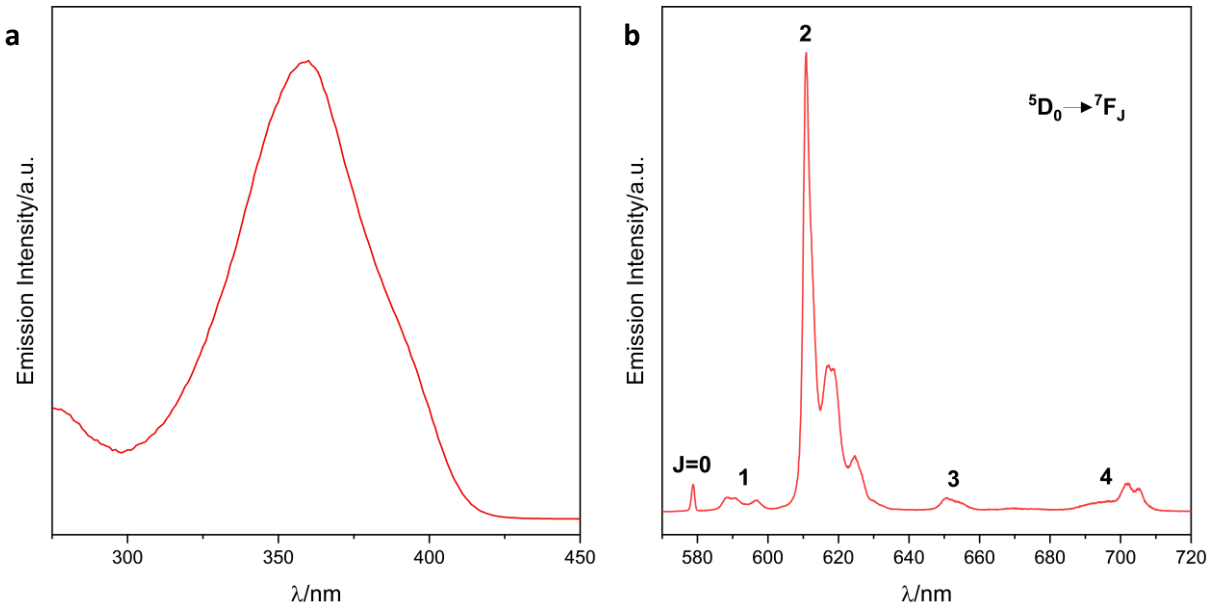


Figure 2.32 – Excitation (**a**) and emission (**b**) spectra of **Eu₂SAcbisDBM₃** in DMF. λ_{exc}: 350 nm, λ_{em}: 611 nm.

The luminescence lifetime of the complex in DMF is 180 µs (**τ** (DMF), Table 2.3), where the monoexponential fitting again suggests the presence of a single species in solution. As already observed for **Eu₂bisDBM₃**, this relatively small value is indicative of H_2O coordination to the Eu(III) centres and thus quenching by O-H oscillators, confirmed by the equivalency (within fitting error) of the longer component (190 µs) in the biexponential fitting of the lifetime in H_2O (0.2% DMF, Table 2.3).[45]

The number of coordinating H_2O molecules **q** is an important parameter to evaluate the coordination sphere of the complex. The Horrocks equation (Equation 2.1) allows for the estimation of **q** by taking into consideration the lower degree of quenching afforded by O-D oscillators.

$$q = A\left(\frac{1}{\tau(H_2O)} - \frac{1}{\tau(D_2O)} - a\right) \quad Equation\ 2.1$$

Where **τ** (H_2O) and **τ** (D_2O) are the lifetimes of the complex in H_2O and D_2O, respectively, **A** is a constant (1.2 ms for Eu(III)) and **a** is the correction factor for outer sphere H_2O molecules (-

0.25 ms^{-1} for Eu(III)).[61-63] From this, we obtain a **q** value of 3.4 for **Eu_2SAcbisDBM$_3$**, which, in addition to the six coordinating oxygen atoms of the **SAcbisDBM** ligand, takes the Eu(III) centres to nine-coordinated in solution. This value is in accordance with the one previously reported for the **Eu_2bisDBM$_3$** complex.[45] The overall quantum yield (**Φ**) of the **Eu_2SAcbisDBM$_3$** complex in DMF was measured to be 5.5%, indicating that the presence of the surface active unit does not significantly affect the value (**Φ**=5% for **Eu_2bisDBM$_3$**).[45] The intrinsic quantum yield of Eu(III) (**Φ_{Eu}**) was not obtained experimentally upon direct *f-f* excitation but from the ratio between the observed lifetime in DMF (**$\tau_{Obs.}$** in Equation 2.3, i.e. **τ** (DMF) in Table 2.3) and the radiative lifetime (**$\tau_{Rad.}$**, Equation 2.2).[56, 64]

$$\frac{1}{\tau_{Rad.}} = A_{MD} n^3 \left(\frac{I_{Tot.}}{I_{MD}}\right) \quad Equation\ 2.2$$

$$\Phi_{Eu} = \frac{\tau_{Obs.}}{\tau_{Rad.}} \quad Equation\ 2.3$$

Where A_{MD} is the spontaneous emission probability of the magnetic dipole transition $^5D_0 \rightarrow {}^7F_1$ (14.65 s^{-1}), n is the refractive index of DMF (1.4305), $I_{Tot.}$ the total integral of the **Eu_2SAcbisDBM$_3$** emission spectrum (570-720 nm), and I_{MD} the one of the $^5D_0 \rightarrow {}^7F_1$ transition (581-601 nm). The obtained value of **Φ_{Eu}** is 17% and is indicative of an unfilled coordination sphere where quenching solvent molecules can coordinate directly to the metal. Finally, from the overall **Φ** and **Φ_{Eu}** we obtain a sensitisation efficiency of 32% (**$\eta_{Sens.}$**, Equation 2.4).

$$\eta_{Sens.} = \frac{\Phi}{\Phi_{Eu}} \quad Equation\ 2.4$$

	Eu_2SAcbisDBM$_3$
τ (DMF)/μs	180
τ (H_2O)[a]/μs	190 (68%), 60 (32%)
τ (D_2O)[a]/μs	380 (70%), 150 (30%)
q[b]	3.4
Φ (DMF)	5.5%
$\tau_{Rad.}$ (DMF)/μs	1040
Φ_{Eu} (DMF)	17%
$\eta_{Sens.}$ (DMF)	32%

Table 2.3 – Summary of: exponential decay analysis of the observed lifetimes (**τ**), radiative lifetime ($\tau_{Rad.}$) number of coordinating water molecules (**q**), overall quantum yield (**Φ**), intrinsic quantum yield (Φ_{Eu}) and sensitisation efficiency ($\eta_{Sens.}$) of **Eu_2SAcbisDBM$_3$**.
[a]0.4% DMF
[b]Calculated considering only the longer component.

2.2.3.2 Luminescence of the NIR emitting Yb_2SAcbisDBM$_3$ and Nd_2SAcbisDBM$_3$ complexes in solution

Compared to Eu(III) and Tb(III) complexes, the preparation of NIR luminescent Yb(III) and Nd(III) complexes is more challenging. This is primarily due to the higher sensitivity of lanthanide(III) NIR luminescence to quenching from O-H, C-H and N-H oscillators.[58] The **SAcbisDBM** ligand is expected to transfer energy to both Yb(III) and Nd(III) due to the suitable energy of its triplet state.

The emission spectra of the complexes were first acquired in DMSOd_6, as the non-radiative energy transfer to C-D and O-D oscillators is very limited compared to C-H and O-H. Upon excitation at 350 nm, we observe five components splitting the $^2F_{5/2} \rightarrow {}^2F_{7/2}$ transition in the emission spectrum of **Yb_2SAcbisDBM$_3$** (921 nm, 950 nm, 976 nm, 1001 nm and 1043 nm, Figure 2.33, **a**), with the splitting at 976 nm dominating the spectrum. The observed profile is ascribed to the m_J splitting of both the emitting and fundamental states of Yb(III), as a result

of the ligand field.[65, 66] In the emission spectrum of **Nd_2SAcbisDBM$_3$**, we identify all $^2F_{3/2}\rightarrow{}^4I_J$ (ΔJ=9/2, 11/2, 13/2) transitions at 882 nm, 1058 nm and 1135 nm, respectively (Figure 2.33, **b**). For both complexes, the excitation spectra display the expected band at 360 nm (Figures 2.86 and 2.87, Appendix), confirming energy transfer from the **SAcbisDBM** ligands to the NIR emissive ions.

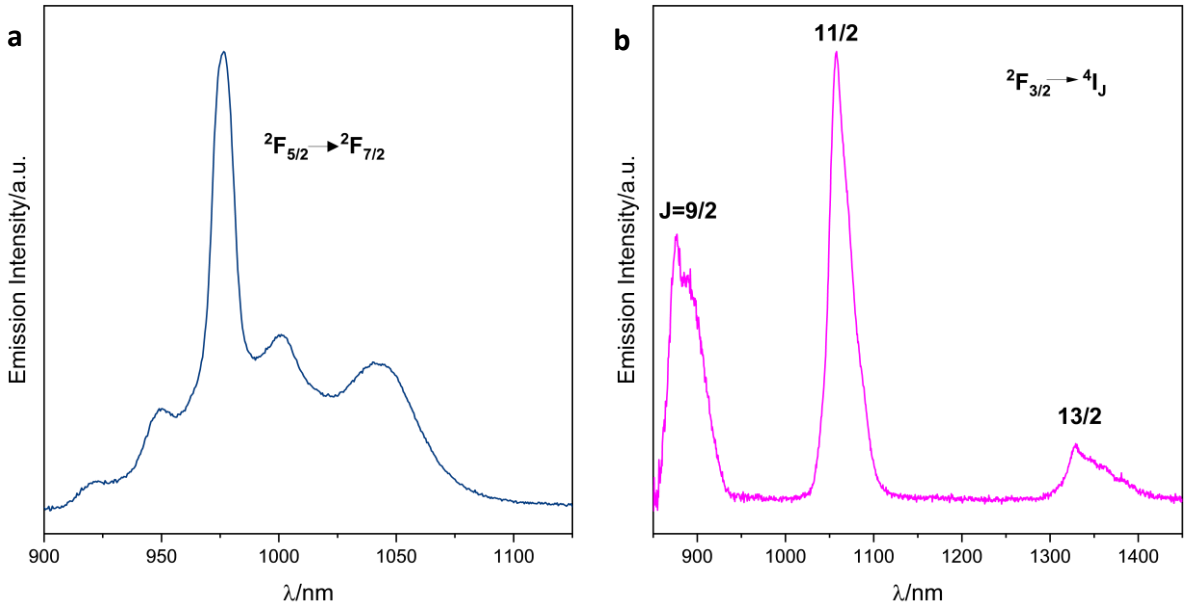


Figure 2.33 – Emission spectra of **Yb_2SAcbisDBM$_3$** (**a**) and **Nd_2SAcbisDBM$_3$** (**b**) in DMSO-d_6. λ_{exc}: 350 nm.

Considering the luminescence lifetimes of **Yb_2SAcbisDBM$_3$** (Figure 2.34 and Table 2.4, Appendix), a stark decrease from DMSOd_6 (17 µs) to H_2O (11 µs, 70%, 3.3 µs, 30%) is recorded and is attributed to the strong deactivating effect of the O-H oscillators in H_2O. The observed overall quantum yield (**Φ**) of **Yb_2SAcbisDBM$_3$** in DMSOd_6 is 0.8%, which is identical to the one measured for the **Yb_2bisDBM$_3$** complex (0.8%). The lifetime of **Nd_2SAcbisDBM$_3$** in DMSOd_6 is 2.1 µs, which is comparable to the one reported for the **Nd_2bisDBM$_3$** complex in DMFd_7 (1.5 µs).[45]

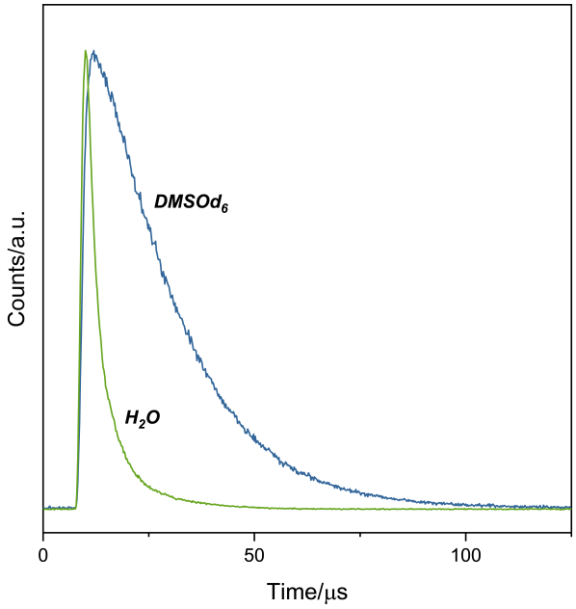


Figure 2.34 – Lifetime spectra of **Yb_2SAcbisDBM$_3$** in DMSOd_6 (blue) and H_2O (0.4% DMF, green). λ_{exc}: 350 nm, λ_{em}: 977 nm.

Interestingly, upon investigation of the luminescence properties of the single crystals of the **Yb_2bisDBM$_3$** complex, the coordination of either H_2O or MeOH at each Yb(III) centre is reflected in the multicomponent decay of the complex (11 μs, 65%, 3.9 μs, 30%, 1.6 μs, 5%, Figure 2.35, **a**). The powder form of the complex, however, displays a monoexponential decay (11 μs, Figure 2.35, **a**) as well as a small difference in the relative intensities and positions of the m_J splitting components of the $^2F_{5/2} \rightarrow {}^2F_{7/2}$ transition (Figure 2.35, **b**). Both observations indicate that the solvent coordination detected in the crystal structure arises from the crystallisation conditions and is different from the powder.

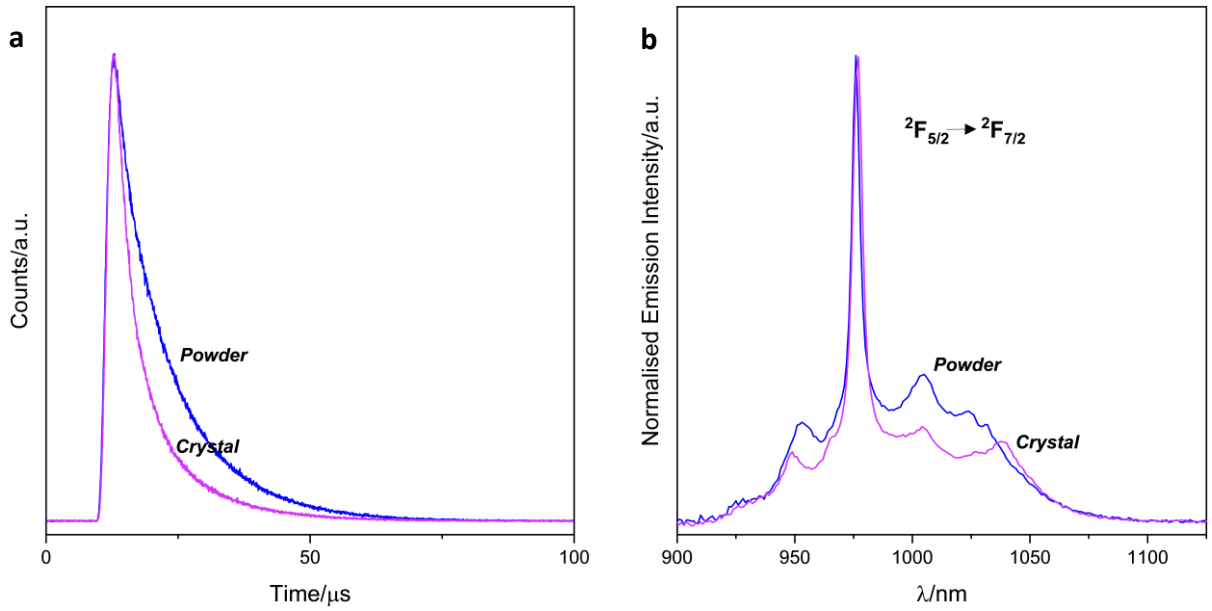


Figure 2.35 – **a** Lifetime spectra of **Yb_2bisDBM$_3$** as powder (blue) or single crystals (pink). λ_{exc}: 400 nm, λ_{em}: 977 nm. **b** Normalised emission spectra of **Yb_2bisDBM$_3$** as powder (blue) or single crystals (pink). λ_{exc}: 350 nm.

2.2.4 Detection and coordination of F^- to Eu(III) diketonates complexes

For the testing of Eu(III) diketonates as probes for F^- detection, steady state and time resolved spectroscopies are employed. As reported in section 1.2, F^- coordination to Eu(III) can be monitored as variations to both the emission profile and luminescence lifetime of the complex, due to the strong effects on the local crystal field and exchange of F^- with quenching solvent molecules.

F^- is commonly found in water supplies and it is thus desirable to detect these anions in aqueous conditions. In a first approach, we consider a 1:1 EtOH:H_2O mixture (0.4% DMF) as solvent and employ NaF as source of F^-. Upon addition of F^- (up to 260 equivalents, 0.8 mM), no change in the luminescence lifetime of the **Eu_2SAcbisDBM$_3$** complex is recorded (Figure 2.101, Appendix). The emission profile of the complex is unaltered, with just a small decrease in the overall emission intensity (1.5-fold, Figure 2.88, Appendix) attributed to either a change

in the polarity and ionic strength of the medium or a dilution effect. We suggest that, in these conditions, the coordination of F^- to Eu(III) is unfavoured, potentially due to the hydrophobicity and uncharged nature of the **Eu_2SAcbisDBM$_3$** complex, which do not allow for the overcoming of the hydration energy barrier of F^-.

In a second approach, we chose a purely organic solvent (THF, 0.2% DMF) and use tetrabutylammonium fluoride (TBAF) as source of F^-. Unlike NaF and other inorganic fluoride salts, the hydration of TBAF is minimal, allowing for the testing in a quasi-anhydrous system.

Upon addition of up to 30 equivalents of F^- (i.e. 60 µM), we observe a large increase in the luminescence lifetime of the **Eu_2SAcbisDBM$_3$** complex (>8-fold, for the longer component, 1500 µs, 3-fold for the shorter component, 500 µs, Figure 2.36, **b** and Table 2.6, Appendix). This is in accordance with the displacement of quenching solvent molecules by F^- to exclude such deactivation pathways.

The initial luminescence lifetime in absence of F^- displays a monoexponential decay, with a value of 170 µs. Upon addition of up to 4 equivalents of F^-, a biexponential decay is recorded, including the initial component (170 µs) and a second longer component (730±30 µs). This indicates that both uncoordinated and F^- coordinated **Eu_2SAcbisDBM$_3$-F$_n$** species are present. After this point, only **Eu_2SAcbisDBM$_3$-F$_n$** species are detected and, due to the complex allowing for multiple solvent molecules to be exchanged, we believe that more than one F^- anion coordinates to the Eu(III) centre. The biexponential decay recorded at all points of the titration indicates that not all Eu(III) centres are equivalent, with multiple species and potentially slow exchange kinetics being present. As expected, the $\tau_{Rad.}$ of the complex sees a considerable

increase (1.8-fold) up to 10 equivalents of F^-, after which a plateau is reached (Figure 2.104, Appendix).

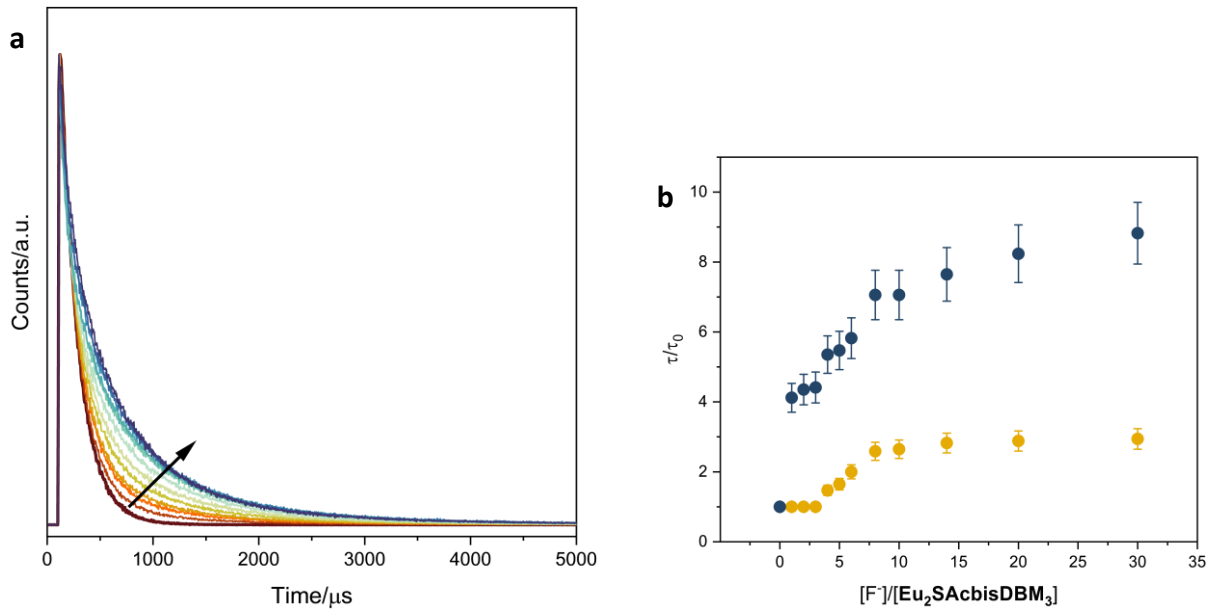


Figure 2.36 – **a** Overlaid time-resolved luminescence of **Eu_2SAcbisDBM$_3$** in THF (0.2% DMF) upon addition of up to 30 equivalents of F^- (60 μM). λ_{exc}: 350 nm, λ_{em}: 611 nm. **b** Plot of the ratios between the lifetime after addition of F^- (τ) and the initial lifetime (τ_0) of **Eu_2SAcbisDBM$_3$** versus the equivalents of F^- added in THF (0.2% DMF). The blue circle represents the long component, while the yellow circle the short component.

To evaluate the effect of the surface active unit, the control **Eu_2bisDBM$_3$** complex was tested in identical conditions. The same increase in luminescence lifetime as for the **Eu_2SAcbisDBM$_3$** complex is observed (Figure 2.108, Appendix), confirming that the recorded response is solely dependent on the coordination environment and geometry of the complex and that the surface active unit is not involved in the sensing event.

Upon examination of the emission spectra of the **Eu_2SAcbisDBM$_3$** complex (Figure 2.37, **a**), a moderate increase in the total emission intensity is detected after 30 equivalents of F^- added (up to 1.5-fold, Figure 2.89, Appendix, for plot). More importantly, the overall emission profile of the complex displays significant perturbations to the splitting pattern.

Focusing on the hypersensitive $^5D_0 \rightarrow {}^7F_2$ transition, up to 5 equivalents of F^- (thick green line, Figure 2.37, **b**), the 611 nm component increases by 2.3-fold (Figure 2.37, **b**, inset, green arrow). Concurrently, a new component at 608.5 nm appears, reaching up to 11-fold the initial value at 30 equivalents of F^- (Figure 2.37, **b**, inset, blue arrow). These new splitting components are accompanied by the decrease in intensity of the ones at 622 nm and 625 nm, with the latter disappearing at 30 equivalents of F^-. The emission spectrum at 30 equivalents (thick blue line, Figure 2.37, **b**) thus comprises five splitting components: 608.5 nm, 611 nm, 613 nm, 622 nm and 630 nm. Such a high number is indicative of a site with low symmetry, as that of a C_1 point group. Furthermore, such significant alterations to the hypersensitive transition are in accordance with the coordination of highly polarising anions such as F^-, while the presence of several steps correlates well with the observations from the time-resolved data that multiple binding events and species are present.

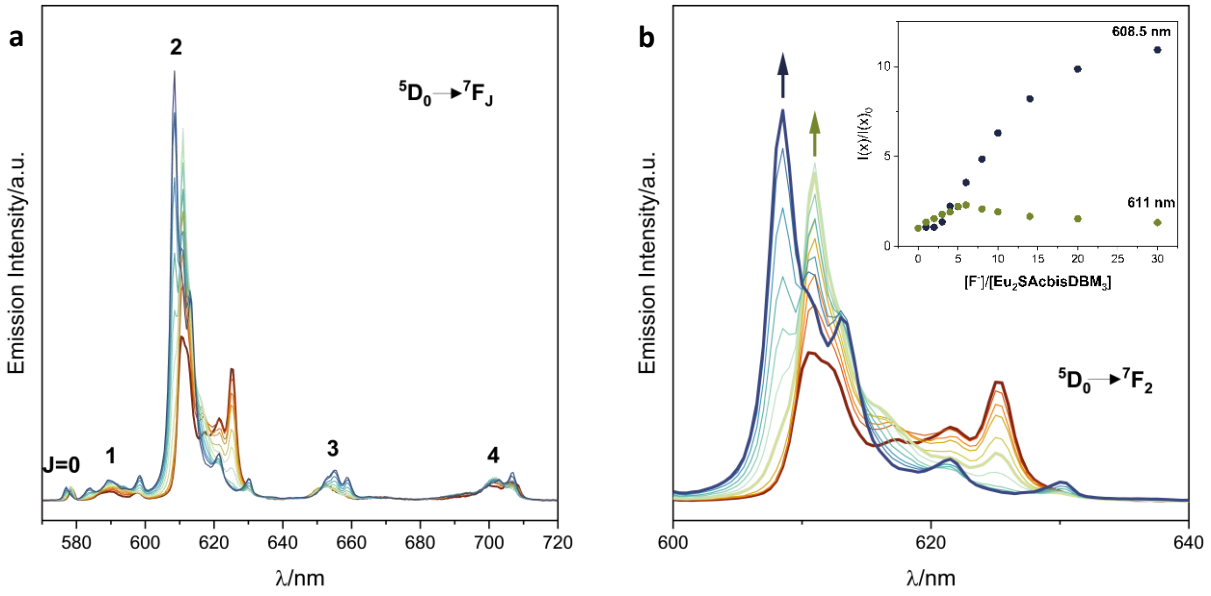


Figure 2.37 – **a** Overlaid emission spectra of **Eu_2SAcbisDBM$_3$** in THF (0.2% DMF) upon addition of equivalents of F^-. λ_{exc}: 350 nm. **b** Section of the overlaid emission spectra of **Eu_2SAcbisDBM$_3$** in THF (0.2% DMF) upon addition of equivalents of F^- showing only the $^5D_0 \rightarrow {}^7F_2$ transition. λ_{exc}: 350 nm. The spectra at 0, 5 and 30 equivalents of F^- are highlighted with thick red, green and blue lines, respectively. The inset depicts the plot of the ratio of emission intensities (either at 611 nm (blue) or 608.5 nm (green)) over the starting value at 0 equivalents versus equivalents of F^- added.

Focusing on the $^5D_0 \rightarrow {}^7F_0$ transition, this can be used to understand the presence of multiple species in solutions. A shoulder or an asymmetry of the peak are related to more than one site of symmetry in the complex.[59] Indeed, an asymmetric peak can be identified in the intermediate states between 5 and 30 equivalents of F^- (Figure 2.38, **a**). At 30 equivalents (thick blue line, Figure 2.38, **a**), a 2 nm blue shift from the initial 579 nm position is detected, confirming the formation of a new species. Upon addition of F^-, the $^5D_0 \rightarrow {}^7F_1$ transition exhibits further splitting from two to three components (583 nm, 590 nm and 598 nm, Figure 2.38, **a**). The approximately equal distance between them indicates that Eu(III) is in a site of low symmetry, as already inferred from the examination of the hypersensitive $^5D_0 \rightarrow {}^7F_2$ transition, and in accordance with the exchange with F^- to form **Eu_2SAcbisDBM$_3$-F_n** species.

The excitation spectra of the **Eu_2SAcbisDBM$_3$** complex display a blue shift (≈3 nm, from 360 nm to 357 nm) upon addition of F^- (Figure 2.38, **b**). As can be seen from the inset of Figure 2.38, **b**, the shift occurs between 0 and 5 equivalents, indicating that coordination of F^- in this range affects the photophysics of the ligands the most, possibly due to small rearrangements in the geometrical conformation of the complex. The validity of the shift was also confirmed by UV-Vis absorption spectroscopy, where an identical magnitude and trend was observed (Figures 2.90 and 2.91, Appendix). It is worth mentioning that the modulation in intensity of the excitation band is proportional to the alteration in emission intensity of the 611 nm component of the $^5D_0 \rightarrow {}^7F_2$ transition, which was set as emission wavelength for the measurements (Figures 2.92 and 2.93 for plots, Appendix).

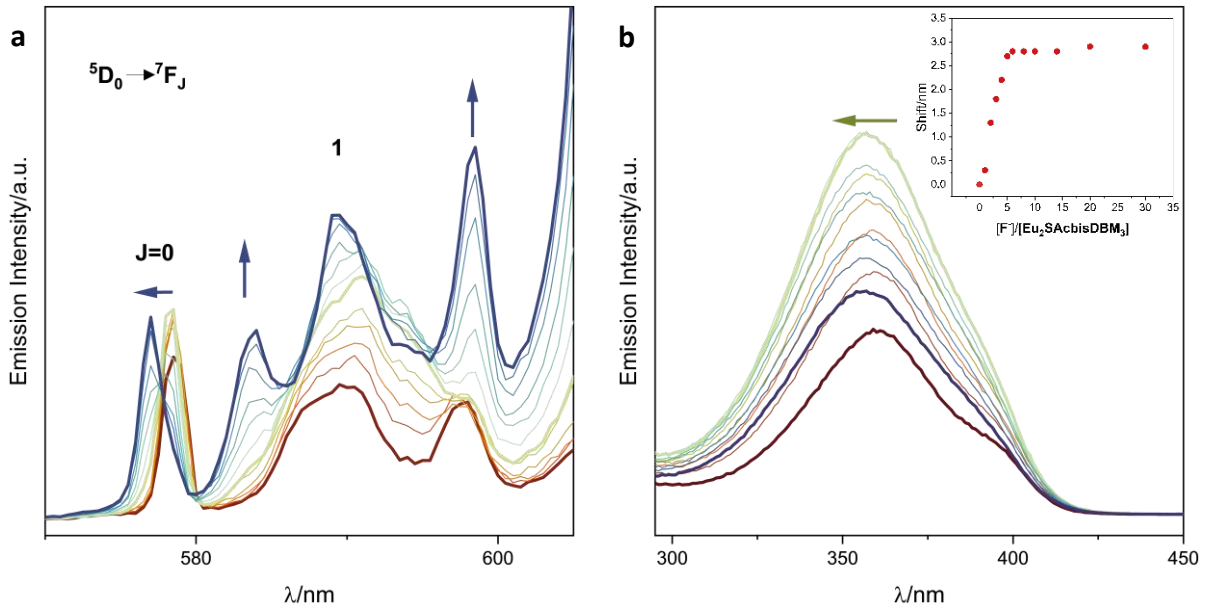


Figure 2.38 – **a** Section of the overlaid emission spectra of **Eu₂SAcbisDBM₃** in THF (0.2% DMF) upon addition of equivalents of F^- showing only the $^5D_0 \rightarrow ^7F_0$ and $^5D_0 \rightarrow ^7F_1$ transitions. λ_{exc}: 350 nm. The spectra at 0, 5 and 30 equivalents of F^- are highlighted with thick red, green and blue lines, respectively. **b** Overlaid excitation spectra of **Eu₂SAcbisDBM₃** in THF (0.2% DMF) upon addition of equivalents of F^-. λ_{em}: 611 nm. The spectra at 0, 5 and 30 equivalents of F^- are highlighted with thick red, green and blue lines, respectively, and the green arrow depicts the direction of the shift. The inset is the plot of the shift of the maximum in the excitation spectra compared to the starting value at 0 equivalents versus equivalents of F^- added.

From the interpretation of the time resolved and steady state measurements, it can be deduced that multiple binding events are present. Two important points are observed at 5 and 10-14 equivalents of F^- (4 μM and 8-12 μM), where the most significant alterations to either the luminescence lifetime or emission and excitation spectra are detected.

From the decay fittings, we gather that, up to 4-5 equivalents, there are some Eu(III) species with no F^- coordination. After this point, it is assumed that coordination of multiple F^- leads to the more dramatic alterations to the emission and luminescence lifetime spectra.

For comparison, addition of tetrabutylammonium bromide (TBAB) to **Eu₂SAcbisDBM₃** elicits only a very small change to the hypersensitive $^5D_0 \rightarrow ^7F_2$ transition, with the 625 nm component displaying a 1.2-fold decrease at 16 equivalents of Br^- and the other components and transitions displaying no change (Figure 2.95, Appendix). Examination of the luminescence

lifetime data reveals the presence of a biexponential decay upon addition of Br^-, with the second component (180-280 µs) consistently making up ≈18% of the decay (Figure 2.110 and Table 2.10, Appendix). From these results, we conclude that the smaller size (1.33 Å for F^- vs 1.96 Å for Br^-) and higher electronegativity of F^- lead to more profound effects to the crystal field and, thus, luminescence properties of **Eu_2SAcbisDBM$_3$** upon coordination. This ensures a selective response for F^- over Br^- in the tested conditions.

To elucidate the coordination state of the **Eu_2SAcbisDBM$_3$-F_n** system, we employ mass spectrometry. As the **Eu_2SAcbisDBM$_3$** and **Eu_2bisDBM$_3$** complexes are neutral, it is believed that only F^- coordinated species will be detected by ESI^--MS. To eliminate any interference from the sulfur groups in **Eu_2SAcbisDBM$_3$** and as it previously displayed identical response to F^-, the **Eu_2bisDBM$_3$** complex is selected. Addition of excess F^- to give the luminescence lifetime and emission spectra observed before 6 equivalents (Figures 2.109 and 2.94, Appendix) produced negatively charged species that could be detected by ESI^--MS (Figure 2.39, **a**). Upon examination of the spectrum, the correct isotope pattern and m/z values for the **Eu_2bisDBM$_3$-F_3** species are observed. Due to the presence of two main components in the exponential decay analysis (long, 1000 µs, 70%, and short 240 µs, 30%), it is deduced that the system includes Eu(III) species with either one or two F^- coordinating. This is in accordance with the conclusions drawn from the analysis of the steady state and time-resolved luminescence spectra of **Eu_2SAcbisDBM$_3$**, where it was hypothesized that after 5 equivalents, only Eu(III) species with F^- coordinated were present in solution.

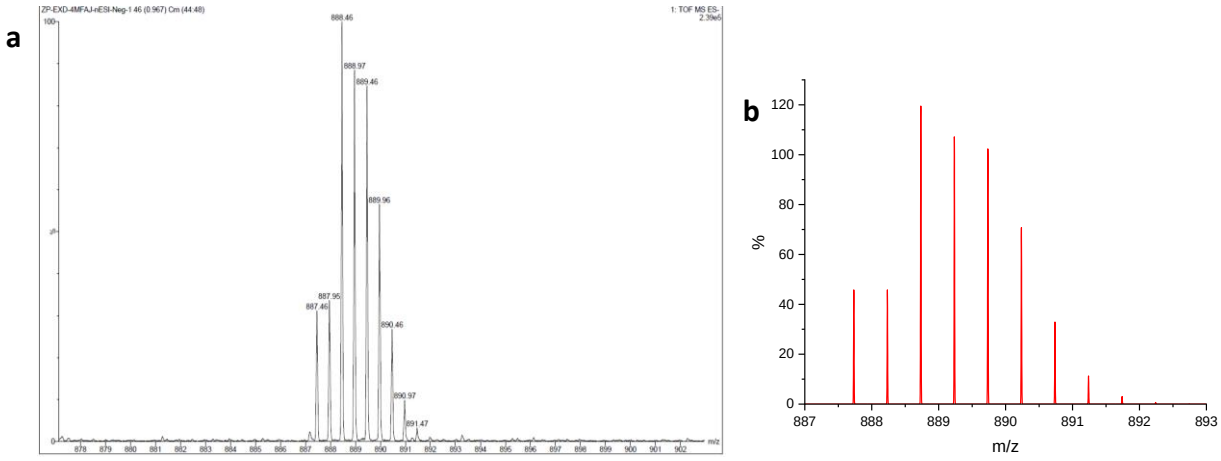


Figure 2.39 – **a** Found (ESI$^-$-MS) and **b** calculated spectra and isotope pattern of **Eu_2bisDBM$_3$** in THF (0.2% DMF) upon addition of excess F^- (i.e. **Eu_2bisDBM$_3$-F$_3$** species).

Finally, to investigate the impact of having two Eu(III) sites in the **Eu_2SAcbisDBM$_3$** and **Eu_2bisDBM$_3$** complexes, the mononuclear **EuDBM$_3$** complex is tested in identical conditions as before. Compared to the dinuclear counterparts, the emission intensity of the **EuDBM$_3$** complex upon addition of 1, 2 and 4 equivalents of F^- dramatically decreases (40-fold, Figure 2.40, **a**), accompanied by no alteration to the emission profile (Figure 2.96, Appendix). From these observations, we suggest that, upon addition of F^-, energy transfer processes from the ligand are interrupted, thus causing the luminescence decrease. Evaluation of the luminescence lifetimes of the complex reveals an extreme decrease (Figure 2.40, **b**) from 130 µs to ≈2 µs, at 0 and 4 equivalents of F^-, respectively.

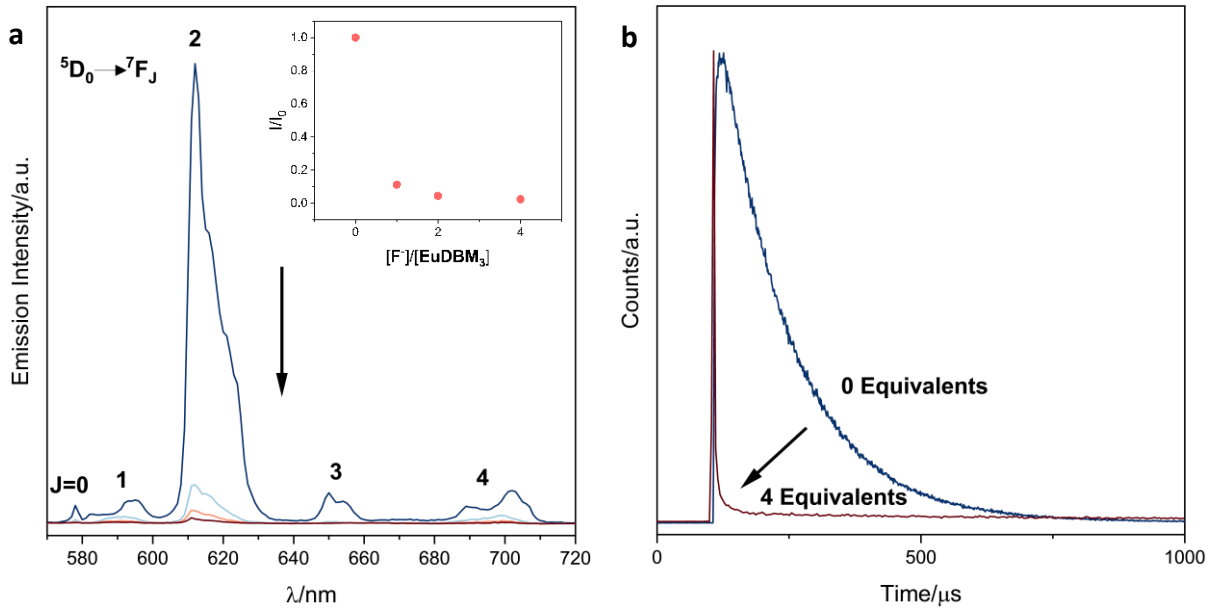


Figure 2.40 – **a** Overlaid emission spectra of **EuDBM$_3$** in THF (0.2% DMF) upon addition of 0, 1, 2 and 4 equivalents of F^-. λ_{exc}: 350 nm. The inset is the plot of the overall emission intensity over the initial one versus equivalents of F^- added. **b** Luminescence lifetime spectra of **EuDBM$_3$** in THF (0.2% DMF) upon addition of 0 (blue) and 4 (maroon) equivalents of F^-. λ_{exc}: 350 nm, λ_{em}: 611 nm. Both emission and luminescence lifetime spectra were acquired by MSc Carys Scott.

From this, we suggest that the complex disassociates in the presence of F^-, also justifying the disruption of energy transfer processes. Mononuclear β-diketonate complexes are reportedly less rigid than dinuclear counterparts. This is often reflected in the longer luminescence lifetimes of bis β-diketonates (i.e. 200 μs for **Eu$_2$bisDBM$_3$** versus 130 μs for **EuDBM$_3$** in THF, 0.2% DMF) due to the reduction of thermal vibrations of the ligands, limiting radiationless deactivation pathways.[60] In the context of F^- coordination, our results indicate that the higher rigidity of the dinuclear **Eu$_2$SAcbisDBM$_3$** and **Eu$_2$bisDBM$_3$** complexes imparts additional stability, allowing to withstand the binding of electronegative and negatively charged anions such as F^-.

2.3 Conclusions and future studies

In this project, we have designed and successfully synthesized a novel surface active bis β-diketone ligand (**SAcbisDBM**) as well as its respective triple stranded **Ln_2SAcbisDBM$_3$** complexes, expanding the potential of dinuclear β-diketonates for incorporation to metallic substrates.

The obtained **Ln_2SAcbisDBM$_3$** complexes were characterised with a range of techniques to evaluate their coordination and geometry. In particular, single crystals of both **Yb_2SAcbisDBM$_3$** and **Yb_2bisDBM$_3$** complexes were obtained and studied by X-ray diffraction, making this the first report of the crystal structure of a **Ln_2bisDBM$_3$** complex. The study of the crystal structures has allowed for a comparison of the two complexes, confirming the equivalency in their coordination state and conformation.

Upon examination of the 77 K phosphorescence spectrum of the **Gd_2SAcbisDBM$_3$** complex, the triplet state energy of the **SAcbisDBM** ligand was obtained and it was found to be consistent with the one of the parent **bisDBM** scaffold. Sensitisation of both visible (Eu(III)) and NIR (Yb(III), Nd(III)) luminescence was confirmed, leading to well resolved emission spectra and quantum yields comparable to the ones of the reported unfunctionalized complex (Eu(III) derivative). The number of coordinating H_2O molecules was determined with the Horrocks equation for the **Eu_2SAcbisDBM$_3$** complex, with ≈3 H_2O molecules coordinating to each Eu(III) centre. The resulting unfilled coordination sphere allowed for the detection of F^- in solution by coordination to Eu(III) and displacement of solvent molecules. Whereas no F^- coordination could be identified in aqueous media, addition of F^- as TBAF in THF afforded significant alterations to both steady state and time-resolved spectra. These were examined

and it was determined that multiple binding events were in place and more than one species were present at any given equivalent of F^-, as confirmed by ESI^--MS. Furthermore, the comparison of the optical properties of dinuclear (**Eu_2SAcbisDBM$_3$**, **Eu_2bisDBM$_3$**) and mononuclear (**EuDBM$_3$**) complexes upon addition of F^- revealed that the rigidity of the former is required to prevent disassociation, highlighting the potential of dinuclear β-diketonate complexes for the development of anion sensing platforms.

Unfortunately, due to the complexity of the system, it was not possible to determine either binding constants or the exact number of F^- coordinating at each stage. However, a clear readout at sub-μM concentrations of F^- could be obtained. Future work should thus focus on the further deconvolution of the system and the determination of both limits of detection and binding constants. Furthermore, from the attempts at F^- detection in aqueous media, we observed that the hydrophobicity of the **Eu_2SAcbisDBM$_3$** complex could represent a limitation for anion sensing in H_2O. The introduction of hydrophilic units to the ligand scaffold could address this, also improving the solubility of the complex in solvents other than DMF or DMSO.

2.4 References

1. D. Parker, J. D. Fradgley and K.-L. Wong, *Chemical Society Reviews*, 2021, **50**, 8193-8213.
2. N. Kwon, D. Kim, K. M. K. Swamy and J. Yoon, *Coordination Chemistry Reviews*, 2021, **427**, 213581.
3. Y. Ning, M. Zhu and J.-L. Zhang, *Coordination Chemistry Reviews*, 2019, **399**, 213028.
4. S. Shuvaev, M. Starck and D. Parker, *Chemistry – A European Journal*, 2017, **23**, 9974-9989.
5. S. E. Bodman and S. J. Butler, *Chemical Science*, 2021, **12**, 2716-2734.
6. M. L. Aulsebrook, B. Graham, M. R. Grace and K. L. Tuck, *Coordination Chemistry Reviews*, 2018, **375**, 191-220.
7. B. Brennecke, Q. Wang, Q. Zhang, H.-Y. Hu and M. Nazaré, *Angewandte Chemie International Edition*, 2020, **59**, 8512-8516.
8. A. G. Cosby, J. J. Woods, P. Nawrocki, T. J. Sørensen, J. J. Wilson and E. Boros, *Chemical Science*, 2021, **12**, 9442-9451.
9. J. D. Routledge, X. Zhang, M. Connolly, M. Tropiano, O. A. Blackburn, A. M. Kenwright, P. D. Beer, S. Aldridge and S. Faulkner, *Angewandte Chemie International Edition*, 2017, **56**, 7783-7786.
10. C. Breen, R. Pal, M. R. J. Elsegood, S. J. Teat, F. Iza, K. Wende, B. R. Buckley and S. J. Butler, *Chemical Science*, 2020, **11**, 3164-3170.
11. S.-Y. Huang and V. C. Pierre, *Chemical Communications*, 2018, **54**, 9210-9213.
12. S.-Y. Huang, M. Qian and V. C. Pierre, *Inorganic Chemistry*, 2020, **59**, 4096-4108.
13. S.-Y. Huang, M. Qian and V. C. Pierre, *Inorganic Chemistry*, 2019, **58**, 16087-16099.
14. S. Hery, L. L. A. Grenier and T. J. Sørensen, *Analysis & Sensing*, 2022, **4**, e202200093.
15. L. L. A. Grenier, L. G. Nielsen and T. J. Sørensen, *Analysis & Sensing*, 2022, **2**, e202200033.
16. S. E. Bodman, C. Breen, S. Kirkland, S. Wheeler, E. Robertson, F. Plasser and S. J. Butler, *Chemical Science*, 2022, **13**, 3386-3394.
17. J. Sahoo, R. Arunachalam, P. S. Subramanian, E. Suresh, A. Valkonen, K. Rissanen and M. Albrecht, *Angewandte Chemie International Edition*, 2016, **55**, 9625-9629.
18. Z. Mandinic, M. Curcic, B. Antonijevic, M. Carevic, J. Mandic, D. Djukic-Cosic and C. P. Lekic, *Science of The Total Environment*, 2010, **408**, 3507-3512.
19. M. Ludlow, G. Luxton and T. Mathew, *Nephrology Dialysis Transplantation*, 2007, **22**, 2763-2767.
20. Y. Zhou, J. F. Zhang and J. Yoon, *Chemical Reviews*, 2014, **114**, 5511-5571.
21. A. Dhillon, M. Nair and D. Kumar, *Analytical Methods*, 2016, **8**, 5338-5352.
22. H. Yahyavi, M. Kaykhaii and M. Mirmoghaddam, *Critical Reviews in Analytical Chemistry*, 2016, **46**, 106-121.
23. S. J. Butler, *Chemical Communications*, 2015, **51**, 10879-10882.
24. L. s. M. P. Lima, A. Lecointre, J.-F. Morfin, A. de Blas, D. Visvikis, L. J. Charbonnière, C. Platas-Iglesias and R. Tripier, *Inorganic Chemistry*, 2011, **50**, 12508-12521.
25. R. Tripier, C. Platas-Iglesias, A. Boos, J.-F. Morfin and L. Charbonnière, *European Journal of Inorganic Chemistry*, 2010, **2010**, 2735-2745.

26. T. Liu, A. Nonat, M. Beyler, M. Regueiro-Figueroa, K. Nchimi Nono, O. Jeannin, F. Camerel, F. Debaene, S. Cianférani-Sanglier, R. Tripier, C. Platas-Iglesias and L. J. Charbonnière, *Angewandte Chemie International Edition*, 2014, **53**, 7259-7263.
27. A. Nonat, T. Liu, O. Jeannin, F. Camerel and L. J. Charbonnière, *Chemistry – A European Journal*, 2018, **24**, 3784-3792.
28. A. Nonat, C. F. Chan, T. Liu, C. Platas-Iglesias, Z. Liu, W.-T. Wong, W.-K. Wong, K.-L. Wong and L. J. Charbonnière, *Nature Communications*, 2016, **7**, 11978.
29. O. A. Blackburn, N. F. Chilton, K. Keller, C. E. Tait, W. K. Myers, E. J. L. McInnes, A. M. Kenwright, P. D. Beer, C. R. Timmel and S. Faulkner, *Angewandte Chemie International Edition*, 2015, **54**, 10783-10786.
30. O. A. Blackburn, A. M. Kenwright, P. D. Beer and S. Faulkner, *Dalton Transactions*, 2015, **44**, 19509-19517.
31. O. A. Blackburn, A. M. Kenwright, A. R. Jupp, J. M. Goicoechea, P. D. Beer and S. Faulkner, *Chemistry – A European Journal*, 2016, **22**, 8929-8936.
32. O. A. Blackburn, J. D. Routledge, L. B. Jennings, N. H. Rees, A. M. Kenwright, P. D. Beer and S. Faulkner, *Dalton Transactions*, 2016, **45**, 3070-3077.
33. C. Alexander, J. A. Thom, A. M. Kenwright, K. E. Christensen, T. J. Sørensen and S. Faulkner, *Chemical Science*, 2023, **14**, 1194-1204.
34. M. J. Langton, O. A. Blackburn, T. Lang, S. Faulkner and P. D. Beer, *Angewandte Chemie International Edition*, 2014, **53**, 11463-11466.
35. S. R. Kiraev, R. R. Weber, J. A. L. Wells, A. Orthaber, D. Kovacs and K. E. Borbas, *Analysis & Sensing*, 2022, **2**, e202200015.
36. A. Cataldo, M. Chvojka, G. Park, V. Šindelář, F. P. Gabbaï, S. J. Butler and H. Valkenier, *Chemical Communications*, 2023, **59**, 4185-4188.
37. W. Chen, X. Tang, W. Dou, B. Wang, L. Guo, Z. Ju and W. Liu, *Chemistry – A European Journal*, 2017, **23**, 9804-9811.
38. Q. Wang, Z. Zhou and Y. Zheng, *Materials Letters*, 2014, **126**, 162-164.
39. L. F. Smith, B. A. Blight, H.-J. Park and S. Wang, *Inorganic Chemistry*, 2014, **53**, 8036-8044.
40. H.-J. Park, S.-B. Ko, I. W. Wyman and S. Wang, *Inorganic Chemistry*, 2014, **53**, 9751-9760.
41. X. Pang, L. Li, Y. Wei, X. Yu and Y. Li, *Dalton Transactions*, 2018, **47**, 11530-11538.
42. Z. Zhou, Y. Zheng and Q. Wang, *Inorganic Chemistry*, 2014, **53**, 1530-1536.
43. S. J. Bradberry, J. P. Byrne, C. P. McCoy and T. Gunnlaugsson, *Chemical Communications*, 2015, **51**, 16565-16568.
44. X. Zeng, J. Hu, M. Zhang, F. Wang, L. Wu and X. Hou, *Analytical Chemistry*, 2020, **92**, 2097-2102.
45. A. P. Bassett, S. W. Magennis, P. B. Glover, D. J. Lewis, N. Spencer, S. Parsons, R. M. Williams, L. De Cola and Z. Pikramenou, *Journal of the American Chemical Society*, 2004, **126**, 9413-9424.
46. K. Binnemans, *Handbook on the Physics and Chemistry of Rare Earths*, 2005, **35**, 107-272.
47. E. Pretsch, P. Bühlmann, M. Badertscher, *Structure Determination of Organic Compounds*, 2009.
48. R. Chinchilla and C. Nájera, *Chemical Society Reviews*, 2011, **40**, 5084-5121.

49. S. Thulasi, A. Savithri and R. L. Varma, *Supramolecular Chemistry*, 2011, **23**, 501-508.
50. P. G. M. Wuts, *Greene's protective groups in organic synthesis / Peter G. M. Wuts*, Hoboken, New Jersey : Wiley, 2014., Fifth edition. edn., 2014.
51. P. Larkin, *Infrared and Raman Spectroscopy: Principles and Spectral Interpretation*, Saint Louis: Elsevier, Saint Louis, 2017.
52. C. F. Liang, E. J. Schmitschek and J. A. Trias, *Journal of Inorganic and Nuclear Chemistry*, 1970, **32**, 811-831.
53. V. A. Grillo, E. J. Seddon, C. M. Grant, G. Aromí, J. C. Bollinger, K. Folting and G. Christou, *Chemical Communications*, 1997, 1561-1562.
54. J. K. Clegg, L. F. Lindoy, J. C. McMurtrie and D. Schilter, *Dalton Transactions*, 2005, 857-864.
55. R. D. Shannon, *Acta Crystallographica Section A*, 1976, **32**, 751-767.
56. J. Shi, Y. Hou, W. Chu, X. Shi, H. Gu, B. Wang and Z. Sun, *Inorganic Chemistry*, 2013, **52**, 5013-5022.
57. J.-C. G. Bünzli and S. V. Eliseeva, in *Lanthanide Luminescence: Photophysical, Analytical and Biological Aspects*, eds. P. Hänninen and H. Härmä, Springer Berlin Heidelberg, Berlin, Heidelberg, 2011, 1-45.
58. M. H. V. Werts, in *Lanthanide Luminescence: Photophysical, Analytical and Biological Aspects*, eds. P. Hänninen and H. Härmä, Springer Berlin Heidelberg, Berlin, Heidelberg, 2011, 133-159.
59. K. Binnemans, *Coordination Chemistry Reviews*, 2015, **295**, 1-45.
60. H. F. Li, P. F. Yan, P. Chen, Y. Wang, H. Xu and G. M. Li, *Dalton Trans*, 2012, **41**, 900-907.
61. W. D. Horrocks, Jr. and D. R. Sudnick, *Journal of the American Chemical Society*, 1979, **101**, 334-340.
62. A. Beeby, I. M. Clarkson, R. S. Dickins, S. Faulkner, D. Parker, L. Royle, A. S. de Sousa, J. A. Gareth Williams and M. Woods, *Journal of the Chemical Society, Perkin Transactions 2*, 1999, 493-504.
63. M. Tropiano, O. A. Blackburn, J. A. Tilney, L. R. Hill, T. Just Sørensen and S. Faulkner, *Journal of Luminescence*, 2015, **167**, 296-304.
64. S. V. Eliseeva and J.-C. G. Bünzli, *Chemical Society Reviews*, 2010, **39**, 189-227.
65. F. R. Silva, O. Malta, C. Reinhard, H. U. Güdel, C. Piguet, J.-E. Moser and J.-C. Bünzli, *The Journal of Physical Chemistry A*, 2002, **106**, 1670-1677.
66. D. Esteban-Gómez, L. A. Büldt, P. Pérez-Lourido, L. Valencia, M. Seitz and C. Platas-Iglesias, *Inorganic Chemistry*, 2019, **58**, 3732-3743.

2.5 Appendix I

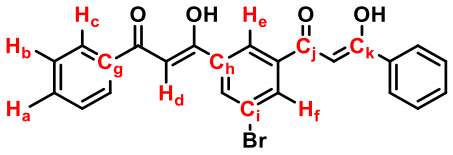
2.5.1 Materials and methods

Solvents and chemicals were purchased from Sigma Aldrich/Merck, VWR, Alfa Aesar and Fisher Scientific. NMR solvents were purchased from Goss Scientific. For both synthesis and photophysical studies, DMF (anhydrous, 99.8%) and THF (anhydrous, ≥99.9%, inhibitor free) were employed. For the syntheses of **3** and **bisDBM**, NaH (60% in mineral oil) was employed and washed 3 times with anhydrous hexane prior to use. For F^- coordination studies in THF, section 2.4, TBAF 1.0 M solution in THF was purchased from Sigma Aldrich/Merck and diluted to the desired stock concentration. For each study, the stock solution was prepared fresh. All organic reactions were conducted under N_2 flow with Schlenk technique, unless stated otherwise, and all glassware was oven dried overnight prior to use. THF and triethylamine for the synthesis of compound **4** and DMF for the synthesis of compound **7** were degassed for 30 minutes prior to use and the reactions were conducted shielded from light with the aid of aluminium foil. Compound **$EuDBM_3$** was synthesised by MSc Carys Scott. Silica gel plates 60 F_{254} for thin layer chromatography were purchased from Merck. Silica gel 0.060-0.2 mm, 70-230 mesh was purchased from Alfa Aesar. NMR spectra were recorded on 400 MHz Bruker AVIII 400 or NEO 400 or a 500 MHz Bruker NEO 500, and analysed with MestReNova software. Electrospray mass spectrometry was conducted on a Waters Micromass Q-TOF. MALDI-TOF was conducted on a Bruker Flextreme MALDI-TOF and using α-cyano-4-hydroxycinnamic acid (i.e. CHCA) as matrix. For calculation of predicted isotope patterns and mass of MALDI-TOF spectra, enviPat was employed. Infrared measurements were obtained on a Perkin Elmer 100FT-IR spectrometer fitted with ATR attachment. Raman spectra were recorded on a

Renishaw InVia Raman microscope at the department of Physics and Astronomy, University of Birmingham, using a 633 nm laser, 50x objective and 600 l/mm grating. UV-Vis absorption spectra were recorded on an Agilent Cary 60 UV-Vis spectrophotometer. Luminescence spectra were recorded either on an Edinburgh Instruments FLSP920 steady state and time resolved spectrometer with F980 software or an Edinburgh Instruments FLS1000 steady state and time resolved spectrometer with Fluoracle software. In both cases, the spectra were corrected for lamp and instrument response. Longpass filters were employed, with cut-on wavelength 550 nm for Eu(III) spectra and 850 nm for Yb(III) and Nd(III) spectra. A 450 W Xenon Arc lamp was employed as excitation source for steady state measurements, while time resolved spectra were acquired with a μF flashlamp. For quantum yield studies, the absorbance value at the excitation wavelength was below 0.1. For all other luminescence studies, absorbance values at the excitation wavelength below 0.2 were used. Quantum yields were obtained with an integrating sphere apparatus from Edinburgh Instruments and analysed with either F980 or Fluoracle software. When appropriate, neutral density filters (OD 0.3 or 0.8) from Thorlabs were used. For 77 K phosphorescence studies, an Oxford Instruments cryostat was employed and the sample was degassed with 10 freeze-pump-thaw cycles prior to analysis. Lifetimes were fitted to mono- or multiexponential decays as appropriate using FAST software, with an estimated error of 10% and with χ^2 between 1.0 and 1.3. When directly comparing optical properties for section 2.4, the measurements were carried out on the same day, with the same software and instrument configurations. When comparing emission intensities, the integral of the whole spectrum was considered, unless a single wavelength was stated. For calculations of $\tau_{Rad.}$, the wavelength range of the $^5D_0 \rightarrow {}^7F_1$ transition of Eu(III) was 581-601 nm. All spectra were plotted and analysed with OriginPro 2023.

2.5.2 Synthetic procedures

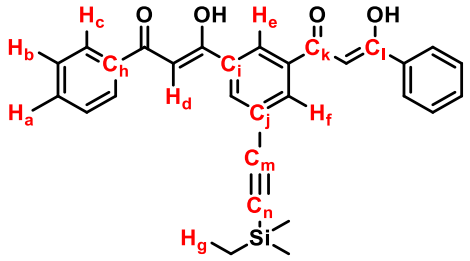
2.5.2.1 Synthesis of 3,3'-(5-bromo-1,3-phenylene)bis(1-phenylpropane-1,3-dione) (3)



3

Dimethyl 5-bromoisophthalate **1** (800 mg, 2.90 mmol) and acetophenone **2** (1.03 mL, 8.79 mmol) in THF (5.8 mL) were added dropwise to NaH (586 mg, 14.6 mmol) at 0-5 °C to give a bright yellow mixture. This was stirred at 0-5 °C for 2 hours and then for an additional 2 hours at room temperature. After this time, H_2O (10 mL) was added to the yellow reaction mixture to give a yellow precipitate. After filtration, the solid was dispersed in MeOH (5 mL) and HCl (5 mL, 2 M) was added to give a pale-yellow precipitate. This was washed with MeOH (3 x 20 mL) to give **3** as a pale-yellow solid (623 mg, 1.40 mmol, 45%). ^{1}H-NMR (400 MHz, $CDCl_3$): δ 8.48 (t, J = 1.6 Hz, H_e, 1H), 8.26 (d, J = 1.6 Hz, H_f, 2H), 8.05 – 8.01 (dt, J = 6.9, 1.8 Hz H_c, 4H), 7.63 – 7.57 (m, H_a, 2H), 7.55 – 7.50 (m, H_b, 4H), 6.88 (s, H_d, 2H). ^{13}C-NMR (101 MHz, $CDCl_3$): δ 186.51 (C_k), 183.39 (C_j), 138.19 (C_h), 135.07 (C_g), 133.56 (C_f), 133.14 (C_a), 128.98 (C_b), 127.52 (C_c), 124.42 (C_e), 123.55 (C_i), 93.66 (C_d). ESI$^-$-MS: calcd. [M-H] 447.0232 found 447.0244. IR (solid): $\tilde{\nu}$ (cm^{-1}) 1598 (s, C=O/C-OH), 1530 (s), 1476 (s), 1417 (m), 1304 (m), 1258 (m), 1232 (m), 1207 (s), 1178 (m), 1152 (w), 1133 (w), 1115 (w), 1097 (w), 1078 (w), 1068 (w), 1050 (w), 1025 (m), 997 (m), 924 (w), 908 (w), 871 (m), 849 (w), 804 (m), 758 (vs), 717 (m), 692 (s), 679 (s).

2.5.2.2 Synthesis of 1,1'-(5-((trimethylsilyl)ethynyl)-1,3-phenylene)bis(3-hydroxy-3-phenylprop-2-en-1-one) (4)

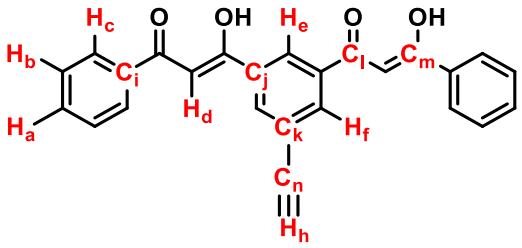


4

Compound **3** (442 mg, 0.89 mmol), $PdPPh_3Cl_2$ (62 mg, 0.09 mmol), PPh_3 (23 mg, 0.09 mmol) and CuI (34 mg, 0.18 mmol), were suspended in a degassed solution of dry THF (2.5 mL) and triethylamine (1.49 mL, 10.68 mmol) to give a deep red mixture. After 15 minutes, trimethylsilylacetylene (0.18 mL, 1.34 mmol) was added dropwise and the black mixture was stirred at 50 °C for 18 hours. After this time, DCM (100 mL) was added, and the solvent removed under reduced pressure. The procedure was repeated three times to give a dark brown solid. This was taken up in ethyl acetate (10 mL) and the black catalyst removed by filtration. After removal of the solvent under reduced pressure, the orange solid was purified by column chromatography (9:1 hexane: ethyl acetate). Compound **4** was isolated as a pale yellow solid (274 mg, 0.58 mmol, 66%). ^{1}H-NMR (400 MHz, $CDCl_3$): δ 8.51 (t, J = 1.7 Hz, H_e, 1H,), 8.21 (d, J = 1.7 Hz, H_f, 2H), 8.05 – 8.01 (m, H_c, 4H), 7.62 – 7.50 (m, H_a, H_b, 6H), 6.92 (s, H_d, 2H), 0.31 (s, H_g, 9H). ^{13}C-NMR (101 MHz, $CDCl_3$) δ 186.47 (C_l), 184.03(C_k), 136.59 (C_i), 135.23 (C_h), 133.87 (C_f), 133.01 (C_a), 128.94 (C_b), 127.50 (C_c), 125.61 (C_e), 124.69 (C_j), 103.23 (C_m), 96.97 (C_n), 93.63 (C_d), 0.00 (C_g). ESI$^-$-MS $C_{29}H_{26}O_4Si$: calcd. $[M-H]^-$ 465.1522 found 465.1535. λ_{max}/nm (DMF): 358 nm (ε (DMF): $4x10^4$ M^{-1} cm^{-1}). IR (solid): $\tilde{\nu}$ (cm^{-1}) 1603 (s, C=O/C-OH), 1530 (s), 1476 (s), 1435 (m), 1307 (m), 1247 (s), 1211 (m), 1191 (w), 1112 (w), 1100 (w), 1074 (w),

1024 (m), 999 (m), 952 (m), 914 (m), 892 (w), 837 (vs, CH_3-Si), 751 (vs), 691 (s), 674 (s), 664 (m), 654 (w).

2.5.2.3 Synthesis of 1,1'-(5-ethynyl-1,3-phenylene)bis(3-hydroxy-3-phenylprop-2-en-1-one) (5)

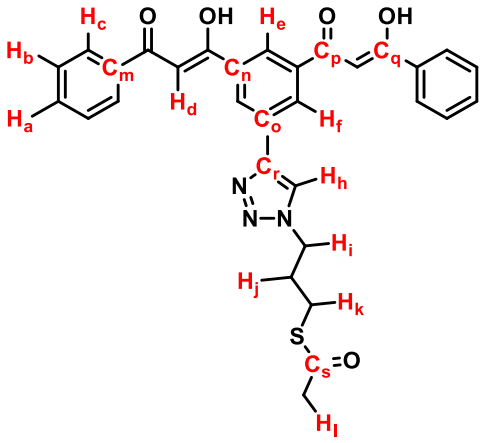


5

Compound **4** (190 mg, 0.40 mmol) was dissolved in dry THF (1.3 mL) and TBAF (0.5 mL, 1 M in THF) was added dropwise at 0 °C to give a dark green solution. The mixture was stirred at 0 °C for 2 hours and at room temperature for additional 2 hours. After this time, the solution was diluted with H_2O (5 mL) and extracted with DCM (3 x 5 mL). The organic layer was washed with brine (10 mL) and dried over Na_2SO_4. After removal of the solvent under reduced pressure, the dark orange solid was purified by column chromatography (8:2 hexane: ethyl acetate) to give compound **5** as an off white solid (105 mg, 0.26 mmol, 65%). ^{1}H-NMR (400 MHz, $CDCl_3$): δ 8.54 (t, J = 1.5 Hz, H_e, 1H), 8.25 (d, J = 1.6 Hz, H_f, 2H), 8.05 – 8.01 (m, H_c, 4H), 7.62 – 7.57 (m, H_a, 2H), 7.56 – 7.49 (m, H_b, 4H), 6.91 (s, H_d, 2H), 3.24 (s, H_h, 1H). ^{13}C-NMR (101 MHz, $CDCl_3$) δ 186.51 (C_m), 183.86 (C_l), 136.74 (C_j), 135.19 (C_i), 134.04 (C_f), 133.05 (C_a), 128.95 (C_b), 127.50 (C_c), 125.95 (C_e), 123.67 (C_k), 93.62 (C_d), 82.10 (C_n), 79.39 (C_h). ESI$^-$-MS $C_{26}H_{18}O_4$: calcd. $[M-H]^-$ 393.1127 found 393.1138. λ_{max}/nm (DMF): 359 nm (ε (DMF): 5x10^4 M^{-1} cm^{-1}). IR (solid): $\tilde{\nu}$ (cm^{-1}) 3269 (m, ≡C-H), 1596 (s, C=O/C-OH), 1523 (s), 1470 (s), 1410 (w), 1304 (w), 1238 (w), 1203

(m), 1184 (w), 1156 (w), 1097 (w), 1074 (w), 1024 (w), 999 (w), 914 (m), 892 (w), 799 (w), 755 (vs), 711 (m), 692 (s), 676 (s).

2.5.2.4 Synthesis of S-(3-(4-(3,5-bis(3-hydroxy-3-phenylacryloyl)phenyl)-1H-1,2,3-triazol-1-yl)propyl) ethanethioate (SAcbisDBM)

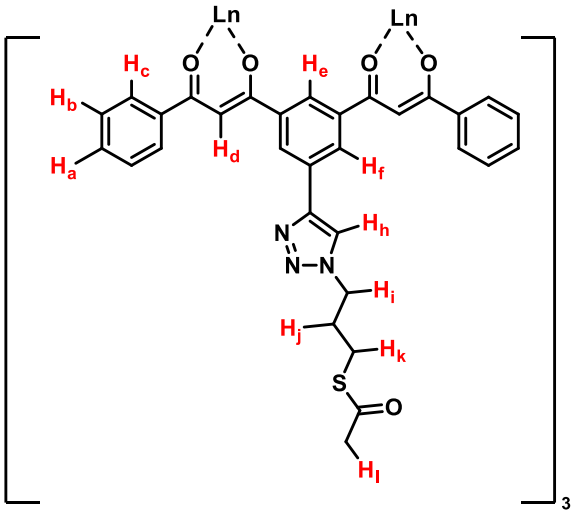


7 (SAcbisDBM)

Compound **5** (100 mg, 0.25 mmol), CuI (4.8 mg, 0.02 mmol), TBTA (20 mg, 0.04 mmol) and L-ascorbic acid (35 mg, 0.20 mmol) were dissolved in dry and degassed DMF (1 mL). S-(3-azidopropyl)thioacetate **6** (0.04 mL, 0.30 mmol) was added to the clear yellow solution and the mixture was stirred at room temperature for 18 hours. After this time, H_2O (5 mL) was added and the mixture extracted with DCM (4 x 5 mL). The organic layer was washed with brine, dried over Na_2SO_4 and the solvent removed under reduced pressure. The red solid was purified by column chromatography (DCM and DCM:MeOH 9.5:0.5). The resultant solid was washed with MeOH (15 mL) to give **SAcbisDBM** as a dark pink solid (70 mg, 0.13 mmol, 50%). ^{1}H-NMR (400 MHz, $CDCl_3$): δ 8.63 (s, H_f, 2H), 8.56 (s, H_e, 1H), 8.06 (m, H_c, H_h, 5H), 7.60 (t, J = 7.3 Hz, H_a, 2H), 7.53 (t, J = 7.3 Hz, H_b, 4H), 7.07 (s, H_d, 2H), 4.53 (t, J = 6.8 Hz, H_i, 2H), 2.95 (t, J = 6.8 Hz, H_k, 2H), 2.38 (s, H_l, 3H), 2.31 (p, J = 6.8 Hz, H_j, 2H). ^{13}C-NMR (101 MHz, $CDCl_3$) δ 195.39

(C_s), 186.37 (C_q), 184.63 (C_p), 146.30 (C_r), 137.08 (C_n), 135.28 (C_m), 132.97 (C_a), 132.03 (C_o), 128.93 (C_b), 127.82 (C_f), 127.55 (C_c), 125.44 (C_e), 120.89 (C_h), 93.77 (C_d), 49.25 (C_i), 30.84 (C_l), 30.45 (C_j), 25.98 (C_k). ESI^--MS $C_{31}H_{27}N_3O_5S$: calcd. $[M-H]^-$ 552.1593 found 552.1603. λ_{max}/nm (DMF): 357.5 nm (ε (DMF): $5x10^4$ M^{-1} cm^{-1}). IR (solid): $\tilde{\nu}$ (cm^{-1}) 1691 (s, *S*-C=O), 1598 (s, C=O/C-OH), 1520 (s), 1482 (s), 1423 (w), 1379 (vw), 1351 (w), 1300 (w), 1266 (w), 1235 (w), 1210 (m), 1178 (w), 1156 (w), 1137 (w), 1093 (m), 1068 (vw), 1049 (vw), 1024 (w), 996 (w), 949 (w), 892 (m), 839 (w), 814 (w), 802 (w), 764 (vs), 723 (m), 695 (s), 676 (s).

2.5.2.5 Synthesis of Ln_2SAcbisDBM$_3$ (Ln=Eu(III), Gd(III), Nd(III), Yb(III))



Ln_2SAcbisDBM$_3$

No Schlenk techniques were employed for this reaction. Ligand **SAcbisDBM** (20 mg, 0.04 mmol) was dissolved in $CHCl_3$ (0.6 mL) and a solution of $LnCl_3$ $6H_2O$ (0.03 mmol) in MeOH (0.3 mL) was added dropwise. A solution of triethylamine (0.01 mL, 0.09 mmol) in MeOH (0.3 mL) was then added to give a pale-yellow precipitate. After two hours of stirring at room temperature, the pale-yellow solid was filtered and washed with $CHCl_3$ (2 mL), MeOH (2 mL), H_2O (2 mL) and Et_2O (2 mL) to give **Ln_2SAcbisDBM$_3$** as a pale-yellow solid (25-30%).

Eu_2SAcbisDBM$_3$

^{1}H-NMR (500 MHz, DMSOd_6) δ 8.04 (s, H_h, 3H) 6.54 (s, H_a, 6H), 6.38 (s, H_b, H_e, 15H), 6.25 (s, H_f, 6H), 4.49 (s, H_c, 12H), 4.04 (br t, J = 6.8 Hz, H_i, 6H), 3.71 (s, H_d, 6H), 2.41 (q, J = 6.8 Hz, H_k, 3H), 2.12 (s, H_l, 9H), 1.74 (p, J = 6.8 Hz, H_j, 6H), 0.92 (s, J = 6.8 Hz, H_k, 3H). MALDI – TOF $C_{93}H_{75}Eu_2N_9O_{15}S_3$: $[M+CH_2O]^{\cdot-}$ calcd. 1989.3 found 1989.3. IR (solid): $\tilde{\nu}$ (cm^{-1}) 1692 (m), 1599 (m), 1524 (s), 1478 (s), 1347 (m), 1301 (m), 1273 (m), 1236 (m), 1217 (s), 1180 (m), 1152 (w), 1133 (w), 1115 (w), 1096 (m), 1078 (w), 1068 (w), 1050 (w), 1022 (m), 994 (m), 947 (m), 891 (w), 836 (w), 817 (w), 808 (w), 761 (vs), 724 (m), 696 (m), 677 (m). λ_{max}/nm (DMF): 359.5 nm (ε (DMF): 1.5x10^5 M^{-1} cm^{-1}). Φ (DMF): 5.5%.

Gd_2SAcbisDBM$_3$

MALDI – TOF $C_{93}H_{75}Gd_2N_9O_{15}S_3$: $[M+CH_2O]^{\cdot-}$ calcd. 1999.3 found 1999.6. λ_{max}/nm (DMF): 359 nm (ε (DMF): 1.6x10^5 M^{-1} cm^{-1}).

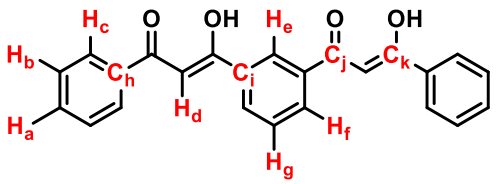
Yb_2SAcbisDBM$_3$

^{1}H NMR (500 MHz, DMSOd_6) δ 7.14-7.05 (m, H_a, H_b, H_e, 21H), 6.03 (s, H_h, 3H), 4.97 (br, H_c, H_d, 18H), 3.00-2.94 (br, m, H_i, H_f, 12H), 1.57 (t, J = 6.8 Hz, H_k, 6H), 1.51 (s, H_l, 9H), 0.67 (p, J = 6.8 Hz, H_j, 6H). MALDI – TOF $C_{93}H_{75}Yb_2N_9O_{15}S_3$: $[M+CH_2O]^{\cdot-}$ calcd. 2031.3 found 2031.4. λ_{max}/nm (DMF): 358.5 nm (ε (DMF): 1.5x10^5 M^{-1} cm^{-1}). Φ (DMSOd_6): 0.8%.

Nd_2SAcbisDBM$_3$

^{1}H NMR (500 MHz, DMSOd_6) δ 12.35-11.21 (br, H_c, H_d, 18H), 10.60 (s, H_f, 6H), 9.72 (s, H_h, 3H), 8.43 (s, H_a, H_b, H_e, 21H), 4.94 (t, J = 6.8 Hz, H_i, 6H), 3.27 (m, 6.8 Hz, H_k, 6H) 2.66-2.54 (br, H_l, H_j, 15H). MALDI – TOF $C_{93}H_{75}Nd_2N_9O_{15}S_3$: $[M\text{-}2Ac+ CH_2O]^{\cdot-}$ calcd. 1885.2 found 1885.0. λ_{max}/nm (DMF): 358.5 nm (ε (DMF): 1.5x10^5 M^{-1} cm^{-1}).

2.5.2.6 Synthesis of 1,3-bis(3-phenyl-3-oxopropanoyl)benzene (bisDBM)[1]



bisDBM

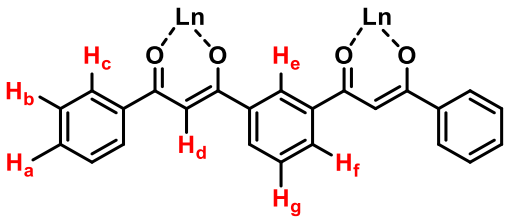
The procedure was followed as reported.[45] Dimethyl isophthalate (500 mg, 2.57 mmol) and acetophenone, **2**, (0.9 mL, 7.72 mmol) were dissolved in THF (5 mL) and the solution was added dropwise to NaH at 0 °C (515 mg, 12.87 mmol) to produce a bright yellow suspension. The mixture was stirred at 0 °C for 2 hours and at room temperature for additional 2 hours to give a deep orange colour. After this time, H_2O (6 mL) was slowly introduced and the yellow sticky precipitate was filtered. This was taken up in MeOH (6 mL) and addition of dilute HCl (5 mL, 2 M) gave a pale yellow precipitate that was filtered and washed with MeOH to give **bisDBM** as a pale yellow solid (430 mg, 1.16 mmol, 45%).

^{1}H-NMR (400 MHz, $CDCl_3$): δ 8.58 (t, J = 1.7 Hz, H_e, 1H), 8.17 (dd, J = 7.8, 1.7 Hz, H_f, 2H), 8.04 – 8.01 (m, H_c, 4H), 7.66 – 7.49 (m, H_a, H_g, H_b, 7H), 6.93 (s, H_d, 2H).

^{13}C NMR (101 MHz, $CDCl_3$): δ 186.24 (C_k), 184.95 (C_j), 136.37 (C_i), 135.37 (C_h), 132.88 (C_f), 130.94 (C_a), 129.31 (C_g), 128.91 (C_b), 127.44 (C_c), 125.94 (C_e), 93.54 (C_d).

The found data are in accordance to the reported data.[45]

2.5.2.7 Synthesis of $Ln_2bisDBM_3$ (Ln=Eu(III), Yb(III), Nd(III))[45]



$Ln_2bisDBM_3$

The synthesis was repeated as reported and no Schlenk techniques were employed for this reaction.[45] **bisDBM** (43 mg, 0.12 mmol) was dissolved in $CHCl_3$ (4 mL) and a solution of $LnCl_3$ $6H_2O$ (0.08 mmol) in MeOH (1 mL) was added. A solution of triethylamine (0.03 mL, 0.23 mmol) in MeOH (1 mL) was introduced dropwise and the solution turned a darker yellow colour, followed by the formation of a pale yellow precipitate after a few seconds. This was stirred at room temperature for 1 hour and, after this time, the yellow precipitate was filtered and washed with $CHCl_3$ (1 mL), MeOH (1 mL), H_2O (1 mL) and Et_2O (1 mL) to give **$Ln_2bisDBM_3$** as a pale yellow solid (29-44%).

$Eu_2bisDBM_3$

^{1}H-NMR (400 MHz, DMSO-d_6): δ 6.52 (t, J = 7.5 Hz, H_a, 6H), 6.36 (br, H_b, H_e, 15H), 6.12 (t, J = 7.3, H_g, 3H), 5.89 (d, J = 7.3, H_f, 6H), 4.48 (s, H_c, 12H), 3.60 (br, H_d, 6H). MALDI – TOF $C_{73}H_{48}Eu_2O_{13}$: $[M+CO]^-$ calcd. 1436.1 found 1436.4.

$Yb_2bisDBM_3$

^{1}H-NMR (400 MHz, DMSO-d_6): δ 7.24-7.09 (m, H_a, H_b, H_e, H_g, 30H), 5.29 (br, H_c, H_d, 18H), 4.89 (br, H_f, 6H). MALDI – TOF $C_{72}H_{50}Yb_2O_{12}$: $[M+Na]^+$ calcd. 1475.2 found 1475.2.

Nd_2bisDBM$_3$

^{1}H-NMR (400 MHz, DMSO-d_6): δ 11.62 (br, H_c, H_d, 18H), 10.21 (br, H_f, 6H), 8.56-8.37 (m, H_g, H_a, H_b, H_e, 24H). MALDI – TOF $C_{72}H_{51}Nd_2O_{12}$: $[M+Na]^+$ calcd. 1416.2 found 1416.6.

The found data are in accordance to the reported data.[45]

2.5.3 Anion coordination procedures

2.5.3.1 Testing with F^- (NaF)

NaF (25 mM in H_2O) was added to **Eu_2SAcbisDBM$_3$** (3.2 μM in H_2O/EtOH 1/1, 0.4% DMF, 3 mL) in small aliquots (6.5 equivalents = 2.5 μL) up to 260 equivalents. Each addition was followed by stirring at room temperature for 5 minutes prior to acquisition of steady state and time resolved spectra.

2.5.3.2 Testing with F^- (TBAF)

*Comparison between **Eu_2SAcbisDBM$_3$** and **Eu_2bisDBM$_3$***

TBAF (3 mM in THF) was added to either **Eu_2SAcbisDBM$_3$** or **Eu_2bisDBM$_3$** (0.83 μM in THF, 0.2% DMF, 3 mL) in small aliquots (6 equivalents = 5 μL) up to 24 equivalents. Each addition was followed by stirring at room temperature for 5 minutes prior to acquisition of steady state and time resolved spectra.

*Smaller additions to **Eu_2SAcbisDBM$_3$***

TBAF (0.5 mM in THF) was added to **Eu_2SAcbisDBM$_3$** (0.83 μM in THF, 0.2% DMF, 3 mL) in small aliquots (1 equivalent = 5 μL) up to 30 equivalents. Each addition was followed by stirring at room temperature for 5 minutes prior to acquisition of steady state and time resolved spectra.

*Addition to **Eu_2bisDBM$_3$** for ESI^--MS*

TBAF (1 mM in THF, 120 µL) was added to **Eu_2bisDBM$_3$** (1 µM in THF, 0.2% DMF, 3 mL), followed by stirring at room temperature for 15 minutes.

2.5.3.3 Testing with Br^- (TBAB)

TBAB (0.5 mM in THF) was added to **Eu_2SAcbisDBM$_3$** (0.5 µM in THF, 0.2% DMF, 3 mL) in small aliquots (2 equivalents = 6 µL) up to 16 equivalents. Each addition was followed by stirring at room temperature for 5 minutes prior to acquisition of steady state and time resolved spectra.

2.5.4 Characterisation data

2.5.4.1 3,3'-(5-bromo-1,3-phenylene)bis(1-phenylpropane-1,3-dione) (3)

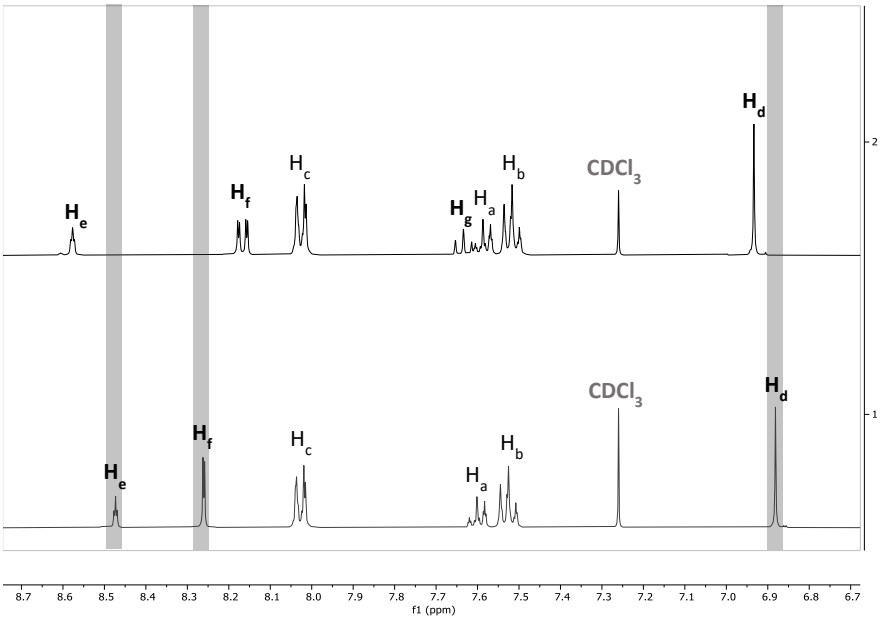


Figure 2.41 – Stacked ^{1}H-NMR spectra (400 MHz, $CDCl_3$) of control **bisDBM** (top) and compound **3** (bottom). Only the aromatic region is shown, and the peaks have been assigned as reported in the experimental section. The grey bands illustrate the position and shift of the H_e, H_f and H_d protons of compound **3**.

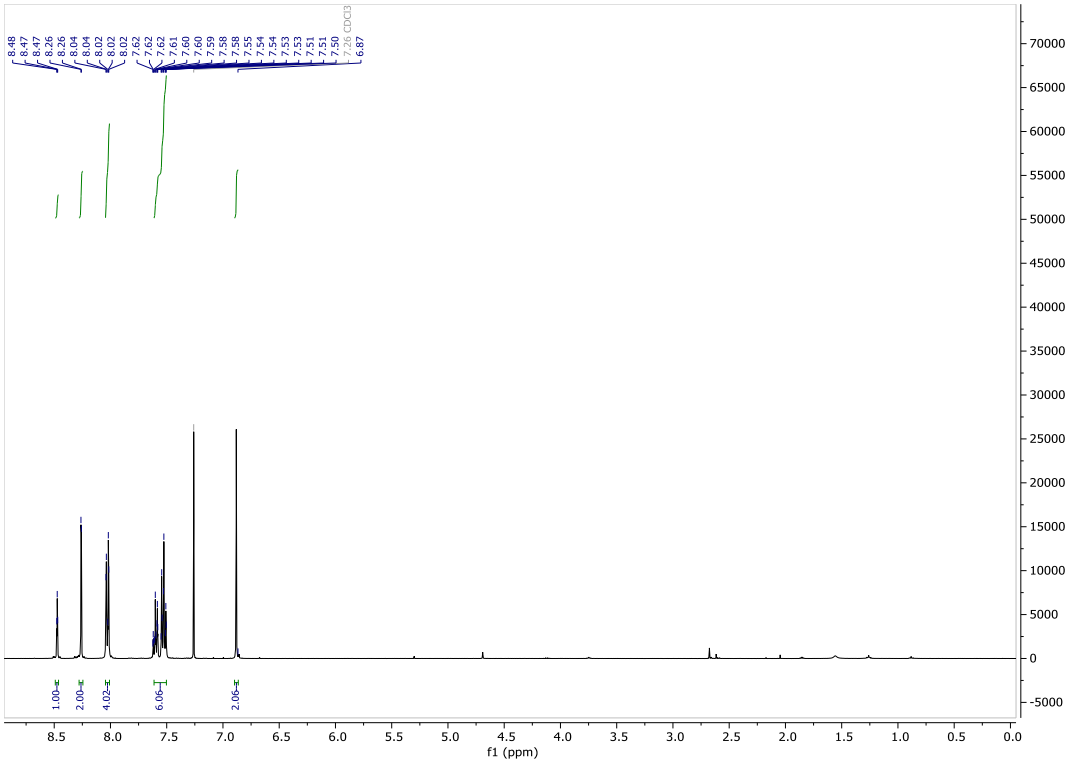


Figure 2.42 –^{1}H-NMR spectrum (400 MHz, $CDCl_3$) of compound **3**.

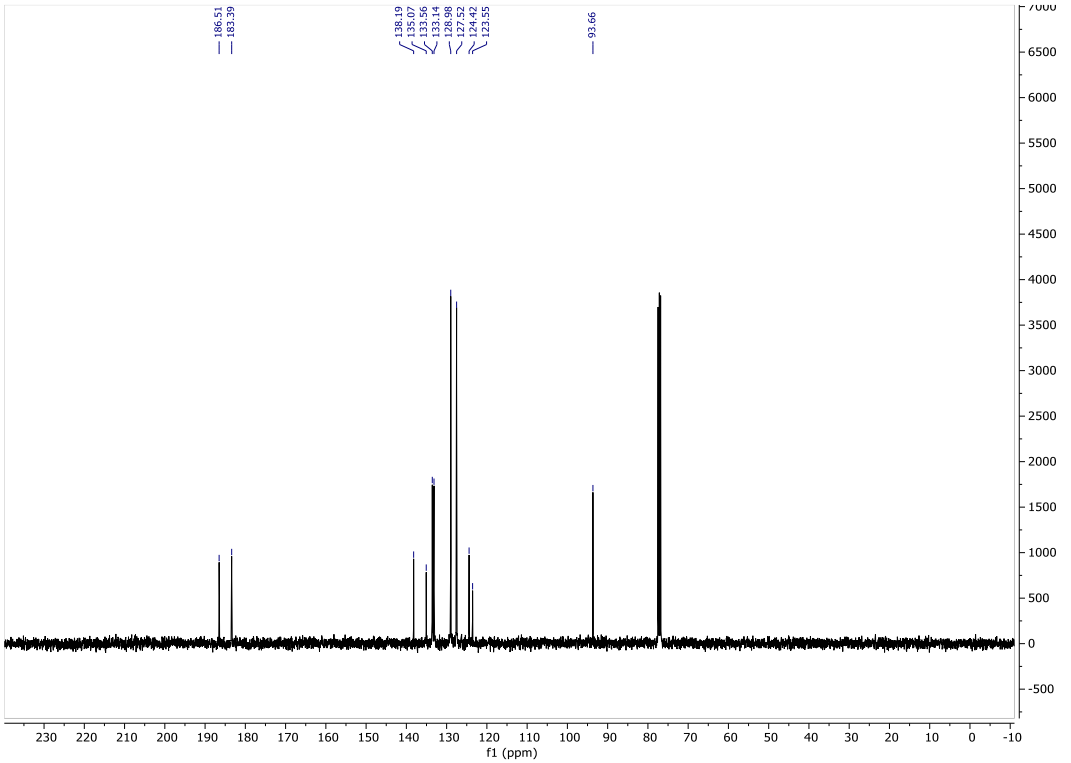


Figure 2.43 –^{13}C-NMR spectrum (101 MHz, $CDCl_3$) of compound **3**.

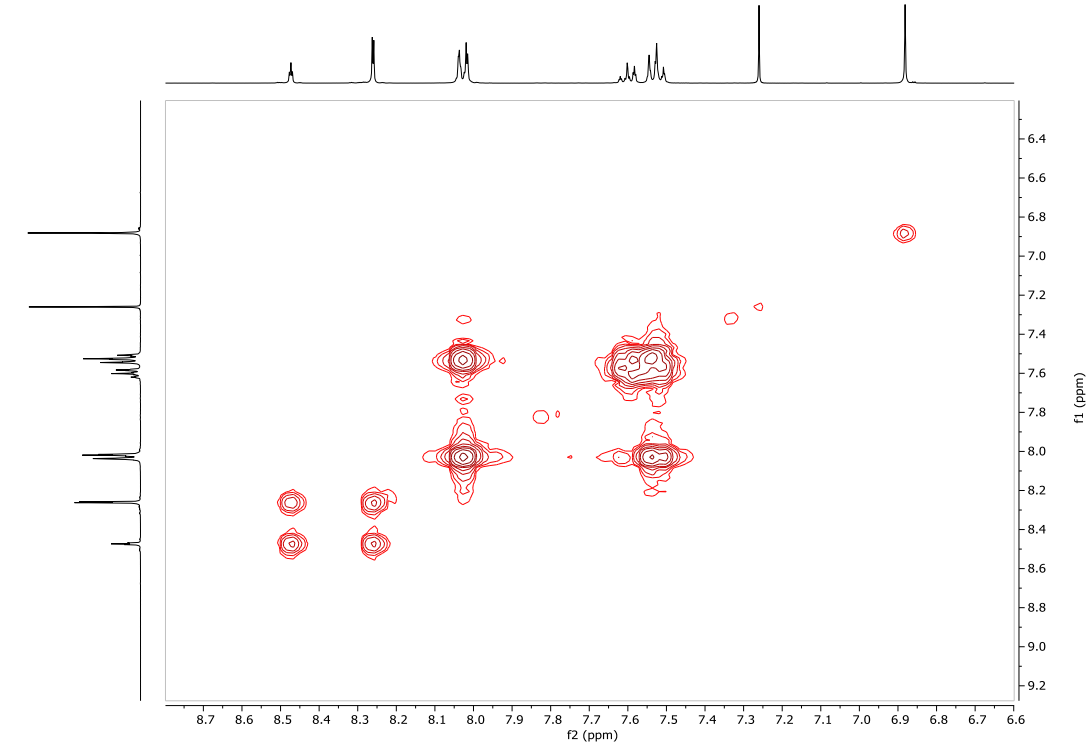


Figure 2.44 – 2D COSY spectrum ($CDCl_3$) of compound **3**.

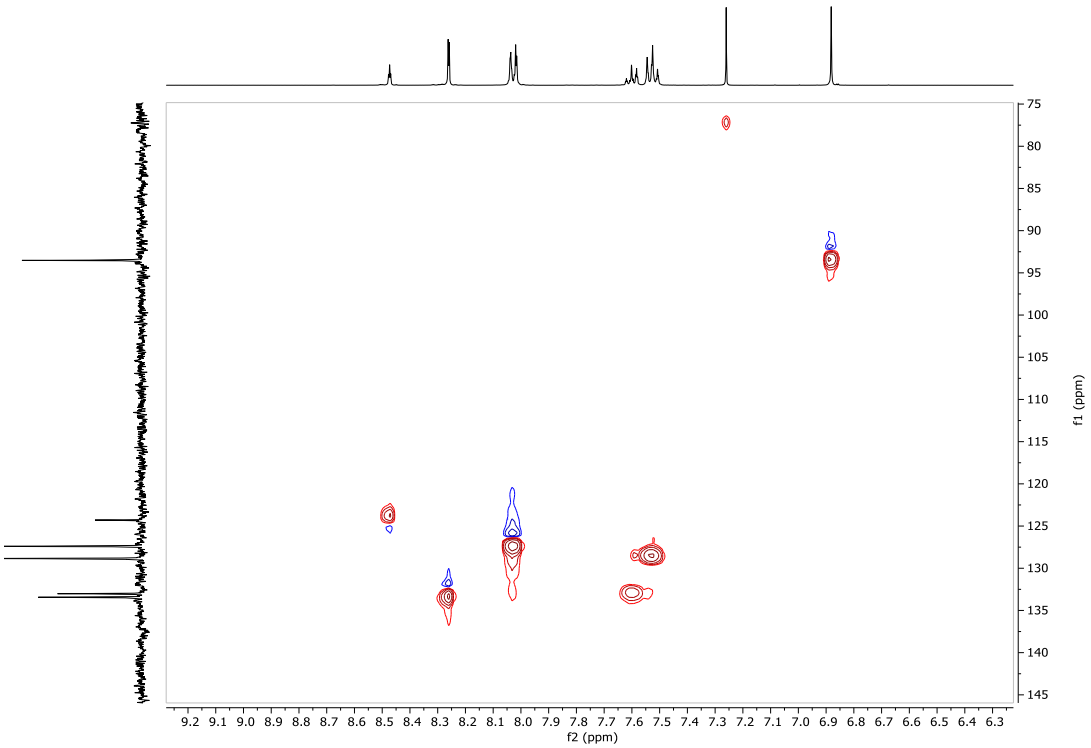


Figure 2.45 – 2D HSQC spectrum ($CDCl_3$) of compound **3**.

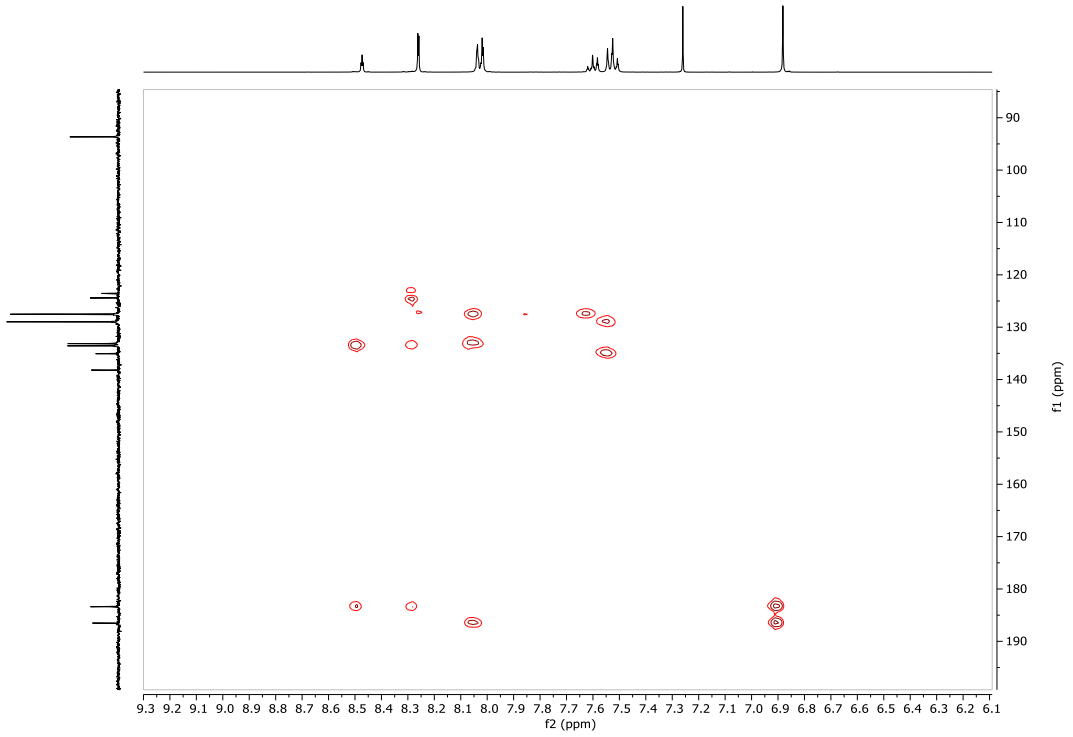


Figure 2.46 – 2D HMBC spectrum ($CDCl_3$) of compound **3**.

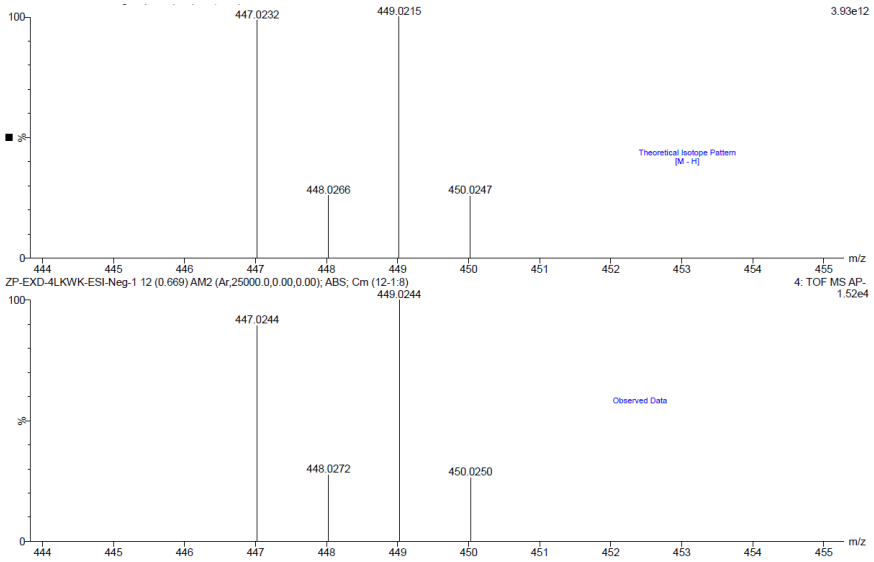


Figure 2.47 – Theoretical (top) and observed (bottom) ESI^--MS spectra of compound **3**.

2.5.4.2 1,1'-(5-((trimethylsilyl)ethynyl)-1,3-phenylene)bis(3-hydroxy-3-phenylprop-2-en-1-one) (4)

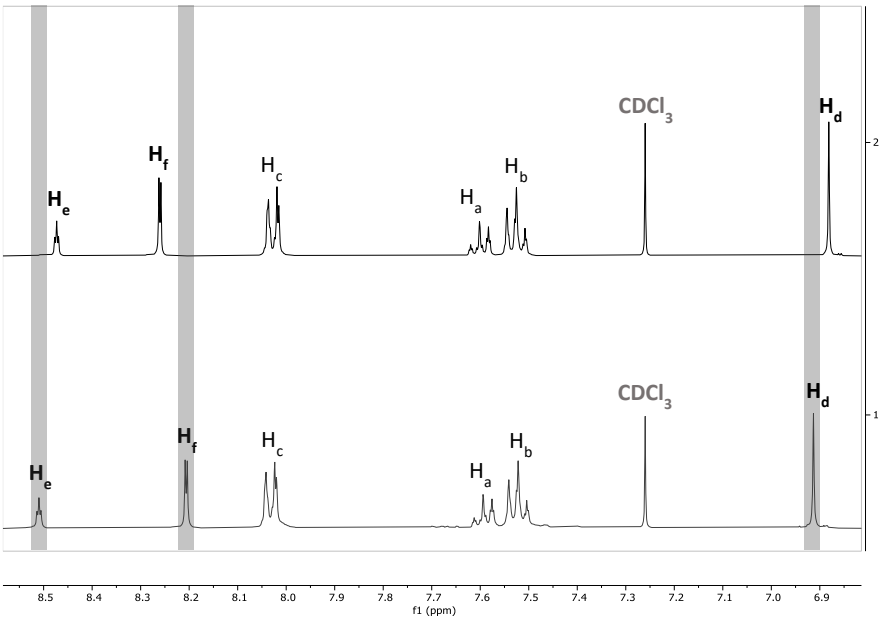


Figure 2.48 – Stacked ^{1}H-NMR spectra (400 MHz, $CDCl_3$) of compound **3** (top) and compound **4** (bottom). Only the aromatic region is shown, and the peaks have been assigned as reported in the experimental section. The grey bands illustrate the position and shift of the H_e, H_f and H_d protons of compound **4**.

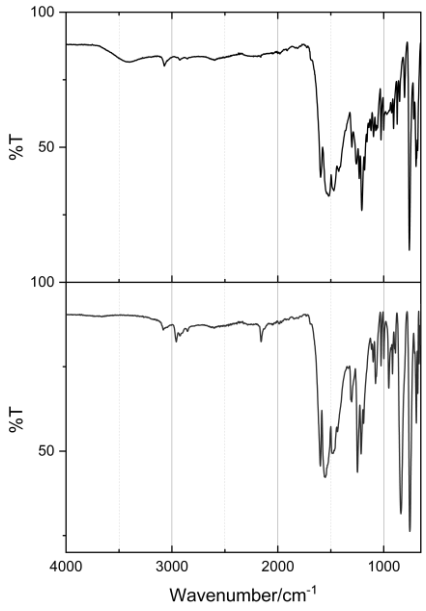


Figure 2.49 – Stacked IR spectra of compound **3** (top) and compound **4** (bottom).

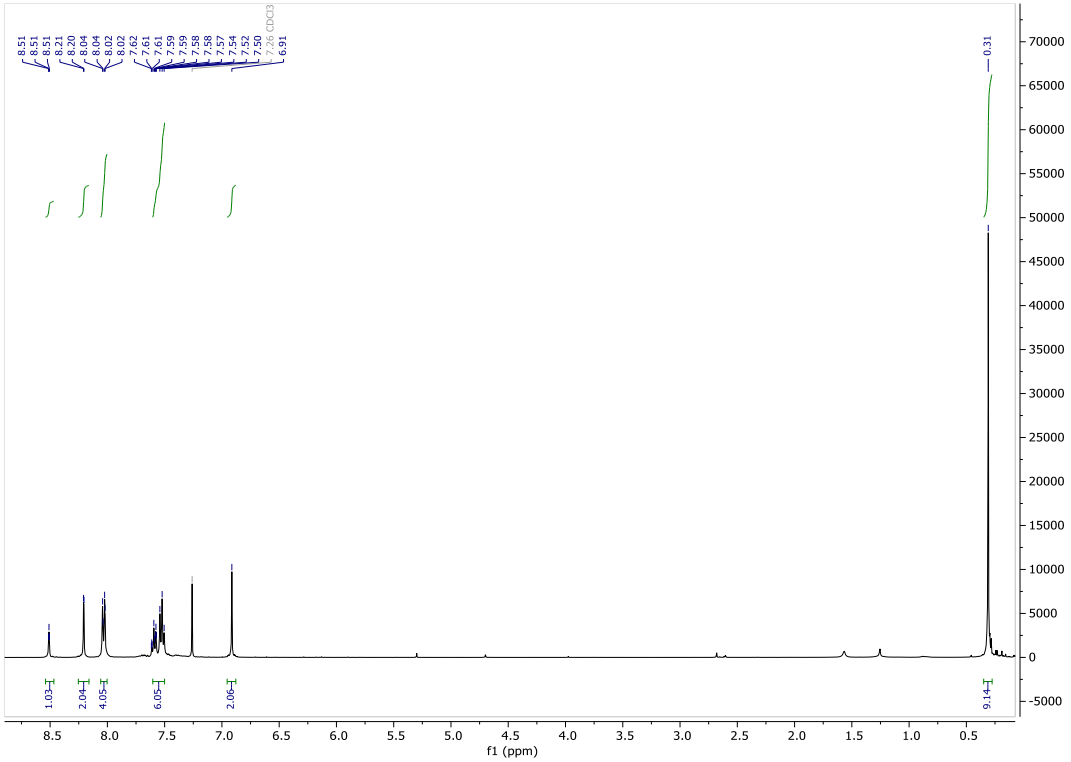


Figure 2.50 –^{1}H-NMR spectrum (400 MHz, $CDCl_3$) of compound **4**.

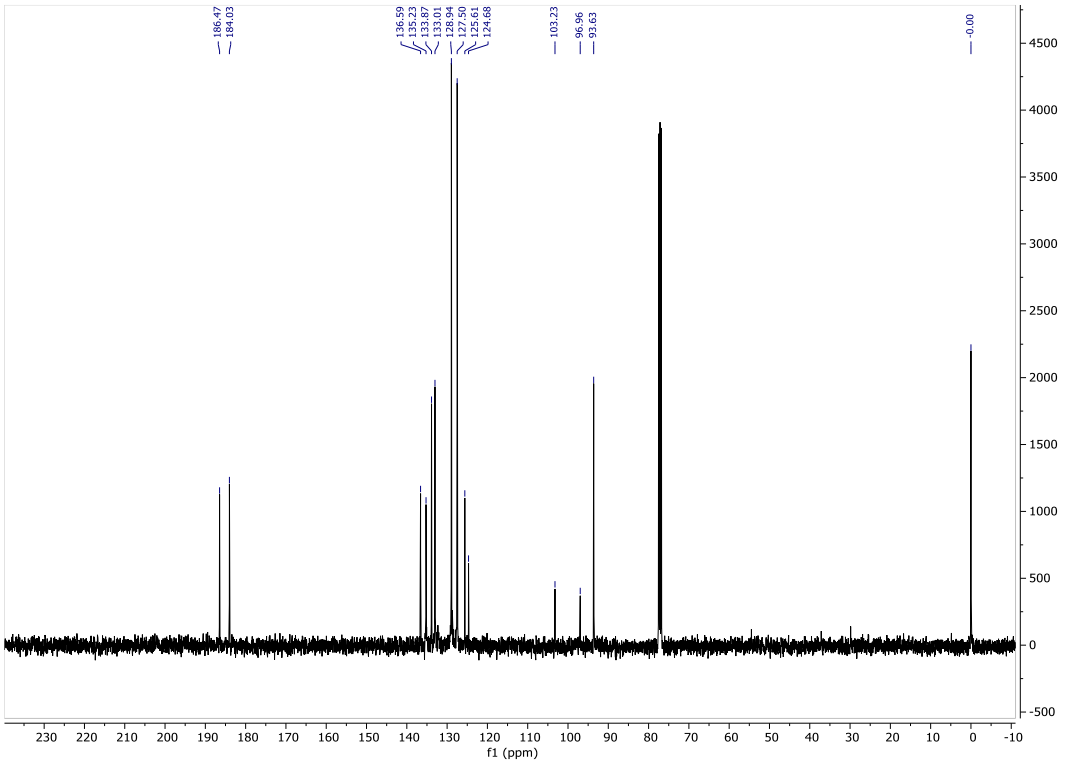


Figure 2.51 –^{13}C-NMR spectrum (101 MHz, $CDCl_3$) of compound **4**.

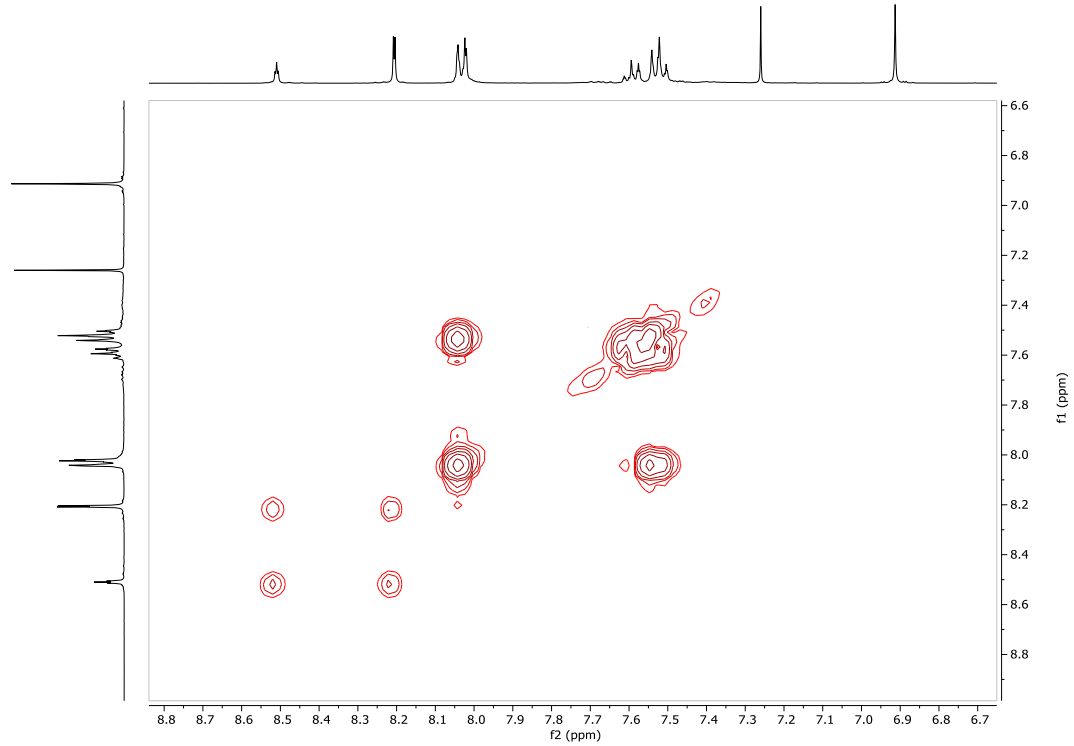


Figure 2.52 – 2D COSY spectrum ($CDCl_3$) of compound **4**.

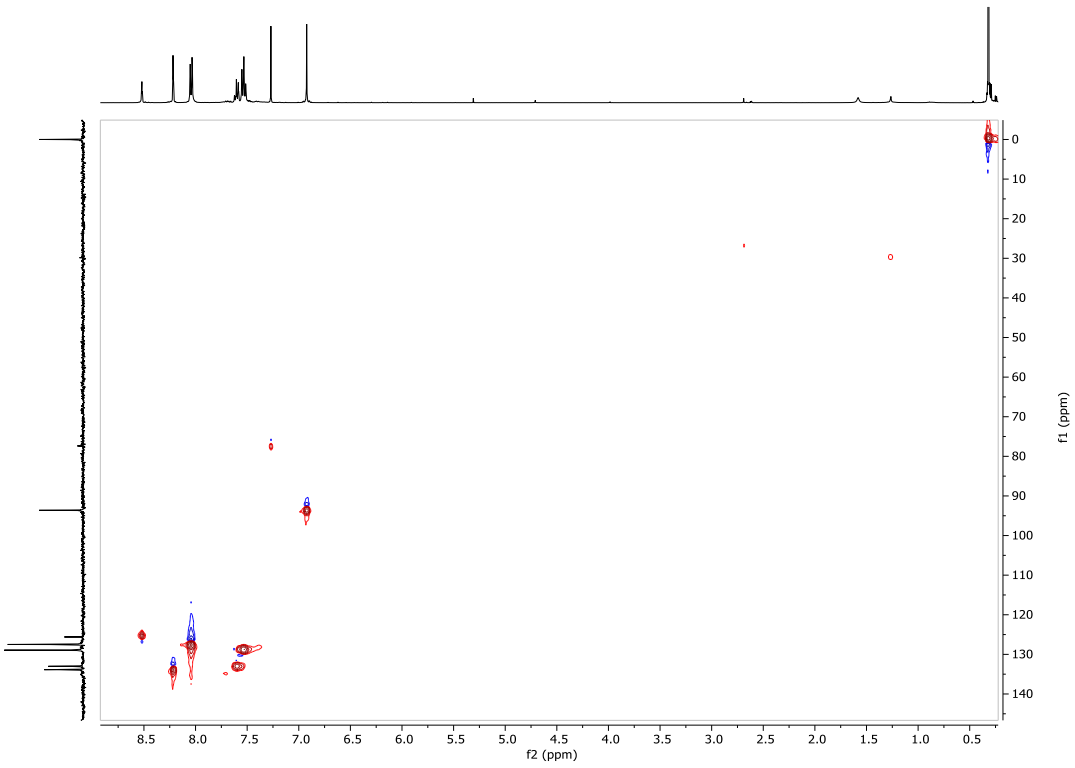


Figure 2.53 – 2D HSQC spectrum ($CDCl_3$) of compound **4**.

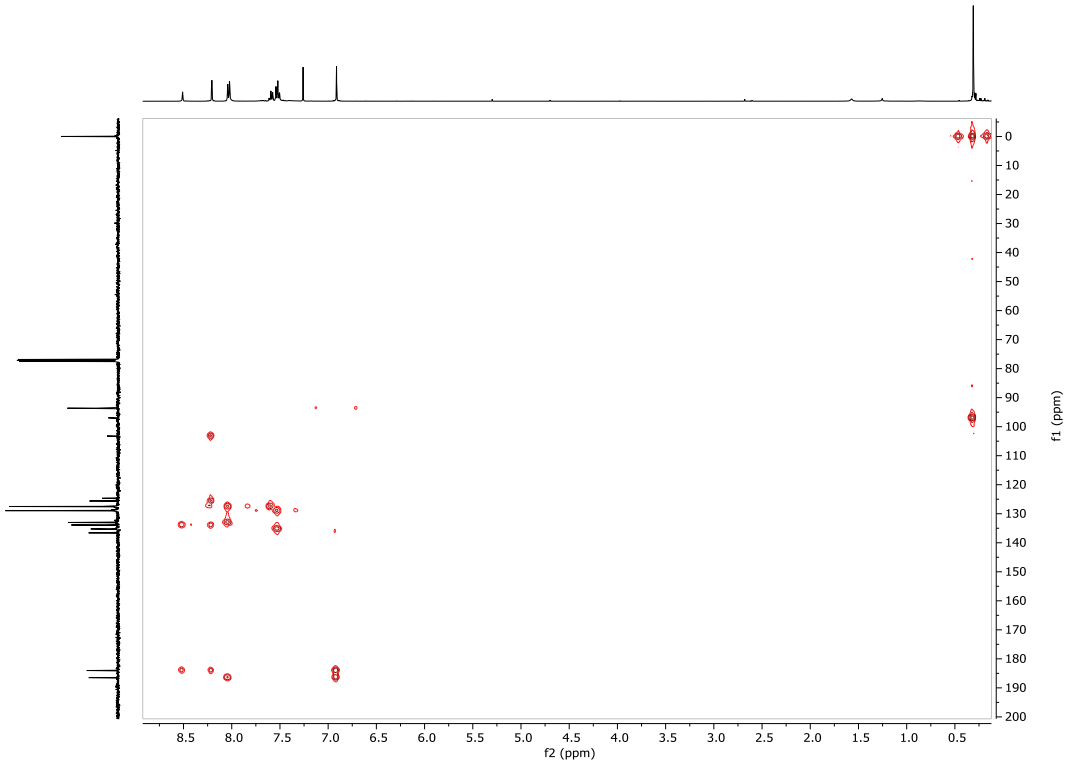


Figure 2.54 – 2D HMBC spectrum ($CDCl_3$) of compound **4**.

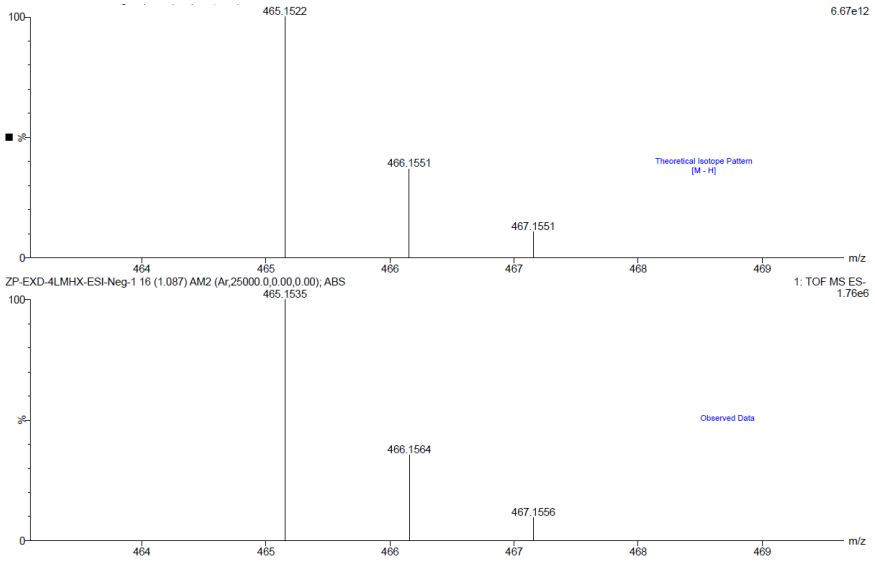


Figure 2.55 – Theoretical (top) and observed (bottom) ESI^--MS spectra of compound **4**.

2.5.4.3 1,1'-(5-ethynyl-1,3-phenylene)bis(3-hydroxy-3-phenylprop-2-en-1-one) (5)

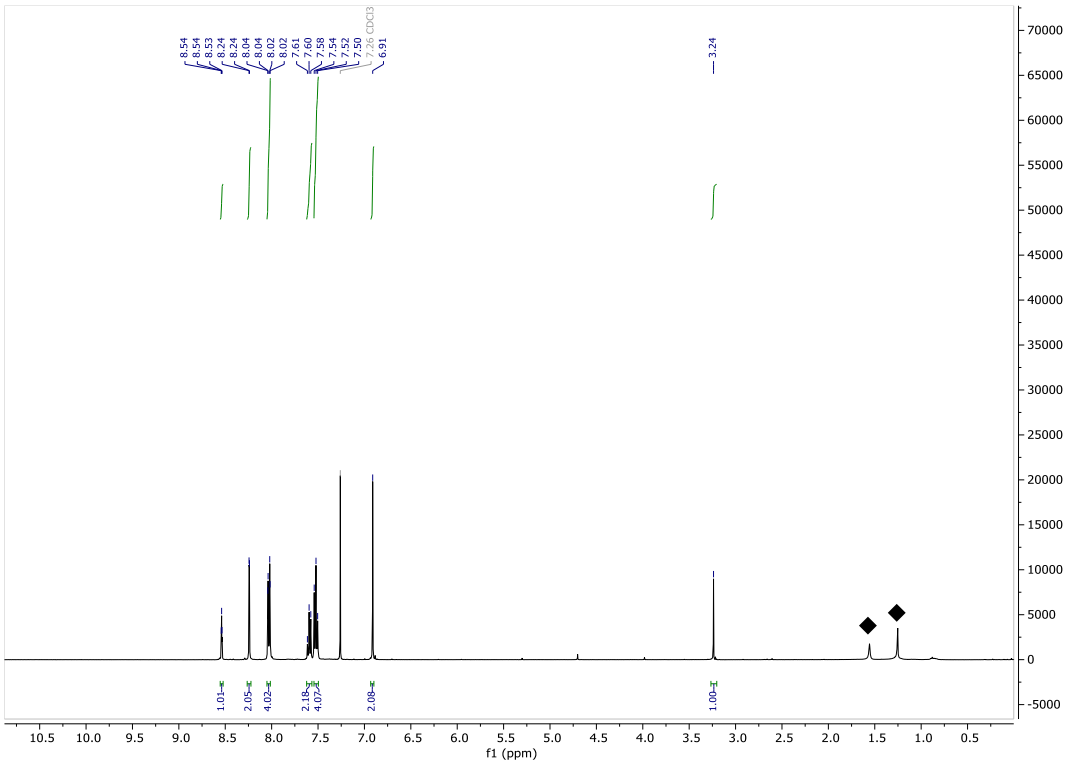


Figure 2.56 –^{1}H-NMR spectrum (400 MHz, $CDCl_3$) of compound **5**. The small peaks at 1.56 ppm and 1.25 ppm (black shape) are attributed to H_2O and grease, respectively.

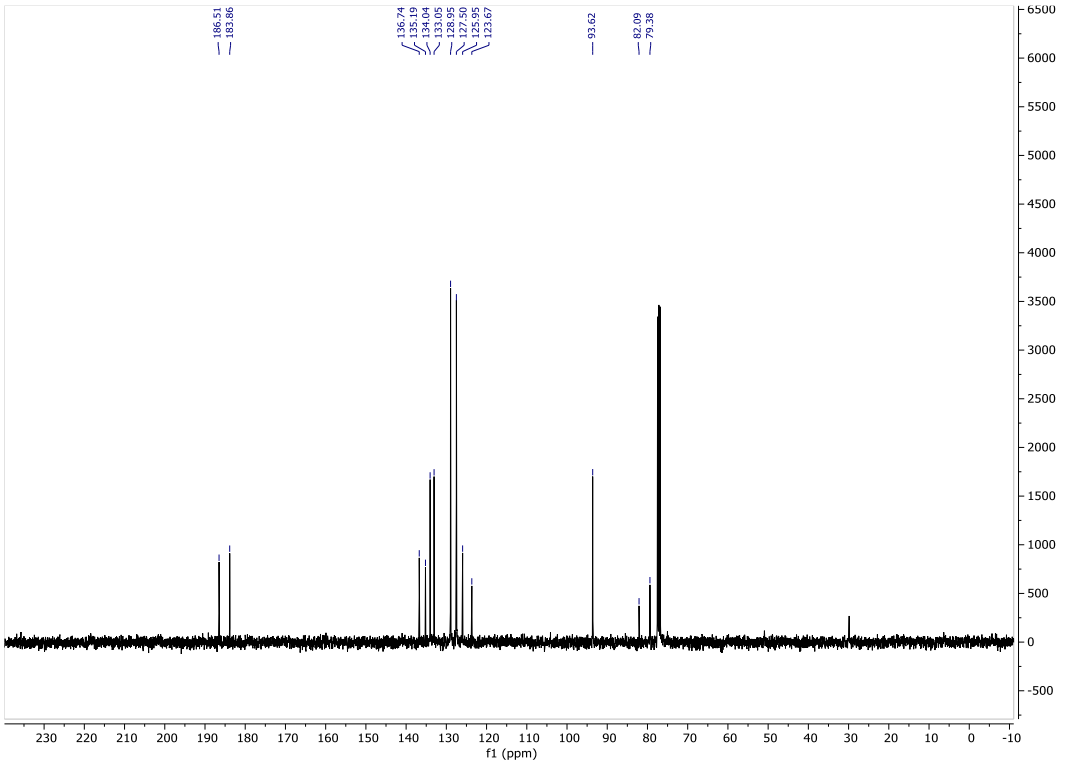


Figure 2.57 –^{13}C-NMR spectrum (101 MHz, $CDCl_3$) of compound **5**.

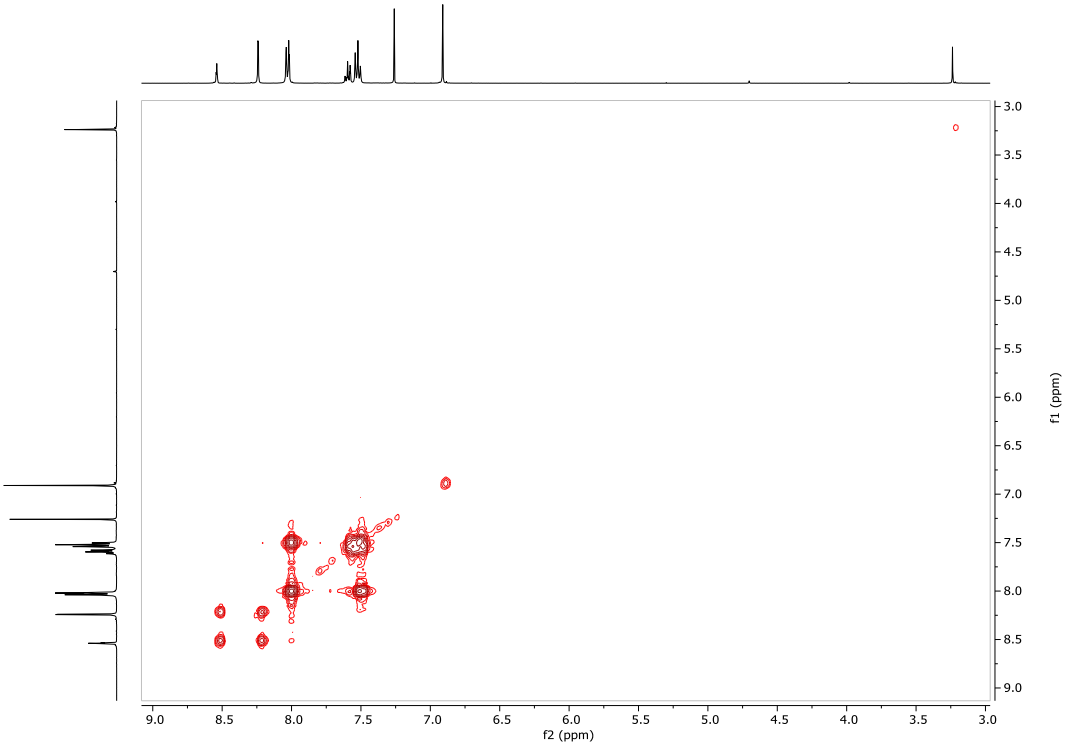


Figure 2.58 – 2D COSY spectrum ($CDCl_3$) of compound **5**.

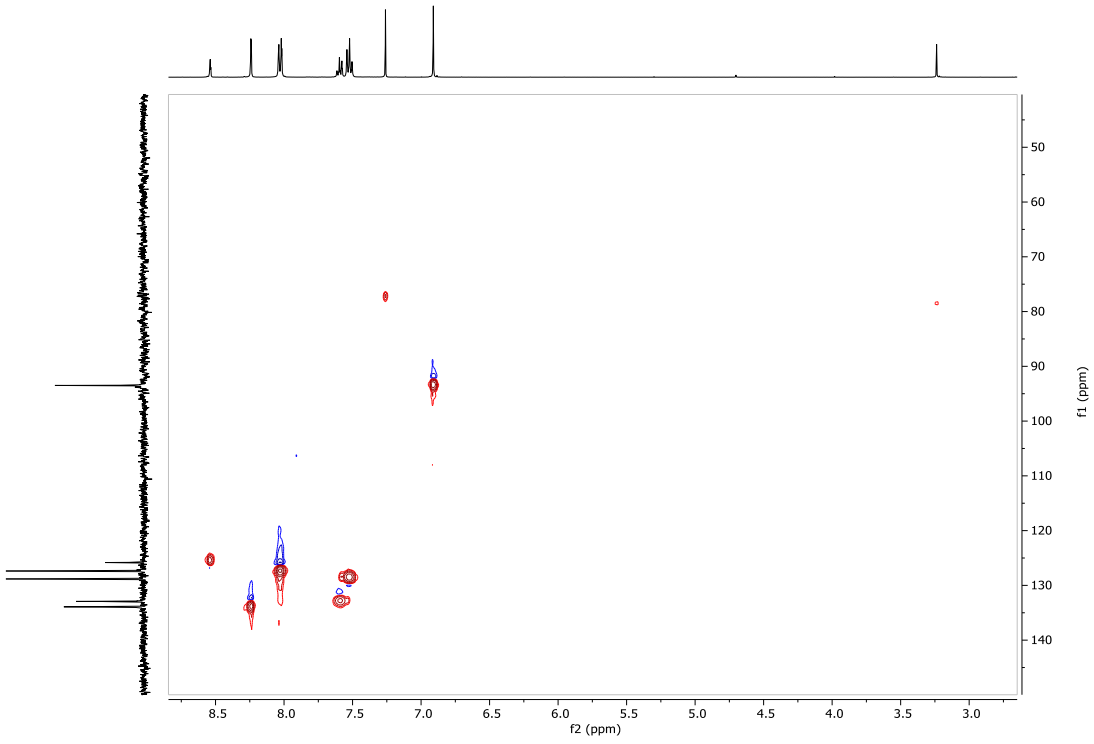


Figure 2.59 – 2D HSQC spectrum ($CDCl_3$) of compound **5**.

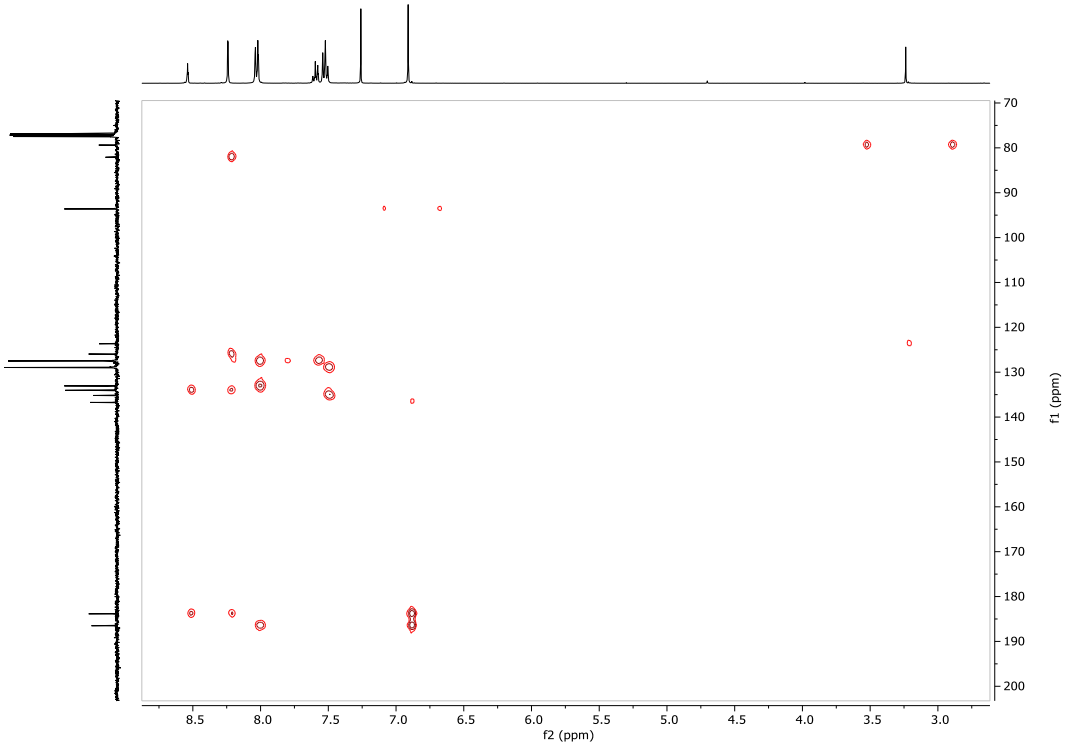


Figure 2.60 – 2D HMBC spectrum ($CDCl_3$) of compound **5**.

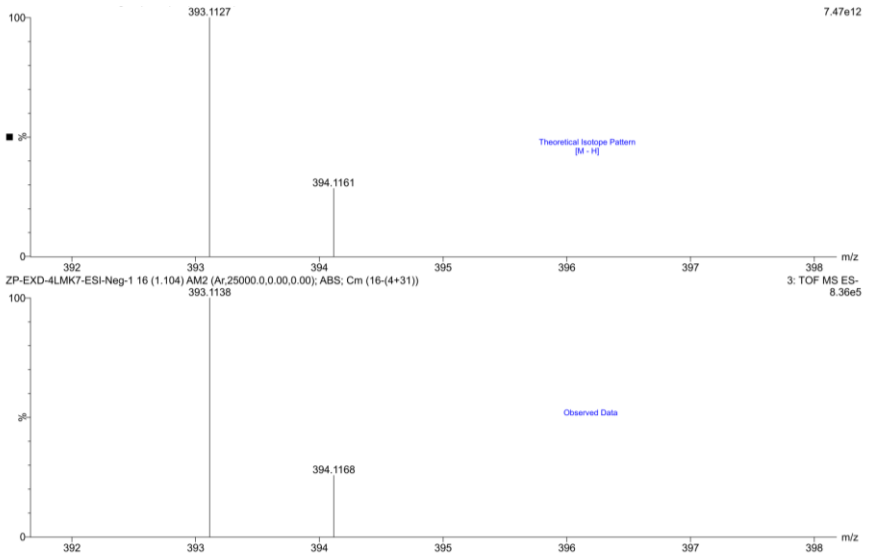


Figure 2.61 – Theoretical (top) and observed (bottom) ESI^--MS spectra of compound **5**.

2.5.4.4 S-(3-(4-(3,5-bis(3-hydroxy-3-phenylacryloyl)phenyl)-1H-1,2,3-triazol-1-yl)propyl) ethanethioate (SAcbisDBM)

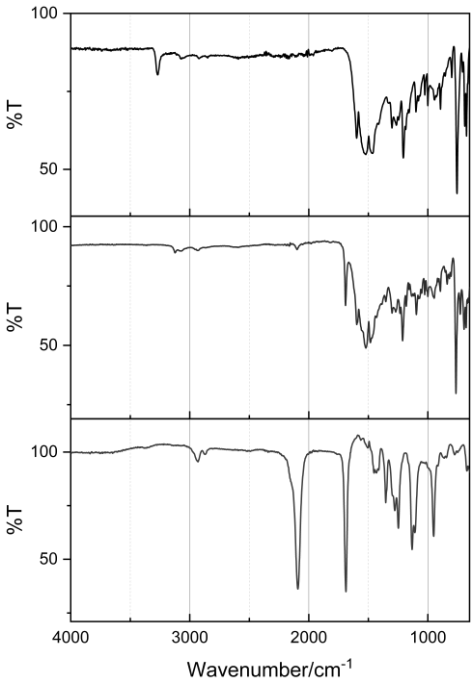


Figure 2.62 – Stacked IR spectra of compound **5** (top), **SAcbisDBM** (middle) and compound **6** (bottom).

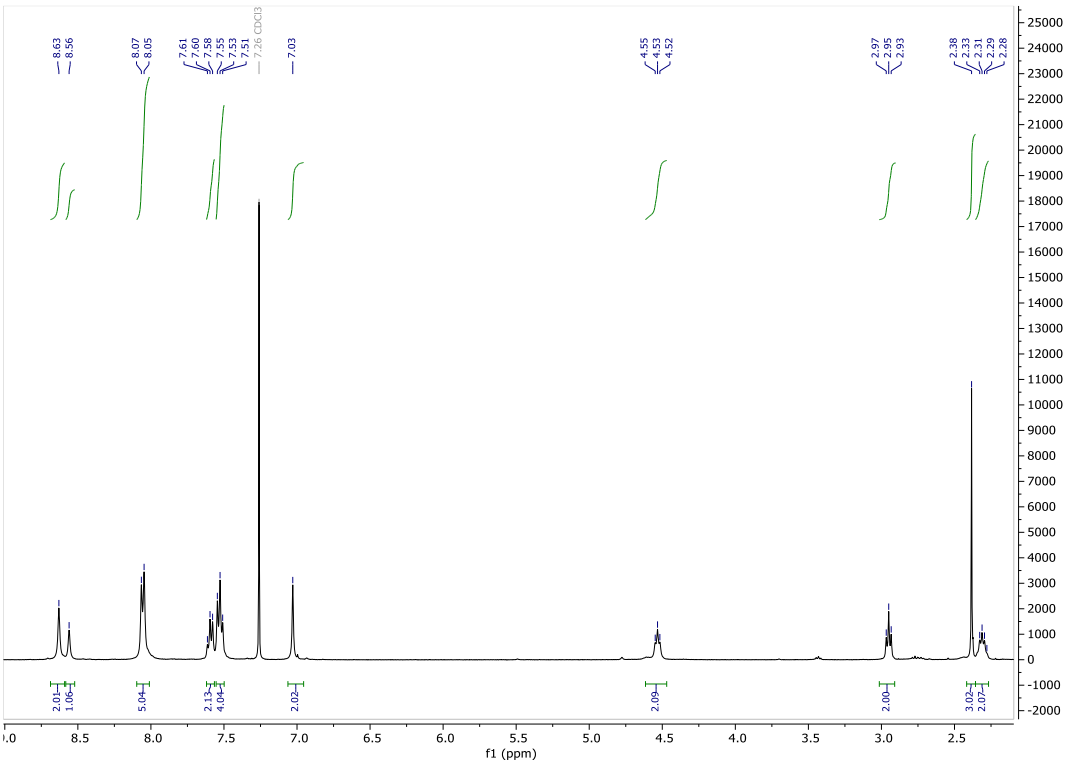


Figure 2.63 –^{1}H-NMR spectrum (400 MHz, $CDCl_3$) of **SAcbisDBM**.

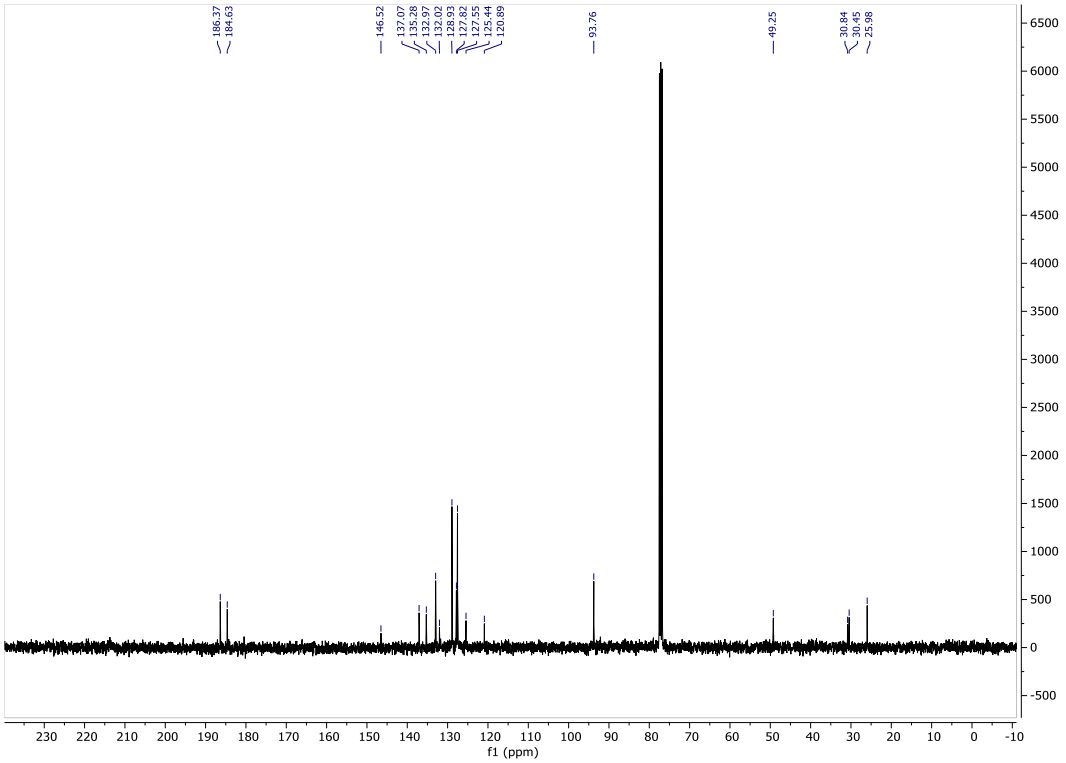


Figure 2.64 –^{13}C-NMR spectrum (101 MHz, $CDCl_3$) of **SAcbisDBM**.

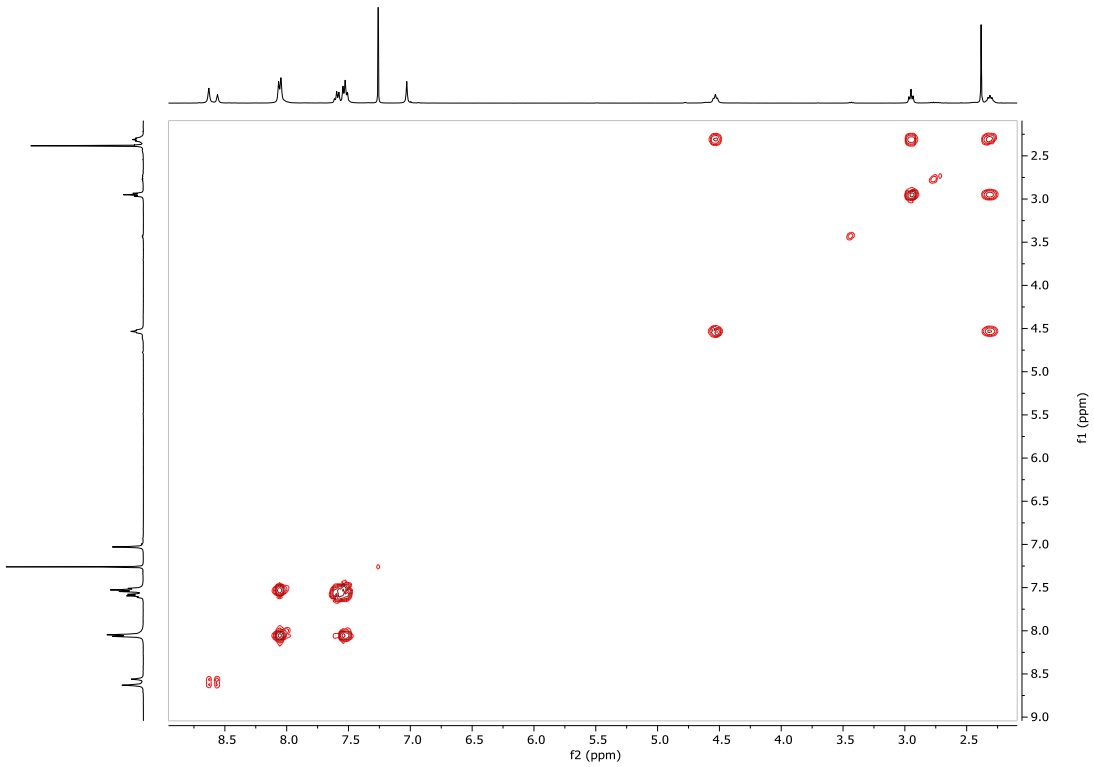


Figure 2.65 – 2D COSY spectrum ($CDCl_3$) of **SAcbisDBM**.

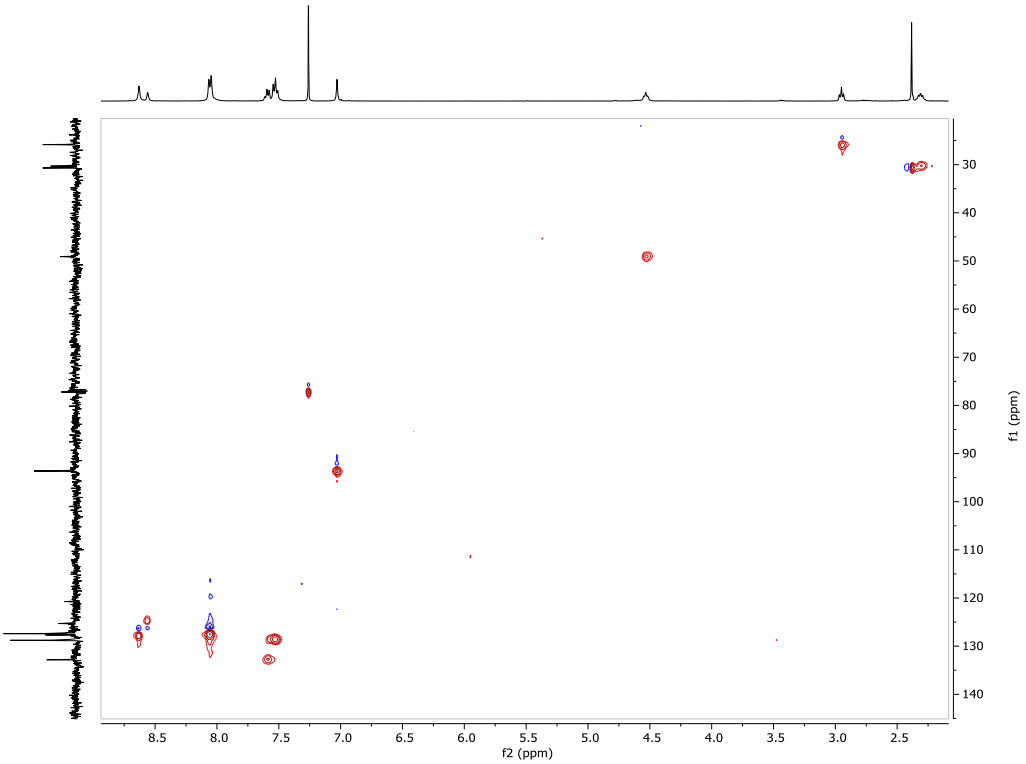


Figure 2.66 – 2D HSQC spectrum ($CDCl_3$) of **SAcbisDBM**.

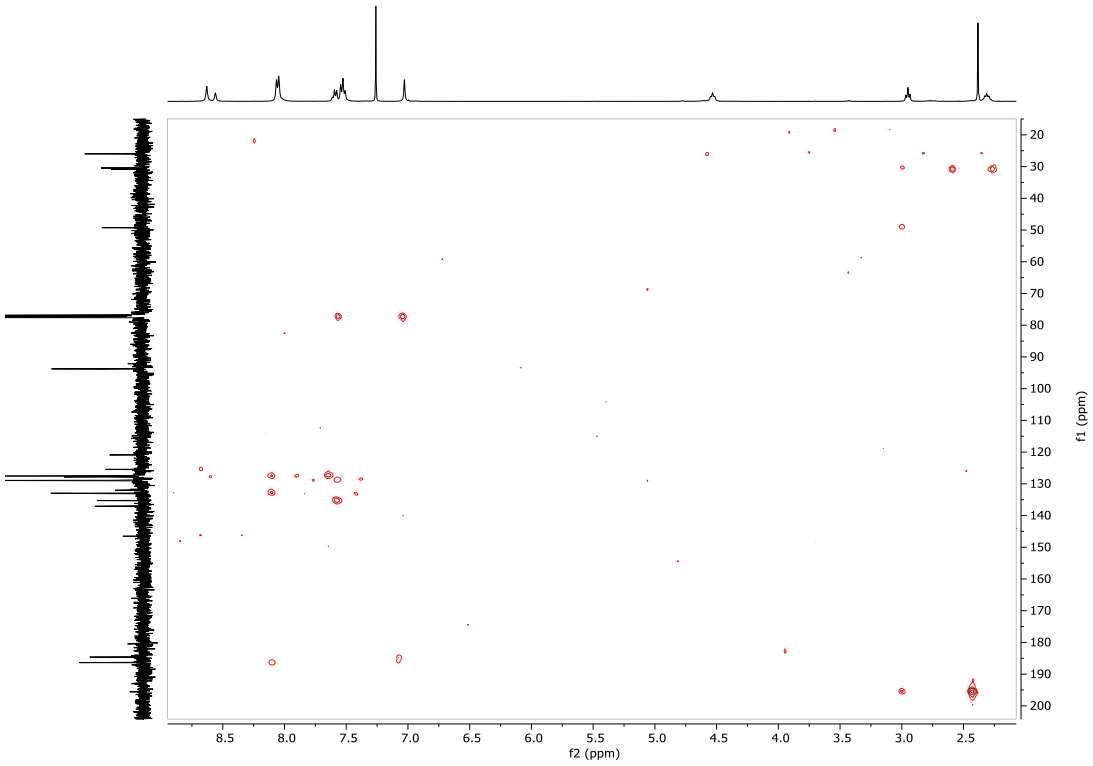


Figure 2.67 – 2D HMBC spectrum ($CDCl_3$) of **SAcbisDBM**.

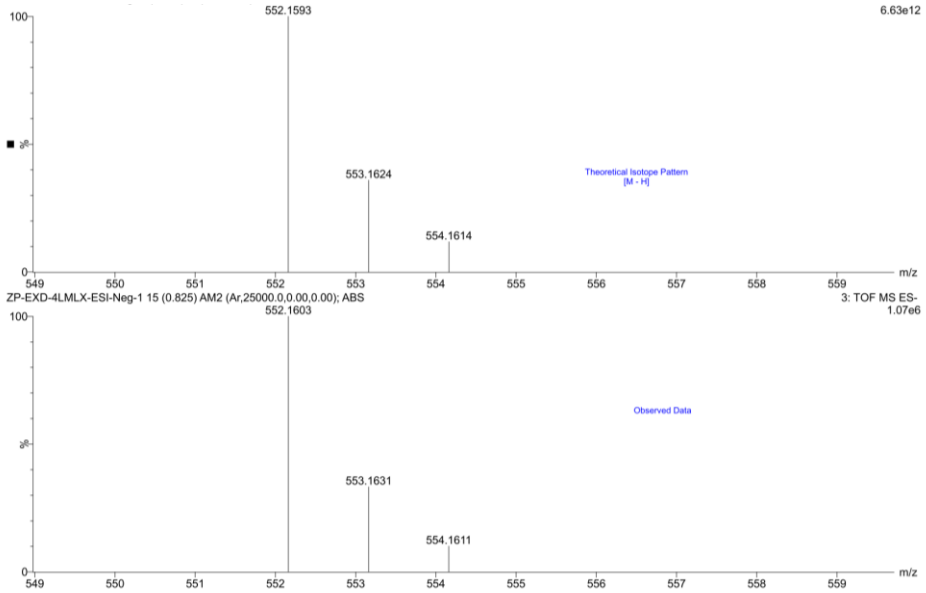


Figure 2.68 – Theoretical (top) and observed (bottom) ESI^--MS spectra of **SAcbisDBM**.

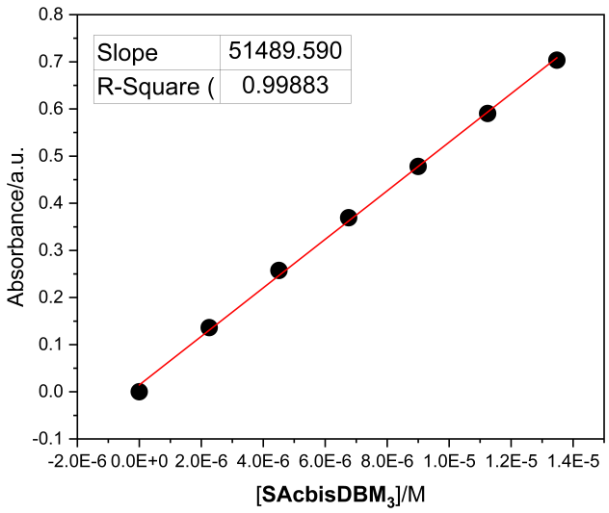


Figure 2.69 – Plot for the calculation of the ε (i.e. "Slope") at 358 nm for **SAcbisDBM** in DMF showing the linear fit.

2.5.4.5 $Eu_2SAcbisDBM_3$

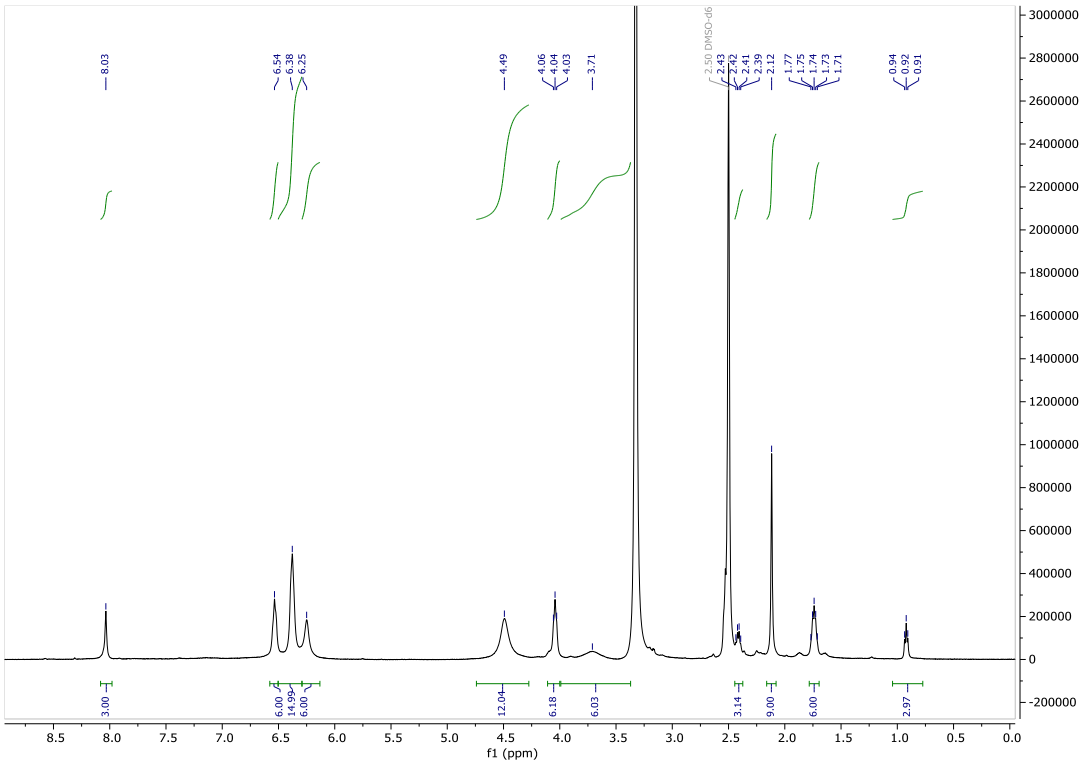


Figure 2.70 –^{1}H-NMR spectrum (500 MHz, DMSOd_6) of **$Eu_2SAcbisDBM_3$**.

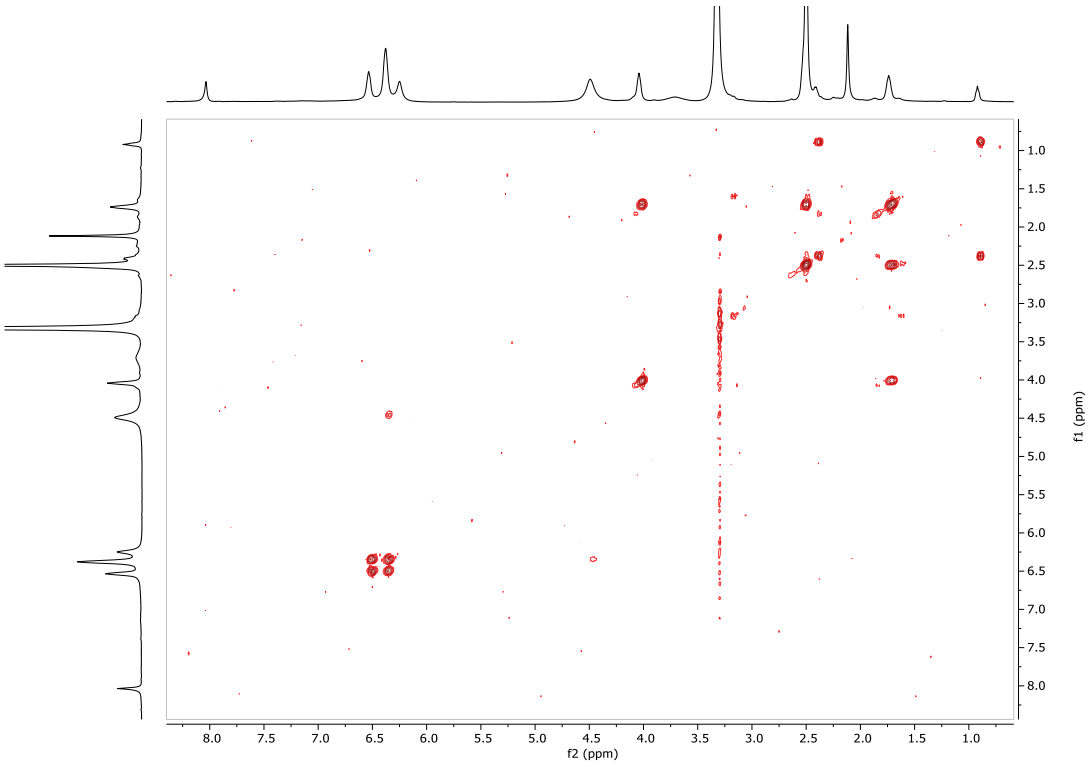


Figure 2.71 – 2D COSY spectrum (DMSOd_6) of compound **$Eu_2SAcbisDBM_3$**.

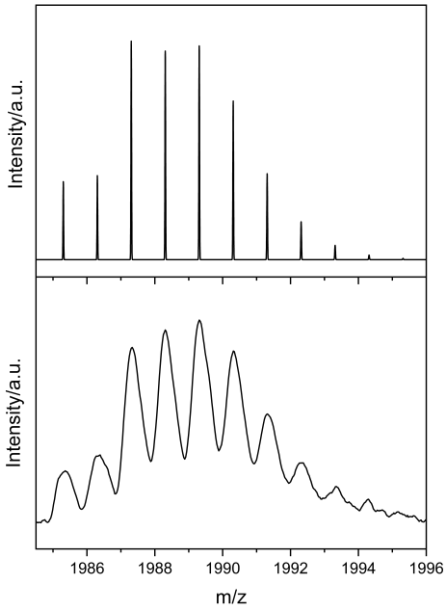


Figure 2.72 – Theoretical (top) and observed (bottom) MALDI-TOF spectra of **Eu_2SAcbisDBM$_3$**.

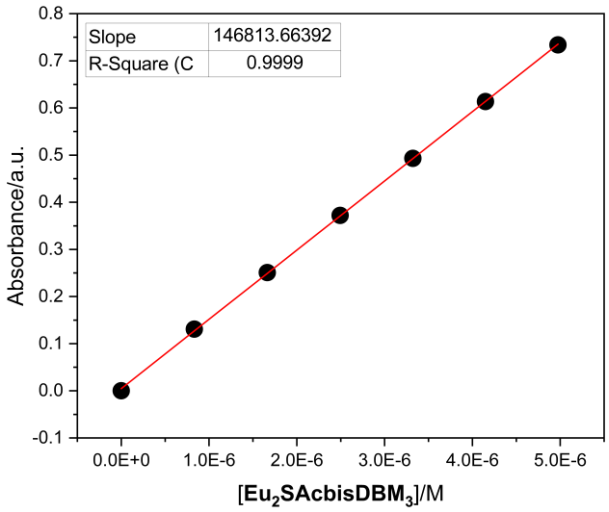


Figure 2.73 – Plot for the calculation of the ε (i.e. "Slope") at 360 nm for **Eu_2SAcbisDBM$_3$** in DMF showing the linear fit.

2.5.4.6 $Yb_2SAcbisDBM_3$

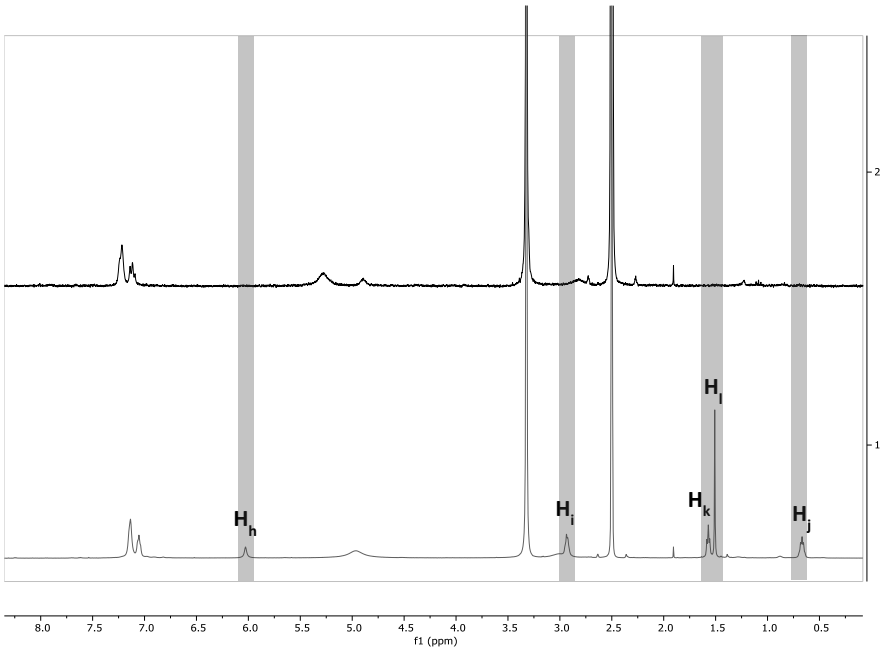


Figure 2.74 – Stacked ^{1}H-NMR spectra (400 and 500 MHz, respectively, DMSOd_6) of **Yb_2bisDBM$_3$** (top) and **Yb_2SAcbisDBM$_3$** (bottom). Highlighted are the additional peaks arising from the **SAcbisDBM** scaffold.

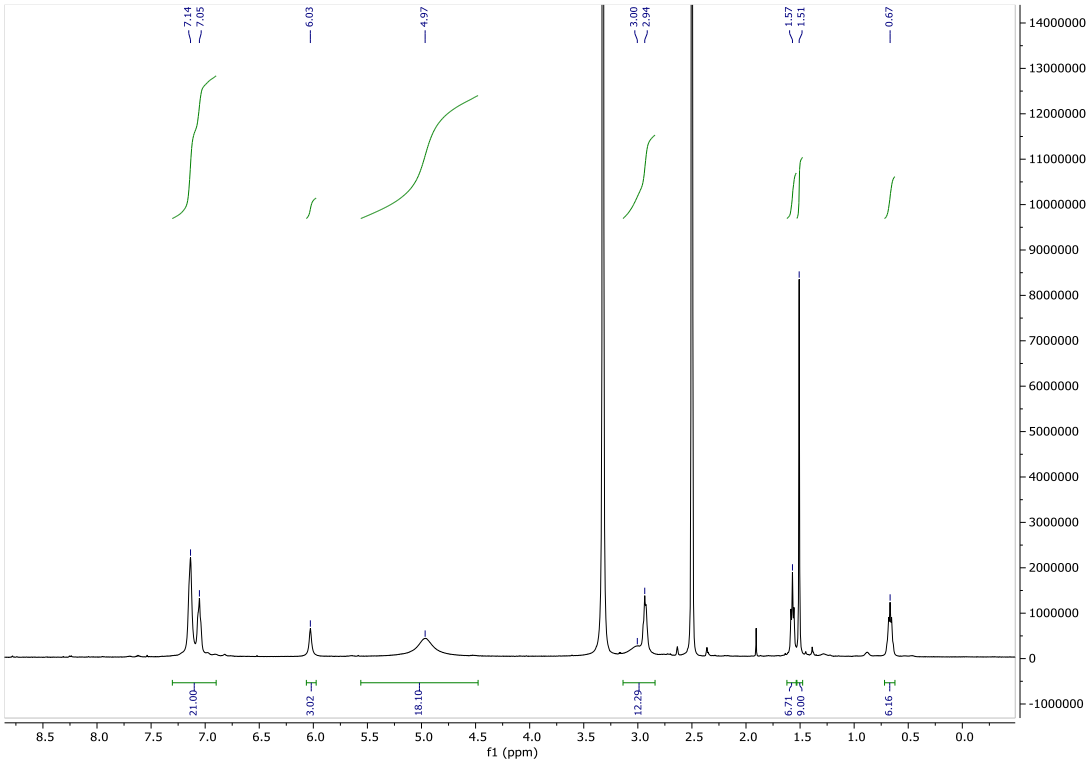


Figure 2.75 –^{1}H-NMR spectrum (500 MHz, DMSOd_6) of **Yb_2SAcbisDBM$_3$**.

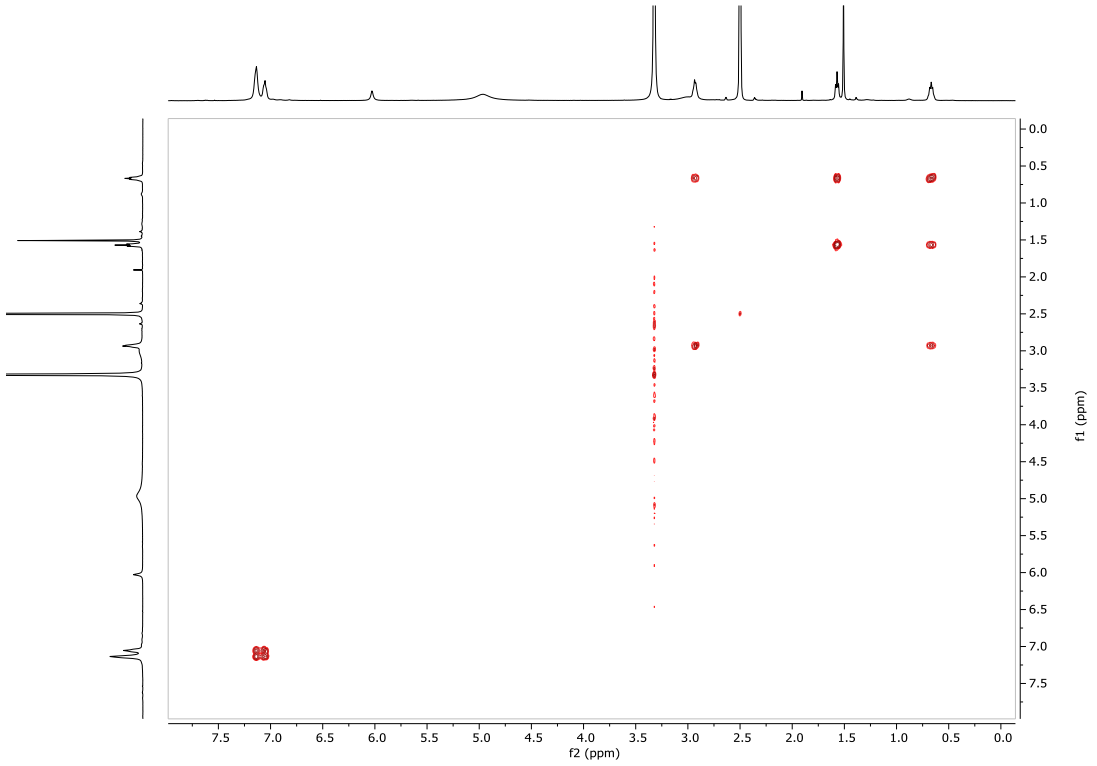


Figure 2.76 – 2D COSY spectrum (DMSOd_6) of compound **Yb_2SAcbisDBM$_3$**.

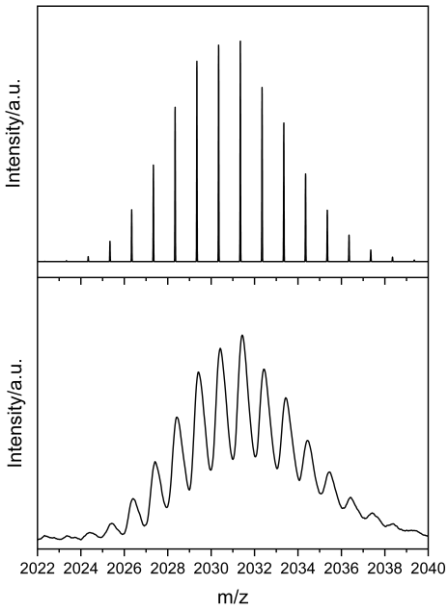


Figure 2.77 – Theoretical (top) and observed (bottom) MALDI-TOF spectra of **Yb_2SAcbisDBM$_3$**.

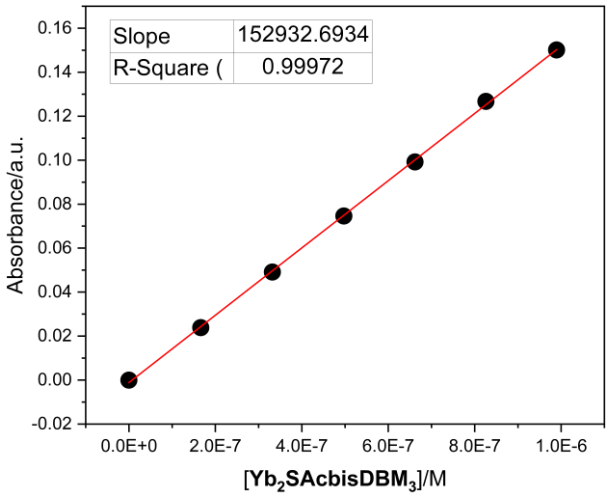


Figure 2.78 – Plot for the calculation of the ε (i.e. "Slope") at 359 nm for **Yb_2SAcbisDBM$_3$** in DMF showing the linear fit.

2.5.4.7 Nd_2SAcbisDBM$_3$

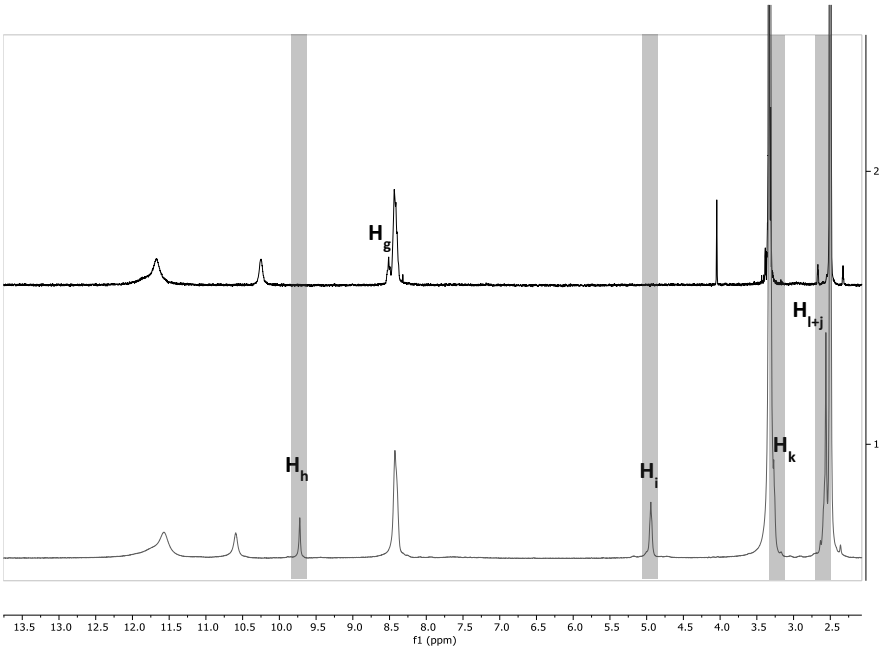


Figure 2.79 – Stacked ^{1}H-NMR spectra (400 and 500 MHz, respectively, DMSOd_6) of **Nd_2bisDBM$_3$** (top) and **Nd_2SAcbisDBM$_3$** (bottom). Highlighted are the additional peaks arising from the **SAcbisDBM** scaffold and **H_g** of the **bisDBM** ligand.

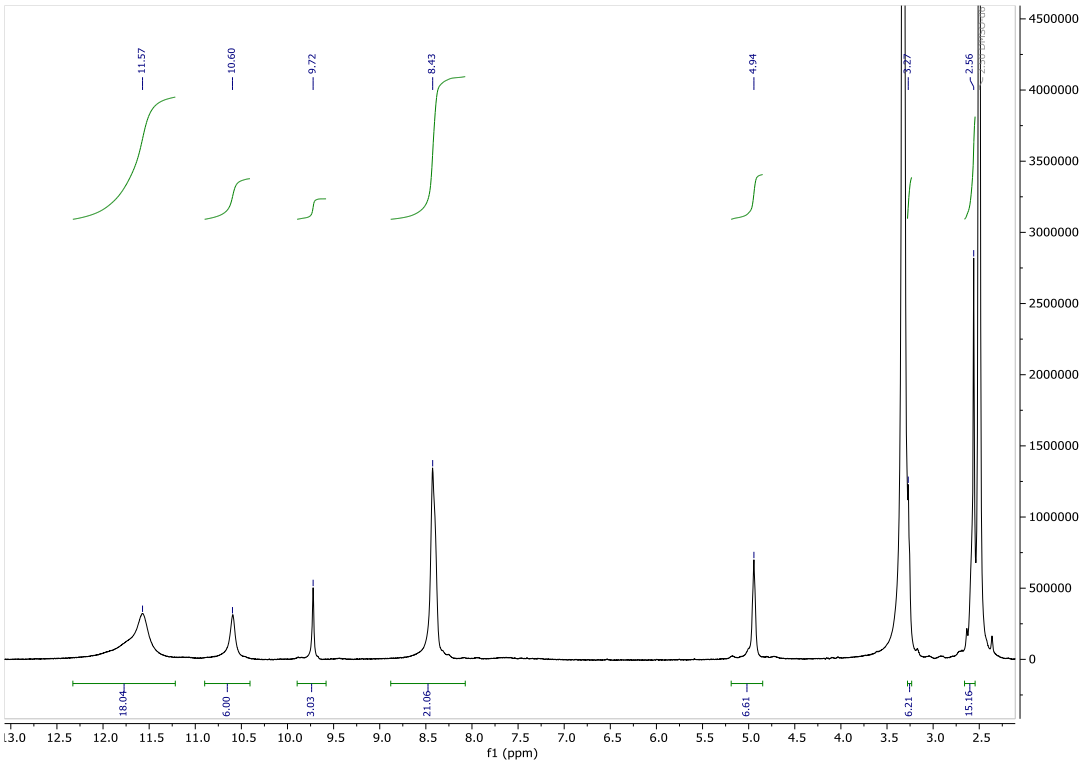


Figure 2.80 –^{1}H-NMR spectrum (500 MHz, DMSOd_6) of **Nd$_2$SAcbisDBM$_3$**.

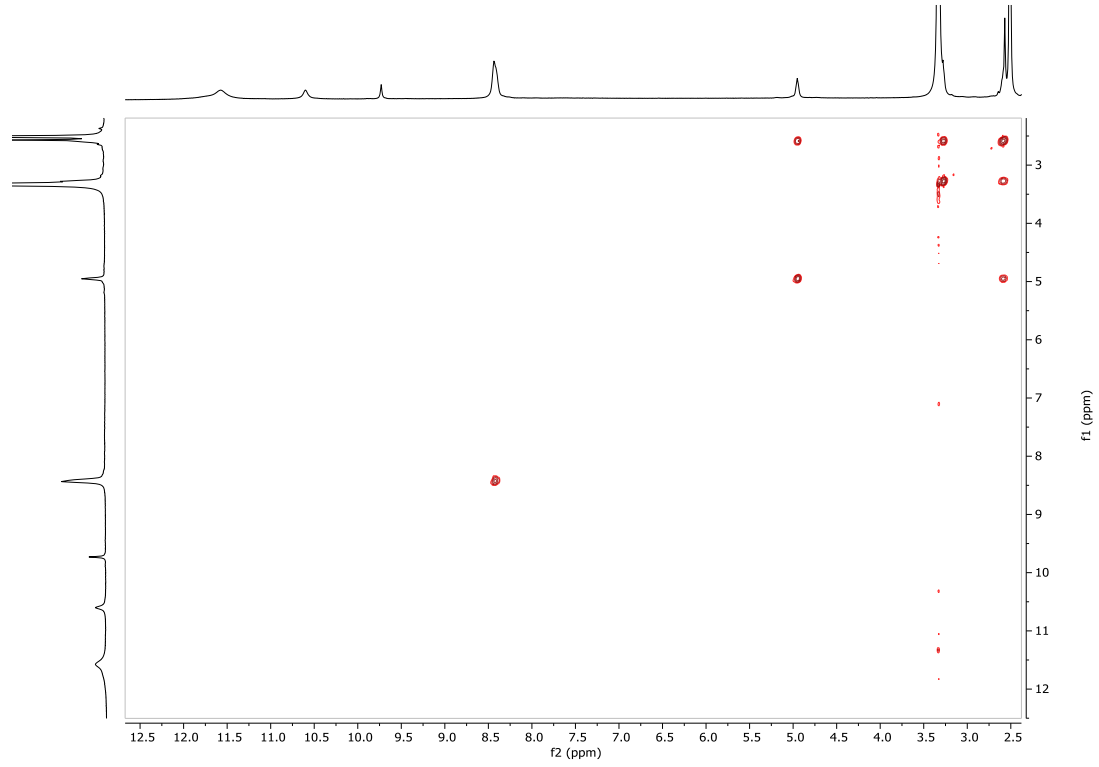


Figure 2.81 – 2D COSY spectrum (DMSOd_6) of compound **Nd$_2$SAcbisDBM$_3$**.

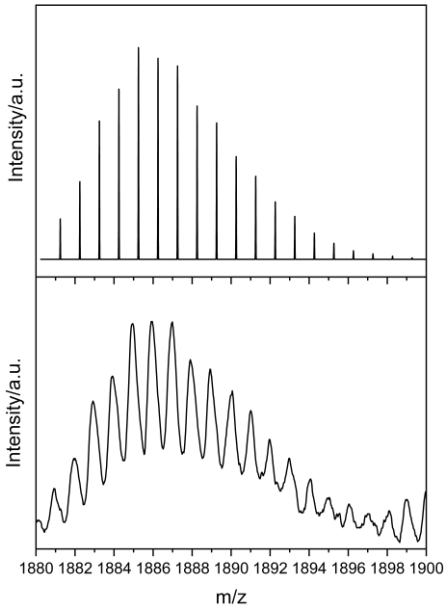


Figure 2.82 – Theoretical (top) and observed (bottom) MALDI-TOF spectra of **Nd_2SAcbisDBM$_3$**.

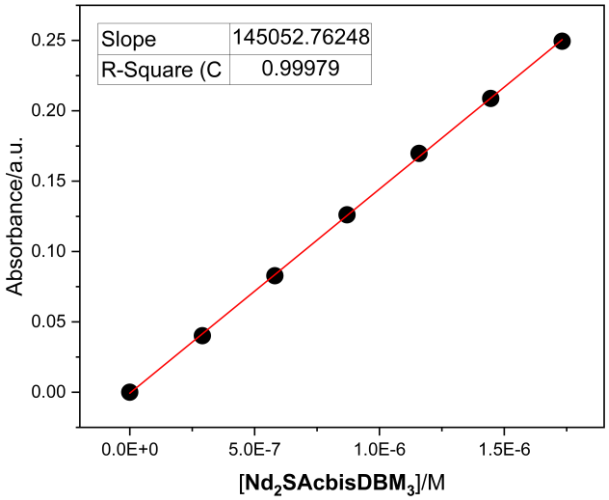


Figure 2.83 – Plot for the calculation of the ε (i.e. "Slope") at 359 nm for **Nd_2SAcbisDBM$_3$** in DMF showing the linear fit.

2.5.4.8 $Gd_2SAcbisDBM_3$

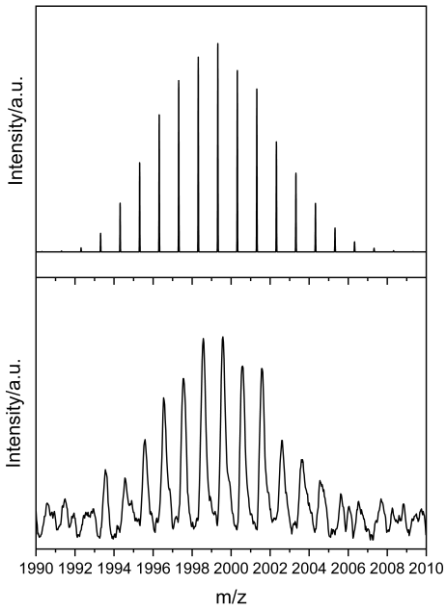


Figure 2.84 – Theoretical (top) and observed (bottom) MALDI-TOF spectra of **$Gd_2SAcbisDBM_3$**.

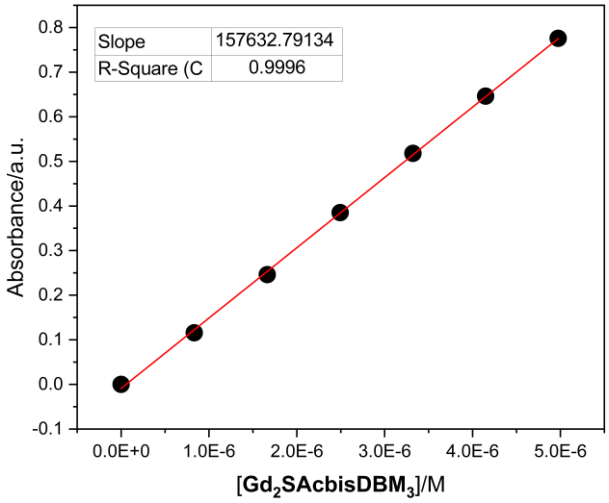


Figure 2.85 – Plot for the calculation of the ε (i.e. "Slope") at 359 nm for **$Gd_2SAcbisDBM_3$** in DMF showing the linear fit.

2.5.5 Additional photophysical data

2.5.5.1 Steady state excitation and emission data

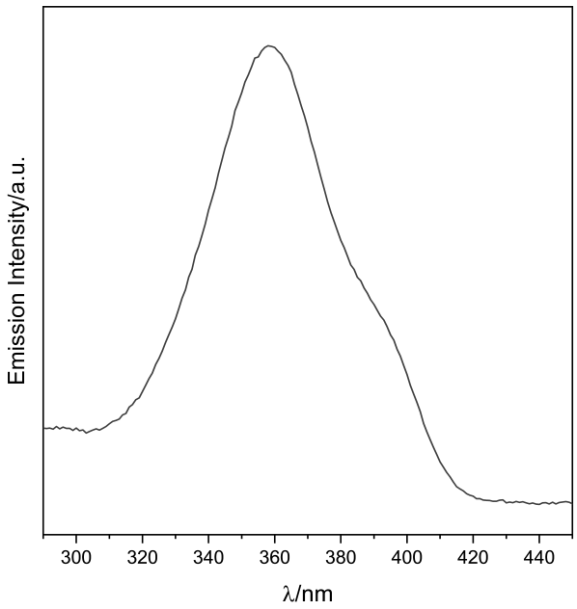


Figure 2.86 – Excitation spectrum of **Yb_2SAcbisDBM$_3$** in DMSOd_6. λ_{em}: 977 nm.

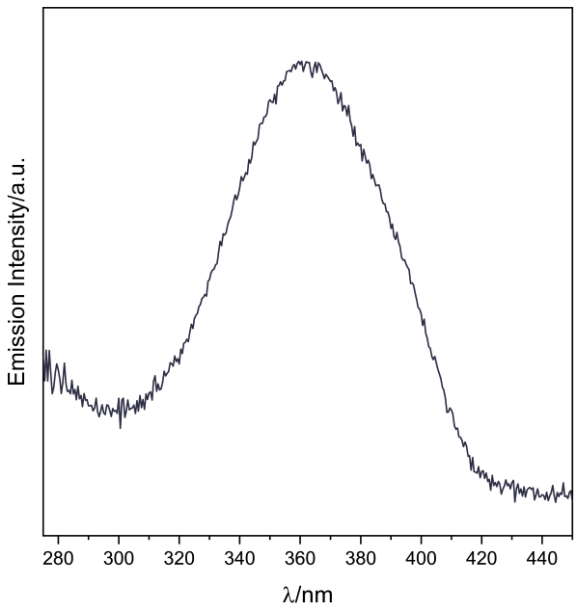


Figure 2.87 – Excitation spectrum of **Nd_2SAcbisDBM$_3$** in DMSOd_6. λ_{em}: 1060 nm.

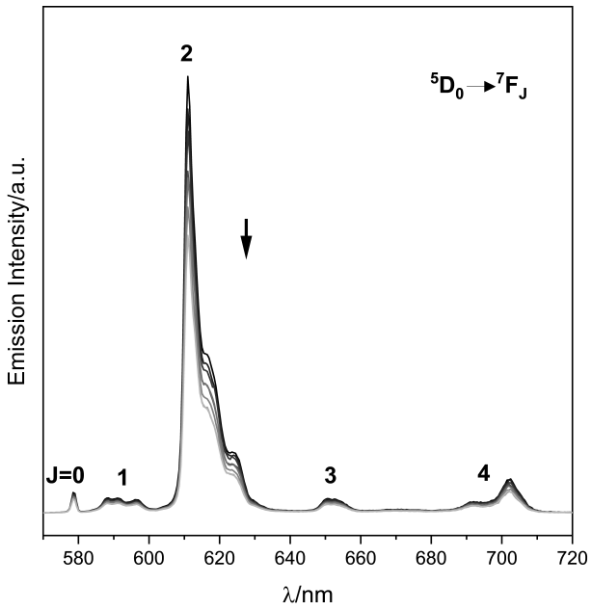


Figure 2.88 – Overlaid emission spectra of **Eu_2SAcbisDBM$_3$** in H_2O/EtOH (1/1, 0.4% DMF) upon addition of F^- as NaF (0 to 260 equivalents). λ_{exc}: 350 nm.

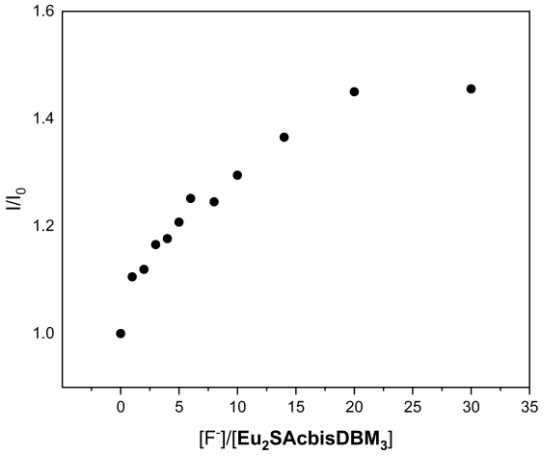


Figure 2.89 – Plot of the ratios between the total emission intensity after addition of F^- as TBAF (I) and the initial total emission intensity (I_0) of **Eu_2SAcbisDBM$_3$** versus the equivalents of F^- added in THF (0.2% DMF).

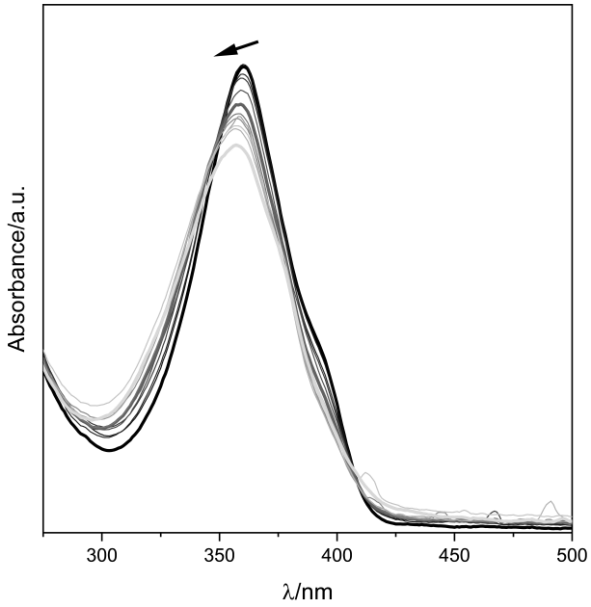


Figure 2.90 – Overlaid absorption spectra of **Eu_2SAcbisDBM$_3$** in THF (0.2% DMF) upon addition of 0-30 equivalents of F^- as TBAF.

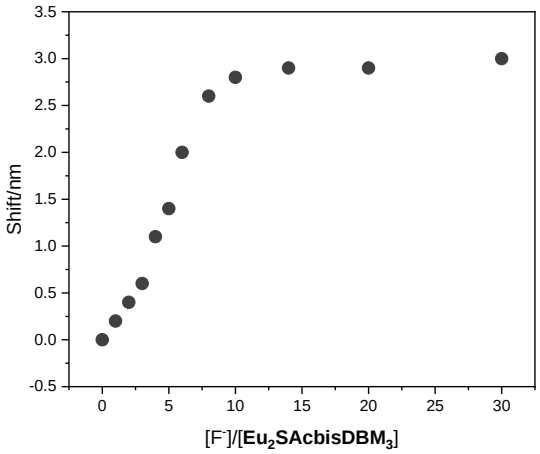


Figure 2.91 – Plot of the shift of the maximum in the absorption spectra of **Eu_2SAcbisDBM$_3$** in THF (0.2% DMF) compared to the starting value at 0 equivalents, versus equivalents of F^- added.

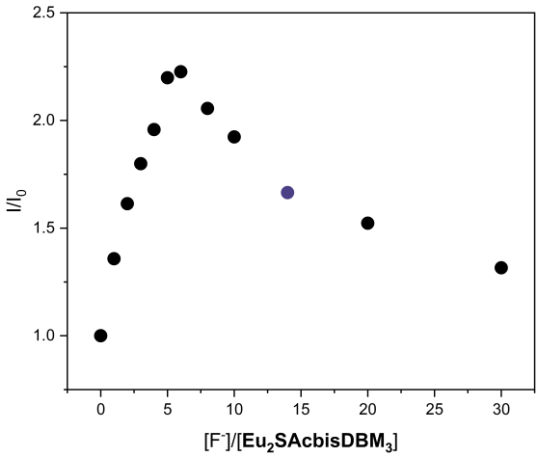


Figure 2.92 – Plot of the modulation in total emission intensity of the excitation spectra of **Eu_2SAcbisDBM$_3$** in THF (0.2% DMF) upon addition of F^- as a ratio over the starting value at 0 equivalents, versus equivalents of F^- added.

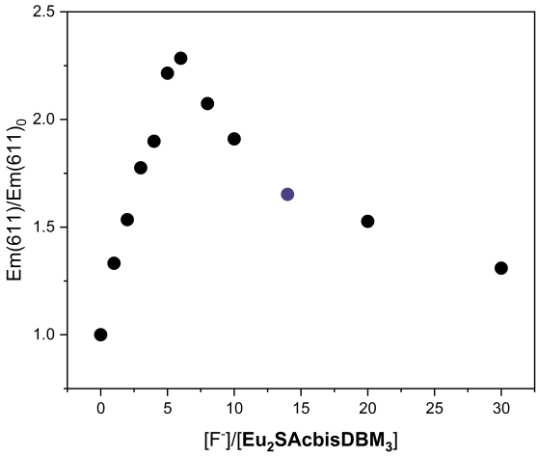


Figure 2.93 – Plot of the modulation in emission intensity of the 611 nm component of the $^5D_0 \rightarrow {}^7F_2$ transition in the emission spectra of **Eu_2SAcbisDBM$_3$** in THF (0.2% DMF) upon addition of F^- as a ratio over the starting value at 0 equivalents, versus equivalents of F^- added.

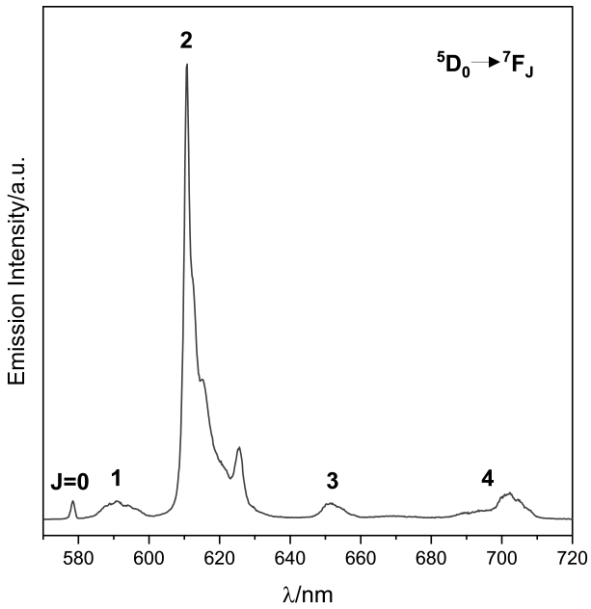


Figure 2.94 – Emission spectrum of **Eu_2SAcbisDBM$_3$** in THF (0.2% DMF) upon addition of excess F^- as sample for ESI^--MS. λ_{exc} 350 nm.

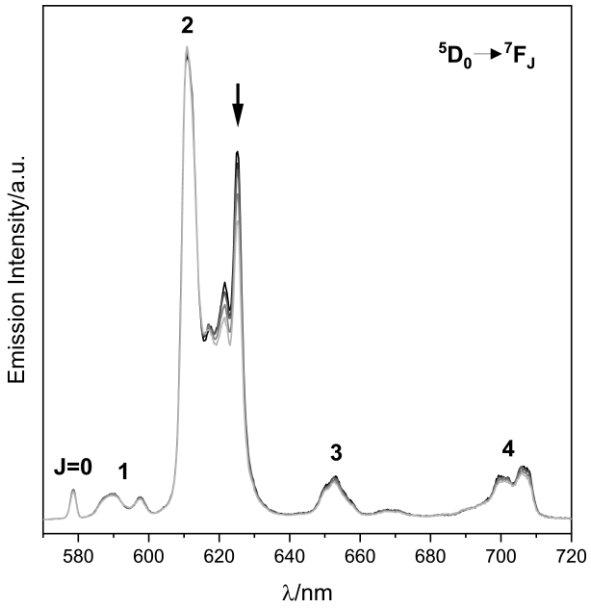


Figure 2.95 – Overlaid emission spectra of **Eu_2SAcbisDBM$_3$** in THF (0.2% DMF) upon addition of 0, 2, 4, 8 and 16 equivalents of Br^-. λ_{exc} 350 nm.

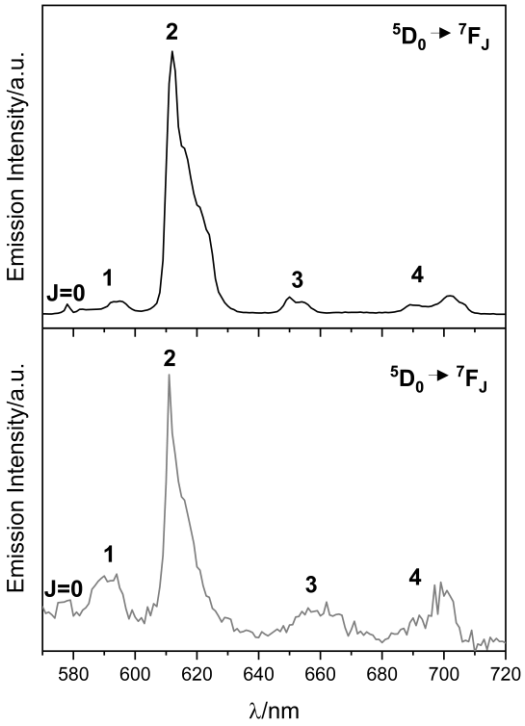


Figure 2.96 – Stacked emission spectra of **EuDBM$_3$** in THF (0.2% DMF) upon addition of 0 (top, black) and 4 (bottom, grey) equivalents of F^-. λ_{exc}: 350 nm. The spectra were acquired by MSc Carys Scott.

2.5.5.2 Time resolved data

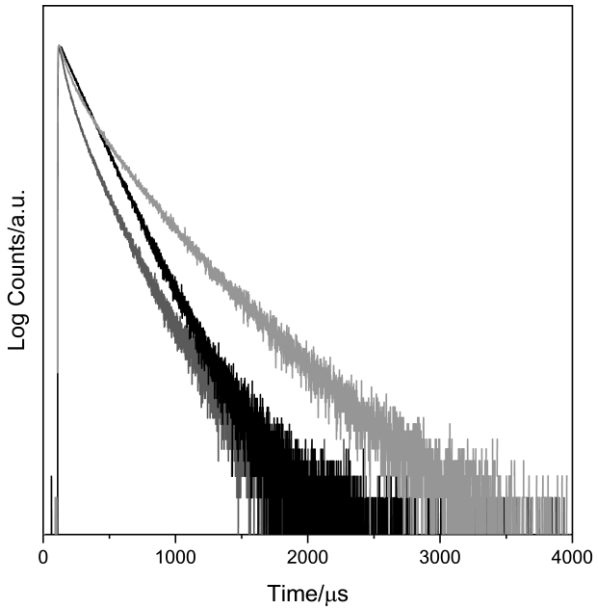


Figure 2.97 – Overlaid luminescence lifetime spectra of **Eu$_2$SAcbisDBM$_3$** in DMF (black), H_2O (dark grey) and D_2O (light grey). 0.4% DMF for H_2O and D_2O, λ_{exc} 350 nm, λ_{em} 611 nm.

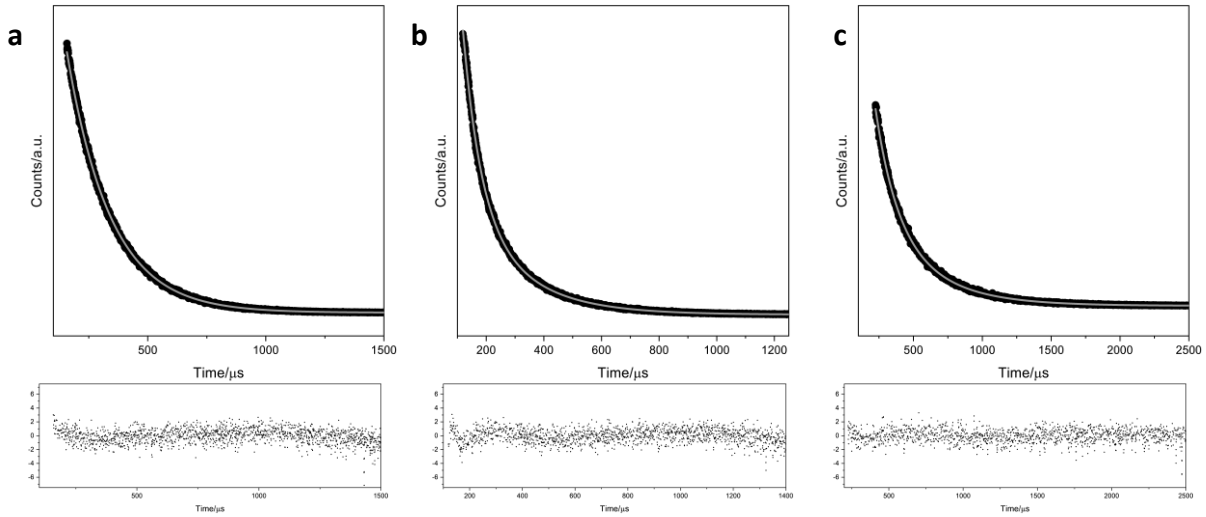


Figure 2.98 – Decay curve fittings of **Eu_2SAcbisDBM$_3$** in DMF (**a**), H_2O (0.2% DMF, **b**) and D_2O (0.2% DMF, **c**). Below are the respective residuals.

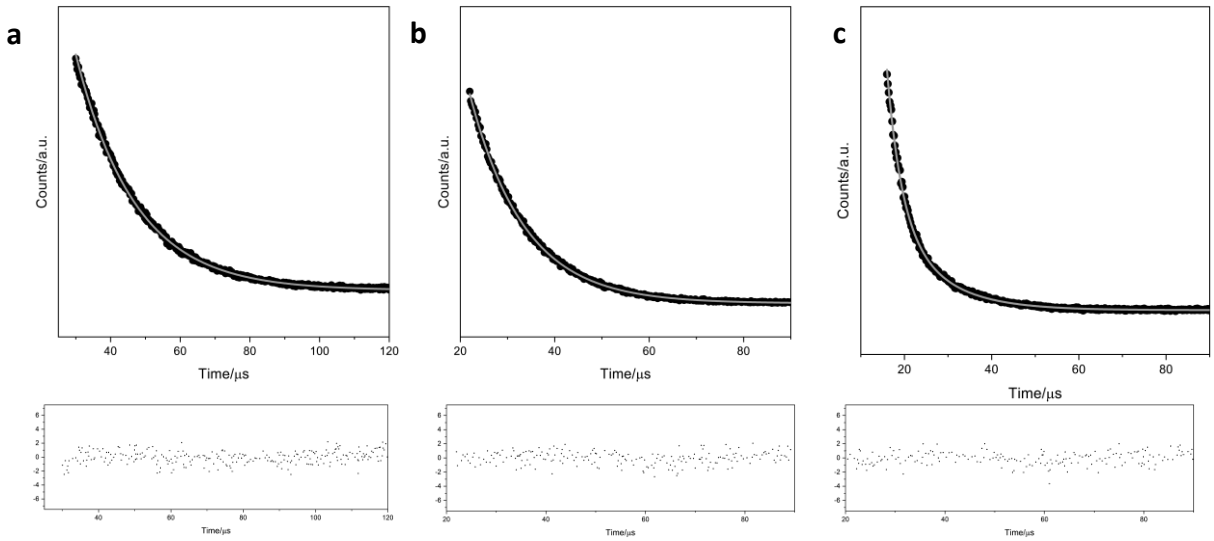


Figure 2.99 – Decay curve fittings of **Yb_2SAcbisDBM$_3$** in DMSOd_6 (**a**), DMF (**b**) and H_2O (0.2% DMF, **c**). Below are the respective residuals.

Solvent	**τ/μs (%)**
DMSOd_6	17 (100%)
DMF	11 (100%)
H_2O	11 (70%), 3.3 (30%)

Table 2.4 – Exponential decay analysis of **Yb_2SAcbisDBM$_3$**. λ_{exc}: 350 nm, λ_{em}: 977 nm.

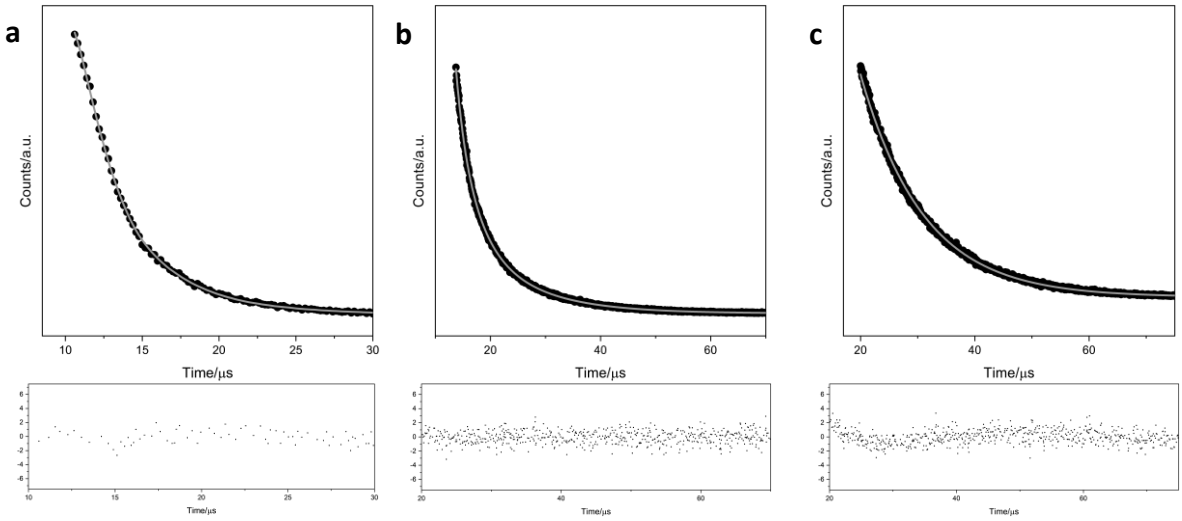


Figure 2.100 – Decay curve fittings of **Nd_2SAcbisDBM$_3$** in DMSOd_6 (**a**) and of **Yb_2bisDBM$_3$** as crystals (**b**) and as powder (**c**). Below are the respective residuals.

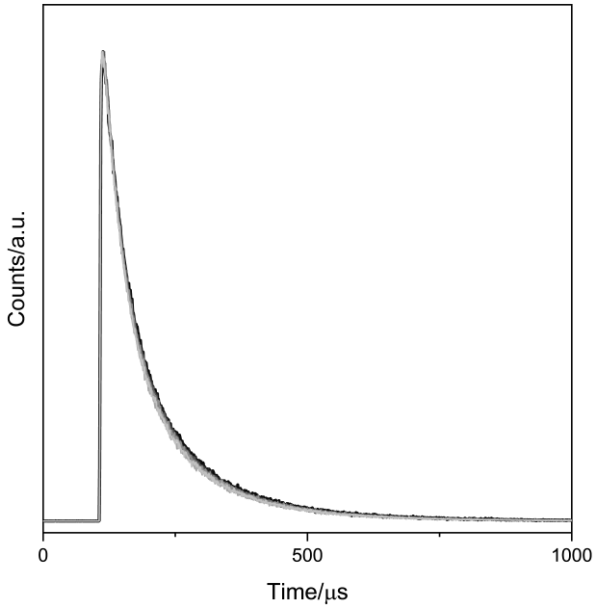


Figure 2.101 – Overlaid lifetime spectra of **Eu_2SAcbisDBM$_3$** in H_2O/EtOH (1/1, 0.4% DMF) upon addition of up to 260 equivalents of F^- as NaF (0.8 mM). λ_{exc}: 350 nm, λ_{em}: 611 nm.

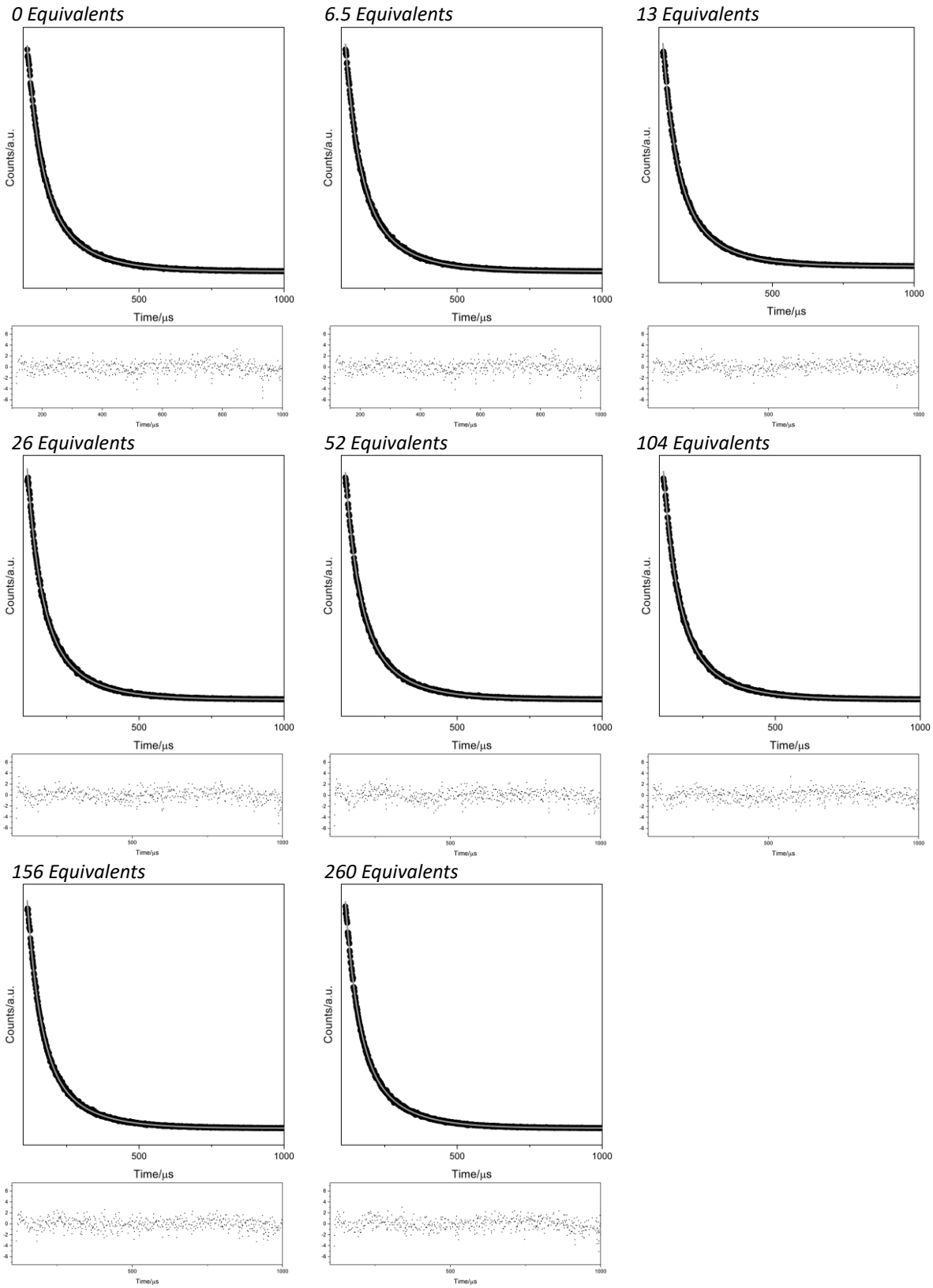
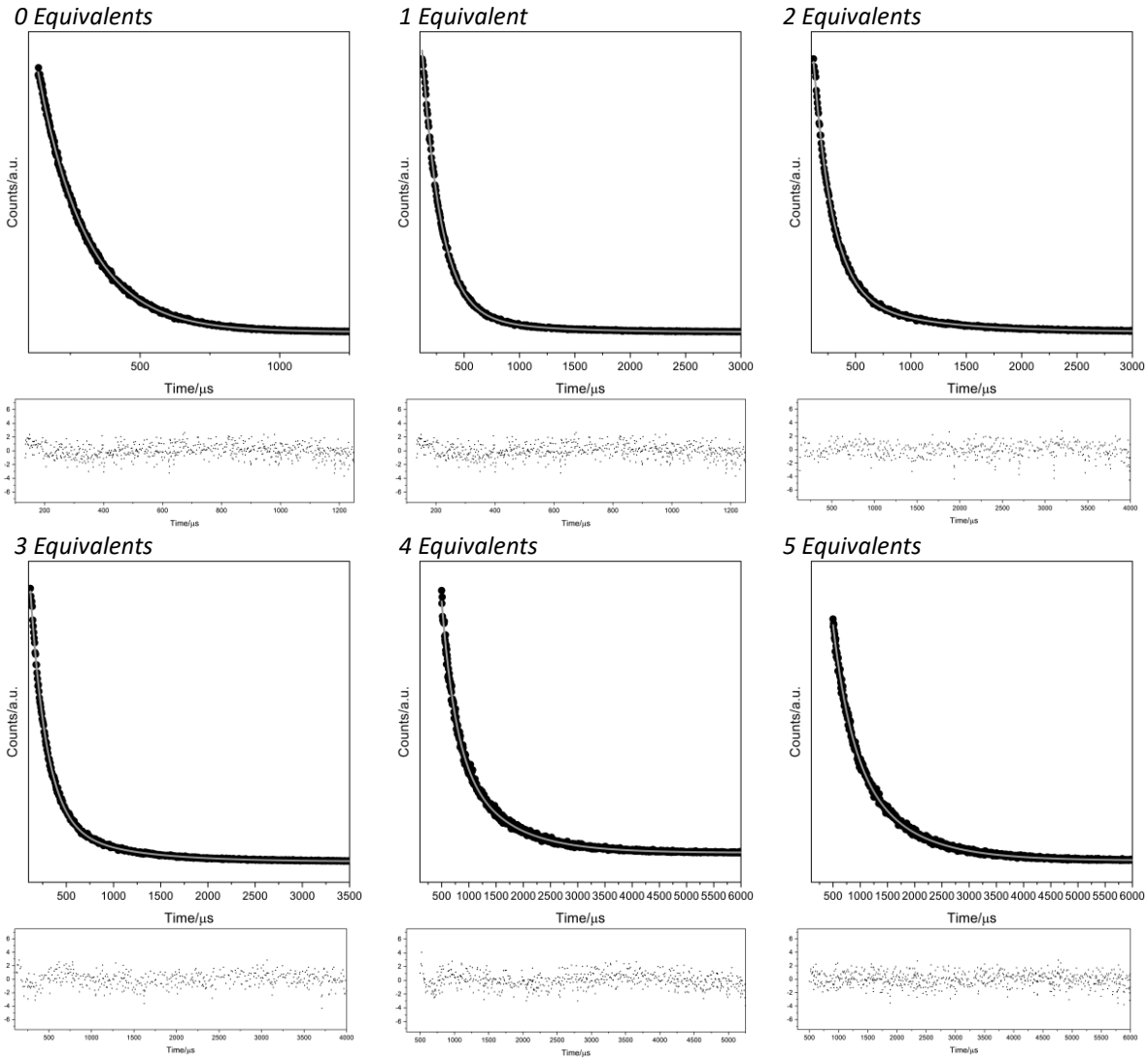


Figure 2.102 – Decay curve fittings of **Eu_2SAcbisDBM$_3$** upon addition of F^- as NaF in H_2O/EtOH (1:1 ratio, 0.4% DMF) at the specified equivalents. Below are the respective residuals.

Equivalents NaF	τ/μs (%)
0	140 (66%), 46 (34%)
6.5	140 (66%), 46 (34%)
13	140 (63%), 47 (37%)
26	130 (68%), 43 (32%)
52	140 (64%), 45 (36%)
104	140 (63%), 46 (37%)
156	140 (63%), 44 (37%)
260	140 (64%), 44 (36%)

Table 2.5 – Exponential decay analysis of **Eu_2SAcbisDBM$_3$** upon addition of F^- as NaF in H_2O/EtOH (1:1 ratio, 0.4% DMF). λ_{exc}: 350 nm, λ_{em}: 611 nm.



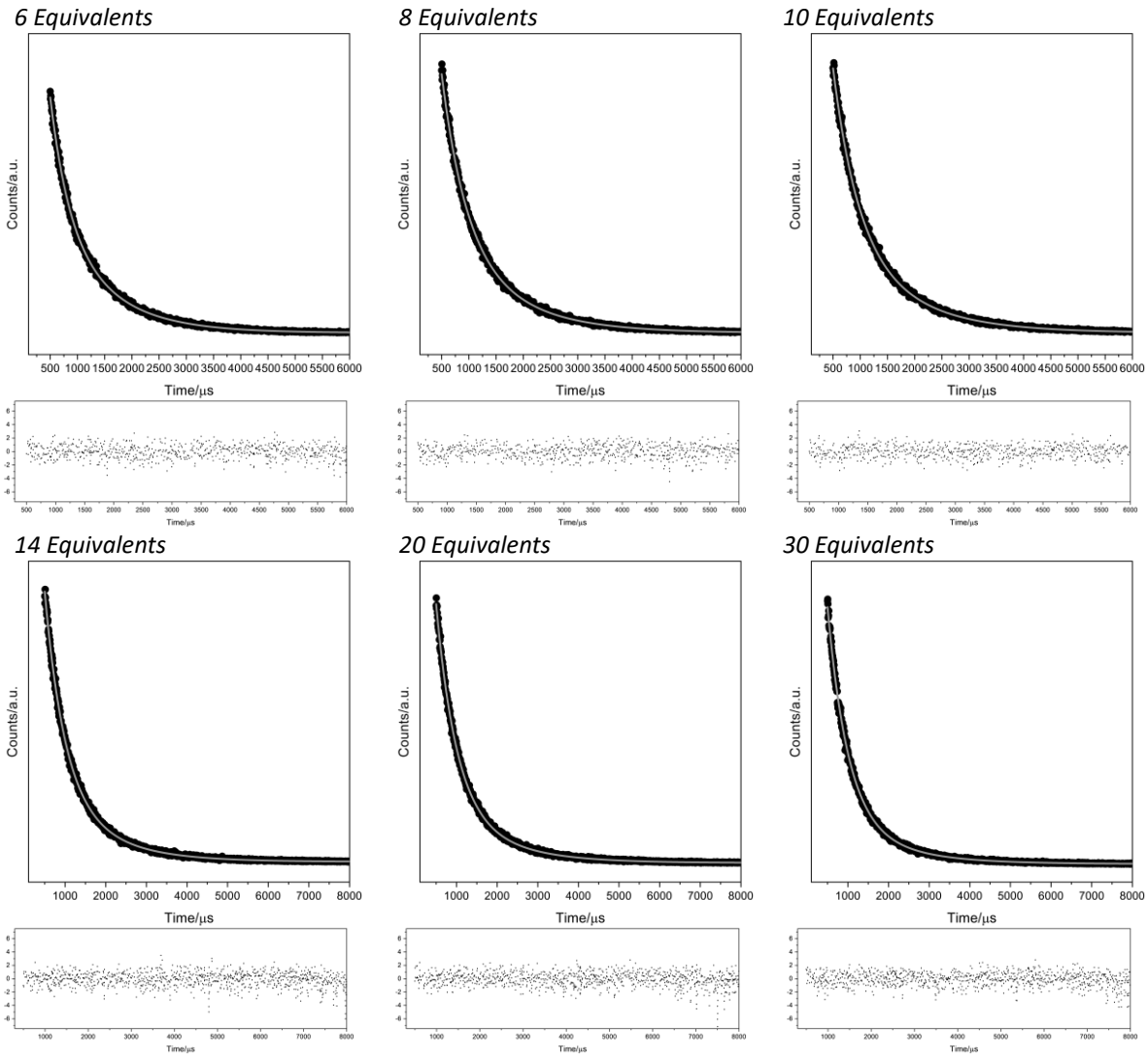


Figure 2.103 – Decay curve fittings of **Eu_2SAcbisDBM$_3$** upon addition of F^- as TBAF in THF (0.2% DMF) at the specified equivalents. Below are the respective residuals.

Equivalents F^-	τ/μs (%)
0	170 (100%)
1	170 (76%), **700** (24%)
2	170 (64%), **740** (36%)
3	170 (56%), **750** (44%)
4	**910** (74%), 250 (26%)
5	**930** (77%), 280 (23%)
6	**990** (75%), 340 (25%)
8	**1200** (63%), 440 (37%)
10	**1200** (63%), 450 (37%)
14	**1300** (53%), 480 (47%)
20	**1400** (47%), 490 (53%)
30	**1500** (40%), 500 (60%)

Table 2.6 – Exponential decay analysis of **Eu_2SAcbisDBM$_3$** upon addition of F^- as TBAF in THF (0.2% DMF). Highlighted are the longer components. λ_{exc}: 350 nm, λ_{em}: 611 nm.

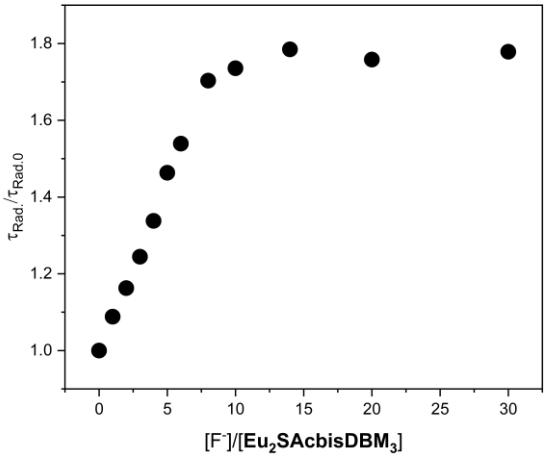


Figure 2.104 – Plot of the ratios between the τ_{Rad} after addition of F^- ($\tau_{Rad.}$) and the initial $\tau_{Rad.}$ ($\tau_{Rad.0}$) of **Eu_2SAcbisDBM$_3$** versus the equivalents of F^- added in THF (0.2% DMF).

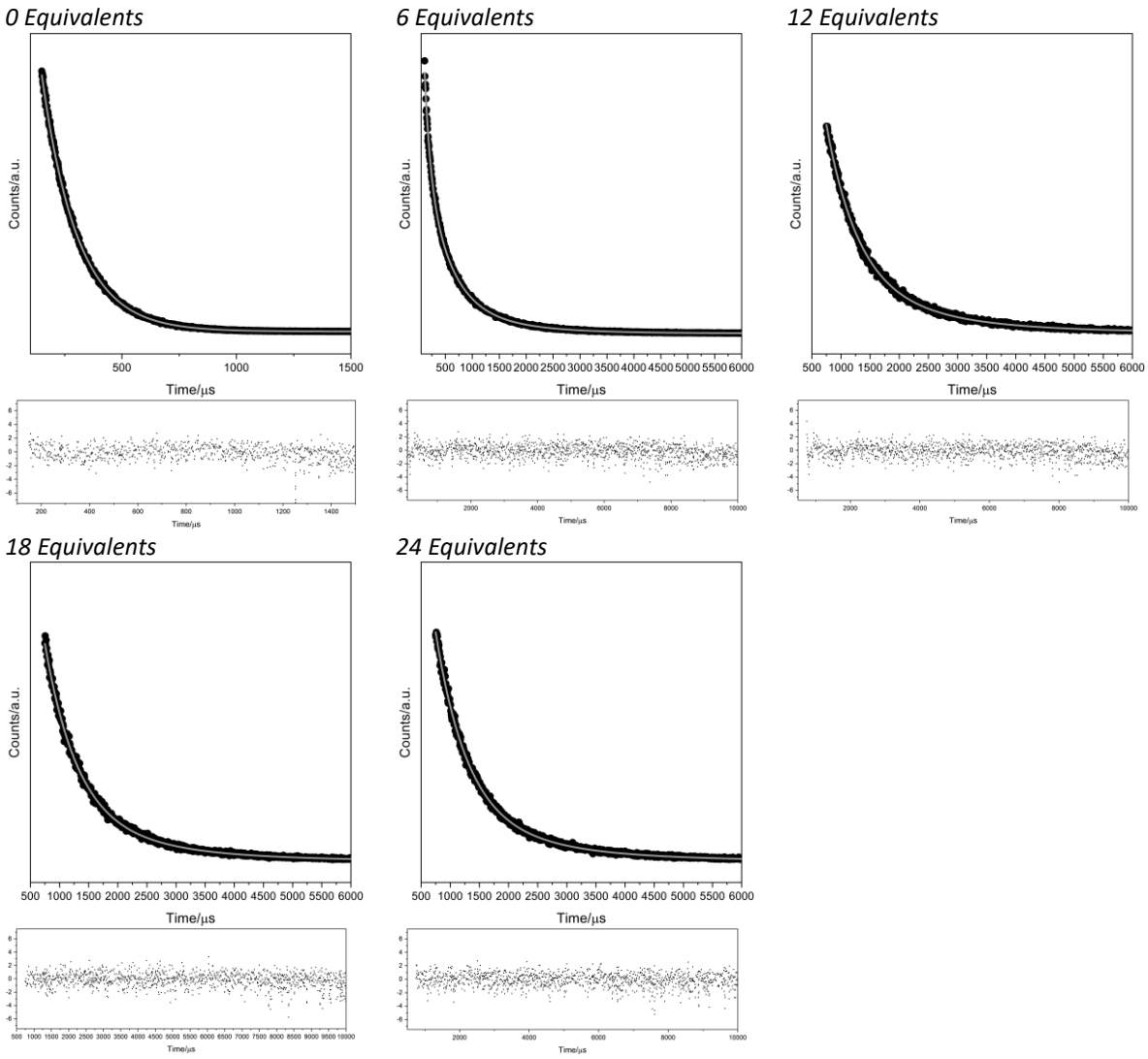


Figure 2.105 – Decay curve fittings of **Eu_2SAcbisDBM$_3$** upon addition of F^- as TBAF in THF (0.2% DMF) at the specified equivalents. Below are the respective residuals.

Equivalents F^-	τ/μs (%)
0	160 (100%)
6	**1200** (34%), 450 (57%), 100 (9%)
12	**1500** (51%), 530 (49%)
18	**1600** (46%), 540 (54%)
24	**1600** (46%), 530 (54%)

Table 2.7 – Exponential decay analysis of **Eu_2SAcbisDBM$_3$** upon addition of F^- as TBAF in THF (0.2% DMF). Highlighted are the longer components. λ_{exc}: 350 nm, λ_{em}: 611 nm.

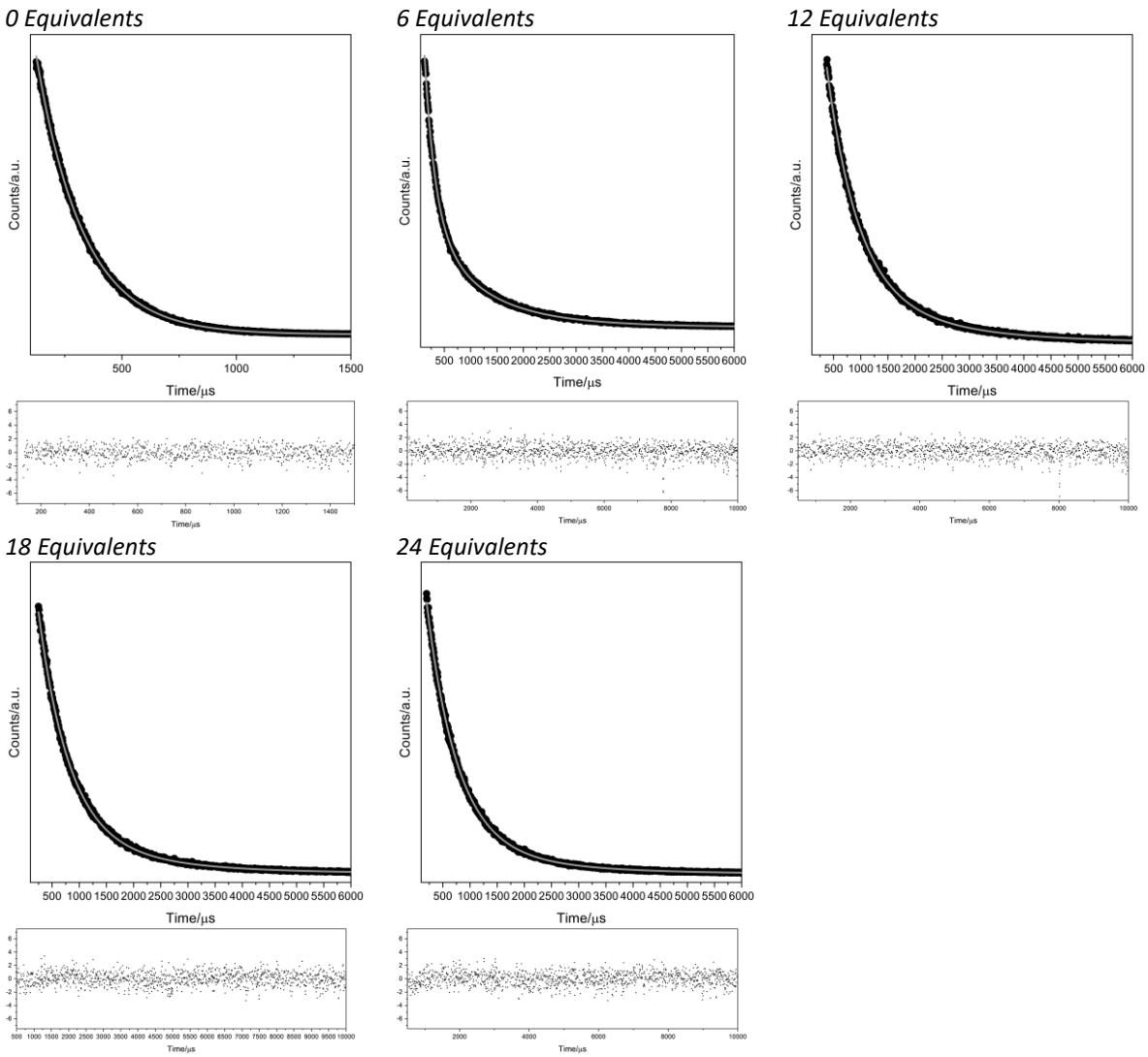


Figure 2.106 – Decay curve fittings of **Eu_2bisDBM$_3$** upon addition of F^- as TBAF in THF (0.2% DMF) at the specified equivalents. Below are the respective residuals.

Equivalents F^-	τ/μs (%)
0	200 (100%)
6	**1500** (41%), 780 (38%), 200 (21%)
12	**1800** (44%), 570 (56%)
18	**1800** (36%), 560 (64%)
24	**1800** (31%), 560 (61%)

Table 2.8 – Exponential decay analysis of **Eu_2bisDBM$_3$** upon addition of F^- as TBAF in THF (0.2% DMF). Highlighted are the longer components. λ_{exc}: 350 nm, λ_{em}: 611 nm.

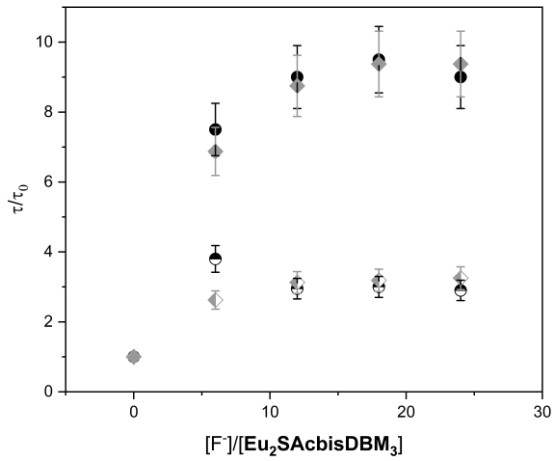


Figure 2.108 – Plot of the ratios between the lifetime after addition of F^- as TBAF (τ) and the initial lifetime (τ_0) of **Eu_2bisDBM$_3$** (black) and **Eu_2SAcbisDBM$_3$** (grey) versus the equivalents of F^- as TBAF added in THF (0.2% DMF). The filled symbol represents the long component, while the half-filled symbol the short component. λ_{exc}: 350 nm, λ_{em}: 611 nm.

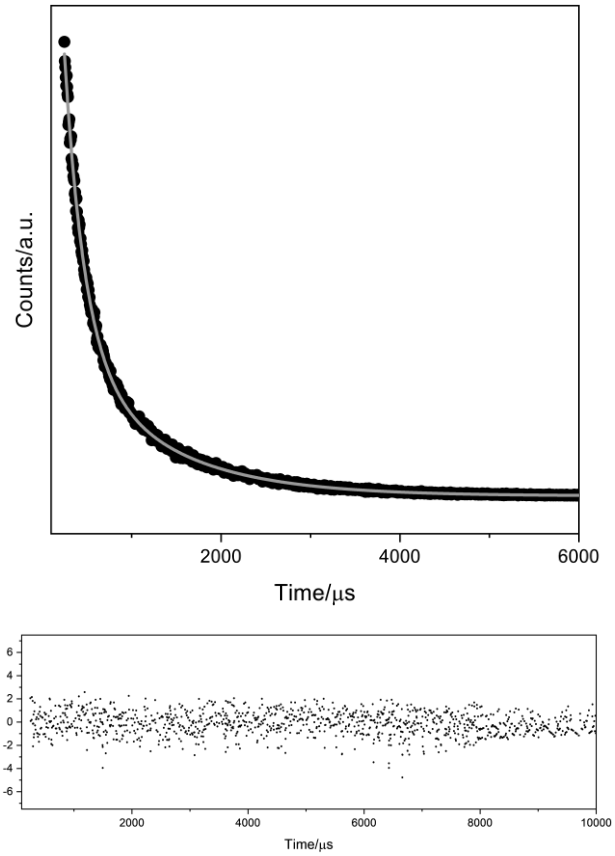


Figure 2.109 – Decay curve fitting of **Eu_2bisDBM$_3$** in THF (0.2% DMF) upon addition of excess F^- as sample for ESI^--MS. λ_{exc} 350 nm, λ_{em} 611 nm. Below are the respective residuals.

τ/μs (%)
1000 μs (70%), 240 μs (30%)

Table 2.9 – Exponential decay analysis of **Eu_2bisDBM$_3$** in THF (0.2% DMF) upon addition of excess F^- as sample for ESI$^-$-MS. λ_{exc} 350 nm, λ_{em} 611 nm.

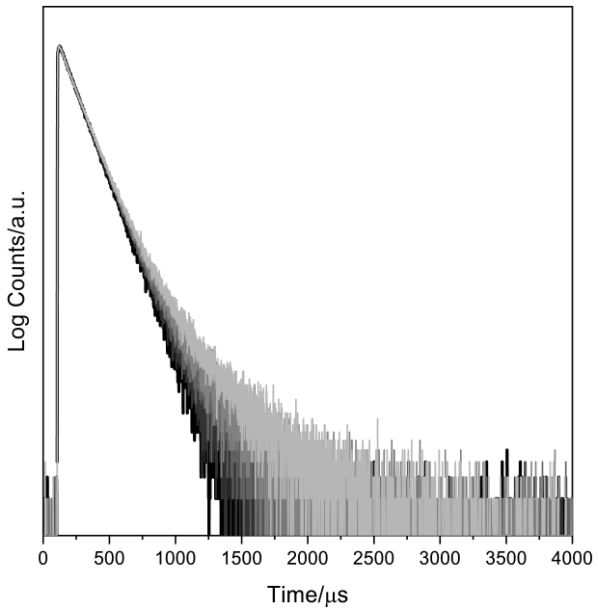
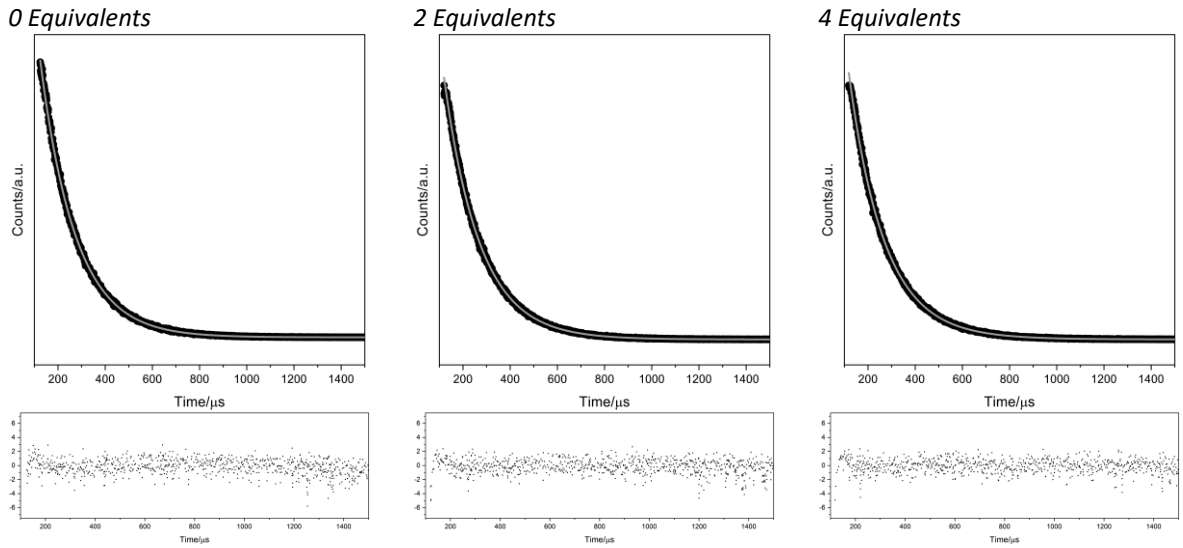


Figure 2.110 – Overlaid lifetime spectra of **Eu_2SAcbisDBM$_3$** in THF (0.2% DMF) upon addition of 0, 2, 4, 8 and 16 equivalents Br^-. λ_{exc} 350 nm, λ_{em} 611 nm.



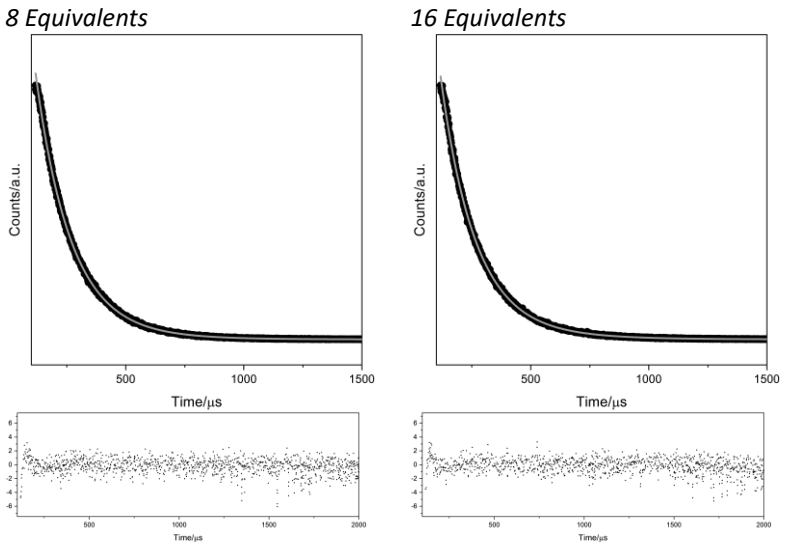


Figure 2.111 – Decay curve fittings of **Eu_2SAcbisDBM$_3$** upon addition of Br^- as TBAB in THF (0.2% DMF) at the specified equivalents. Below are the respective residuals.

Equivalents TBAB	**τ/μs (%)**
0	160 (100%)
2	160 (82%), 190 (18%)
4	160 (77%), 210 (23%)
8	150 (88%), 280 (12%)
16	140 (82%), 280 (18%)

Table 2.10 – Exponential decay analysis of **Eu_2SAcbisDBM$_3$** in THF (0.2% DMF) upon addition of Br^-.

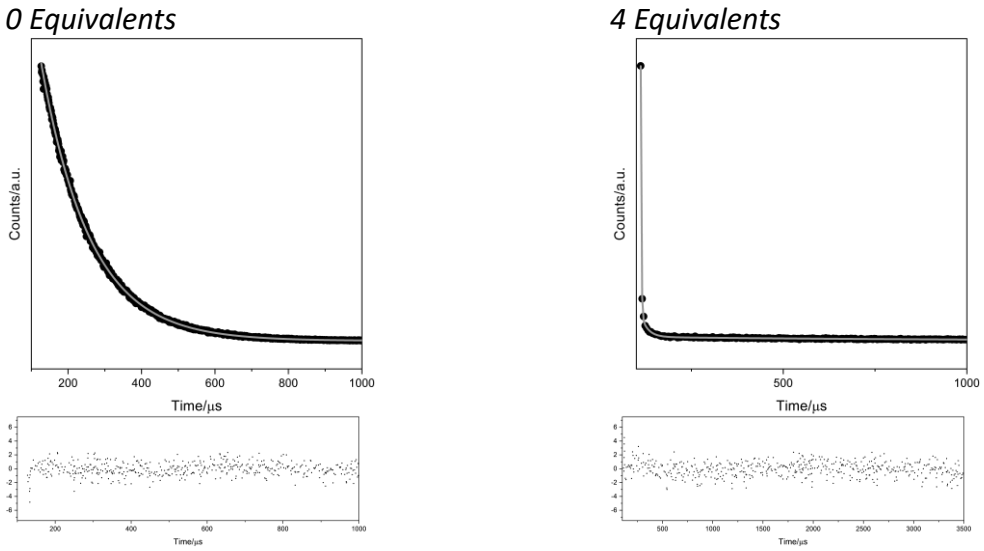


Figure 2.112 – Decay curve fittings of **EuDBM$_3$** upon addition of F^- as TBAF in THF (0.2% DMF) at the specified equivalents. Below are the respective residuals.

2.5.6 Crystal structures data

	Yb_2bisDBM$_3$	**Yb_2SAcbisDBM$_3$**
Formula	C_{73} H_{53} O_{14} Yb_2,2(C_3 H_7 N O)	C_{97} H_{87} N_9 O_{17} S_5 Yb_2
Space group	P 2_1/c	P -1
Cell lengths/Å	**a** 13.33830(10) **b** 28.53550(10) **c** 18.11090(10)	**a** 16.26780(10) **b** 16.69170(10) **c** 16.99930(10)
Cell angles/deg	α 90 β 103.0530(10) γ 90	α 91.5590(10) β 93.7960(10) γ 99.6380(10)
Cell volume/Å^3	6715.17	4537.36
Z	4	2

Table 2.11 – Crystal structure data of **Yb_2bisDBM$_3$** and **Yb_2SAcbisDBM$_3$**.

Yb_2bisDBM$_3$		Bond length/Å
Yb1	O2	2.242(3)
Yb1	O1	2.231(3)
Yb1	O7	2.265(2)
Yb1	O4	2.225(3)
Yb1	O6	2.236(3)
Yb1	O3	2.275(3)
Yb1	O5	2.355(4)
Yb2	O8	2.223(3)
Yb2	O9	2.223(3)
Yb2	O13	2.248(3)
Yb2	O14	2.228(3)
Yb2	O11	2.220(3)
Yb2	O12	2.253(3)
Yb2	O10	2.340(5)
O2	C9	1.268(5)
O1	C7	1.268(5)
O8	C16	1.270(5)
O7	C57	1.270(5)
O9	C18	1.264(5)
O4	C33	1.269(4)
O6	C55	1.270(5)
O13	C64	1.267(5)
O14	C66	1.263(5)
O3	C31	1.272(5)
O11	C40	1.262(5)
O12	C42	1.265(5)
O5	C78	1.301(9)
O10	H10A	0.87
O10	H10B	0.869
C17	H17	0.95
C17	C18	1.411(5)
C17	C16	1.409(5)
C18	C19	1.499(5)
C8	H8	0.951
C8	C9	1.411(5)
C8	C7	1.399(5)
C12	H12	0.95
C12	C13	1.388(5)
C12	C11	1.390(5)

Yb_2SAcbisDBM$_3$		Bond length/Å
Yb1	O1	2.240(3)
Yb1	O1S	2.297(5)
Yb1	O2	2.248(4)
Yb1	O6	2.250(5)
Yb1	O7	2.238(3)
Yb1	O11	2.232(3)
Yb1	O12	2.229(4)
Yb2	O2S	2.281(4)
Yb2	O4	2.235(3)
Yb2	O5	2.236(3)
Yb2	O9	2.250(4)
Yb2	O10	2.254(3)
Yb2	O14	2.256(3)
Yb2	O15	2.252(4)
S1	C17	1.837(9)
S1	C18	1.71(1)
S2	C48	1.819(9)
S2	C49	1.69(1)
S3	C79	1.86(1)
S3	C80	1.73(1)
S3S	O2S	1.503(4)
S3S	C5S	1.758(7)
S3S	C6S	1.804(8)
O1	C7	1.261(7)
O1S	S1S	1.546(6)
O2	C9	1.262(6)
O3	C18	1.24(1)
O4	C23	1.255(6)
O5	C25	1.256(6)
O6	C38	1.252(8)
O7	C40	1.282(7)
O8	C49	1.25(1)
O9	C54	1.274(6)
O10	C56	1.266(6)
O11	C69	1.258(6)
O12	C71	1.281(6)
O13	C80	1.23(1)
O14	C85	1.268(6)
O15	C87	1.273(6)

C10	C9	1.500(5)
C10	C15	1.402(5)
C10	C11	1.393(6)
C35	H35	0.95
C35	C34	1.388(5)
C35	C36	1.387(5)
C56	H56	0.95
C56	C55	1.401(5)
C56	C57	1.403(5)
C16	C14	1.505(5)
C14	C13	1.390(6)
C14	C15	1.391(5)
C5	H5	0.949
C5	C6	1.388(6)
C5	C4	1.401(5)
C30	C31	1.506(5)
C30	C25	1.380(6)
C30	C29	1.392(7)
C19	C20	1.391(6)
C19	C24	1.400(5)
C34	C39	1.393(5)
C34	C33	1.506(5)
C58	C57	1.509(5)
C58	C63	1.393(5)
C58	C59	1.398(7)
C13	H13	0.95
C6	C7	1.506(5)
C6	C1	1.394(5)
C66	C65	1.396(6)
C66	C67	1.504(5)
C15	H15	0.95
C55	C54	1.500(5)
C41	H41	0.95
C41	C42	1.400(5)
C41	C40	1.402(5)
C11	H11	0.95
C65	H65	0.951
C65	C64	1.402(5)
C38	C39	1.397(5)
C38	C37	1.396(5)
C38	C40	1.498(5)
C20	H20	0.95
C20	C21	1.391(5)
C68	H68	0.95
C68	C67	1.393(6)
C68	C69	1.389(6)
C54	C53	1.388(6)
C54	C49	1.389(6)
C39	H39	0.95
C64	C62	1.508(7)
C37	H37	0.95
C37	C36	1.387(5)
C63	H63	0.95
C63	C62	1.389(5)
C33	C32	1.391(6)
C53	H53	0.95
C53	C52	1.383(6)
C2	H2	0.951

N1	N2	1.321(9)
N1	C13	1.346(7)
N2	N3	1.313(8)
N3	C14	1.358(8)
N3	C15	1.459(9)
N4	N5	1.310(7)
N4	C44	1.371(7)
N5	N6	1.333(7)
N6	C45	1.351(7)
N6	C46	1.470(9)
N7	N8	1.317(9)
N7	C75	1.347(7)
N8	N9	1.327(8)
N9	C76	1.350(7)
N9	C77	1.46(1)
C1	H1	0.95
C1	C2	1.378(9)
C1	C6	1.400(9)
C2	H2	0.95
C2	C3	1.376(9)
C3	H3	0.95
C3	C4	1.36(1)
C4	H4	0.949
C4	C5	1.379(9)
C5	H5	0.951
C5	C6	1.394(8)
C5S	H5SA	0.98
C5S	H5SB	0.98
C5S	H5SC	0.981
C6	C7	1.497(7)
C6S	H6SA	0.98
C6S	H6SB	0.98
C6S	H6SC	0.98
C7	C8	1.415(8)
C8	H8	0.95
C8	C9	1.399(7)
C9	C10	1.498(8)
C10	C11	1.397(8)
C10	C22	1.406(7)
C11	H11	0.951
C11	C12	1.394(8)
C12	C13	1.488(8)
C12	C20	1.382(7)
C13	C14	1.35(1)
C14	H14	0.95
C15	H15A	0.99
C15	H15B	0.99
C15	C16	1.50(1)
C16	H16A	0.99
C16	H16B	0.99
C16	C17	1.49(1)
C17	H17A	0.99
C17	H17B	0.99
C18	C19	1.52(2)
C19	H19A	0.98
C19	H19B	0.98
C19	H19C	0.98
C20	H20	0.949

C2	C1	1.393(5)
C2	C3	1.381(6)
C1	H1	0.95
C36	H36	0.95
C31	C32	1.396(6)
C62	C61	1.389(8)
C4	H4	0.95
C4	C3	1.394(5)
C42	C43	1.500(6)
C25	H25	0.95
C25	C26	1.388(7)
C67	C72	1.393(7)
C21	H21	0.95
C21	C22	1.386(6)
C32	H32	0.95
C24	H24	0.95
C24	C23	1.389(5)
C3	H3	0.95
C26	H26	0.95
C26	C27	1.373(8)
C52	H52	0.95
C52	C51	1.386(6)
C69	H69	0.95
C69	C70	1.379(8)
C23	H23	0.95
C23	C22	1.389(7)
C22	H22	0.95
C43	C48	1.391(7)
C43	C44	1.392(7)
C70	H70	0.95
C70	C71	1.380(8)
C49	H49	0.95
C49	C50	1.383(9)
C59	H59	0.95
C59	C60	1.384(7)
C48	H48	0.95
C48	C47	1.389(9)
C29	H29	0.95
C29	C28	1.387(9)
C71	H71	0.949
C71	C72	1.383(7)
C72	H72	0.95
C61	H61	0.95
C61	C60	1.39(1)
C51	H51	0.95
C51	C50	1.380(8)
C27	H27	0.95
C27	C28	1.381(8)
C60	H60	0.95
C44	H44	0.95
C44	C45	1.392(9)
C50	H50	0.95
C46	H46	0.95
C46	C45	1.38(1)
C46	C47	1.37(1)
C45	H45	0.95
C47	H47	0.95
C28	H28	0.951

C20	C21	1.398(8)
C21	C22	1.376(8)
C21	C23	1.504(7)
C22	H22	0.95
C23	C24	1.397(7)
C24	H24	0.95
C24	C25	1.409(7)
C25	C26	1.500(7)
C26	C27	1.38(1)
C26	C31	1.394(9)
C27	H27	0.95
C27	C28	1.39(1)
C28	H28	0.95
C28	C29	1.37(1)
C29	H29	0.95
C29	C30	1.34(1)
C30	H30	0.951
C30	C31	1.385(9)
C31	H31	0.951
C32	H32	0.95
C32	C33	1.38(2)
C32	C37	1.39(1)
C33	H33	0.95
C33	C34	1.35(1)
C34	H34	0.95
C34	C35	1.36(1)
C35	H35	0.949
C35	C36	1.39(1)
C36	H36	0.949
C36	C37	1.37(1)
C37	C38	1.50(1)
C38	C39	1.400(9)
C39	H39	0.949
C39	C40	1.38(1)
C40	C41	1.501(7)
C41	C42	1.411(7)
C41	C53	1.389(8)
C42	H42	0.95
C42	C43	1.380(7)
C43	C44	1.462(7)
C43	C51	1.391(7)
C44	C45	1.366(8)
C45	H45	0.95
C46	H46A	0.991
C46	H46B	0.989
C46	C47	1.51(1)
C47	H47A	0.991
C47	H47B	0.99
C47	C48	1.52(1)
C48	H48A	0.99
C48	H48B	0.99
C49	C50	1.54(2)
C50	H50A	0.98
C50	H50B	0.98
C50	H50C	0.98
C51	H51	0.95
C51	C52	1.401(7)
C52	C53	1.393(7)

C78	H78A	0.98
C78	H78B	0.98
C78	H78C	0.98
C74	H	0.98
C74	HA	0.98
C74	HB	0.98
C74	N4	1.450(7)
N4	C73	1.264(7)
N4	C75	1.479(9)
C73	HC	0.95
C73	O80	1.335(6)
C75	HD	0.979
C75	HE	0.98
C75	HF	0.98
O16	C79	1.23(1)
N6	C77	1.44(1)
N6	C79	1.29(1)
N6	C76	1.43(2)
C77	HG	0.98
C77	HH	0.98
C77	HI	0.98
C79	HJ	0.95
C76	HK	0.98
C76	HL	0.98
C76	HM	0.98

C52	C54	1.507(8)
C53	H53	0.949
C54	C55	1.397(7)
C55	H55	0.951
C55	C56	1.390(8)
C56	C57	1.500(7)
C57	C58	1.390(9)
C57	C62	1.36(1)
C58	H58	0.95
C58	C59	1.37(1)
C59	H59	0.95
C59	C60	1.34(1)
C60	H60	0.95
C60	C61	1.39(1)
C61	H61	0.95
C61	C62	1.389(9)
C62	H62	0.95
C63	H63	0.95
C63	C64	1.34(1)
C63	C68	1.42(1)
C64	H64	0.95
C64	C65	1.37(1)
C65	H65	0.951
C65	C66	1.36(1)
C66	H66	0.951
C66	C67	1.389(9)
C67	H67	0.95
C67	C68	1.381(8)
C68	C69	1.485(7)
C69	C70	1.415(8)
C70	H70	0.95
C70	C71	1.389(7)
C71	C72	1.497(8)
C72	C73	1.391(7)
C72	C84	1.389(7)
C73	H73	0.949
C73	C74	1.408(8)
C74	C75	1.459(7)
C74	C82	1.393(7)
C75	C76	1.376(8)
C76	H76	0.951
C77	H77A	0.989
C77	H77B	0.989
C77	C78	1.51(1)
C78	H78A	0.99
C78	H78B	0.99
C78	C79	1.50(1)
C79	H79A	0.99
C79	H79B	0.99
C80	C81	1.48(1)
C81	H81A	0.98
C81	H81B	0.98
C81	H81C	0.98
C82	H82	0.951
C82	C83	1.382(7)
C83	C84	1.405(8)
C83	C85	1.508(7)
C84	H84	0.95

C85	C86	1.397(8)
C86	H86	0.95
C86	C87	1.402(7)
C87	C88	1.497(9)
C88	C89	1.385(9)
C88	C93	1.370(9)
C89	H89	0.95
C89	C90	1.37(1)
C90	H90	0.95
C90	C91	1.34(1)
C91	H91	0.95
C91	C92	1.37(1)
C92	H92	0.95
C92	C93	1.39(1)
C93	H93	0.949
S1S	C1S	1.75(2)
S1S	C2S	1.80(1)
C1S	H1SA	0.97
C1S	H1SB	0.98
C1S	H1SC	0.99
C2S	H2SA	0.98
C2S	H2SB	0.98
C2S	H2SC	0.98

Tables 2.12 and 2.13 – Bond lengths of **Yb_2bisDBM$_3$** and **Yb_2SAcbisDBM$_3$**.

Chapter 3 – Plasmonic enhancement of visible and NIR lanthanide(III) emission on nanostructured surfaces

3.1 Introduction

3.1.1 Lanthanide(III) complexes on Au surfaces

Among other molecular components, fluorophores, including metal complexes, have been anchored on Au surfaces, with some studies displaying the retention of the luminescence on the surface.[1-4] In an example by Pikramenou and co-workers, Ru(II) and Ir(III) bipyridyl complexes **1** and **2** (Figure 3.1) were attached to Au substrates *via* S-Au bonds. The complexes include an alkyl spacing unit to reduce the quenching from the metal to produce emissive surfaces. Importantly, the surfaces were found to be responsive to albumins as a modulation of both lifetime and surface plasmon resonance (SPR), thus reporting the potential of such materials as multimodal sensing devices.[5, 6]

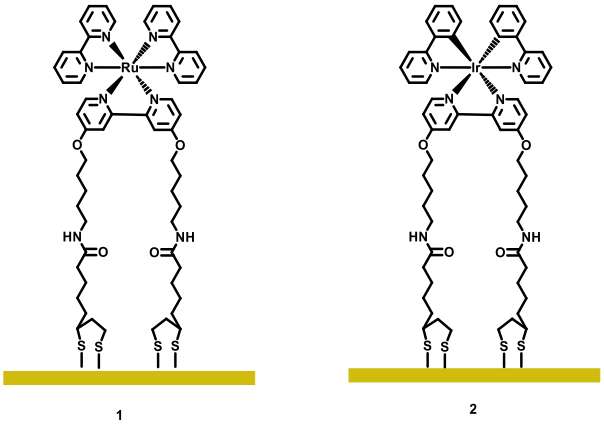


Figure 3.1 – Chemical structures and sketch of the systems presented by Pikramenou and co-workers.[5, 6]

Despite their excellent optical properties, examples of lanthanide(III) complexes anchored on Au surfaces are rare. Gunnlaugsson and co-workers reported a macrocyclic Eu(III) complex

anchored on Au with a C12 spacing unit (**3**, Figure 3.2).[7] Upon excitation at 281 nm, the surfaces displayed characteristic Eu(III) luminescence solely in the presence of a β-diketonate antenna (**4**) and a switch-on/off mechanism was demonstrated by introduction of a competitive ligand (**5**) to displace the sensitiser.[7]

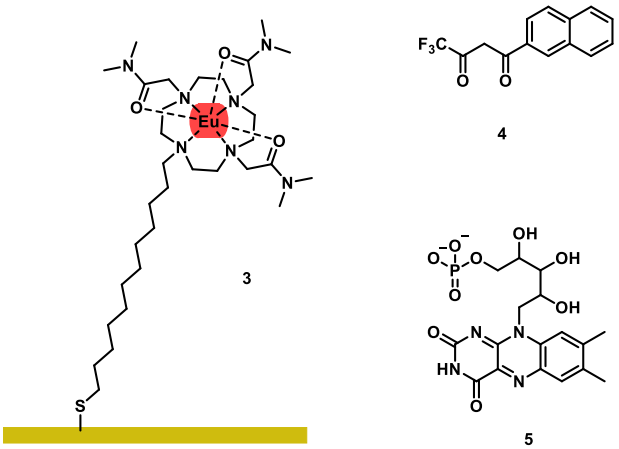


Figure 3.2 – Chemical structures of the complex and molecules presented by Gunnlaugsson and co-workers.[7]

Lehr *et al.* have presented the functionalisation of an Au surface with binuclear Eu(III) and Tb(III) complexes by means of a film of surface active isophthalic acid units on the substrate.[8] In their work, after anchoring the isophthalic acid units **7** *via* S-Au bonds, complex **6** was introduced and, due to its unfilled coordination sphere, could coordinate to the carboxylic acid units exposed on the surface and produce characteristic Eu(III) or Tb(III) luminescence. Furthermore, the authors report a dependence of the emission intensity of the Tb(III) derivative to the length of the spacing unit. Significant improvements in emission signal were recorded upon increase of the carbon chain length (from 5 to 15 CH_2 units), indicating a decrease in the quenching from the Au surface at longer distances.[8]

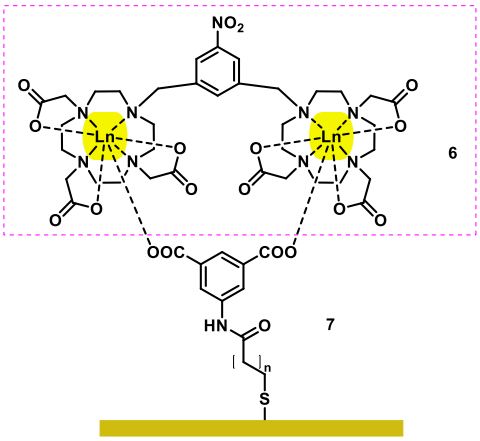


Figure 3.3 – Chemical structure and sketch of the system presented by Lehr *et al.*.[8] Ln=Eu(III) or Tb(III), n=5-15.

In the same report, the authors present the reversible coordination of mononuclear Tb(III) complex **8** by electrochemical modulation of the recruiting catechol units **9** (Figure 3.4). Indeed, Tb(III) luminescence could be deactivated by dissociation of the formed complex, due to the conversion from catechol to quinone.[8]

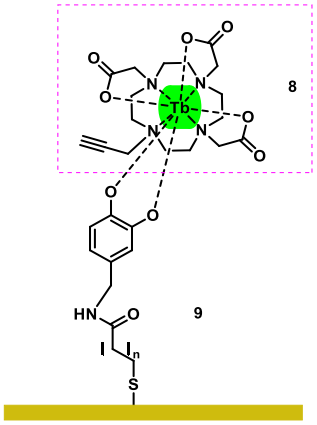


Figure 3.4 – Chemical structure and sketch of the system presented by Lehr *et al.*.[8]

Further work by the group concerned the electrochemical modulation of Eu(III) emission by means of a ferrocene unit (Figure 3.5). Here, Eu(III) complex **10** was anchored on the surface by photogeneration of a reactive nitrene at the terminal aryl azide which, in turn, would react with aromatic C-H units of the ferrocene component on the Au surface. Upon electrochemical oxidation of the functionalised surface, Eu(III) emission decreased by ≈35%, in accordance with the conversion to a ferrocenium unit and quenching of the luminescence. The process was

found to be reversible and the surface is an excellent example of incorporation of responsive units to surfaces.[9]

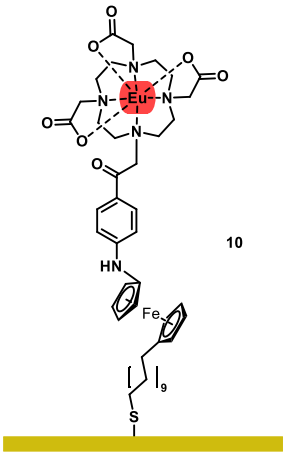


Figure 3.5 – Chemical structure and sketch of the system presented by Lehr *et al.*.[9]

In another example of functionalisation of Au surfaces with both *d* block and *f* block elements, Mulas *et al.* have presented the electrochemical detection of coordinating Eu(III) or Yb(III) β-diketonate complexes **11** by means of a Ru(II) organometallic ligand (**12**, Figure 3.6). Unfortunately, no luminescence arising from the lanthanide(III) unit could be observed upon coordination to **12** when anchored on Au, drawing attention to the challenges encountered when fabricating luminescent surfaces.[10]

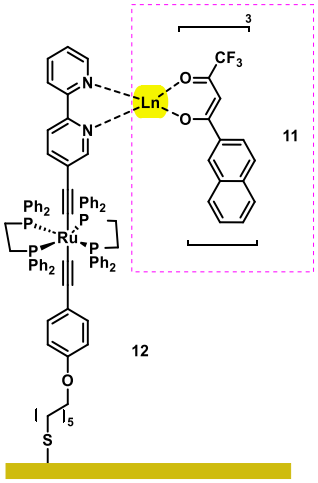


Figure 3.6 – Chemical structure and sketch of the system presented by Mulas *et al.*. Ln(III)= Eu(III) or Yb(III).[10]

3.1.2 Plasmonic enhancement of lanthanide(III) luminescence

There are significant efforts to produce highly emissive materials by means of plasmon enhanced fluorescence, and, in addition to organic dyes, examples of luminescence enhancement of emitters such as quantum dots, perovskites and metal complexes, among others, are well reported.[11-14] The impressive sensitivity of lanthanides(III) to changes in their coordination state and environment has driven the study of sensing probes based on lanthanide(III) luminescence.[15-17] As for other emitters, the plasmonic enhancement of lanthanide(III) luminescence has been reported, with most studies concerning upconversion materials or the embedding of ions and complexes in glasses and polymeric matrices for the production of photonic devices (Figure 3.7).[18-26] However, the direct anchoring of lanthanide(III) complexes on plasmonic materials is more scarcely addressed, hindering the advance of such systems into sensing applications and neglecting the benefits of lanthanide(III) coordination chemistry.

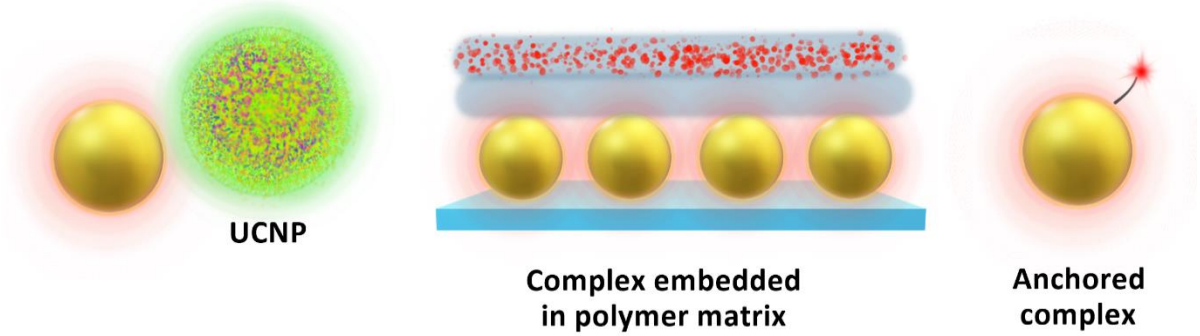


Figure 3.7 – Sketches of most common lanthanide(III) – plasmonic systems. UCNP: UpConversion NanoParticle.

3.1.2.1 Plasmon enhanced upconversion luminescence

Upconversion luminescence (UCL) is an anti-Stokes process, where excitation at lower frequencies produces higher energy emission. Lanthanides(III) have long been employed for the preparation of upconversion nanomaterials due to their characteristic sharp emission and

wide spectral coverage, allowing for multicolour emission upon NIR excitation. The potential of lanthanide(III) doped nanomaterials has been demonstrated in a variety of fields, ranging from bioimaging to anticounterfeiting barcoding, among others.[27] However, the narrow excitation cross-sections of *f-f* transitions lead to limited upconversion efficiencies, requiring prohibitively high excitation powers and hindering their inclusion in practical applications.[28] The coupling of upconversion nanomaterials to plasmonic materials has displayed impressive results for the enhancement of such processes.[19] In an example by Chen *et al.*, a 180-fold upconversion enhancement was reported by evaporation of $NaYF_4$: Yb(III), Tm(III)/Er(III) upconversion nanoparticles (UCNPs) films on highly irregular Au/Ag alloy nanoislands (Figure 3.8, **a**).[29] In this approach, the near field amplification is maximised by the presence of both Au and Ag and the surface plasmon extinction extends over the 350-1100 nm region, covering both emission (350-800 nm) and excitation (Yb(III), 980 nm) processes. The enhancement, however, is mostly attributed to the coupling with the excitation component, and the prepared composite material was used for the high quality identification of fingerprints (Figure 3.8 **c**), not possible when the UCNPs were coated on glass (Figure 3.8, **b**).[29] Kang *et al.* have reported the fine colour modulation of upconversion nanocrystals (UCNCs) doped with Yb(III), Nd(III) and Er(III) and electrostatically assembled on SiO_2 coated Au nanorods (AuNRs) (25x80 nm, Figure 3.8, **e**).[30] Here, the intensity of the green (525 and 545 nm), blue (410 nm) and red (660 nm) emitting transitions of Er(III) are individually tuned by variation of the SiO_2 shell thickness and resultant plasmonic enhancement arising from the AuNRs. The change in overall colour of the material from pale yellow to green (Figure 3.8, **f**) is due to the better overlap of the green component with the transversal LSPR mode of the AuNRs (T-LSPR, 530 nm, Figure 3.8 **d**), while

the longitudinal LSPR (L-LSPR, 700-900 nm) ensures excitation enhancement at 808 nm, with a maximum collective enhancement factor of 20.[30]

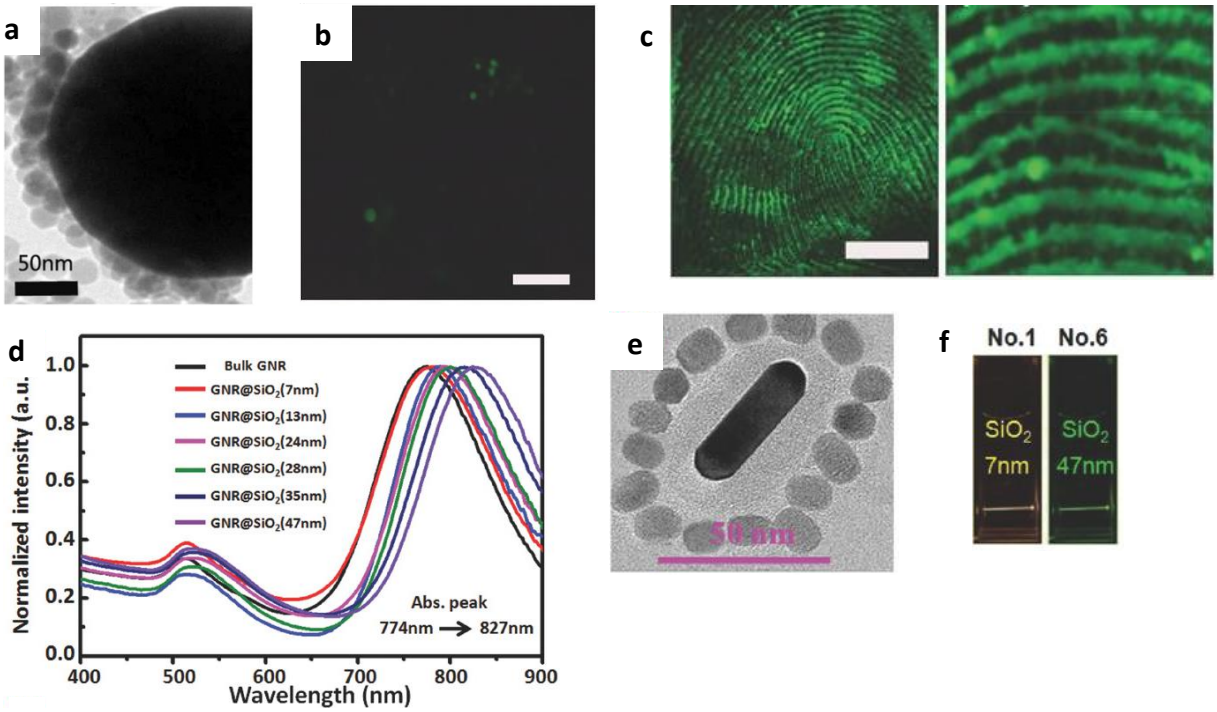


Figure 3.8 – **a** TEM image of one Au/Ag alloy nanoisland coated with $NaYF_4$: Yb(III), Tm(III) UCNPs as reported by Chen *et al.*. The image was taken from [29]. **b-c** UCL digital images of a fingerprint on a $NaYF_4$: Yb(III), Er(III) UCNPs film on glass (**b**) and on a Au/Ag alloy nanoislands surface (**c**), showing the UCL enhancement. The scale bars are 2 mm. The images were taken from [29]. **d** Extinction spectra of the prepared AuNRs reported by Kang *et al.* with increasing SiO_2 shell thickness, displaying a shift in the L-LSPR in the 700-900 nm region and the T-LSPR at 530 nm. The image was taken from [30]. **e** TEM image of the assembled UCNCs-AuNRs showing the central SiO_2 coated AuNR surrounded by the electrostatically assembled UCNCs. The image was taken from [30]. **f** Images of the assembled UCNCs-AuNRs displaying pale yellow emission with 7 nm SiO_2 shell and green emission with 47 nm SiO_2 shell. The image was taken from [30].

Whereas the reported examples rely on the assembly of the upconverting elements on the plasmonic substrates, the direct incorporation of both components in a single nanostructure has also been explored. The preparation of core-shell UCNPs has been reported by either inclusion of a plasmonic core or decoration of the UCNPs with plasmonic NPs. The first approach has been employed by Yin *et al.*, where a 30-fold enhancement was recorded for the red and green emission of a Lu_2O_3: Gd(III), Yb(III), Er(III) shell around SiO_2 (30 nm) coated

AgNPs (20 nm, Figures 3.9, **a** and **b**).[31] Qin *et al.*, on the other hand, have demonstrated a 15-fold upconversion luminescence enhancement upon embedding of AgNPs (10 nm) in the SiO_2 shell (10 nm) of $NaYF_4$: Nd(III), Yb(III), Ho(III) UCNPs (Figures 3.9, **c** and **d**).[32] Despite both methods displaying encouraging results, the controlled preparation of such core-shell assemblies has been reported to be particularly challenging.[28]

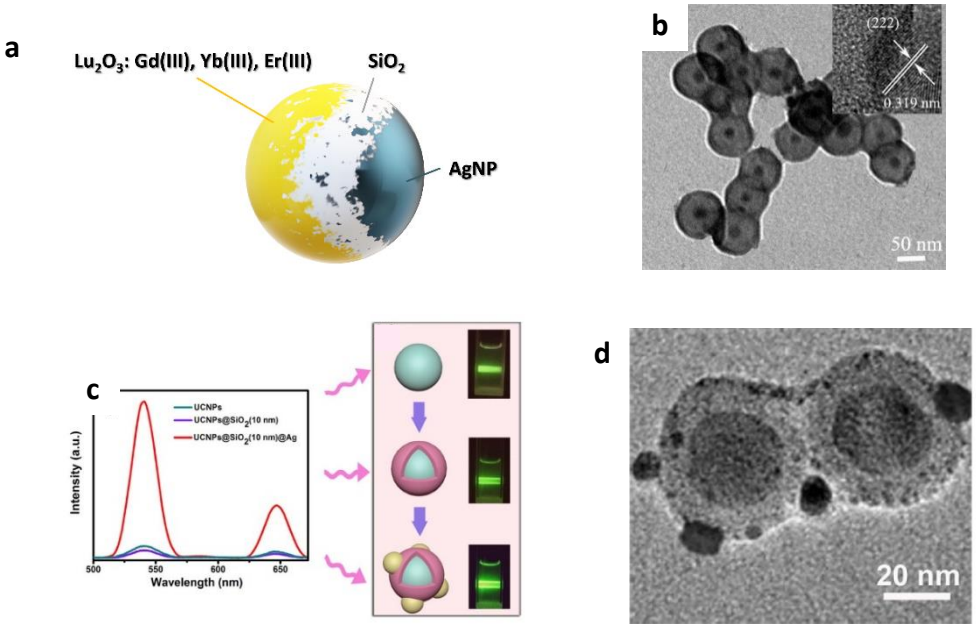


Figure 3.9 – **a** Sketch of the core shell system proposed by Yin *et al.*, where an UC shell surrounds the SiO_2 coated AgNP. **b** TEM image of the core shell NPs reported by Yin *et al.*, with inset showing the HRTEM of Lu_2O_3. The image was taken from [31]. **c** Emission spectra with corresponding sketches and UCL of the UCNPs reported by Qin *et al.* without a shell (blue NP), with the SiO_2 shell (pink shell) and the embedded AgNPs (yellow NPs). The same system is displayed also in the TEM image (**d**). Both **c** and **d** images were taken from [32].

3.1.2.2 Plasmon enhanced emission of lanthanide(III) molecular complexes

The doping of lanthanides(III) in a dielectric shell or layer has not been limited to upconversion luminescence. Lakowicz and co-workers have presented the adsorption of β-diketonate Eu(III) complex **13** (Figure 3.10, **a**) in the SiO_2 shell (5-10 nm) of either AgNPs (130 nm) or Ag nanorods (AgNRs).[33, 34] Whereas a modest 8-fold enhancement of Eu(III) emission was recorded on the SiO_2-AgNP substrates, the presence of both the L- (≈600-800 nm) and T- (380-500 nm) LSPRs of AgNRs (80x18 nm) allowed for the overlap with both absorption (300-400 nm) and emission

(570-720 nm) processes of the complex, resulting in a 240-fold overall enhancement.[34] The same group also reported the optimisation of the spectral overlap by modulation of the aspect ratio of AgNRs (Figure 3.10, **a** and **b**). Here, AgNRs (38x15 nm) were again coated with a SiO_2 shell (5 nm) and the Eu(III) complex **13** was adsorbed on the surface of SiO_2-AgNRs in approximately a 1:20 ratio (**13**:SiO_2-AgNRs). The improved overall 280-fold enhancement could be ascribed to the better overlap with the L-LSPR (≈500-750 nm) of the coated AgNRs and the system was employed for the detection of single lanthanide(III) luminescence, aided by the low **13**:SiO_2-AgNRs ratio.[35] In all these examples, the luminescence enhancement was measured by comparing the optical properties of the complex on SiO_2-AgNP/NR and after treatment with NaCN, leading to dissolution of the AgNP/NR core and thus assessment of the doped **13**-SiO_2 system alone.

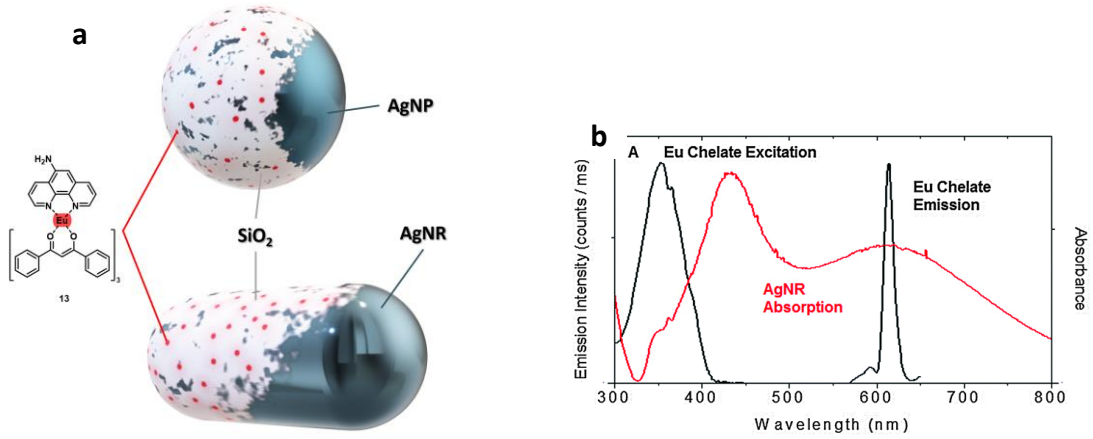


Figure 3.10 – **a** Sketch of the systems presented by Lakowicz and co-workers where an AgNP or AgNR (grey inner NP or NR) is coated with a SiO_2 shell (white layer) embedded with β-diketonate Eu(III) complex **13** (red dots).[33-35] **b** Absorption spectrum of AgNRs (red) as reported by Lakowicz and co-workers, displaying the wavelengths of the plasmon resonances of AgNRs suitable for overlap with both excitation and emission spectra (black) of Eu(III) complex **13**. The image has been taken from [35].

In similar approaches, Deng *et al*. and Zhao *et al.* included complexes **14** and **15** to SiO_2 coated AgNPs, respectively.[36, 37] In the first case (Figure 3.11, **a**), the authors doped Eu(III) complex **14** in a third SiO_2 shell (3 nm), which surrounds the original SiO_2 coated AgNP core (12 nm and 52 nm, respectively). A 3.5-fold decrease in lifetime was observed, accompanied by an 11-fold

increase in emission intensity. Both effects were attributed to the overlap of the AgNP extinction with the absorption (350-450 nm) and, partially, emission processes of the Eu(III) complex. Interestingly, the authors report the time gated fluorescence of single coated AgNPs by correlation with TEM imaging (Figure 3.11, **b**).[36]

In the approach by Zhao *et al.*, the Eu(III) or Tb(III) complexes **15** (Figure 3.11, **c**) are doped in the SiO_2 shell of AgNPs (46 nm, system as in Figure 3.11 **a**). By comparing the enhancement factors for each lanthanide(III) and modulating the SiO_2 shell thickness, the authors report a maximum 26-fold enhancement for Tb(III) and up to 6-fold for Eu(III) with a SiO_2 shell of 24 nm (Figure 3.11, **d**). The larger enhancement values for Tb(III) are ascribed to the overlap of both Tb(III) excitation and emission with the extinction of the AgNPs (350-600 nm), offering a dual enhancement mechanism.[37]

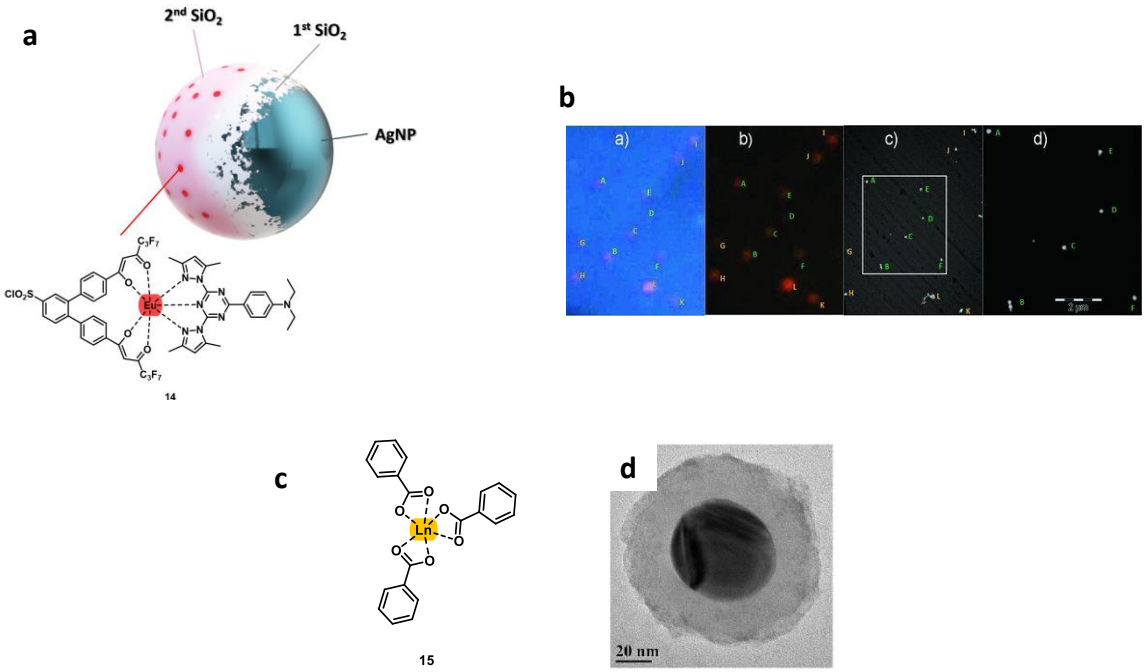


Figure 3.11 – **a** Sketch of the systems presented by Deng *et al.* where an AgNP (grey inner NP) is coated with a SiO_2 shell (white layer) followed by a second SiO_2 layer doped with Eu(III) complex **14** (red dots). For clarity, the second SiO_2 shell is depicted in pink.[36] **b** Fluorescence a), time gated fluorescence b) and TEM images c)-d) of the nanocomposites proposed by Deng *et al.*, showing the luminescence of single NP units. d) is an enlargement the area in the white rectangle of c). The image was taken from [36]. **c** Molecular structure of complex **15** reported by Zhao *et al.*.[37] **d** TEM image of an AgNP (46 nm) with a SiO_2 shell (24 nm) doped with complex **15**.

Yan *et al.* have optimised the blood compatibility of similar nanocomposites (25 nm SiO_2 shell on 50-60 nm AgNP core) by addition of a lysozyme as a fourth layer (Figure 3.12, **a**). The authors report that, after adsorption of a layer of Eu(III) complex **16**, the lysozyme can interact with **16** to stabilise the formation of a fourth more biocompatible shell (Figure 3.12, **b**). Although a very modest emission enhancement is reported (≈2-fold), the anticoagulant activity of the nanocomposite is significantly improved by inclusion of the lysozyme layer.[38] As an alternative to AgNPs and AgNRs, Zhang *et al.* incorporated complex **16** to Ag nanowires (Figure 3.12, **c**).[39] **16** was coated on the SiO_2 shell (15 nm) of Ag nanowires (70-100 nm diameter), displaying a 9-fold enhancement compared to the complex alone. Although the enhancement mechanism was not declared, the overlap between the absorption of the Eu(III) complex at 350 nm with the extinction of the Ag nanowires at 325-500 nm suggests that excitation enhancement is in place. Importantly, these processes were preserved upon immobilisation in an isotactic polypropylene matrix, improving the handling and commercial relevance of the material.[39] In the context of Ag nanomaterials, the effects of Ag nanoislands constitute some of the early work on the plasmonic enhancement of lanthanide(III) luminescence. These substrates (irregular sizes of Ag nanoislands on glass, 100-500 nm across, ≈60 nm height), were found to lead to both moderate emission increases (5-10-fold) as well as a decrease in the lifetime of the complexes proposed to be *via* radiative decay enhancement.[40, 41]

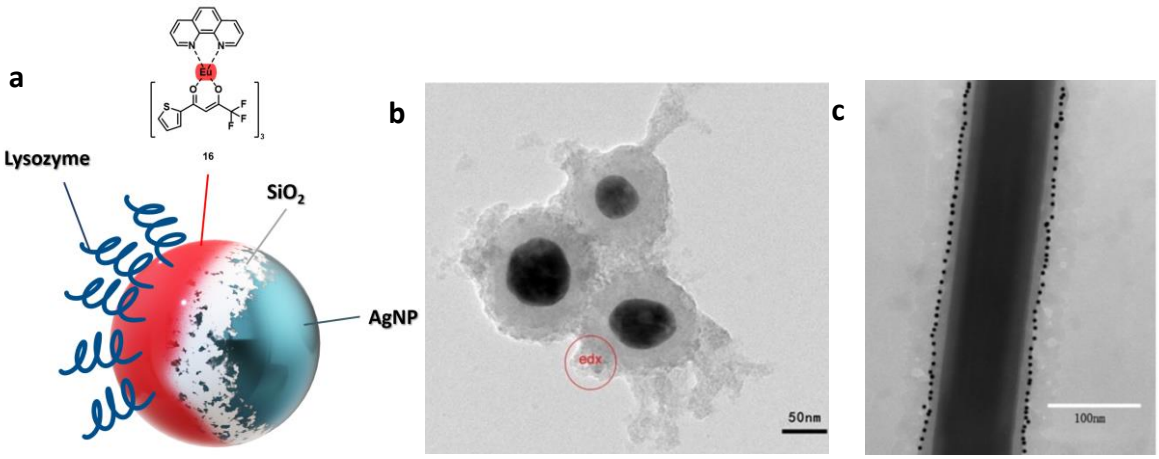


Figure 3.12 – **a** Sketch of the systems presented by Yan *et al.* where an AgNP (grey inner NP) is coated with a SiO_2 shell (white layer) followed by a layer of complex **16** (red layer) and lysozyme (blue spirals).[38] **b** TEM image of the nanocomposite presented by Yan *et al.*. The authors indicate that the irregular features surrounding the circular SiO_2 layer represent the lysozyme. The image was taken from [38]. **c** TEM image of SiO_2 shell Ag nanowires doped with complex **16** reported by Zhang *et al.*. The image was taken from [39].

Wang *et al.* investigated the effects of AuNRs to both Tb(III) and Eu(III) luminescence.[42, 43] AuNRs (50 nm) were drop casted on silicon wafers and complexes **17** and **18**, were spin coated in a polymethyl methacrylate (PMMA) matrix (Figure 3.13). The T- and L-LSPR wavelengths of the AuNRs were observed in the 450-550 nm and 575-800 nm regions, overlapping with the emissions of Tb(III) (450-650 nm) and Eu(III) (570-720 nm), respectively. In addition to the evaluation of plasmonic enhancement, the energy transfer from Tb(III) to Eu(III) is also assessed by varying the ratios of the respective complexes. The authors report that, whereas the L-LSPR does enhance Eu(III) luminescence, the T-LSPR amplifies the energy transfer from Tb(III), as observed in the decrease in the emission of complex **17** upon increase in the Eu(III) complex **18** concentration.[42] The incorporation of Eu(III) complexes in a PMMA layer was also reported for the lifetime modulation of complex **19** by AuNRs of varying aspect ratios (1.1 to 2.8) deposited on glass (Figure 3.13). Lifetime optical multiplexing was demonstrated with this system, where different degrees of decay rate enhancement were achieved by tuning the overlap between L-LSPR frequency of the AuNRs and Eu(III) emission.[44]

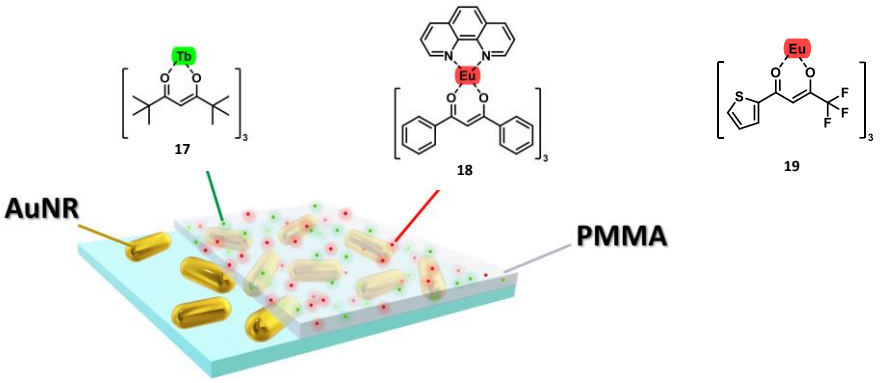
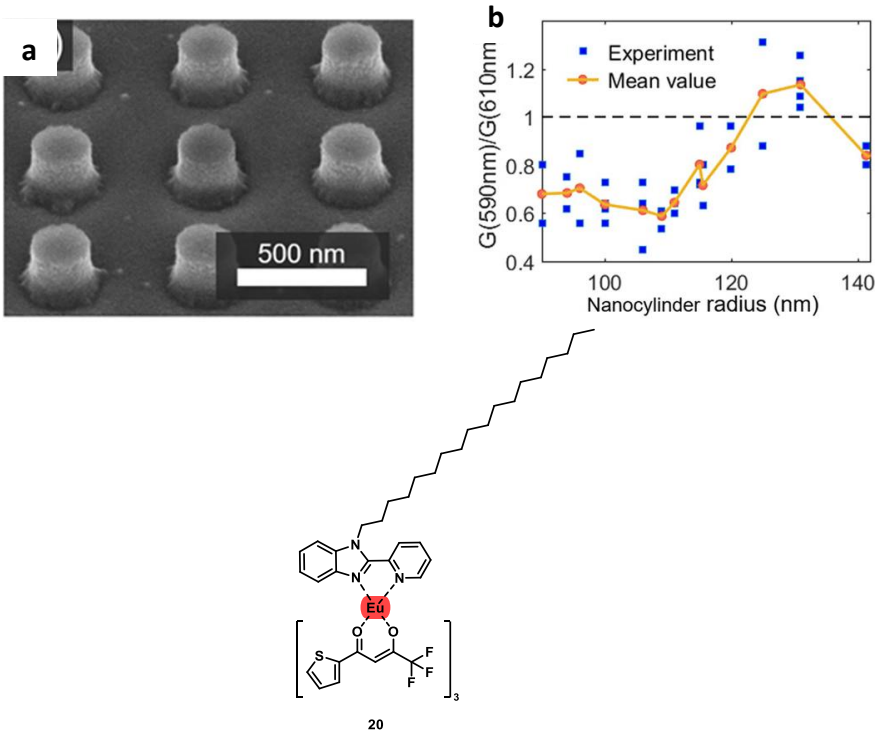


Figure 3.13 – Sketch of the systems presented by Wang *et al.*, where complexes **17** (green dots) and **18** (red dots) are spin coated in a PMMA matrix on drop casted AuNRs (gold NRs on blue glass substrate).[42] A similar system was adopted by Zhang *et al.* for the coating of complex **19** in a PMMA matrix on AuNRs with varying aspect ratios.[44]

In addition to dielectric layers such as SiO_2 or PMMA, biomolecules have also been employed for the incorporation of lanthanide(III) complexes to plasmonic substrates. Antibodies have been attached on plasmonic surfaces to drive the capture and detection of biomarkers as well as to provide a spacing layer to reduce quenching of the label dye.[45] Deng *et al.* have proposed a system where AgNPs (≈8 nm) grown on SiO_2NPs (400 nm) are used as substrate for the capture and plasmonic enhancement of the biotin labelled Eu(III) complex to goat anti-mouse IgG antibody. The authors report an enhancement factor of 11, obtained from both excitation and emission contributions. Despite the modest enhancement, this example reports the coupling of lanthanide(III) labelled biomolecules and plasmonic substrates, which could further the development of lanthanide(III) based bioassays.[46]

The luminescence of some lanthanides(III) is characterised by the presence of both electric and magnetic dipole character (ED and MD, respectively).[47, 48] Electric and magnetic dipoles can be differently and separately affected by the confined EM field of nanostructures and significant effort has been devoted to the enhancement of the magnetic character of light, with Eu(III) and Er(III) complexes serving as optimal probes to assess the optical behaviour of

such plasmonic surfaces.[25] Vaskin *et al.* prepared arrays of silicon nanocylinders (Figure 3.14, **a**) coated with Eu(III) complex **20** embedded in a polystyrene matrix.[22] The enhancement of the MD $^5D_0 \rightarrow {}^7F_1$ transition over the ED $^5D_0 \rightarrow {}^7F_2$ reported here (Figure 3.14, **b**) is a prime example of light manipulation attainable with plasmonic nanostructures and lanthanides(III). Several more examples are reported, including the modulation of Er(III) transitions.[23-26, 49, 50]



20

Figure 3.14 – **a** SEM image of the silicon nanocylinders arrays fabricated by Vaskin *et al.*. The image has been taken from [22]. **b** Emission enhancement ratios of the MD $^5D_0 \rightarrow {}^7F_1$ transition over the ED $^5D_0 \rightarrow {}^7F_2$ transition of complex **20** as a function of nanocylinder radius. The image has been taken from [22].

A different approach to the manipulation of Eu(III) luminescence has been recently reported by Zhang *et al.*.[51] In their study, the degree enhancement of each $^5D_0 \rightarrow {}^7F_J$ transition for a $Y(V,P)O_4$:Eu phosphor was modulated by the size of the AuNP core (from 53 nm to 194 nm). As larger AuNPs lead to a red shift of the LSPR band, the overlap with Eu(III) emission varies, so that the transitions are affected differently (Figure 3.15, **b**). This system is particularly relevant for the development of material relying on luminescence intensity ratio (LIR) readouts, such as for optical temperature sensors and anticounterfeiting materials.[51]

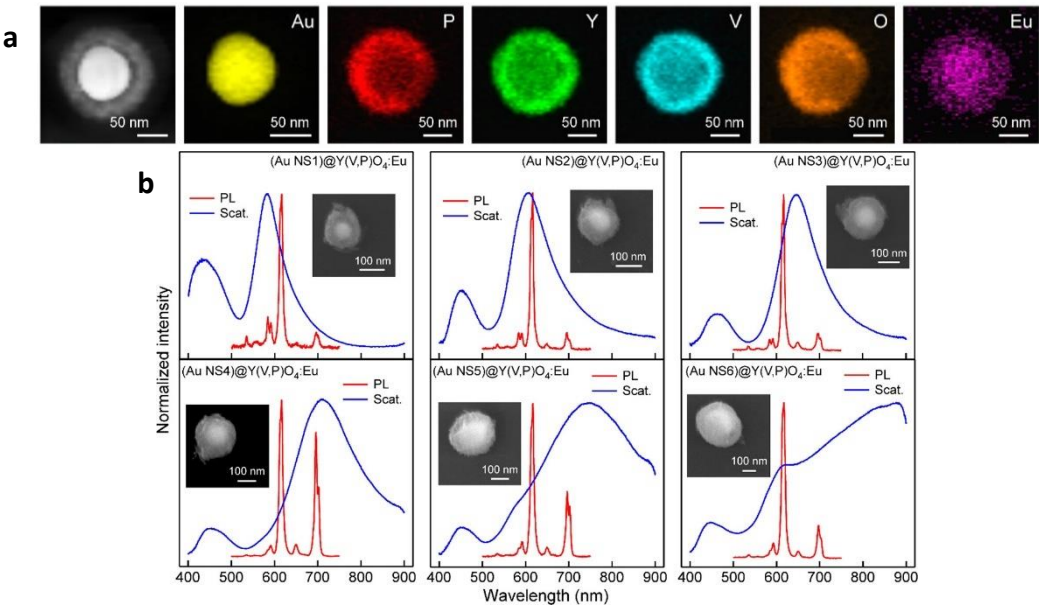


Figure 3.15 – **a** HAADF-STEM image of a nanocomposite presented by Zhang *et al.* with the EDX elemental analysis, displaying the AuNP core surrounded by the $Y(V,P)O_4$:Eu phosphor. The image was taken from [51]. **b** Emission spectra of the nanocomposites with increasing AuNP core size (53 nm, 75 nm, 91 nm, 121 nm, 156 nm and 194 nm, from top left to right bottom). The overlaid extinction spectra of the materials are correlated to the varying degree of enhancement for each transition. The image was taken from [51].

In the examples reported up to now, the emitting lanthanide(III) complexes are doped in a polymeric or SiO_2 spacing layer. This disordered arrangement and orientation of molecules, however, leads to a lack of control over the distance and distribution of complexes on the nanostructures and, as mentioned before, limits their applications in sensing.[52, 53] In an improved approach, Zhang *et al.* covalently linked Eu(III) complex **21** to the SiO_2 shell of Ag nanoparticles by means of a surface active phenanthroline unit (Figure 3.16).[54] The authors report that grafting the complex affords more control over the distance and distribution, confirmed by the correlation between thickness of the SiO_2 shell and variation in lifetime and quantum yield of the complex. Indeed, a synergistic effect of quenching and enhancement was observed at short distances (below 10 nm), after which point the complex was not significantly affected by the AgNP core. Such pronounced lifetime variations were efficiently utilised for security printing, where optical multiplexing afforded the hidden letters of an image (Figure 3.16 **b**).[54]

Similarly, Li *et al.* presented the attachment of complex **22** (Figure 3.16, **a**) to the SiO_2 shell of AuNPs (10 nm). Comparing different SiO_2 shell sizes, a 30 nm thickness displayed the maximum enhancement of 4.2.

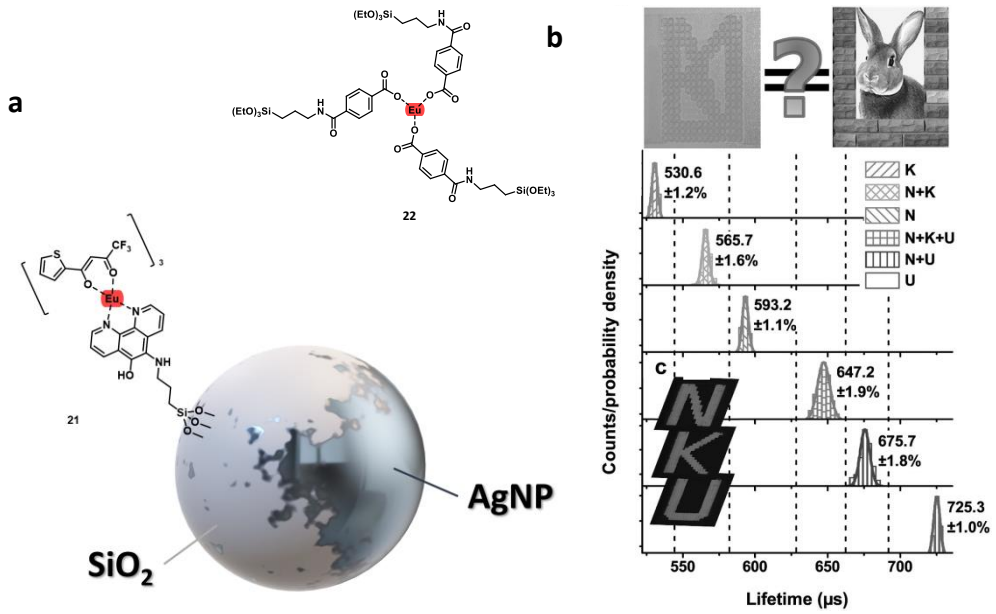


Figure 3.16 – **a** Sketch of the system presented by Zhang *et al.* with complex **21**[54]. The metallic grey portion illustrates the Ag nanoparticle, while the white part the SiO_2 shell coating. Five shell thicknesses are investigated. The complex reported by Li *et al.* (**22**) is also portrayed here. **b** Example of optical multiplexing, where the system presented in **a** is printed in a pattern and then deconvoluted by means of the different luminescence lifetimes obtained by varying the SiO_2 shell thickness. The image was taken from [54].

Finally, Jenie *et al.* have attached a modified Eu(III) DO3A complex on porous silicon resonant microcavities, obtaining a 3-fold emission enhancement (Figure 3.17).[55] Porous silicon resonant microcavities are photonic materials consisting of periodic layers of low and high porosity silicon with high and low refractive indices to form distributed Bragg reflectors, separated by a microcavity layer to confine incident light.[56] After the thermal hydrosilation of the surface to incorporate the alkyl spacing chain and conversion of the terminal bromo group in an azide, the alkyne functionalised Eu(III) complex **23** was anchored on the surface by CuAAC click reaction to give complex **24** (Figure 3.17).

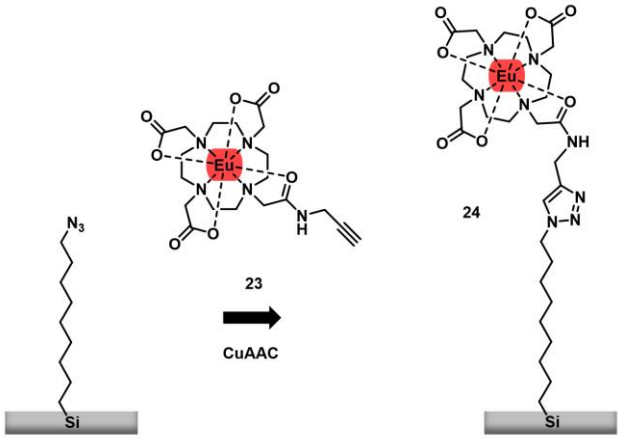


Figure 3.17 – Sketch of the system presented by Jenie *et al.*, where a surface active DO3A Eu(III) complex has been grafted to porous silicon resonant microcavities by means of a click reaction.[55]

Despite the modest emission enhancements and not involving plasmonic processes, this example combines the chemistry of grafting molecules on a substrate with the enhancement of luminescence.[55, 57] Furthermore, a highly similar system has been subsequently reported for the detection of singlet oxygen, highlighting the importance of anchored complexes for the development of sensing platforms.[57]

3.1.3 Introduction to polyaniline (PANI)

Polyaniline (PANI) is one of the most studied conjugated polymers of the past decades. Prepared from the oxidation of aniline, PANI displays high thermal and environmental stability, straightforward synthesis and diverse redox behaviour, making it relevant for a range of applications, particularly in optoelectronic and sensing devices.[58-60] PANI can be found in a series of redox forms, distinguishable by their quinonoid to benzenoid ratio and characteristic colours. Leucoemeraldine base (LB) is the fully reduced colourless PANI; partial oxidation of LB PANI gives the blue emeraldine base (EB) and full oxidation the violet pernigraniline (PB) form (Figure 3.18). Furthermore, the EB form of PANI can be doped to give the conductive green emeraldine salt (ES) form.[61]

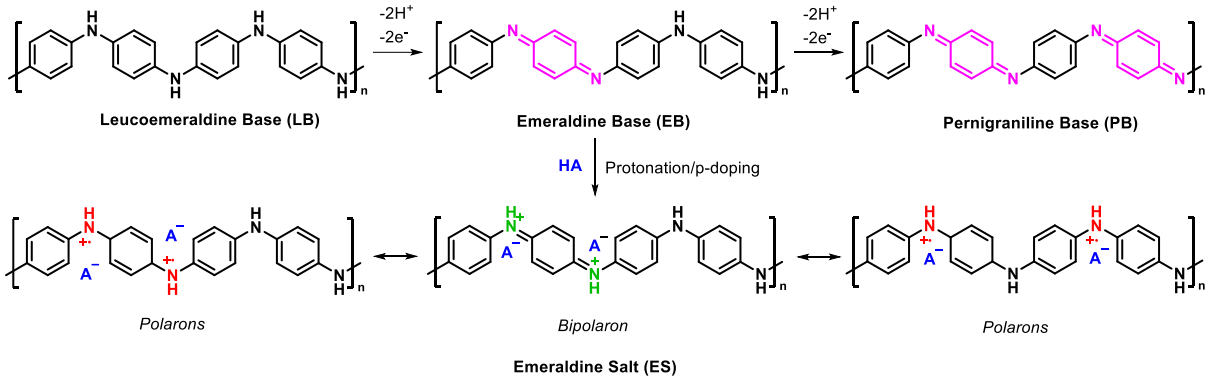


Figure 3.18 – Molecular structures of the tetramer of PANI in its various redox and doped states.[61]

Despite its strong absorption in the UV-Vis and NIR regions, PANI is only weakly luminescent, thus limiting its role in photonic devices to the conductive properties of the doped ES form of the polymer.[62] By including the lanthanides(III) to polymer matrices, the unique properties of the lanthanides(III) are combined with the processability and applications of polymers such as PANI. Furthermore, the effect of complex and polymer on their respective tridimensional structures is highly fascinating and can lead to new morphologies and novel luminescence properties.[63]

3.1.3.1 PANI, lanthanides(III) and their assemblies

Few examples on the interaction between PANI and lanthanides(III) are reported and, to the best of our knowledge, none concern their assembly and behaviour on gold surfaces. The independent incorporation of PANI and lanthanide(III) complexes to composite materials has been mostly reported for the preparation of electrospun polymer nanostructures, conferring new optical and magnetic properties to the material. In these examples, the authors have reported a quenching of Eu(III) and Tb(III) luminescence, due to both the CT absorption of PANI and inorganic nanoparticles overlapping with the lanthanide(III) emission peaks.[64-66] The direct interaction of PANI and lanthanides(III), however, is the focus of much of the early work on the polymer. The nitrogen atoms of PANI can be easily seen as coordination pockets for the

lanthanides(III) salts, which, in turn, can act as doping agents and convert the insulating EB PANI to its conductive ES form. Not only a rearrangement of the polymer to more ordered and rigid structures has been observed, but, as the luminescence of PANI is in the 375-475 nm region, weak energy transfer from the polymer to Eu(III) or Tb(III) ions has been recorded upon excitation at the PANI absorption.[67-71]

Although PANI can reassemble into novel structures by maximising dispersion interactions or, as reported above, in response to coordination, the control of its morphology is typically driven by the synthesis conditions.[72, 73] Conventional methods for the preparation of PANI mostly lead to granular and amorphous assemblies, while template assisted, pH controlled or self-assembled based syntheses can produce PANI in micro- and nanostructures.[59] Similarly to the template assisted synthesis, the addition of lanthanide (III) salts such as $EuNO_3$ or $GdCl_3$ during the synthesis of PANI can drive the formation of nanofibers, whereas granular and irregular particles have been observed in the absence of Eu(III) ions.[74, 75] On surfaces, PANI is commonly deposited by *in situ* polymerisation. DNA as a template can impart string-like qualities to the newly synthesised polymer. Alternatively, mechanical stretching and electrospinning can be used for the preparation of nanofibres and nanowires.[76-79]

Finally, the layer by layer assembly of PANI does not require *in situ* polymerisation but relies solely on the interactions between PANI and other molecules. The necessity for spin coating or specialised instruments is thus avoided as dip coating is the common method for layer by layer assembly.[80] Although it is often based on electrostatic interactions between the two components, examples of layer by layer assembly *via* hydrogen bonding have been reported, opening the field for non-charged molecules.[61, 81-83]

3.1.4 Aims of the project

In this project, we first investigate the luminescence and assembly of surface active bis β-diketonate **Ln_2SAcbisDBM$_3$** complexes (Figure 3.19) on Au surfaces (**Ln_2SAcbisDBM$_3$@Au**). The **Ln_2SAcbisDBM$_3$** complexes (Ln = Eu(III), Yb(III) and Nd(III)) have displayed good quantum yields in the visible and NIR, with well resolved emission detected in solution. The assembly of **Ln_2SAcbisDBM$_3$** complexes on Au surfaces is examined with two coating approaches (i.e. dip coating and spin coating) to determine the better coating method. Furthermore, our aim is to examine the possibility of fluoride sensing as a modulation of the optical properties of visible emitting **Eu_2SAcbisDBM$_3$@Au** surfaces. The **Eu_2SAcbisDBM$_3$** complex has an unfilled coordination sphere (q≈3) and has previously displayed a strong response to fluoride coordination. The translation of the readout to Au surfaces would allow for the development of handheld sensing platforms, raising the potential of the prepared materials.

Furthermore, we strive to enhance both visible and NIR luminescence of anchored **Ln_2SAcbisDBM$_3$** complexes by means of either Ag nanoIslands (AgNIs) or Au nanoislands (pGold) surfaces. Our aim is to examine the plasmonic effect of nanostructured surfaces on the luminescence of **Ln_2SAcbisDBM$_3$** complexes, evaluating the versatility of the substrates for a wide emission range (570-1540 nm) and comparing the different enhancement processes. Enhanced emission signals and resolutions are highly desirable for future applications, especially in the NIR, where the detection is often troublesome. Additionally, the surface enhanced Raman spectroscopy (SERS) of the prepared pGold surfaces is examined, aiming to identify a multimodal view of the enhancement processes.

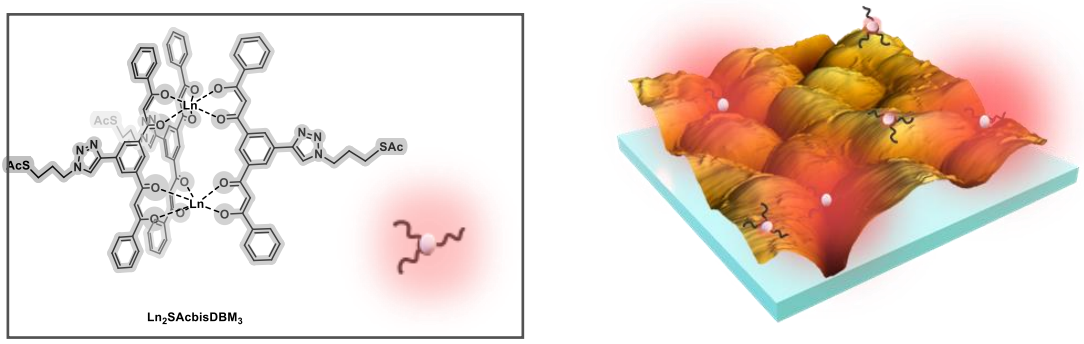


Figure 3.19 – Chemical structure of the **Ln_2SAcbisDBM$_3$** complexes (Ln= Eu(III), Yb(III) and Nd(III)) and sketch of the proposed system, where the maximum luminescence enhancement is expected in the gaps between nanostructures. The golden substrate depicted here is a 3D AFM image of pGold, obtained by Dr. James Churm at the School of Engineering at the University of Birmingham.

In a third and final section, we propose an alternative method for the coating of Au surfaces with unfunctionalized **Ln_2bisDBM$_3$** complexes. Our aim is to investigate the polymer aided deposition of **Ln_2bisDBM$_3$** complexes by physisorption (Figure 3.20), thus combining the luminescence properties of lanthanides(III) with the functionality of conjugated polymers. Polyaniline (PANI) is selected as polymer due to its diverse and important applications, particularly in optoelectronic devices and photovoltaics, as well as its reported dependence on dispersion interactions, which could promote the formation of assemblies with **Ln_2bisDBM$_3$** at the surface interface.

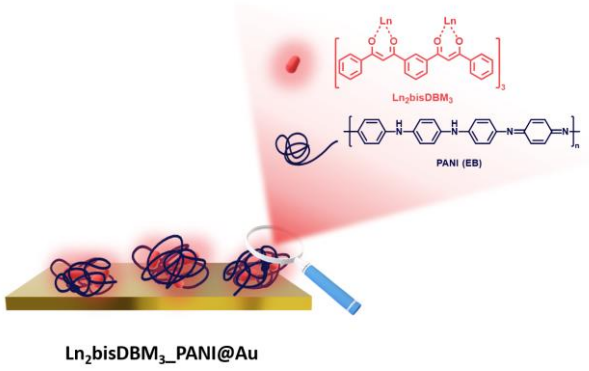


Figure 3.20 – Sketch of the presented system, displaying the assembly of PANI and **Ln_2bisDBM$_3$** complexes on Au surfaces

3.2 Results and discussion

3.2.1 Visible and NIR luminescent dip coated Ln_2SAcbisDBM$_3$@Au surfaces

The visible and NIR luminescence of **Ln_2SAcbisDBM$_3$** (Ln = Eu(III), Yb(III) and Nd(III)) complexes on Au surfaces was examined. Au surfaces were coated by immersion in a solution of **Ln_2SAcbisDBM$_3$** (1 mM) in DMF overnight. DMF was initially selected due to the high solubility of the complexes in this solvent and, after coating, the surfaces were washed with DMF to remove unbound complex. The **Eu_2SAcbisDBM$_3$@Au** surface displays the same excitation maximum as in solution (360 nm, Figure 3.21), thus confirming both the energy transfer from **SAcbisDBM** ligands to the Eu(III) centre and the presence of the assembled complex on the Au surface. Characteristic Eu(III) emission is observed upon excitation at 350 nm and all $^5D_0 \rightarrow {}^7F_J$ (ΔJ=0-4) transitions can be identified (Figure 3.21).

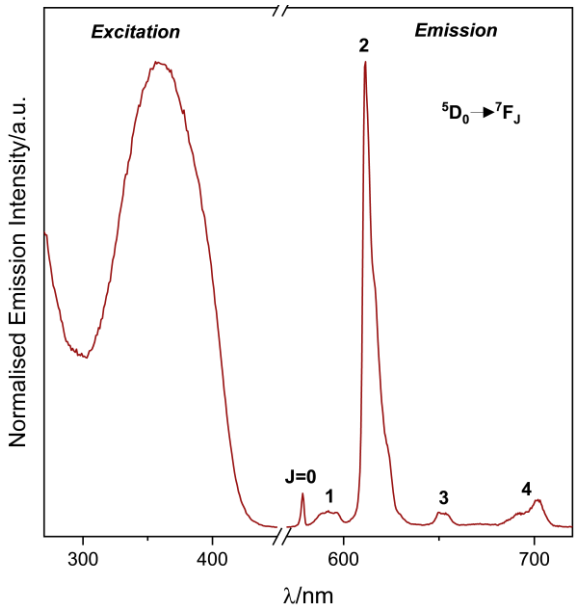


Figure 3.21 – Normalised excitation (**Excitation**) and emission (**Emission**) spectra of **Eu_2SAcbisDBM$_3$@Au**. λ_{exc}: 350 nm, λ_{em}: 611 nm.

Furthermore, the hypersensitive $^5D_0 \rightarrow {}^7F_2$ transition dominates the spectrum, characteristic of β-diketonate complexes, and its relative intensity to the $^5D_0 \rightarrow {}^7F_1$ transition is identical to the

one in DMF ($I_{\Delta J=2}$/ $I_{\Delta J=1}$ = 26 in both spectra). Similarly, good NIR luminescence is observed for **Yb-** and **Nd_2SAcbisDBM$_3$@Au** surfaces (Figures 3.22 **a** and **b**) and the characteristic $^2F_{5/2} \rightarrow {}^2F_{7/2}$ and $^2F_{3/2} \rightarrow {}^4I_J$ (ΔJ = 9/2, 11/2, 13/2) transitions are identified in both spectra, respectively. The sharp rise in Nd(III) luminescence at lower wavelengths (Figure 3.22, **b**) is ascribed to the longpass filter.

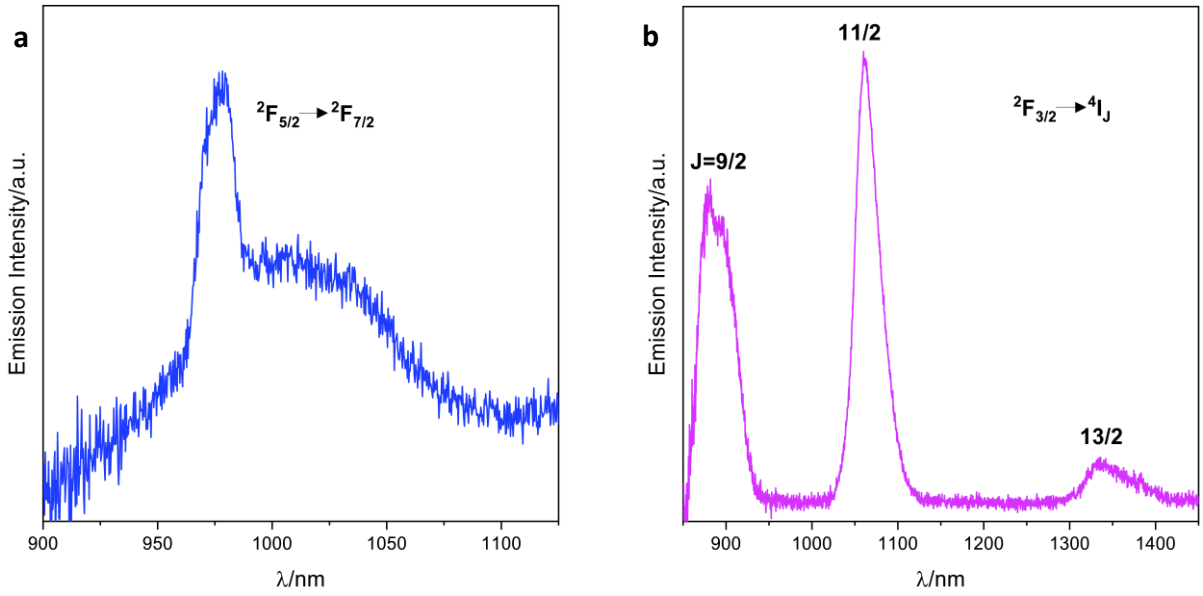


Figure 3.22 – Emission spectra of **Yb_2SAcbisDBM$_3$@Au** (**a**) and **Nd_2SAcbisDBM$_3$@Au** (**b**). λ_{exc}: 350 nm.

NIR luminescence is often problematic to record, especially with weakly emissive solid state samples. The well-defined NIR emission of the **Yb_2SAcbisDBM$_3$@Au** and **Nd_2SAcbisDBM$_3$@Au** surfaces, however, highlights the potential of **Ln_2SAcbisDBM$_3$** complexes for the progress and development of NIR probes and materials.

Time-resolved luminescence studies of the **Eu_2SAcbisDBM$_3$@Au** surface were conducted and a multiexponential decay was recorded (Table 3.1). In DMF, the single value of 180 µs was ascribed to the identification of a single species. On the Au surface, a longer component (140 µs) is accompanied by shorter values of 57 µs and 21 µs. This multiexponential decay reflects

the complex photophysical processes occurring on the Au surface, where a decrease in lifetime and the presence of multiple components can both be attributed to the non-radiative energy transfer from the emitter to the metal surface.[8]

	τ/μs (%)
Eu_2SAcbisDBM$_3$ in DMF	180 (100%)
Eu_2SAcbisDBM$_3$@Au	140 (29%), 57 (46%), 21 (25%)

Table 3.1 – Exponential decay analysis of **Eu_2SAcbisDBM** in DMF and of **Eu_2SAcbisDBM$_3$@Au**.

The **Eu_2SAcbisDBM$_3$@Au** surface was immersed in increasing concentrations of tetrabutylammonium fluoride (TBAF, as source of F^-) in THF (0-100 μM) for 15 minutes to evaluate the sensing performance of the surface. No variations in luminescence lifetime could be recorded (Figure 3.86, Appendix). Therefore, testing of these surfaces for F^- sensing did not prove successful. This is believed to be due to the strong coordinating behaviour of DMF to form an extended network of complexes. Consequently, an alternative approach to pure DMF for the preparation of the coating solution was considered. As the sensing of F^- with the **Eu_2SAcbisDBM$_3$** complex was previously conducted in THF, 0.2% DMF, the new coating solution was prepared in THF (0.1 mM). A small percentage of DMF (1%) was required to allow solubilisation of the complex.

The excitation spectrum (Figure 3.67, Appendix) displays a maximum at 360 nm and all the $^5D_0 \rightarrow {}^7F_J$ (ΔJ=0-4) transitions can be well identified in the emission spectrum of the surface (Figure 3.23, **a**). It was also possible to obtain confocal images of the surface, which display bright spots of average size 1.4 ± 0.4 μm upon excitation at 405 nm and are attributed to small assemblies of complex on the Au surface (Figure 3.23, **b**).

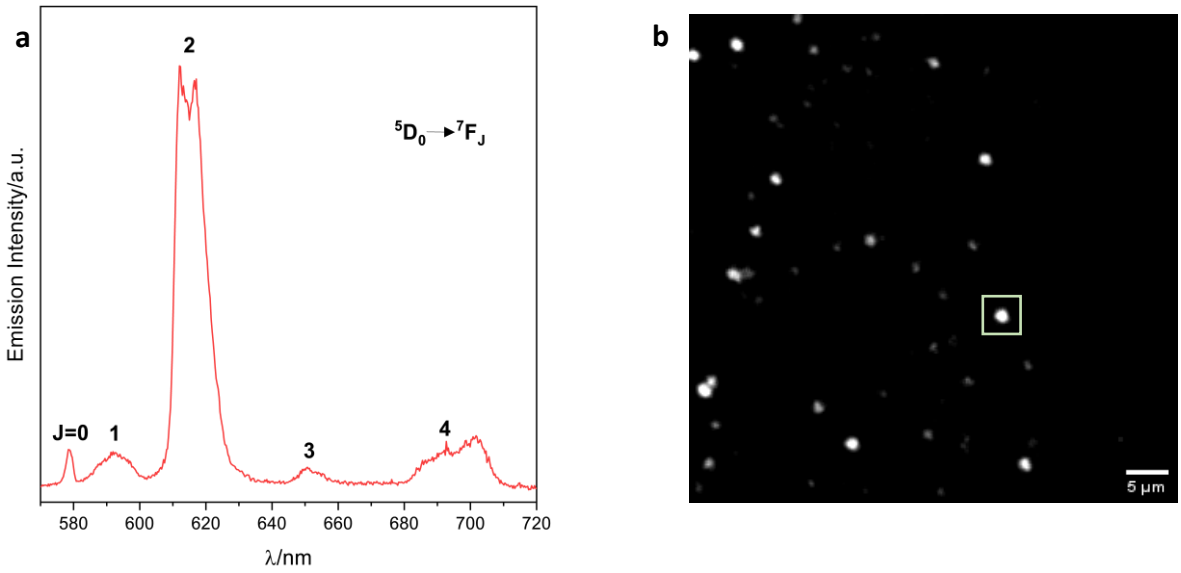


Figure 3.23 – **a** Emission spectrum of **Eu_2SAcbisDBM$_3$@Au** coated in THF (1% DMF). λ_{exc}: 350 nm. **b** Confocal image of **Eu_2SAcbisDBM$_3$@Au** coated in THF (1% DMF). λ_{exc} 405 nm. The green square represents the feature size compared with the AFM and SEM images in Figures 3.24 **a** and **b**, respectively.

The **Eu_2SAcbisDBM$_3$@Au** surface is further analysed by AFM (Figure 3.24 **a**) and SEM (Figure 3.25 **a**) to determine the distribution and morphology of complex anchored on the Au substrate and correlate any findings with the luminescent areas observed by confocal microscopy.

Large aggregates are found by AFM imaging (Figure 3.24 **a**). A Root Mean Square (RMS) roughness of 68 nm is measured, contrasting to the RMS roughness of 1 nm of a bare Au surface (Figure 3.101, Appendix), and correlating well with the visual distribution of irregular features. Indeed, both smaller features with heights of 0.13 ± 0.04 µm (0.50 ± 0.10 µm width, blue square in Figure 3.24 **a**) and larger ones with heights up to 0.95 µm (1.4 ± 0.3 µm width, green square in Figure 3.24 **a**) are identified. The second set of feature sizes can be correlated with the average width of the luminescent spots observed in the confocal microscopy image (green square in Figure 3.23, **a** for comparison). These feature sizes and heights, however, indicate significant stacking of **Eu_2SAcbisDBM$_3$** complexes. This behaviour is not surprising: the presence of multiple surface active units per complex promotes the interaction and stacking

of complexes, while the poor solubility of **Eu_2SAcbisDBM$_3$** in solvents other than pure DMF and DMSO can lead to the formation of aggregates on the surface. The comparison with the **Eu_2SAcbisDBM$_3$@Au** surface coated in DMF, however, indicates that the first process is potentially predominant. In the AFM image of this surface (Figure 3.24 **b**), the average feature width and height are 0.53 ± 0.26 µm and 0.11 ± 0.04 µm, respectively, with a RMS roughness of 45 nm. These parameters are comparable with the ones of the surface coated in THF, suggesting that a more solubilising solvent such as DMF does not prevent the formation of such large assemblies.

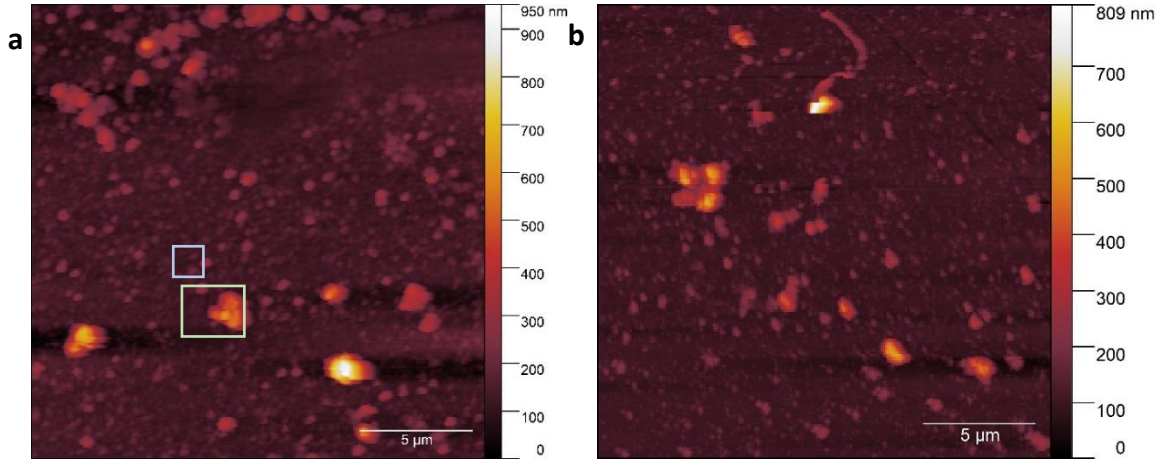


Figure 3.24 – **a** AFM image (20 µm x 20 µm) of **Eu_2SAcbisDBM$_3$@Au** coated in THF (1% DMF). The image was obtained by Dr. Simon Connell and Dr. Pallavi Kumari at the School of Physics and Astronomy at the University of Leeds. **b** AFM image (20 µm x 20 µm) of **Eu_2SAcbisDBM$_3$@Au** coated in DMF. The image was obtained by Christopher Jones at the department of Chemical Engineering at the University of Birmingham.

Similarly, the feature sizes observed by AFM imaging are identified in the SEM image of the **Eu_2SAcbisDBM$_3$@Au** surface coated in THF (blue and green squares in Figure 3.25 **a**). In addition to these assemblies, a more complex "honeycomb" pattern is found, whose absence in AFM and confocal images is attributed to the different focal plane for the latter and the limited resolution in the presence of such larger features for the former. Interestingly, addition of hydrazine as thioacetate reducing agent does not lead to evident differences in the morphology and assembly of **Eu_2SAcbisDBM$_3$** on the surface (Figure 3.104, Appendix). Finally,

the elemental analysis by EDX of the imaged features in SEM confirms the presence of the expected elements for the **Eu_2SAcbisDBM$_3$** complex (C, N, O, Eu and S, Figure 3.105, Appendix).

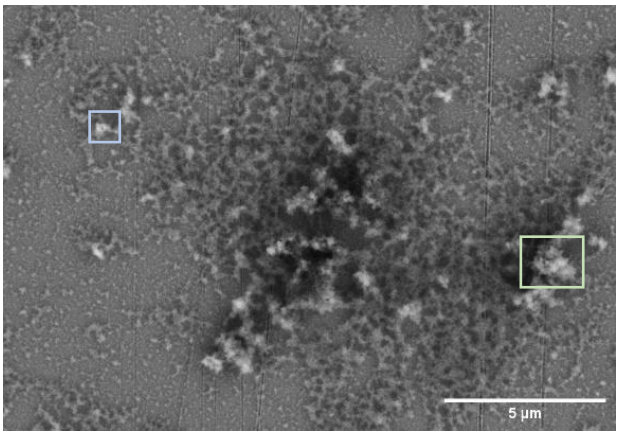


Figure 3.25 – **a** SEM image of **Eu_2SAcbisDBM$_3$@Au** coated in THF (1% DMF). The image was obtained by Sigrid Benemann at BAM.

A quantitative elemental analysis of the **Eu_2SAcbisDBM$_3$@Au** surface was acquired by XPS. The wide survey analysis (Figure 3.118, Appendix) confirms the elemental composition already observed in the EDX spectra, with the Eu 3d, O 1s, N 1s, C 1s, S 2p and Au 4f peaks found in the 1120-1170 eV, 530-535 eV, 395-405 eV, 280-290 eV, 160-170 eV and 80-90 eV regions, respectively. The X/Eu ratios are calculated from the atomic percentages of each element for three regions of interest (ROIs) and are found to be in strong agreement with the expected values for the chemical formula of the complex ($C_{93}H_{75}Eu_2N_9O_{15}S_3$, Tables 3.17-18, Appendix).

An exception is the O/Eu ratio, where a 32% increase from the expected value is observed. This is primarily attributed to the oxidation of sulfur to form sulfoxide and sulfone species, as can be confirmed in the high resolution S 2p spectrum (Figure 3.26, **a**).

Indeed, the peak at 168.5 eV is assigned to the oxidised species of sulfur, while the components at 163.6 eV and 165.1 eV are characteristic of thioacetate groups (C-S, Figure 3.26, **a**), in accordance with the chemical structure of the **Eu_2SAcbisDBM$_3$** complex. It is worth

mentioning that strong S-Au bonds (161-163 eV) would be very hard to detect with the current **Eu_2SAcbisDBM$_3$@Au** surfaces. This is due to both the considerable attenuation of the signal caused by the overlaying multi-layered assemblies and the depth of XPS analysis (5-10 nm) compared to the thickness of **Eu_2SAcbisDBM$_3$** assemblies (average of 150±70 nm), preventing analysis of the complexes closest to the Au surface.[84]

The Eu 3d spectrum display the characteristic spin orbit $Eu(III)_{5/2}$ component at 1134.7 eV (Figure 3.26, **b**), while the C 1s and N 1s spectra are distinctive for a ligand containing a β-diketone and a 1,2,3-triazole ring. Indeed, the peak component of the C 1s spectrum at 286.4 eV is ascribable to both C-N and C-O contributions (Figure 3.26, **c**), while the two components at 399.7 eV and 401.0 eV in the N 1s spectrum are typical of the N-N bonds in 1,2,3-triazole rings (Figure 3.26, **d**).[85, 86]

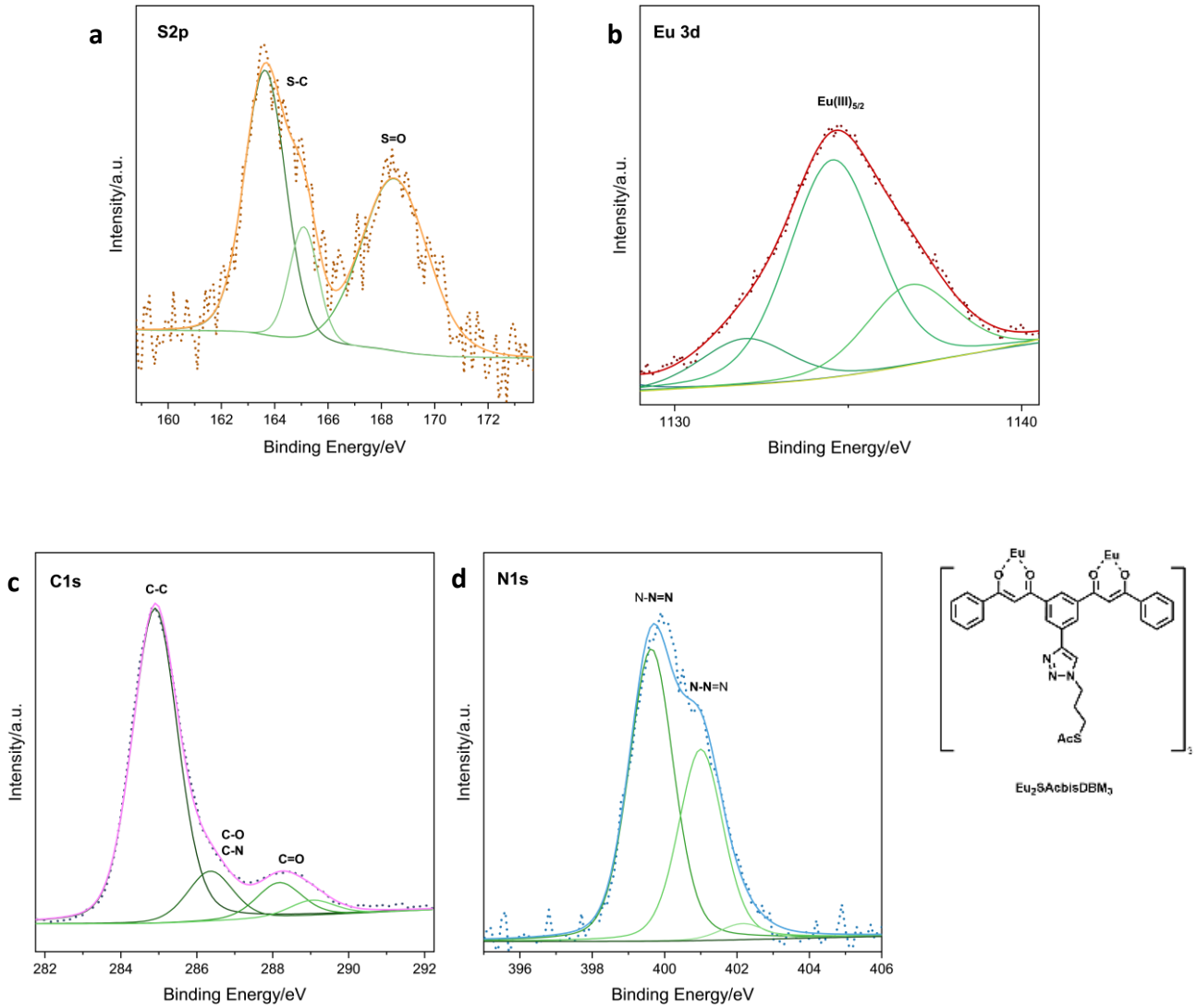


Figure 3.26 – XPS S 2p (**a**), C 1s (**b**), N 1s (**c**) and Eu 3d (**d**) spectra of **Eu_2SAcbisDBM$_3$@Au** coated in THF (1% DMF) showing the recorded spectrum (dotted), the fitting components (green), and the sum curve (orange, pink, blue and red, respectively). The data were recorded and processed by M.Eng. Jörg M. Stockmann at BAM. The molecular structure of the **Eu_2SAcbisDBM$_3$** complex is included for clarity.

3.2.2 F^- sensing with Eu_2SAcbisDBM$_3$@Au surfaces

The prepared **Eu_2SAcbisDBM$_3$@Au** surfaces coated in THF (1% DMF) were employed for the sensing of F^-. The **Eu_2SAcbisDBM$_3$@Au** surfaces were incubated for 15 minutes in known concentrations of TBAF in THF as source of F^- before measurement of their luminescence properties.

Our first approach is to immerse the same surface in increasing concentrations of F^- in THF (5 μM increase), with the purpose of assessing the response of the **Eu_2SAcbisDBM$_3$@Au** surface to F^- and calibrating this to known fluoride concentrations. Indeed, a steady increase in the luminescence lifetime of the complex is observed (Figure 3.27 **a** and Table 3.13, Appendix) which is in accordance with the sensing event by coordination to the Eu(III) centre and displacement of quenching solvent molecules. Considering the longer component of the triexponential decay for comparison, a statistically significant increase is recorded: from 160 ± 10 μs of the pristine surface to 250 ± 10 μs at 20 μM F^- concentration, with repeats (n=3) of the experiment displaying a consistent trend (Figure 3.27, **a**, inset). In the second approach, after assessment of the initial optical properties of pristine **Eu_2SAcbisDBM$_3$@Au**, the surface is immersed in known concentrations of F^- in THF (5 μM, 10 μM, 15 μM and 20 μM). Again, at least three surfaces per concentration are analysed, obtaining both averages and standard deviations of the luminescence lifetime readouts (Figure 3.27, **b**). A response similar to the one observed in the calibration experiment is recorded and a 1.5-fold increase from the starting luminescence lifetime can be measured already from 15 μM (Table 3.14, Appendix).

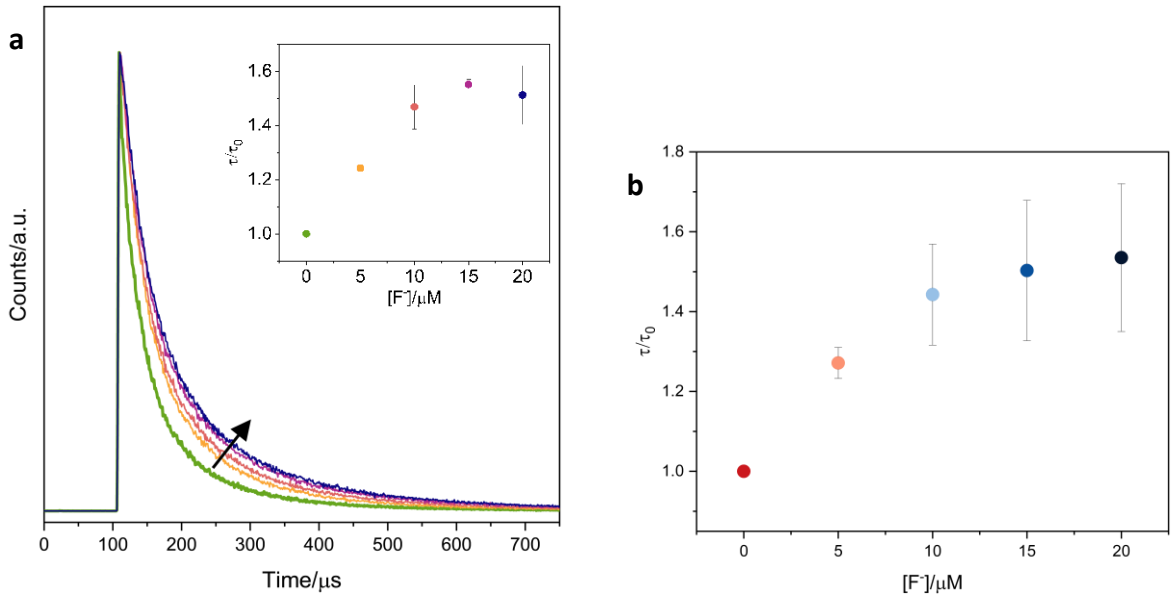


Figure 3.27 – **a** Overlaid luminescence lifetime spectra of one **Eu_2SAcbisDBM$_3$@Au** surface before and after immersion in increasingly concentrated solutions of F^-. λ_{exc}: 350 nm, λ_{em}: 611 nm. The inset is the plot of the ratio between found lifetimes over initial values versus concentrations of F^- solutions. Each point corresponds to n=3, apart from 5 µM where, due to an outlier, n=2. The error bar is the standard deviation of the average. Only the longest component is considered for calculation of ratios. **b** Plot of the ratio between found luminescence lifetimes over initial values versus concentrations of F^- solutions. Each point corresponds to n>3, with the error bar being the standard deviation of the average. Only the longest component is considered for calculation of ratios.

Considering the emission properties of the surface, an increase in intensity (3.5 ± 0.5-fold at 20 µM of F^-) is accompanied by a sharper profile of the hypersensitive $^5D_0 \rightarrow {}^7F_2$ transition (Figure 3.28). Although the resolution of the spectrum does not allow for further analysis of the emission profile, both the signal increase and the variation in the shape of the $^5D_0 \rightarrow {}^7F_2$ transition further indicate the exclusion of quenching solvent molecules and the perturbation of the crystal field, which can both be associated with the coordination of F^- ions to the Eu(III) centre.

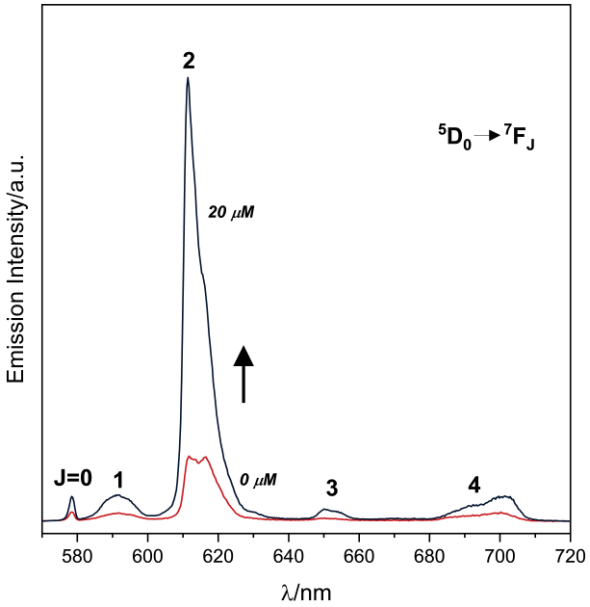


Figure 3.28 – Emission spectra of a **Eu_2SAcbisDBM$_3$@Au** surface before (red) and after (dark blue) immersion in a 20 μM solution of F^-, displaying the increase in emission intensity and the variation in the emission profile.

These experiments confirm that the **Eu_2SAcbisDBM$_3$@Au** surfaces can give a readout to different concentrations of F^- as a variation in their luminescence lifetimes and are found to be fairly consistent over different batches of surfaces. A multimodal readout is also proposed, where changes in emission intensity and profile of Eu(III) luminescence can be used to complement the sensing response.

Comparison of the wide survey XPS spectra of a **Eu_2SAcbisDBM$_3$@Au** surface confirms the appearance of the F 1s peak in the 680-690 eV region after immersion in a 15 μM solution of F^-(**Eu_2SAcbisDBM$_3$@Au-F**, Figure 3.119, Appendix). As for the pristine **Eu_2SAcbisDBM$_3$@Au**, the atomic percentages of **Eu_2SAcbisDBM$_3$@Au-F** obtained by XPS are used to calculate the ratios between Eu and each element (Tables 3.19-20). The F/Eu ratio is 0.6 ± 0.0: two Eu(III) atoms compose the complex, so that such a value indicates that around one F atom per **Eu_2SAcbisDBM$_3$** complex is present. However, in addition to the deviation from the expected value for O/Eu already discussed in section 3.2.1, considerably higher C/Eu and C/N ratios are also detected. We ascribe this to the residual tetrabutylammonium counterion from

immersion in the TBAF solution and calculate an increase of +1.2 in the N/Eu ratio, suggesting that an excess of counterion is found on the surface.

From the high resolution F 1s spectrum (Figure 3.29), the peak can be deconvoluted into two components, indicating the presence of two chemical states for the anion. The major component (68%) centred at 685.1 eV is characteristic of metal fluorides. Several Ln-F_3 materials report such binding energies and we thus ascribe it to Eu-F coordination.[87-90]

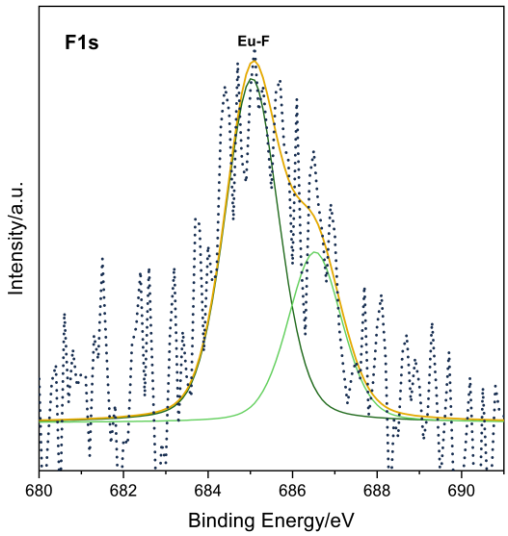


Figure 3.29 – XPS F 1s spectrum of **Eu_2SAcbisDBM$_3$@Au-F** showing the recorded spectrum (blue, dotted), the fitting components (green) and the sum curve (orange).The data were recorded and processed by M.Eng. Jörg M. Stockmann at BAM.

The presence of residual tetrabutylammonium counterion is confirmed by comparison of the high resolution C 1s and N 1s spectra with the one of the pristine **Eu_2SAcbisDBM$_3$@Au** surface (Figure 3.30, **b**). In the C 1s spectrum of **Eu_2SAcbisDBM$_3$@Au-F**, we observe a steep increase in the C-N component at 286.0 eV, in accordance with the molecular structure of the tetrabutylammonium counterion (Figure 3.30). The interpretation of the N 1s spectrum is more complex due to the overlap of the C-N bond peaks with the ones of the 1,2,3-triazole ring. However, the increase at 401.0 eV and the new component at 402.1 eV can both be ascribed to the presence of C-N^+ species.

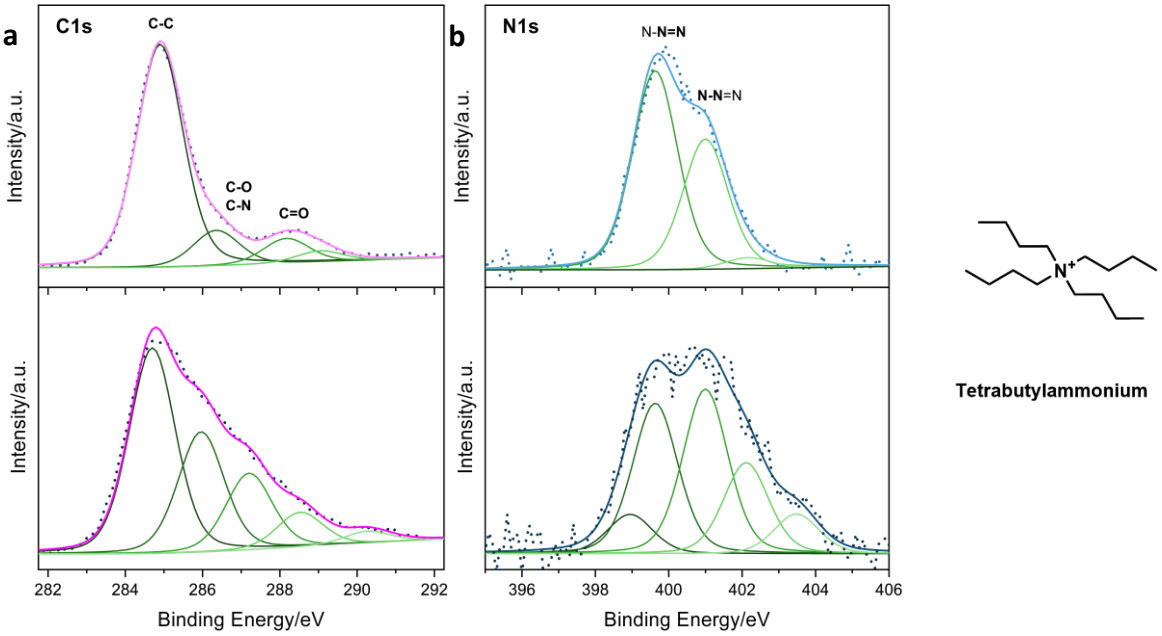


Figure 3.30 – XPS spectra of the C 1s (**a**) and N 1s (**b**) regions of **Eu₂SAcbisDBM₃@Au** (top, lighter colours) and **Eu₂SAcbisDBM₃@Au-F** (bottom, darker colours). The figures include the recorded spectra (blue, dotted), the fitting components (green) and the sum curves (pink for C 1s and blue for N 1s). The data were recorded and processed by M.Eng. Jörg M. Stockmann at BAM.

The presence of both Eu and F is also detected by SEM/EDX. No F was present in the pristine **Eu₂SAcbisDBM₃@Au** surface (Figure 3.105, Appendix) and, importantly, no F signal is recorded in the control Au area of the **Eu₂SAcbisDBM₃@Au-F** surface (green, Figure 3.31), further suggesting co-localisation of the two elements in the same features. Quantification of the atomic percentages of Eu and F in the imaged features by EDX analysis reveals an identical Eu/F ratio to the one observed by XPS (0.6±0.1, n=8), further validating the results.

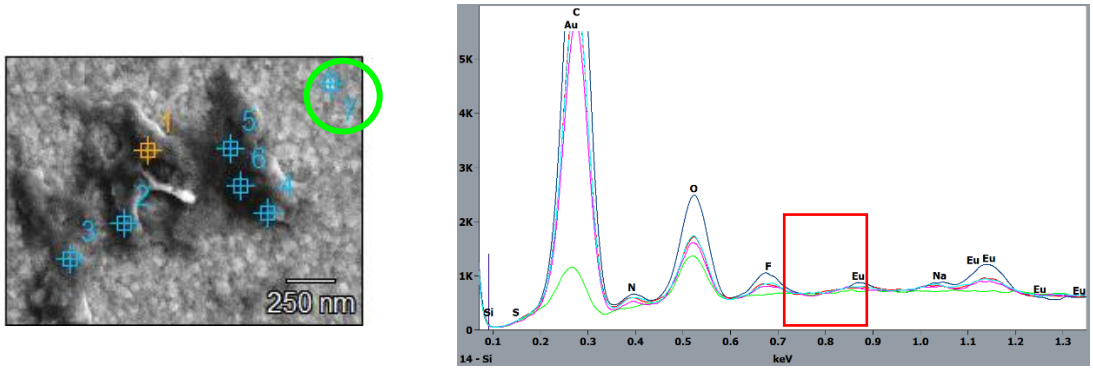


Figure 3.31 – EDX spectra of the imaged areas of **Eu₂SAcbisDBM₃@Au**. The green spectrum is the control area with no features, showing absence of F. The image and the EDX spectra were acquired by Sigrid Benemann at BAM.

3.2.3 Spin coating as a robust coating method for Au surfaces

Having assessed dip coated **Ln_2SAcbisDBM$_3$@Au** surfaces and their detection of F^-, we set out to investigate the spin coating of **Ln_2SAcbisDBM$_3$** complexes for a more uniform film formation. In the dip coated **Eu_2SAcbisDBM$_3$@Au** surfaces, large (>1 μm) and irregular features were observed, indicating the formation of big aggregates on the substrates. On the other hand, spin coating allows for the deposition of a thin and even layer of material on a surface. After placing a drop of solution on the substrate, a centrifugal force is applied, spreading the mixture and driving any excess out of the edges. As the concentration of complex in the added aliquot is known, spin coating represents a more controlled film formation approach for the coating of surfaces.

For the spin coating of the surfaces presented here, a solution of **Ln_2SAcbisDBM$_3$** in THF (0.1 mM, 1% DMF) was employed. SEM and AFM imaging of spin coated **SP_Eu_2SAcbisDBM$_3$@Au** surfaces reveals that the complex is distributed as thin branch-like features on the Au surface (Figures 3.32, **a** and **b**). The average feature height and roughness of the spin coated sample measured by AFM are both significantly lower than the dip coated **Eu_2SAcbisDBM$_3$@Au** surface (Table 3.2). Furthermore, the values are close to the ones of a plain Au surface, suggesting that the coating does not significantly alter the height distribution on the substrate. Approximating the footprint of a single **Eu_2SAcbisDBM$_3$** complex from the crystal structure of **Yb_2SAcbisDBM$_3$**, the found average feature height of 7±2 nm indicates that ≈2-3 complexes are stacked on the substrate. Focusing on the pattern, whereas the branch-like features extend up to several μm, their widths are measured to be 220±40 nm, which equals to approximately 100 complexes if stacked along the direction of the surface active chain.

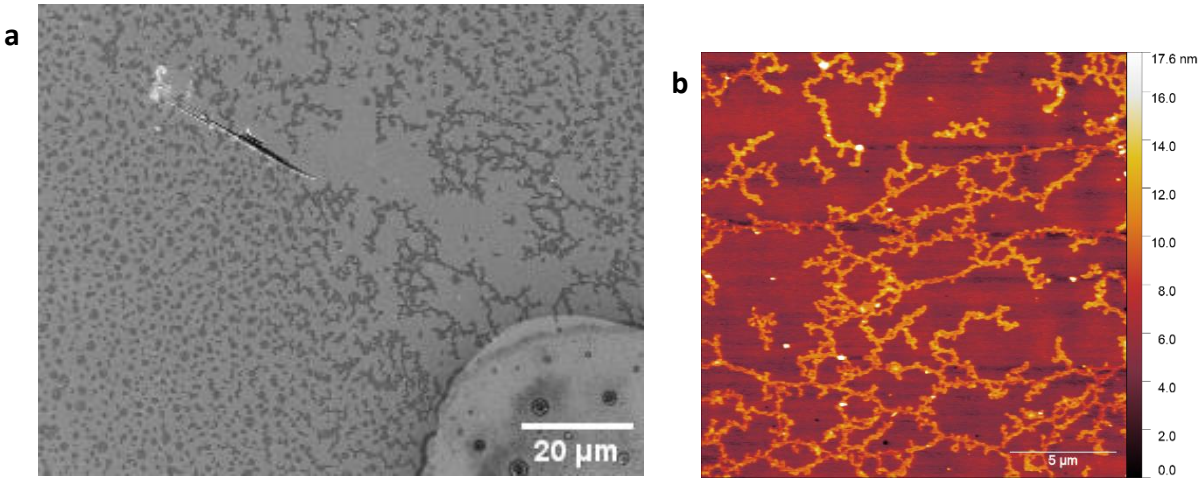


Figure 3.32 – **a** SEM image of **SP_Eu₂SAcbisDBM₃@Au** obtained by Sigrid Benemann at BAM. **b** AFM image (20 µm x 20 µm) of **SP_Eu₂SAcbisDBM₃@Au**. The image was obtained by Dr. Simon Connell and Dr. Pallavi Kumari at the School of Physics and Astronomy at the University of Leeds

Sample	Average Height	Roughness
Plain Au	4 nm	1 nm
Eu₂SAcbisDBM₃@Au	150 nm	68 nm
SP_Eu₂SAcbisDBM₃@Au	7 nm	2 nm

Table 3.2 – Average feature height and roughness of AFM images.

In addition to these patterns, SEM reveals the presence of regular and circular features, with most sizes averaging 500±60 nm in diameter. Imaging of one of the larger features (2 µm, Figure 3.33, **a**) reveals the presence of assemblies with smaller widths (28±4 nm) than the ones observed in Figures 3.32 **a** and **b** and containing approximately 10 complexes.

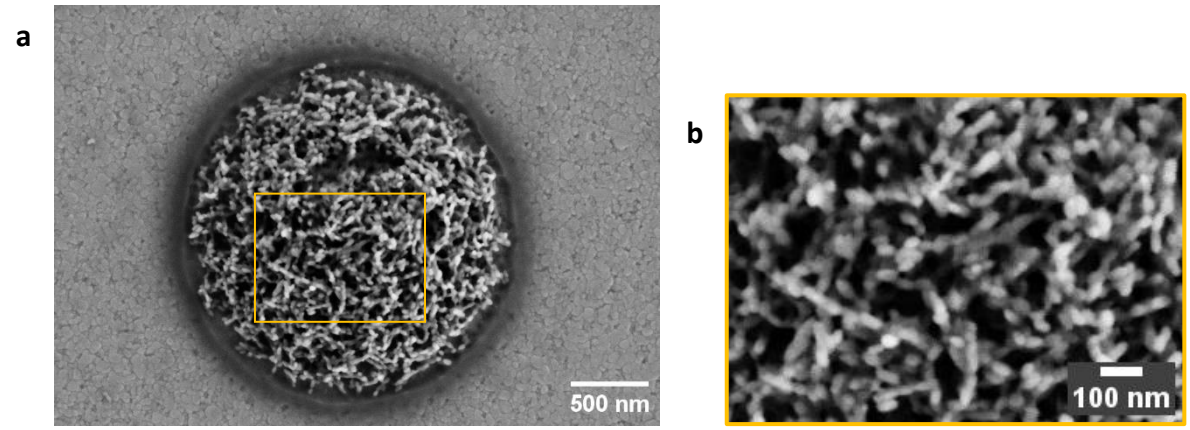


Figure 3.33 – **a** SEM image of **SP_Eu₂SAcbisDBM₃@Au** displaying a large circular feature of around 2 µm in diameter. **b** A section of the SEM image **a** (orange rectangle) of **SP_Eu₂SAcbisDBM₃@Au** to display the morphology. Both images were acquired by Sigrid Benemann at BAM.

The elemental composition of the features is obtained by EDX, confirming the presence of the predicted elements for the **Eu_2SAcbisDBM$_3$** complex (Eu, C, N, S and O, Figure 3.107, Appendix). The considerable intensity of the oxygen Kα peak at 0.525 keV and high atomic percentage of oxygen (28±4%) are attributed to residual solvent and the potential presence of H_2O in the solvent and coordinating to the lanthanide(III).

Comparing the optical properties of the spin coated **SP_Eu_2SAcbisDBM$_3$@Au** surface with the dip coated **Eu_2SAcbisDBM$_3$@Au** surface, the excitation spectrum of the spin coated surface displays the expected band with maximum at 359 nm (Figure 3.34), attributed to the energy transfer from the **SAcbisDBM** ligand to Eu(III). Furthermore, the emission profile of **SP_Eu_2SAcbisDBM$_3$@Au** displays all $^5D_0 \rightarrow {}^7F_J$ (ΔJ=0-4) transitions with the hypersensitive $^5D_0 \rightarrow {}^7F_2$ transition being characteristically prevalent (Figure 3.34). The lifetime values correlate well with the average ones of a set of 15 **Eu_2SAcbisDBM$_3$@Au** dip coated surfaces (190 μs and 170±20 μs for the longest components of spin coated and dip coated surfaces, respectively. For the full analysis, Table 3.15, Appendix).

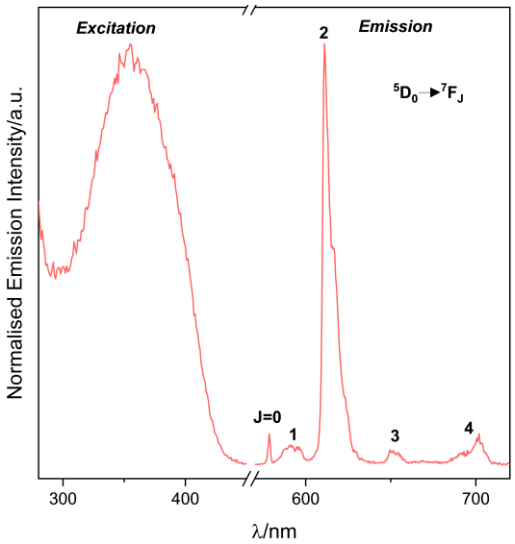


Figure 3.34 – Normalised excitation (**Excitation**) and emission (**Emission**) spectra of spin coated **SP_Eu_2SAcbisDBM$_3$@Au**. λ_{exc} 350 nm, λ_{em} 611 nm.

These comparisons suggest that the different coating method does not significantly affect the luminescence of the surfaces. NIR emitting **SP_Yb$_2$SAcbisDBM$_3$@Au** and **SP_Nd$_2$SAcbisDBM$_3$@Au** surfaces, however, are found to be very weakly luminescent (Figures 3.73 and 3.74, Appendix).

Finally, to investigate the reliability of the spin coating approach on Au surfaces, the effect of concentration (0.05-1 mM) of the spin coating solution on the emission intensity of **Eu$_2$SAcbisDBM$_3$** is evaluated. The visible emitting **Eu$_2$SAcbisDBM$_3$** complex was selected as, compared to its NIR emitting counterparts, it displays well resolved and easily detectable emission on Au surfaces. Furthermore, due to the higher solubility of the complex in DMF compared to THF, higher concentrations are possible in this solvent, hence it was chosen for the preparation of coating solutions in this experiment. From the dependence of **Eu$_2$SAcbisDBM$_3$** emission on the concentration of coating solution, a linear trend is observed, correlating well with the increase in concentration of complex on both substrates (Figure 3.35). The data can be approximated with a linear fit (R^2 = 0.96), indicating that spin coating can provide a reliable approach to the film formation of **Ln$_2$SAcbisDBM$_3$** complexes on Au surfaces.

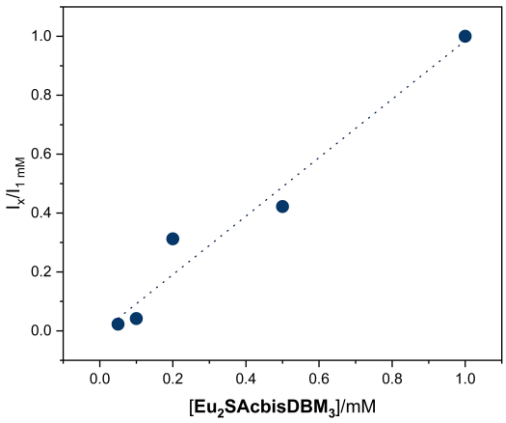


Figure 3.35 – Emission intensity of spin coated **SP_Eu$_2$SAcbisDBM$_3$@Au** (blue circle) as a function of the concentration of the spin coated **Eu$_2$SAcbisDBM$_3$** complex solution in DMF. For clarity, the emission intensities are normalised by their respective 1 mM value. The linear fit is shown as a dashed line and is obtained with OriginPro 2023. The fitting parameters are reported in Table 3.10, Appendix.

3.2.4 Characterisation and modelling of plasmonic Au (pGold) surfaces

Having investigated the properties of both dip coated and spin coated **Ln_2SAcbisDBM$_3$@Au** surfaces, we set out to explore the plasmonic enhancement of visible and NIR **Ln_2SAcbisDBM$_3$** luminescence on plasmonic pGold surfaces, starting with the characterisation of the pGold substrates.

From the correlation between concentration of spin coated **Eu_2SAcbisDBM$_3$** solution (0.05 mM, 0.1 mM, 0.2 mM, 0.5 mM and 1 mM in DMF) and emission intensity on pGold (Figure 3.36, orange triangles), a similar response to the **SP_Eu_2SAcbisDBM$_3$@Au** surfaces is recorded. Indeed, a linear fit can be applied, displaying good correlation with the experimental data (R^2 = 0.98), and equivalent slopes for both **Eu_2SAcbisDBM$_3$@Au** and **Eu_2SAcbisDBM$_3$@pGold** are observed (0.99 in both cases). Spin coating is thus deemed a suitable approach for the functionalisation of both Au and plasmonic substrates with **Ln_2SAcbisDBM$_3$** complexes.

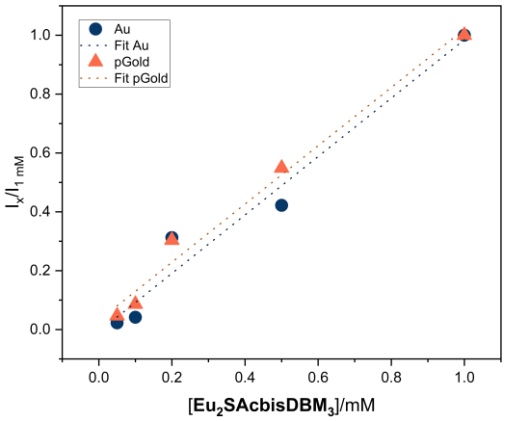


Figure 3.36 – Emission intensity of spin coated **SP_Eu_2SAcbisDBM$_3$@Au** (blue circle) and **SP_Eu_2SAcbisDBM$_3$@pGold** (orange triangle) as a function of the concentration of the spin coated **Eu_2SAcbisDBM$_3$** complex solution (0.05 mM, 0.1 mM, 0.2 mM, 0.5 mM and 1 mM in DMF). For clarity, the emission intensities are normalised by their respective 1 mM value. The linear fits are shown as dashed lines and are obtained with OriginPro 2023. The fitting parameters are reported in Table 3.10, Appendix.

pGold surfaces were studied with both SEM and AFM to examine their morphology. Whereas a mostly uniform layer of Au is observed for plain Au surfaces (Figure 3.101, Appendix), the imaging of pGold surfaces reveals a random distribution of Au islands on the glass substrate, which is in accordance with previous reports.[45] SEM analysis shows that the gap (a in Figure 3.37 **a**) between the nanostructures is 20 ± 7 nm, while the width of the nanoislands (b in Figure 3.37 **a**) is 83 ± 16 nm and AFM imaging reveals the average height of Au to be 41 ± 6 nm. These parameters will be used for the modelling and simulation of the pGold and Ln(III)/pGold system.

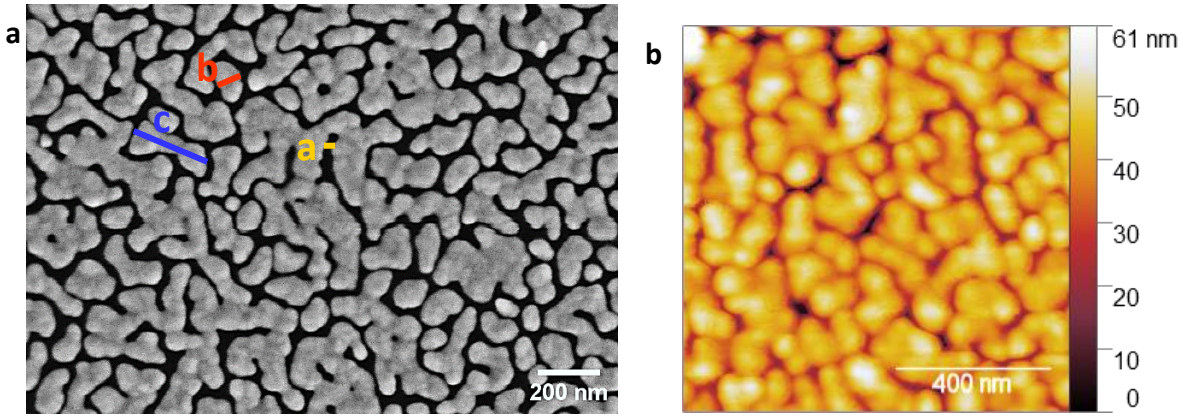


Figure 3.37 – **a** SEM image of a plain pGold surface acquired at BAM. a, b and c represent the gap size, width and length, respectively, of Au nanostructures. **b** AFM image (1 µm x 1 µm) of a plain pGold surface. The image was obtained by Dr. James Churm at the School of Engineering at the University of Birmingham.

Due to the random distribution and dimensions of the nanostructures, along with their non-spherical nature, Mie theory cannot be directly applied to predict the plasmon resonance of the surface.[91, 92] Indeed, a very broad band is observed by UV-Vis absorption spectroscopy, as reported, and is attributed to the collective plasmon modes of the surface (Figure 3.38).[45] The broadness of the extinction band from 550 nm to over 1200 nm allows for the overlap with the signal range of Eu(III) (570-720 nm) emission, as well as the NIR emitting Yb(III) (900-1125 nm) and Nd(III) (850-1450 nm, Figure 3.38).

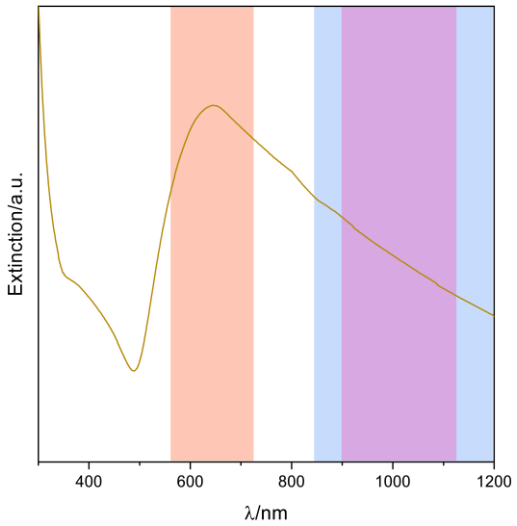


Figure 3.38 – Extinction spectrum of pGold (gold). The coloured overlaid sections represent the emission ranges of Eu(III) (orange), Yb(III) (lilac) and, partially, Nd(III) (blue).

Simulations of pGold under plane-wave illumination, however, reflect the complexity of the system (Figure 3.39, **a**). For the modelling, the dimensions reported above were used, with the thickness of the Au layer being 60 nm. Considering the simulated absorption spectrum, a peak above 700 nm is found. Experimentally, a broad band at 600 nm is observed, although the same trend of declining absorbance up to 1000 nm is present. The difference between simulation and experiment highlights how the randomness of the nanostructures leads to a difficult prediction of the system's optical properties. For comparison, the simulation of an ordered array of 60 nm AuNPs was also conducted (Figure 3.39, **b**). As expected, a well-defined extinction band is observed, in sharp contrast to the broad and complex extinction spectrum of pGold.

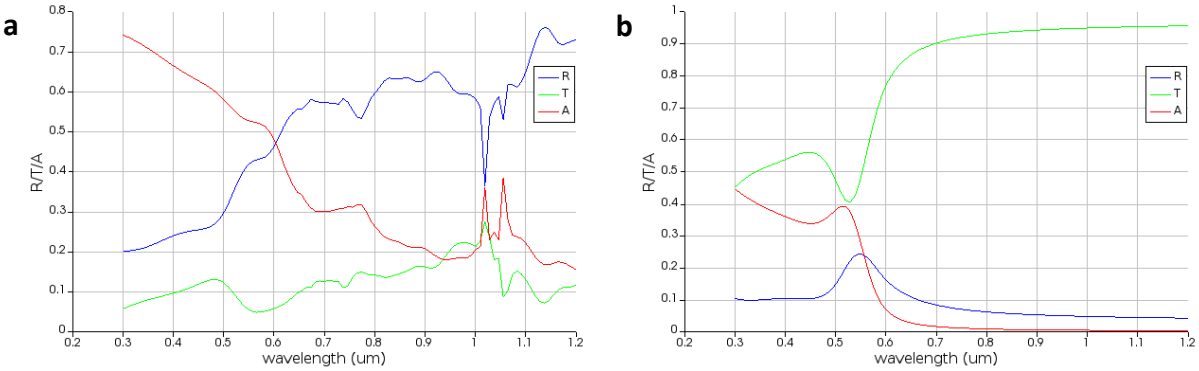


Figure 3.39 – Simulated reflectance (blue, R), transmittance (green, T) and absorption (red, A) spectra of a modelled pGold surface (**a**) and an array of AuNPs with 60 nm diameter and 80 nm periodicity. The simulations and images were made by Dr. Miguel Navarro-Cía at the School of Physics and Astronomy and School of Engineering at the University of Birmingham.

To evaluate the localisation of EM field on the pGold surface, simulations of the system were carried out with the plane-wave excitation and monitoring the electric field enhancement on the substrate for a set wavelength. Both visible and NIR wavelengths were selected to further assess the suitability of pGold for a broad wavelength range enhancement. From the simulations, it is observed that the maximum electric field confinement is found in the gaps between the Au islands with emission set at 609 nm (Figure 3.40 **a**). This is in accordance with previous theory and evidence that, when nanostructures are in proximity of each other (20 ± 7 nm, here), the incident electromagnetic field is localised in the gaps to give hot spots of maximum enhancement. Furthermore, the electric field is found to quickly decay upon increasing distance from the gaps and the surface.

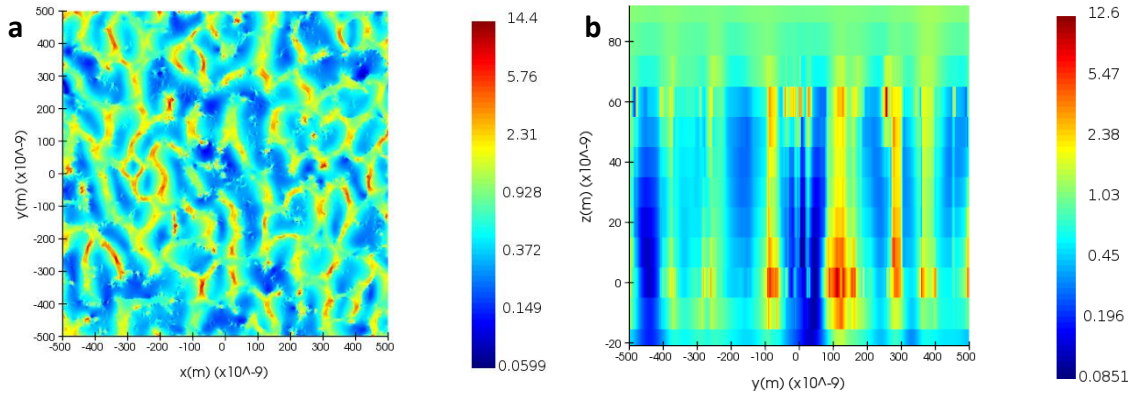


Figure 3.40 – Simulated localised electric field (scalebar, absolute value in logarithmic scale) over pGold surface for the emission at 609 nm, as seen from the top of the surface (**a**) and from the side (**b**). The simulations and images were made by Dr. Miguel Navarro-Cía at the School of Physics and Astronomy and School of Engineering at the University of Birmingham.

When the emission wavelength is set in the NIR (982 nm and 1055 nm for Yb(III) and Nd(III), Figures 3.41 **a** and **b**, respectively), the simulations display an excellent localisation of electric field in the gaps. Here, the confinement is more defined, compared to the 609 nm emission, and the magnitude is amplified.

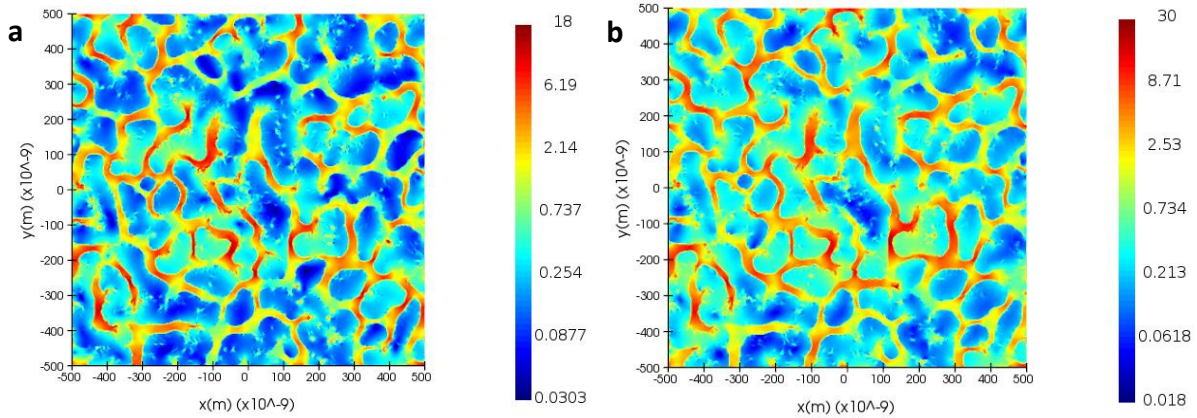


Figure 3.41 – Simulated localised electric field (scalebar, absolute value in logarithmic scale) over pGold surface for the emission at 982 nm (**a**) and at 1055 nm (**b**), as seen from the top of the surface. The simulations and images were made by Dr. Miguel Navarro-Cía at the School of Physics and Astronomy and School of Engineering at the University of Birmingham.

This is in accordance with the reported examples of pGold for the enhancement of the fluorescence of organic dyes, where modest enhancements were observed for visible emitting dyes (≈3-fold in the 500-700 nm range), while more significant increases could be found in the

NIR (≈100-fold in the 700-900 nm region) and thus supporting our choice of pGold as an enhancing substrate for both visible and NIR emitting lanthanides(III).[93]

3.2.5 Effect of pGold surfaces on lanthanide(III) luminescence

3.2.5.1 Visible Eu_2SAcbisDBM$_3$ luminescence

Upon excitation at 350 nm, the luminescence of the **SP_Eu_2SAcbisDBM$_3$@pGold** surface (orange, Figure 3.42), is significantly enhanced compared to the control **SP_Eu_2SAcbisDBM$_3$@Au** surface (blue, Figure 3.42).

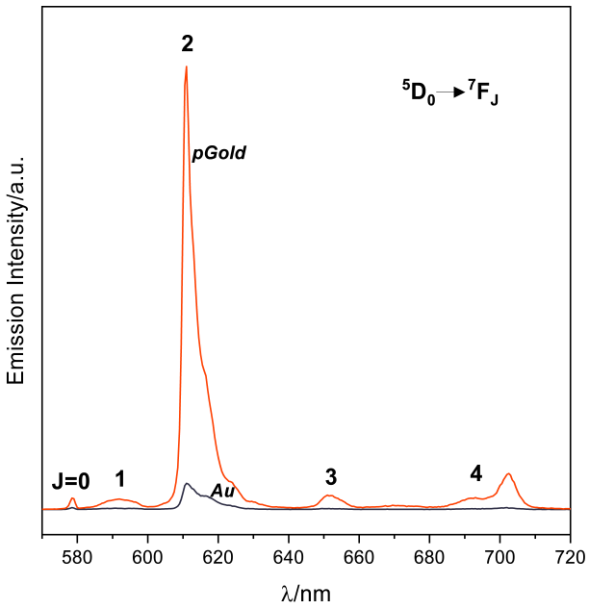


Figure 3.42 – Overlaid emission spectra of **SP_Eu_2SAcbisDBM$_3$@Au** (blue) and **SP_Eu_2SAcbisDBM$_3$@pGold** (orange). λ_{exc}: 350 nm.

To estimate the enhancement factor, the emission intensity (as the overall emission integral) is compared and a 12-fold enhancement is found.

By assessing the wavelengths of the plasmon modes of the pGold surface and the emission spectrum of the **Eu_2SAcbisDBM$_3$** complex (Figure 3.43), a strong overlap between the plasmon resonance and Eu(III) emission is observed. As mentioned above, such a condition has as its

basis the Purcell effect, where the non-radiative energy transfer from emitter to nanostructure lead to resonant and enhanced light emission.

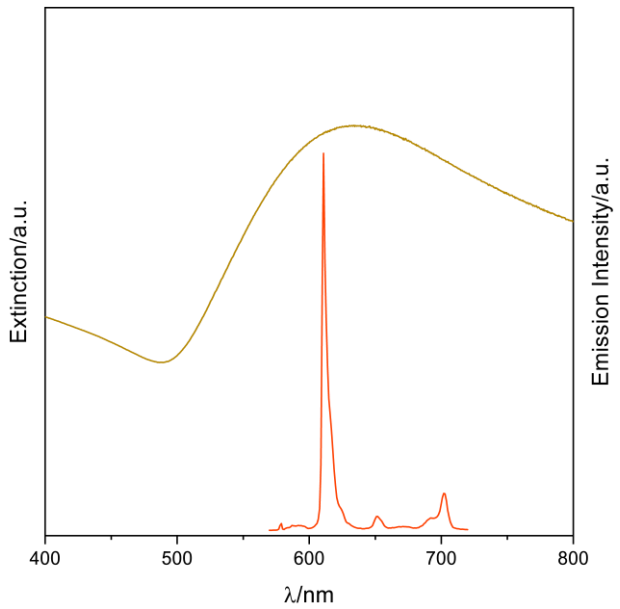
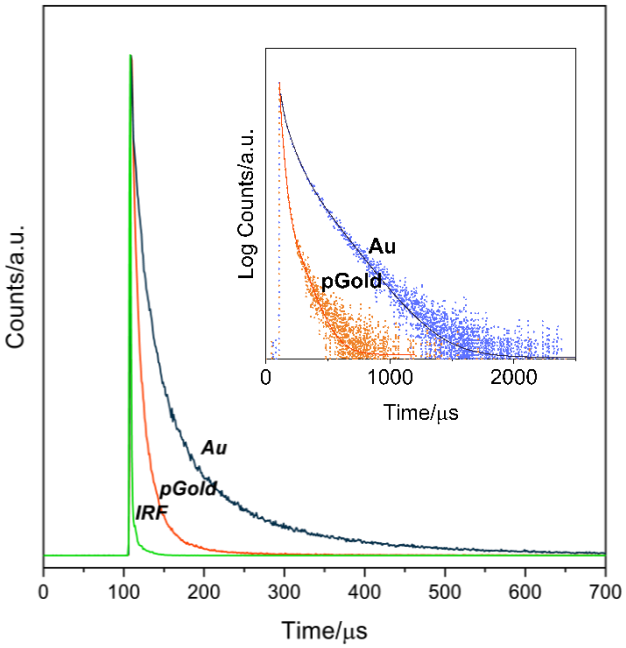


Figure 3.43 – Overlaid extinction (gold) and emission (orange) spectra of **SP_Eu$_2$SAcbisDBM$_3$@pGold**. λ_{exc}: 350 nm.

To confirm the Purcell enhancement mechanism, the lifetime of the **Eu$_2$SAcbisDBM$_3$@pGold** surface was also considered. Characteristic of the Purcell effect is an increase in the radiative decay rate of the emitter, which, in turn, is often reflected in a decreased lifetime. As already seen for the dip coated **Eu$_2$SAcbisDBM$_3$@Au** surfaces in Section 2.1, the lifetime of **Eu$_2$SAcbisDBM$_3$** becomes significantly more complex on the surface than in solution. Indeed, a similar triexponential decay is observed for the spin coated **SP_Eu$_2$SAcbisDBM$_3$@Au** (Table 3.3), with the shorter lifetime values (69 µs and 20 µs) suggesting the presence of non-radiative decay pathways due to the proximity of the metal surface. A triexponential decay is also found for the **SP_Eu$_2$SAcbisDBM$_3$@pGold** surface (Table 3.3) where, however, all values are reduced compared to the reference. The over 2-fold decrease cannot be ascribed to quenching processes alone and is in accordance with the enhancement in emission intensity observed in

Figure 3.42 **a**. Consequently, we attribute the overall photophysical properties of **Eu$_2$SAcbisDBM$_3$@pGold** to the Purcell effect.[94, 95]



Sample	τ/μs (%)
Au	**190** (33%), 61 (46%), 13 (21%)
pGold	**86** (10%), 20 (48%), 5.3 (42%)

Figure 3.44 – Overlaid lifetime spectra of **SP_Eu$_2$SAcbisDBM$_3$@Au** (blue) and **SP_Eu$_2$SAcbisDBM$_3$@pGold** (orange) with IRF (green). λ_{exc}: 350 nm, λ_{em}: 611 nm. The inset shows the fitting in the logarithmic scale. **Table 3.3** – Exponential decay analysis of **SP_Eu$_2$SAcbisDBM$_3$@Au** and **SP_Eu$_2$SAcbisDBM$_3$@pGold**. Highlighted are the main longer components.

As mentioned in section 3.1.2.2, the confined EM field at the nanostructures can enhance the ED and MD transitions of Eu(III) differently. Indeed, in the overlaid and normalised emission spectra in Figure 3.45, the emission profile of **Eu$_2$SAcbisDBM$_3$** is altered on the pGold surface. From the spectra in Figure 3.45, the following differences are visually observed on pGold: the hypersensitive $^5D_0 \rightarrow {}^7F_2$ transition appears sharper, the $^5D_0 \rightarrow {}^7F_{0\text{-}1}$ transitions are significantly reduced and the $^5D_0 \rightarrow {}^7F_{3\text{-}4}$ transitions are unaffected. A common method to monitor variations in the emission profile of Eu(III) spectra is to use the MD $^5D_0 \rightarrow {}^7F_1$ transition as reference. Here, however, it is one of the most affected transitions. We thus take the $^5D_0 \rightarrow {}^7F_4$ transition as reference, because its intensity and shape appear unaltered.

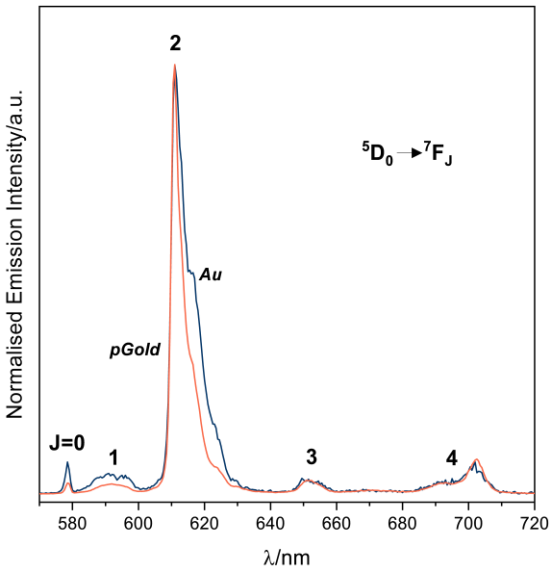


Figure 3.45 – Overlaid and normalised emission spectra of spin coated **SP_Eu₂SAcbisDBM₃@Au** (blue) and **SP_Eu₂SAcbisDBM₃@pGold** (orange). λ_{exc}: 350 nm.

The ratios reported in Table 3.4 confirm the visual observations from Figure 3.45. Indeed, a more than 2-fold decrease in the relative intensity of the $^5D_0 \rightarrow ^7F_1$ transition is found, suggesting that pGold surfaces do not enhance MD transitions. The decrease in relative intensity of the hypersensitive $^5D_0 \rightarrow ^7F_2$ transition is attributed to the lower integral value, due to the narrowing of the peak. The $^5D_0 \rightarrow ^7F_3$ transition is confirmed unaltered, while the $^5D_0 \rightarrow ^7F_0$ transition displays a 2-fold decrease, similarly to the MD $^5D_0 \rightarrow ^7F_1$ transition. From these observations, we suggest that the optical modes of the pGold surface strongly couple with the ED component of Eu(III), enhancing the intensity of these transitions.

	$^5D_0 \rightarrow ^7F_0$	**$^5D_0 \rightarrow ^7F_1$**	**$^5D_0 \rightarrow ^7F_2$**	**$^5D_0 \rightarrow ^7F_3$**	**$^5D_0 \rightarrow ^7F_4$**
Au	0.18	0.73	9.95	0.40	1.00
pGold	0.07	0.34	7.08	0.34	1.00

Table 3.4 – Ratio of selected transitions over the $^5D_0 \rightarrow ^7F_4$ transition (i.e. $^5D_0 \rightarrow ^7F_J/^5D_0 \rightarrow ^7F_4$) of spin coated **SP_Eu₂SAcbisDBM₃@Au** and **SP_Eu₂SAcbisDBM₃@pGold**.

3.2.5.2 NIR Yb_2SAcbisDBM$_3$ and Nd_2SAcbisDBM$_3$ luminescence

After confirming and investigating the effect of pGold on the visible **Eu_2SAcbisDBM$_3$** luminescence, we evaluated the enhancement of NIR emitting Yb(III) and Nd(III) **Ln_2SAcbisDBM$_3$** complexes. From the simulation results in section 2.4 and the reported trends, a significant enhancement is expected in the NIR region.

Indeed, the **SP_Yb_2SAcbisDBM$_3$@pGold** surface displays a 41-fold emission enhancement from its **Yb_2SAcbisDBM$_3$@Au** counterpart (Figure 3.46). As seen with the **SP_Eu_2SAcbisDBM$_3$@pGold** surface, the luminescence enhancement allows for the clear observation of the splitting for the $^2F_{5/2}\rightarrow{}^2F_{7/2}$ transition of Yb(III), which is unprecedented for us on a surface. Furthermore, considering the limited quantum yield of the complex (0.8% in DMSOd_6) and the approximate maximum amount of **Yb_2SAcbisDBM$_3$** complex on the chip (0.4 nmol/cm^2, average size of the chip 1.5 cm x 1.5 cm), the obtained signal and its resolution are astounding.

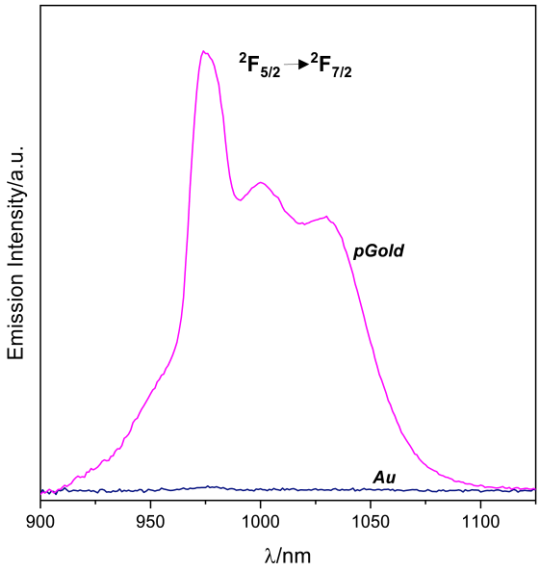


Figure 3.46 – Overlaid emission spectra of **SP_Yb_2SAcbisDBM$_3$@Au** (blue) and **SP_Yb_2SAcbisDBM$_3$@pGold** (pink). λ_{exc}: 350 nm.

Considering time-resolved measurements, only the lifetime of the **SP_Yb$_2$SAcbisDBM$_3$@pGold** surface could be recorded. This is due to the extremely low signal detected for the **SP_Yb$_2$SAcbisDBM$_3$@Au** surface, not allowing for reliable lifetime measurements. Instead, we compare the **SP_Yb$_2$SAcbisDBM$_3$@pGold** lifetime to the one of the complex as a powder, which is unaffected by any plasmonic processes. Here, the sharp decrease in all decay components, as observed for the visible emitting **SP_Eu$_2$SAcbisDBM$_3$@pGold** surface, is not recorded. Instead, the lifetime is mostly unaltered from the control powder (Table 3.5). The additional shorter components in the powder sample are attributed to the presence of solvent coordinating to the complex, thus partially quenching the Yb(III) luminescence. As the values observed for the **SP_Yb$_2$SAcbisDBM$_3$@pGold** surface are very similar, and as no strong reduction in lifetime values is found, we cannot attribute the short components of the surface sample to the Purcell effect.

Sample	τ/μs (%)
Yb$_2$SAcbisDBM$_3$ Powder	**11** (84%), 2.6 (16%)
SP_Yb$_2$SAcbisDBM$_3$@pGold	**11** (42%), 3.6 (48%), 1.4 (10%)

Table 3.5 – Exponential decay analysis of **Yb$_2$SAcbisDBM$_3$** as powder and of **SP_Yb$_2$SAcbisDBM$_3$@pGold**. Highlighted is the main longer component. λ_{exc}: 350 nm, λ_{em}: 977 nm.

Similarly to the **SP_Yb$_2$SAcbisDBM$_3$@pGold** surface, **SP_Nd$_2$SAcbisDBM$_3$@pGold** displays well defined and enhanced emission peaks (Figure 3.47, **a**). As for the enhancement factor, if the whole spectrum is considered, a 214-fold increase is calculated by comparing both spectral integrals. However, due to the extremely poor resolution and intensity of the $^4F_{3/2}\rightarrow{}^4I_{9/2}$ and $^4F_{3/2}\rightarrow{}^4I_{13/2}$ transitions of the **SP_Nd$_2$SAcbisDBM$_3$@Au** surface (Figure 3.47, **b**), these are neglected in the integral calculations and an overestimation is likely. If only the better resolved

and most intense $^4F_{3/2} \rightarrow {}^4I_{11/2}$ transition is considered, a more modest – but still impressive – 64-fold enhancement is recorded.

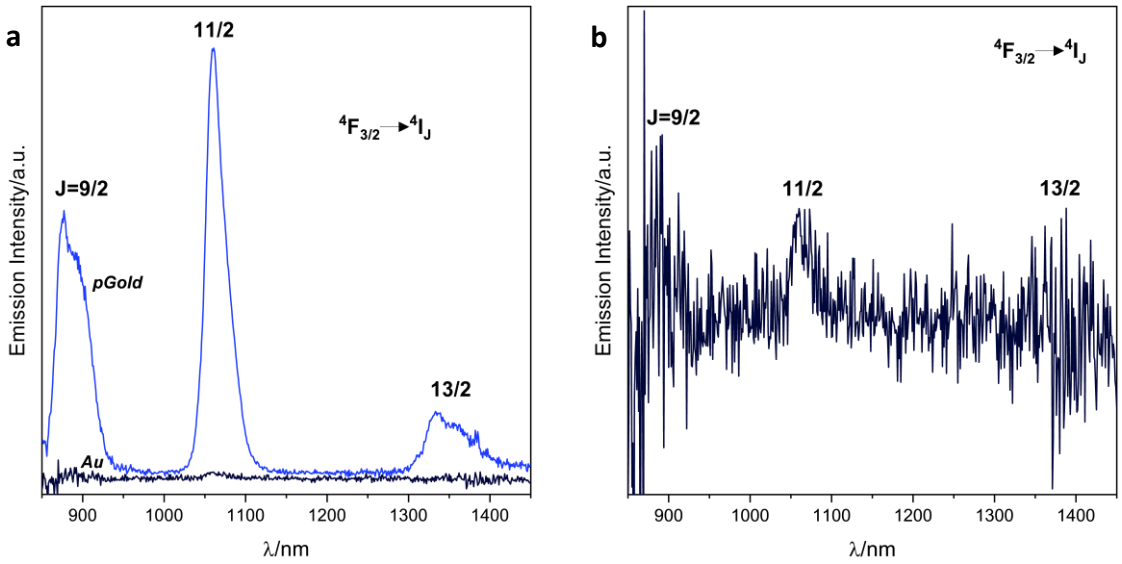


Figure 3.47 – **a** Overlaid emission spectra of **SP_Nd$_2$SAcbisDBM$_3$@Au** (dark blue) and **SP_Nd$_2$SAcbisDBM$_3$@pGold** (light blue). λ_{exc}: 350 nm. **b** Emission spectrum of **SP_Nd$_2$SAcbisDBM$_3$@Au**. λ_{exc}: 350 nm.

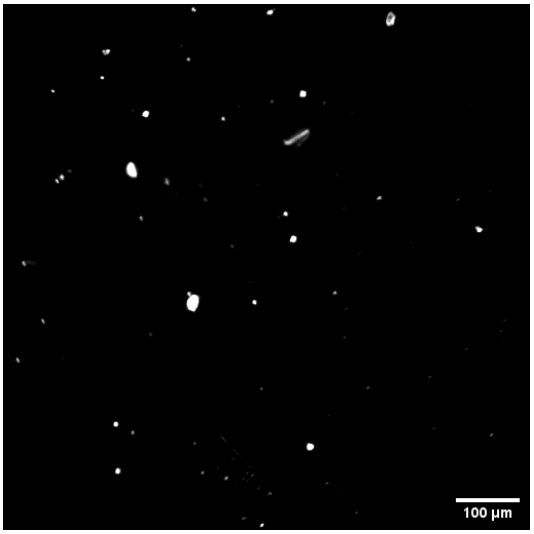
These results are extremely significant. Here, the NIR luminescence of lanthanide(III) complexes on solid substrates is enhanced to the point where remarkable resolutions are attainable, similar to the ones of the same samples in solution. Such enhancement of emission intensity has enormous potential for the advancement of NIR emitting lanthanides(III) to practical applications, where weaker detection systems would preclude the use of more weakly luminescent materials, like the ones on Au surfaces.

3.2.5.3 Further studies on SP_Eu$_2$SAcbisDBM$_3$@pGold: epifluorescence microscopy and SERS

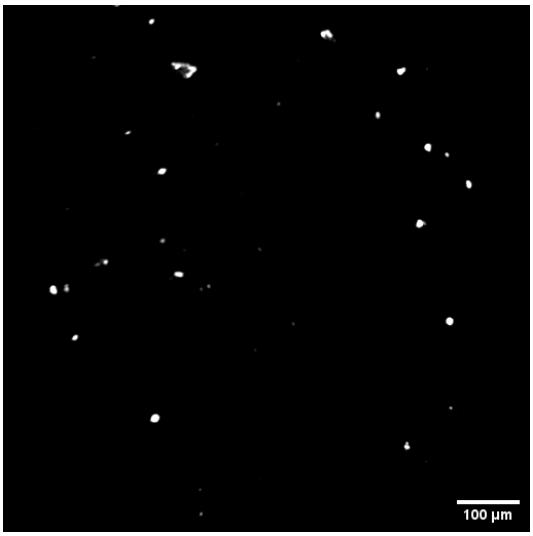
To further compare the luminescence arising from the **SP_Eu$_2$SAcbisDBM$_3$@Au** and **SP_Eu$_2$SAcbisDBM$_3$@pGold** surfaces, fluorescence microscopy images of the two samples were acquired. Furthermore, by connecting the epifluorescence microscope to a steady state

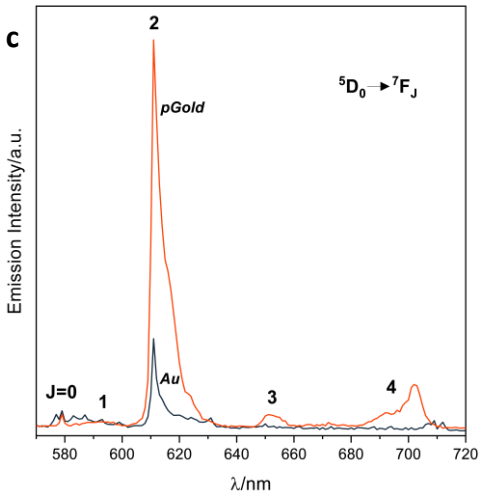
and time-resolved spectrophotometer *via* liquid light guides, emission and lifetime spectra of the surfaces were also obtained, confirming the nature of the luminescence observed in the images. Bright luminescent spots are observed upon excitation at 350 nm (Figures 3.48 **a** and **b**). The size (5±2 μm and 6±2 μm for Au and pGold, respectively) and distribution of the luminescent areas is comparable regardless of the substrate. To confirm the nature of the luminescence, we employed steady state spectroscopy. Characteristic Eu(III) luminescence is observed in both cases but a significantly higher emission intensity for the complex on pGold is recorded (3-fold increase). Indeed, compared to the **SP_Eu$_2$SAcbisDBM$_3$@Au** surface, where only the most intense $^5D_0 \rightarrow {}^7F_2$ can be clearly identified, the enhanced emission of **SP_Eu$_2$SAcbisDBM$_3$@pGold** leads to an extremely well resolved emission profile, where all the $^5D_0 \rightarrow {}^7F_J$ (J=0-4) transitions can be assigned. As a further result of the enhanced luminescence, the lifetime of the **SP_Eu$_2$SAcbisDBM$_3$@pGold** surface can be recorded, whereas no reliable lifetime measurements could be obtained for the **SP_Eu$_2$SAcbisDBM$_3$@Au** surface due to the weak emission signal. The lifetime of **SP_Eu$_2$SAcbisDBM$_3$@pGold** is in strong agreement with what was observed previously (Tables 3.3 and 3.6).

a



b





Sample	τ/µs
SP_Eu$_2$SAcbisDBM$_3$@Au	N/A
SP_Eu$_2$SAcbisDBM$_3$@pGold	**90** (17%), 22 (62%), 7.7 (21%)

Figure 3.48 – Epifluorescence images (10x) of **SP_Eu$_2$SAcbisDBM$_3$@Au** (**a**) and **SP_Eu$_2$SAcbisDBM$_3$@pGold** (**b**). λ_{exc}: 350 nm. Exposure and gain were adjusted for each surface to obtain comparable brightness. **c** Overlaid emission spectra of the imaged regions of **SP_Eu$_2$SAcbisDBM$_3$@Au** (blue) and **SP_Eu$_2$SAcbisDBM$_3$@pGold** (orange) from Figures **a** and **b**. **Table 3.6** – Exponential decay analysis of **SP_Eu$_2$SAcbisDBM$_3$@pGold**. Highlighted is the main longer component. λ_{exc}: 350 nm, λ_{em}: 611 nm.

These results further highlight the significance of our system. The emission profile and lifetime of lanthanides(III) enclose so much information regarding the environment and coordination state of the system, tremendously useful in sensing platforms, as seen in Section 2.2. However, we have shown here that, often, this information is lost due to insufficient signal. The luminescence enhancement offered by plasmonic surfaces allows for the detection of the optical properties of the metal complex with as high resolution and reliability as with a specialised spectrophotometer, so that the unique luminescence of the lanthanides(III) can be fully recorded and applied.

In addition to enhanced fluorescence, plasmonic materials can also act as Raman scattering enhancing substrates. Surface Enhanced Raman Spectroscopy (SERS) is a technique where the inelastic Raman scattering of a molecule is amplified due to the enhanced fields created by localised surface plasmons, such as those in the gaps between nanostructures.[96] Here we aim to evaluate whether any SERS processes are in place, which would further indicate that the

complex is found in the gaps. As portrayed in Figure 3.49, it was possible to acquire Raman spectra for both Au and pGold surfaces. The **Eu_2SAcbisDBM$_3$** complex as powder was used as control as the peaks were previously assigned in Chapter 2 and reported in Table 3.7. A higher laser power was required for the acquisition of the Raman spectrum for **SP_Eu_2SAcbisDBM$_3$@Au**, compared to pGold (750 µW vs 150 µW for Au and pGold, respectively, at the same excitation wavelength). This could be attributed to a higher scattering efficiency given by SERS, thus requiring a less powerful source to obtain a sufficiently resolved spectrum.

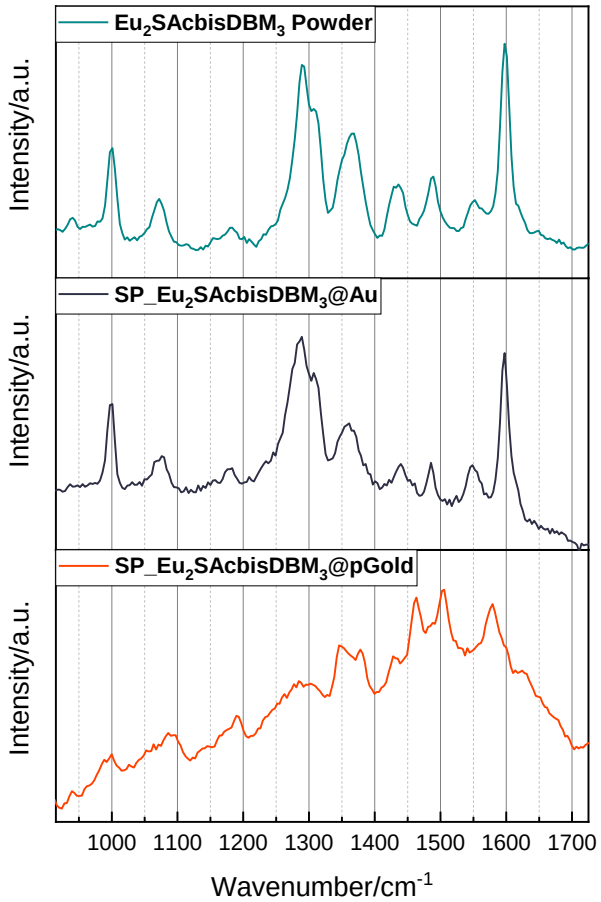


Figure 3.49 – Stacked Raman spectra of **Eu_2SAcbisDBM$_3$** as powder (top, green), **SP_Eu_2SAcbisDBM$_3$@Au** (middle, blue) and **SP_Eu_2SAcbisDBM$_3$@pGold** (bottom, orange). The laser power (633 nm) required for the acquisition of the **SP_Eu_2SAcbisDBM$_3$@Au** spectrum is five-fold (750 µW vs 150 µW), compared to **SP_Eu_2SAcbisDBM$_3$@pGold**.

As can be seen from both Figure 3.49 and the peak positions in Table 3.7, the spectrum of **SP_Eu$_2$SAcbisDBM$_3$@pGold** appears significantly different compared to the other two samples. Indeed, the position and relative intensity of peaks belonging to bonds with large dipole strengths, such as C=O and triazole in the 1300-1600 cm^{-1} region, are significantly shifted and their intensity altered for the pGold sample. Although it is not possible to assign with complete certainty the peaks for the **SP_Eu$_2$SAcbisDBM$_3$@pGold** surface, due to their shift from the control complex, a similar pattern is present. For example, the peaks at 1462 and 1504 cm^{-1} have a similar pattern to the ring stretching at 1435 and 1488 cm^{-1} of the **Eu$_2$SAcbisDBM$_3$** powder, while the strong peak at 1579 cm^{-1} could either be assigned to the C=O or triazole ring at 1598 and 1551 cm^{-1}, respectively. In any case, such significant shifts and intensity differences are attributed to the complex being in the gaps of the nanostructured pGold surface, thus confirming the experimental and simulated observations.

	Wavenumber/cm^{-1}		
Assignment	**Eu$_2$SAcbisDBM$_3$ Powder**	**SP_Eu$_2$SAcbisDBM$_3$@Au**	**SP_Eu$_2$SAcbisDBM$_3$@pGold**
C=O	1598 (vs)	1598 (vs)	1579 (s)
Triazole ring **C=C**	1551 (m)	1550 (m)	Broad band
Ring stretching	1488 (m)	1486 (m)	1504 (s)
Ring stretching	1435 (m)	1441 (m)	1462 (s)
Triazole ring **C-N + C-H def.**	1365 (s)	1364 (s)	1380 (m), 1347 (m)
C-H in plane deformation	1309 (sh)	1309 (sh)	1237-1317 (vw)
Triazole ring **N=N**	1291 (vs)	1290 (vs)	1237-1317 (vw)
-	1181 (w)	1181 (w)	1192 (w)
C-H ring bending	1072 (m)	1073 (m)	1093 (w)
Ring breathing	1000 (s)	1000 (s)	1000 (w)

Table 3.7 – Peak positions and assignments of the Raman spectra of **Eu$_2$SAcbisDBM$_3$** as powder and **SP_Eu$_2$SAcbisDBM$_3$@Au**. For **SP_Eu$_2$SAcbisDBM$_3$@pGold**, we suggest the peak assignments from the ones that are shifted due to SERS. Sh: shoulder, vs: very strong, s: strong, m: medium, w: weak.

3.2.6 Preparation of Ag nanoislands (AgNIs) surfaces

After investigating the effects of the plasmonic gold (pGold) surfaces on both visible and NIR lanthanide(III) luminescence, we assess the plasmonic effects of AgNIs surfaces. The plasmon resonance of Ag nanostructures is usually observed at lower wavelengths than Au nanostructures. This is optimal for the overlap with the excitation spectrum of the **Ln_2SAcbisDBM$_3$** complexes, whose absorption and excitation bands extend in the 300-425 nm region.

The Ag nanoislands (AgNIs) surfaces were prepared as in reported procedures.[97-99] Briefly, the reduction of silver nitrate *via* Tollens' reagent preparation and addition of glucose results in the deposition of elemental silver as a nanostructured silver mirror on the glass substrate.

$2Ag^+$ (aq) + $2OH^-$ (aq) → **Ag_2O** (s) + H_2O (l)

Ag_2O (s) + $4NH_3$ (aq) + H_2O (l) → **$2[Ag(NH_3)_2]^+$** (aq) + $2OH^-$ (aq)

$2[Ag(NH_3)_2]^+$ (aq) + RCHO (s) → **2Ag** (s) + RCOOH (aq)

Equation 3.1 – Reactions for the formation of Tollens' reagent and its reaction with glucose to give elemental Ag. $AgNO_3$ is used as source of Ag^+ and glucose as RCHO.

Pre-treatment of the glass substrates with (3-aminopropyl)triethoxysilane (APTES) allows for a better adhesion of the AgNIs layer, due to the weak interaction between the amino groups of APTES and the metal, very important to maintain the coating of the surface upon washing and sonication. The relevance of the sonication step to remove excess reagents and contaminants is exemplified by the larger scale SEM images of the AgNIs surfaces before and after sonication (Figure 3.109 and 3.110, Appendix). Imaging of the prepared surfaces by SEM and AFM (Figures 3.50, **a** and **b**) reveals the presence of large islands with random distribution and sizes. Considering the width of the features (as indicated by the red line b in Figure 3.50 **a**), an

average of 270 ± 35 nm is measured, with an average height of 66 ± 17 nm. For comparison, the width of pGold features was calculated to be 83 ± 16 nm with an average height of 41 ± 6 nm. In addition to the differences in sizes, the AgNIs surface has a RMS roughness of 24 nm, 3 times the one of pGold (8 nm), which is indicative of greater height irregularities. Finally, the gap shape and size of the AgNIs surface is more irregular than the one of pGold. For an estimation of the gap sizes, two sets are considered: wider and more circular gaps ($\underline{a_1}$ in Figure 3.50, **a**), and narrow and elongated gaps ($\underline{a_2}$ in Figure 3.50, **a**). The sizes of each type are, respectively, 210 ± 29 nm and 50 ± 10 nm, with the latter being more comparable to the gaps of pGold (20 ± 7 nm, Figure 3.37 **a**).

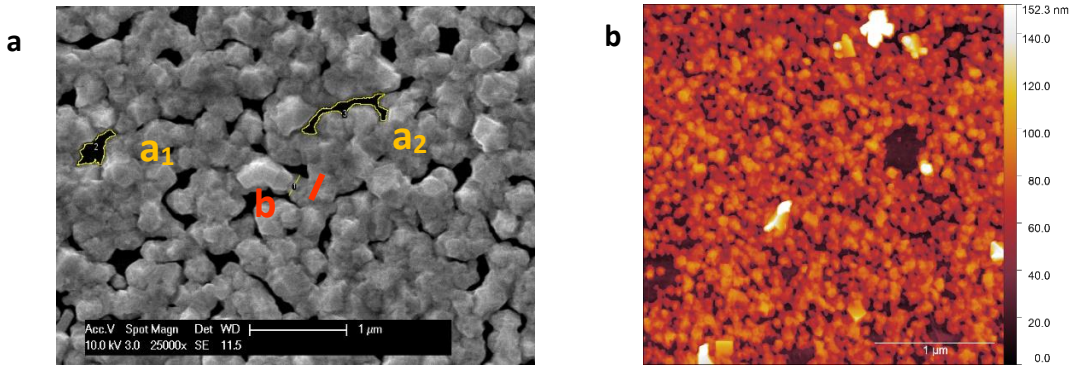


Figure 3.50 – **a** SEM image of AgNIs surface. The red line indicates the width of the nanostructures ($\underline{b}$) and the yellow sections the two considered gap shapes $\underline{a_1}$ and $\underline{a_2}$. **b** AFM image (3 µm x 3 µm) of a plain pGold surface. The image was obtained by Dr. Simon Connell and Dr. Pallavi Kumari at the School of Physics and Astronomy at the University of Leeds.

The extinction spectrum of AgNIs (Figure 3.51) displays a sharp peak at 375 nm. This correlates well with what has been reported for other AgNIs surfaces and is promising for the excitation enhancement of **Ln_2SAcbisDBM$_3$**, due to the overlap with the absorption and excitation spectra of the complexes (green section in Figure 3.51).[97]

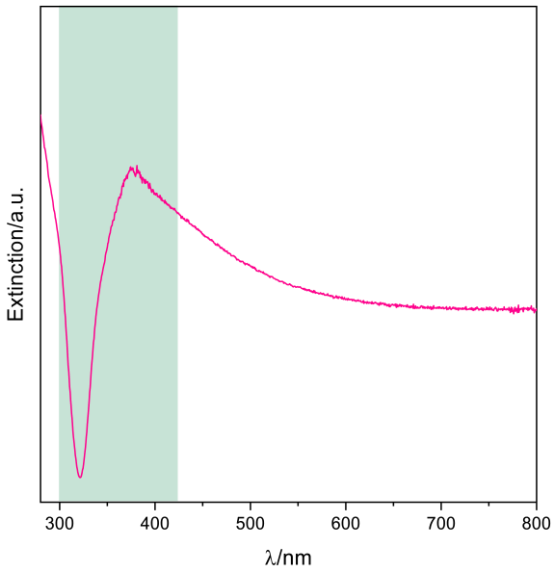


Figure 3.51 – Extinction spectrum of AgNIs. The green overlaid section represents the absorption/excitation ranges of **Ln_2SAcbisDBM$_3$** complexes.

3.2.7 Effect of Ag nanostructured surfaces (AgNIs) on lanthanide(III) luminescence and comparison with pGold

For the evaluation of the plasmonic enhancement of **Ln_2SAcbisDBM$_3$** luminescence with AgNIs, a similar approach to pGold surfaces was adopted and spin coated **SP_Ln_2SAcbisDBM$_3$@AgNIs** surfaces were compared to their **SP_Ln_2SAcbisDBM$_3$@Au** counterparts. Compared to the Purcell effect observed on pGold, the excitation enhancement expected with AgNIs surfaces does not directly involve the emission processes, often making for a harder identification. From the excitation spectra of **SP_Eu_2SAcbisDBM$_3$@Au** and **SP_Eu_2SAcbisDBM$_3$@AgNIs** surfaces, a significant shift from 355 nm to 390 nm for the π→π* band of the complex is observed on the AgNIs substrate (Figure 3.52, **a**). Excitation at 350 nm and 390 nm reveals an increase in emission intensity for **SP_Eu_2SAcbisDBM$_3$@AgNIs** (Figure 3.52, **b**), whereas a decrease in emission for both **SP_Eu_2SAcbisDBM$_3$@Au** and **SP_Eu_2SAcbisDBM$_3$@pGold** is recorded (Figures 3.78 and 3.79, respectively, Appendix). This is in accordance with the respective excitation spectra (Figure 3.34 and Figure 3.77, Appendix)

and confirming the authenticity of the shift for the **SP_ Eu_2SAcbisDBM$_3$@AgNIs** surface. Indeed, an excellent overlap is observed between the excitation spectrum of **SP_Eu_2SAcbisDBM$_3$@AgNIs** and extinction spectrum of AgNIs (green, solid, and pink, dashed, respectively). The collective data suggests that the shift is potentially caused by an enhancement of the high wavelength components of the excitation band of the complex, offered by a better overlap with the plasmon modes of the AgNIs surface at such frequencies.

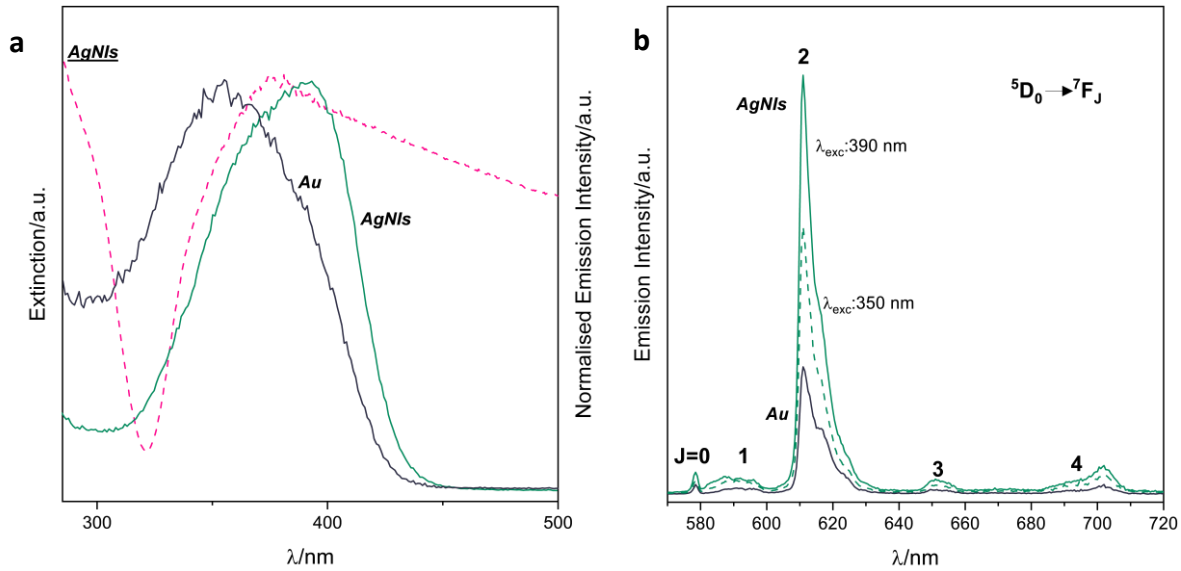


Figure 3.52 – **a** Overlaid extinction spectrum of AgNIs (dashed, pink) and normalised excitation spectra of **SP_Eu_2SAcbisDBM$_3$@AgNIs** (solid, green) and **SP_Eu_2SAcbisDBM$_3$@Au** (solid, blue). λ_{em}: 611 nm. **b** Overlaid emission spectra of **SP_Eu_2SAcbisDBM$_3$@Au** (blue, λ_{exc}: 350 nm) and **SP_Eu_2SAcbisDBM$_3$@AgNIs** upon λ_{exc}: 350 nm (dashed, green) and λ_{exc}: 390 nm (solid, green).

A 3-fold enhancement is recorded for AgNIs upon excitation at 390 nm, while a more modest 2-fold enhancement is found if the excitation wavelength is set as 350 nm. This is significantly lower than the one of pGold (12-fold, Figure 3.53).

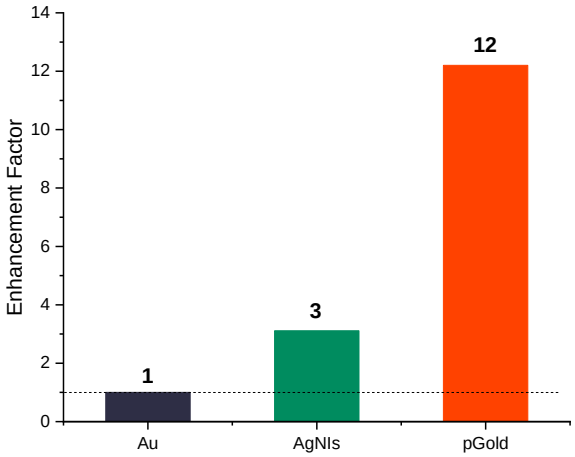


Figure 3.53 – Graph of the enhancement of **Eu_2SAcbisDBM$_3$** luminescence on AgNIs and pGold relative to Au. For **SP_Eu_2SAcbisDBM$_3$@Au** (blue) and **SP_Eu_2SAcbisDBM$_3$@pGold** (orange), λ_{exc} is 350 nm, while for **SP_Eu_2SAcbisDBM$_3$@AgNIs** (teal), λ_{exc} is 390 nm.

As expected, no significant effects on the emission profile of the complex are recorded (Figure 3.80, Appendix). Table 3.8 below reports the ratio of integrals for $^5D_0 \rightarrow {}^7F_J$ Eu(III) transitions relative to the hypersensitive $^5D_0 \rightarrow {}^7F_2$ one. Compared to pGold, the MD $^5D_0 \rightarrow {}^7F_1$ transition is substantially unchanged, further supporting the enhancement mechanisms of the two substrates.

	$^5D_0 \rightarrow {}^7F_0$	**$^5D_0 \rightarrow {}^7F_1$**	**$^5D_0 \rightarrow {}^7F_2$**	**$^5D_0 \rightarrow {}^7F_3$**	**$^5D_0 \rightarrow {}^7F_4$**
Au	0.18	0.73	9.95	0.40	1.00
AgNIs	0.14	0.65	7.84	0.38	1.00

Table 3.8 – Ratio of selected transitions over the $^5D_0 \rightarrow {}^7F_4$ transition (i.e. $^5D_0 \rightarrow {}^7F_J / {}^5D_0 \rightarrow {}^7F_4$) of spin coated **SP_$Eu_2$SAcbisDBM$_3$@Au** and **SP_$Eu_2$SAcbisDBM$_3$@AgNIs**.

Considering the NIR emissive **Nd_2SAcbisDBM$_3$@AgNIs**, a moderate enhancement is observed on the AgNIs substrate (Figure 3.54, **a**). For the calculation of the enhancement factor, we consider again only the $^4F_{3/2} \rightarrow {}^4I_{11/2}$ transition, due to the poor resolution of the other transitions on both substrates. An enhancement factor of 4 is found here, comparable to the one observed for the **SP_Eu_2SAcbisDBM$_3$@AgNIs** surface (3-fold). By comparing the

enhancement factors of **Nd_2SAcbisDBM$_3$** on both AgNIs and pGold substrates, an enormous difference between AgNIs (4-fold) and pGold (64-fold) is recorded (Figure 3.54, **b**).

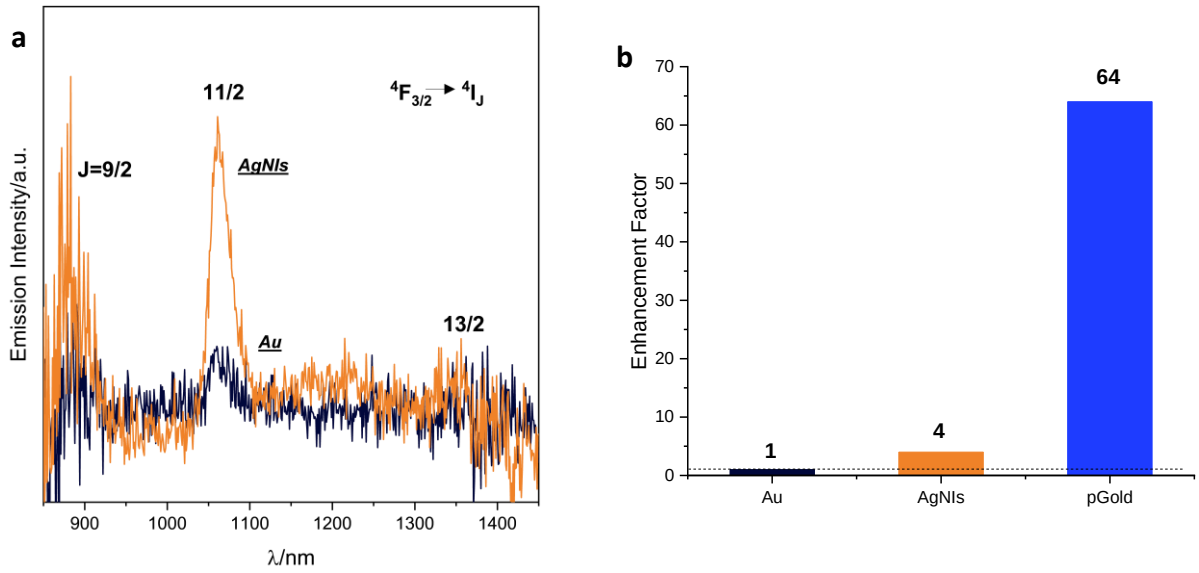


Figure 3.54 – **a** Overlaid emission spectra of **SP_Nd_2SAcbisDBM$_3$@Au** (dark blue, λ_{exc}: 350 nm) and **SP_Nd_2SAcbisDBM$_3$@AgNIs** (orange, λ_{exc}: 390 nm). **b** Graph of the enhancement of **Nd_2SAcbisDBM$_3$** luminescence on AgNIs and pGold relative to Au, calculated considering the $^4F_{3/2}\rightarrow{}^4I_{11/2}$ transition only. For **SP_Nd_2SAcbisDBM$_3$@Au** (dark blue) and **SP_Nd_2SAcbisDBM$_3$@pGold** (light blue), λ_{exc} is 350 nm, while for **SP_Nd_2SAcbisDBM$_3$@AgNIs** (orange), λ_{exc} is 390 nm.

Although not as large with the visible emitting **Eu_2SAcbisDBM$_3$** complex (3-fold versus 12-fold for the complex on AgNIs and pGold, respectively), the pGold surface clearly has a tremendous effect on Nd(III) and Yb(III) luminescence, also reflected in the exceptional resolution of their emission spectra (Figures 3.46 **a** and **b**).The comparison between visible and NIR emissive surfaces gives a further insight in the enhancement mechanisms. The enhancement arising from AgNIs surfaces is independent of the emission range of the emitters and, as the absorption and excitation spectra for both visible and NIR emitting complexes are essentially identical, the enhancement factors are very similar (3-fold vs 4-fold). This is in accordance with a process that only involves the excitation component of the complex's photophysics. On the other hand, the enhancement provided by pGold surfaces solely relies on the emission

processes, so that more impressive enhancements occurs in the NIR region where better spectral overlap is provided (from 12-fold for **SP_Eu$_2$SAcbisDBM$_3$@pGold** to 41- and 64-fold for **SP_Yb$_2$SAcbisDBM$_3$@pGold** and **SP_Nd$_2$SAcbisDBM$_3$@pGold**, respectively).

3.2.8 Polymer assisted deposition of Ln$_2$bisDBM$_3$ complexes on Au surfaces

Having investigated and characterised both Au and plasmonic surfaces coated with surface active thiolated **Ln$_2$SAcbisDBM$_3$** complexes, here we present an alternative approach for the deposition on Au surfaces of unfunctionalized **Ln$_2$bisDBM$_3$** complexes with PANI (Ln=Eu(III), Yb(III) and Nd(III)).

3.2.8.1 Evaluation of the supramolecular assembly of Ln$_2$bisDBM$_3$ and PANI

As described in Chapter 2, the crystal structure of the **Yb$_2$bisDBM$_3$** complex displays a distorted helical conformation, with one of the ligands possessing opposite twist (pink, Figure 3.55, **a**) and the two Yb atoms coordinating to one H_2O or MeOH molecule (here described as Yb^H and Yb^M, respectively). Analysis of the packing in the crystal structure of the complex reveals an extensive hydrogen bonding network (blue dashed lines, Figure 3.55, **a**), mediated by the Yb coordinated solvent molecules and DMF. Due to the presence of coordinating solvent molecules at either side, the ligand with the opposite twist (pink, Figure 3.55, **a**) is significantly involved in the hydrogen bonding network, and we hypothesise that this contributes to the disruption of helicity in the complex. Furthermore, as the same DMF molecule hydrogen bonds with both the MeOH of one complex and the H_2O molecule of another complex, the orientation of the Yb^H-Yb^M axis alternates in space and extensive π-π stacking is observed between complexes with opposite orientation along the Yb^H-Yb^M axis (orange and yellow ligands, Figure 3.55, **b**).

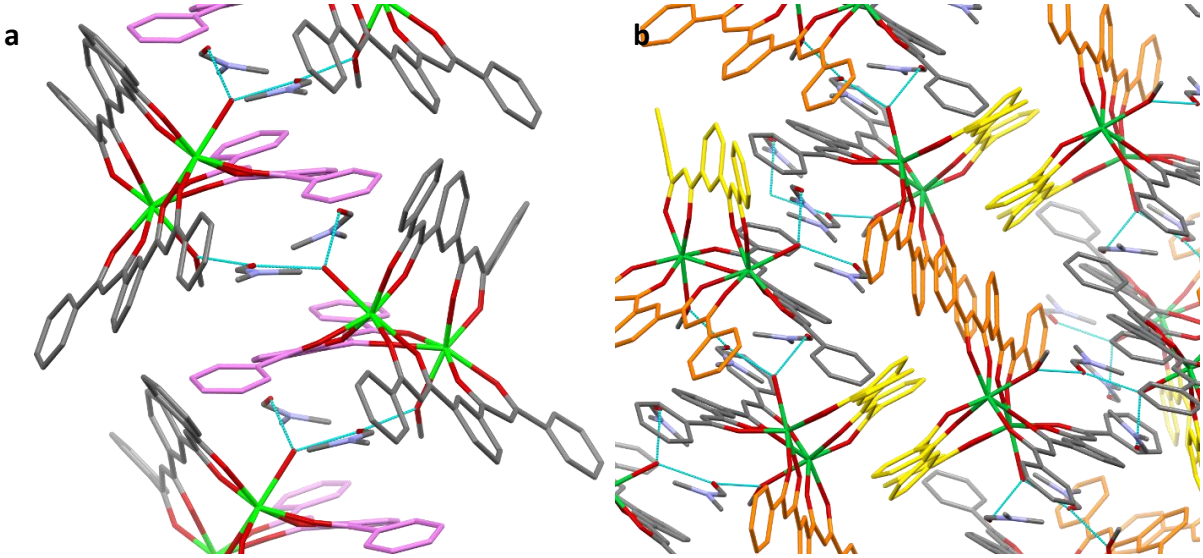


Figure 3.55 – Crystal structure of **Yb_2bisDBM$_3$** displaying the hydrogen bonding network (**a**) and π-π stacking (**b**). These were collected by Dr. Sarah Griffin at the University of Birmingham. The elements colours are as follows: grey – carbon, lilac – nitrogen, yellow – sulphur, red – oxygen and green – ytterbium. For clarity, hydrogen atoms have been omitted.

From this analysis, we suggest that **Ln_2bisDBM$_3$** complexes can form extensive networks and thus participate in supramolecular interactions. To assess a potential interaction between the **Ln_2bisDBM$_3$** complexes and PANI, we employ UV-Vis spectroscopy. As a conjugated polymer, the colours of PANI arise from its tuneable UV-Vis absorption: whereas the π-π* transition below 350 nm is characteristic of all forms containing benzenoid units, the charge transfer (CT, **π_Q-π_B**) absorption above 550 nm is pH and redox sensitive. This is particularly evident in the emeraldine form where, in the change from EB quinoid to ES polaronic semi-quinoids, the CT band shifts accordingly from the characteristic EB 550-750 nm region to the 700-900 nm region for ES.[61]

The ES form of PANI was dispersed by sonication in DMF to give a dark green mixture. Equivalents aliquots of the PANI dispersion were added to DMF, as control, and to 1 mM solutions of **$EuCl_3 \cdot 6H_2O$**, **bisDBM**, **Eu_2bisDBM$_3$** and **EuDBM$_3$** in DMF. Prior to addition of PANI, all five solutions were transparent and colourless. As can be observed from the photograph in Figure 3.56, upon addition of PANI, a precipitate is present in all mixtures and is attributed to

the poor dispersion of the polymer in absence of sonication. However, the **EuDBM$_3$**+PANI mixture develops a very weak blue colour, while an intense deep blue shade is observed for the **Eu$_2$bisDBM$_3$**+PANI sample (Figure 3.56, second to last).

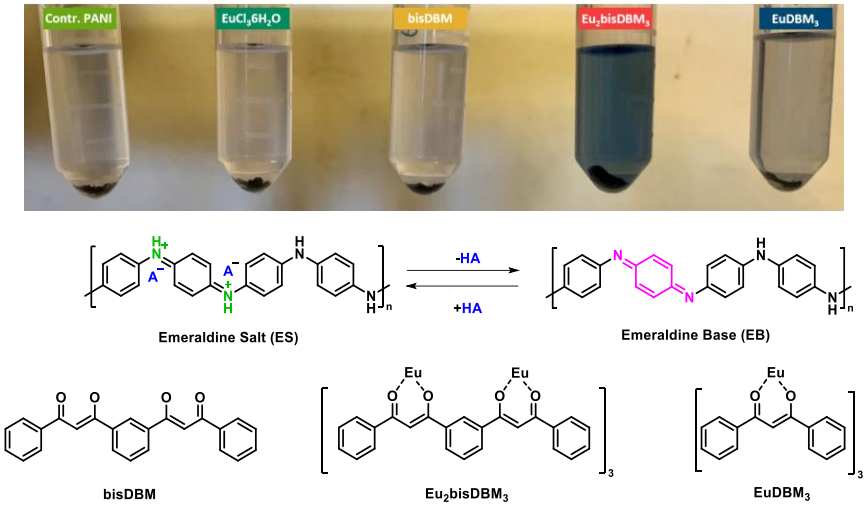


Figure 3.56 – Photograph of Eppendorf vials containing DMF (far left) or 1 mM solutions in DMF of (from second left to right): **EuCl$_3$·6H$_2$O**, **bisDBM**, **Eu$_2$bisDBM$_3$** and **EuDBM$_3$** after the addition of equivalent aliquots of the ES PANI dispersion. Below are reported the chemical structures of the ligand and complexes, as well as the ES and EB forms of PANI.

To consider the fraction of polymer that is well dispersed, the mixtures were centrifuged and the supernatant analysed by UV-Vis spectroscopy. As can be seen in the spectra in Figure 3.57, only the **Eu$_2$bisDBM$_3$**+PANI and **EuDBM$_3$**+PANI mixtures display intense absorption bands in the 420-800 nm range (Figure 3.57, **a**). Strong absorption at 630 nm is observed for the **Eu$_2$bisDBM$_3$**+PANI supernatant (pink, Figure 3.57, **a**), which is attributed to the charge transfer (CT) quinoid exciton π_B-π_Q of the EB form. Concentration dependence is observed upon addition of equivalents amounts of ES PANI to 0.01 mM, 0.5 mM and 1 mM solutions of **Eu$_2$bisDBM$_3$** in DMF (Figure 3.57, **b**), with the observation of a linear increase in intensity of the PANI CT band at 630 nm (R^2>0.99, inset of Figure 3.57, **b** and Table 3.11, Appendix). The benzenoid units of PANI absorb light below 350 nm, with a maximum around 330 nm. Due to the strong absorption of the complex in that region, it is not possible to identify any of these

bands and we do not report them here. The CT band at 630 nm is also observed in the absorption spectrum of the **EuDBM$_3$**+PANI mixture (blue, Figure 3.57, **a**). However, this is considerably less intense (over 3-fold) than for **Eu$_2$bisDBM$_3$**+PANI, in accordance with the weaker colour observed by eye, and indicating that less polymer is present in the supernatant.

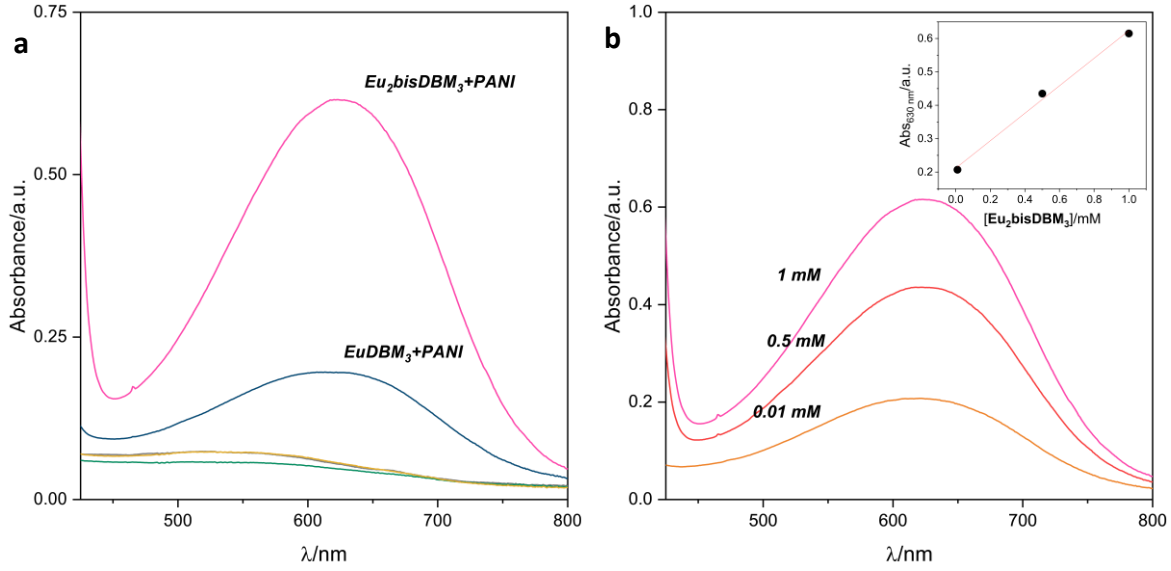


Figure 3.57 – **a** Absorption spectra of the supernatants retrieved after addition of equivalents aliquots of ES PANI and centrifugation in DMF (grey) and 1 mM solutions in DMF of **EuCl$_3$·6H$_2$O** (green), **bisDBM** (yellow), **Eu$_2$bisDBM$_3$** (pink) and **EuDBM$_3$** (blue). **b** Absorption spectra of the supernatants retrieved after addition of equivalents aliquots of ES PANI and centrifugation to 1 mM (pink), 0.5 mM (red) and 0.01 mM (orange) solutions of **Eu$_2$bisDBM$_3$** in DMF. The inset is the plot of the absorbance at 630 nm versus concentration of **Eu$_2$bisDBM$_3$** in DMF.

From these results, we conclude that the investigated Eu(III) β-diketone complexes drive the conversion of ES PANI to its EB form, promoting its dispersion in DMF. This effect is not observed for the bisDBM ligand or the Eu(III) salt alone, indicating that it arises solely from an interaction with the structures of the complexes. As PANI reportedly forms assemblies by π-π stacking, we believe such interactions could be at the basis of our observations. Furthermore, as a significant difference is found between the dinuclear **Eu$_2$bisDBM$_3$** complex and the mononuclear **EuDBM$_3$**, it is deduced that the more rigid geometry of the dinuclear complex,

as well as its extended aromatic structure, promote interactions with PANI and result in the higher absorbance and dispersion of the polymer.

3.2.8.2 Luminescence of Au surfaces coated with Ln_2bisDBM$_3$ complexes and PANI

Au surfaces can be a substrate for the investigation of potential **Ln_2bisDBM$_3$**-PANI assemblies formed in solution. Here, we employ two coating methodologies, namely dip coating and spin coating. Spin coating is selected as a highly reproducible method for the formation of thin films on the surface, while dip coating is believed to encourage the deposition of assemblies and more accurately reflect the events in the solution state.

In the first approach, the Au surface is first dip coated in an ES PANI dispersion to produce **PANI@Au**, followed by dip coating in 1 mM solutions of **Ln_2bisDBM$_3$** in DMF (i.e. **Ln_2bisDBM$_3$_PANI@Au**). In the second approach, a layer of ES PANI is first spin coated on the Au surface, followed by a second layer of **Ln_2bisDBM$_3$** (**SP_Ln_2bisDBM$_3$_PANI@Au**). Alternatively, a mixture of **Ln_2bisDBM$_3$**+PANI is spin coated on the Au surface (**SP_Ln_2bisDBM$_3$+PANI@Au**).

Upon excitation at 350 nm, all three **Eu_2bisDBM$_3$_PANI@Au**, **SP_Eu_2bisDBM$_3$_PANI@Au** and **SP_Eu_2bisDBM$_3$+PANI@Au** surfaces display well resolved Eu(III) luminescence, with the $^5D_0 \rightarrow {}^7F_J$ (ΔJ=0-4) transitions identified at the characteristic wavelengths (i.e. 578 nm, 592 nm, 611 nm, 652 nm and 695 nm, respectively, Figure 3.58). This indicates that the energy transfer processes from the **bisDBM** units are maintained in the presence of PANI. The luminescence lifetime of all three surfaces displays a multiexponential decay (Table 3.16, Appendix), ascribed to the quenching arising from the Au surface, and, considering the longer component (200±20

μs, including standard deviation between samples), no significant differences from the luminescence lifetime of **Eu_2bisDBM$_3$** in DMF are recorded (i.e. 220 μs).

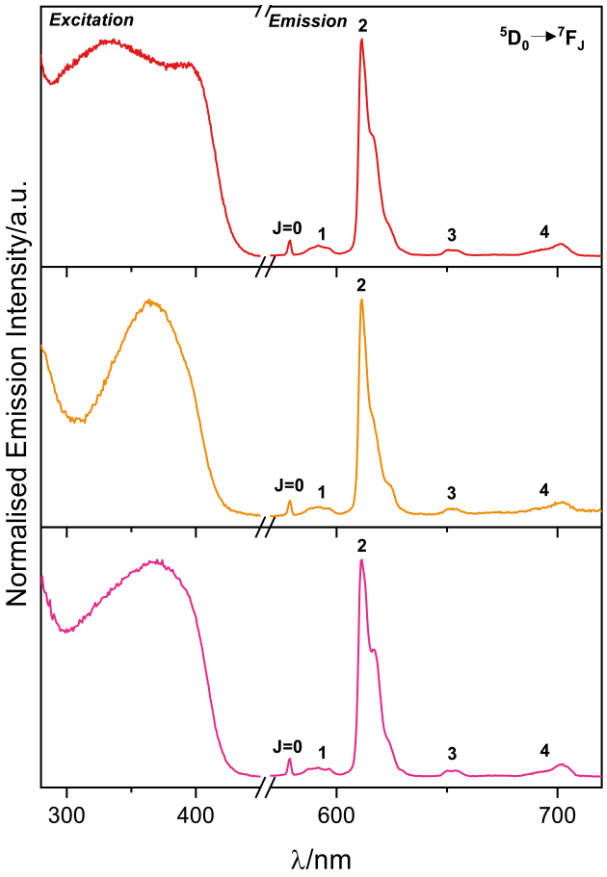


Figure 3.58 – Excitation (left) and emission (right) spectra of **Eu_2bisDBM$_3$_PANI@Au** (top, red), **SP_Eu_2bisDBM$_3$_PANI@Au** (middle, yellow) and **SP_Eu_2bisDBM$_3$+PANI@Au** (bottom, pink). λ_{exc}: 350 nm, λ_{em}: 611 nm.

The excitation spectrum of **SP_Eu_2bisDBM$_3$_PANI@Au** (yellow in Figure 3.58) displays a small red shift from the maximum of the complex in DMF (365 nm versus 359 nm, respectively). Significant broadening of the band, however, is observed for both the dip coated **Eu_2bisDBM$_3$_PANI@Au** and spin coated **SP_Eu_2bisDBM$_3$+PANI@Au** (red and pink in Figure 3.58). The excitation of **Eu_2bisDBM$_3$_PANI@Au**, in particular, displays two peak components at 330 nm and 400 nm. As the ES and EB forms of PANI reportedly absorb light at 330 nm, both the broadening of **SP_Eu_2bisDBM$_3$+PANI@Au** to cover this region, as well as the excitation component of **Eu_2bisDBM$_3$_PANI@Au** at 330 nm, indicate that the polymer could be involved

in the energy transfer processes.[61] It is worth mentioning, however, that similar band broadenings and shifts have been previously reported for lanthanide(III) β-diketonate complexes in the solid state and attributed to aggregation of complexes.[100-102]

Well resolved NIR emission could be detected from both dip coated **Yb_2bisDBM$_3$_PANI@Au** and **Nd_2bisDBM$_3$_PANI@Au** surfaces, upon excitation at 350 nm. Here, the $^4F_{5/2}\rightarrow{}^2F_{7/2}$ transition of Yb(III) was identified at 977 nm (Figure 3.59, **a**), while the Nd(III) $^4F_{3/2}\rightarrow{}^4I_J$ (ΔJ=9/2, 11/2, 13/2) transitions were observed at the characteristic 888, 1060 and 1355 nm wavelengths (Figure 3.59, **b**). The **Yb_2bisDBM$_3$** complex was also spin coated with PANI, and well resolved emission was recorded for both **SP_Yb_2bisDBM$_3$_PANI@Au** and **SP_Yb_2bisDBM$_3$+PANI@Au** surfaces (Figures 3.82 and 3.83, Appendix), indicating that all three methods can produce NIR emitting Au surfaces.

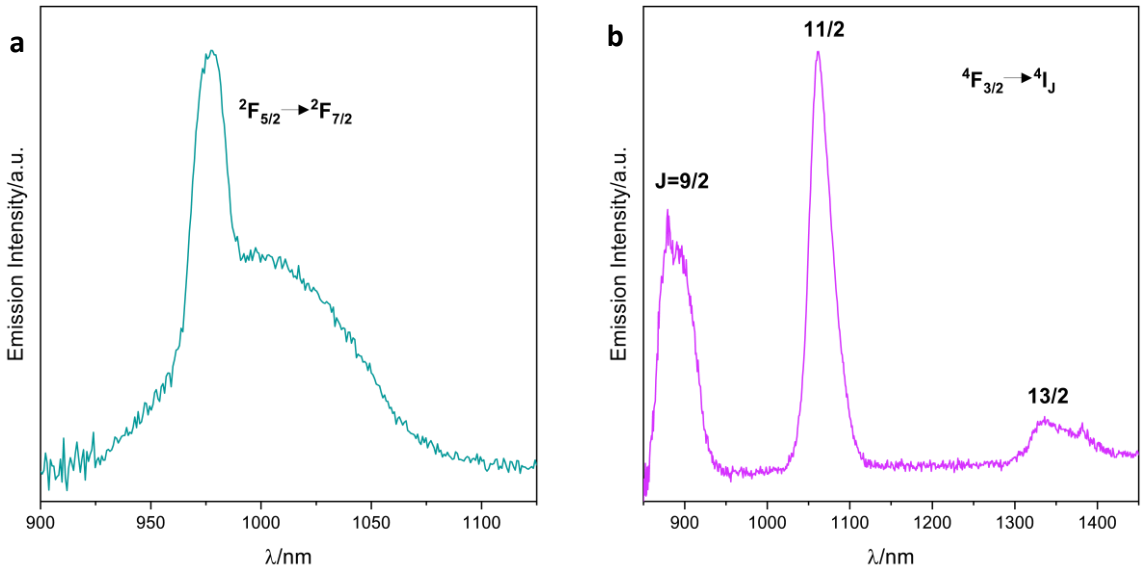


Figure 3.59 – Emission spectra of **Yb_2bisDBM$_3$_PANI@Au** (**a**) and **Nd_2bisDBM$_3$_PANI@Au** (**b**). λ_{exc}: 350 nm.

3.2.8.3 Morphology and characterisation of the surfaces

The prepared surfaces were first characterised by Raman spectroscopy. Owing to their "fingerprint" Raman peaks and vibrational modes, the redox and doping states of PANI are routinely monitored by Raman spectroscopy.[61] Only an extremely weak signal was recorded for the spin coated surfaces (Figure 3.121, Appendix), thus not allowing for interpretation of the spectra. On the other hand, the dip coated **Eu_2bisDBM$_3$_PANI@Au** surface displayed well resolved Raman peaks and the spectrum was compared to the one of **PANI@Au** (i.e. the surface prior to immersion in the **Ln_2bisDBM$_3$** solution) and ES PANI employed for coating. As can be seen in Figure 3.60, the spectrum of **PANI@Au** matches well with the one of ES PANI. Specifically, the bands at 1333 cm^{-1} and 1375 cm^{-1} are characteristic of C-$N^{+\cdot}$ vibrations, solely present in the delocalised polaronic structures of the ES form.[61] In the spectrum of **Eu_2bisDBM$_3$_PANI@Au**, no peaks belonging to the **Eu_2bisDBM$_3$** complex can be identified. Furthermore, the C-$N^{+\cdot}$ bands are extremely weak, indicating a significant loss of the polymer doped state. The spectrum is dominated by the quinoid stretching at 1463 cm^{-1}, which is characteristic of the EB form of PANI. This is in agreement with the conclusions drawn from the absorption spectra of **Eu_2bisDBM$_3$**-PANI in section 3.2.8.1 (Figure 3.57), where the characteristic absorption of EB PANI was observed and it was suggested that **Eu_2bisDBM$_3$** could drive the conversion from ES to EB in DMF.

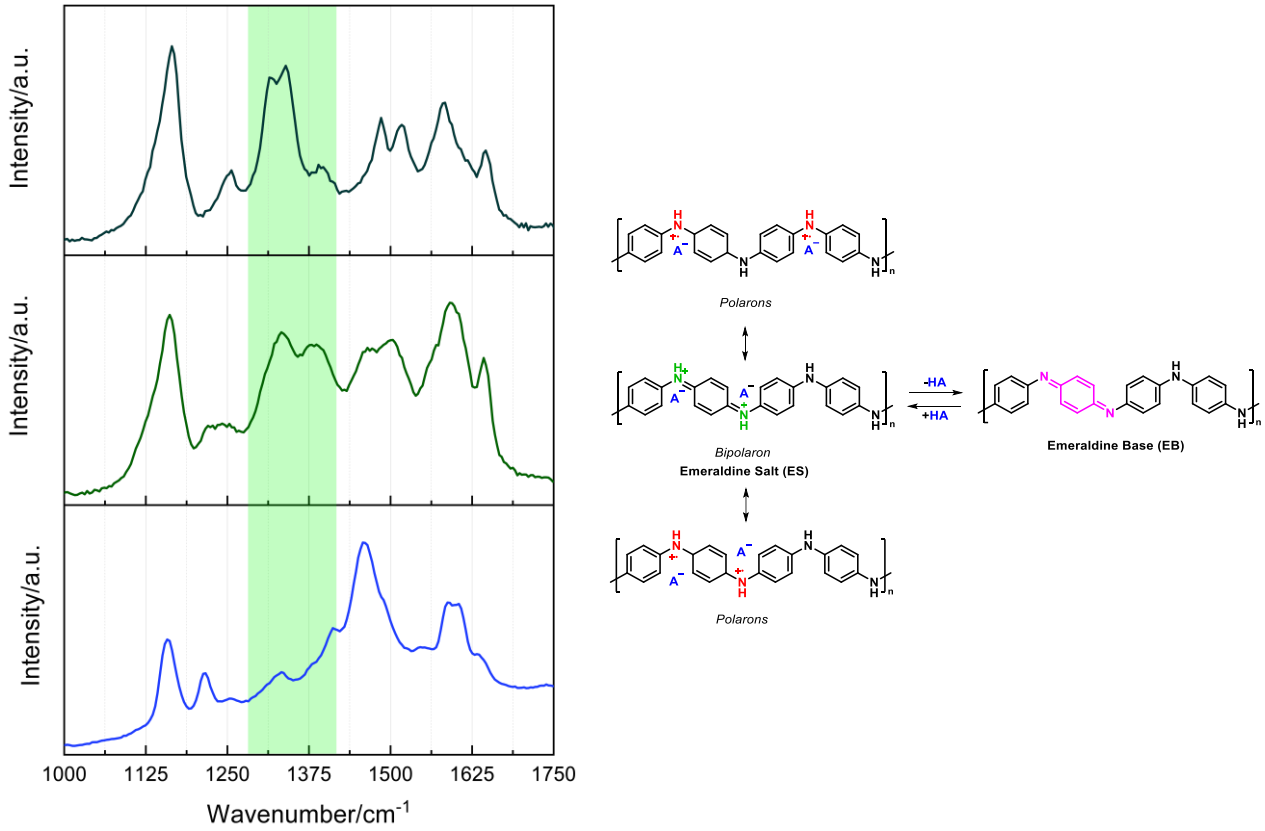


Figure 3.60 – Stacked Raman spectra of PANI ES as powder (top, dark green), **PANI@Au** (middle, green) and **Eu_2bisDBM$_3$_PANI@Au** (bottom, blue). Laser excitation λ: 633 nm. On the right are reported the chemical structures of the ES and EB forms of PANI.

SEM imaging of the dip coated **Yb_2bisDBM$_3$_PANI@Au** surface revealed the presence of extended and fibre-like features on the substrate (>10 µm, Figure 3.61, **b**), while a different morphology was observed for the **PANI@Au** surface, with granular and irregular assemblies (>3 µm, Figure 3.61, **a**). In an attempt to simulate the conditions for the **Yb_2bisDBM$_3$** coating step, the **PANI@Au** surface was immersed in DMF overnight. Upon examination of the respective SEM image (Figure 3.113, Appendix), large and flat features were found, unlike the ones observed in Figure 3.61, **b**. This revealed that the structures observed on the **Yb_2bisDBM$_3$_PANI@Au** surface were due to the presence of the complex in the coating solution, and not from the long immersion time or the solvent itself.

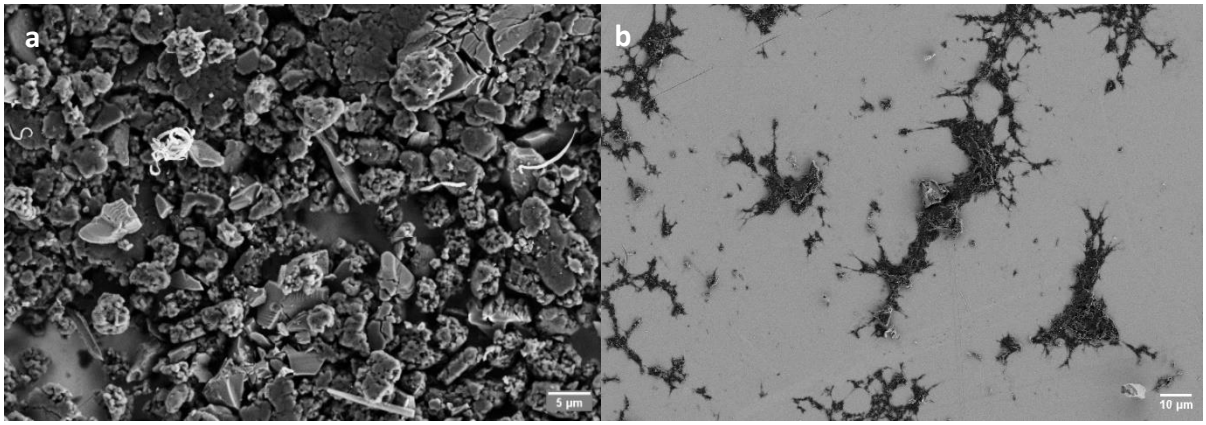


Figure 3.61 – SEM images of **PANI@Au** (**a**) and **Eu_2bisDBM$_3$_PANI@Au** (**b**). The images were obtained by Sigrid Benemann at BAM.

EDX analysis of **PANI@Au** indicated the presence of carbon and nitrogen, backbones of the polymer, at 277 eV and 392 eV, respectively (Figure 3.115, Appendix). The presence of sulfur and oxygen Kα peaks at 2.31 keV and 525 eV, respectively, was ascribed to the doping sulfonic acid used to produce ES PANI. This confirmed the observation from the Raman spectrum (Figure 3.60) that the ES form of PANI is the one found in **PANI@Au**.

As expected for the presence of the complex on the surface, Yb was detected in the EDX spectrum of **Yb_2bisDBM$_3$_PANI@Au**, as well as in its EDX mapping (Figures 3.114, Appendix, and Figure 3.62), with the Mα peak observed at 1.52 keV. However, no sulfur Kα peak was detected at 2.31 keV. This is in accordance with the loss of doping agent and formation of EB PANI, as indicated by the Raman spectrum of **Eu_2bisDBM$_3$_PANI@Au** (Figure 3.60).

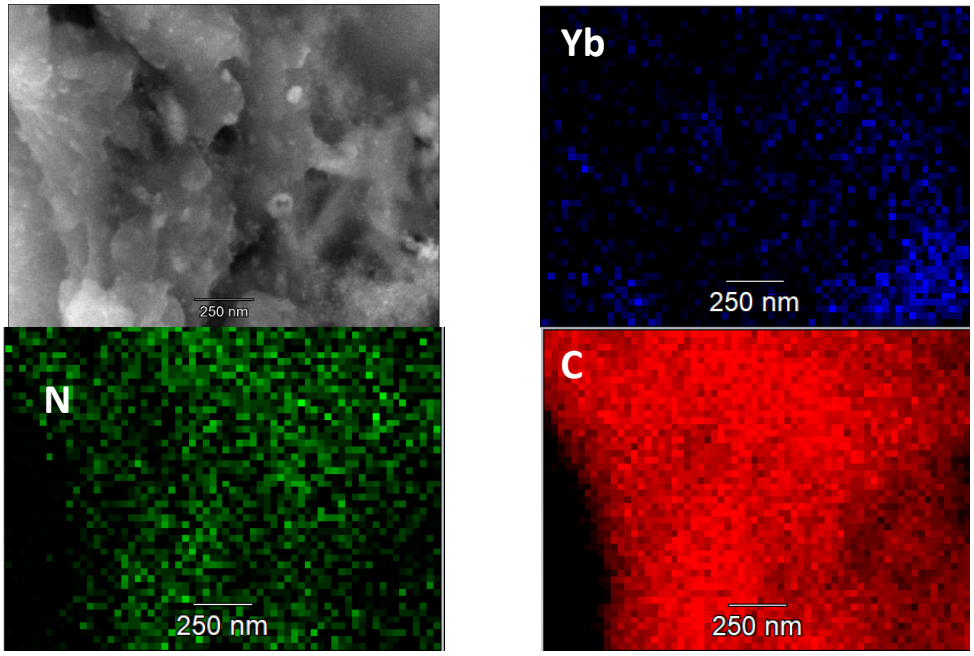


Figure 3.62 – SEM image of **Yb_2bisDBM$_3$_PANI@Au** with respective EDX mapping of the imaged area of **Yb_2bisDBM$_3$_PANI@Au**. The blue colour represents Yb, green is nitrogen and red is carbon. The data were obtained by Sigrid Benemann at BAM.

For the large (>1 µm) assemblies attributed to PANI, no significant differences were observed in the SEM images of the spin coated **SP_Eu_2bisDBM$_3$_PANI@Au** and **SP_Eu_2bisDBM$_3$+PANI@Au** surfaces (Figures 3.63, **a** and **c**). However, the spin coated **SP_Eu_2bisDBM$_3$+PANI@Au** surface prepared by mixing PANI and **Eu_2bisDBM$_3$** also contained small clusters (52±9 nm) on the polymer assemblies (yellow circle in Figure 3.63, **b**). EDX analysis confirmed the presence of Eu in the features (Mα peak at 1.14 keV, Figure 3.116, Appendix), indicating that the **Eu_2bisDBM$_3$** complex assembled in such geometries upon mixing with PANI and spin coating on the surface. By comparison, only sparse and branched features were attributed by EDX to the **Eu_2bisDBM$_3$** complex in the SEM image of **SP_Eu_2bisDBM$_3$_PANI@Au** (Figure 3.63, **d**).

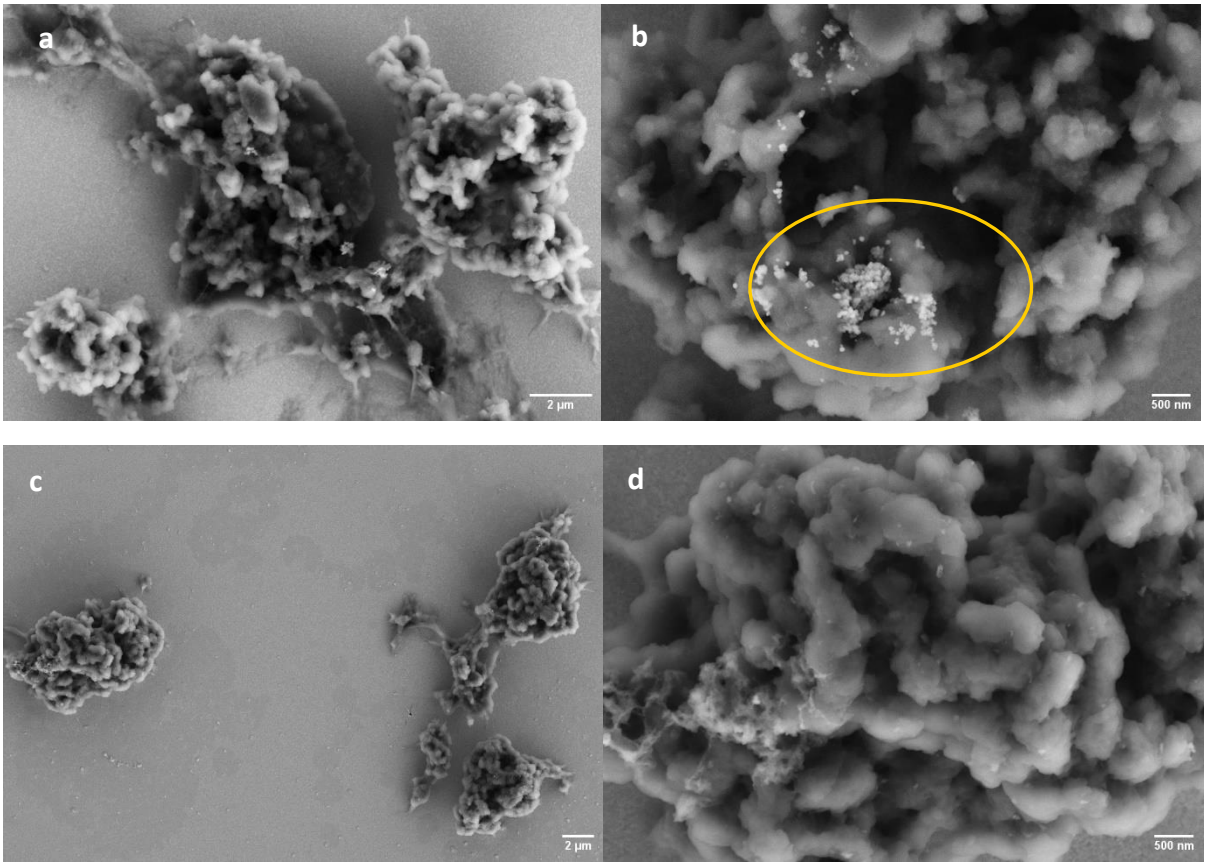


Figure 3.63 – SEM images of **SP_Eu$_2$bisDBM$_3$+PANI@Au** (**a**, **b**) and **SP_Eu$_2$bisDBM$_3$_PANI@Au** (**c**, **d**). The images were obtained by Sigrid Benemann at BAM.

These results indicated that, by combining **Ln$_2$bisDBM$_3$** complexes and PANI, the resulting morphology and assembly on Au surfaces could be affected, regardless of the coating method. **Ln$_2$bisDBM$_3$** complexes were also found to determine the doping state of the polymer, driving the formation of the EB PANI form. As no indication of polymer coordination to the lanthanide(III) was found, we ascribe these effects to hydrophobic interactions in solution, which are translated in the properties of the observed assemblies on the Au surface. Finally, epifluorescence images of **SP_Eu$_2$bisDBM$_3$+PANI@Au**, as a representative surface, were obtained (Figure 3.85, Appendix, and 3.64, **a**). The observed luminescent spots were found to be grouped in small assemblies with diameter ≈1 µm (Figure 3.64, **a**) and correlating well with the AFM images of the surface (Figure 3.64, **b**, and Figure 3.117, Appendix, for larger area). In the steady state emission spectrum of the imaged areas it was possible to clearly identify the

intense $^5D_0 \rightarrow {}^7F_2$ transition (Figure 3.64, **c**), indicating that the small assemblies observed in the epifluorescence images of Figure 3.64, **a**, arise from the **Eu_2bisDBM$_3$** complex luminescence.

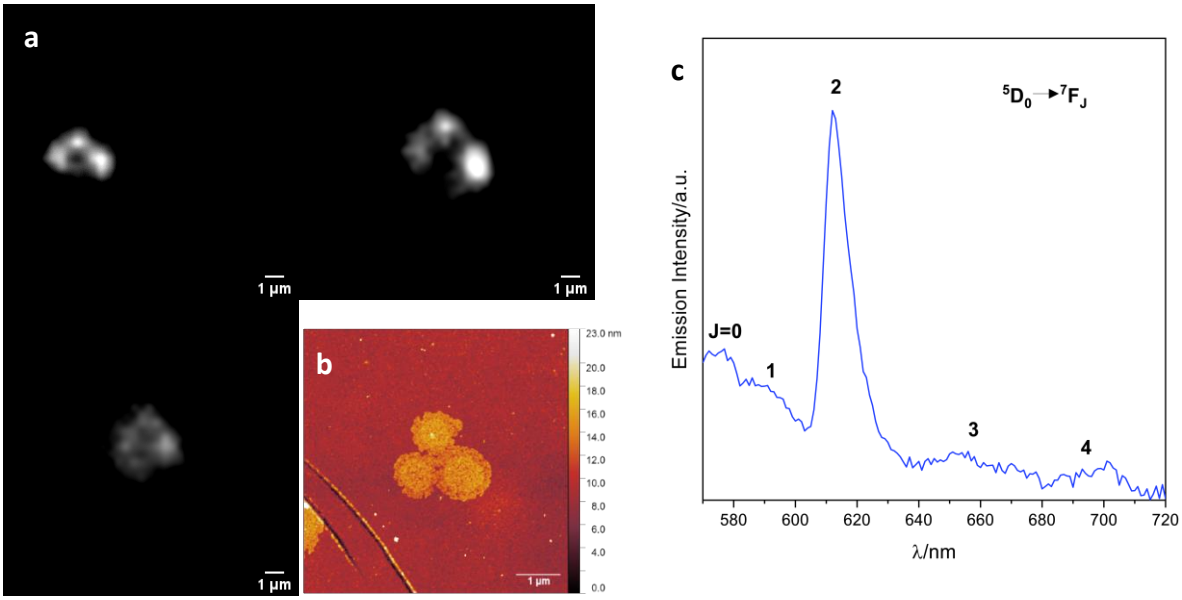


Figure 3.64 – Areas of the epifluorescence image and AFM image of **SP_Eu_2bisDBM$_3$+PANI@Au** (**a**, **b**) with respective emission spectrum (**c**). λ_{exc}: 350 nm. The AFM image was obtained by Dr. Simon Connell and Dr. Pallavi Kumari at the School of Physics and Astronomy at the University of Leeds.

3.3 Conclusions and future studies

In this chapter we have presented the incorporation of surface active **Ln_2SAcbisDBM$_3$** complexes to Au and plasmonic surfaces, as well as the assembly of unfunctionalized visible and NIR emitting **Ln_2biDBM$_3$** complexes and PANI on Au surfaces.

First, we investigated the properties of **Ln_2SAcbisDBM$_3$@Au** surfaces coated by immersion in the **Ln_2SAcbisDBM$_3$** solution overnight. SEM and AFM imaging of the surfaces have revealed a multi-layered assembly of complexes on the Au substrates, possibly promoted by the presence of multiple surface active units in the molecular structure and the low solubility of **Ln_2SAcbisDBM$_3$** complexes. Furthermore, the **Eu_2SAcbisDBM$_3$@Au** surfaces were tested for F^- sensing. The recognition of different concentrations of F^- in THF solutions has thus been achieved by monitoring the luminescence lifetime of the surfaces, which displayed considerable reproducibility over triplicate repeats. A time-resolved sensing readout is particularly advantageous for solid samples, as it does not rely on a variation of emission intensity, which is instead more prone to errors in the solid state. XPS analysis of **Eu_2SAcbisDBM$_3$@Au-F** (i.e. after immersion in a 15 µM F^- solution) has confirmed the presence of F species on the surface. The atomic ratios have revealed that a 1:2 ratio (F:Eu) is present and the Eu-F interaction has been identified by analysis of the high resolution F 1s peak. Furthermore, co-localisation of Eu and F has been confirmed by SEM/EDX analysis of the features observed on the surface.

In the second part, the effects of both Au and Ag nanostructured substrates (i.e. pGold and AgNIs) were explored and compared. pGold was found to provide exceptional enhancement factors for NIR emitting complexes, in particular (up to 64-fold for the Nd(III) complex). To our

knowledge, this is the first example of plasmonic enhancement of a NIR emitting complex by direct coating on the surface and without a dielectric spacing layer.

The effect of pGold on the visible emitting **Eu_2SAcbisDBM$_3$** complex has been investigated to elucidate the enhancement process. In addition to the expected decrease in lifetime and increase in emission intensity associated with the Purcell effect, the emission profile of the surface is also altered. The **Eu_2SAcbisDBM$_3$** complex acts here as a probe, indicating a strong interaction with the electric component of the focused field and resulting in higher enhancements of the ED transitions. Raman spectroscopy is an optimal tool for the further analysis of the **SP_Eu_2SAcbisDBM$_3$@pGold** surface. A moderate SERS enhancement has indeed been observed, alongside the variation of peak intensities and wavenumbers, given by the presence of the complex in the gaps.

The comparison of pGold enhancement with the effects of AgNIs surfaces has provided an excellent platform for the further assessment of the plasmonic processes of both materials. Indeed, whereas the NIR enhancement factors on pGold are impressive (41- and 64-fold for the Yb(III) and Nd(III) **Ln_2SAcbisDBM$_3$** complexes, respectively) the one of the **SP_Nd_2SAcbisDBM$_3$@AgNIs** surface is significantly lower (4-fold). Furthermore, this is found to be analogous to the one of the visible emitting **SP_Eu_2SAcbisDBM$_3$@AgNIs** surface, emphasizing the independence of the AgNIs enhancement mechanism from any emission processes.

By comparing the two substrates, pGold and AgNIs, we find that pGold provides a significantly better enhancing platform for visible and NIR emitting complexes. Additionally, despite the ease of preparation of AgNIs surfaces, their storage is limited to a maximum of a month due to the lower stability of Ag compared to Au, reducing their shelf life.

In a third and final section, unfunctionalized **Ln_2bisDBM$_3$** complexes and the conjugated polymer PANI were assembled on Au surfaces. By UV-Vis spectroscopy, it was determined that the bis β-diketonate **Eu_2bisDBM$_3$** complex was able to induce the conversion from ES PANI to the EB PANI form in DMF. The Au surface dip coated in ES PANI and **Ln_2bisDBM$_3$** was studied with both Raman spectroscopy and SEM/EDX. It was confirmed that the coating step with the complex would drive the formation of ES PANI and removal of doping agent, with the concurrent variation of the polymer morphology on the surface. Furthermore, spin coating of PANI and **Eu_2bisDBM$_3$** on Au resulted in the detection of different morphologies for the complex on the polymer assemblies, depending on whether the two components were coated in a layer by layer approach or as a mixture. Importantly, all investigated surfaces displayed well resolved emission in both the visible and NIR regions, thus combining the optical properties of the lanthanides(III) with the functionality and relevance of a polymer such as PANI. Further studies should concern the study of the resulting electric and mechanical properties of PANI in the prepared surfaces, advancing the studied assemblies to applications in optoelectronics or sensing.

Impressive luminescence enhancements have been described here by means of plasmonic surfaces. Further studies should concern the modulation of the spacer length between emitter and nanostructures, allowing for an estimation of the optimal distance with **Ln_2SAcbisDBM$_3$** complexes. Reportedly, quenching processes are predominant at short distances (< 5 nm), although strong enough enhancement at hot spots have been found to overcome such short distance quenching.[103] Nonetheless, the design of our synthesis allows for the facile interchange with different spacers by click chemistry, without the development of a novel synthetic route. Furthermore, by avoiding the presence of polymer spacing layers as reported

in most examples, the nanostructure is fully exposed. This is extremely useful for the preparation of sensing platforms, as a multimodal readout can be obtained from both the emitter's luminescence and changes to the plasmon resonance of the exposed nanostructures. As the **Eu_2SAcbisDBM$_3$** complex has displayed the capability of sensing F^- on an Au surface, the **SP_Eu_2SAcbisDBM$_3$@pGold** surfaces should be tested for the detection of F^-. Furthermore, we have shown how the resolution and optical properties of **Eu_2SAcbisDBM$_3$** luminescence are wholly preserved on the pGold surface, whereas the low signal arising from **SP_Eu_2SAcbisDBM$_3$@Au** surfaces can, in some cases, prevent this. Our system has thus excellent potential for such sensing applications, where the fine modulation of the emission profile or lifetime of the complex are found to be an excellent readout. This potential is further strengthened by the impressive NIR luminescence of pGold samples, where such high signal and resolution are essential to advance the applications of lanthanides(III) NIR light. Finally, as both Ag and Au nanostructured surfaces have displayed visible and NIR emission enhancements, the combination of both elements in a single material could amplify the magnitude of such enhancement. Indeed, Ag/Au alloys would offer at least two plasmon peaks or a broader plasmon peak, with the possibility of overlap with both excitation and emission of the complexes.[104]

3.4 References

1. S. Ramachandra, K. C. Schuermann, F. Edafe, P. Belser, C. A. Nijhuis, W. F. Reus, G. M. Whitesides and L. De Cola, *Inorganic Chemistry*, 2011, **50**, 1581-1591.
2. A. Schramm, C. Stroh, K. Dössel, M. Lukas, M. Fischer, F. Schramm, O. Fuhr, H. v. Löhneysen and M. Mayor, *European Journal of Inorganic Chemistry*, 2013, **2013**, 70-79.
3. K. C. F. Toledo and J. A. Bonacin, *Inorganic Chemistry Communications*, 2019, **99**, 52-59.
4. R. Cao, A. M. Díaz-García and R. Cao, *Coordination Chemistry Reviews*, 2009, **253**, 1262-1275.
5. S. J. Adams, A. J. Carrod, L. A. Rochford, M. Walker and Z. Pikramenou, *ChemistrySelect*, 2018, **3**, 3251-3257.
6. S. J. Adams, D. J. Lewis, J. A. Preece and Z. Pikramenou, *ACS Applied Material & Interfaces*, 2014, **6**, 11598-11608.
7. N. S. Murray, S. P. Jarvis and T. Gunnlaugsson, *Chemical Communications*, 2009, 4959-4961.
8. J. Lehr, J. Bennett, M. Tropiano, T. J. Sorensen, S. Faulkner, P. D. Beer and J. J. Davis, *Langmuir*, 2013, **29**, 1475-1482.
9. J. Lehr, M. Tropiano, P. D. Beer, S. Faulkner and J. J. Davis, *Chemical Communications*, 2015, **51**, 6515-6517.
10. A. Mulas, G. V. Dubacheva, H. Al Sabea, F. Miomandre, J. F. Audibert, L. Norel, S. Rigaut and C. Lagrost, *Langmuir*, 2019, **35**, 13711-13717.
11. L. Gu, K. Wen, Q. Peng, W. Huang and J. Wang, *Small*, 2020, **16**, 2001861.
12. M. A. Fusella, R. Saramak, R. Bushati, V. M. Menon, M. S. Weaver, N. J. Thompson and J. J. Brown, *Nature*, 2020, **585**, 379-382.
13. O. S. Ojambati, W. M. Deacon, R. Chikkaraddy, C. Readman, Q. Lin, Z. Koczor-Benda, E. Rosta, O. A. Scherman and J. J. Baumberg, *ACS Photonics*, 2020, **7**, 2337-2342.
14. N. Hildebrandt, M. Lim, N. Kim, D. Y. Choi and J.-M. Nam, *Chemical Communications*, 2023, **59**, 2352-2380.
15. M. L. Aulsebrook, B. Graham, M. R. Grace and K. L. Tuck, *Coordination Chemistry Reviews*, 2018, **375**, 191-220.
16. N. Kwon, D. Kim, K. M. K. Swamy and J. Yoon, *Coordination Chemistry Reviews*, 2021, **427**, 213581.
17. Y. Ning, M. Zhu and J.-L. Zhang, *Coordination Chemistry Reviews*, 2019, **399**, 213028.
18. X. Qin, A. N. Carneiro Neto, R. L. Longo, Y. Wu, O. L. Malta and X. Liu, *The Journal of Physical Chemistry Letters*, 2021, **12**, 1520-1541.
19. J. Liu, Q. Wang, X. Sang, H. Hu, S. Li, D. Zhang, C. Liu, Q. Wang, B. Zhang, W. Wang and F. Song, *Nanomaterials*, 2021, **11**, 1037.
20. P. Singh, S. Kachhap, P. Singh and S. K. Singh, *Coordination Chemistry Reviews*, 2022, **472**, 214795.
21. S. J. Kwon, G. Y. Lee, K. Jung, H. S. Jang, J.-S. Park, H. Ju, I. K. Han and H. Ko, *Advanced Materials*, 2016, **28**, 7899-7909.

22. A. Vaskin, S. Mashhadi, M. Steinert, K. E. Chong, D. Keene, S. Nanz, A. Abass, E. Rusak, D.-Y. Choi, I. Fernandez-Corbaton, T. Pertsch, C. Rockstuhl, M. A. Noginov, Y. S. Kivshar, D. N. Neshev, N. Noginova and I. Staude, *Nano Letters*, 2019, **19**, 1015-1022.
23. B. Kalinic, T. Cesca, I. G. Balasa, M. Trevisani, A. Jacassi, S. A. Maier, R. Sapienza and G. Mattei, *ACS Photonics*, 2023, **10**, 534-543.
24. D. Genchi, B. Kalinic, I. G. Balasa, T. Cesca and G. Mattei, *Materials*, 2022, **15**, 4923.
25. D. G. Baranov, R. S. Savelev, S. V. Li, A. E. Krasnok and A. Alù, *Laser & Photonics Reviews*, 2017, **11**, 1600268.
26. C. Ernandes, H.-J. Lin, M. Mortier, P. Gredin, M. Mivelle and L. Aigouy, *Nano Letters*, 2018, **18**, 5098-5103.
27. J.-C. G. Bünzli, *European Journal of Inorganic Chemistry*, 2017, **2017**, 5058-5063.
28. H. Peng, S. Li, J. Xing, F. Yang and A. Wu, *Journal of Materials Chemistry B*, 2023, **11**, 5238-5250.
29. X. Chen, W. Xu, L. Zhang, X. Bai, S. Cui, D. Zhou, Z. Yin, H. Song and D.-H. Kim, *Advanced Functional Materials*, 2015, **25**, 5462-5471.
30. F. Kang, J. He, T. Sun, Z. Y. Bao, F. Wang and D. Y. Lei, *Advanced Functional Materials*, 2017, **27**, 1701842.
31. D. Yin, C. Wang, J. Ouyang, X. Zhang, Z. Jiao, Y. Feng, K. Song, B. Liu, X. Cao, L. Zhang, Y. Han and M. Wu, *ACS Applied Materials & Interfaces*, 2014, **6**, 18480-18488.
32. Y. Qin, Z. Dong, D. Zhou, Y. Yang, X. Xu and J. Qiu, *Optical Materials Express*, 2016, **6**, 1942-1955.
33. K. Aslan, M. Wu, J. R. Lakowicz and C. D. Geddes, *Journal of the American Chemical Society*, 2007, **129**, 1524-1525.
34. J. Zhang, Y. Fu, K. Ray, Y. Wang and J. R. Lakowicz, *The Journal of Physical Chemistry C*, 2013, **117**, 9372-9380.
35. J. Zhang, K. Ray, Y. Fu and J. R. Lakowicz, *Chemical Communications*, 2014, **50**, 9383-9386.
36. W. Deng, D. Jin, K. Drozdowicz-Tomsia, J. Yuan, J. Wu and E. M. Goldys, *Advanced Materials*, 2011, **23**, 4649-4654.
37. Y. Zhao, A. Wang, J. Kang, H. Chu, H. Zhang and Y. Zhao, *Journal of Photochemistry and Photobiology A: Chemistry*, 2020, **400**, 112678.
38. P. Yan, J. Tang, Y. Zhang, W. Shen, Y. Wang, L. Hou, R. Tian, Y. Wang, H. Li, L. Huang and L. A. Belfiore, *Micro & Nano Letters*, 2018, **13**, 1447-1452.
39. Y. Zhang, X. Wang, J. Tang, W. Wang, J. Wang and L. A. Belfiore, *Optical Materials*, 2017, **66**, 17-22.
40. D. A. Weitz, S. Garoff, C. D. Hanson, T. J. Gramila and J. I. Gersten, *Optics Letters*, 1982, **7**, 89-91.
41. M. Wu, J. R. Lakowicz and C. D. Geddes, *Journal of Fluorescence*, 2005, **15**, 53-59.
42. Q. Wang, J. Liu, K. Huang, Q. Chen, H. Dong, D. Zhang, Q. Shi, S. Li and W. Wang, *Spectrochimica Acta Part A: Molecular and Biomolecular Spectroscopy*, 2020, **235**, 118260.
43. Q. Wang, X. Sang, S. Li, Y. Liu, W. Wang, Q. Wang, K. Liu, Z. An and W. Huang, *Optics Express*, 2019, **27**, 27726-27736.
44. J. Zhang, F. Song, S. Lin, S. Liu and Y. Liu, *Optics Express*, 2016, **24**, 8228-8236.

45. W. Xu, L. Wang, R. Zhang, X. Sun, L. Huang, H. Su, X. Wei, C. C. Chen, J. Lou, H. Dai and K. Qian, *Nature Communications*, 2020, **11**, 1654.
46. W. Deng, D. Jin, K. Drozdowicz-Tomsia, J. Yuan and E. M. Goldys, *Langmuir*, 2010, **26**, 10036-10043.
47. J.-C. G. Bünzli and S. V. Eliseeva, in *Lanthanide Luminescence: Photophysical, Analytical and Biological Aspects*, eds. P. Hänninen and H. Härmä, Springer Berlin Heidelberg, Berlin, Heidelberg, 2011, 1-45.
48. K. Binnemans, *Coordination Chemistry Reviews*, 2015, **295**, 1-45.
49. H. Sugimoto and M. Fujii, *ACS Photonics*, 2021, **8**, 1794-1800.
50. F. T. Rabouw, P. T. Prins and D. J. Norris, *Nano Letters*, 2016, **16**, 7254-7260.
51. J. Zhang, X. Cheng, H. Zhang, J. Zheng and J. Wang, *ACS Nano*, 2023, **11**, 10546–10559.
52. Q. Su, C. Jiang, D. Gou and Y. Long, *ACS Applied Bio Materials*, 2021, **4**, 4684-4705.
53. M. Dass, F. N. Gür, K. Kołątaj, M. J. Urban and T. Liedl, *The Journal of Physical Chemistry C*, 2021, **125**, 5969-5981.
54. J. Zhang, F. Song, Z. He, Y. Liu, Z. Chen, S. Lin, L. Huang and W. Huang, *Small*, 2016, **12**, 397-404.
55. S. N. A. Jenie, S. Pace, B. Sciacca, R. D. Brooks, S. E. Plush and N. H. Voelcker, *ACS Applied Materials & Interfaces*, 2014, **6**, 12012-12021.
56. F. S. H. Krismastuti, S. Pace and N. H. Voelcker, *Advanced Functional Materials*, 2014, **24**, 3639-3650.
57. S. N. A. Jenie, S. E. Plush and N. H. Voelcker, *Langmuir*, 2017, **33**, 8606-8613.
58. B. L. Guo and P. X. Ma, *Biomacromolecules*, 2018, **19**, 1764-1782.
59. C. O. Baker, X. Huang, W. Nelson and R. B. Kaner, *Chemical Society Reviews*, 2017, **46**, 1510-1525.
60. Z. B. Yang, J. Ren, Z. T. Zhang, X. L. Chen, G. Z. Guan, L. B. Qin, Y. Zhang and H. S. Peng, *Chemical Reviews*, 2015, **115**, 5159-5223.
61. W. A. Marmisollé and O. Azzaroni, *Nanoscale*, 2016, **8**, 9890-9918.
62. M. Abdelhameed, A. Langlois, D. Fortin, P.-L. Karsenti and P. D. Harvey, *Chemical Communications*, 2014, **50**, 11214.
63. *Luminescence of Lanthanide Ions in Coordination Compounds and Nanomaterials*, John Wiley & Sons Ltd, Chichester, 2014.
64. L. Han, Q. Ma and X. Dong, *RSC Advances*, 2015, **5**, 95674-95681.
65. X. Xi, Q. Ma, X. Dong, D. Li, W. Yu, J. Wang and G. Liu, *ChemPlusChem*, 2018, **83**, 108-116.
66. Y. Xie, Q. Ma, H. Qi, Y. Song, J. Tian, M. A. Musa, W. Yu, X. Dong, D. Li and G. Liu, *RSC Advances*, 2019, **9**, 30890-30904.
67. C. M. S. Izumi, H. F. Brito, A. M. D. C. Ferreira, V. R. L. Constantino and M. L. A. Temperini, *Synthetic Metals*, 2009, **159**, 377-384.
68. O. P. Dimitriev and V. V. Kislyuk, *Synthetic Metals*, 2002, **132**, 87-92.
69. J. Dominic, M. Karthikeyan and K. K. Satheesh Kumar, *Journal of Energy Storage*, 2022, **48**, 103971.
70. K. Gupta, G. Chakraborty, S. Ghatak, P. C. Jana, A. K. Meikap and R. Babu, *Journal of Applied Physics*, 2010, **108**, 073701.

71. J. Zhang, H. Wang, S. Yang, S. Wang and S. Yang, *Journal of Applied Polymer Science*, 2012, **125**, 2494-2501.
72. Y. Tao, J. Li, A. Xie, S. Li, P. Chen, L. Ni and Y. Shen, *Chemical Communications*, 2014, **50**, 12757-12760.
73. H.-J. Lee, S.-O. Hur, M.-K. Ahn, M. Changez and J.-S. Lee, *Nanoscale*, 2017, **9**, 6545-6550.
74. W. Zhang, G. Li, C. She, A. liu, J. Cheng, H. Li, S. Liu, C. Jing, Y. Cheng and J. Chu, *Analytica Chimica Acta*, 2020, **1093**, 115-122.
75. S. Zhang, S. Kan and J. Kan, *Journal of Applied Polymer Science*, 2006, **100**, 946-953.
76. G. Wang, H. Tanaka, L. Hong, Y. Matsuo, K. Niikura, M. Abe, K. Matsumoto, T. Ogawa and K. Ijiro, *Journal of Materials Chemistry*, 2012, **22**, 13691-13697.
77. C. J. Whitfield, M. Zhang, P. Winterwerber, Y. Wu, D. Y. W. Ng and T. Weil, *Chemical Reviews*, 2021, **121**, 11030-11084.
78. Z.-G. Wang, P. Zhan and B. Ding, *ACS Nano*, 2013, **7**, 1591-1598.
79. J. Huang and R. B. Kaner, *Chemical Communications*, 2006, 367-376.
80. J. Borges and J. F. Mano, *Chemical Reviews*, 2014, **114**, 8883-8942.
81. W. B. Stockton and M. F. Rubner, *Macromolecules*, 1997, **30**, 2717-2725.
82. G. Zaldivar and M. Tagliazucchi, *ACS Macro Letters*, 2016, **5**, 862-866.
83. J. J. Richardson, J. Cui, M. Björnmalm, J. A. Braunger, H. Ejima and F. Caruso, *Chemical Reviews*, 2016, **116**, 14828-14867.
84. M. I. Béthencourt, L.-o. Srisombat, P. Chinwangso and T. R. Lee, *Langmuir*, 2009, **25**, 1265-1271.
85. M. James, S. Ciampi, T. A. Darwish, T. L. Hanley, S. O. Sylvester and J. J. Gooding, *Langmuir*, 2011, **27**, 10753-10762.
86. T. Heinrich, C. H. H. Traulsen, E. Darlatt, S. Richter, J. Poppenberg, N. L. Traulsen, I. Linder, A. Lippitz, P. M. Dietrich, B. Dib, W. E. S. Unger and C. A. Schalley, *RSC Advances*, 2014, **4**, 17694-17702.
87. P. Sun, J. Bai, J. He, M. Yang, J. Su, Y. Ji and H. Liu, *Coatings*, 2022, **12**, 1693.
88. N. Chen, L. Cai, F. Xie, W. Wang, H. Wei, Y. Hong, H. Shen and Z. Liang, *ACS Applied Energy Materials*, 2022, **5**, 4351-4357.
89. J. R. McCreary and R. J. Thorn, *Journal of Electron Spectroscopy and Related Phenomena*, 1976, **8**, 425-436.
90. C. D. Wagner and G. E. Muilenberg, *Handbook of X-ray Photoelectron Spectroscopy: A Reference Book of Standard Data for Use in X-ray Photoelectron Spectroscopy*, Perkin-Elmer, 1979.
91. G. Mie, *Annalen der Physik*, 1908, **330**, 377-445.
92. L. Wang, M. Hasanzadeh Kafshgari and M. Meunier, *Advanced Functional Materials*, 2020, **30**, 2005400.
93. B. Koh, X. Li, B. Zhang, B. Yuan, Y. Lin, A. L. Antaris, H. Wan, M. Gong, J. Yang, X. Zhang, Y. Liang and H. Dai, *Small*, 2016, **12**, 457-465.
94. M. Pelton, *Nature Photonics*, 2015, **9**, 427-435.
95. M. Agio, *Nanoscale*, 2012, **4**, 692-706.
96. A. I. Pérez-Jiménez, D. Lyu, Z. Lu, G. Liu and B. Ren, *Chemical Science*, 2020, **11**, 4563-4577.

97. H. Mishra, B. L. Mali, J. Karolin, A. I. Dragan and C. D. Geddes, *Physical Chemistry Chemical Physics*, 2013, **15**, 19538-19544.
98. K. Aslan and C. D. Geddes, *Analytical Chemistry*, 2005, **77**, 8057-8067.
99. K. Ray, R. Badugu and J. R. Lakowicz, *Langmuir*, 2006, **22**, 8374-8378.
100. A. J. Brock, I. M. Etchells, E. G. Moore and J. K. Clegg, *Dalton Transactions*, 2021, **50**, 4874-4879.
101. B. Rajamouli, R. Devi, A. Mohanty, V. Krishnan and S. Vaidyanathan, *New Journal of Chemistry*, 2017, **41**, 9826-9839.
102. Y. Wan, H. Lyu, H. Du, D. Wang and G. Yin, *Research on Chemical Intermediates*, 2019, **45**, 1669-1687.
103. M. Jahn, S. Patze, I. J. Hidi, R. Knipper, A. I. Radu, A. Muhlig, S. Yuksel, V. Peksa, K. Weber, T. Mayerhofer, D. Cialla-May and J. Popp, *Analyst*, 2016, **141**, 756-793.
104. M. Ha, J. H. Kim, M. You, Q. Li, C. Fan and J. M. Nam, *Chemical Reviews*, 2019, **119**, 12208-12278.

3.5 Appendix II

3.5.1 Materials and methods

3.5.1.1 Fabrication

Ln_2SAcbisDBM$_3$ complexes were prepared and characterised as reported in Chapter 2. DMF (anhydrous, 99.8%) and THF (anhydrous, ≥99.9%, inhibitor free) were purchased from Sigma Aldrich/Merck and used fresh. Other chemicals and solvents were purchased from Sigma Aldrich, VWR, Alfa Aesar and Fisher Scientific. Au surfaces, 30 nm Au layer on silicon with a 5 nm Ti priming layer, were purchased from Georg Albert PVD. After cutting in smaller pieces of approximately 1.5x1.5 cm size, the surfaces were cleaned as reported in section 3.5.2. pGold surfaces were purchased from Nirmidas Biotech and cut to smaller pieces of approximately 1.5x1.5 cm size. After coating, the surfaces were stored under inert atmosphere in the dark. For the preparation of AgNIs surfaces, glass microscope slides were cut in smaller pieces of approximately 1.5x1.5 cm size and cleaned as reported in section 3.5.2. The cleaned glass surfaces and all glassware used for the preparation of AgNIs were washed with aqua regia (3:1 HCl 37% and HNO_3 65-70%) for a minimum of 5 hours and rinsed with milliQ H_2O. For the synthesis of AgNIs surfaces, milliQ H_2O was employed and the reaction was conducted in the dark. Spin coating was carried out in a clean room using a WS-650-23B spin coater. All surfaces were spin coated at 4000 rpm for 30 seconds.

3.5.1.2 Characterisation

SEM images were acquired on 1) a Zeiss Supra 40 SEM at BAM, Berlin, Germany or 2) a Philips XL30 FEG ESEM at the University of Birmingham. In case 2), the samples were sputtered

with gold using a Quorum Emscope SC500 prior to imaging. EDX data were recorded at BAM, Berlin, Germany with a Thermo Fisher Scientific EDS (Waltham, MA, USA) and processed with Thermo Scientific Pathfinder X-ray Microanalysis Software. AFM images were acquired on either a Asylum Research Cypher S at the Department of Engineering, University of Birmingham, a Digital Instruments Dimension 3100, at the Department of Chemical Engineering, University of Birmingham, or an Asylum Research MFP-3D-BIO and a Bruker Dimension FastScan at the Department of Physics and Astronomy, University of Leeds. The images were processed with Gwyddion software. XPS spectra were acquired at BAM, Berlin, Germany, with an AXIS Ultra DLD photoelectron spectrometer manufactured by Kratos Analytical (Manchester, UK) and with a monochromatized aluminium Kα radiation for excitation, at a pressure of approximately 5×10^{-9} mbar. The electron emission angle was 0° and the source-to-analyser angle was 60°, with a 300 × 700 μm² analysis area. The data was analysed and fitted with CasaXPS. Epifluorescence images were recorded on an Olympus IX71 inverted microscope fitted with ImagEM Hamamatsu EM-CCD digital camera and using a 510 nm dichroic mirror. For the acquisition of steady state and time-resolved spectra of the area in the field of view, the microscope was connected to an Edinburgh Instruments FLS1000 *via* liquid light guides. A 450 W Xenon Arc lamp or μF flashlamp were used as excitation source for steady state and time-resolved acquisitions, respectively. Confocal images were obtained on a Leica SP8 confocal microscope. The images were processed with ImageJ. Raman spectra were recorded on a Renishaw InVia Raman microscope at the department of Physics and Astronomy, University of Birmingham, using a 633 nm laser, 50x objective and 600 l/mm grating. UV-Vis absorption and extinction spectra were recorded on an Agilent Cary 60 or Cary 5000 UV-Vis-NIR spectrophotometers. Luminescence spectra were recorded either on an Edinburgh

Instruments FLSP920 steady state and time-resolved spectrophotometer with F980 software or an Edinburgh Instruments FLS1000 steady state and time-resolved spectrometer with Fluoracle software. The spectra were corrected for lamp and instrument response in both cases. A 450 W Xenon Arc lamp was employed as excitation source for steady state measurements, while time-resolved spectra were acquired with a μF flashlamp. Lifetimes were fitted to mono- or multiexponential decays as appropriate using FAST or Fluoracle software, with an estimated error of 10% and with χ^2 between 1.0 and 1.3. When comparing plasmonic enhancement, surfaces spin coated on the same day and with the same coating solutions were used. All optical measurements were carried out for both samples on the same day with the same software and instrument configurations. When comparing emission intensities, the integral of the whole spectrum was considered, unless stated otherwise. For the relative ratios of $^5D_0 \rightarrow {}^7F_J$ transitions in **Eu_2SAcbisDBM$_3$** spectra of sections 2.3.1 and 2.5, the integrals of each transition were divided by the one of the $^5D_0 \rightarrow {}^7F_4$ transition. The wavelength ranges of each transition are as follows: J=0 575-581 nm, J=1 581-601 nm, J=2 601-640 nm, J=3 643-662 nm, J=4 680-713 nm. All spectra were plotted and analysed with OriginPro 2023.

3.5.2 Cleaning of surfaces

Au and glass surfaces were immersed in a Piranha solution (3:1 H_2SO_4 and H_2O_2 30%) at 50 °C for 30 minutes. This was followed by three washes in MilliQ H_2O and one in acetonitrile. Finally, the surfaces were dried under N_2 flow and were stored in glass vials under inert atmosphere.

3.5.3 Coating of surfaces

Dip coating:

A. DMF: a dip coating solution of **Eu_2SAcbisDBM$_3$** (1 mM in 2 mL DMF) was prepared. An Au surface was immersed in the coating solution and the vial sealed under inert atmosphere. After 18 hours, the surface was retrieved, washed copiously with DMF and dried with N_2 flow.

B. THF: a dip coating solution of **Eu_2SAcbisDBM$_3$** (0.1 mM in THF, 1% DMF) was prepared by diluting a concentrated solution of **Eu_2SAcbisDBM$_3$** (20 µl, 10 mM in DMF) in THF (2 mL). An Au surface was immersed in the coating solution and the vial sealed under inert atmosphere. After 18 hours, the surface was retrieved, washed copiously with THF and dried with N_2 flow. The solution was only used once and was stored for a maximum of 24 hours.

C. PANI and **Ln_2bisDBM$_3$**: the Au surface was immersed in a sonicated dispersion of ES PANI (≈0.07 mM in DMF) for 30 minutes. The surface was retrieved, washed with a drop of DMF and dried with N_2 flow. The prepared **PANI@Au** surface was then immersed in a **Ln_2bisDBM$_3$** solution (1 mM in DMF, Ln(III)=Eu(III), Yb(III), Nd(III)) for 18 hours. After this time, the surface was washed with a drop of DMF and dried with N_2 flow.

Spin coating

A. *For the monitoring of emission intensity versus concentration of coating solution in section 3.2.2.*

   Five coating solutions of **Eu_2SAcbisDBM$_3$** with increasing concentration (0.05 mM, 0.1 mM, 0.2 mM, 0.5 mM and 1 mM) were prepared by diluting 10 µL, 20 µL, 40 µL, 100

µL or 200 µL, respectively, of a stock solution (1 mM in DMF) in DMF (190 µL , 180 µL, 160 µL, 100 µL or 0 µL, respectively). 10 µL of coating solution were spin coated on each surface (Au or pGold) followed by air drying.

B. *For the evaluation of plasmonic enhancement in sections 3.2.3-5.*

A coating solution of **Ln_2SAcbisDBM$_3$** (0.1 mM in THF, 1% DMF, Ln=Eu(III), Yb(III), Nd(III)) was prepared by diluting a concentrated **Ln_2SAcbisDBM$_3$** solution (2.5 µl, 10 mM in DMF) in THF (250 µL). For **Eu_2SAcbisDBM$_3$**, 10 µL of the coating solution were spin coated on the surface (Au, pGold or AgNIs). For **Yb_2SAcbisDBM$_3$** or **Nd_2SAcbisDBM$_3$**, 20 µL of the coating solution were spin coated on the surface (Au, pGold or AgNIs).

C. *For the layer by layer coating of PANI and **Ln_2bisDBM$_3$** on Au surfaces (i.e. **SP_Ln_2bisDBM$_3$_PANI@Au**)*

A diluted and sonicated dispersion of ES PANI (≈3 µM in DMF) was prepared by addition of a sonicated dispersion of ES PANI (10 µL, ≈0.07 mM in DMF) in DMF (250 µl). 10 µL of the diluted ES PANI solution were spin coated on the Au surface, followed by air drying (i.e. SP_PANI@Au). 10 µL of a **Ln_2bisDBM$_3$** solution (1 mM in DMF, Ln(III)=Eu(III), Yb(III)) were spin coated on the SP_PANI@Au surface, followed by air drying.

D. *For the mixed coating of PANI and **Ln_2bisDBM$_3$** on Au surfaces (i.e. **SP_Ln_2bisDBM$_3$+PANI@Au**)*

A mixture of ES PANI (3 µM in DMF) and **Ln_2bisDBM$_3$** was prepared by addition of a sonicated dispersion of ES PANI (10 µL, ≈0.07 mM in DMF) in a **Ln_2bisDBM$_3$** solution (250 µl, 1 mM in DMF, Ln(III)=Eu(III), Yb(III)). 10 µL of the mixture were spin coated on the Au surface, followed by air drying.

3.5.4 Fluoride sensing

Approach A.

This approach was used for both **Eu_2SAcbisDBM$_3$@Au** surfaces coated in DMF or THF (1% DMF) solutions.

A stock solution of TBAF in THF (3 mM, 3 mL) was prepared by dilution of the purchased solution of TBAF (1.0 M in THF, 9 µL). A solution (**A**) of increasing TBAF concentration (5 µM, 10 µM, 15 µM and 20 µM) for the testing of the sensing performance of the **Eu_2SAcbisDBM$_3$@Au** surface was prepared as follows. The solution with lowest concentration of TBAF (5 µM) was prepared by dilution of the stock TBAF solution (5 µL, 3 mM) in THF (3 mL) to give solution **A**. Increasing concentrations (10 µM, 15 µM and 20 µM) were attained by addition of stock TBAF solution (5 µL for each concentration increase) to solution **A**. Prior to incubation in the TBAF solution of lowest concentration (5 µM), the excitation, emission and lifetime spectra of the pristine **Eu_2SAcbisDBM$_3$@Au** surface were recorded. For the sensing, the surface was immersed in the solution of TBAF with lowest concentration (5 µM) and incubated for 15 minutes. After this time, the surface was removed, dried with air stream and the optical properties of the surface were acquired. The surface was then immersed in the same solution (**A**) after addition of 5 µL of TBAF stock solution (3 mM) to give the next concentration point and the procedure repeated. The instrument settings were maintained identical for each acquisition of the same surface.

Approach B.

This approach was used solely for **Eu_2SAcbisDBM$_3$@Au** surfaces coated in THF (1% DMF) solutions.

A stock solution of TBAF in THF (3 mM, 3 mL) was prepared by dilution of the purchased solution of TBAF (1.0 M in THF, 9 µL). Four TBAF solutions for the evaluation of the sensing performance of **Eu_2SAcbisDBM$_3$@Au** surfaces were prepared as follows. Aliquots of stock solution (5 µL, 10 µL, 15 µL and 20 µL, respectively) were diluted in THF (3 mL) to give the desired TBAF concentrations (5 µM, 10 µM, 15 µM and 20 µM, respectively). For each surface, the optical properties of the pristine surface were recorded prior to incubation in the TBAF solution. For the sensing, each surface was incubated in the TBAF solution of the selected concentration for 15 minutes. After this time, the surface was removed, dried with air stream and the optical properties were acquired. The instrument settings were maintained identical for each acquisition of the same surface.

3.5.5 Preparation of AgNIs surfaces

AgNIs surfaces were prepared by a modification of the reported procedures.[98, 99] Clean glass surfaces were immersed in an APTES solution (0.2 mM in MeOH) for 18 hours and the vial was sealed under inert atmosphere. After this time, the surface was retrieved and copiously rinsed with MeOH and dried under N_2 flow.

In a 20 mL vial, $AgNO_3$ (42 mg, 250 µmol) was dissolved in H_2O (5 mL) and the solution vigorously stirred. A NaOH solution (1.0 M, 50 µL) was quickly added to give a dark brown precipitate. NH_4OH (201 µL) was added drop by drop to completely redissolve the dark brown precipitate. The APTES coated glass surface was inserted in the vial and immersed in the clear and colourless solution, the system was stirred at 0-5 °C for 5 minutes. After this time, a solution of D-glucose (0.5 M, 1.5 mL) was added and the vial was moved to a heating bath at 55 °C where the mixture was stirred for 3 minutes. During this time, the contents of the vial

went from colourless and transparent to green-brown and to finally produce a silver mirror on the walls of the glass vial. The coated surface was removed and copiously rinsed with H_2O, followed by sonication in H_2O for 1 minute and further washing with H_2O. The prepared AgNIs surface displayed a green-silver coating, it was dried under N_2 flow and stored in a glass vial under inert atmosphere and in the dark for up to 1 month.

3.5.6 Addition of PANI to Eu_2bisDBM$_3$ for UV-Vis absorption spectroscopy

Additions to 1 mM solutions

A sonicated dispersion of ES PANI (40 µL, ≈0.07 mM in DMF) was added to either DMF (1 mL), **bisDBM** (1 mL, 1 mM in DMF), **$EuCl_3 \cdot 6H_2O$** (1 mL, 1 mM in DMF), **EuDBM$_3$** (1 mL, 1 mM in DMF) or **Eu_2bisDBM$_3$** (1 mL, 1 mM in DMF). The mixtures were mixed with a vortex for 10 seconds and then centrifuged for 10 minutes (9000 rpm). The supernatant was retrieved and analysed by absorption spectroscopy.

*Additions to **Eu_2bisDBM$_3$** solutions of increasing concentration*

Three solutions of **Eu_2bisDBM$_3$** (1 mL, 1 mM, 0.5 mM, 0.01 mM in DMF) were prepared by dilution of 0 µL, 500 µL, 10 µL, respectively, of a concentrated **Eu_2bisDBM$_3$** solution (1 mM in DMF) in DMF (1 mL, 500 µL, 990 µL). A sonicated dispersion of ES PANI (40 µL, ≈0.07 mM in DMF) was added to each solution and the mixtures were mixed with a vortex for 10 seconds and then centrifuged for 10 minutes (9000 rpm). The supernatant was retrieved and analysed by absorption spectroscopy.

3.5.7 Additional photophysical data

3.5.7.1 Steady state excitation and emission data

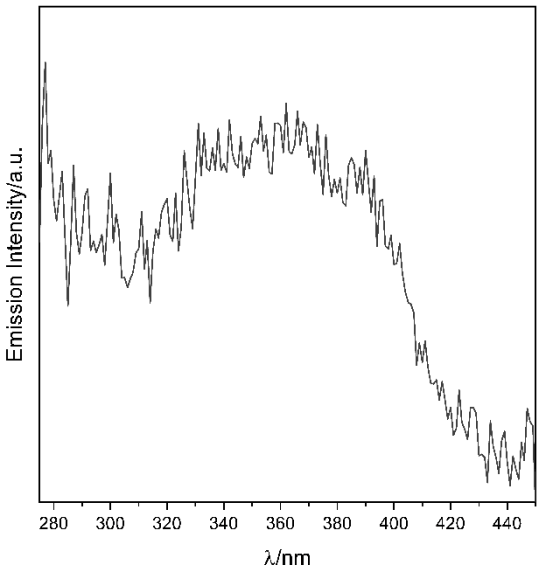


Figure 3.65 – Excitation spectrum of **Yb_2SAcbisDBM$_3$@Au** coated in DMF. λ_{em}: 977 nm.

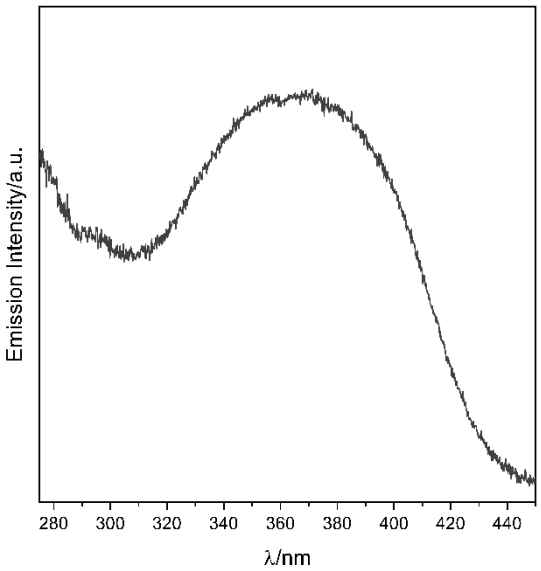


Figure 3.66 – Excitation spectrum of **Nd_2SAcbisDBM$_3$@Au** coated in DMF. λ_{em}: 1060 nm.

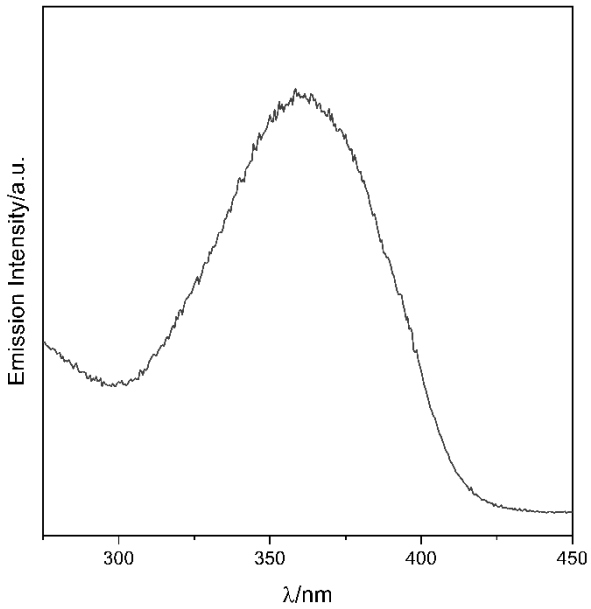


Figure 3.67 – Excitation spectrum of **Eu_2SAcbisDBM$_3$@Au** coated in THF (1% DMF). λ_{em}: 611 nm.

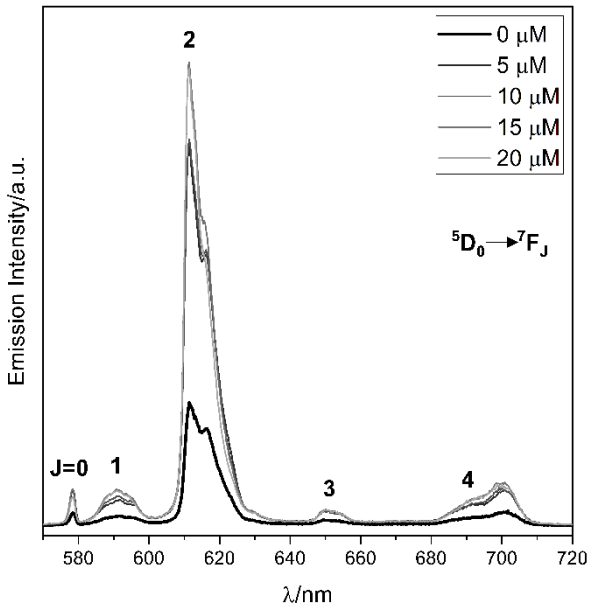


Figure 3.68 – Overlaid emission spectra of **Eu_2SAcbisDBM$_3$@Au** (surface A in Figure 3.27 and Table 3.13) before (black, thick) and after immersion in solutions of increasing concentration of TBAF. λ_{exc} 350 nm.

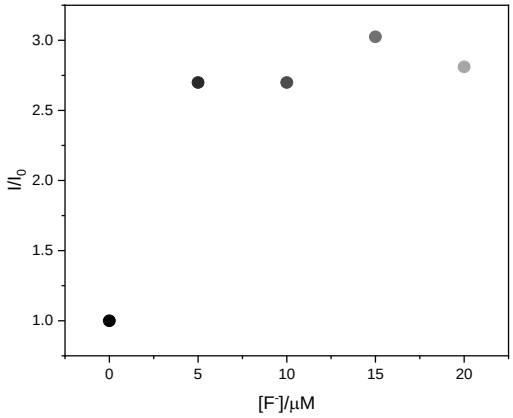


Figure 3.69 – Plot of the ratio of integrals of the whole **Eu_2SAcbisDBM$_3$@Au** (surface A in Figure 3.27) spectrum over initial value versus concentration of TBAF.

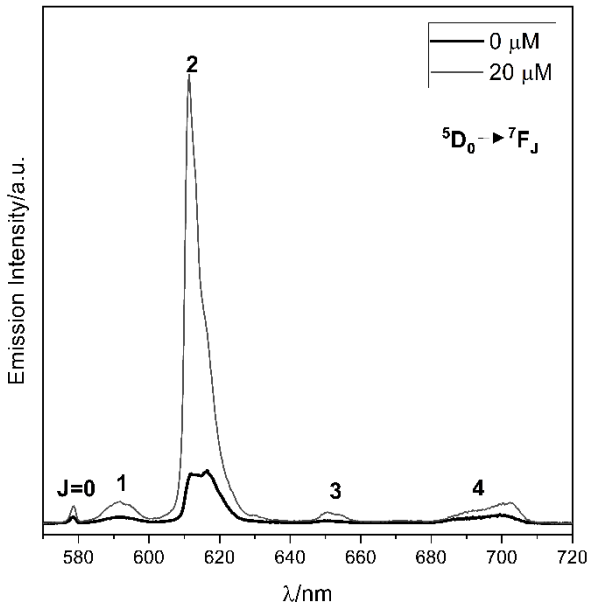


Figure 3.70 – Overlaid emission spectra of **Eu_2SAcbisDBM$_3$@Au** (surface 13 in Table 3.14) before (black, thick) and after (grey) immersion in a 20 μM solution of TBAF. λ_{exc} 350 nm.

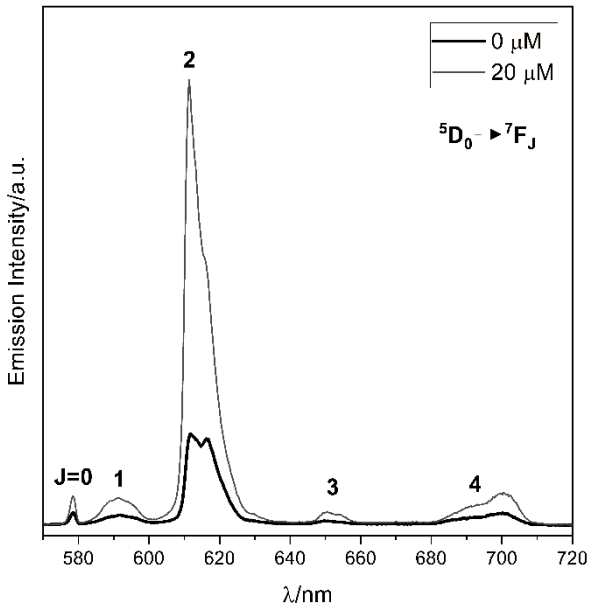


Figure 3.71 – Overlaid emission spectra of **Eu_2SAcbisDBM$_3$@Au** (surface 14 in Table 3.14) before (black, thick) and after (grey) immersion in a 20 μM solution of TBAF. λ_{exc} 350 nm.

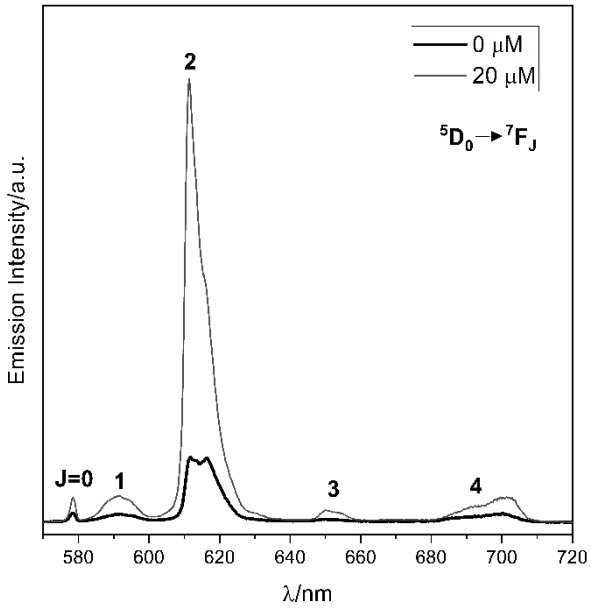


Figure 3.72 – Overlaid emission spectra of **Eu_2SAcbisDBM$_3$@Au** (surface 15 in Table 3.14) before (black, thick) and after (grey) immersion in a 20 μM solution of TBAF. λ_{exc} 350 nm.

Surface No.	Ratio I_{20}/I_0	Average
13	3.9	3.5±0.5
14	3.0	
15	3.6	

Table 3.9 – Ratio of the full integrals of the emission spectra of selected **Eu_2SAcbisDBM$_3$@Au** surfaces after immersion in a 20 µM solution of TBAF (I_{20}) over the initial value (I_0).

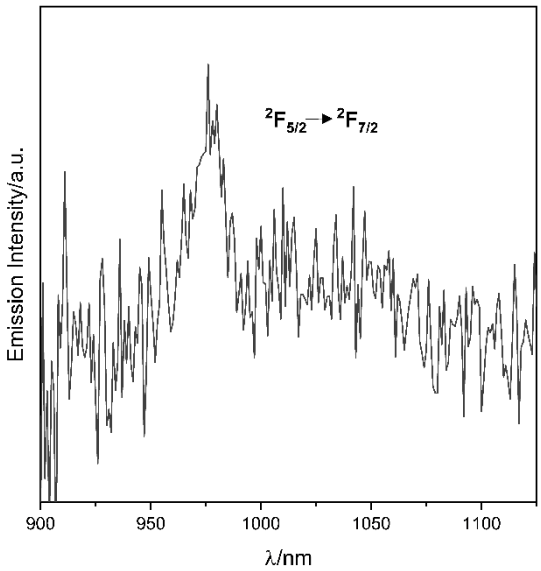


Figure 3.73 – Emission spectrum of spin coated **SP_Yb_2SAcbisDBM$_3$@Au**. λ_{exc}: 350 nm.

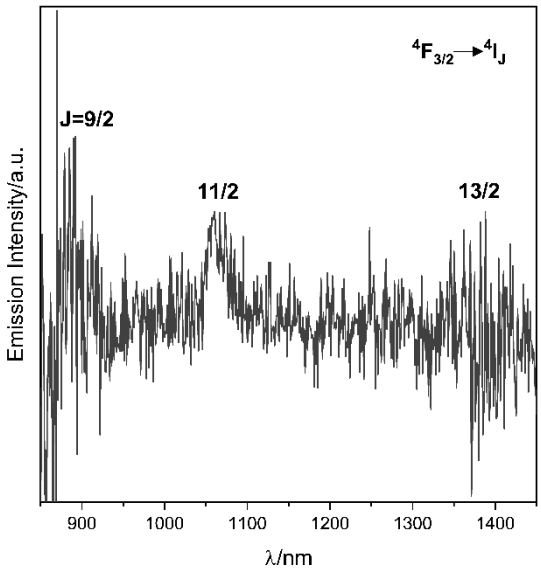


Figure 3.74 – Emission spectrum of spin coated **SP_Nd_2SAcbisDBM$_3$@Au**. λ_{exc}: 350 nm.

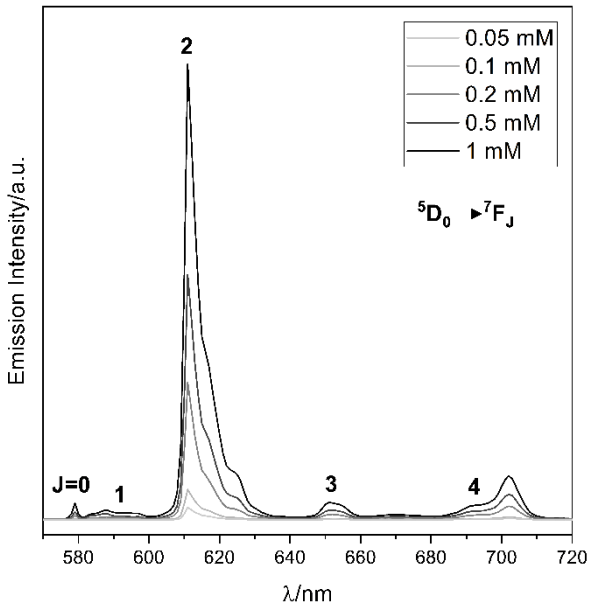


Figure 3.75 – Overlaid emission spectra of **SP_Eu$_2$SAcbisDBM$_3$@pGold** with increasing concentration of spin coated solution. λ_{exc}: 350 nm.

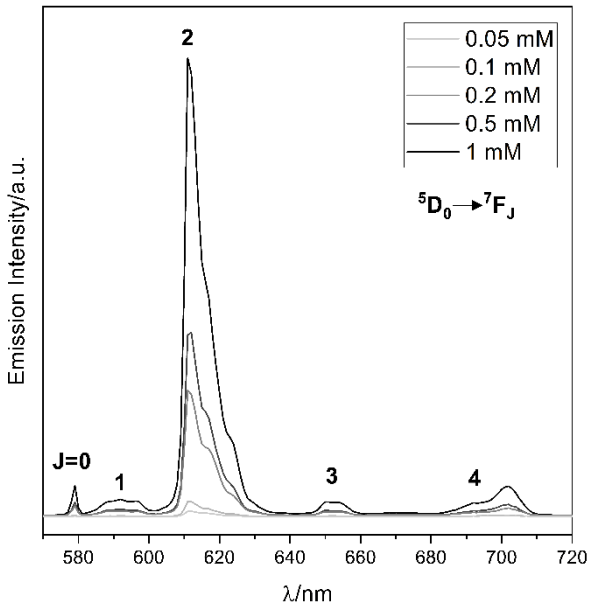


Figure 3.76 – Overlaid emission spectra of **SP_Eu$_2$SAcbisDBM$_3$@Au** with increasing concentration of spin coated solution. λ_{exc}: 350 nm.

Equations for fitting in Figures 3.35-36 (section 2.3-4)

	Au	**pGold**
Equation	y=a+bx	y=a+bx
a	-0.00743 ± 0.05595	0.03075 ± 0.03674
b	0.99236 ± 0.10962	0.98972 ± 0.07199
R^2	0.96469	0.98438

Table 3.10 – Parameters for the linear fit of the emission response of **Eu$_2$SAcbisDBM$_3$** on Au and pGold upon increasing concentrations of complex. The fit has been carried out with OriginPro 2023.

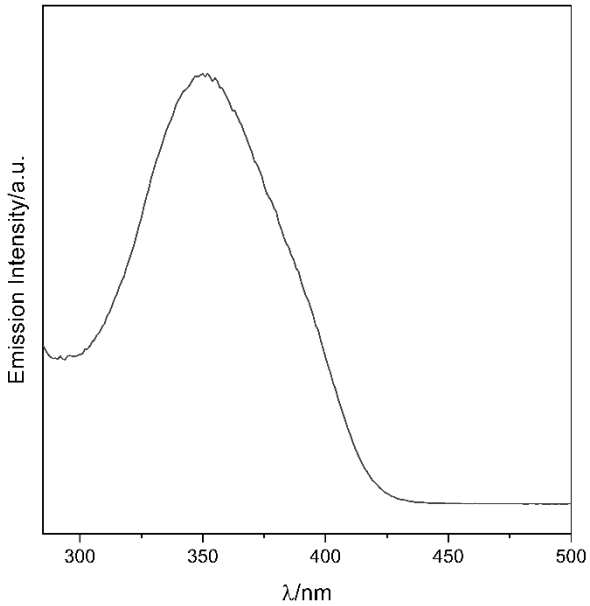


Figure 3.77 – Excitation spectrum of spin coated **SP_Eu$_2$SAcbisDBM$_3$@pGold**. λ_{em}: 611 nm.

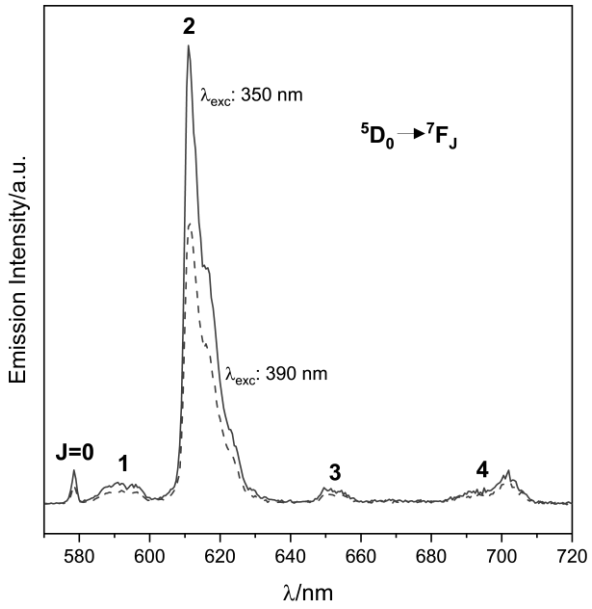


Figure 3.78 – Overlaid emission spectra of spin coated **SP_Eu$_2$SAcbisDBM$_3$@Au** upon excitation at 350 nm (solid line) and 390 nm (dashed line).

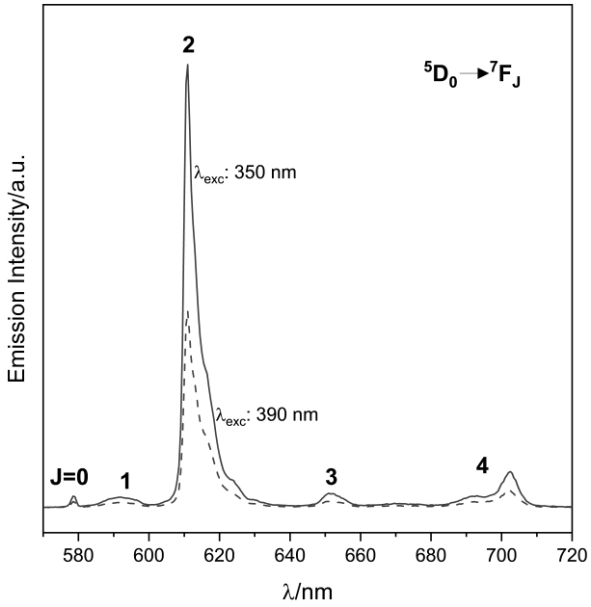


Figure 3.79 – Overlaid emission spectra of spin coated **SP_Eu$_2$SAcbisDBM$_3$@pGold** upon excitation at 350 nm (solid line) and 390 nm (dashed line).

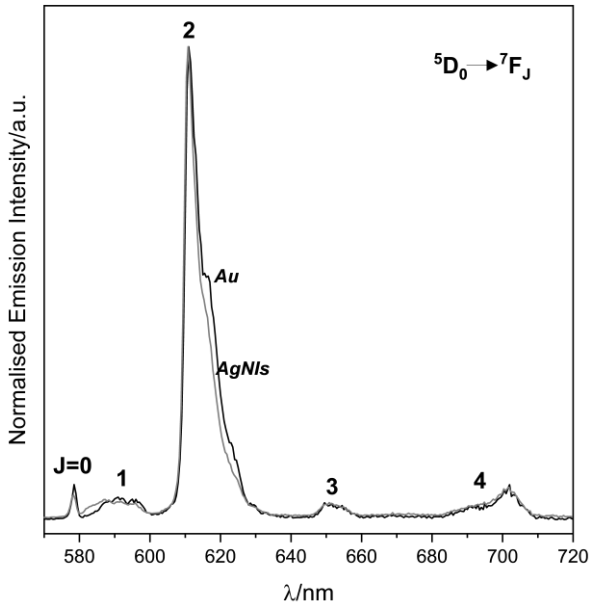


Figure 3.80 – Overlaid and normalised emission spectra of spin coated **SP_Eu$_2$SAcbisDBM$_3$@Au** (black, λ_{exc}: 350 nm) and **SP_Eu$_2$SAcbisDBM$_3$@AgNIs** (light grey, λ_{exc}: 390 nm).

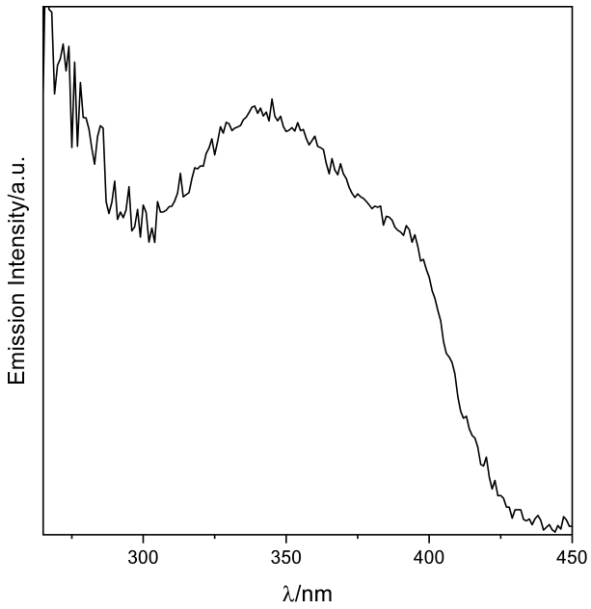


Figure 3.81 – Excitation spectrum of **Yb_2bisDBM$_3$_PANI@Au**. λ_{em}: 977 nm.

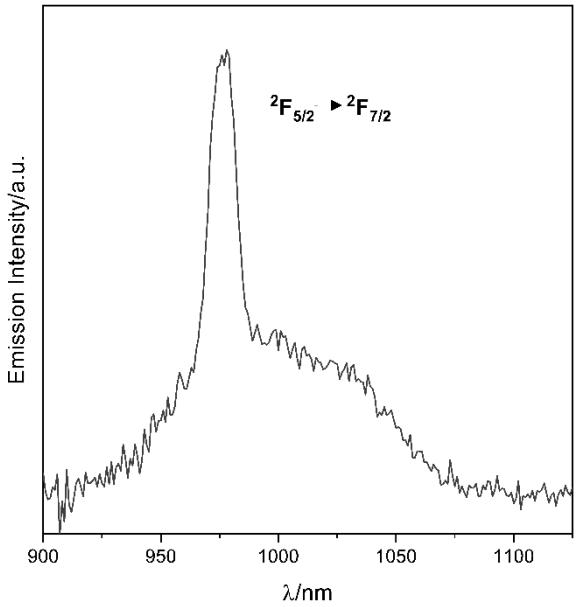


Figure 3.82 – Emission spectrum of **SP_Yb_2bisDBM$_3$_PANI@Au**. λ_{exc}: 350 nm.

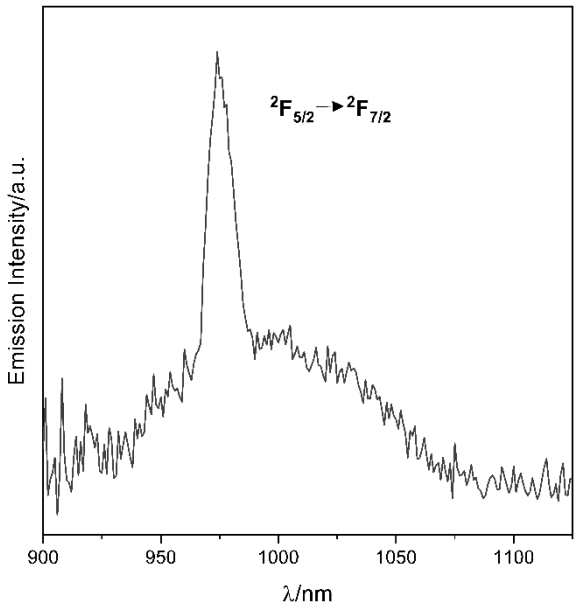


Figure 3.83 – Emission spectrum of **SP_Yb$_2$bisDBM$_3$+PANI@Au**. λ_{exc}: 350 nm.

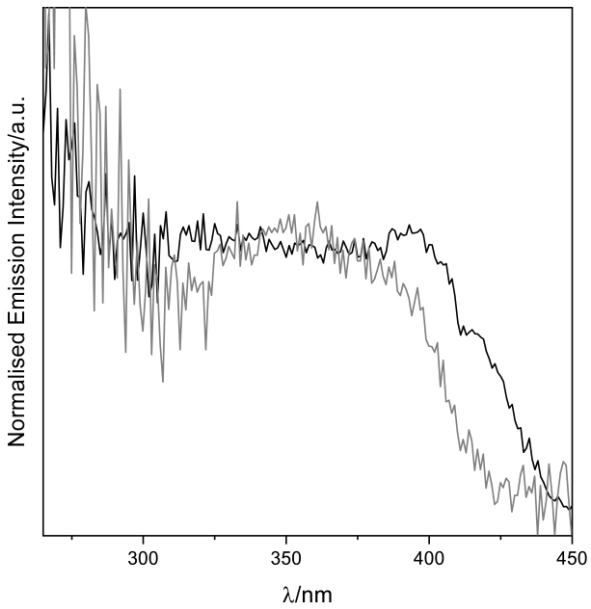


Figure 3.84 – Emission spectra of **SP_Yb$_2$bisDBM$_3$_PANI@Au** (black) and **SP_Yb$_2$bisDBM$_3$+PANI@Au** (grey). λ_{em}: 977 nm.

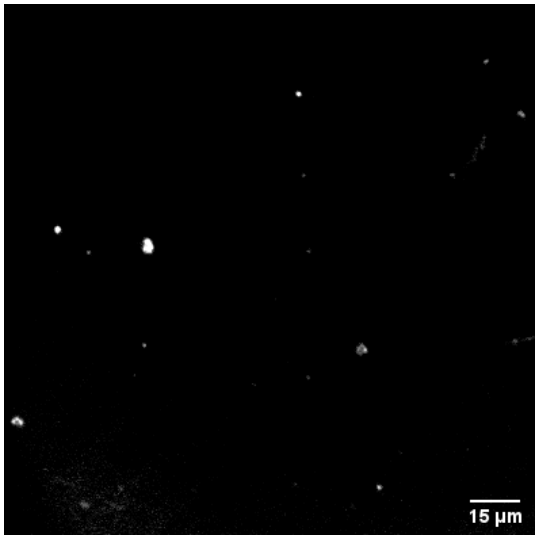


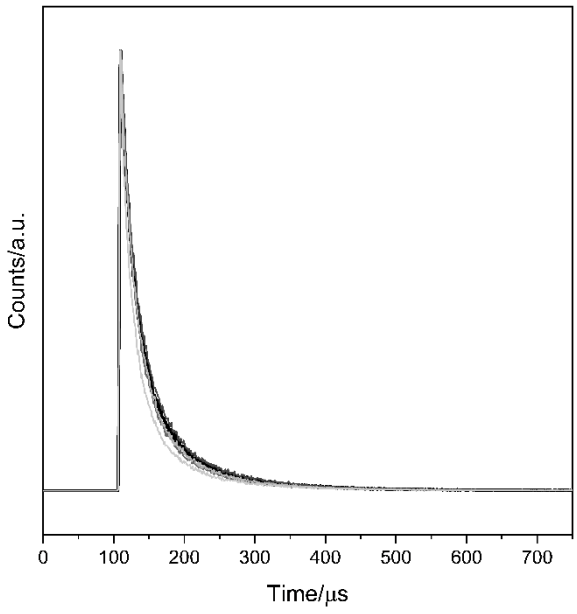
Figure 3.85 – Epifluorescence image of **SP_Eu₂bisDBM₃+PANI@Au**. λ_{exc}: 350 nm.

Equations for fitting in Figure 3.57 (section 2.8.1)

	Au
Equation	y=a+bx
a	0.21165 ± 0.01962
b	0.41194 ± 0.0304
R^2	0.99459

Table 3.11 – Parameters for the linear fit of the absorbance at 630 nm of **Eu₂bisDBM₃**-PANI in DMF upon increasing concentration of **Eu₂bisDBM₃** (0.01 mM-1 mM). The fit has been carried out with OriginPro 2023.

3.5.7.2 Time resolved data



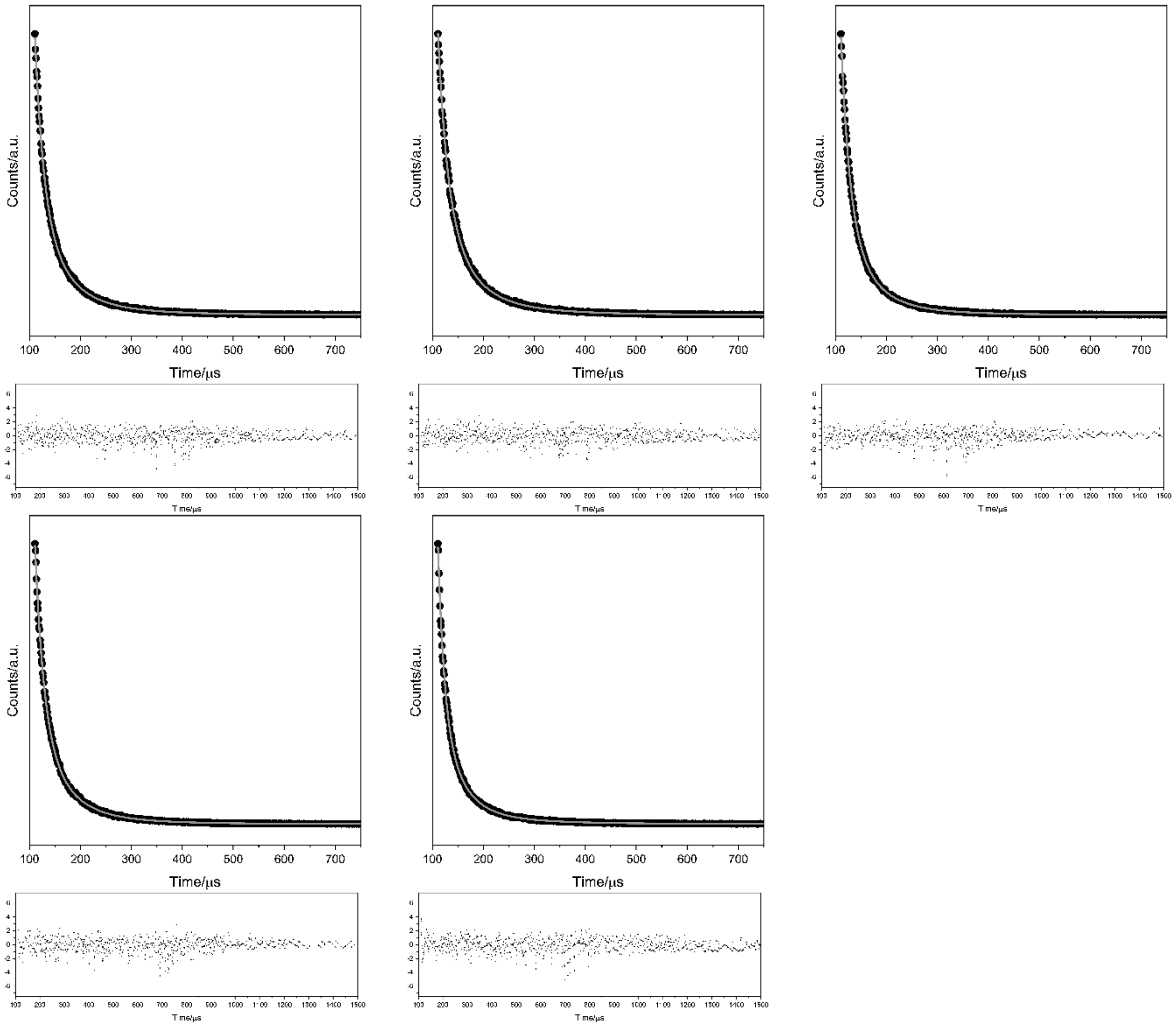


Figure 3.86 – Lifetime spectra of **Eu_2SAcbisDBM$_3$@Au** coated in DMF before (black, thick) and after (grey) immersion in solutions of increasing concentrations of F^- as TBAF (10 μM, 20 μM, 80 μM, 100 μM). λ_{exc}: 350 nm, λ_{em}: 611 nm. Below are reported the respective fitting curves and residuals.

[F^-]/μM	**τ/μs (%)**
0	140 (29%), 57 (46%), 21 (25%)
10	120 (31%), 45 (47%), 17 (22%)
20	110 (24%), 43 (48%), 16 (28%)
80	120 (24%), 47 (47%), 17 (29%)
100	130 (24%), 39 (50%), 12 (26%)

Table 3.12 – Exponential decay analysis of **Eu_2SAcbisDBM$_3$@Au** coated in DMF before (black, thick) and after (grey) immersion in solutions of increasing concentrations of F^- as TBAF.

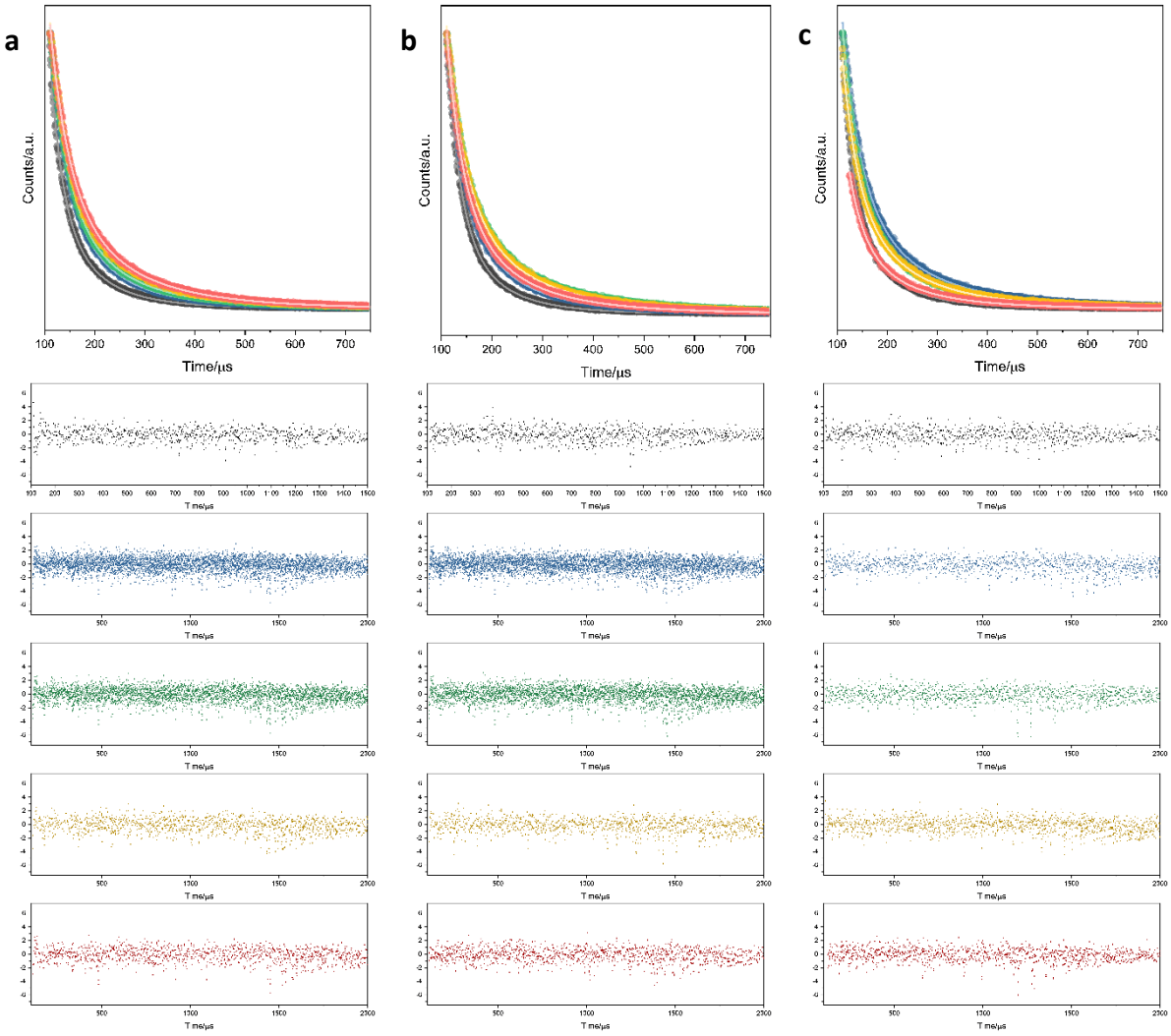
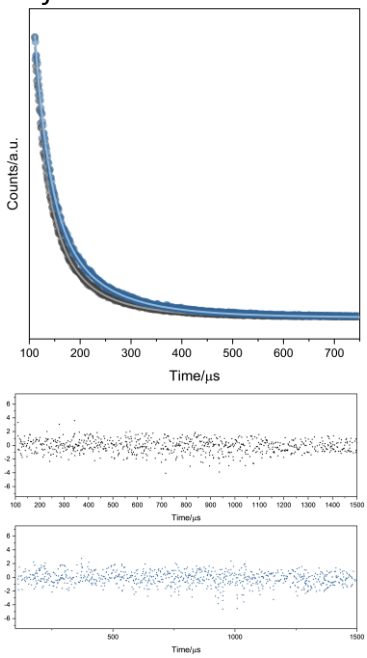


Figure 3.87 – Decay curves of **Eu_2SAcbisDBM$_3$@Au** coated in THF (1% DMF, i.e. surfaces A, **a**, B, **b** and C, **c**) before (black) and after immersion in solutions of increasing concentrations of F^- as TBAF (5 µM, blue, 10 µM, green, 15 µM, yellow and 20 µM, red). λ_{exc}: 350 nm, λ_{em}: 611 nm. Below each curve are reported the respective residuals.

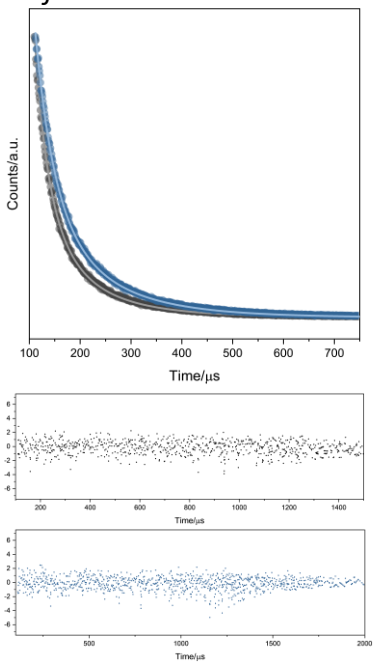
[F^-]/µM	**τ/µs** *(Surface A)*	**τ/µs** *(Surface B)*	**τ/µs** *(Surface C)*
0	160 (30%), 61 (48%), 22 (22%)	170 (22%), 70 (47%), 24 (31%)	160 (26%), 63 (50%), 20 (24%)
5	200 (26%), 85 (49%), 29 (25%)	210 (28%), 84 (49%), 28 (23%)	270 (30%), 110 (47%), 34 (23%)
10	220 (29%), 92 (47%), 31 (24%)	260 (38%), 97 (44%), 32 (18%)	240 (27%), 95 (49%), 30 (23%)
15	250 (29%), 100 (49%), 34 (22%)	260 (31%), 100 (47%), 33 (22%)	250 (34%), 90 (48%), 27 (18%)
20	260 (29%), 110 (48%), 36 (23%)	240 (29%), 94 (49%), 30 (22%)	240 (28%), 84 (48%), 26 (23%), 1.4 (2%)

Table 3.13 – Exponential decay analysis of **Eu_2SAcbisDBM$_3$@Au** upon immersion in solutions of increasing concentration of TBAF.

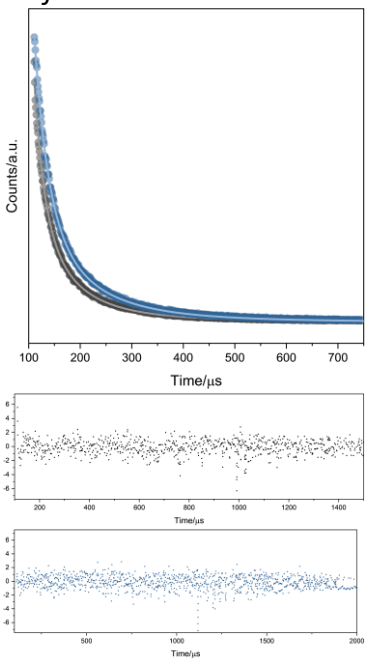
Surface 1



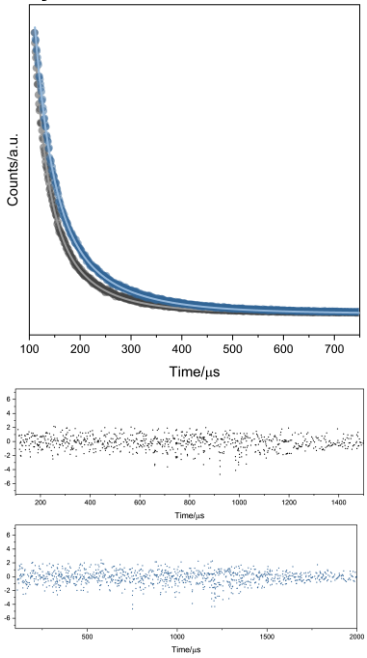
Surface 2



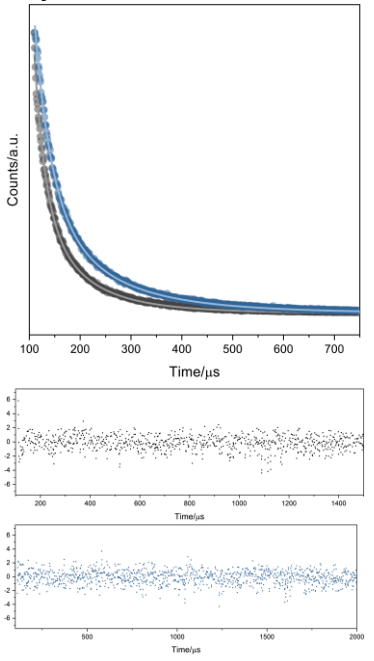
Surface 3



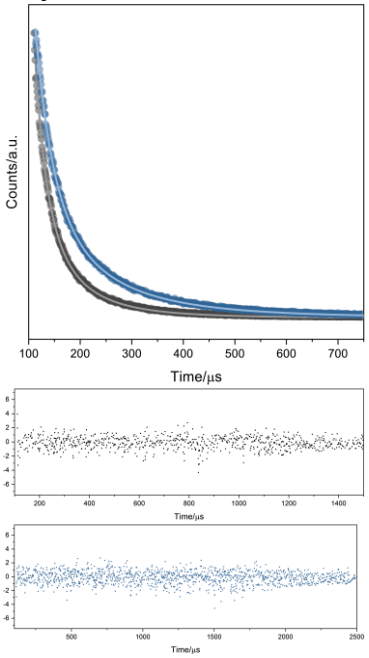
Surface 4



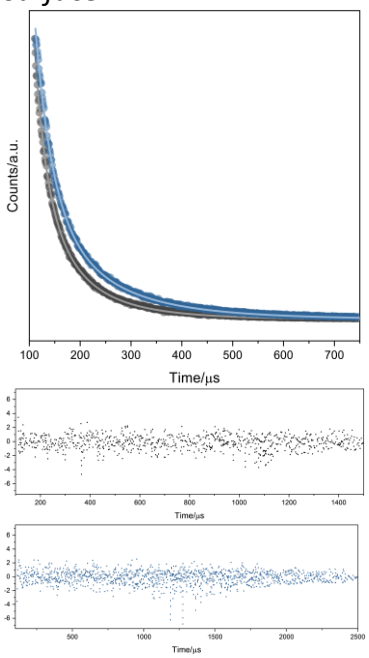
Surface 5



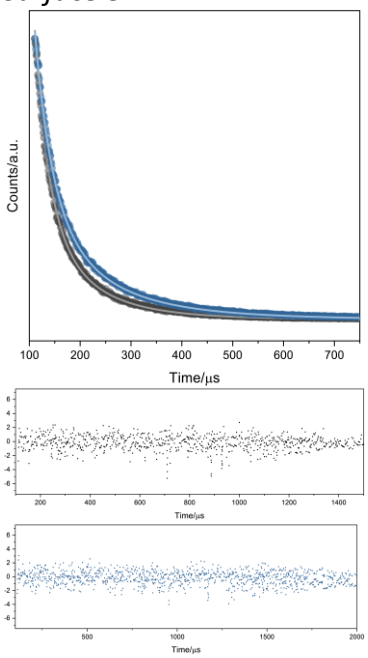
Surface 6



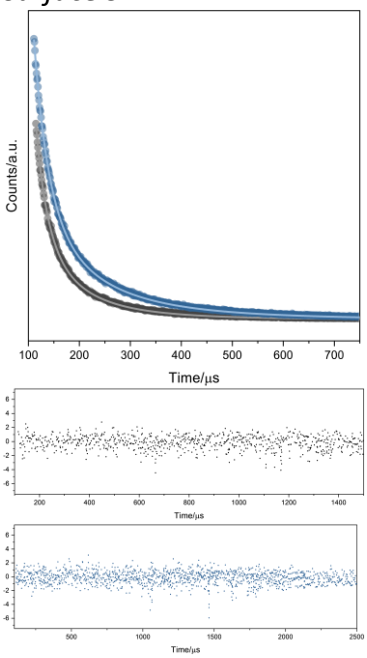
Surface 7



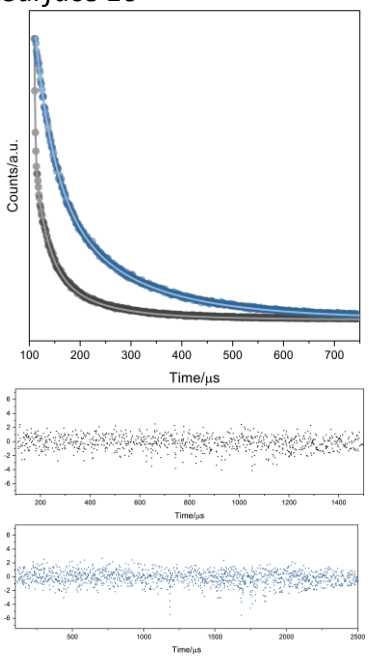
Surface 8



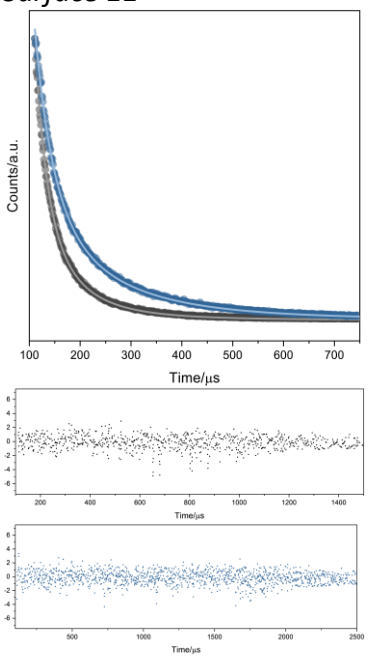
Surface 9



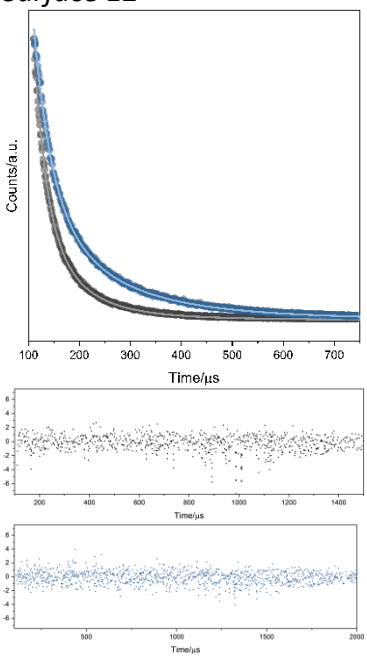
Surface 10



Surface 11



Surface 12



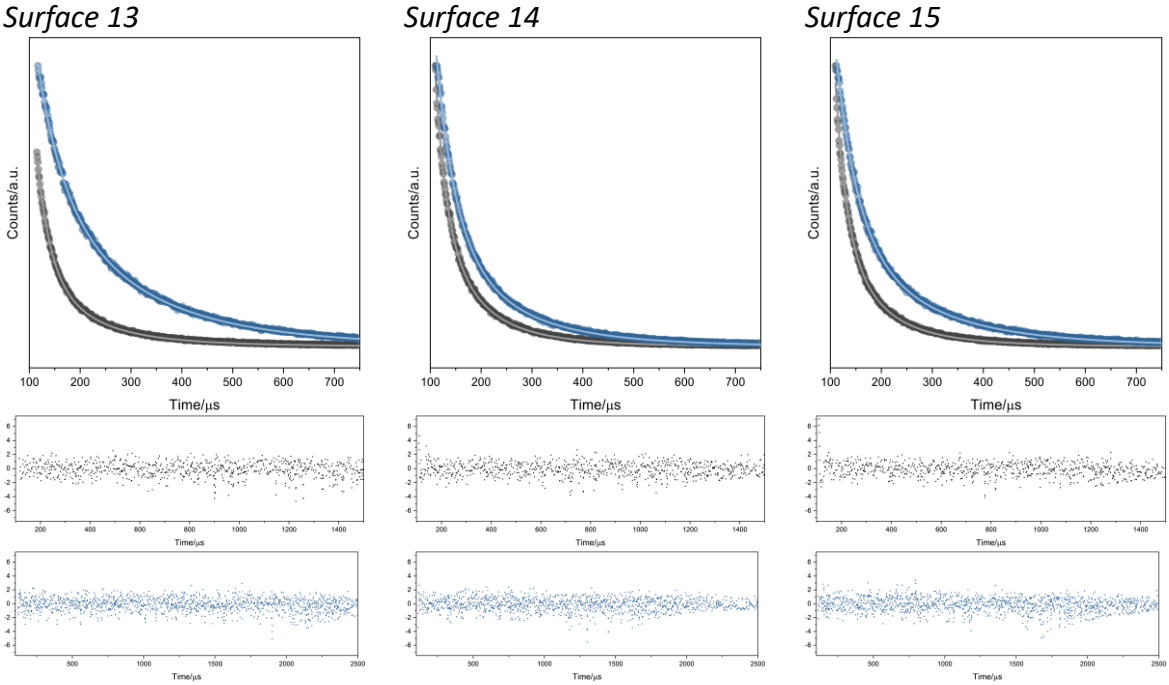


Figure 3.88 – Decay curves of **Eu_2SAcbisDBM$_3$@Au** coated in THF (1% DMF) before (black) and after (blue) immersion in solutions of F^- as TBAF (5 μM, surfaces 1-3, 10 μM, surfaces 4-7, 15 μM, surfaces 8-11 and 20 μM, surfaces 12-15). λ_{exc}: 350 nm, λ_{em}: 611 nm. Below each curve are reported the respective residuals.

[F^-]/μM	**τ/μs** *(Surface 1)*	**τ/μs** *(Surface 2)*	**τ/μs** *(Surface 3)*
0	150 (32%), 58 (46%), 22 (22%)	160 (33%), 66 (44%), 24 (22%)	170 (33%), 57 (50%), 16 (17%)
5	190 (26%), 80 (50%), 27 (24%)	210 (22%), 100 (51%), 36 (27%)	210 (26%), 83 (48%), 26 (26%)
Ratio	1.3	1.3	1.2
Avg. Ratio	1.3 ± 0.0(4)		

[F^-]/μM	**τ/μs** *(Surface 4)*	**τ/μs** *(Surface 5)*	**τ/μs** *(Surface 6)*	**τ/μs** *(Surface 7)*
0	150 (31%), 62 (46%), 22 (23%)	200 (28%), 73 (50%), 21 (22%)	160 (23%), 65 (48%), 23 (29%)	170 (31%), 66 (50%), 22 (19%)
10	200 (25%), 88 (49%), 31 (26%)	280 (28%), 100 (48%), 31 (23%)	260 (30%), 100 (47%), 32 (23%)	240 (28%), 100 (47%), 32 (25%)
Ratio	1.3	1.4	1.6	1.4
Avg. Ratio	1.4 ± 0.1			

[F^-]/µM	τ/µs *(Surface 8)*	τ/µs *(Surface 9)*	τ/µs *(Surface 10)*	τ/µs *(Surface 11)*
0	170 (25%), 77 (47%), 26 (28%)	200 (31%), 70 (48%), 21 (21%)	200 (26%), 75 (45%), 24 (25%), 1.8 (4%)	160 (25%), 63 (49%), 21 (26%)
15	240 (29%), 98 (47%), 32 (24%)	270 (32%), 99 (46%), 27 (22%)	300 (33%), 130 (48%), 37 (19%)	280 (31%), 110 (46%), 34 (23%)
Ratio	1.4	1.4	1.5	1.8
Avg. Ratio	1.5 ± 0.2			

[F^-]/µM	τ/µs *(Surface 12)*	τ/µs *(Surface 13)*	τ/µs *(Surface 14)*	τ/µs *(Surface 15)*
0	180 (26%), 83 (46%), 30 (28%)	220 (31%), 82 (47%), 25 (22%)	170 (31%), 67 (49%), 21 (20%)	170 (31%), 65 (49%), 20 (20%)
20	240 (24%), 100 (49%), 34 (27%)	320 (35%), 150 (51%), 47 (14%)	270 (24%), 110 (51%), 36 (25%)	300 (28%), 130 (49%), 40 (23%)
Ratio	1.3	1.5	1.6	1.8
Avg. Ratio	1.5 ± 0.2			

Table 3.14 – Exponential decay analysis of **Eu_2SAcbisDBM$_3$@Au** surfaces upon immersion in solutions of different concentrations of TBAF. The ratios are calculated considering the longest underlined component only.

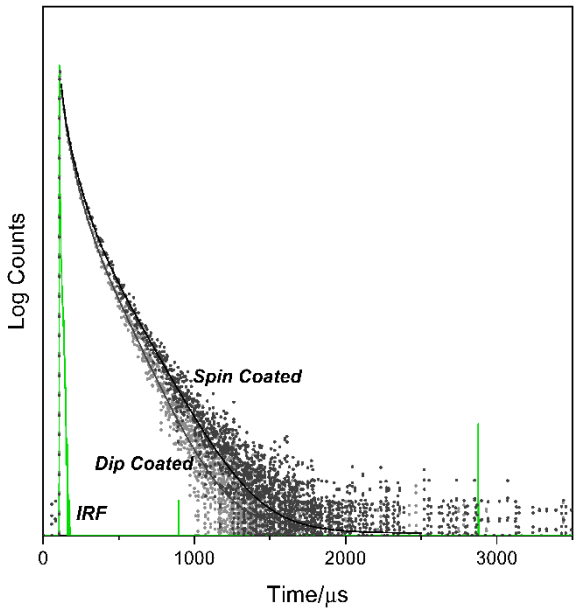


Figure 3.89 – Overlaid lifetime spectra with fitting curves of dip coated **Eu_2SAcbisDBM$_3$@Au** (light grey) and spin coated **SP_Eu_2SAcbisDBM$_3$@Au** (dark grey) with IRF (green). λ_{exc}: 350 nm, λ_{em}: 611 nm.

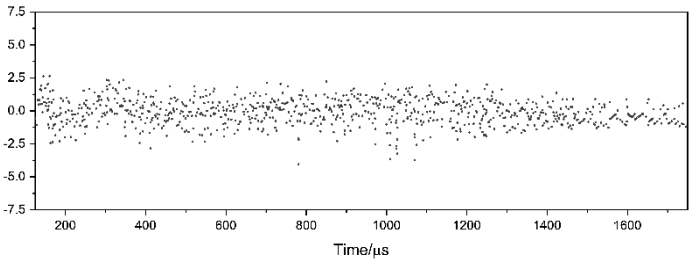


Figure 3.90 – Residuals of the fitting for the lifetime of dip coated **Eu_2SAcbisDBM$_3$@Au**.

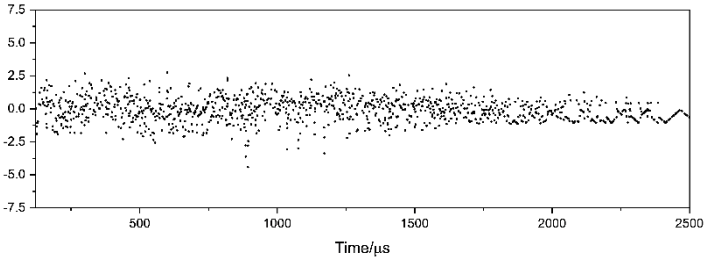


Figure 3.91 – Residuals of the fitting for the lifetime of spin coated **SP_Eu_2SAcbisDBM$_3$@Au**.

Sample	**τ/μs (%)**
Eu_2SAcbisDBM$_3$@Au	**170±20** (29±4%), 68±8 (48±2%), 23±3 (23±4%)
SP_Eu_2SAcbisDBM$_3$@Au	**190** (33%), 61 (46%), 13 (21%)

Table 3.15 – Exponential decay analysis of **Eu_2SAcbisDBM$_3$@Au** (average and standard deviation of n=18) and **SP_Eu_2SAcbisDBM$_3$@Au**.

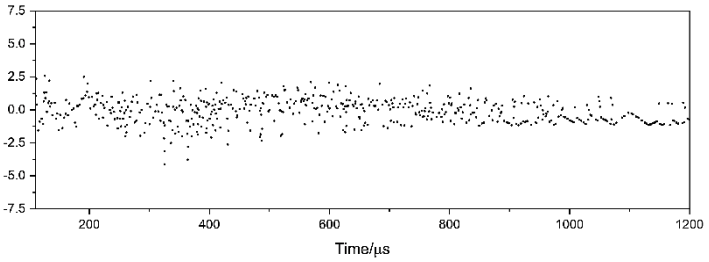


Figure 3.92 – Residuals for the fitting of **SP_Eu_2SAcbisDBM$_3$@pGold**.

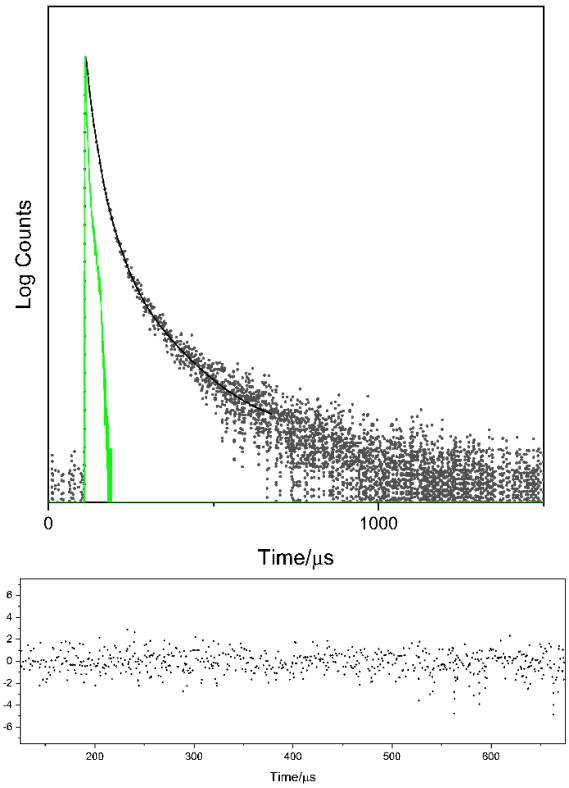


Figure 3.93 – Lifetime spectrum with fitting of **SP_Eu$_2$SAcbisDBM$_3$@pGold** of the imaged area in the epifluorescence image of Figure 3.48 and IRF (green). λ_{exc}: 350 nm, λ_{em}: 611 nm. Below are the residuals of the fitting.

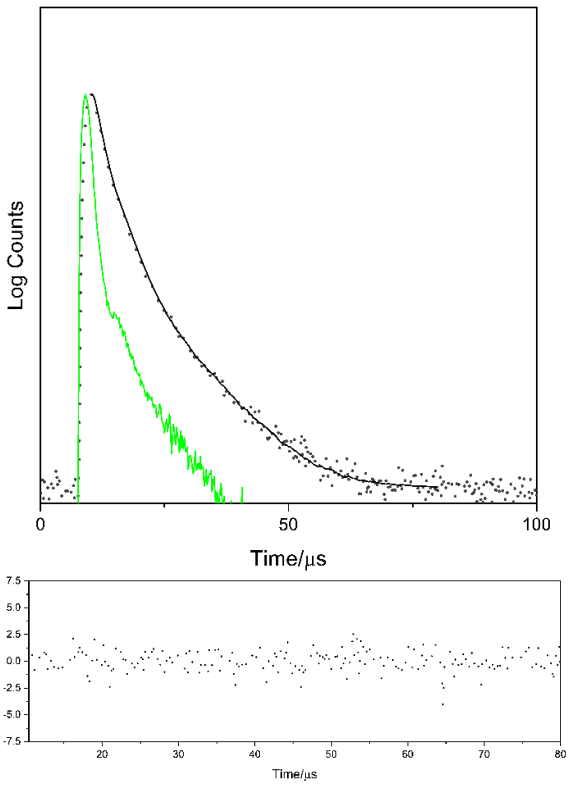


Figure 3.94 – Lifetime spectrum with fitting of **SP_Yb$_2$SAcbisDBM$_3$@pGold** and IRF (green). λ_{exc}: 350 nm, λ_{em}: 977 nm. Below are the residuals of the fitting.

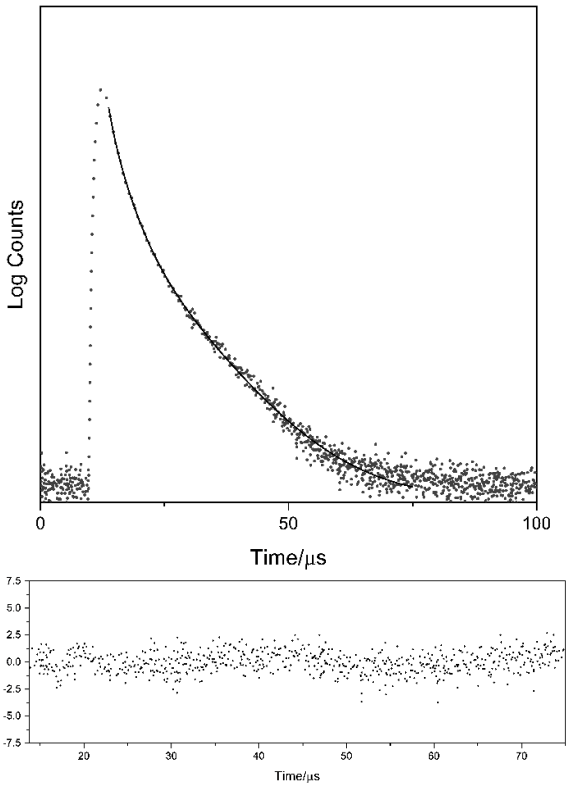


Figure 3.95 – Lifetime spectrum with fitting of **Yb_2SAcbisDBM$_3$** as powder. λ_{exc}: 350 nm, λ_{em}: 977 nm. Below are the residuals of the fitting.

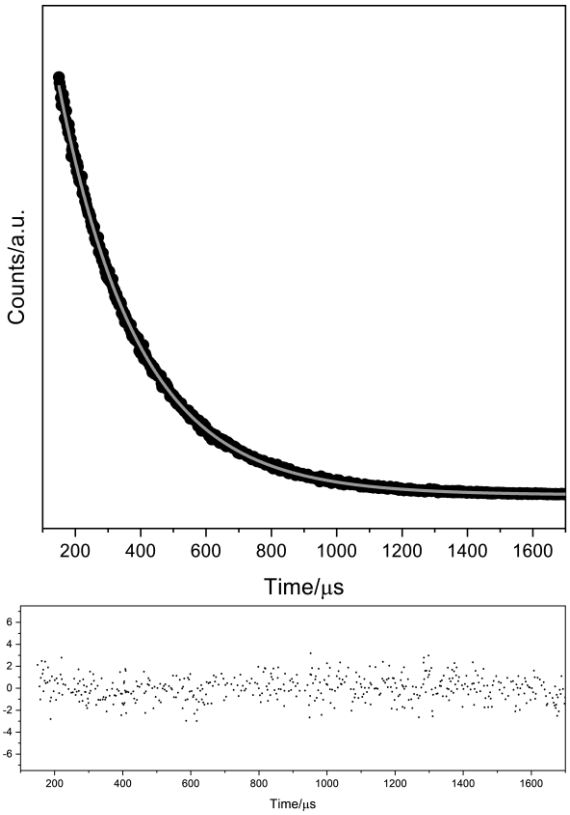


Figure 3.96 – Lifetime spectrum with fitting of **Eu_2bisDBM$_3$** in DMF. λ_{exc}: 350 nm, λ_{em}: 611 nm. Below are the residuals of the fitting.

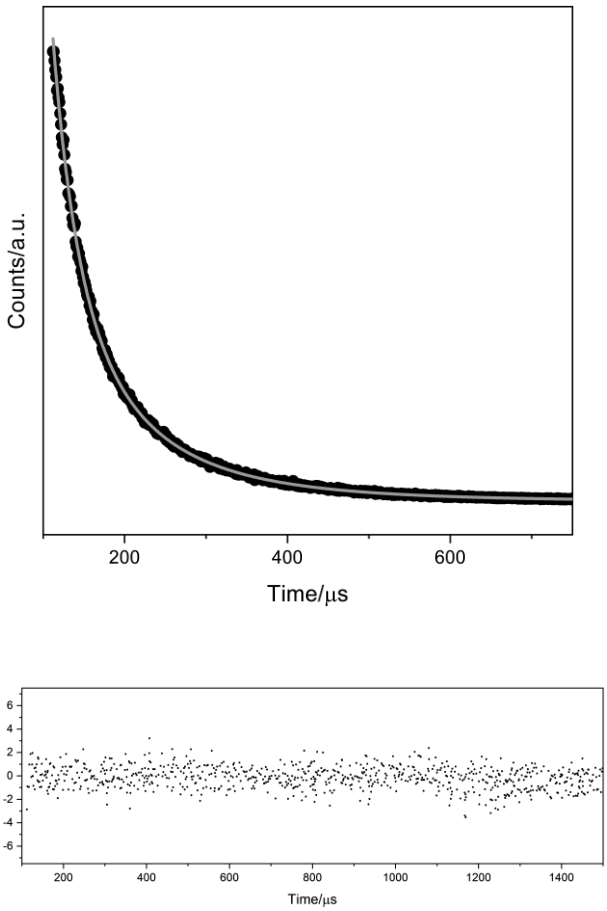
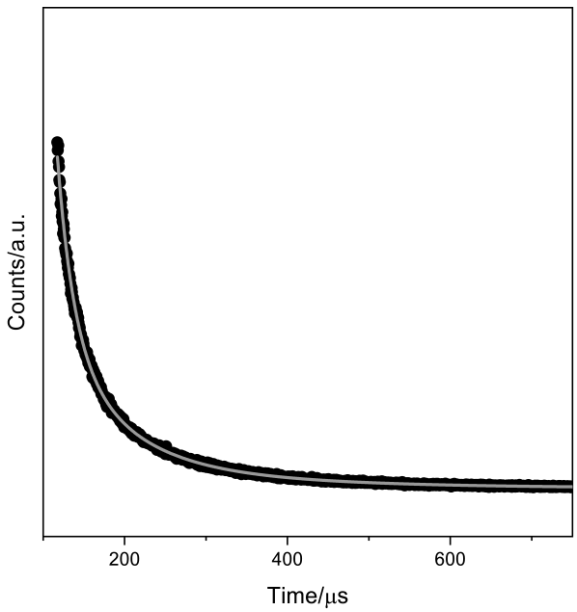


Figure 3.97 – Lifetime spectrum with fitting of **Eu_2bisDBM$_3$_PANI@Au** in DMF. λ_{exc}: 350 nm, λ_{em}: 611 nm. Below are the residuals of the fitting.



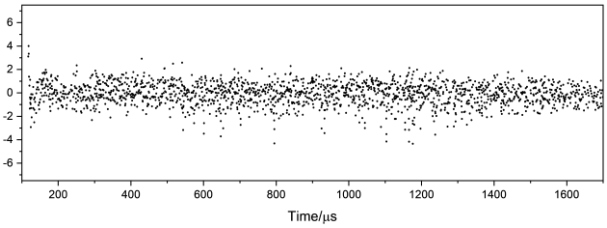


Figure 3.98 – Lifetime spectrum with fitting of **SP_Eu₂bisDBM₃_PANI@Au** in DMF. λ_{exc}: 350 nm, λ_{em}: 611 nm. Below are the residuals of the fitting.

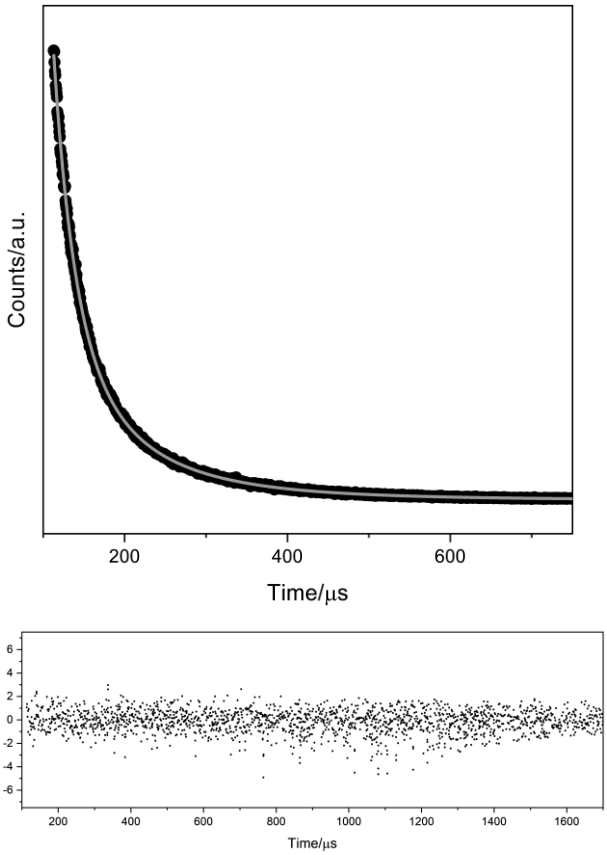


Figure 3.99 – Lifetime spectrum with fitting of **SP_Eu₂bisDBM₃+PANI@Au** in DMF. λ_{exc}: 350 nm, λ_{em}: 611 nm. Below are the residuals of the fitting.

Sample	**τ/μs (%)**
Eu₂bisDBM₃ in DMF	220 (100%)
Eu₂bisDBM₃_PANI@Au	**180** (34%), 80 (45%), 29 (21%)
SP_Eu₂bisDBM₃_PANI@Au	**210** (34%), 73 (48%), 20 (18%)
SP_Eu₂bisDBM₃+PANI@Au	**200** (24%), 79 (49%), 23 (27%)

Table 3.16 – Exponential decay analysis of **Eu₂bisDBM₃** in DMF, **Eu₂bisDBM₃_PANI@Au**, **SP_Eu₂bisDBM₃_PANI@Au** and **SP_Eu₂bisDBM₃+PANI@Au**. λ_{exc}: 350 nm, λ_{em}: 611 nm.

3.5.8 Additional imaging data

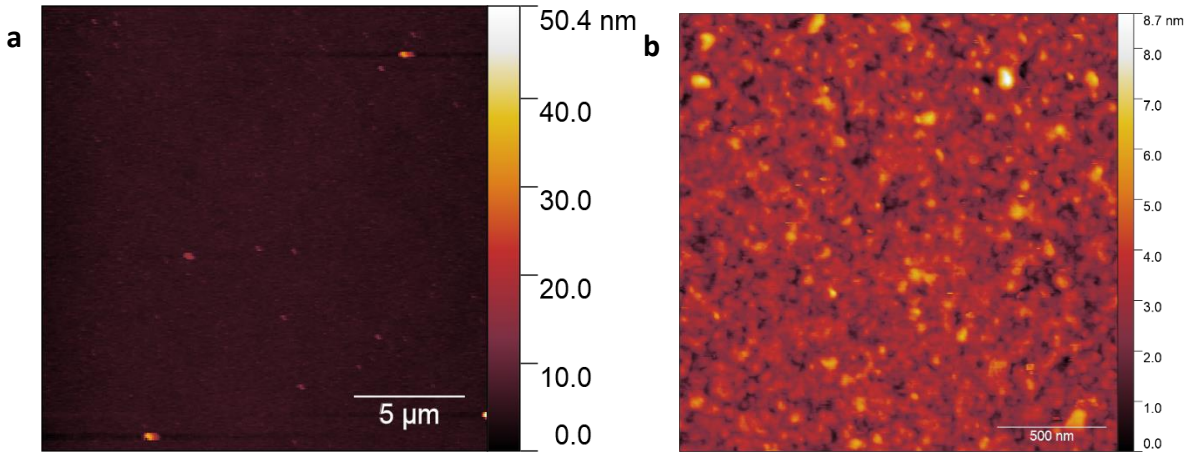


Figure 3.101 – AFM images (20 µm x 20 µm, **a**, and 2 µm x 2 µm, **b**) of a plain Au surface. The images were obtained by Dr. Simon Connell and Dr. Pallavi Kumari at the School of Physics and Astronomy at the University of Leeds.

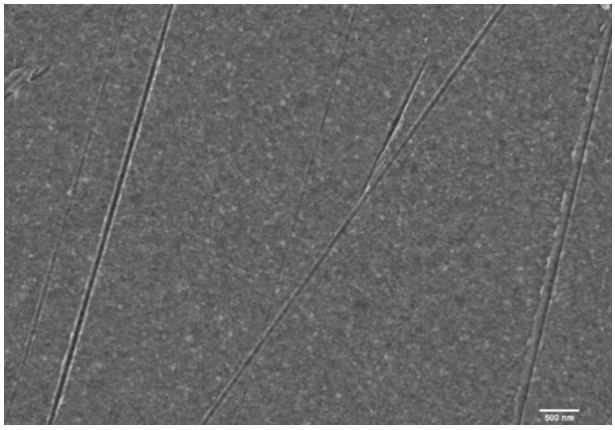


Figure 3.102 – SEM image of a plain Au surface. The image was obtained by Sigrid Benemann at BAM.

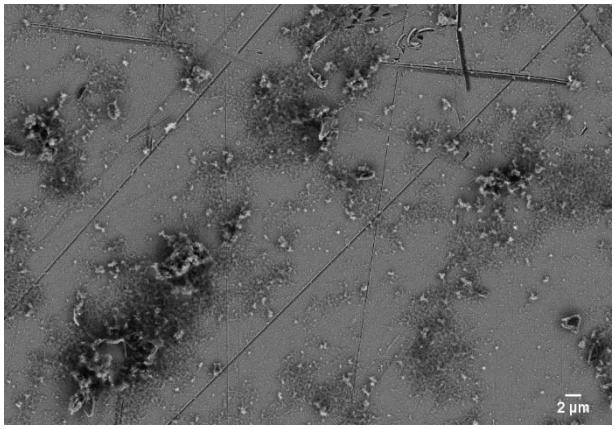


Figure 3.103 – SEM image of **Eu_2SAcbisDBM$_3$@Au** coated in THF (1% DMF). The image was obtained by Sigrid Benemann at BAM.

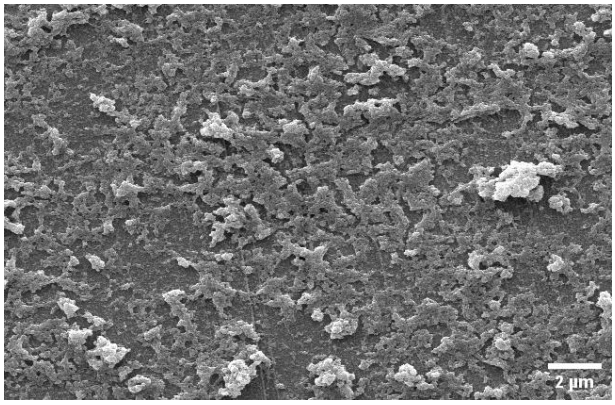


Figure 3.104 – SEM image of **Eu_2SAcbisDBM$_3$@Au** coated in THF (1% DMF) and with addition of hydrazine (0.1 mM).

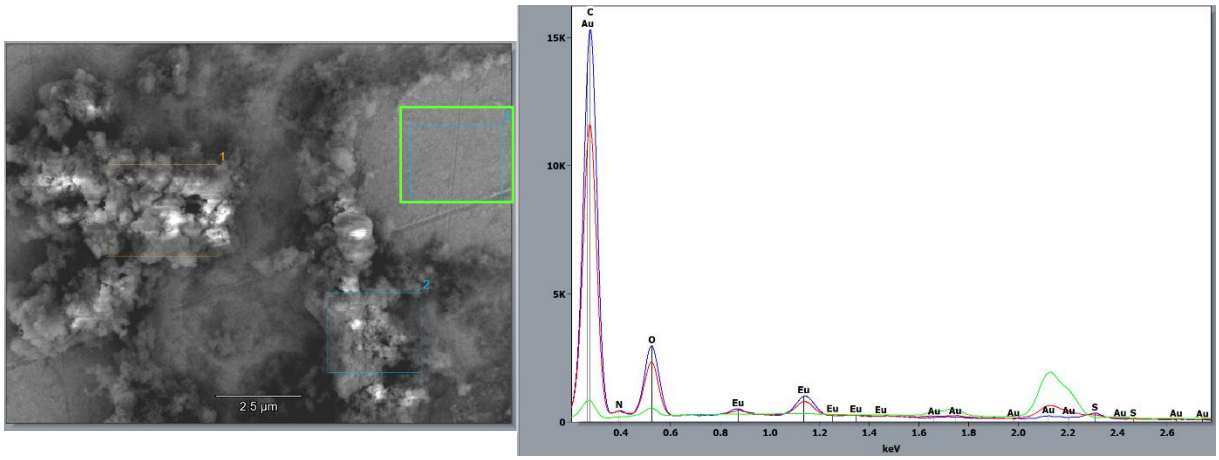


Figure 3.105 – SEM image of **Eu_2SAcbisDBM$_3$@Au** with EDX spectrum of the selected areas (1-3). Area number 3 (green) is highlighted as the control region which does not include the features analysed in the other areas. The image and the EDX spectra were acquired by Sigrid Benemann at BAM.

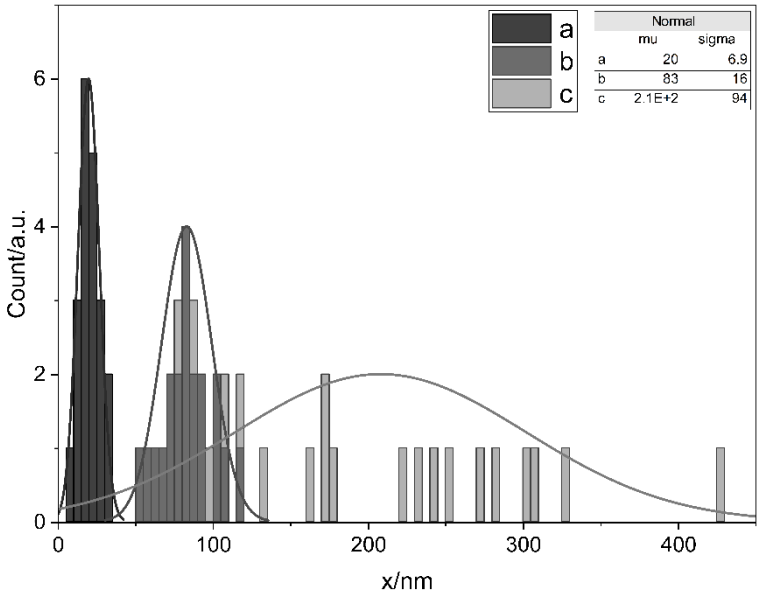


Figure 3.106 – Distributions of measured sizes and distances as reported in the SEM image of pGold (Figure 3.37, section 2.4). a, b and c represent the gap size, width and length, respectively, of Au nanostructures.

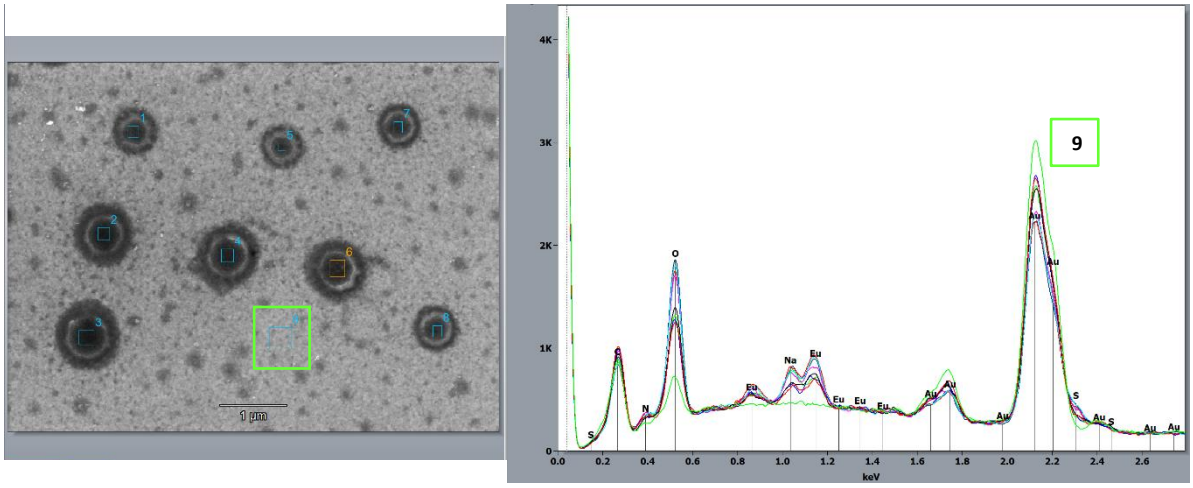


Figure 3.107 – SEM image of **SP_Eu$_2$SAcbisDBM$_3$@Au** with EDX spectrum of the selected areas (1-9). Area number 9 (green) is highlighted as the control region which does not include the features analysed in the other areas. The image and the EDX spectra were acquired at BAM.

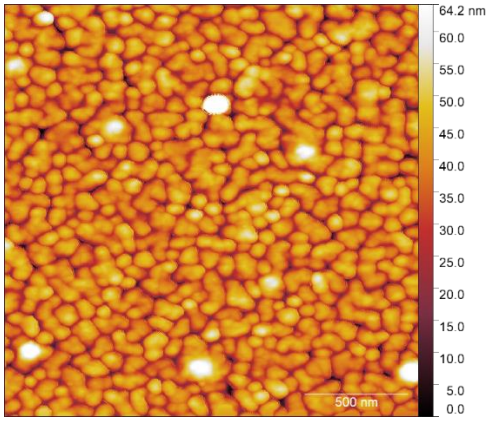


Figure 3.108 – AFM image (2 µm x 2 µm) of **SP_Eu$_2$SAcbisDBM$_3$@pGold**. The image was obtained by Dr. Simon Connell and Dr. Pallavi Kumari at the School of Physics and Astronomy at the University of Leeds.

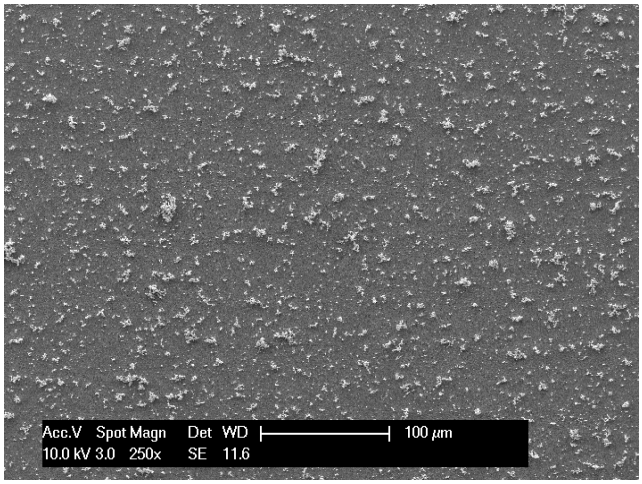


Figure 3.109 – SEM image of a plain AgNIs surface (glass pre-treated with APTES) without the sonication step after coating.

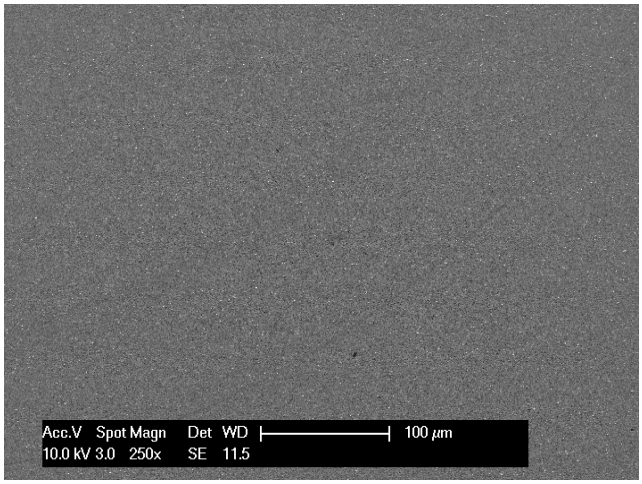


Figure 3.110 – SEM image of a plain AgNIs surface (glass pre-treated with APTES) with the sonication step after coating.

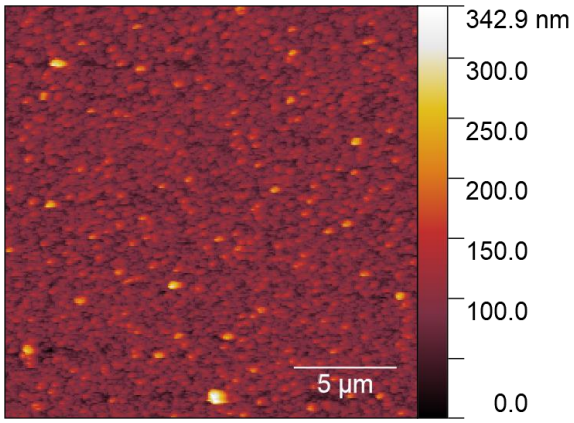


Figure 3.111 – AFM image (20 µm x 20 µm) of **SP_Eu$_2$SAcbisDBM$_3$@AgNIs**. The image was obtained by Dr. Simon Connell and Dr. Pallavi Kumari at the School of Physics and Astronomy at the University of Leeds.

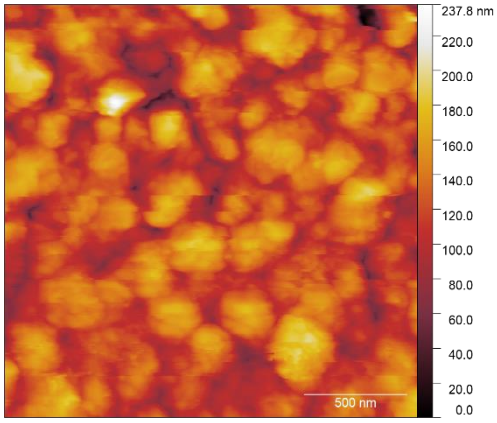


Figure 3.112 – AFM image (2 µm x 2 µm) of **SP_Eu$_2$SAcbisDBM$_3$@AgNIs**. The image was obtained by Dr. Simon Connell and Dr. Pallavi Kumari at the School of Physics and Astronomy at the University of Leeds.

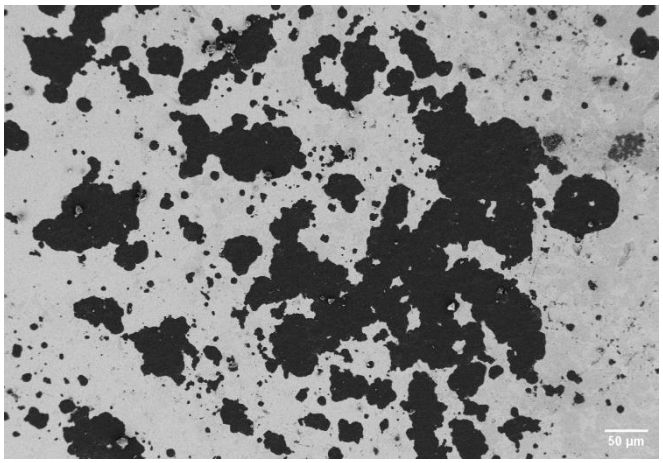


Figure 3.113 – SEM images of **PANI@Au** after overnight immersion in DMF. The images were obtained by Sigrid Benemann at BAM.

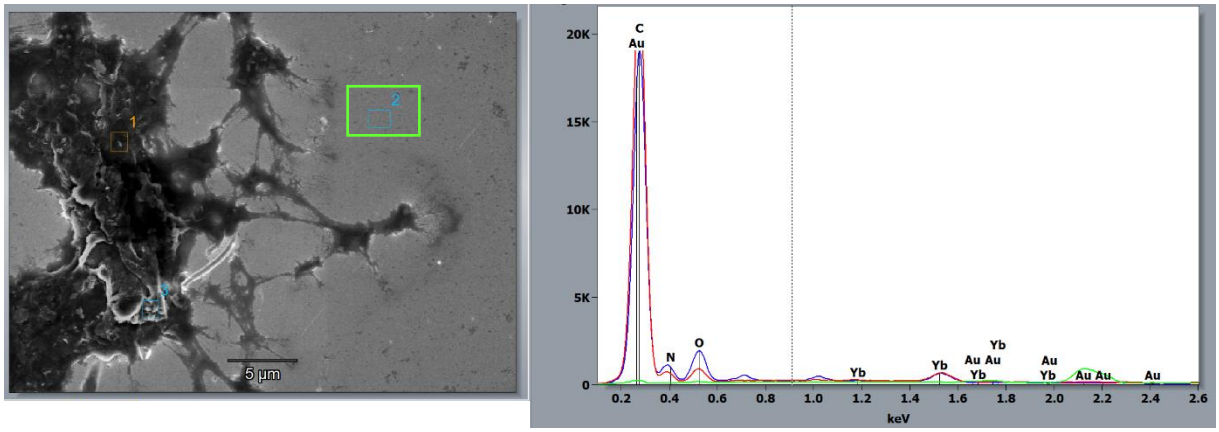


Figure 3.114 – SEM image of **Eu$_2$SAcbisDBM$_3$_PANI@Au** with EDX spectrum of the selected areas (1-3). Area number 2 (green) is highlighted as the control region which does not include the features analysed in the other areas. The image and the EDX spectra were acquired by Sigrid Benemann at BAM.

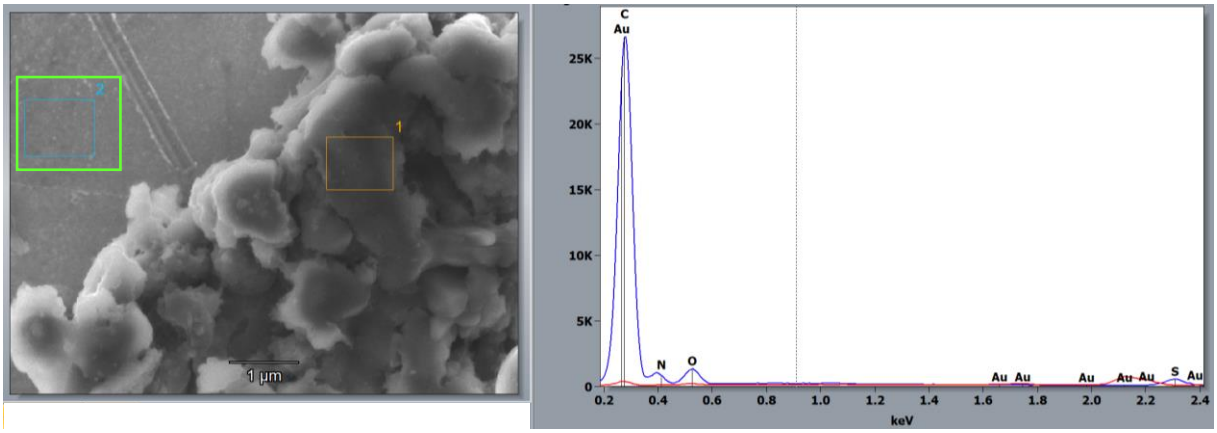


Figure 3.115 – SEM image of **PANI@Au** with EDX spectrum of the selected areas (1-2). Area number 2 (green) is highlighted as the control region which does not include the features analysed in the other areas. The image and the EDX spectra were acquired by Sigrid Benemann at BAM.

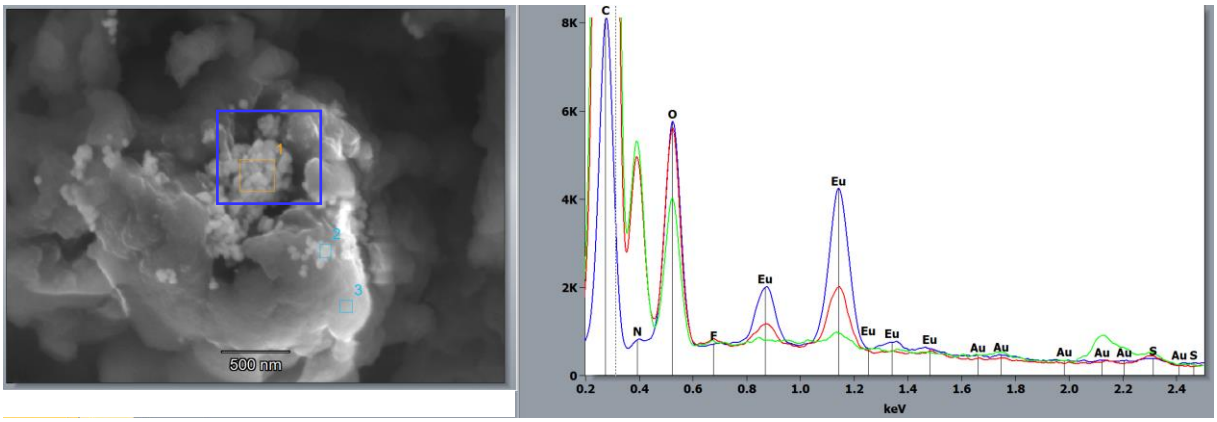


Figure 3.116 – SEM image of **SP_Eu$_2$bisDBM$_3$+PANI@Au** with EDX spectrum of the selected areas (1-5). Area number 1 (blue) is highlighted as the one including the cluster features of interest. The image and the EDX spectra were acquired by Sigrid Benemann at BAM.

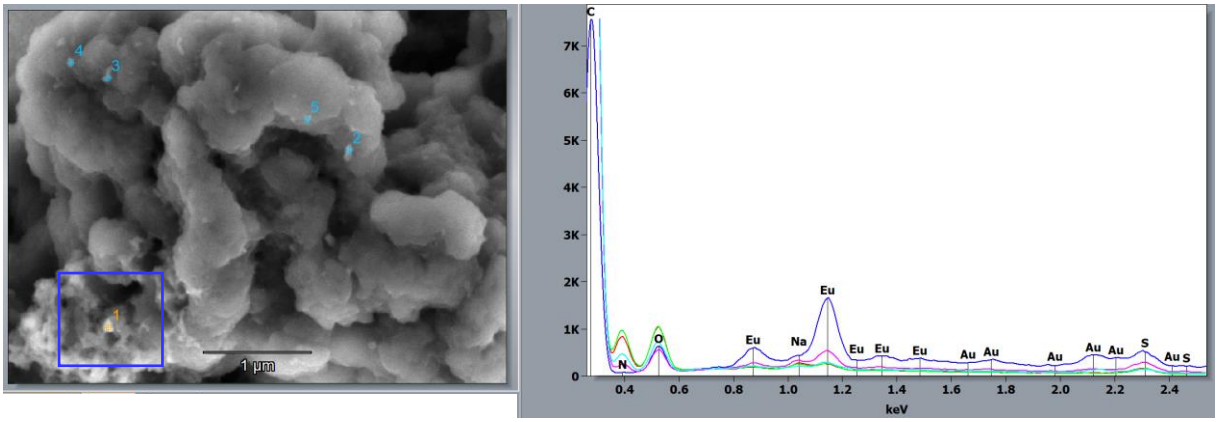


Figure 3.116 – SEM image of **SP_Eu$_2$bisDBM$_3$_PANI@Au** with EDX spectrum of the selected areas (1-5). Area number 1 (blue) is highlighted as the one including the branched features of interest. The image and the EDX spectra were acquired by Sigrid Benemann at BAM.

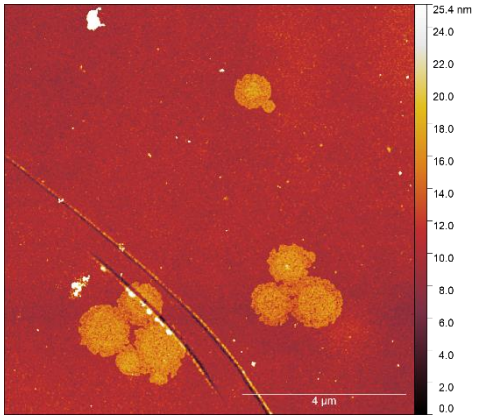


Figure 3.117 – AFM image (20 µm x 20 µm) of **SP_Eu$_2$bisDBM$_3$+PANI@Au**. The image was obtained by Dr. Simon Connell and Dr. Pallavi Kumari at the School of Physics and Astronomy at the University of Leeds.

3.5.9 XPS data

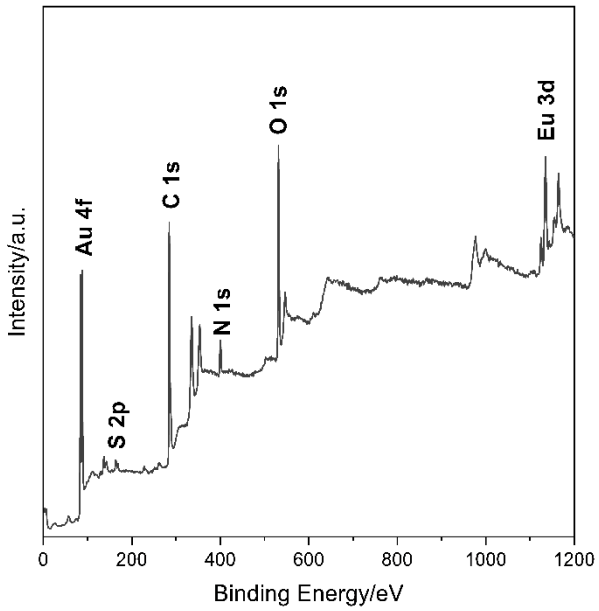


Figure 3.118 – Wide survey XPS spectra of **Eu$_2$SAcbisDBM$_3$@Au**. The spectrum was acquired by M.Eng. Jörg M. Stockmann at BAM.

C (At.%)	N (At.%)	O (At.%)	S (At.%)	Eu (At.%)
71.1±2.3	6.4±0.3	18.5±2.6	2.5±0.1	1.5±0.1

Table 3.17 – Atomic percentages measured in the wide survey XPS spectrum of **Eu$_2$SAcbisDBM$_3$@Au**. Three ROIs were analysed and the reported values are the averages with standard deviation.

	C/Eu	N/Eu	O/Eu	S/Eu
Expected	46.5	4.5	7.5	1.5
Found	48.3 ± 1.4	4.4 ± 0.2	12.6 ± 2.5	1.7 ± 0.0

Table 3.18 – Elemental ratios as calculated from the atomic percentages measured in the wide survey XPS spectrum of **Eu_2SAcbisDBM$_3$@Au**. Three ROIs were analysed and the reported values are the averages with standard deviation. The expected values are calculated from the chemical formula of the **Eu_2SAcbisDBM$_3$** complex ($C_{93}H_{75}Eu_2N_9O_{15}S_3$).

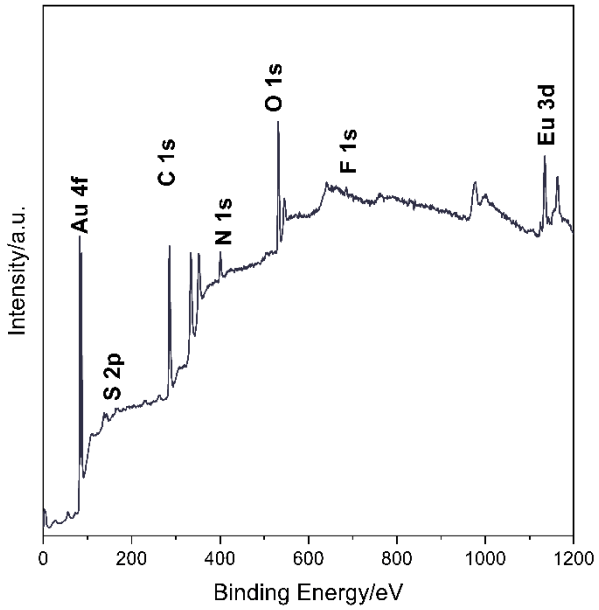


Figure 3.119 – Wide survey XPS spectra of **Eu_2SAcbisDBM$_3$@Au-F**. The spectrum was acquired by M.Eng. Jörg M. Stockmann at BAM.

C (At.%)	N (At.%)	O (At.%)	S (At.%)	F (At.%)	Eu (At.%)
72.9±0.8	6.4±0.5	16.8±0.9	1.8±0.1	0.6±0.0	1.1±0.0

Table 3.19 – Atomic percentages measured in the wide survey XPS spectrum of **Eu_2SAcbisDBM$_3$@Au-F**. Three ROIs were analysed and the reported values are the averages with standard deviation.

		C/Eu	N/Eu	O/Eu	S/Eu	F/Eu
	Expected	46.5	4.5	7.5	1.5	-
Eu_2SAcbisDBM$_3$@Au-F	**Found**	65.8 ± 2.8	5.7 ± 0.5	15.2 ± 0.7	1.6 ± 0.1	0.6 ± 0.0
	Deviation	+19.3	+1.2			

Table 3.20 – Elemental ratios as calculated from the atomic percentages measured in the wide survey XPS spectrum of **Eu_2SAcbisDBM$_3$@Au-F**. Three ROIs were analysed and the reported values are the averages with standard deviation. The expected values are calculated from the chemical formula of the **Eu_2SAcbisDBM$_3$** complex ($C_{93}H_{75}Eu_2N_9O_{15}S_3$).

3.5.10 Additional simulations of pGold

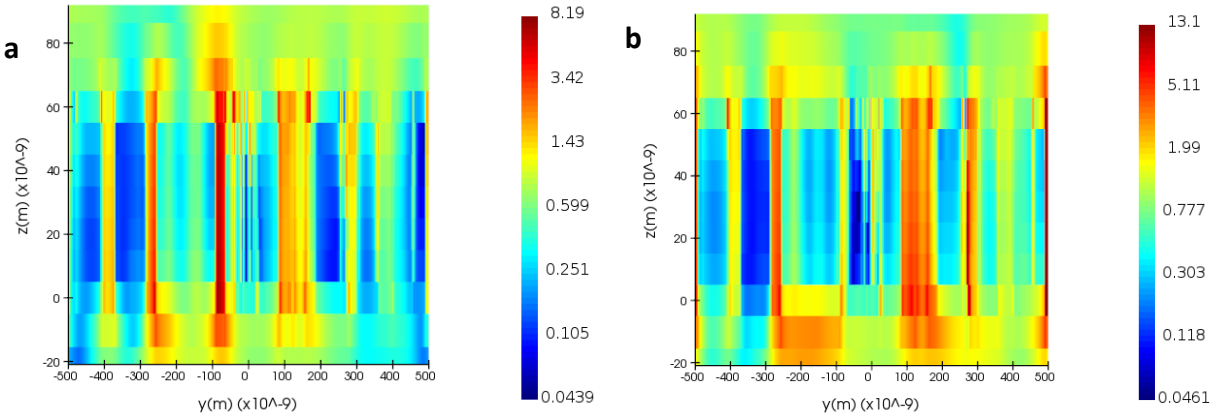


Figure 3.120 – Simulated localised electric field (scalebar, absolute value in logarithmic scale) over pGold surface for the emission at 982 nm (**a**) and 1055 (**b**), as seen from the side of the surface. The simulation and image were made by Dr. Miguel Navarro-Cía at the School of Physics and Astronomy and School of Engineering at the University of Birmingham.

3.5.11 Addition Raman data and assignments

	Wavenumber/cm^{-1}	
Assignment	**PANI ES/PANI@Au**	**Eu$_2$bisDBM$_3$_PANI@Au**
C-C B ring or C=O	1643 (m)	-
C=C Q stretching	1595 (vs)	1634 (sh), 1604 (m), 1589 (m)
C=N Q stretching	1502 (s), 1464 (m)	1463 (vs), 1411 (w)
Phenazine-like unit	-	1411 (sh)
C-N$^{+\cdot}$ stretching	1380 (s), 1333 (s)	1378 (w), 1333 (w)
C-N B and Q stretchings	1220-1255 (w)	1216 (m)
C-H bending	1161 (vs)	1160 (s)

Table 3.21 – Peak positions and assignments of the Raman spectra of PANI ES (powder)/**PANI@Au** and **Eu$_2$bisDBM$_3$_PANI@Au**. Sh: shoulder, vs: very strong, s: strong, m: medium, w: weak.

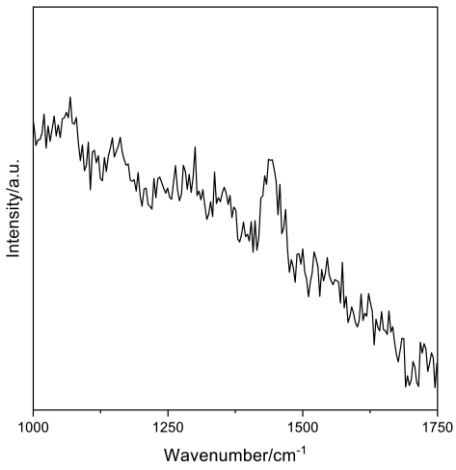


Figure 3.121 – Raman spectrum of **Eu$_2$bisDBM$_3$+PANI@Au**. λ laser excitation: 633 nm.

Chapter 4 – Lanthanide(III) coated luminescent Au nanoparticles (AuNPs)

4.1 Introduction

4.1.1 General principles of AuNPs

Au nanoparticles (AuNPs) have received much attention in recent decades. Their excellent chemical and physical stabilities, distinctive optical properties, and ease of synthesis and functionalisation have driven their incorporation to a range of systems, from biomedical and therapeutical applications to sensing and catalysis.[1-6]

The behaviour of AuNPs stems from their nanoscale nature, affording their characteristic LSPR frequencies and distinctive colours.[7, 8] It is indeed the presence of LSPRs that make nanomaterials, including AuNPs, stand out from other substrates. The high sensitivity of LSPR frequencies to changes in the medium is an excellent sensing readout, while the confinement of the incident electromagnetic (EM) field on the surface of AuNPs can enhance optical and catalytic processes.[9, 10]

4.1.1.1 The fabrication of AuNPs

The large scale preparation of AuNPs is routinely performed, affording highly monodispersed AuNPs with controlled sizes and shapes. The methods for the synthesis of AuNPs can be divided in three classes. These are:

- Physical methods, such as laser ablation and lithography. These methods rely on the nanoscale patterning of films or pellets of metal (bulk) to produce AuNPs of

predetermined sizes and shapes with high precision and control. The high cost and significant amounts of waste material produced with these techniques constitute the main drawbacks for this class of methods.[11-13]

- Biological methods, also referred to as "green methods". In this approach, microorganisms (e.g. bacteria and fungi), plant extracts or polysaccharides are used to reduce Au salts and drive the nucleation and formation of AuNPs. This method is of high interest due to the environmentally friendly synthesis conditions. However, the poor monodispersities of the prepared AuNPs represent a significant setback.[14-16]
- Chemical methods, such as the Turkevich or Brust methods. Similarly to the green method, these routes rely on the reduction of Au salts by means of reducing agents such as trisodium citrate or $NaBH_4$. Chemical methods produce highly monodispersed AuNPs with controlled sizes and shapes, although the toxicity of the reactants is considered a primary issue.[17, 18]

Due to the low cost and accessibility of the required materials, as well as the extensive studies conducted to fine tune the synthetic conditions, the chemical route is one of the preferred methods for the fabrication of AuNPs.[19, 20] Since its introduction in 1951, the Turkevich method has seen tremendous popularity for the simple and highly reproducible preparation of small AuNPs (10-20 nm).[21, 22] In this method, Au(III) atoms are reduced to Au(0) by a reducing (and capping) agent, promoting the nucleation and growth into well dispersed AuNPs in the aqueous phase.[23] $HAuCl_4$ is the traditional source of Au(III), while trisodium citrate and ascorbic acid are the most common reducing agents.[17, 21] The Turkevich method is optimal for the preparation of smaller AuNPs, while sizes above 20 nm are easily obtained by the seed mediated growth approach. The size of the seeds (i.e. AuNPs with smaller dimensions than the

desired one) is step-wise increased by addition of Au(III) salt and a reducing agent. [20, 24] Tuning the rates of addition and temperature have produced highly reproducible methods for the preparation of AuNPs up to 200 nm in size.[20, 24]

4.1.1.2 The optical properties of AuNPs

The absorption spectra of AuNPs are characterised by large extinction cross sections dominated by the LSPR band (Figure 4.1), whose frequencies (in the range of 515-572 nm) are extremely sensitive to changes in composition, size, shape and coating.[25]

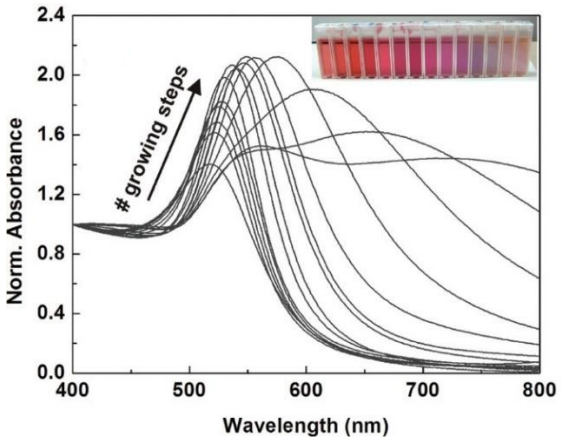


Figure 4.1 – UV-Vis spectra of AuNPs of sizes from 10 nm to 200 nm. The inset is a photograph of the AuNP samples. The spectra and image have been taken from [20].

In 1908, Mie first described the extinction cross sections (σ_{Ext}) of metallic NPs as a combination of both absorption (σ_{Abs}) and scattering (σ_{Scat}) contributions (Equation 4.1), whose ratio is highly dependent on the size of the NP and can be deconvoluted with Mie theory calculations.[6, 26, 27]

$$\sigma_{Ext} = \sigma_{Scat} + \sigma_{Abs} \quad Equation\ 4.1$$

For smaller AuNPs (radius << λ), the absorption component is dominant ($\sigma_{Ext} \approx \sigma_{Abs}$), while the scattering contribution prevails at larger sizes. This is exemplified in Figure 4.2, **a** with AuNP

sizes from 40 nm to 100 nm and is also reflected in the dichroic behaviour observed in Figure 4.2, **b**.[7, 28, 29] AuNPs can thus be tailored to exhibit the degree of absorption or scattering component intended for the purpose of the nanomaterial.

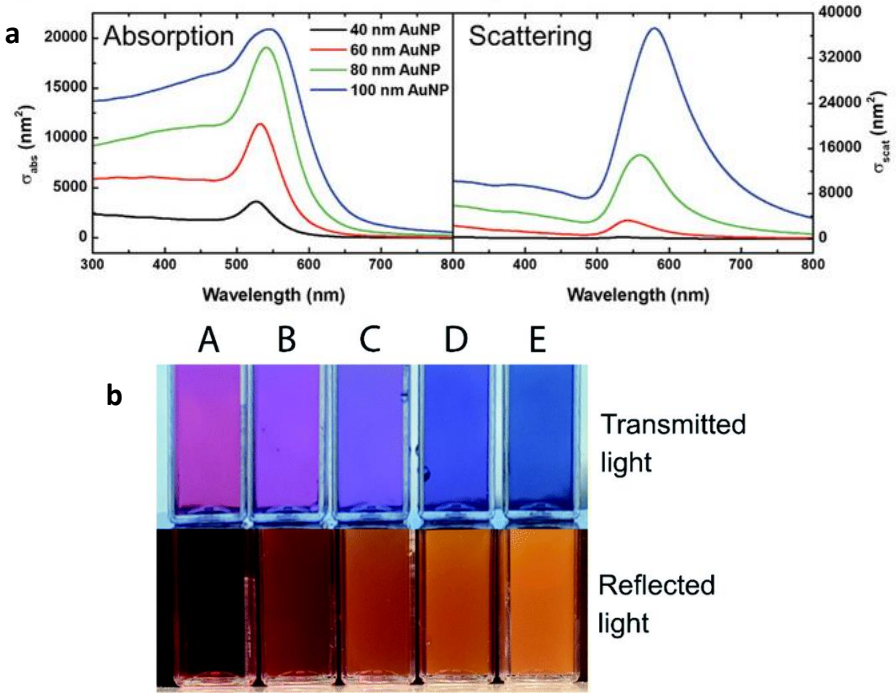


Figure 4.2 – **a** Calculated absorption and scattering cross sections (σ_{Abs} and σ_{Scat}, respectively) as a function of AuNP size. The spectra have been taken from [29]. **b** Photograph of AuNP samples with increasing sizes and scattering components (from A to E) as seen under daylight (transmitted light) and in front of a dark background (reflected light). The image has been taken from [7].

For AuNPs with high $\boldsymbol{\sigma_{Abs}}$, upon irradiation at the LSPR a local increase in temperature (i.e. hyperthermia) occurs. This effect has been utilised for the elimination of e.g. cancer cells and bacterial infections in tissues. Importantly, the functionalisation of AuNPs with targeting antibodies, as well as the efficient and localised thermal conversion of AuNPs upon irradiation, have prevented the damaging of surrounding tissues. [29-31] The local heat generation of AuNPs upon light absorption has also been associated with the generation of acoustic signals by thermal-induced expansion of the surrounding medium (i.e. photoacoustic signal) and photoacoustic imaging has been demonstrated, for example, in the intraoperative detection and removal of tumour cells *in vivo*.[32, 33] The scattering component of the $\boldsymbol{\sigma_{Ext}}$ has been

associated with enhanced light-coupling efficiencies, both in the far- and near-fields. These have been applied for the improved light absorption of photovoltaics, affording lower physical thicknesses of absorber layers and thus producing more cost-efficient materials.[34, 35] Furthermore, the scattering of AuNPs is substantially more intense than the one of biological samples and it can be detected under dark-field illumination. Imaging agents based on this principle have displayed exceptional chemical and photostabilities compared to organic dye probes, as well as tuneable colours due to the signal's being shape and composition dependent.[36]

4.1.1.3 The functionalisation of AuNPs

In addition to their intrinsic features, the extraordinary potential of AuNPs lies in their ease of functionalisation to impart novel properties and purposes. A range of functionalisation methods can be employed, based on both chemi- and physisorption, with interactions between thiols, amines or carboxylic acids and Au being the most popular approaches for the conjugation of molecules to the nanostructure.[37] Among others, antibodies, carbohydrates and drugs have been conjugated to AuNPs, tailoring the nanomaterial composition to the application.[38-43] Vetro *et al.* have presented a glycol-AuNP vaccine against *Streptococcus pneumoniae* by attachment of two synthetic carbohydrate antigens *via* thiol-Au bonds to 2 nm AuNPs. The functionalised AuNPs elicited a stronger immune response in mice than the one of the single antigens and this was comparable to the one of commercially available vaccines.[44] Incorporation of antibiotics and their intermediates to AuNPs allows for higher loadings, due to the high surface to volume ratios, and improved delivery in bacteria.[45] Yang *et al.* have prepared 6-aminopenicillanic acid coated AuNPs (3 nm) to target multi-drug resistant bacteria. By doping the coated AuNPs in electrospun fibres of poly(ε-caprolactone) and gelatine, a

dressing was fabricated, displaying substantial inhibition of multi-drug resistant wound infections and improved wound-healing effects compared to other dressings.[46]

Unlike bulk Au, the colloidal stability of AuNPs must be considered to avoid aggregation and preserve the original physical and chemical properties of the nanomaterial.[47, 48] During the synthesis of AuNPs *via* most chemical methods, capping agents (e.g. trisodium citrate, cetyltrimethylammonium bromide, or polyvinylpyrrolidone) are introduced, providing stabilisation by either electrostatic or steric effects.[49-51] Some of these capping agents, however, can be easily displaced, especially in biological settings of high ionic strengths. To impart further stability, a range of polymers, surfactants and biomolecules have been reported.[47, 52] In an example by Wang *et al.*, the poor stability of cetyltrimethylammonium bromide on the surface of Au nanorods (AuNRs, 58x13 nm) was reported to lead to a partial release of the molecules, with subsequent intercalation and disruption of biological membranes. However, such cytotoxicity was not detected when the AuNRs were coated with a more stable polyelectrolyte poly(diallyldimethylammonium chloride) ligand, highlighting the importance of evaluating stabilities if biological settings are considered.[53] The importance and role of the capping ligand was also exemplified for catalysis purposes by the groups of Baker and Murphy, where the attachment of dodecanethiol to AuNPs (2 nm) led to a 100-fold increase in yield compared to polycrystalline Au for the reduction of CO_2.[54]

4.1.2 The functionalisation of AuNPs with luminescent lanthanide(III) complexes

In addition to biologically active units, such as drugs and antibodies, AuNPs have been functionalised with luminescent components, thus combining their plasmonic properties and high surface to volume ratios with the luminescent signal of optical probes.[6, 29, 55, 56] Such luminescent materials have been prepared by the coupling to molecular emitters, e.g. organic dyes and metal complexes, as well as optically active materials like upconversion nanoparticles (UCNPs).[3, 57-61]

Pikramenou and Osborne have anchored Ru(II) complexes *via* thiol groups to AuNPs (13 nm, 50 nm and 100 nm, Figure 4.3, **a**).[61] In their work, the authors investigate the effect of longer spacer chains to improve the luminescence lifetime of the probe (**1**-**3**). The Ru(II) complex with the longest chain (**3**, Figure 4.3, **a**) displayed the largest enhancement (70%) upon attachment on the AuNPs, ascribed to the reduced quenching from the metal surface at longer distance and the effect of the fluorinated surfactant on the AuNPs. Interestingly, the luminescence lifetime was not found to be dependent on AuNP size.[61] In another example, the group anchored a Ir(III) cyclometalated complex (**4**) to AuNPs (13 nm, 25 nm and 100 nm, Figure 4.3, **b**) to produce probes for two-photon lifetime imaging.[62] The short-lived (ps range) and long-lived (ns range) luminescence lifetimes of the Au and Ir(III) components, respectively, allowed for multichannel detection in cancer cells. Furthermore, the luminescence lifetime of Ir(III) was found to be sensitive to the local cell environment, so that mapping of the imaged cells at long excitation wavelengths (λ_{exc}: 760 nm) was achieved.[62]

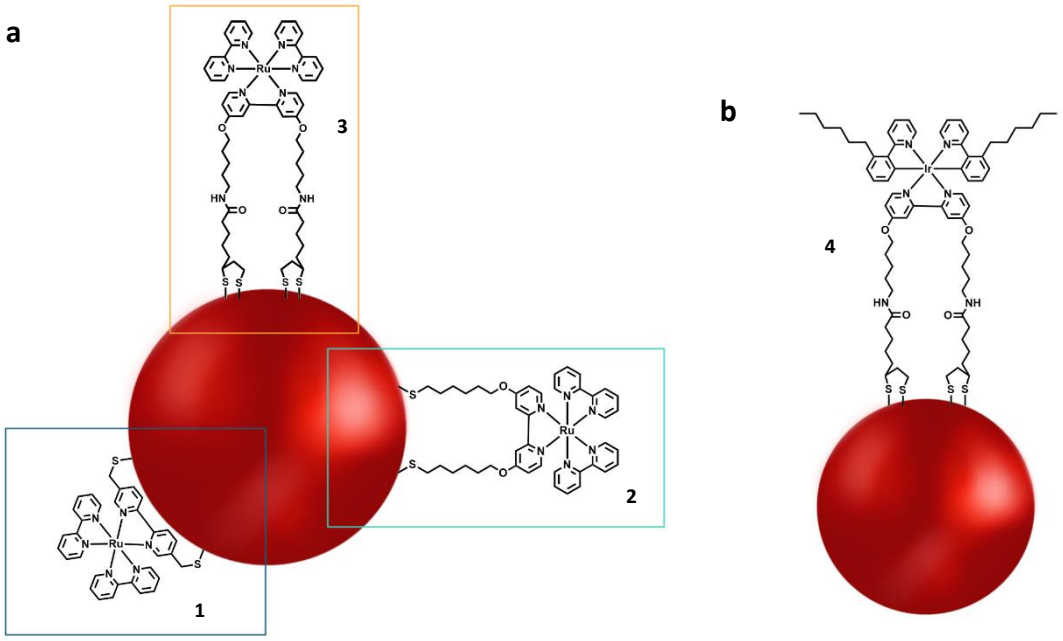


Figure 4.3– **a** Chemical structures of the surface active Ru(II) complexes on AuNPs (13 nm, 50 nm, 100 nm) reported by Pikramenou and Osborne.[61] **b** Chemical structure of the Ir(III) complex reported by Pikramenou and co-workers.[62]

Mendez-Gonzalez *et al.* have investigated the effect of AuNPs sizes on the luminescence of UCNPs ($NaYF_4$:Yb,Er).[58] SiO_2 coated UCNPs (≈18 nm core, ≈4 nm shell) were functionalised with APTES for interaction with AuNPs, whose sizes ranged from 4 nm to 66 nm. Upon excitation at 980 nm, the green luminescence at 525 nm and 540 nm arising from Er(III) $^2H_{11/2} \rightarrow {}^4I_{15/2}$ and $^4S_{3/2} \rightarrow {}^4I_{15/2}$ transitions was found to be quenched by small AuNPs (size below 41 nm, 40% quenching efficiencies), using the UCNPs not coupled to AuNPs as reference. Interestingly, the trend reversed with big enough sizes (above 50 nm) and was ascribed to a moderate plasmonic enhancement of luminescence due to the small overlap with the LSPR of AuNPs (≈540 nm).[58]

In addition to UCNPs, also molecular complexes of lanthanides(III) have been anchored on AuNPs. One of the first examples of ligands for lanthanide(III) complexation on AuNPs has been reported by Ipe *et al.*.[63] In their design, the authors coat AuNPs (4 nm diameter) with high

concentrations of surface active 2,2'-bipyridine ligands. Upon addition of Eu(III) or Tb(III), the ions coordinate to the 2,2'-bipyridine units in a 1:3 ratio (Ln(III): 2,2'-bipyridine, Figure 4.4, **5**), affording well resolved luminescence. The functionalised AuNPs were then employed for the sensing of divalent cations (e.g. Ca(II), Zn(II) and Cu(II)) by displacement of the Eu(III) or Tb(III) ions and resulting in a luminescence decrease.[63]

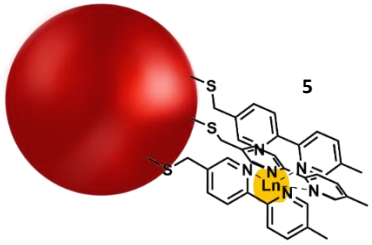


Figure 4.4 – Chemical structures of the surface active 2,2'-bipyridine ligands upon complexation of Ln(III) ions in a 3:1 ratio, i.e. **5**, reported by Ipe *et al.*. Ln(III)=Eu(III), Tb(III).[63]

In an optimised approach relying on the formation of thermodynamically stable complexes prior to attachment on AuNPs, Pikramenou and co-workers have presented a novel surface active Eu(III) complex (**6**, Figure 4.5). The ligand scaffold was based on a substituted DTPA fitted with thiophenols for anchoring on AuNPs (13 nm). The conjugation of the complexes to AuNPs was efficiently monitored by tracking the shift of the LSPR band and, importantly, a purification step by size exclusion chromatography was introduced prior to the assessment of the optical properties of the material, removing excess unbound complex and producing luminescence data of the Eu-AuNP system alone.[64] Complex **6** and its Ce(IV) analogue were also employed by the group for the investigation of DNA damage caused by AuNPs and PtNPs. Here, the Eu(III) coated AuNPs could be localised and detected in cells by high resolution synchrotron X-ray fluorescence microscopy and the genotoxicity of internalised NPs could be assessed.[65] The same group has introduced longer surface active spacers to aminoquinoline substituted DTPA

Eu(III) complexes (**7**, Figure 4.5), to reduce short distance quenching. The addition of a pH low insertion peptide to the AuNPs has produced luminescent nanomaterials that can be delivered into platelets and tracked by bioimaging.[66]

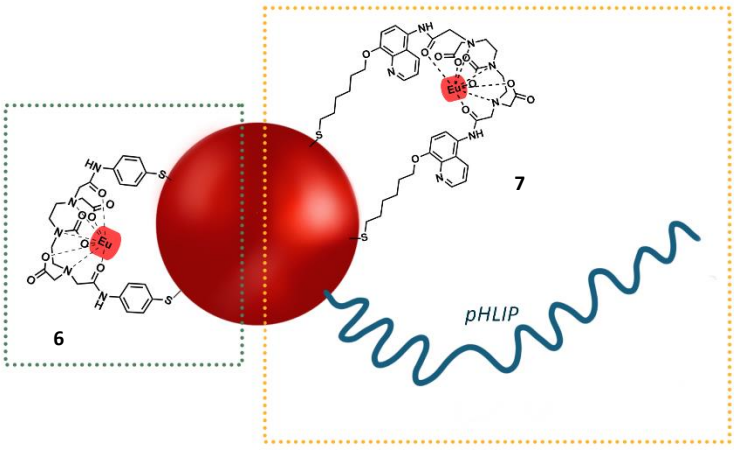


Figure 4.5 – Chemical structures of the surface active "short legs" (**6**) and "long legs" (**7**) Eu(III) DTPA complexes on AuNPs (13 nm) reported by Pikramenou and co-workers.[64, 66]

Whereas these approaches are based on a DTPA scaffold, Gunnlaugsson and co-workers have focused on the incorporation of substituted cyclen complexes to AuNPs (≈4 nm diameter, Figure 4.6). The AuNPs were synthesised with the two-phase Brust method in toluene and H_2O and with 4-dimethylaminopyridine (DMAP) as capping agent, which readily exchanges upon addition of the complex (**8**). The scaffold of **8** does not include an antenna, so that the system is only weakly luminescent. Upon addition and coordination of an ancillary naphthalene β-diketonate unit (Nta, Figure 4.6), the luminescence is sensitised and characteristic Eu(III) emission is recorded.[67] This approach has been used for the sensing of biologically relevant analytes, i.e. flavin monophosphate and bovin serum albumin, where the red luminescence of the nanomaterial was reduced by either displacement of the antenna or interaction with it.[68, 69] The addition to the cyclen scaffold of disodium iminodiacetate chelators for Ca(II) binding (**9**, Figure 4.6) further advanced this system, targeting Ca(II) accumulations found in bone

microcracks.[70] Bovine bone was imaged by two photon excitation microscopy, producing 3D fluorescence images of the microdamaged areas of the bone. Importantly, the authors report that the immobilisation of Eu(III) complexes on AuNPs leads to lower concentrations of complex required for imaging, compared to the free probe, which is highly beneficial for *in vivo* applications.[70] The advantages of AuNPs as supports for the anchoring of molecules have been utilised in the development of logic gate mimics. The attachment of both Eu(III) and Tb(III) complexes **10**, alongside the introduction of lanthanide(III) specific antennae (Nta for Eu(III) and 4-(dimethylamino)benzoic acid, DMAB, for Tb(III)) have produced a system where red or green luminescence is independently turned on or off and thus acting as a logic gate (Figure 4.6).[71]

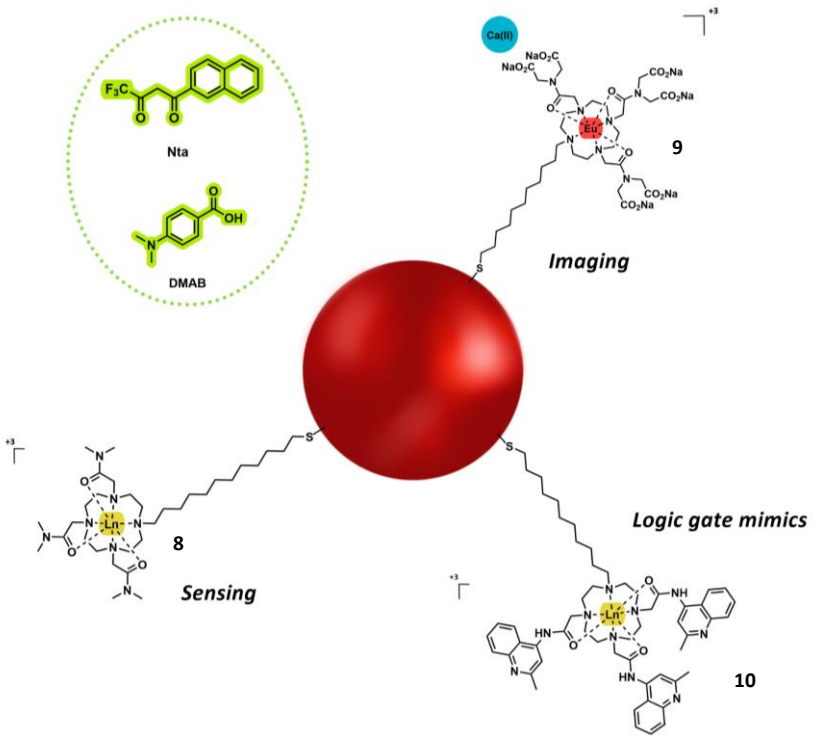


Figure 4.6 – Chemical structures of the Ln(III) complexes for sensing (**8**, Ln(III) = Eu(III) or Yb(III))[67-69, 72], imaging, **9**,[70] and logic gate mimics (**10**, Ln(III) = Eu(III) or Tb(III))[71] with the proposed antennae (Nta and DMAB) reported by Gunnalaugsson and co-workers for attachment on AuNPs.[68-72]

The combination on AuNPs of Eu(III) complexes and biomolecules has been reported for the highly selective sensing of enzymes. The attachment to AuNPs of peptides for the coordination of lanthanides(III) was first reported by Pikramenou and co-workers. Dithiol functionalised peptides were anchored on AuNPs (13 nm diameter) and the subsequent coordination to Eu(III) ions led to characteristic luminescence.[73] Wang *et al.* have attached a diketonate based Eu(III) complex (**11**, Figure 4.7) and a 7-amino-4-methylcoumarin dye (AMC, blue in Figure 4.7) to the N- and C-termini of a peptide, respectively, for dual emission at a single excitation wavelength (400-500 nm for AMC and 570-720 nm for Eu(III) complex, λ_{exc}: 350 nm). When anchored on AuNPs (13 nm diameter) *via* cysteine units, the luminescence of **11** and AMC was severely quenched *via* non-radiative energy transfer to the AuNPs, while in the presence of specific metalloproteinases (MMP2 and MMP7), the cleavage of the peptide would release the probes, reinstating their luminescence.[74] With a similar detection approach, Feng *et al.* have proposed the ultrasensitive detection and quantification of Caspase-3 by anchoring an analogous Eu(III) complex **11** to a Caspase-3 specific peptide spacer on AuNPs, leading to luminescence increase upon cleavage of the peptide by the enzyme. In addition to an imaging readout, ICP-MS analysis of the Eu(III) content in the supernatant allowed for the quantification of Caspase-3.[75]

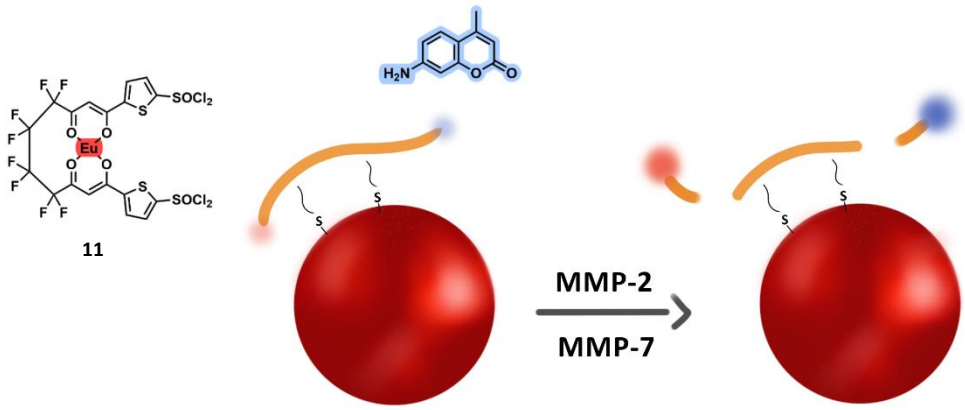


Figure 4.7 – Sketch of the system designed by Wang *et al.* for the detection of MMP2 and MMP7 on AuNPs. The full emission intensity of the two probes (**11**, red, and AMC, blue) is reinstated upon cleavage of the peptide (orange) by MMP-2 and MMP-7.[74]

An in depth study of the quenching efficiencies of different sizes of AuNPs and their non-radiative energy transfer mechanism has been reported by the groups of Werts and Hildebrandt.[76] Here, Tb(III) labelled streptavidin was assembled on biotinylated AuNPs of increasing sizes *via* streptavidin-biotin interactions (5, 30, 50 and 80 nm, Figure 4.8). The authors report that the size of the AuNPs does not influence the energy transfer efficiencies from Tb(III) to AuNPs. Importantly, although quenching is present, as observed in the shorter lifetime components of the lanthanide(III), a significant portion of the initial luminescence is retained and can still be utilised.[76]

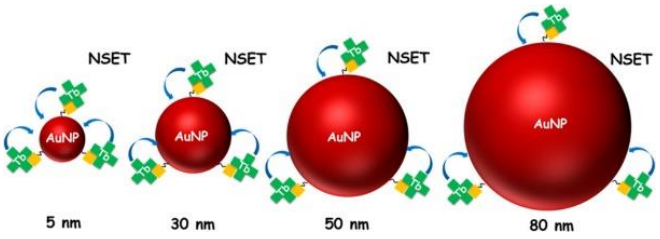
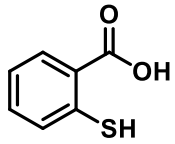


Figure 4.8 – Sketch of the AuNPs coated with Tb(III) labelled streptavidin-biotin assemblies reported by the groups of Werts and Hildebrandt to investigate the effect of AuNP size on the optical processes of Tb(III). The image was taken from [76].

In addition to their quenching efficiencies, the optical properties of AuNPs have been used for the development of colorimetric assays. Although not solely relying on lanthanide(III) luminescence, Nath *et al.* have taken advantage of the coordination chemistry of Eu(III) for the detection of As(III, V) on paper. In their study, they report that hydrated As(III, V) species can coordinate and bridge between Eu(III) ions anchored on different AuNPs, thus driving the aggregation and visual colour change.[77] It is worth mentioning that such a mechanism has also been used for the fabrication of colorimetric sensing devices for the detection of lanthanide(III) ions.[78-80]

The luminescent AuNPs reported above all rely on the visible emission of Eu(III) or Tb(III). To our knowledge, only two systems with a NIR emitting complex anchored to AuNPs have been reported. Gunnlaugsson and co-workers have attached the surface active Yb(III) complex **8** (Figure 4.6) to AuNPs (8 nm diameter). Here, Xylenol Orange was used as both sensitising antenna for Yb(III) emission and as sensing unit to detect pH changes, thus reversibly modulating the NIR emission.[72] Crawford *et al.* have shown energy transfer from small NIR emitting AuNPs (1-3 nm) to Yb(III). Upon addition of Yb(III) to *ortho*-mercaptobenzoic acid capped AuNPs, the increase in Yb(III) emission was accompanied by a decrease in AuNPs luminescence, which was also dependent on both spectral overlap and distance, and thus ascribed as Dexter type energy transfer.[81]



***ortho*-mercaptobenzoic acid**

Figure 4.9 – Chemical structure of *ortho*-mercaptobenzoic acid.

4.1.3 Aims of the project

In this project, we present the attachment of Ln(III) complexes based on **bisDBM** scaffolds to AuNPs to prepare a new class of highly luminescent nanomaterials with emission ranges in both the visible and NIR. Our aim is to first develop a robust coating method for the preparation of luminescent AuNPs and then to evaluate different approaches for the optimisation of the overall luminescence of the system.

The first approach involves the attachment of surface active **Ln_2SAcbisDBM$_3$** complexes to AuNPs of increasing sizes (from 14 nm to 100 nm, Figure 4.10). Our aim is to asses the visible and NIR luminescence of the complexes on AuNPs, as well as to evaluate the effect of the different optical properties of the AuNPs series on the overall luminescence.

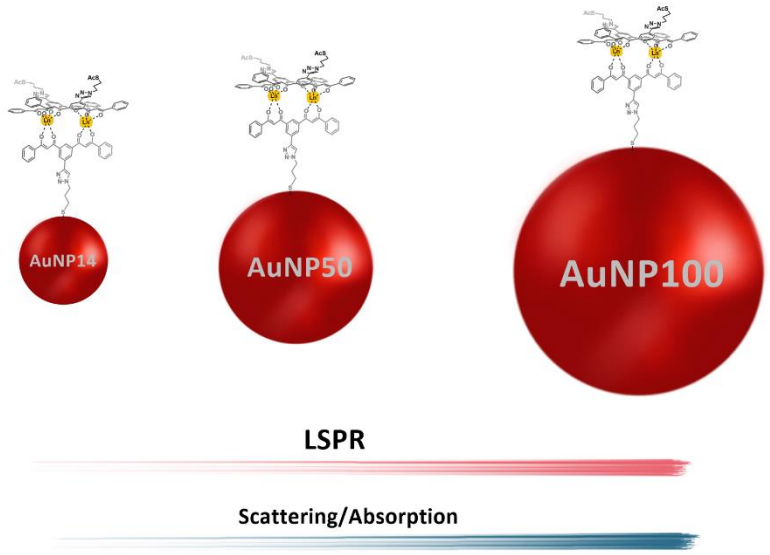


Figure 4.10 – Sketch of **Ln_2SAcbisDBM$_3$** complexes on AuNPs of increasing size (14 nm, 50 nm and 100 nm) alongside the different properties of AuNPs (red shifting LSPR and higher scattering/absorption ratios for larger AuNPs).

In the second approach, we present an ancillary ligand (**PhenSS**, Figure 4.11) for the one-step preparation of surface active complexes from the unfunctionalized **Eu_2bisDBM$_3$** derivative. Here, we rely on the unfilled coordination sphere of the **Eu_2bisDBM$_3$** complex (q≈3), which

allows for the binding of an ancillary ligand and, importantly, exclusion of quenching O-H oscillators to afford higher quantum yields and longer lifetimes in aqueous media. The **PhenSS** ligand is designed to include an alkyl spacer chain bearing a terminal dithiol group for anchoring on AuNPs and is prepared in a one-step reaction.

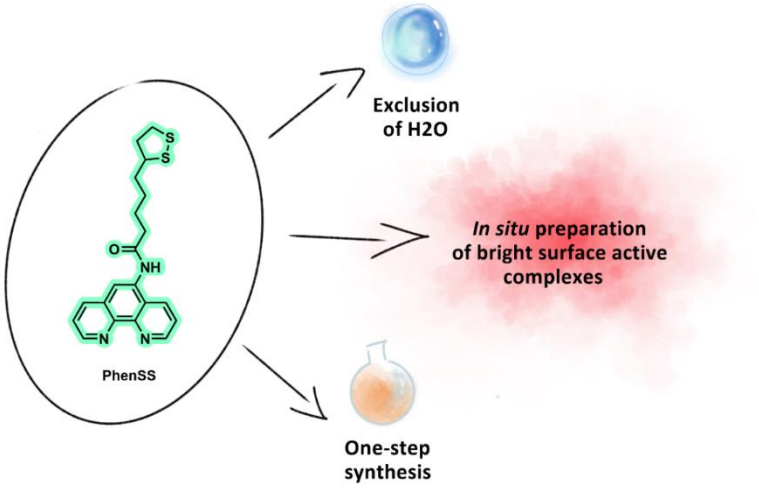


Figure 4.11 – Sketch of **PhenSS** displaying its main advantages.

4.2 Results and Discussion

4.2.1 Preparation, optimisation and luminescence of Eu_2SAcbisDBM$_3$ coated AuNP14

4.2.1.1 Direct coating of AuNPs: Eu_2SAcbisDBM$_3$@AuNP14

Monodispersed AuNPs with size of 14±1 nm (AuNP14) and polydispersity index (PDI) of 0.06 (as measured by TEM) were synthesized by a modified Turkevich method and characterised by UV-Vis absorption, DLS and TEM (Figure 4.37, Appendix).[61, 66, 82] In a first attempt, citrate stabilised AuNPs are coated by the stepwise addition of a solution of **Eu_2SAcbisDBM$_3$** complex in DMF to the AuNP14 dispersion, to give **Eu_2SAcbisDBM$_3$@AuNP14**.[66, 82]

As can be observed from Figures 4.12 **a** and **b** below, a shift of the LSPR band of AuNP14 is found, alongside the appearance and increase of the **Eu_2SAcbisDBM$_3$** absorption band at 350 nm. The shift of the LSPR band is attributed to the change in environment at the AuNP surface, indicating the presence of a coating event. Furthermore, the shift is accompanied by the broadening of the LSPR band. This effect is commonly attributed to flocculation, where AuNPs aggregate to form bigger particles or entities and lose their original plasmonic and morphological properties.

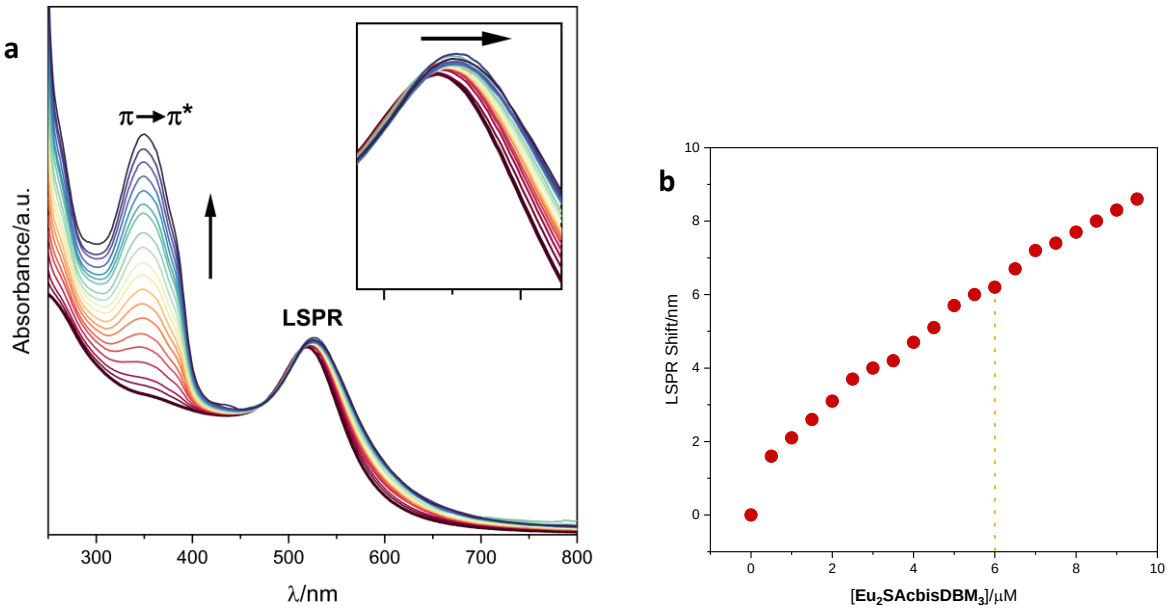


Figure 4.12 – **a** Absorption spectra of AuNP14 (2 nM) upon addition of **Eu_2SAcbisDBM$_3$** (0.2 mM in DMF) from 0.5 µM to 9.5 µM to give **Eu_2SAcbisDBM$_3$@AuNP14** in H_2O (maximum 4.7% DMF). **b** LSPR shift of **Eu_AuNP14** as a function of **Eu_2SAcbisDBM$_3$** concentration. The dashed line represents the concentration of **Eu_2SAcbisDBM$_3$** used for TEM imaging (6 µM).

Indeed, from TEM imaging of **Eu_2SAcbisDBM$_3$@AuNP14** at 6 µM **Eu_2SAcbisDBM$_3$** concentrations (Figure 4.13, **a**), two populations of sizes can be distinguished. The first (blue, Figure 4.13 **b**) with a size distribution centred at 15±1 nm, and the second (yellow) at 24±2 nm.

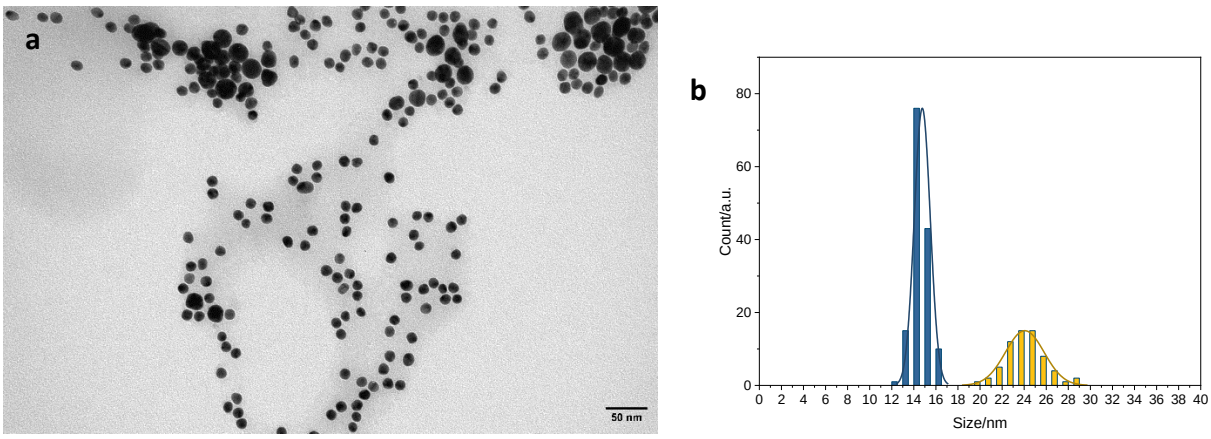


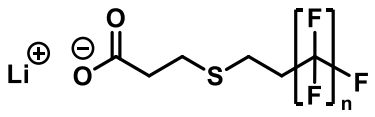
Figure 4.13 – **a** TEM image of **Eu_2SAcbisDBM$_3$@AuNP14** after stepwise coating with 6 µM of **Eu_2SAcbisDBM$_3$** (Figure 4.12, **b**). The image was acquired by Sarah Akponasa at the University of Birmingham. **b** Size distribution of **Eu_2SAcbisDBM$_3$@AuNP14** as measured by TEM. n=145 and PDI=0.06 for blue population, n=65 and PDI=0.05 for yellow population.

Aggregation of AuNPs can be driven by a variety of factors, such as pH, temperature and nature of the coating molecules.[83-85] The **Eu_2SAcbisDBM$_3$** complex is neutral and has low solubility in solvents other than DMF and DMSO. This effect, in addition to the presence of multiple and, likely free, thioacetate groups per molecule, could drive the interaction between different AuNPs by having one complex binding to more than one AuNP.[86]

4.2.1.2 Coating and characterisation of Zonyl FSA stabilised AuNPs: Eu_2SAcbisDBM$_3$●Z@AuNP14

The partial coating of AuNPs with a fluorinated surfactant (Zonyl FSA, Figure 4.14) has been introduced by our group to improve the colloidal stability of AuNPs coated with charged transition metals.[61, 62] This also promotes the separation between particles, reducing the probability of multiple binding events, and thus aggregation, as suggested in section 4.2.1.1.

Zonyl FSA is a fluorosurfactant bearing a perfluorinated chain and a sulphur atom for interaction with Au (Figure 4.14). In our case, the presence of C-F bonds over C-H is expected to limit the quenching of NIR luminescence, compared to popular non-fluorinated polymers such as PEG.



Zonyl FSA

Figure 4.14 – Chemical structure of Zonyl FSA.

As indicated in previous reports, the partial coating of AuNP14 with Zonyl FSA affords monodispersed Z@AuNP14 with sizes of 15±1 nm by TEM (Figure 4.39, Appendix). The

stepwise addition of a solution of **Eu_2SAcbisDBM$_3$** in DMF to Z@AuNP14 displays a steady shift in the LSPR band of the Z@AuNP14 (Figure 4.15), in accordance with the binding of **Eu_2SAcbisDBM$_3$** complexes to form **Eu_2SAcbisDBM$_3$●Z@AuNP14**, and reaching a plateau at 4 µM of complex added.

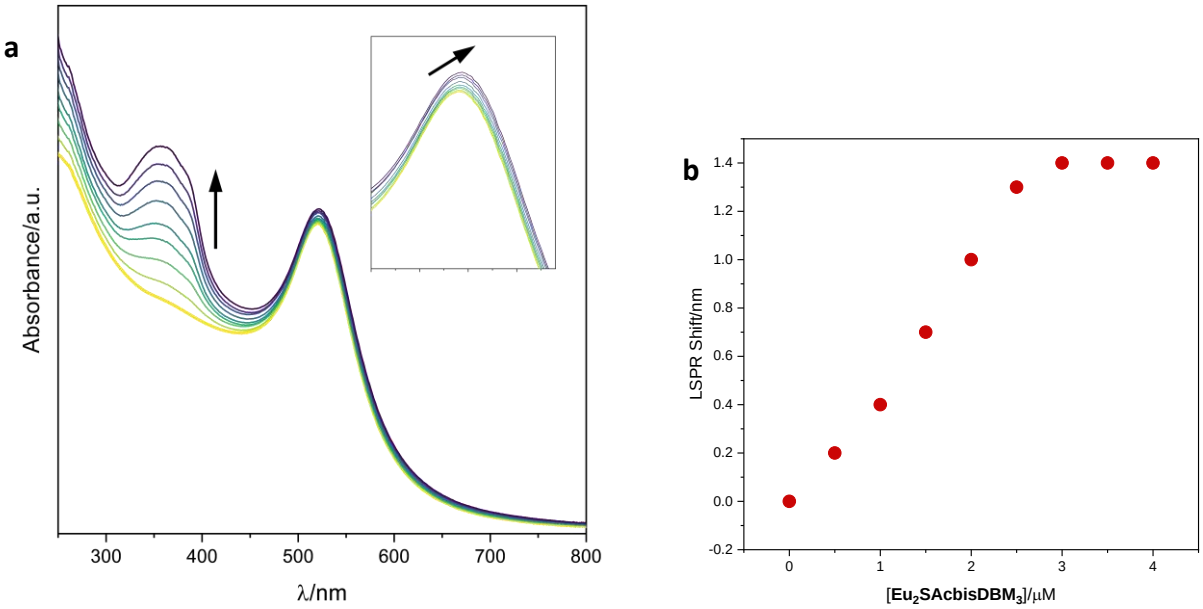


Figure 4.15 – **a** Absorption spectra of Z@AuNP14 (3 nM) upon addition of **Eu_2SAcbisDBM$_3$** (0.2 mM in DMF) from 0.5 µM to 4 µM to give **Eu_2SAcbisDBM$_3$●Z@AuNP14** in H_2O (maximum 2% DMF). **b** LSPR shift of **Eu_2SAcbisDBM$_3$●Z@AuNP14** as a function of **Eu_2SAcbisDBM$_3$** concentration.

The maximum LSPR shift is 1.4 nm, to give the final LSPR wavelength of 520 nm. This is a significantly less pronounced effect compared to the direct addition of the **Eu_2SAcbisDBM$_3$** to citrate AuNP14 (i.e. **Eu_2SAcbisDBM$_3$@AuNP14** Figure 4.12, **b**) and is attributed to the presence of Zonyl FSA. The LSPR shift is accompanied by the expected appearance and increase of the **Eu_2SAcbisDBM$_3$** absorption band at 350 nm. The molar absorption coefficient (**ε**) for the **Eu_2SAcbisDBM$_3$** complex in the **Eu_2SAcbisDBM$_3$●Z@AuNP14** system is derived by subtracting the Z@AuNP14 absorption spectrum, and is in accordance with the expected value for **Eu_2SAcbisDBM$_3$** (1.1×10^5 M^{-1} cm^{-1}).

After purification by size exclusion chromatography, the absorption spectrum of **Eu_2SAcbisDBM$_3$●Z@AuNP14** reveals a drop in the absorption band at 350 nm (Figure 4.16). The decrease was calculated to be 33%, suggesting that not all **Eu_2SAcbisDBM$_3$** anchors during the titration and that the purification process is indeed effective at removing any unbound complex. Importantly, no shift in the LSPR was recorded after purification.

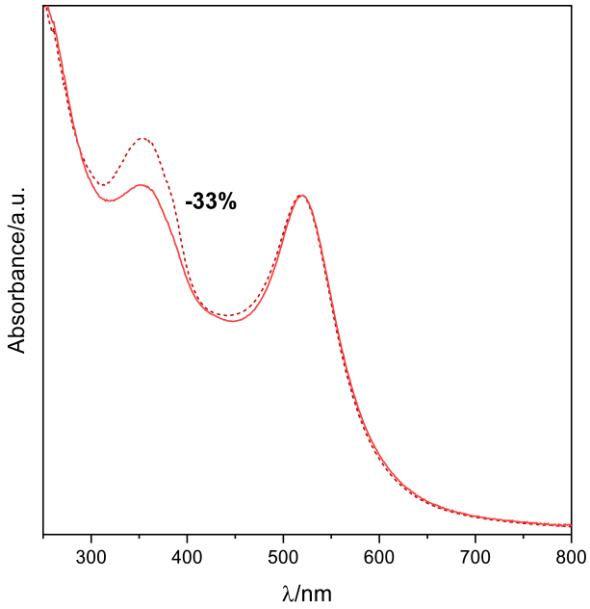


Figure 4.16 – Absorption spectra of **Eu_2SAcbisDBM$_3$●Z@AuNP14** before (dashed) and after (solid) purification by size exclusion chromatography. For clarity and to estimate the absorbance reduction, the spectrum before purification was scaled at the LSPR band. The concentration of **Eu_2SAcbisDBM$_3$●Z@AuNP14** after purification is 0.5 nM in H_2O.

TEM imaging of **Eu_2SAcbisDBM$_3$●Z@AuNP14** does not show the large aggregates observed for **Eu_2SAcbisDBM$_3$@AuNP14** (Figure 4.17 and 4.13, respectively), revealing instead monodispersed particles with sizes of 15±1 nm and PDI of 0.05 (Figures 4.17 **a**, **b** and Figure 4.40, Appendix).

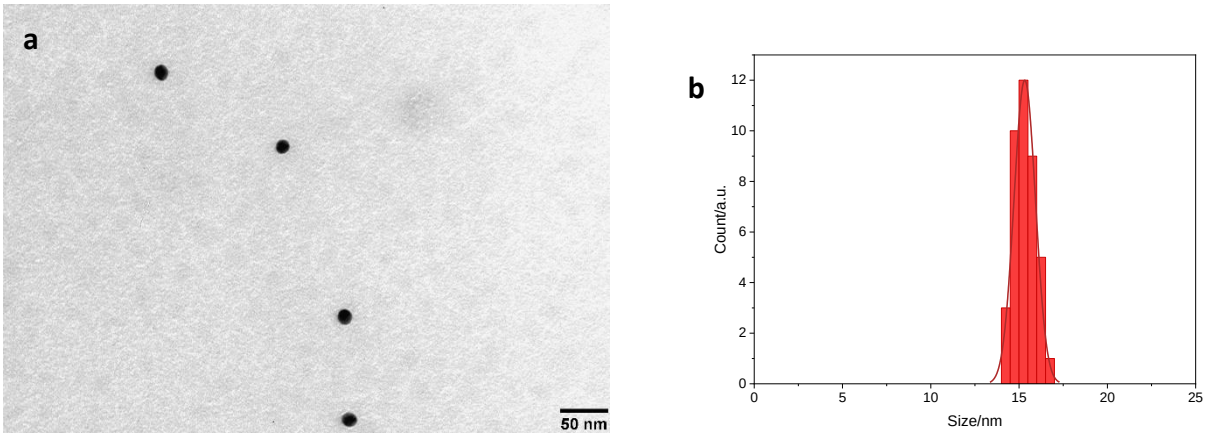


Figure 4.17 – **a** TEM image of **Eu_2SAcbisDBM$_3$●Z@AuNP14** after purification by size exclusion chromatography. **b** Size distribution of **Eu_2SAcbisDBM$_3$●Z@AuNP14** as measured by TEM. n=40.

To further investigate the coating of **Eu_2SAcbisDBM$_3$●Z@AuNP14** system, we employed Super Scanning Transmission Electron Microscopy (SuperSTEM) imaging. Whereas in conventional TEM imaging a parallel beam of electrons is perpendicularly projected on the entire imaged area, in STEM the beam is focused to a very narrow spot and scanned over the sample. Single atom resolution can be achieved in the annular dark-field imaging mode of STEM and in high-angle annular dark-field (HAADF) mode, the contrast is directly linked to the atomic number (Z) of the atoms in the sample.[87] As the electrostatic interactions between the nuclei and the electron beam increase at higher Z, the electrons of heavier atoms will be scattered at higher angles, resulting in brighter spots for those elements in the image.

The SuperSTEM-HAADF images of **Eu_2SAcbisDBM$_3$●Z@AuNP14** reveal small "clouds" surrounding the bright AuNP14 cores and these are attributed to the Eu signal (yellow arrow, Figure 4.18).

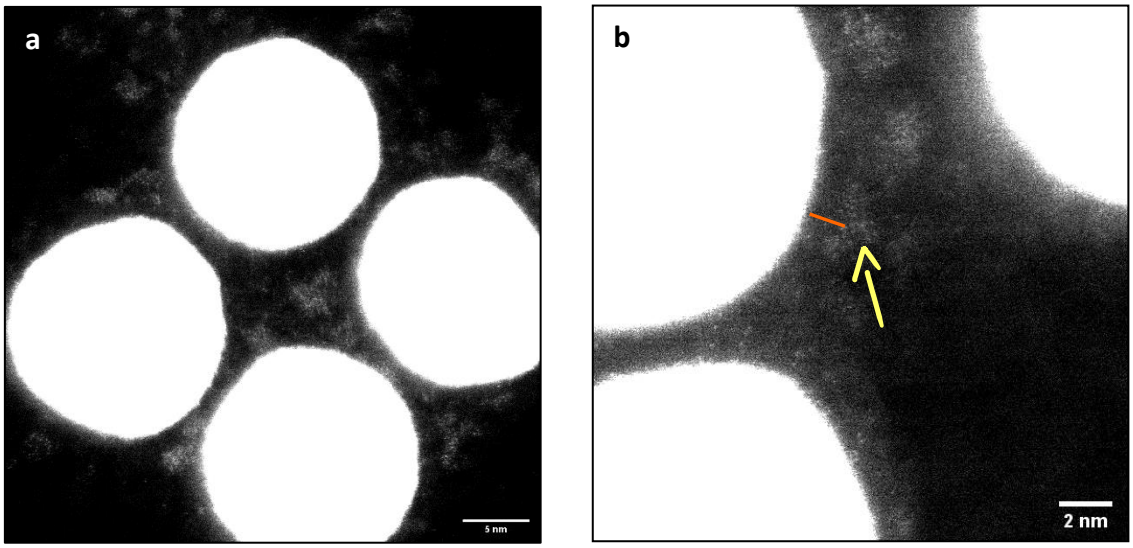
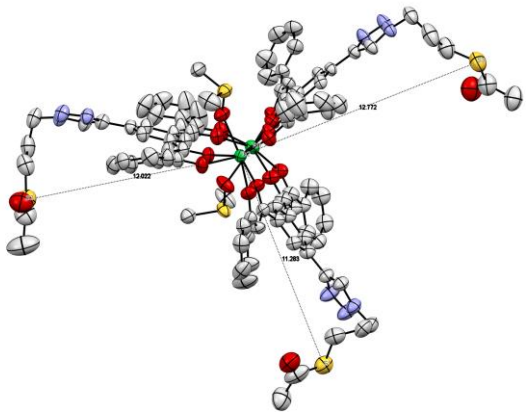


Figure 4.18 – SuperSTEM-HAADF images of **Eu_2SAcbisDBM$_3$●Z@AuNP14**. The yellow arrow indicates the spots attributed to Eu, while the orange line represents an example of Eu-Au distance considered for the calculations in Table 4.19. The images were acquired by Dr. Demie Kepaptsoglou at SuperSTEM, Daresbury.

The distances between these and the Au core are ≈ 1.5±0.3 nm, highly comparable to the Yb-S distance in the **Yb_2SAcbisDBM$_3$** crystal structure (Figure 4.19), suggesting that what is observed is **Eu_2SAcbisDBM$_3$** anchored on AuNP14. It is not possible to image Zonyl FSA due to the low atomic number of its composing elements.



	Measured Distance
Crystal Structure *Yb-S*	1.2 ± 0.1 nm
SuperSTEM-HAADF *Eu-Au*	1.5 ± 0.3 nm

Figure 4.19 – Crystal structure of **Yb_2SAcbisDBM$_3$** collected by Dr. Sarah Griffin at the University of Birmingham. The displayed Yb-S distances are in Ångström and measured for both Yb(III) atoms. The elements colours are as follows: white – carbon, lilac – nitrogen, yellow – sulphur, red – oxygen and green – ytterbium. For clarity, hydrogen atoms have been omitted. **Table 4.1** – Table showing the distances between Yb and S atoms in the crystal structure and average of the distances of Eu and Au (n = 10) as measured in the SuperSTEM-HAADF images.

STEM can be coupled to spectroscopy techniques such as Electron Energy Loss Spectroscopy (EELS). Similarly to EDX, this technique can provide a map of elements in the image: upon exposure of the sample to the incident beam, some electrons undergo inelastic scattering. The energy loss is quantified and, as different elements display characteristic values and patterns we can obtain, among other information, the elemental composition of the sample.[88]

Further indication of the presence of Eu surrounding AuNP14 is thus given by EELS (Figure 4.20). The Eu map of the respective SuperSTEM-HAADF image confirms the elemental composition of the features considered before. Indeed, the signal arising from the Eu $M_{4,5}$-edges of the EELS spectrum (blue, Figure 4.20) is localised around the Au core (yellow, Figure 4.20), validating the distance measurements from Table 4.1 and the assignment of the "clouds" to the **Eu_2SAcbisDBM$_3$** complexes.

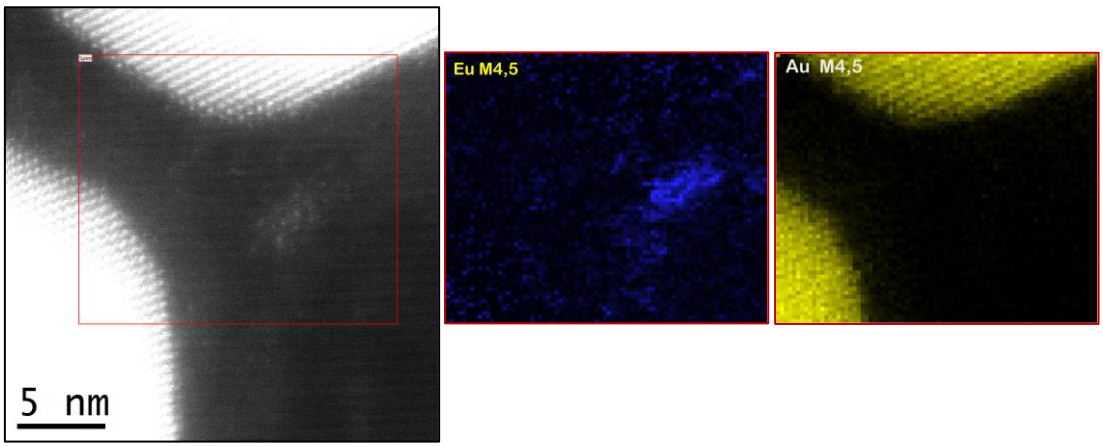


Figure 4.20 – SuperSTEM–HAADF image of **Eu_2SAcbisDBM$_3$●Z@AuNP14** with the respective EELS mappings for Eu (blue) and Au (yellow). The mapped area is represented by the red rectangle. The images were acquired by Dr. Demie Kepaptsoglou at SuperSTEM, Daresbury.

Whereas common characterisation methods such as absorption spectroscopy, XPS or zeta potential can provide important data on the chemical state of the system, they all lack the visual execution of electron microscopy. Furthermore, conventional TEM imaging like the one of Figure 4.17 is intrinsically limited to the study of essential parameters, such as size

distributions and morphologies or, if coupled with EDX, elemental compositions. On the other hand, the superb resolution of SuperSTEM-HAADF, coupled to the identification of single atoms and elements, is extremely powerful. Indeed, the visual observation and characterisation of the arrangement of Eu atoms around the AuNP14 allows for a unique perspective of the **Eu_2SAcbisDBM$_3$●Z@AuNP14** system, not attainable with any other technique.

4.2.1.3 Visible luminescence of Eu_2SAcbisDBM$_3$●Z@AuNP14

The luminescence properties of **Eu_2SAcbisDBM$_3$●Z@AuNP14** were investigated and compared to the ones of the **Eu_2SAcbisDBM$_3$** complex in H_2O. From examination of the excitation spectrum of **Eu_2SAcbisDBM$_3$●Z@AuNP14** (Figure 4.21), we observe a maximum at 360 nm, identical to the one of the complex in H_2O (Figure 4.70, **b**, Appendix) and indicating that the energy transfer processes are maintained on the AuNP14. The emission spectrum of **Eu_2SAcbisDBM$_3$●Z@AuNP14** displays all the $^5D_0 \rightarrow {}^7F_J$ (ΔJ=0-4) transitions with the same relative intensities and splitting pattern as the one of the **Eu_2SAcbisDBM$_3$** complex in H_2O.

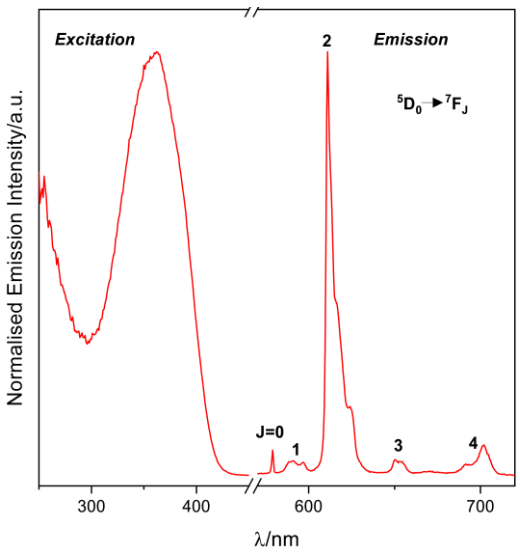


Figure 4.21 – Normalised excitation and emission spectra of purified **Eu_2SAcbisDBM$_3$●Z@AuNP14** in H_2O. λ_{em}: 611 nm, λ_{exc}: 350 nm.

Compared to the complex in H_2O, the luminescence lifetime of **Eu_2SAcbisDBM$_3$●Z@AuNP14** is unchanged (within 10% fitting error, Table 4.2 and Figure 4.72, Appendix), displaying a biexponential decay with values of 180 µs (68%) and 64 µs (32%). This result alludes to the effectiveness of the spacing chain in the ligand scaffold to limit the quenching from the AuNP14 surface. The similarity between the two lifetime values, however, also suggest that the presence of Zonyl FSA on the AuNP14 does not interfere with the coordination of H_2O molecules to the Eu(III) centre.

Sample	**τ/µs**
Eu_2SAcbisDBM$_3$ in H_2O	190±20 (68%), 60±6 (32%)
Eu_2SAcbisDBM$_3$●Z@AuNP14	180±20 (68%), 64±6 (32%)

Table 4.2 – Exponential decay analysis with estimated fitting error of the lifetimes (**τ**) of **Eu_2SAcbisDBM$_3$** in H_2O (0.2% DMF) and of purified **Eu_2SAcbisDBM$_3$●Z@AuNP14** in H_2O. λ_{exc}: 350 nm, λ_{em}: 611 nm.

Finally, the quantum yields of **Eu_2SAcbisDBM$_3$●Z@AuNP14** and **Eu_2SAcbisDBM$_3$** in H_2O (0.2% DMF) were obtained with an integrating sphere. The choice of this approach over the relative method lies in the intrinsic limitations of using a reference standard, which instead is not required for absolute quantum yield measurements with an integrating sphere. The overall quantum yield **Φ** is thus obtained as:

$$\Phi = \frac{E_{Sample} - E_{Blank}}{S_{Blank} - S_{Sample}} \quad Equation\ 4.2$$

Where *E* is the integrated emission and *S* the integrated scattering peak of either the sample or the blank. Whereas for the **Eu_2SAcbisDBM$_3$** complex in H_2O (0.2% DMF) the pure solvent was selected as blank, for **Eu_2SAcbisDBM$_3$●Z@AuNP14** we employed Z@AuNP14. Taken at the same concentration as the sample, the choice of Z@AuNP14 allows for consideration of the AuNP14 own absorption and scattering at the excitation wavelength. Absolute quantum yields

of 1.1% for **Eu_2SAcbisDBM$_3$●Z@AuNP14** and 2.4% for **Eu_2SAcbisDBM$_3$** in H_2O (0.2% DMF) were thus obtained. From these results, it appears that lower quantum yields are to be expected for **Eu_2SAcbisDBM$_3$●Z@AuNP14**, although very similar lifetimes are recorded.

4.2.2 Effect of AuNP size on Eu_2SAcbisDBM$_3$ luminescence and NIR emitting Ln_2SAcbisDBM$_3$●Z@AuNPs (Ln(III)=Yb(III), Nd(III))

Variation of the size of AuNPs is a method to tune the resulting optical properties of the nanomaterial. Matching the LSPR frequencies with the emission or excitation spectra of a fluorophore can afford enhanced luminescence signal. For AuNP14, the LSPR is centred at 520 nm, so that there is only a very small overlap with Eu(III) emission (Figure 4.22). Two sets of monodispersed AuNPs with sizes of 50±2 nm and 103±6 nm by TEM (AuNP50 and AuNP100, respectively) were synthesized by the seed-mediated growth method (Figures 4.43 and 4.44, Appendix).[61, 66, 82] AuNP50 display a LSPR at 525 nm, whereas a red shift at 550 nm is observed for AuNP100, providing a better overlap with the emission range of Eu(III) (Figure 4.22).

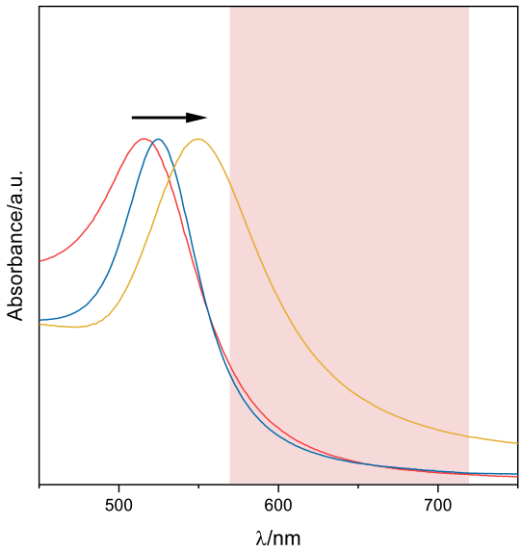


Figure 4.22 – **a** Overlaid absorption spectra of AuNP14 (red), AuNP50 (yellow) and AuNP100 (blue). For clarity, the spectra have been scaled at the LSPR. The red area represents the range of Eu(III) emission.

AuNP50 and AuNP100 were coated with Zonyl FSA as reported to give monodispersed Z@AuNP50 and Z@AuNP100 (Figures 4.45 and 4.46, Appendix).[61] The coating of Z@AuNP50 and Z@AuNP100 with **Eu_2SAcbisDBM$_3$** is carried out by the stepwise addition of the complex as for Z@AuNP14 (Figures 4.23 **a**-**d**). Similarly, the LSPR shift plateaus at 4 µM of complex. For the bigger **Eu_2SAcbisDBM$_3$●Z@AuNP100**, however, the maximum shift reaches 2.3 nm, significantly higher than for **Eu_2SAcbisDBM$_3$●Z@AuNP14** and **Eu_2SAcbisDBM$_3$●Z@AuNP50** (1.3 –1.4 nm).

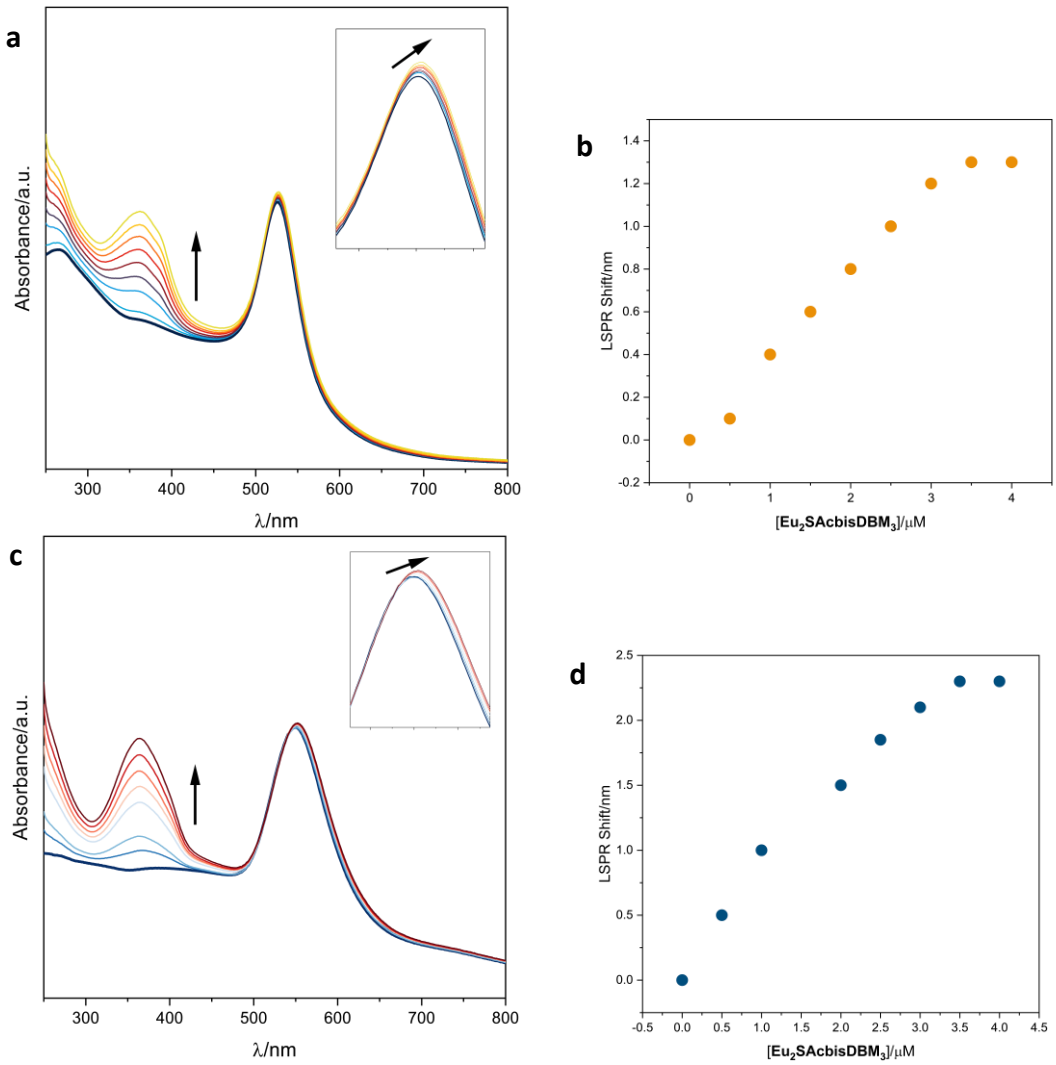


Figure 4.23 – Absorption spectra of Z@AuNP50 (40 pM, **a**) and Z@AuNP100 (6 pM, **c**) upon addition of **Eu_2SAcbisDBM$_3$** (0.2 mM in DMF) from 0.5 µM to 4 µM to give **Eu_2SAcbisDBM$_3$_Z@AuNP50** and **Eu_2SAcbisDBM$_3$_Z@AuNP100** in H_2O (maximum 2% DMF). **b** and **d** Plots of the LSPR shift of Z@AuNP50 and Z@AuNP100, respectively, as a function of **Eu_2SAcbisDBM$_3$** concentration.

After purification by size exclusion chromatography, **Eu_2SAcbisDBM$_3$●Z@AuNP50** display a drop in the 350 nm **Eu_2SAcbisDBM$_3$** absorption band similar to **Eu_2SAcbisDBM$_3$●Z@AuNP14** (-32%). A more significant decrease (-69%) is recorded for **Eu_2SAcbisDBM$_3$●Z@AuNP100** (Figures 4.53 and 4.54, Appendix).

For the comparison of Eu(III) luminescence between AuNPs of different sizes after purification, the absolute quantum yield method did not prove successful. Due to their considerable size and thus tendency to diffuse downwards, the larger **Eu_2SAcbisDBM$_3$●Z@AuNP50** and **Eu_2SAcbisDBM$_3$●Z@AuNP100** require stirring during the collection of the spectra, so that reliable emission intensities are obtained. In an integrating sphere, this is not possible. Instead, **Eu_2SAcbisDBM$_3$●Z@AuNP14-50-100** were diluted to give isoabsorptive dispersions at the **Eu_2SAcbisDBM$_3$** absorption band (350 nm, absorbance = 0.05 for all sizes by subtraction of the respective Z@AuNP14-50-100 spectrum). An estimation of the concentration of **Eu_2SAcbisDBM$_3$** on the AuNPs was obtained from the found absorbance values and the **ε** of the complex, affording a concentration of 0.5 μM for all sizes (Figures 4.51, 4.53 and 4.54, Appendix). Additionally, the prepared **Eu_2SAcbisDBM$_3$●Z@AuNP14-50-100** samples were analysed with inductively coupled plasma mass spectrometry (ICP-MS), where a **Eu_2SAcbisDBM$_3$** concentration of 0.3 μM was obtained for all AuNP sizes. This value is very close to the one estimated by UV-Vis absorption and, most importantly, confirms that any comparison between samples is free from concentration effects, as this is constant along the series. Finally, the number of **Eu_2SAcbisDBM$_3$** molecules per AuNP is also obtained from the ICP-MS results. Higher numbers are recorded for bigger AuNPs, in accordance with their higher surface area (from 572 for **Eu_2SAcbisDBM$_3$●Z@AuNP14**, to 53,950 and 155,604 for **Eu_2SAcbisDBM$_3$●Z@AuNP50** and **Eu_2SAcbisDBM$_3$●Z@AuNP100**, respectively).

Upon excitation at 350 nm, characteristic Eu(III) emission is observed for all AuNP sizes and all $^5D_0 \rightarrow {}^7F_J$ (ΔJ=0-4) transitions can be identified (Figure 4.24, **a**). Interestingly, a higher total emission intensity is recorded for **Eu_2SAcbisDBM$_3$●Z@AuNP100** (1.7-fold, compared to **Eu_2SAcbisDBM$_3$●Z@AuNP14**, Figure 4.24, **b**). As the concentration of **Eu_2SAcbisDBM$_3$** complex is the same over the AuNP series, the higher emission intensity for **Eu_2SAcbisDBM$_3$●Z@AuNP100** cannot be ascribed to such an effect.

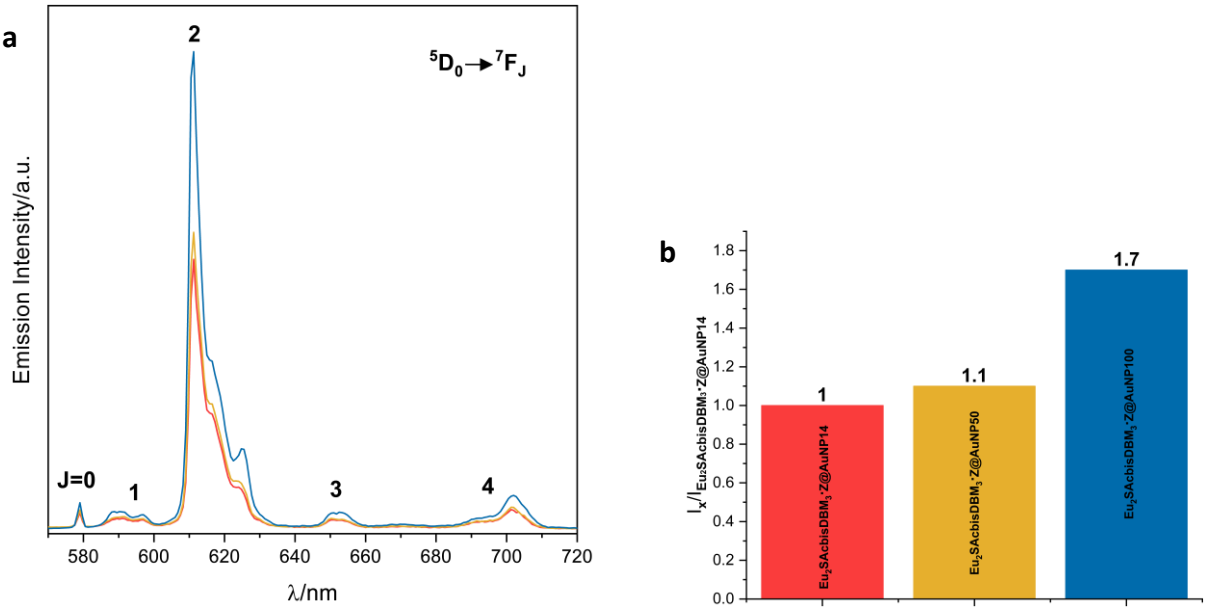


Figure 4.24 – **a** Overlaid emission spectra of isoabsorptive **Eu_2SAcbisDBM$_3$●Z@AuNP14** (red), **Eu_2SAcbisDBM$_3$●Z@AuNP50** (yellow) and **Eu_2SAcbisDBM$_3$●Z@AuNP100** (blue) in H_2O. λ_{exc}: 350 nm. **b** Graph displaying the emission ratios of the **Eu_2SAcbisDBM$_3$●Z@AuNP** systems over **Eu_2SAcbisDBM$_3$●Z@AuNP14**.

Analysis of the luminescence lifetimes of the three sets of AuNPs confirms the biexponential decay already observed for **Eu_2SAcbisDBM$_3$●Z@AuNP14** (Table 4.3). No significant variation (i.e. within 10% fitting error) is identified.

Sample	τ/μs
Eu_2SAcbisDBM$_3$●Z@AuNP14	180 (68%), 64 (32%)
Eu_2SAcbisDBM$_3$●Z@AuNP50	180 (66%), 63 (34%)
Eu_2SAcbisDBM$_3$●Z@AuNP100	160 (69%), 54 (31%)

Table 4.3 – Exponential decay analyses of **Eu_2SAcbisDBM$_3$●Z@AuNP14**, **Eu_2SAcbisDBM$_3$●Z@AuNP50** and **Eu_2SAcbisDBM$_3$●Z@AuNP100**. λ_{exc}: 350 nm, λ_{em}: 611 nm.

To deconvolute the results, we consider the absorbance lost at 350 nm from the overlap between the extinction spectrum of the AuNPs and the absorption of the complex. Correction of the emission spectra by the absorbance loss factor as calculated in section 4.5.5, Experimental, gives a trend similar to the one of Figure 4.25, with the **Eu_2SAcbisDBM$_3$●Z@AuNP100** displaying a 1.8-fold emission increase compared to the **Eu_2SAcbisDBM$_3$●Z@AuNP14** (Figure 4.65, Appendix) and indicating that this parameter does not significantly affect the resulting emission intensity. The small overlap between the LSPR and Eu(III) emission in **Eu_2SAcbisDBM$_3$●Z@AuNP100**, however, could justify the 1.7-fold increase in emission intensity recorded. Coupled to the higher percentage of scattering component at such longer wavelengths (82% at 608 nm, Figure 4.25), which has been associated with near- and far-field enhancement processes, AuNP100 appear to be a better substrate for the fabrication of highly luminescent nanomaterials.

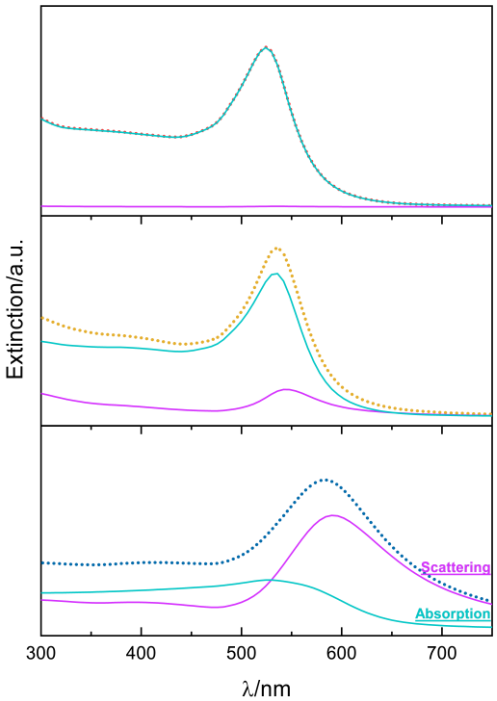


Figure 4.25 –Stacked simulated extinction spectra of AuNP14 (top, red), AuNP50 (middle, yellow) and AuNP100 (bottom, blue). The teal and purple lines represent the absorption and scattering components, respectively, as simulated by Mie theory.[89]

After examination of the luminescence properties of the visible emitting **Eu_2SAcbisDBM$_3$●Z@AuNPs**, we set out to investigate the NIR luminescence of the **Yb_2SAcbisDBM$_3$** and **Nd_2SAcbisDBM$_3$** complexes on AuNP14. The preparation of NIR emissive AuNPs is of high interest, due to the advantages of NIR light in both bioimaging and telecommunication applications. Nonetheless, to our knowledge, only two examples of NIR emitting lanthanide(III) coated AuNPs are reported.[72, 81]

Yb_2SAcbisDBM$_3$●Z@AuNP14 and **Nd_2SAcbisDBM$_3$●Z@AuNP14** were prepared and purified as reported for **Eu_2SAcbisDBM$_3$●Z@AuNP14**, giving comparable LSPR shifts (1.5-1.9 nm) after coating and, for **Yb_2SAcbisDBM$_3$●Z@AuNP14**, analogous sizes and monodispersities by TEM (Figure 4.49, Appendix).

Upon excitation at 350 nm, the emission spectrum of **Yb_2SAcbisDBM$_3$●Z@AuNP14** is dominated by the well resolved $^2F_{5/2}\rightarrow{}^2F_{7/2}$ transition (Figure 4.26, **a**). A biexponential decay is

recorded (11 µs (86%), 2.9 (14%)), which, as already seen with **Eu_2SAcbisDBM$_3$●Z@AuNP14**, displays no significant change to the one of the complex in H_2O (i.e. 11 µs (70%), 3.3 (30%), Table 4.17, Appendix). The emission spectrum of **Nd_2SAcbisDBM$_3$●Z@AuNP14** was recorded and, despite the intense noise, the $^4F_{3/2}\rightarrow{}^4I_J$ (ΔJ=9/2, 11/2, 13/2) transitions of Nd(III) can be identified (Figure 4.26, **b**).

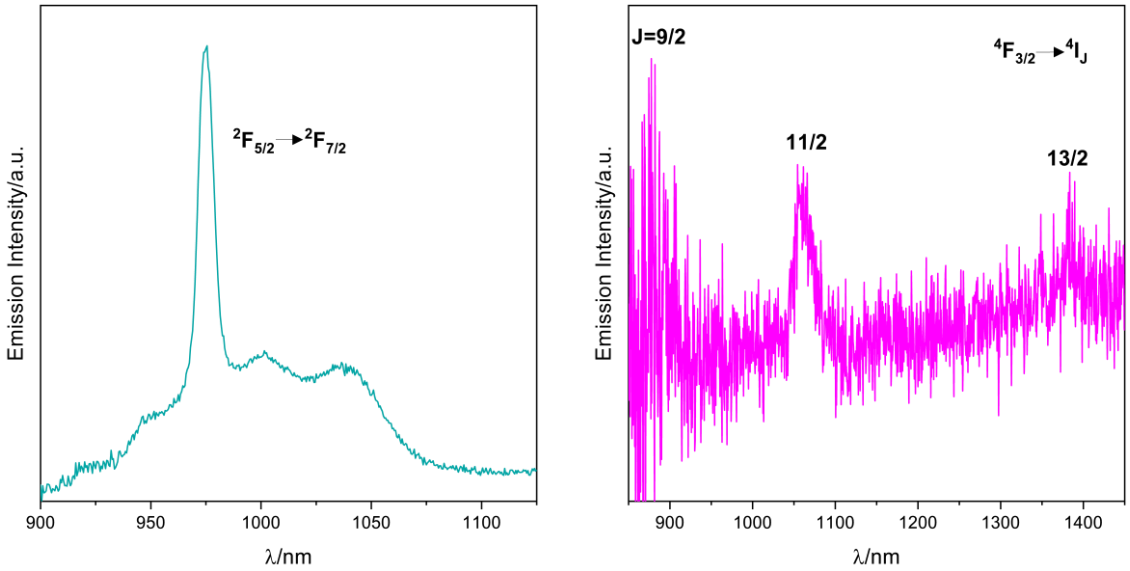


Figure 4.26 – Emission spectrum of **Yb_2SAcbisDBM$_3$●Z@AuNP14** (**a**) and **Nd_2SAcbisDBM$_3$●Z@AuNP14** (**b**) in H_2O. λ_{exc}: 350 nm.

The excitation spectrum of **Yb_2SAcbisDBM$_3$●Z@AuNP14** displays the presence of the characteristic band at 360 nm (Figure 4.66, Appendix). This indicates that the energy transfer from the **SAcbisDBM** units to the lanthanide(III) is present also for NIR emission in the **Ln_2SAcbisDBM$_3$●Z@AuNP14** systems.

Yb_2SAcbisDBM$_3$ was coated on Z@AuNP50 and Z@AuNP100, employing the same conditions as reported for **Eu_2SAcbisDBM$_3$●Z@AuNP50** and **Eu_2SAcbisDBM$_3$●Z@AuNP100**. After purification, characteristic emission displaying the $^2F_{5/2}\rightarrow{}^2F_{7/2}$ transition is observed for the two sets of larger AuNPs (**Yb_2SAcbisDBM$_3$●Z@AuNP50** and **Yb_2SAcbisDBM$_3$●Z@AuNP100**,

Figure 4.27). The prepared **Yb_2SAcbisDBM$_3$●Z@AuNPs**, however, are not isoabsorptive, so the emission intensity is not directly compared.

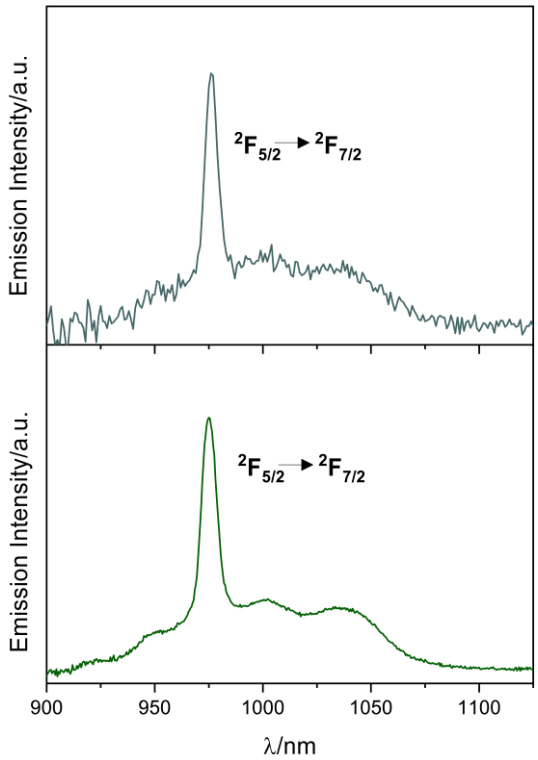


Figure 4.27 – Emission spectra of **Yb_2SAcbisDBM$_3$●Z@AuNP50** (top, grey) and **Yb_2SAcbisDBM$_3$●Z@AuNP100** (bottom, green) in H_2O. λ_{exc}: 350 nm.

As for the **Yb_2SAcbisDBM$_3$●Z@AuNP14** system, the excitation spectra of both **Yb_2SAcbisDBM$_3$●Z@AuNP50** and **Yb_2SAcbisDBM$_3$●Z@AuNP100** are dominated by the characteristic band at 360 nm, confirming energy transfer also with larger sizes of AuNPs (Figure 4.66, Appendix). Furthermore, **Yb_2SAcbisDBM$_3$●Z@AuNP100** exhibits analogous luminescence lifetimes to the one of **Yb_2SAcbisDBM$_3$●Z@AuNP14** and the complex in H_2O, 0.2% DMF (10 µs (89%), 2.3 µs (10%), Figure 4.74 and Table 4.17, Appendix). This indicates that the decay is not affected by the anchoring on AuNPs, as also seen for **Eu_2SAcbisDBM$_3$●Z@AuNP14**, and is independent of the AuNP size.

Finally, although the luminescence of the **Nd_2SAcbisDBM$_3$** complex on larger AuNPs was not investigated, the well resolved emission recorded for the **Yb_2SAcbisDBM$_3$●Z@AuNP14-50-100**

is extremely promising. As NIR luminescence is particularly affected by the quenching by O-H oscillators in H_2O, these results highlight how the dinuclear surface active **Ln_2SAcbisDBM$_3$** complexes are excellent candidates for the preparation of luminescent and NIR emissive materials.

4.2.3 Design and preparation of bright surface active Eu$_2$bisDBM$_3$_PhenSS$_2$ and Eu$_2$bisDBM$_3$_PhenSS$_2$●Z@AuNP14

To enhance the visible luminescence signal of Eu(III) complexes, here we present an alternative system based on the coordination of 1,10-phenanthroline as ancillary ligand for **Eu$_2$bisDBM$_3$** (**PhenSS**, Figure 4.28).

The coordination of 1,10-phenanthroline and its derivatives to lanthanide(III) complexes, including mono- and dinuclear β-diketonates, is widely reported. The displacement of quenching solvent molecules upon coordination of 1,10-phenanthroline affords significantly improved quantum yields and, in some cases, the ancillary ligand acts as additional light harvesting unit.[90-94] Furthermore, the anchoring of mononuclear **EuDBM$_3$** complexes on SiO_2 NPs and attapulgite has been achieved by means of H_2O exchange with a surface active 1,10-phenanthroline ligand.[95]

4.2.3.1 Synthesis and characterisation of PhenSS

The synthesis of **PhenSS** is carried out the by 1-ethyl-3-(3-dimethylaminopropyl)carbodiimide (i.e. EDCI) mediated coupling of 1,10-phenanthrolin-5-amine (**1**) and α-lipoic acid (**2**, Figure 4.28). The reaction was adapted from the reported procedure of a similarly functionalised 1,10-phenanthroline.[96]

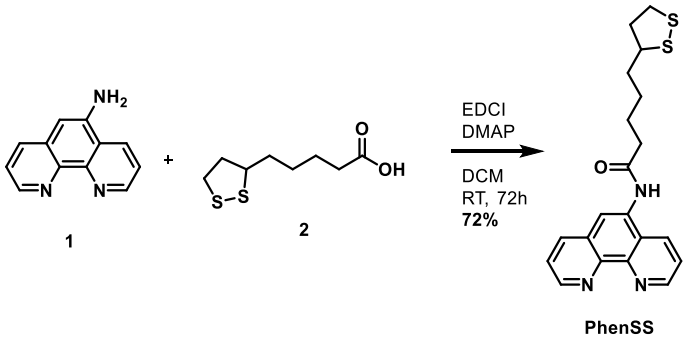


Figure 4.28 – Reaction scheme for the synthesis of **PhenSS**.

A reaction for the preparation of **PhenSS** has been reported before.[97] This relied on the coupling of 1,10-phenanthrolin-5-amine (**1**) and α-lipoic acid (**2**) by means of hydroxybenzotriazole (HOBT). However, the reported procedure could not be reproduced here.

The successful preparation and isolation of **PhenSS** can be confirmed by ^{1}H-NMR. Significant shifts compared to the spectrum of the starting material **1** are observed (Figure 4.29). Specifically, the H_d proton is shifted by +1.31 ppm, in accordance with the change in substituent at the adjacent amine position. Furthermore, the peak ascribed to the amine protons in **1** (NH_2, yellow in Figure 4.29) is not present in the ^{1}H-NMR spectrum of **PhenSS**, while the appearance of a peak at 10.12 ppm is assigned to the amide proton (NH, red in Figure 4.29) and in accordance with the coupling event. Further characterisation is provided by 2D NMR, ESI^{+}-MS and UV-Vis absorption spectroscopy (Section 4.5.12, Appendix).

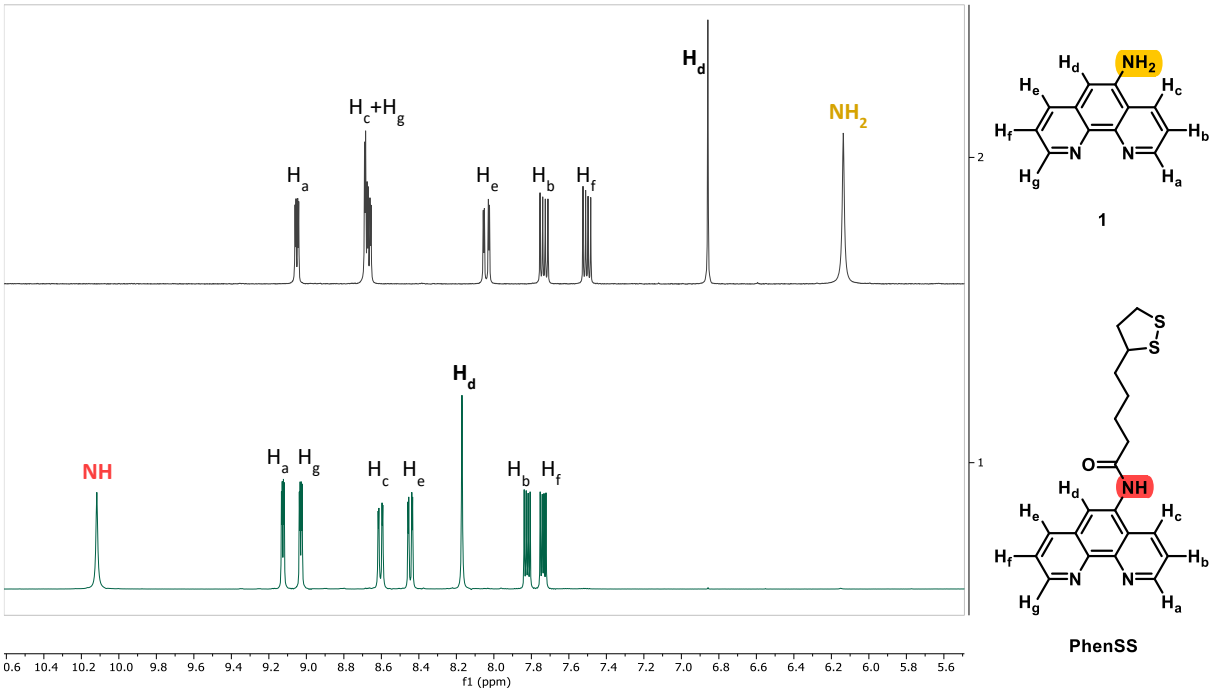


Figure 4.29 – Stacked ^{1}H-NMR spectra (400 MHz, DMSOd_6) of **1** (top) and **PhenSS** (bottom) with the respective assignments. Only the aromatic region is shown, for the full spectrum see Figure 4.83, Appendix. The proton names are as reported in the chemical structures on the right. The amine and amide groups are highlighted in yellow and red for **1** and **PhenSS**, respectively.

4.2.3.2 Spectroscopic studies on the coordination of PhenSS to Eu_2bisDBM$_3$

After successful synthesis and isolation of the **PhenSS** ligand, we set out to prepare the fully coordinated **Eu_2bisDBM$_3$_PhenSS$_2$** complex (Figure 4.30).

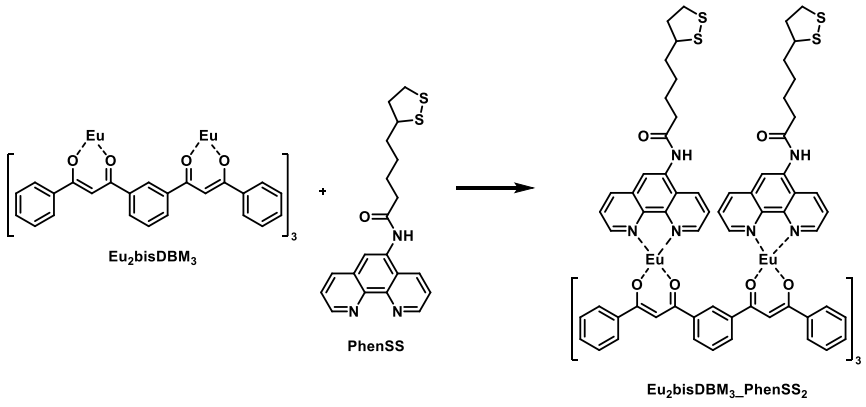


Figure 4.30 – Reaction scheme for the coordination of **PhenSS** to **Eu_2bisDBM$_3$** and preparation of **Eu_2bisDBM$_3$_PhenSS$_2$**.

Although the coordination behaviour of 1,10-phenanthroline ligands and derivatives is well known, the poor solubility of **Eu_2bisDBM$_3$** represents a remarkable challenge for the preparation of such complexes. Due to the positive results of F^- coordination in THF, 0.2% DMF (Chapter 2), this solvent system is selected for the assessment of **PhenSS** coordination to **Eu_2bisDBM$_3$**. Steady state and time resolved spectroscopies are employed to study the coordination behaviour of **PhenSS**. The sensitivity and speed of these techniques, coupled to the response of Eu(III) to changes in its coordination environment as variations in both its emission and lifetime spectra, make this approach ideal for the monitoring of the coordination state of **Eu_2bisDBM$_3$**.

In THF, 0.2% DMF, the **Eu_2bisDBM$_3$** complex displays a monoexponential decay (190 μs), associated with the presence of one species in solution and the equivalence of the two Eu(III) sites. Upon addition of 0.5 equivalents of **PhenSS**, the decay becomes biexponential and the percentage of the second longer component (420±20 μs) steadily increases with further addition of **PhenSS** (Figure 4.31). This is in accordance with the coordination of one **PhenSS** to each Eu(III) centre, which displaces quenching solvent molecules to form the **Eu_2bisDBM$_3$_PhenSS$_2$** species. Upon examination of the curve in Figure 4.31, **b**, the formation of the **Eu_2bisDBM$_3$_PhenSS$_2$** species can be monitored as increase in percentage of the long component of the decay. This is concurrent to the decrease of **Eu_2bisDBM$_3$** species (i.e. short component of the decay), until achievement of full binding at 10 equivalents, reflected in the monoexponential decay (Table 4.18, Appendix).

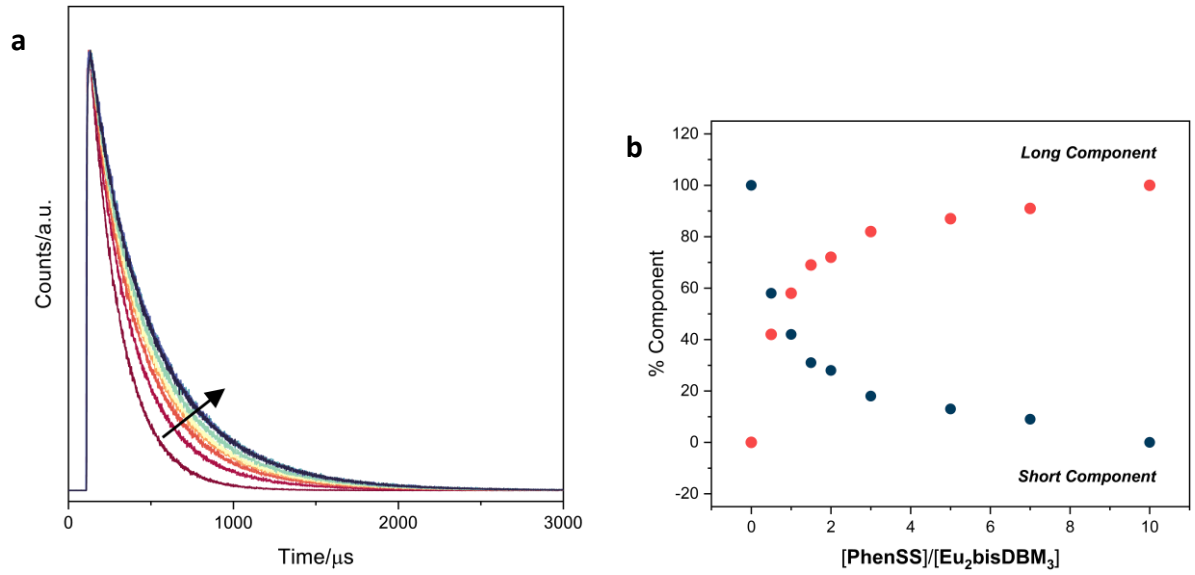


Figure 4.31 – **a** Overlaid lifetime spectra of **Eu₂bisDBM₃** upon addition of 0-10 equivalents of **PhenSS** in THF (0.2% DMF). λ_{exc}: 350 nm, λ_{em}: 611 nm. **b** Plot of the percentage of the short (blue, 420±20 µs) or long (red, 210±10 µs) components in the exponential decay analysis of the lifetimes of **Eu₂bisDBM₃** upon addition of **PhenSS** in THF (0.2% DMF).

The coordination of **PhenSS** is also monitored by steady state spectroscopy where, upon addition of **PhenSS,** the emission profile of **Eu₂bisDBM₃** displays a steady increase in the 611 nm component of the $^5D_0 \rightarrow {}^7F_2$ transition (Figure 4.32, **b**), which is attributed to the coordination of **PhenSS** and subsequent disruption of the symmetry of the complex. By monitoring the ratio between the emission intensity at 611 nm and 625.5 nm, a plateau is reached at 3-5 equivalents (Figure 4.32, **b**), which is in accordance with the curve obtained from the time-resolved data in Figure 4.31, **b**. Furthermore, considering the emission spectrum at 10 equivalents of **PhenSS** (Figure 4.32, **a**) we observe a particularly sharp $^5D_0 \rightarrow {}^7F_0$ transition, in accordance with the presence of a single species in solution and confirming the completion of the binding events. Interestingly, the intensity of this transition surpasses the one of the MD $^5D_0 \rightarrow {}^7F_1$, not seen for the **Eu₂bisDBM₃** complex alone in THF but that is instead observed in DMF (Figure 4.71, Appendix). The stronger polarity of DMF can explain the differences in transition intensities when comparing solvents, whereas the effect of the coordinating

nitrogen atoms of **PhenSS** and exclusion of solvent molecules justifies the increase in Figure 4.32, **a**. Finally, the Stark levels splittings of the transitions and relative intensities observed here are comparable to the ones of reported β-diketonate Eu(III) complexes bearing a 1,10-phenanthroline ancillary ligand, supporting our observations.[98, 99]

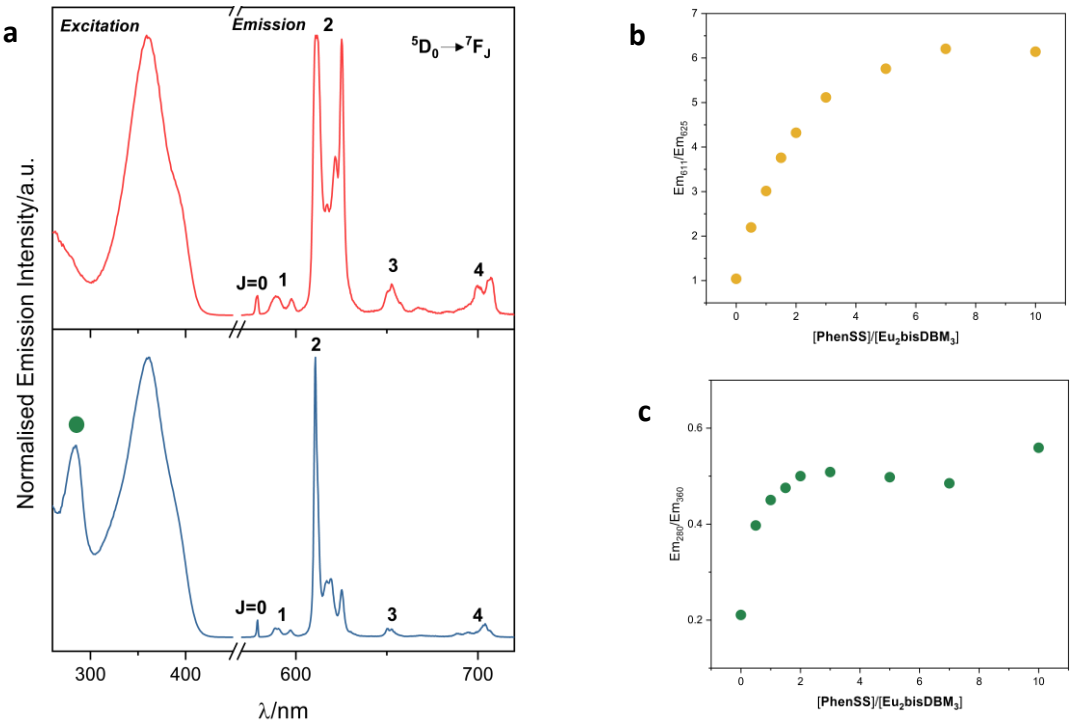


Figure 4.32 – **a** Stacked emission spectra of **Eu_2bisDBM$_3$** before (top, red) and after (bottom, blue) addition of 10 equivalents of **PhenSS** in THF (0.2% DMF). λ_{exc}: 350 nm. Highlighted by a green dot is the excitation band assigned to energy transfer from **PhenSS** to **Eu_2bisDBM$_3$**. **b** Plot of the ratio of intensities at 611 nm over 625.5 nm versus equivalents of **PhenSS** from the emission spectra. **c** Plot of the ratio of intensities at 280 nm over 360 nm versus equivalents of **PhenSS** from the excitation spectra.

From the excitation spectra of **Eu_2bisDBM$_3$** upon addition of **PhenSS**, we observe the appearance of a band at 280 nm (Figure 4.32, **a**), in addition to the one ascribed to the π-π* transitions of the **bisDBM** ligand at 360 nm. The new band at 280 nm is attributed to the energy transfer from the **PhenSS** ligand to the Eu(III) centre upon formation of the **Eu_2bisDBM$_3$_PhenSS$_2$** complex. Similarly to the curves in Figure 4.32, **b**, the intensity of the band eventually plateaus after 3-5 equivalents of **PhenSS** added (Figure 4.32, **c**).

The quantum yield of the **Eu_2bisDBM$_3$_PhenSS$_2$** complex, as prepared after addition of 10 equivalents of **PhenSS** to ensure full coordination, is measured to be 10% in THF, 0.2% DMF. This is more than double the one of **Eu_2bisDBM$_3$** in THF, 0.2% DMF (3.5%) and correlates well with both the increase in lifetime (>2-fold) and in emission intensity (2-fold after 2 equivalents) observed in this solvent system. Furthermore, the intrinsic quantum yield (Φ_{Eu}) of Eu(III) in **Eu_2bisDBM$_3$** is calculated to be 23% in THF, 0.2% DMF. In the **Eu_2bisDBM$_3$_PhenSS$_2$** system, however, Φ_{Eu} doubles to 46%, due to the exclusion of quenching solvent molecules and in accordance with previously reported data for similar systems.[93] Finally, comparisons of **Eu_2bisDBM$_3$_PhenSS$_2$** after dilution in H_2O and D_2O (0.5% THF, < 0.05% DMF) reveal that there is no significant change in lifetime values between the two solvents (biexponential decay, 360 (72%), 120 (28%), within error, Figure 4.77, Appendix), showing that O-H oscillators do not affect the **Eu_2bisDBM$_3$_PhenSS$_2$** complex due to the full coordination of Eu(III).

4.2.3.3 Preparation of Eu_2bisDBM$_3$_PhenSS$_2$●Z@AuNP14 and comparisons with Eu_2SAcbisDBM$_3$●Z@AuNP14

Eu_2bisDBM$_3$_PhenSS$_2$ is prepared by addition of excess **PhenSS** (10 equivalents) to ensure full coordination and the complex is added stepwise to Z@AuNP14, as for **Eu_2SAcbisDBM$_3$●Z@AuNP14**, to give **Eu_2bisDBM$_3$_PhenSS$_2$●Z@AuNP14** (Figure 4.33, **a**). From the UV-Vis spectra in Figure 4.33, **a**, a similar binding behaviour to **Eu_2SAcbisDBM$_3$** is observed. Indeed, a plateau is found at 3-4 μM concentrations of complex, with a maximum LSPR shift of 2 nm (Figure 4.33, **b**).

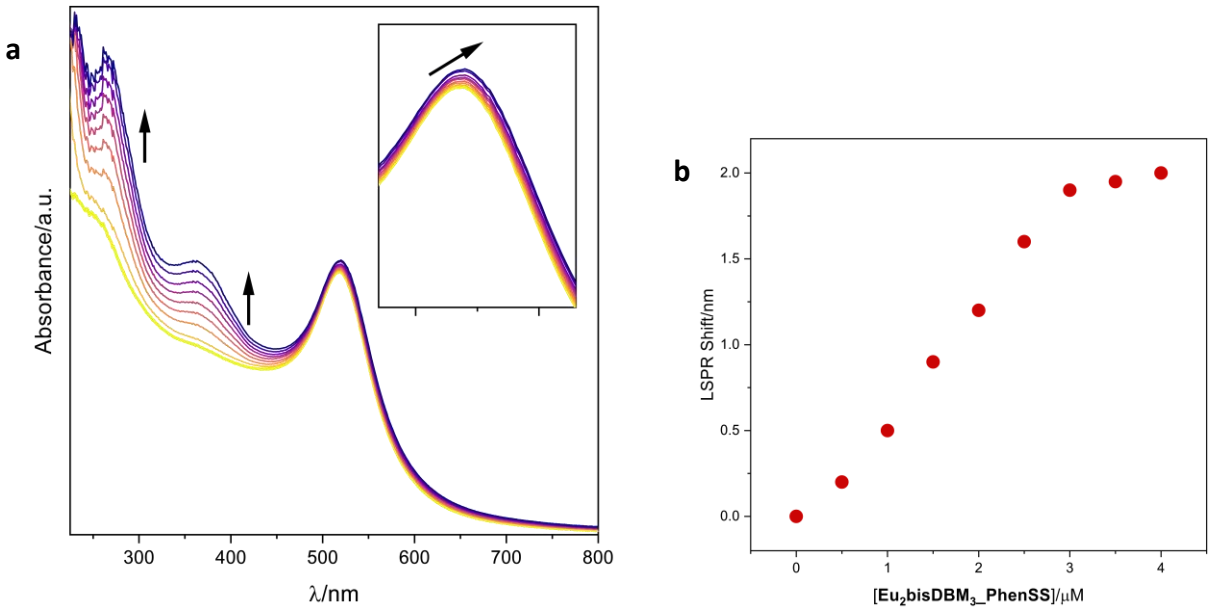


Figure 4.33 – **a** Absorption spectra of Z@AuNP14 (3 nM) upon addition of **Eu_2bisDBM$_3$_PhenSS$_2$** (0.2 mM in THF, 4% DMF) from 0.5 μM to 4 μM to give **Eu_2bisDBM$_3$_PhenSS$_2$●Z@AuNP14** in H_2O (maximum 2% THF, <0.1% DMF). **b** LSPR shift of Z@AuNP14 as a function of **Eu_2bisDBM$_3$_PhenSS$_2$** concentration.

ICP-MS was then employed for the estimation of the number of complex molecules per AuNP14 after purification, and the values were compared to the **Eu_2SAcbisDBM$_3$ ●Z@AuNP14** system. From the ICP-MS results, the **Eu_2bisDBM$_3$_PhenSS$_2$●Z@AuNP14** systems contains 613 complexes per AuNP14, which is a close value to the one for **Eu_2SAcbisDBM$_3$ ●Z@AuNP14** (572 complexes per AuNP14). These also correlate well with the ones reported for AuNPs with similar sizes and co-coated with a peptide and a Eu(III)-DTPA complex (640 complexes per AuNP).[66] In the reported example the complex is mononuclear, suggesting that dinuclear β-diketonate complexes such as **Eu_2SAcbisDBM$_3$** and **Eu_2bisDBM$_3$_PhenSS$_2$** can efficiently pack to give highly coated **Eu_2SAcbisDBM$_3$ ●Z@AuNP14** and **Eu_2bisDBM$_3$_PhenSS$_2$●Z@AuNP14** after purification.

TEM imaging reveals highly monodispersed **Eu_2bisDBM$_3$_PhenSS$_2$●Z@AuNP14** with sizes of 15±1 nm and PDI of 0.06 (Figures 4.34 **a** and **b** and Figure 4.41, Appendix). Unlike **Eu_2SAcbisDBM$_3$●Z@AuNP14** and Z@AuNP14 (Figures 4.17 and 4.39, Appendix), however,

string-like assemblies are observed for **Eu_2bisDBM$_3$_PhenSS_2●Z@AuNP14**. As the AuNPs were deposited in comparable concentrations, this is not attributed to a concentration effect. Furthermore, where the gap between single **Eu_2bisDBM$_3$_PhenSS_2●Z@AuNP14** could be measured, values of 1.4±0.7 nm were recorded. Unfortunately, single crystals of **Eu_2bisDBM$_3$_PhenSS_2** were not obtained, so accurate sizes of the complex are not available. By modelling the 3D structure of the **PhenSS** ligand, it is estimated that the unit can provide 1 nm spacing from the surface of the AuNP14. As coordination of **PhenSS** to both Eu(III) centres is expected, one of the **PhenSS** units is potentially free, anchoring to another AuNP14. Alternatively, the π-π stacking of phenanthroline ligands could also lead to the interaction with other **Eu_2bisDBM$_3$_PhenSS_2●Z@AuNP14** to give such assemblies. As no sign of aggregation is observed in the UV-Vis spectra of **Eu_2bisDBM$_3$_PhenSS_2●Z@AuNP14**, we believe that Zonyl FSA effectively limits this effect during coating, with the slow evaporation of solvent on the TEM grids driving the assembly of **Eu_2bisDBM$_3$_PhenSS_2●Z@AuNP14** into ordered assemblies.

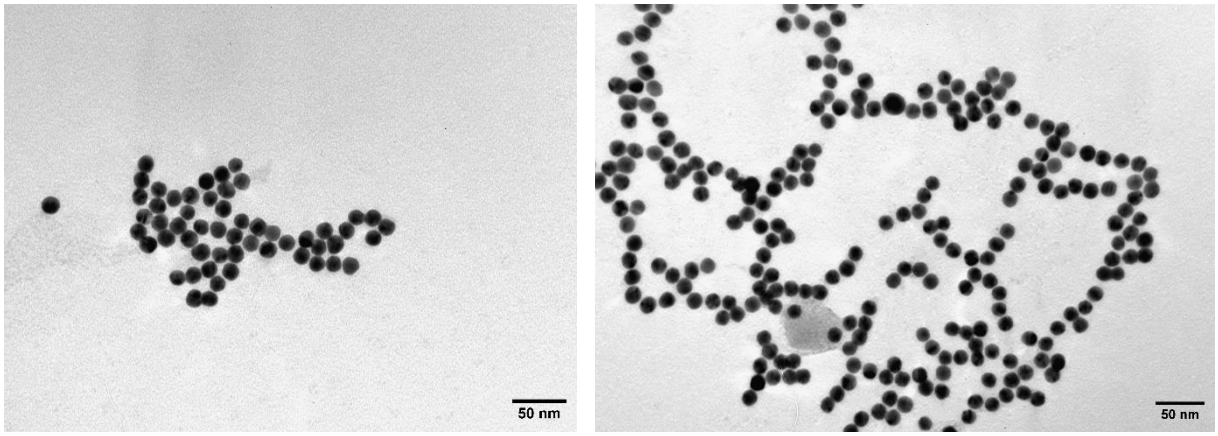


Figure 4.34 – TEM images of purified **Eu_2bisDBM$_3$_PhenSS_2●Z@AuNP14**.

Although this was not further characterised or investigated, it is an extremely interesting concept, which could be utilised for the development of AuNP assemblies with controlled

interparticle distances on surfaces or incorporated in sensing platforms relying on such assembly behaviour.[100-103]

4.2.3.4 Luminescence properties of Eu_2bisDBM$_3$_PhenSS_2●Z@AuNP14

The luminescence properties of **Eu_2bisDBM$_3$_PhenSS_2●Z@AuNP14** were evaluated and compared to **Eu_2SAcbisDBM$_3$ ●Z@AuNP14** as isoabsorptive dispersions at 350 nm (Figure 4.60, Appendix). Upon excitation at 350 nm, a significantly higher emission intensity (3-fold) is recorded for **Eu_2bisDBM$_3$_PhenSS_2●Z@AuNP14**, as expected for a system where quenching H_2O molecules are excluded, and that can be visually observed by irradiation in Figure 4.35, **d**. Indeed, the quantum yield of **Eu_2bisDBM$_3$_PhenSS_2●Z@AuNP14** reports a 4-fold increase (4.3%) compared to the **Eu_2SAcbisDBM$_3$ ●Z@AuNP14** system (1.1%). Finally, a 7 nm red shift in the excitation spectrum of **Eu_2bisDBM$_3$_PhenSS_2●Z@AuNP14** (λ_{max}: 367 nm) is accompanied by a new peak at 280 nm, attributable to the energy transfer from **PhenSS** to Eu(III) (Figure 4.35, **b**). The energy transfer is also visually portrayed in the emission map of **Eu_2bisDBM$_3$_PhenSS_2●Z@AuNP14** (Figure 4.35, **c**). Here, a series of emission spectra are obtained by the stepwise variation of the excitation wavelength, affording an effective representation of the emission intensity as a function of both variables.

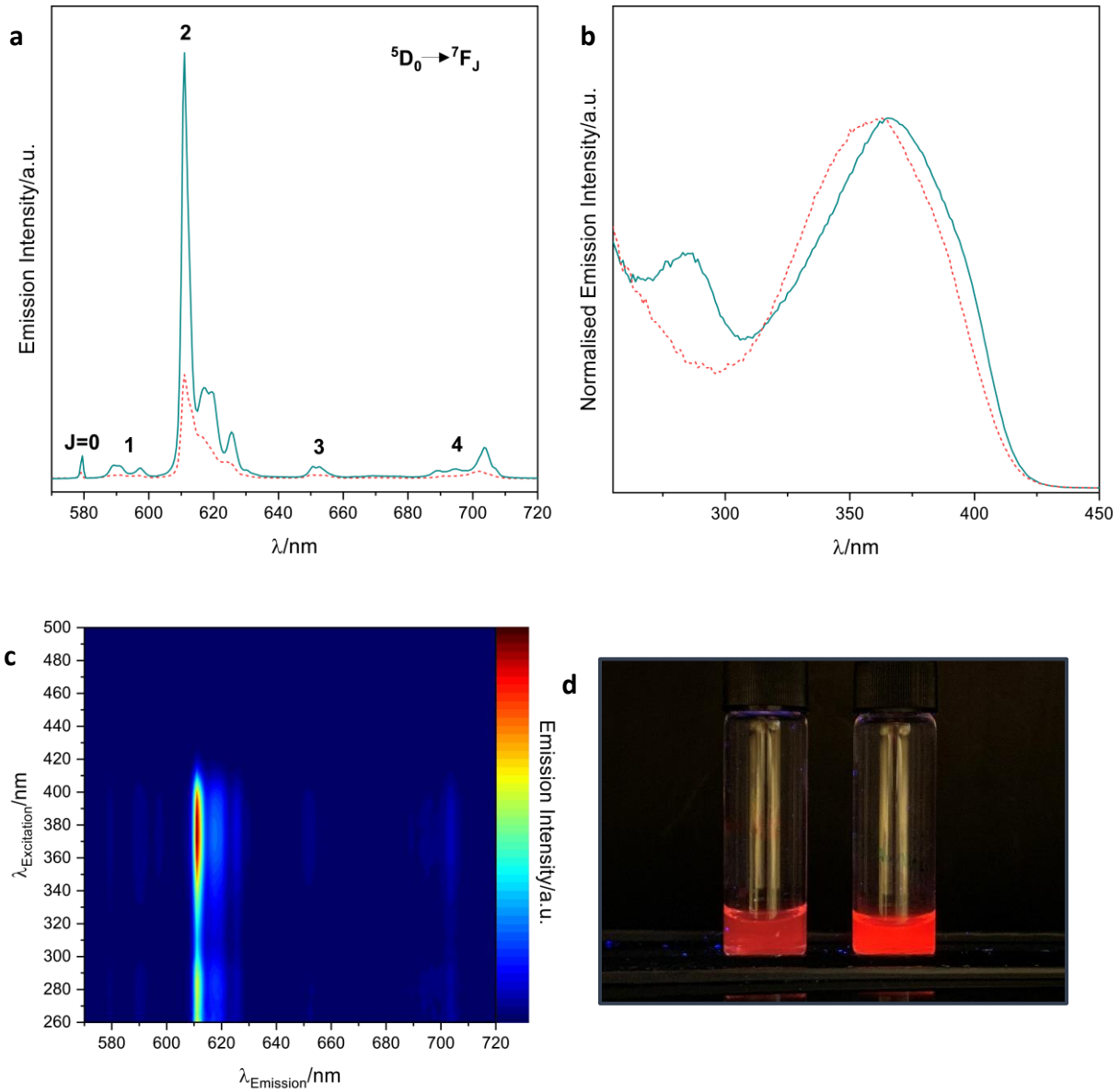
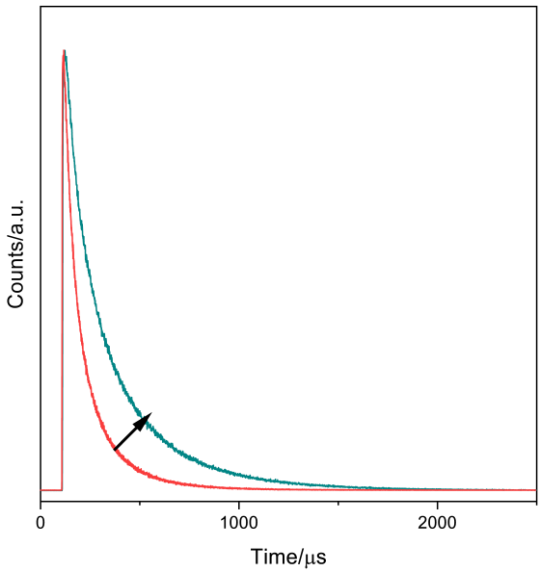


Figure 4.35 – Overlaid emission (**a**) and excitation (**b**) spectra of purified isoabsorptive dispersions of **Eu_2bisDBM$_3$_PhenSS_2●Z@AuNP14** (green, solid) and **Eu_2SAcbisDBM$_3$●Z@AuNP14** (red, dashed) in H_2O. λ_{exc}: 350 nm, λ_{em}: 611 nm. For clarity, the excitation spectra have been normalised. **c** Excitation – Emission map of purified **Eu_2bisDBM$_3$_PhenSS_2●Z@AuNP14** in H_2O. **d** Image of purified **Eu_2SAcbisDBM$_3$●Z@AuNP14** (left) and **Eu_2bisDBM$_3$_PhenSS_2●Z@AuNP14** (right) in H_2O upon illumination at 365 nm.

As expected from the quantum yield values, the lifetime of **Eu_2bisDBM$_3$_PhenSS_2●Z@AuNP14** displays a 2-fold increase from **Eu_2SAcbisDBM$_3$ ●Z@AuNP14**, which is in accordance to the values observed in H_2O (Table 4.4) and confirming the stability of the **Eu_2bisDBM$_3$_PhenSS_2** system on Z@AuNP14 to exclude quenching H_2O molecules.



Sample	τ/μs
Eu_2SAcbisDBM$_3$●Z@AuNP14	180 (68%), 64 (32%)
Eu_2bisDBM$_3$_PhenSS_2●Z@AuNP14	350 (72%), 110 (28%)
Eu_2bisDBM$_3$_PhenSS_2 in H_2O	360 (72%), 120 (28%)

Figure 4.36 – Overlaid lifetime spectra of purified isoabsorptive dispersions of **Eu_2bisDBM$_3$_PhenSS_2●Z@AuNP14** (green) and **Eu_2SAcbisDBM$_3$●Z@AuNP14** (red) in H_2O. λ_{exc}: 350 nm, λ_{em}: 611 nm. **Table 4.4** – Exponential decay analyses of **Eu_2SAcbisDBM$_3$●Z@AuNP14**, **Eu_2bisDBM$_3$_PhenSS_2●Z@AuNP14** and **Eu_2bisDBM$_3$_PhenSS_2** in H_2O.

4.3 Conclusions and future studies

In this chapter, we have presented the optimised incorporation of dinuclear **Ln_2SAcbisDBM$_3$** complexes to AuNPs. The **Eu_2SAcbisDBM$_3$●Z@AuNP14** system was studied, in addition to more traditional techniques, with SuperSTEM and EELS, to reveal the distribution of **Eu_2SAcbisDBM$_3$** complexes around the Z@AuNP14. This has provided a unique perspective of the system, allowing for the direct and visual comparison between the crystal structure of the respective Yb(III) complex and the recorded images.

Two methods for the improvement of Eu(III) luminescence were proposed. The first relied on the intrinsic optical properties of AuNPs and their correlation to the size of the nanostructure. Compared to the smaller sizes, an almost 2-fold increase in the emission intensity of the **Eu_2SAcbisDBM$_3$●Z@AuNP100** was recorded and is suggested to be due to the better overlap with the LSPR of the Z@AuNP100 as well as the high scattering component at Eu(III) emission (570-720 nm). Our second approach involved the synthesis and incorporation of a surface active ancillary ligand (**PhenSS**) for the exclusion of quenching H_2O molecules. This afforded a 4-fold increase in quantum yield for **Eu_2bisDBM$_3$_PhenSS$_2$●Z@AuNP14**, as well as a 2-fold increase in luminescence lifetime.

Finally, the NIR emission of **Yb_2SAcbisDBM$_3$** and **Nd_2SAcbisDBM$_3$** was tested on Z@AuNP14 and, for the Yb(III) derivative, on Z@AuNP50 and Z@AuNP100. Whereas **Nd_2SAcbisDBM$_3$●Z@AuNP14** displayed very weak luminescence, well resolved emission could be recorded for the **Yb_2SAcbisDBM$_3$●Z@AuNP14-50-100** samples, with lifetimes similar to the ones of the complex in H_2O. This example is added to the only other two reports, to the best

of our knowledge, of NIR emissive lanthanide(III) complexes anchored on AuNPs and highlights the value of **Ln_2SAcbisDBM$_3$** complexes for the development of highly emissive materials.

In future studies, the **PhenSS** ligand should be employed for the preparation of surface active NIR emissive **Ln_2SAcbisDBM$_3$_PhenSS$_2$** complexes. This would be particularly relevant for the Nd(III) derivative, where only very weak emission could be recorded in **Nd_2SAcbisDBM$_3$●Z@AuNP14**. Furthermore, the anchoring of **Eu_2SAcbisDBM$_3$** or **Eu_2bisDBM$_3$_PhenSS$_2$** to larger AuNPs (> 100 nm) should be explored, as the red shift obtained by the use of such sizes would allow for an even greater overlap and better plasmonic enhancement. Finally, the inclusion of **Ln_2SAcbisDBM$_3$●Z@AuNP** and **Eu_2bisDBM$_3$_PhenSS$_2$●Z@AuNP** as applied materials should be the focus of future research. As reported in section 1.3, additional units can be easily incorporated to AuNPs to impart functionality. The introduction of antibodies on **Ln_2SAcbisDBM$_3$●Z@AuNP**, for example, would allow for the targeted recognition of biomarkers and the development of diagnostic assays or imaging nanoagents based on a single visible or NIR emitting system.

4.4 References

1. C. Pezzato, S. Maiti, J. L. Y. Chen, A. Cazzolaro, C. Gobbo and L. J. Prins, *Chemical Communications*, 2015, **51**, 9922-9931.
2. A. Amendoeira, L. R. García, A. R. Fernandes and P. V. Baptista, *Advanced Therapeutics*, 2020, **3**, 1900153.
3. R. Sanchis-Gual, M. Coronado-Puchau, T. Mallah and E. Coronado, *Coordination Chemistry Reviews*, 2023, **480**, 215025.
4. H. W. Tan, J. An, C. K. Chua and T. Tran, *Advanced Electronic Materials*, 2019, **5**, 1800831.
5. Z. R. Goddard, M. J. Marín, D. A. Russell and M. Searcey, *Chemical Society Reviews*, 2020, **49**, 8774-8789.
6. V. Montes-García, M. A. Squillaci, M. Diez-Castellnou, Q. K. Ong, F. Stellacci and P. Samorì, *Chemical Society Reviews*, 2021, **50**, 1269-1304.
7. E. G. Wrigglesworth and J. H. Johnston, *Nanoscale Advances*, 2021, **3**, 3530-3536.
8. V. Amendola, R. Pilot, M. Frasconi, O. M. Maragò and M. A. Iatì, *Journal of Physics: Condensed Matter*, 2017, **29**, 203002.
9. X. Wu, C. Hao, J. Kumar, H. Kuang, N. A. Kotov, L. M. Liz-Marzán and C. Xu, *Chemical Society Reviews*, 2018, **47**, 4677-4696.
10. Y. Wy, H. Jung, J. W. Hong and S. W. Han, *Accounts of Chemical Research*, 2022, **55**, 831-843.
11. D. Zhang, Z. Li and K. Sugioka, *Journal of Physics: Photonics*, 2021, **3**, 042002.
12. I. Ielo, G. Rando, F. Giacobello, S. Sfameni, A. Castellano, M. Galletta, D. Drommi, G. Rosace and M. R. Plutino, *Molecules*, 2021, **26**, 5823.
13. X. Yu, J. T. Pham, C. Subramani, B. Creran, Y.-C. Yeh, K. Du, D. Patra, O. R. Miranda, A. J. Crosby and V. M. Rotello, *Advanced Materials*, 2012, **24**, 6330-6334.
14. T. Kunoh, M. Takeda, S. Matsumoto, I. Suzuki, M. Takano, H. Kunoh and J. Takada, *ACS Sustainable Chemistry & Engineering*, 2018, **6**, 364-373.
15. N. M. El-Deeb, S. M. Khattab, M. A. Abu-Youssef and A. M. A. Badr, *Scientific Reports*, 2022, **12**, 11518.
16. S. Ying, Z. Guan, P. C. Ofoegbu, P. Clubb, C. Rico, F. He and J. Hong, *Environmental Technology & Innovation*, 2022, **26**, 102336.
17. C. Daruich De Souza, B. Ribeiro Nogueira and M. E. C. M. Rostelato, *Journal of Alloys and Compounds*, 2019, **798**, 714-740.
18. Y. Ding, P.-J. J. Huang, M. Zandieh, J. Wang and J. Liu, *Langmuir*, 2023, **39**, 256-264.
19. S. Yazdani, A. Daneshkhah, A. Diwate, H. Patel, J. Smith, O. Reul, R. Cheng, A. Izadian and A. R. Hajrasouliha, *ACS Omega*, 2021, **6**, 16847-16853.
20. N. G. Bastús, J. Comenge and V. Puntes, *Langmuir*, 2011, **27**, 11098-11105.
21. J. Turkevich, P. C. Stevenson and J. Hillier, *Discussions of the Faraday Society*, 1951, **11**, 55-75.
22. F. Schulz, T. Homolka, N. G. Bastús, V. Puntes, H. Weller and T. Vossmeyer, *Langmuir*, 2014, **30**, 10779-10784.

23. J. Polte, *CrystEngComm*, 2015, **17**, 6809-6830.
24. M.-Q. He, Y. Ai, W. Hu, L. Guan, M. Ding and Q. Liang, *Advanced Materials*, 2023, **n/a**, 2211915.
25. S. A. Bansal, V. Kumar, J. Karimi, A. P. Singh and S. Kumar, *Nanoscale Advances*, 2020, **2**, 3764-3787.
26. J. Langer, S. M. Novikov and L. M. Liz-Marzán, *Nanotechnology*, 2015, **26**, 322001.
27. G. Mie, *Annalen der Physik*, 1908, **330**, 377-445.
28. J. Olson, S. Dominguez-Medina, A. Hoggard, L.-Y. Wang, W.-S. Chang and S. Link, *Chemical Society Reviews*, 2015, **44**, 40-57.
29. L. Wang, M. Hasanzadeh Kafshgari and M. Meunier, *Advanced Functional Materials*, 2020, **30**, 2005400.
30. C. Darviot, P. Hardy and M. Meunier, *Journal of Biophotonics*, 2019, **12**, e201900193.
31. P. Yuan, X. Ding, Z. Guan, N. Gao, R. Ma, X.-F. Jiang, Y. Y. Yang and Q.-H. Xu, *Advanced Healthcare Materials*, 2015, **4**, 674-678.
32. W. Li and X. Chen, *Nanomedicine*, 2015, **10**, 299-320.
33. E. Y. Lukianova-Hleb, Y.-S. Kim, I. Belatsarkouski, A. M. Gillenwater, B. E. O'Neill and D. O. Lapotko, *Nature Nanotechnology*, 2016, **11**, 525-532.
34. H. A. Atwater and A. Polman, *Nature Materials*, 2010, **9**, 205-213.
35. S. Li, H. Huang, L. Shao and J. Wang, *ACS Nano*, 2021, **15**, 10759-10768.
36. K. A. Willets, A. J. Wilson, V. Sundaresan and P. B. Joshi, *Chemical Reviews*, 2017, **117**, 7538-7582.
37. B. Zhou, X. Guo, N. Yang, Z. Huang, L. Huang, Z. Fang, C. Zhang, L. Li and C. Yu, *Journal of Materials Chemistry B*, 2021, **9**, 5583-5598.
38. S.-C. Wei, L. Chang, C.-C. Huang and H.-T. Chang, *Biomaterials Science*, 2019, **7**, 4482-4490.
39. C. Arib, A. Griveau, J. Eyer and J. Spadavecchia, *Nanoscale Advances*, 2022, **4**, 3010-3022.
40. A. L. Parry, N. A. Clemson, J. Ellis, S. S. R. Bernhard, B. G. Davis and N. R. Cameron, *Journal of the American Chemical Society*, 2013, **135**, 9362-9365.
41. K. R. Trabbic, K. A. Kleski and J. J. Barchi, Jr., *ACS Bio & Med Chem Au*, 2021, **1**, 31-43.
42. X. Zhao, Y. Jia, J. Li, R. Dong, J. Zhang, C. Ma, H. Wang, Y. Rui and X. Jiang, *ACS Applied Materials & Interfaces*, 2018, **10**, 29398-29406.
43. J. Zhang, Z. Huang, Y. Xie and X. Jiang, *Chemical Science*, 2022, **13**, 1080-1087.
44. M. Vetro, D. Safari, S. Fallarini, K. Salsabila, M. Lahmann, S. Penadés, L. Lay, M. Marradi and F. Compostella, *Nanomedicine*, 2017, **12**, 13-23.
45. J. Zhang, L. Mou and X. Jiang, *Chemical Science*, 2020, **11**, 923-936.
46. X. Yang, J. Yang, L. Wang, B. Ran, Y. Jia, L. Zhang, G. Yang, H. Shao and X. Jiang, *ACS Nano*, 2017, **11**, 5737-5745.
47. A. Heuer-Jungemann, N. Feliu, I. Bakaimi, M. Hamaly, A. Alkilany, I. Chakraborty, A. Masood, M. F. Casula, A. Kostopoulou, E. Oh, K. Susumu, M. H. Stewart, I. L. Medintz, E. Stratakis, W. J. Parak and A. G. Kanaras, *Chemical Reviews*, 2019, **119**, 4819-4880.
48. H. Kang, J. T. Buchman, R. S. Rodriguez, H. L. Ring, J. He, K. C. Bantz and C. L. Haynes, *Chemical Reviews*, 2019, **119**, 664-699.
49. J.-W. Park and J. S. Shumaker-Parry, *Journal of the American Chemical Society*, 2014, **136**, 1907-1921.

50. M. R. Hormozi-Nezhad, P. Karami and H. Robatjazi, *RSC Advances*, 2013, **3**, 7726-7732.
51. K. M. Koczkur, S. Mourdikoudis, L. Polavarapu and S. E. Skrabalak, *Dalton Transactions*, 2015, **44**, 17883-17905.
52. F. Höeg, J. Schulz, S. Graf, D. Salah, S. Chandralingam, W. Maison, W. J. Parak and F. Schulz, *The Journal of Physical Chemistry C*, 2022, **126**, 20594-20604.
53. L. Wang, P. Quan, S. H. Chen, W. Bu, Y.-F. Li, X. Wu, J. Wu, L. Zhang, Y. Zhao, X. Jiang, B. Lin, R. Zhou and C. Chen, *ACS Nano*, 2019, **13**, 8680-8693.
54. H. Shang, S. K. Wallentine, D. M. Hofmann, Q. Zhu, C. J. Murphy and L. R. Baker, *Chemical Science*, 2020, **11**, 12298-12306.
55. Y. Wu, M. R. K. Ali, K. Chen, N. Fang and M. A. El-Sayed, *Nano Today*, 2019, **24**, 120-140.
56. K. Saha, S. S. Agasti, C. Kim, X. Li and V. M. Rotello, *Chemical Reviews*, 2012, **112**, 2739-2779.
57. C. Quintana, M. P. Cifuentes and M. G. Humphrey, *Chemical Society Reviews*, 2020, **49**, 2316-2341.
58. D. Mendez-Gonzalez, S. Melle, O. G. Calderón, M. Laurenti, E. Cabrera-Granado, A. Egatz-Gómez, E. López-Cabarcos, J. Rubio-Retama and E. Díaz, *Nanoscale*, 2019, **11**, 13832-13844.
59. Y. Zhang, X. Zhu and Y. Zhang, *ACS Nano*, 2021, **15**, 3709-3735.
60. A. Rahman, P. P. Praveen Kumar, P. Yadav, T. Goswami, A. Shanavas, H. N. Ghosh and P. P. Neelakandan, *ACS Applied Nano Materials*, 2022, **5**, 6532-6542.
61. S. A. M. Osborne and Z. Pikramenou, *Faraday Discussions*, 2015, **185**, 219-231.
62. S. M. King, S. Claire, R. I. Teixeira, A. N. Dosumu, A. J. Carrod, H. Dehghani, M. J. Hannon, A. D. Ward, R. Bicknell, S. W. Botchway, N. J. Hodges and Z. Pikramenou, *Journal of the American Chemical Society*, 2018, **140**, 10242-10249.
63. B. I. Ipe, K. Yoosaf and K. G. Thomas, *Journal of the American Chemical Society*, 2006, **128**, 1907-1913.
64. D. J. Lewis, T. M. Day, J. V. MacPherson and Z. Pikramenou, *Chemical Communications*, 2006, 1433-1435.
65. D. J. Lewis, C. Bruce, S. Bohic, P. Cloetens, S. P. Hammond, D. Arbon, S. Blair-Reid, Z. Pikramenou and B. Kysela, *Nanomedicine*, 2010, **5**, 1547-1557.
66. A. Davies, D. J. Lewis, S. P. Watson, S. G. Thomas and Z. Pikramenou, *Proceedings of the National Academy of Sciences*, 2012, **109**, 1862-1867.
67. C. S. Bonnet, J. Massue, S. J. Quinn and T. Gunnlaugsson, *Organic & Biomolecular Chemistry*, 2009, **7**, 3074-3078.
68. J. Massue, S. J. Quinn and T. Gunnlaugsson, *Journal of the American Chemical Society*, 2008, **130**, 6900-6901.
69. S. Comby and T. Gunnlaugsson, *ACS Nano*, 2011, **5**, 7184-7197.
70. Esther M. Surender, S. Comby, B. L. Cavanagh, O. Brennan, T. C. Lee and T. Gunnlaugsson, *Chem*, 2016, **1**, 438-455.
71. L. K. Truman, S. J. Bradberry, S. Comby, O. Kotova and T. Gunnlaugsson, *ChemPhysChem*, 2017, **18**, 1746-1751.
72. L. K. Truman, S. Comby and T. Gunnlaugsson, *Angewandte Chemie International Edition*, 2012, **51**, 9624-9627.
73. A. C. Savage and Z. Pikramenou, *Chemical Communications*, 2011, **47**, 6431-6433.

74. X. Wang, Y. Xia, Y. Liu, W. Qi, Q. Sun, Q. Zhao and B. Tang, *Chemistry – A European Journal*, 2012, **18**, 7189-7195.
75. D. Feng, F. Tian, W. Qin and X. Qian, *Chemical Science*, 2016, **7**, 2246-2250.
76. C. Chen, C. Midelet, S. Bhuckory, N. Hildebrandt and M. H. V. Werts, *The Journal of Physical Chemistry C*, 2018, **122**, 17566-17574.
77. P. Nath, N. Priyadarshni and N. Chanda, *ACS Applied Nano Materials*, 2018, **1**, 73-81.
78. R. M. Pallares, K. P. Carter, S. E. Zeltmann, T. Tratnjek, A. M. Minor and R. J. Abergel, *Inorganic Chemistry*, 2020, **59**, 2030-2036.
79. C. E. Lisowski and J. E. Hutchison, *Analytical Chemistry*, 2009, **81**, 10246-10253.
80. P. Mondal and J. L. Yarger, *The Journal of Physical Chemistry C*, 2019, **123**, 20459-20467.
81. S. E. Crawford, C. M. Andolina, D. C. Kaseman, B. H. Ryoo, A. M. Smith, K. A. Johnston and J. E. Millstone, *Journal of the American Chemical Society*, 2017, **139**, 17767-17770.
82. D. J. Lewis and Z. Pikramenou, *Coordination Chemistry Reviews*, 2014, **273-274**, 213-225.
83. S. Okyem, O. Awotunde, T. Ogunlusi, M. B. Riley and J. D. Driskell, *Langmuir*, 2021, **37**, 2993-3000.
84. H. M. Zakaria, A. Shah, M. Konieczny, J. A. Hoffmann, A. J. Nijdam and M. E. Reeves, *Langmuir*, 2013, **29**, 7661-7673.
85. A. Dutta, A. Paul and A. Chattopadhyay, *RSC Advances*, 2016, **6**, 82138-82149.
86. N. Maiti, R. Chadha, A. Das and S. Kapoor, *RSC Advances*, 2016, **6**, 62529-62539.
87. D. A. Muller, *Nature Materials*, 2009, **8**, 263-270.
88. S. J. Pennycook, C. Li, M. Li, C. Tang, E. Okunishi, M. Varela, Y.-M. Kim and J. H. Jang, *Journal of Analytical Science and Technology*, 2018, **9**, 11.
89. S. J. Oldenburg, Dissertation, Rice University, 2000.
90. J. Shi, Y. Hou, W. Chu, X. Shi, H. Gu, B. Wang and Z. Sun, *Inorganic Chemistry*, 2013, **52**, 5013-5022.
91. K. Binnemans, *Handbook on the Physics and Chemistry of Rare Earths*, 2005, **35**, 107-272.
92. Y. Hou, J. Shi, W. Chu and Z. Sun, *European Journal of Inorganic Chemistry*, 2013, **2013**, 3063-3069.
93. H. Ma, Y. Zhou, T. Gao, H. Li and P. Yan, *Inorganica Chimica Acta*, 2021, **525**, 120495.
94. L. Ruan, X. Gao, J. Zhao, C. Xu and D. Liang, *Journal of Molecular Structure*, 2017, **1149**, 265-272.
95. J. Xu, Z. Sun, L. Jia, B. Li, L. Zhao, X. Liu, Y. Ma, H. Tian, Q. Wang, W. Liu and Y. Tang, *Dalton Transactions*, 2011, **40**, 12909-12916.
96. R. B. P. Elmes, K. N. Orange, S. M. Cloonan, D. C. Williams and T. Gunnlaugsson, *Journal of the American Chemical Society*, 2011, **133**, 15862-15865.
97. M. Pal, V. Ramu, D. Musib, A. Kunwar, A. Biswas and M. Roy, *Inorganic Chemistry*, 2021, **60**, 6283-6297.
98. R. Ilmi, S. Kansız, N. Dege and M. S. Khan, *Journal of Photochemistry and Photobiology A: Chemistry*, 2019, **377**, 268-281.
99. O. T. Alexander, R. E. Kroon, A. Brink and H. G. Visser, *Dalton Transactions*, 2019, **48**, 16074-16082.

100. I. Blakey, Z. Merican and K. J. Thurecht, *Langmuir*, 2013, **29**, 8266-8274.
101. J. Lai, Y. Xu, X. Mu, X. Wu, C. Li, J. Zheng, C. Wu, J. Chen and Y. Zhao, *Chemical Communications*, 2011, **47**, 3822-3824.
102. H. Xia, Y. Gao, L. Yin, X. Cheng, A. Wang, M. Zhao, J. Ding and H. Shi, *ChemBioChem*, 2019, **20**, 667-671.
103. J. Yi and Y. Xianyu, *Advanced Functional Materials*, 2022, **32**, 2113012.
104. W. Haiss, N. T. K. Thanh, J. Aveyard and D. G. Fernig, *Analytical Chemistry*, 2007, **79**, 4215-4221.

4.5 Appendix III

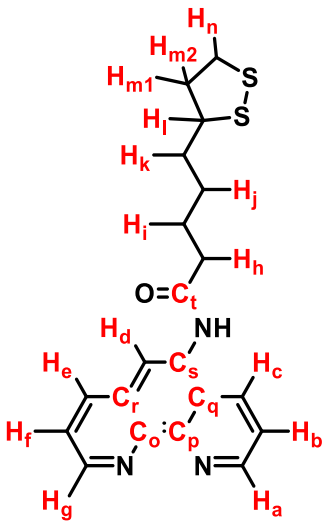
4.5.1 Materials and methods

Solvents and chemicals were purchased from Sigma Aldrich/Merck, VWR, Alfa Aesar, Honeywell and Fisher Scientific, NMR solvents were purchased from Goss Scientific. **Ln_2SAcbisDBM$_3$** and **Eu_2bisDBM$_3$** complexes were prepared and characterised as reported in Chapter 2. For the synthesis, coating and dilution of AuNPs, MilliQ H_2O was employed. All glassware intended for AuNPs was cleaned with aqua regia (3:1 HCl 37% and HNO_3 65-70%) for a minimum of 5 hours and then rinsed with MilliQ H_2O 10 times. For ICP-MS, ultrapure H_2O, aqua regia (3:1 TraceSelect HCl and HNO_3) and HNO_3 4% (TraceSelect) were employed. Reactions for the synthesis of AuNPs were conducted in the dark and shielded from light with aluminium foil. All reported concentrations of AuNPs have a 10% error. For the synthesis of **PhenSS**, Schlenk technique was employed and the reaction was carried out under N_2 atmosphere. NMR spectra were recorded on a Bruker AV400 and analysed with MestreNova software. Electrospray mass spectrometry was conducted on a Waters Micromass Q-TOF. Infrared measurements were obtained on a Perkin Elmer 100FT-IR spectrometer fitted with ATR attachment. UV-Vis absorption spectra were recorded on an Agilent Cary 60 UV-Vis spectrophotometer. DLS data were obtained on a Malvern Panalytical Zetasizer ZS instrument and sizes are reported as a collection of 5 measurements. TEM imaging was conducted on a Jeol 1400 Bio Electron Microscope and using carbon coated Cu 200 mesh grids. TEM images were analysed with ImageJ and at least 20 sizes were measured for the calculation of mean sizes and standard deviation. ICP-MS was conducted on a Perkin Elmer 300X Nexion ICP-MS at the Department of Geography, Earth and Environmental Sciences at the University of

Birmingham and the data were acquired with Perkin Elmer Syngistix for ICP-MS Version 3.1 software. During the measurements, Terbium and Rhodium *Trace*CERT® internal standards from Merck were used. SuperSTEM imaging and EELS analysis were carried out at the SuperSTEM laboratory, EPSRC National Research Facility for Advanced Electron Microscopy, in Daresbury, UK. A Nion UltraSTEM100 instrument was employed, equipped with a Gatan Enfina ELL spectrometer. The convergence semi-angle was 27 mrad for SuperSTEM-HAADF measurements and 36 mrad for EELS acquisitions. Luminescence spectra were recorded either on an Edinburgh Instruments FLSP920 steady state and time resolved spectrometer with F980 software or an Edinburgh Instruments FLS1000 steady state and time resolved spectrometer with Fluoracle software. In both cases, the spectra were corrected for lamp and instrument response. A 450 W Xenon Arc lamp was employed as excitation source for steady state measurements, while time resolved spectra were acquired with a μF flashlamp. Lifetimes were fitted to mono- or multiexponential decays as appropriate using FAST software, with an estimated error of 10% and with χ^2 between 1.0 and 1.2. Quantum yields were obtained with an integrating sphere apparatus from Edinburgh Instruments. The modelling of the absorption and scattering components for **Eu_2SAcbisDBM$_3$●Z@AuNP14-50-100** in section 4.2.2 was obtained and plotted with the Mie theory calculator from nanoComposix[1]

4.5.2 Synthetic procedures

4.5.2.1 Synthesis of 5-(1,2-dithiolan-3-yl)-N-(1,10-phenanthrolin-5-yl)pentanamide (PhenSS)



PhenSS

1,10-Phenanthrolin-5-amine (500 mg, 2.56 mmol) was dissolved in DCM (95 mL) and the pale yellow solution was cooled to 0-5 °C. α-Lipoic acid (528 mg, 2.56 mmol), EDCI (1.23 g, 6.40 mmol) and DMAP (313 mg, 2.56 mmol) were added and the solution was stirred at room temperature for 72 hours. After this time, the solvent was removed under reduced pressure and the orange residue taken up in H_2O (50 mL) and centrifuged (30 minutes, 7800 rpm). After removing the supernatant, the solid was resuspended in MeCN (3x50 mL) and centrifuged (15 minutes, 7800 rpm), repeating the process three times. **PhenSS** was isolated as a pale yellow solid (726 mg, 1.89 mmol, 74%).

^{1}H-NMR (400 MHz, DMSOd_6): δ 10.12 (s, NH, 1H), 9.13 (dd, J = 4.3, 1.7 Hz, H_a, 1H), 9.03 (dd, J = 4.3, 1.7 Hz, H_g, 1H), 8.60 (dd, J = 8.4, 1.7 Hz, H_c, 1H), 8.45 (dd, J = 8.1, 1.7 Hz, H_e, 1H), 8.17 (s, H_d, 1H), 7.82 (dd, J = 8.4, 4.3 Hz, H_b, 1H), 7.74 (dd, J = 8.1, 4.3 Hz, H_f, 1H), 3.68 (dq, J = 8.7, 6.2 Hz, H_l, 1H), 3.26 – 3.08 (m, H_n, 2H), 2.55 (t, J = 7.3 Hz, H_h, 2H), 2.48 (dq, J = 12.9, 6.6 Hz, H_{m1}, 1H), 1.90 (dq, J = 12.9, 6.6 Hz, H_{m2}, 1H), 1.82 – 1.57 (m, H_i, H_j, 4H), 1.56 – 1.44 (m, H_k, 2H). ^{13}C-

NMR (101 MHz, DMSOd_6) δ 172.30 (C_t), 149.87 (C_a), 149.31 (C_g), 145.86 (C_s), 143.79(C_o), 135.79 (C_e), 131.79 (C_p), 131.65 (C_c), 128.10 (C_r), 124.66 (C_q), 123.59(C_f), 122.83 (C_b), 120.05 (C_d), 56.17 (C_l), 40.00 (C_m) 38.17 (C_n), 35.80 (C_h), 34.22 ($C_{i/j}$), 28.44 (C_k), 25.02 ($C_{i/j}$). m/z ESI$^+$-TOF $C_{20}H_{21}N_3OS_2$: calcd. $[M+H]^+$ 384.12 found 384.12. Calcd. $[M+Na]^+$ 406.10 found 406.10. λ_{max} (DMF): 270 nm, 315 (sh).

4.5.2.2 Synthesis of AuNP14

The synthesis was reproduced as reported in [61, 62].

Citric acid (13.3 mg, 0.07 mmol), EDTA (1.6 mg, 0.005 mmol) and trisodium citrate (60.6 mg, 0.23 mmol) were dissolved in H_2O (100 mL). The colourless solution was heated to strong reflux at 150 °C for 15 minutes. $HAuCl_4$ (8.0 mg, 0.02 mmol) was dissolved in H_2O (25 mL) and heated at 100 °C. The yellow $HAuCl_4$ solution was quickly added to the citrate/EDTA solution in reflux and after a few minutes the mixture changed from very pale yellow to pink and finally to wine red. The strong reflux was maintained for 30 minutes and, after this time, the mixture was slowly cooled to room temperature under continuous stirring for 1 hour, to give 125 mL of AuNP14 (2 nM). λ_{max} (H_2O): 518 nm (LSPR).

4.5.2.3 Synthesis of AuNP25, AuNP50 and AuNP100

The synthesis was reproduced as in [61, 62].

Three stock solutions were prepared and used for the synthesis of all three sizes:

(**A**) $HAuCl_4$ in H_2O (5.0 mM).

(**B**) Ascorbic acid in H_2O (57.2 mM).

(**C**) Trisodium citrate in H_2O (34.0 mM).

AuNP25

A diluted $HAuCl_4$ solution was prepared by diluting stock solution **A** (4 mL) in H_2O (16 mL) (solution **A1**). Stock solutions **B** (1 mL) and **C** (0.5 mL) were diluted in H_2O (18.5 mL) (solution **BC1**). AuNP14 (2 nM, 34 mL) were diluted in H_2O (6 mL) and vigorously stirred at room temperature in a three neck round bottom flask. Solutions **A1** and **BC1** were simultaneously added dropwise to the diluted AuNP14 under vigorous stirring. After additions were complete, the deep red mixture was stirred and heated to reflux for 30 minutes at 150 °C. After this time, the vessel was allowed to cool to room temperature for 1 hour while stirring was maintained, to give 80 mL of AuNP25 (0.7 nM). λ_{max} (H_2O): 519 nm (LSPR).

AuNP50

A diluted $HAuCl_4$ solution was prepared by diluting stock solution **A** (4 mL) in H_2O (16 mL) (solution **A1**). Stock solutions **B** (1 mL) and **C** (0.5 mL) were diluted in H_2O (18.5 mL) (solution **BC1**). AuNP25 (0.7 nM, 9 mL) were diluted in H_2O (31 mL) and vigorously stirred at room temperature in a three neck round bottom flask. Solutions **A1** and **BC1** were simultaneously added dropwise to the diluted AuNP25 under vigorous stirring. After additions were complete, the bright red mixture was stirred and heated to reflux for 30 minutes at 150 °C. After this time, the vessel was allowed to cool to room temperature for 1 hour while stirring was maintained, to give 80 mL of AuNP50 (80 pM). λ_{max} (H_2O): 525 nm (LSPR).

AuNP100

A diluted $HAuCl_4$ solution was prepared by diluting stock solution **A** (16 mL) in H_2O (4 mL) (solution **A2**). Stock solutions **B** (4 mL) and **C** (2 mL) were diluted in H_2O (14 mL) (solution **BC2**). AuNP50 (80 pM, 40 mL) were vigorously stirred at room temperature in a three neck round

bottom flask. Solutions **A2** and **BC2** were simultaneously added dropwise to the AuNP50 under vigorous stirring. After additions were complete, the brown mixture was stirred and heated to reflux for 30 minutes at 150 °C. After this time, the vessel was allowed to cool to room temperature for 1 hour while stirring was maintained, to give 80 mL of AuNP100 (40 pM). λ_{max} (H_2O): 550 nm (LSPR).

4.5.3 PhenSS coordination studies

4.5.3.1 Addition of PhenSS to Eu_2bisDBM$_3$ for spectroscopic studies

PhenSS (0.25 mM in THF) was added to **Eu_2bisDBM$_3$** (1.2 µM in THF, 0.2% DMF or 100% DMF, 3 mL) in small aliquots (1 equivalent = 14 µL). Each addition was followed by stirring at room temperature for 5 minutes prior to acquisition of steady state and time resolved spectra.

4.5.3.2 Preparation of Eu_2bisDBM$_3$_PhenSS$_2$ for coating on Z@AuNP14

Eu_2bisDBM$_3$ (5 mM in DMF, 35 µL) was diluted in THF (500 µL) to give a 0.35 µM solution in THF, 7% DMF. **PhenSS** (5 mM in THF, 350 µL, 10 equivalents) was added to the **Eu_2bisDBM$_3$** solution in aliquots of 50 µL each. After each addition, the solution was stirred for 5 minutes. The final concentration of **Eu_2bisDBM$_3$** in the mixture is 0.2 mM in THF, 4% DMF.

4.5.4 Coating procedures

4.5.4.1 Coating of AuNP14 and AuNP50 with Zonyl FSA: Z@AuNP14-50

AuNPs (2 mL) were centrifuged (30 minutes, 9000 rpm). The supernatant was removed, taking care not to disturb the pellet at the bottom. The pellet was then resuspended in H_2O (1 mL) and Zonyl FSA (0.05 mM, 10 µL) was added, followed by stirring at room temperature for 20 minutes. After centrifugation (30 minutes, 9000 rpm) and removal of the supernatant, the pellet was resuspended in H_2O (1 mL).

Z@AuNP14 (3 nM). λ_{max} (H_2O): 519 nm (LSPR).

Z@AuNP50 (76 pM). λ_{max} (H_2O): 526 nm (LSPR).

4.5.4.2 Coating of AuNP100 with Zonyl FSA: Z@AuNP100

AuNP100 (2 mL) were centrifuged (90 seconds, 9000 rpm). The supernatant was removed, taking care not to disturb the pellet at the bottom. The pellet was resuspended in H_2O (1 mL) and Zonyl FSA (0.05 mM, 10 µL) was added, followed by stirring at room temperature for 20 minutes. After centrifugation (90 seconds, 9000 rpm) and removal of the supernatant, the pellet was resuspended in H_2O (1 mL).

Z@AuNP100 (30 pM). λ_{max} (H_2O): 550 nm (LSPR).

4.5.4.3 Coating of Z@AuNP14, Z@AuNP50 and Z@AuNP100 with Ln_2SAcbisDBM$_3$: Ln_2SAcbisDBM$_3$●Z@AuNP14-50-100

Ln_2SAcbisDBM$_3$ (0.2 mM in DMF, 20 µL) was added in 2.5 µL aliquots to Z@AuNP14 (1 mL, 3 nM), Z@AuNP50 (1 mL, 38 pM) or Z@AuNP100 (1 mL, 6 pM). Each intermediate addition was followed by 3 minutes stirring and, after the final addition, the mixture was stirred for 20 minutes at room temperature. **Ln_2SAcbisDBM$_3$●Z@AuNP14-50-100** were purified by size exclusion chromatography (Sephadex G-25) and, if necessary, diluted to the desired concentrations as reported for the specific experiment.

4.5.4.4 Coating of Z@AuNP14 with Eu_2bisDBM$_3$_PhenSS$_2$: Eu_2bisDBM$_3$_PhenSS$_2$●Z@AuNP14

A solution of **Eu_2bisDBM$_3$_PhenSS$_2$** was prepared as described in section 4.5.3.2. **Eu_2bisDBM$_3$_PhenSS$_2$** (0.2 mM in THF, 4% DMF, 20 µL) was added in 2.5 µL aliquots to

Z@AuNP14 (1 mL, 3 nM). Each intermediate addition was followed by 3 minutes stirring and, after the final addition, the mixture was stirred for 20 minutes at room temperature. **Eu_2bisDBM$_3$_PhenSS$_2$●Z@AuNP14** were purified by size exclusion chromatography (Sephadex G-25) and, if necessary, diluted to the desired concentrations as reported for the specific experiment.

4.5.5 Correction of emission spectra by absorbance loss

For comparisons of **Eu_2SAcbisDBM$_3$●Z@AuNP14**, **Eu_2SAcbisDBM$_3$●Z@AuNP50** and **Eu_2SAcbisDBM$_3$●Z@AuNP100**, the spectra were corrected by the absorbance loss. The integrals of the entire emission spectra were multiplied by a correction factor (F_{TOT}) that considered the total absorption of AuNPs at 350 nm.

$$F_{TOT} = \frac{100}{\left[100 - \left(\frac{Abs_{Z@AuNP} \cdot 100}{Abs_{Eu_2SAcbisDBM_3 \cdot Z@AuNP}}\right)\right]} \quad Equation\ 4.3$$

Where $Abs_{Z@AuNP}$ is the absorption of Z@AuNP at 350 nm, while $Abs_{Eu_2SAcbisDBM_3 \bullet Z@AuNP}$ is the absorption of **Eu_2SAcbisDBM$_3$●Z@AuNP** at 350 nm.

4.5.6 Calculation of concentration of AuNPs from UV-Vis absorption spectra

$$[AuNP] = \frac{Abs_{450}}{\varepsilon_{450}} \quad Equation\ 4.4$$

Where Abs_{450} is the absorbance value at 450 nm and the ε_{450} is the molar absorption coefficient of AuNPs at 450 nm, reported according to size in [104].

4.5.7 ICP-MS experiments

4.5.7.1 Preparation of samples and calibration

Standard solutions of Au and Eu were prepared by diluting the stock standards in HNO_3 4% to reach 10 mL.

AuNP samples were prepared by digestion in aqua regia until a colourless solution was obtained and then dilution in HNO_3 to reach 5 mL.

4.5.7.2 Calculations of AuNP concentration and number of complex molecules per AuNP

For the calculation of the concentration of AuNPs in molarity ([AuNP/M]) by ICP-MS:

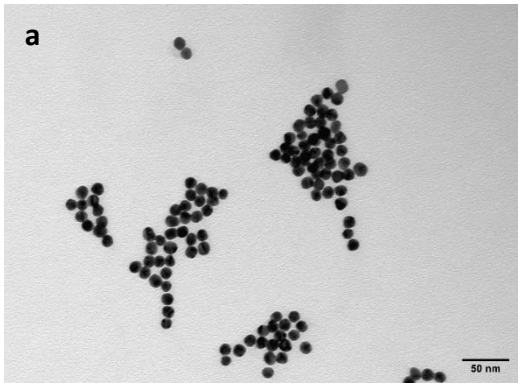
$$[\mathrm{AuNP/M}] = \frac{[\mathrm{AuNP/ppb}] \cdot 10^{-6} \cdot \mathrm{d.f.}}{m_{Au} \cdot N} \cdot \frac{1}{N_A} \quad Equation\ 4.5$$

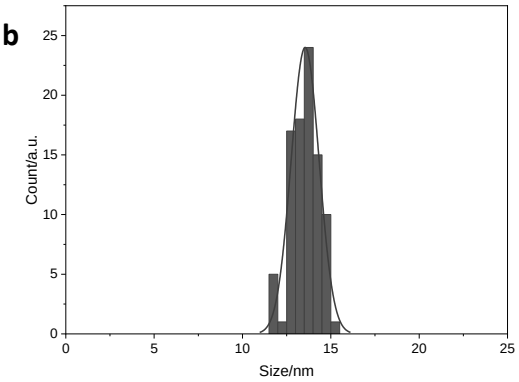
Where d.f. is the dilution factor, m_{Au} is the mass of the Au atom, N the number of Au atoms per AuNP and N_A is Avogadro number. The number of Eu atoms per AuNP is obtained as follows:

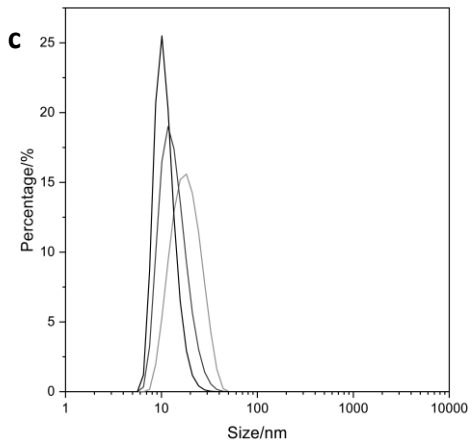
$$\frac{\mathrm{Eu}}{\mathrm{AuNP}} = \frac{N \cdot [\mathrm{Eu}]}{[\mathrm{Au}]} \quad Equation\ 4.6$$

Where [Eu] and [Au] are the concentrations in ppb of Eu and Au, respectively. To obtain the number of dinuclear complexes per AuNP, this value is divided by 2.

4.5.8 Size distributions of AuNPs

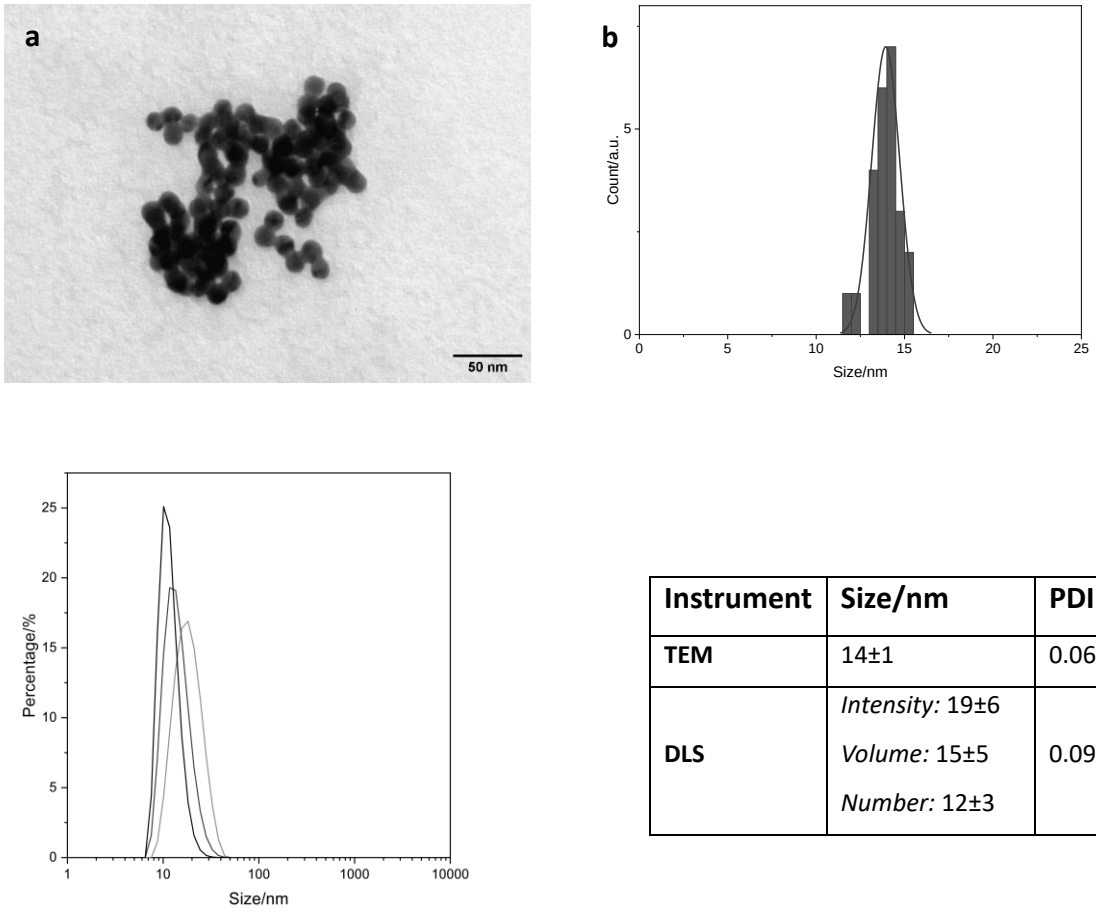






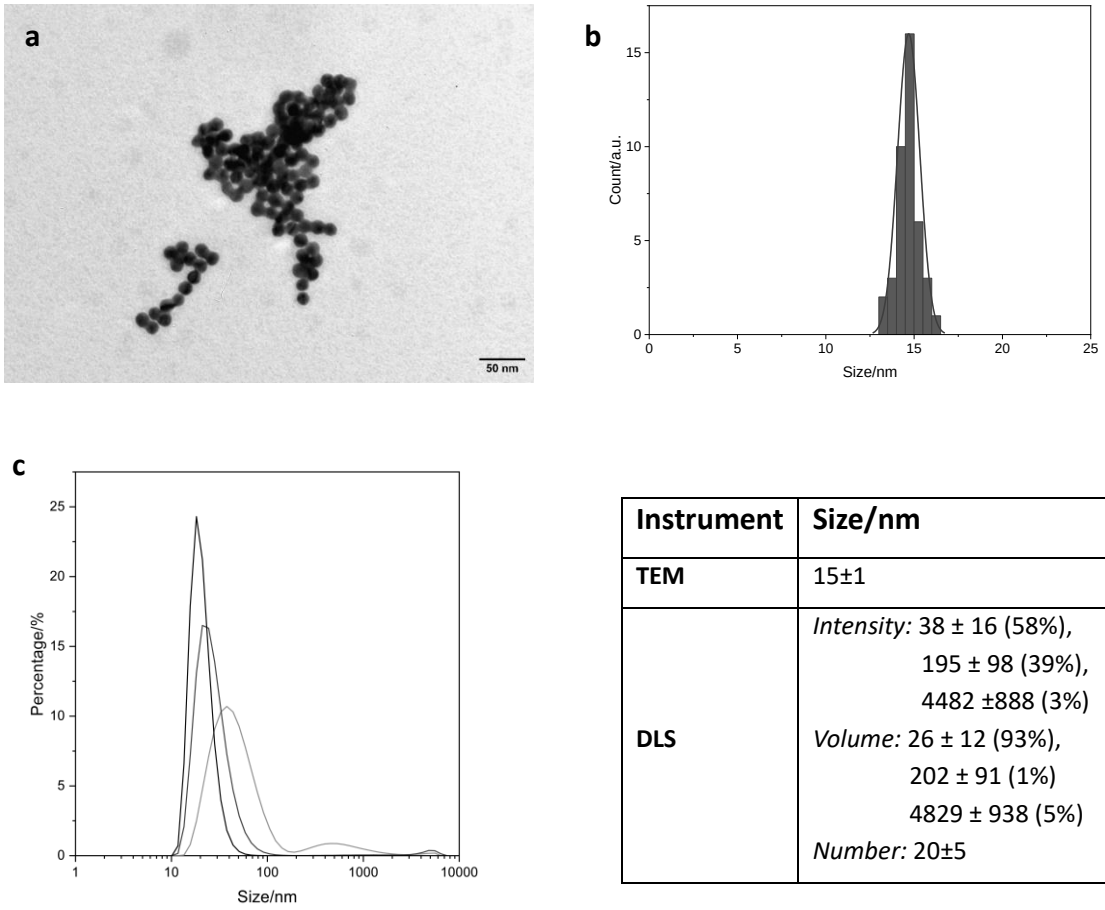
Instrument	Size/nm	PDI
TEM	14±1	0.06
DLS	*Intensity:* 19±6 *Volume:* 14±5 *Number:* 11±3	0.12

Figure 4.37 – **a** TEM image of AuNP14 for direct coating with **Eu_2SAcbisDBM$_3$**. The image was acquired by Sarah Akponasa at the University of Birmingham. **b** Size distribution of synthesized AuNP14 for direct coating with **Eu_2SAcbisDBM$_3$** as measured by TEM. n=90. **c** Intensity (light grey), volume (dark grey) and number (black) distributions of hydrodynamic diameter of synthesized AuNP14 for direct coating with **Eu_2SAcbisDBM$_3$** (DLS). **Table 4.5** – Sizes (as measured by TEM and DLS) of synthesized AuNP14 for direct coating with **Eu_2SAcbisDBM$_3$**.



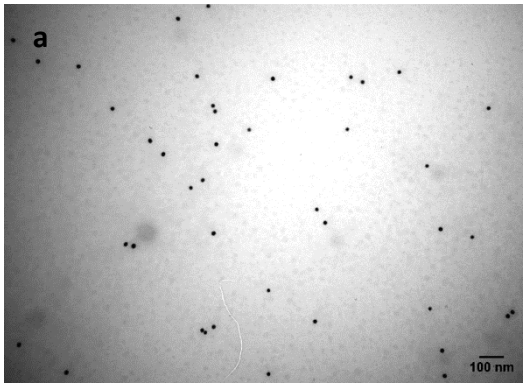
Instrument	Size/nm	PDI
TEM	14±1	0.06
DLS	*Intensity:* 19±6 *Volume:* 15±5 *Number:* 12±3	0.09

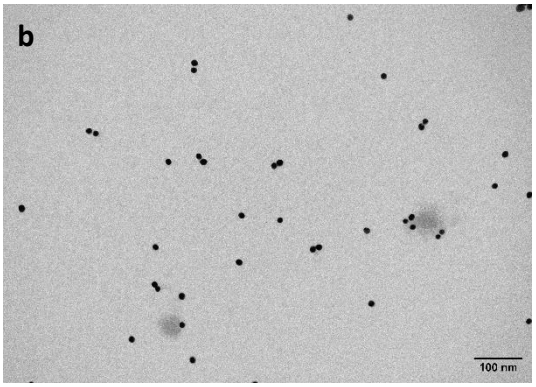
Figure 4.38 – **a** TEM image of AuNP14 for coating with Zonyl FSA and **Ln_2SAcbisDBM$_3$**. **b** Size distribution of synthesized AuNP14 for coating with Zonyl FSA and **Ln_2SAcbisDBM$_3$** as measured by TEM. n=24. **c** Intensity (light grey), volume (dark grey) and number (black) distributions of hydrodynamic diameter of AuNP14 for coating with Zonyl FSA and **Ln_2SAcbisDBM$_3$** (DLS). **Table 4.6** – Sizes (as measured by TEM and DLS) of synthesized AuNP14 for coating with Zonyl FSA and **Ln_2SAcbisDBM$_3$**.

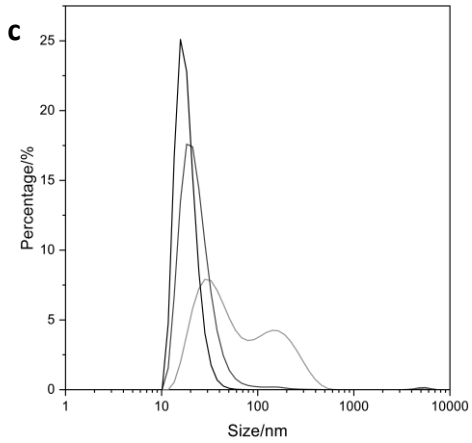


Instrument	Size/nm	PDI
TEM	15±1	0.05
DLS	*Intensity:* 38 ± 16 (58%), 195 ± 98 (39%), 4482 ±888 (3%) *Volume:* 26 ± 12 (93%), 202 ± 91 (1%) 4829 ± 938 (5%) *Number:* 20±5	0.44

Figure 4.39 – **a** TEM image of Z@AuNP14. **b** Size distribution of Z@AuNP14 as measured by TEM. n=41. **c** Intensity (light grey), volume (dark grey) and number (black) distributions of hydrodynamic diameter of Z@AuNP14 (DLS).
Table 4.7 – Sizes (as measured by TEM and DLS) of Z@AuNP14.

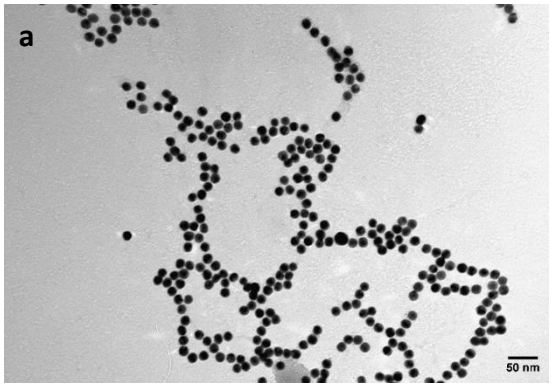


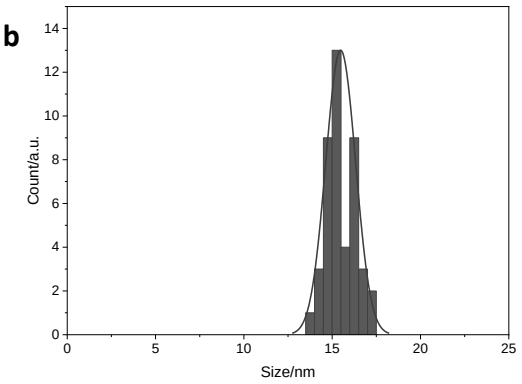


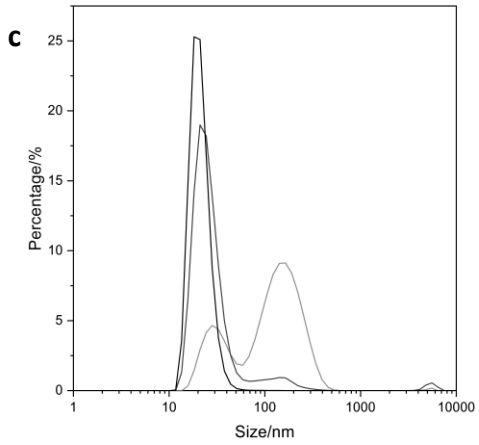


Instrument	Size/nm	PDI
TEM	15±1	0.05
DLS	*Intensity:* 36 ± 15 (58%) 140 ± 62 (63%) 5046 ± 583 (1%) *Volume:* 25 ± 18 (98%) 5199 ± 756 (2%) *Number:* 18 ± 5	0.41

Figure 4.40 – **a**, **b** Additional TEM image of **Eu_2SAcbisDBM$_3$●Z@AuNP14**. Image **b** was acquired by Sarah Akponasa at the University of Birmingham. **c** Intensity (light grey), volume (dark grey) and number (black) distributions of hydrodynamic diameter of **Eu_2SAcbisDBM$_3$●Z@AuNP14** (DLS). **Table 4.8** – Sizes (as measured by TEM and DLS) of **Eu_2SAcbisDBM$_3$●Z@AuNP14**.

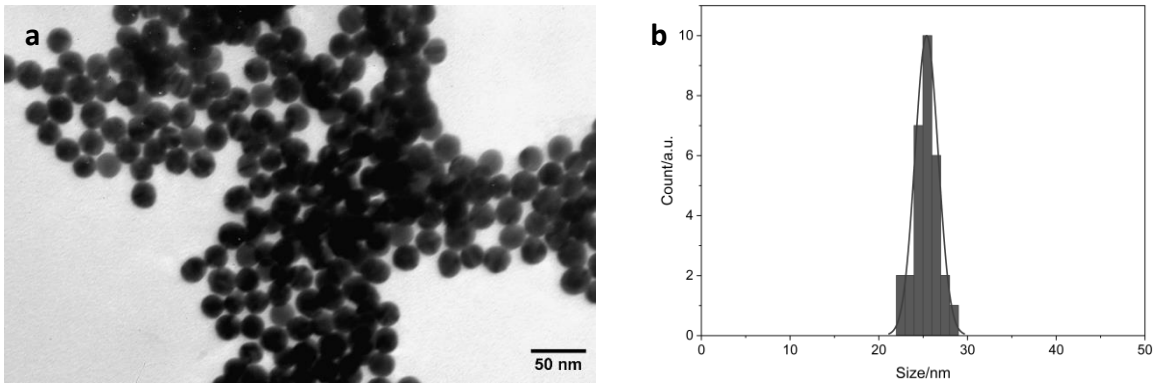






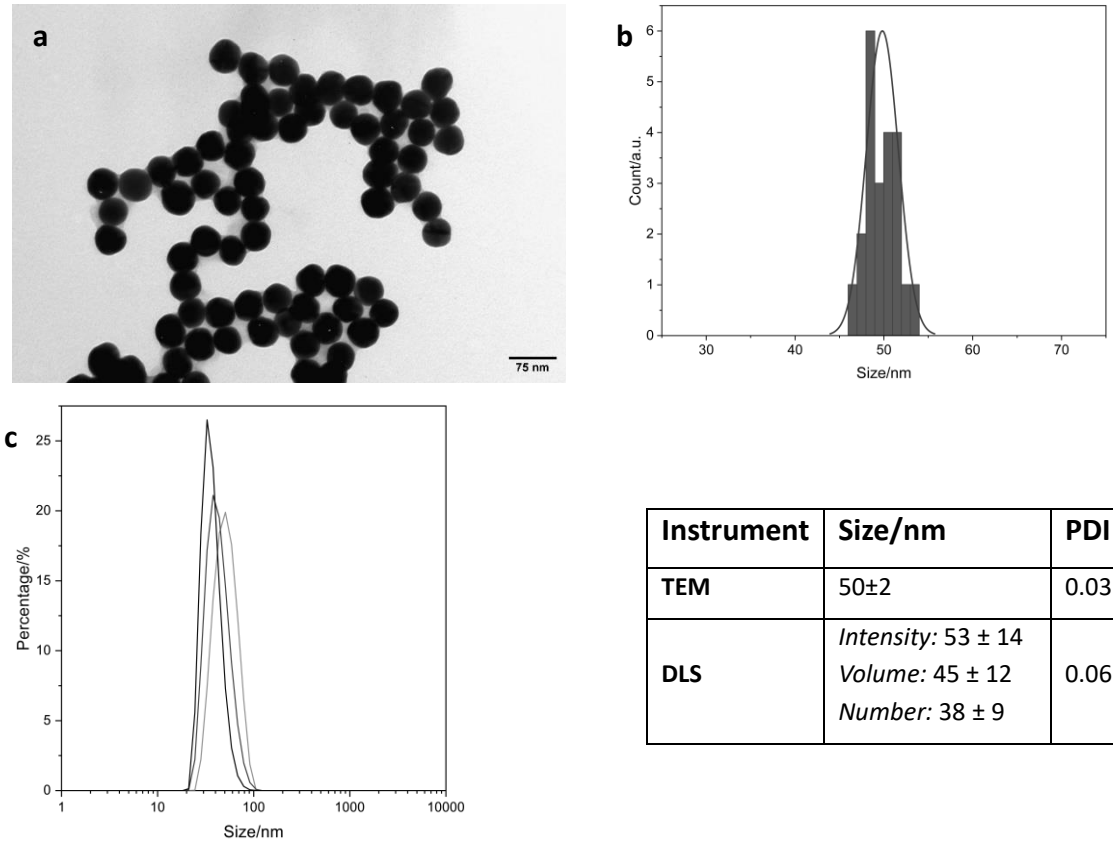
Instrument	Size/nm	PDI
TEM	15±1	0.06
DLS	*Intensity:* 35 ± 11 (29%) 152 ± 62 (70%) 5311 ± 391 (1%) *Volume:* 27 ± 9 (86%) 132 ± 54 (7%) 5394 ± 664 (6%) *Number:* 23 ± 6	0.48

Figure 4.41 – **a** TEM image of **Eu_2bisDBM$_3$_PhenSS_2●Z@AuNP14**. **b** Size distribution of **Eu_2bisDBM$_3$_PhenSS_2●Z@AuNP14** as measured by TEM. n=44. **c** Intensity (light grey), volume (dark grey) and number (black) distributions of hydrodynamic diameter of **Eu_2bisDBM$_3$_PhenSS_2●Z@AuNP14** (DLS). **Table 4.9** – Sizes (as measured by TEM and DLS) of **Eu_2bisDBM$_3$_PhenSS_2●Z@AuNP14**.



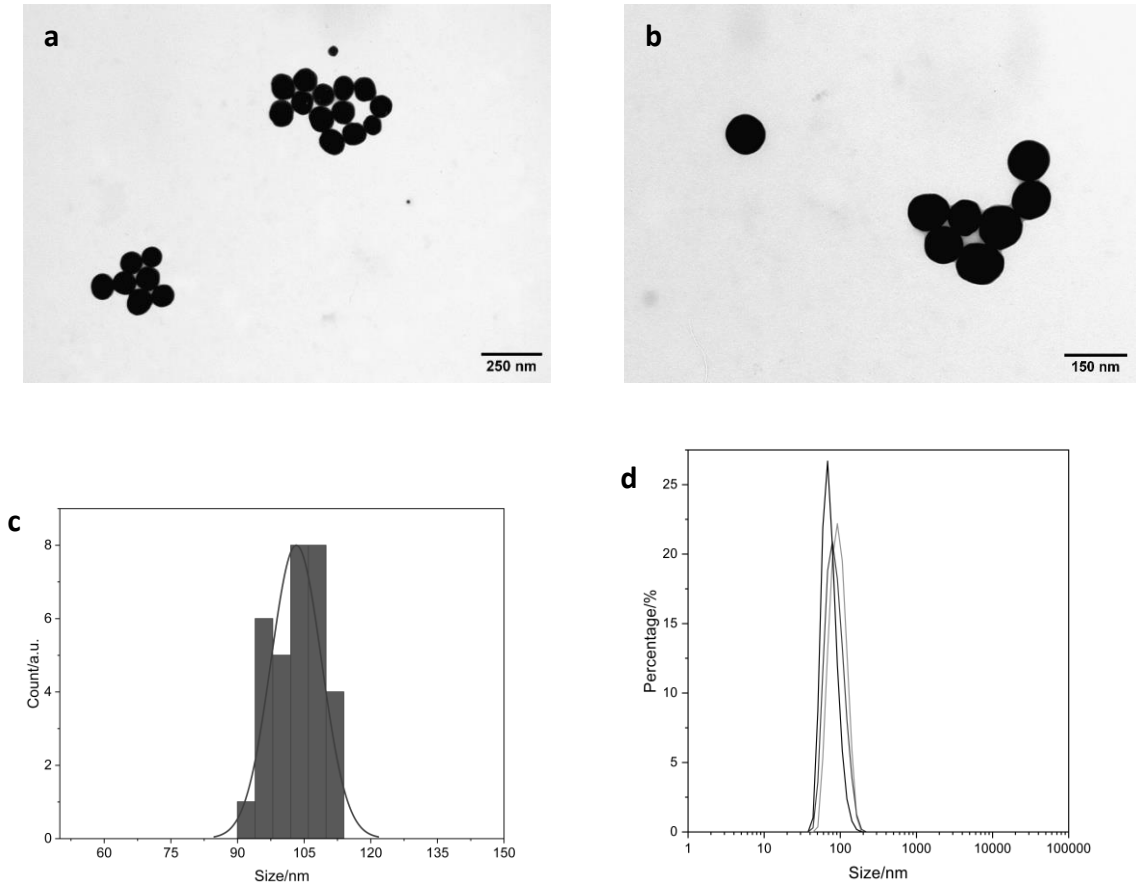
Instrument	Size/nm	PDI
TEM	25±1	0.04
DLS	*Intensity:* 33 ± 13 *Volume:* 22 ± 8 *Number:* 17 ± 5	0.17

Figure 4.42 – **a** TEM image of AuNP25. **b** Size distribution of AuNP25 as measured by TEM. n=30. **Table 4.10** – Sizes (as measured by TEM and DLS) of AuNP25.



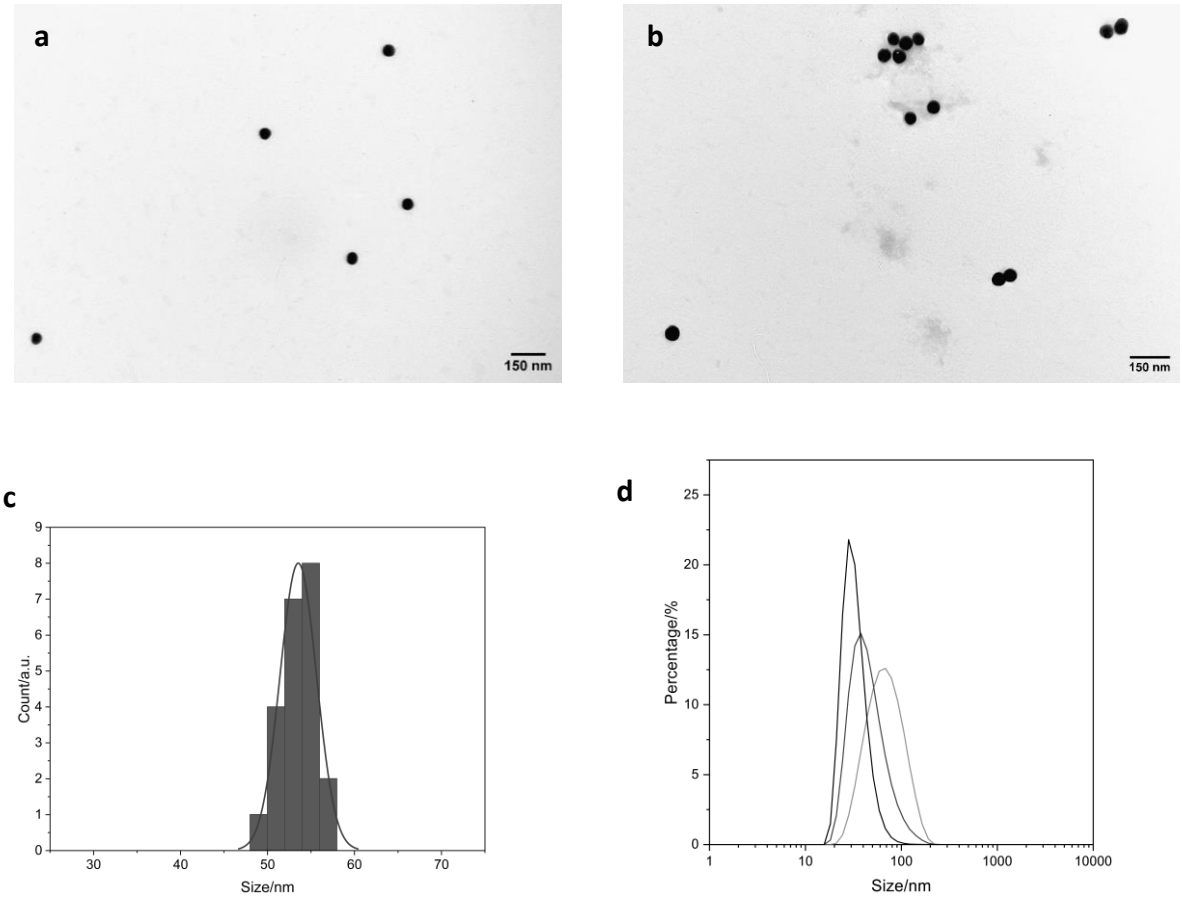
Instrument	Size/nm	PDI
TEM	50±2	0.03
DLS	*Intensity:* 53 ± 14 *Volume:* 45 ± 12 *Number:* 38 ± 9	0.06

Figure 4.43 – **a** TEM image of AuNP50. **b** Size distribution of AuNP50 as measured by TEM. n=22. **c** Intensity (light grey), volume (dark grey) and number (black) distributions of hydrodynamic diameter of AuNP50 (DLS). **Table 4.11** – Sizes (as measured by TEM and DLS) of AuNP50.



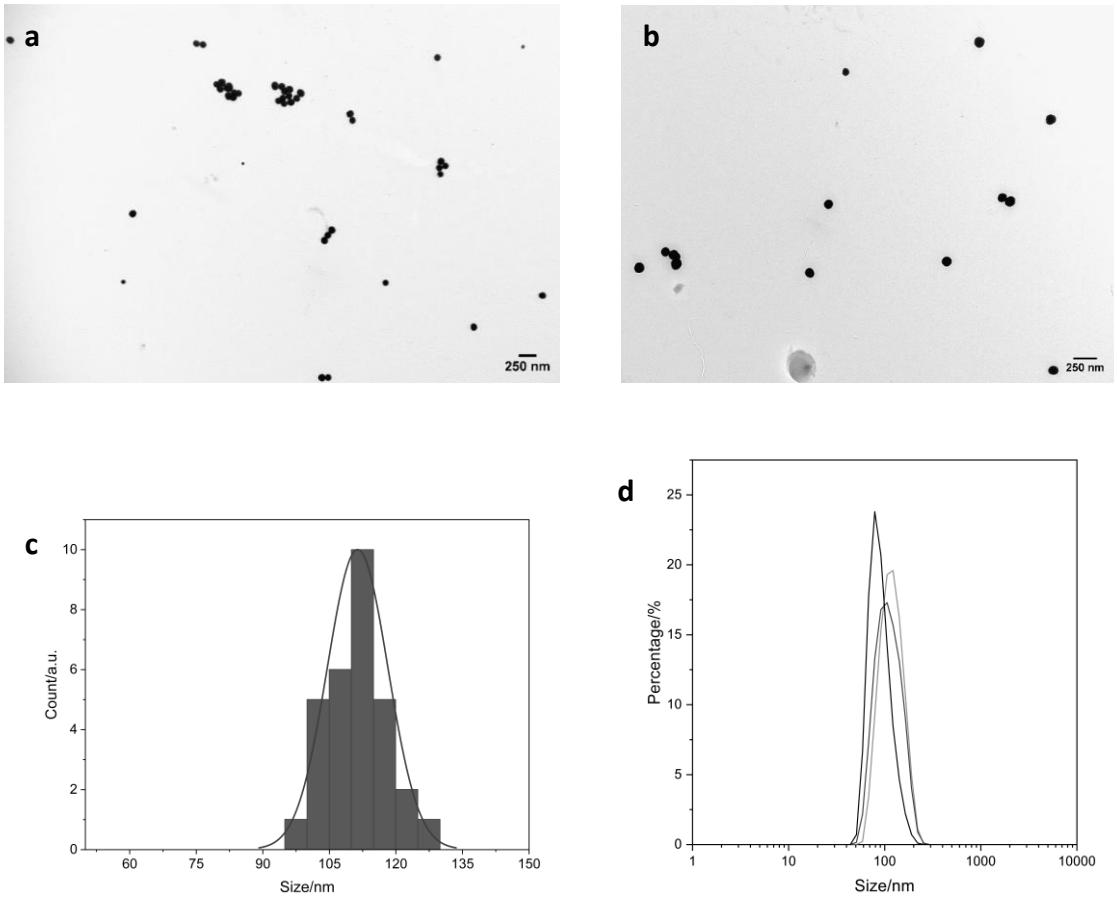
Instrument	Size/nm	PDI
TEM	103±6	0.02
DLS	*Intensity:* 94 ± 22 *Volume:* 86 ± 23 *Number:* 74 ± 18	0.03

Figure 4.44 – **a, b** TEM images of AuNP100. **c** Size distribution of AuNP100 as measured by TEM. n=32. **d** Intensity (light grey), volume (dark grey) and number (black) distributions of hydrodynamic diameter of AuNP100 (DLS).
Table 4.12 – Sizes (as measured by TEM and DLS) of AuNP100.



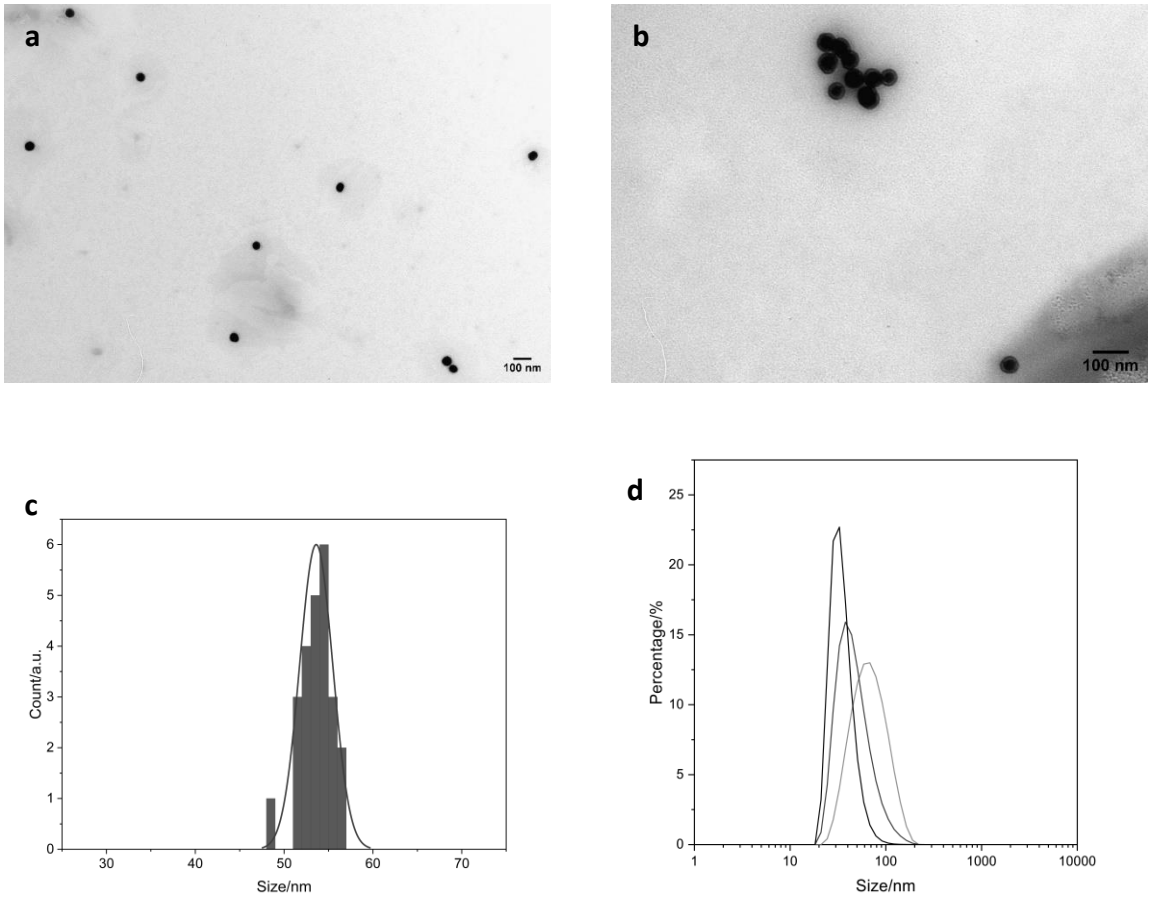
Instrument	Size/nm	PDI
TEM	54±2	0.03
DLS	*Intensity:* 74 ± 33 *Volume:* 46 ± 24 *Number:* 31 ± 10	0.18

Figure 4.45 – **a, b** TEM images of Z@AuNP50. **c** Size distribution of Z@AuNP50 as measured by TEM. n=22. **d** Intensity (light grey), volume (dark grey) and number (black) distributions of hydrodynamic diameter of Z@AuNP50 (DLS). **Table 4.13** – Sizes (as measured by TEM and DLS) of Z@AuNP50.



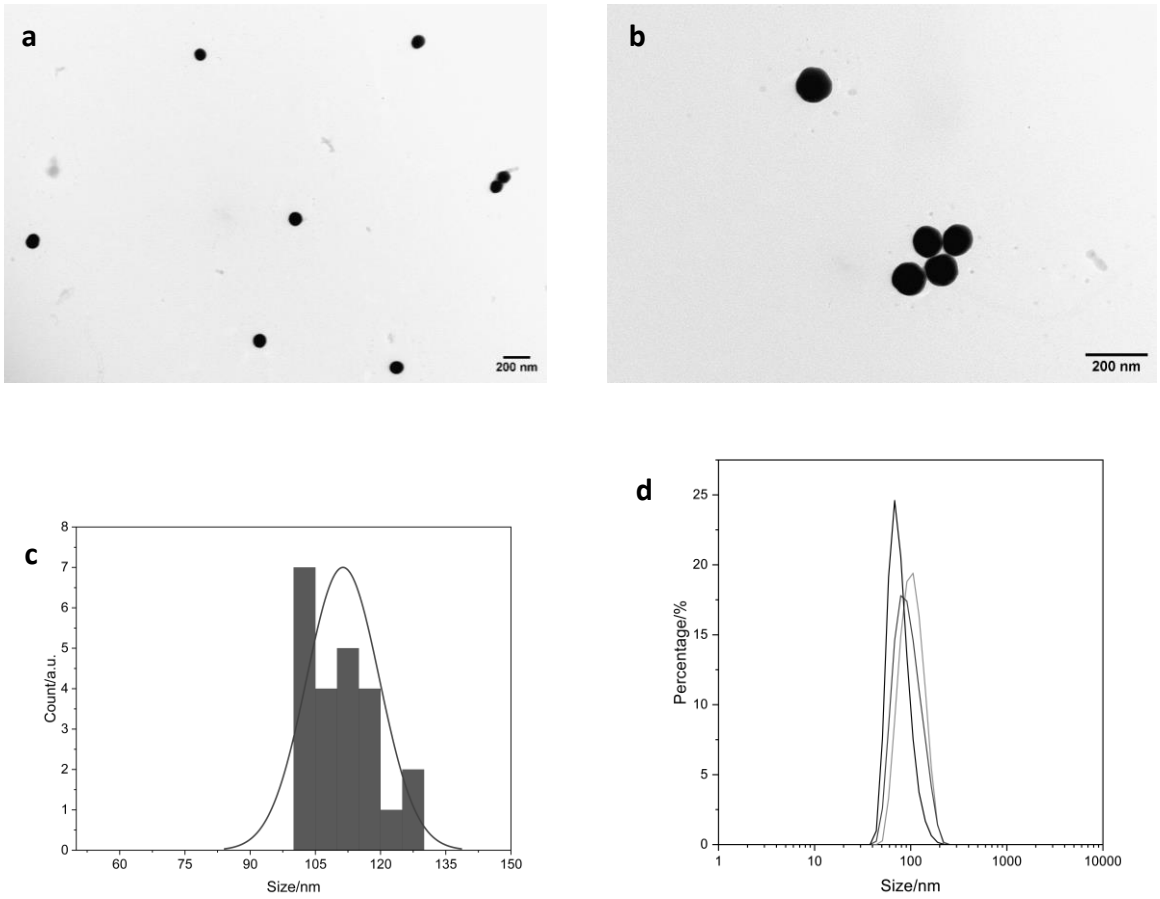
Instrument	Size/nm	PDI
TEM	111±7	0.02
DLS	*Intensity:* 120 ± 32 *Volume:* 113 ± 34 *Number:* 93 ± 25	0.07

Figure 4.46 – **a, b** TEM images of Z@AuNP100. **c** Size distribution of Z@AuNP100 as measured by TEM. n=30. **d** Intensity (light grey), volume (dark grey) and number (black) distributions of hydrodynamic diameter of Z@AuNP100 (DLS). **Table 4.14** – Sizes (as measured by TEM and DLS) of Z@AuNP100.



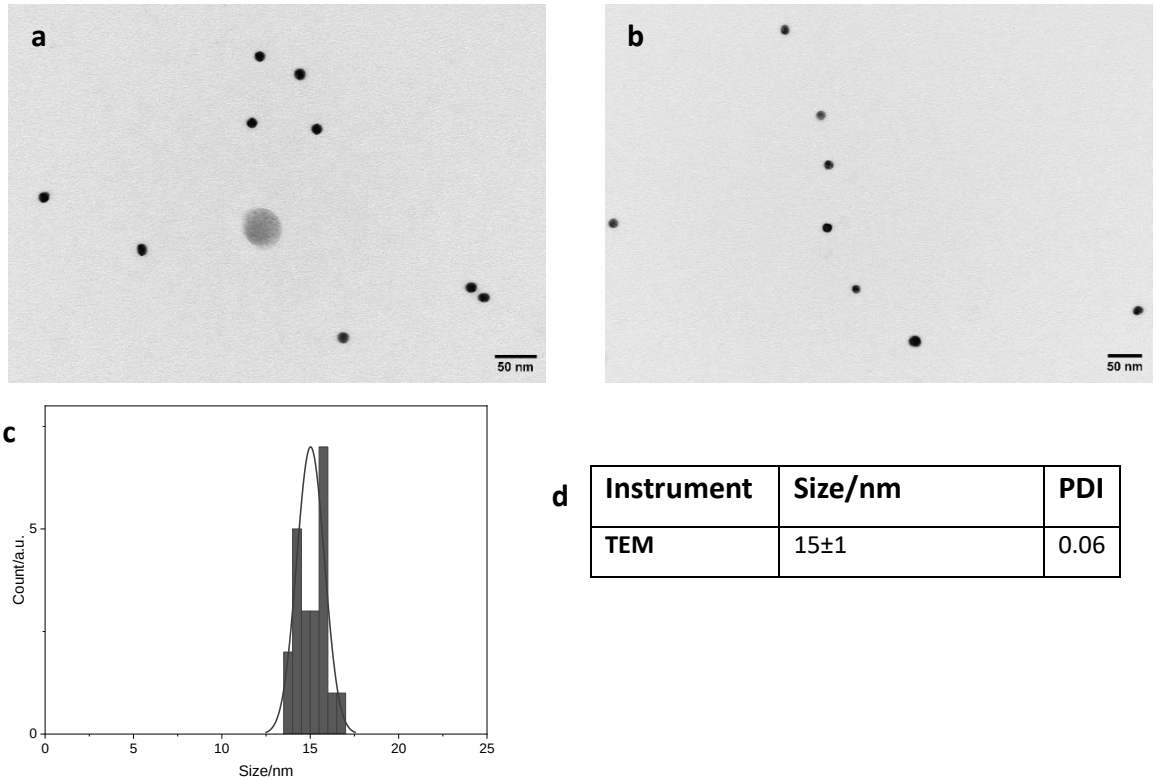
Instrument	Size/nm	PDI
TEM	54±2	0.02
DLS	*Intensity:* 72 ± 29 *Volume:* 51 ± 22 *Number:* 37 ± 11	0.18

Figure 4.47 – **a, b** TEM images of **Eu_2SAcbisDBM$_3$●Z@AuNP50**. **c** Size distribution of **Eu_2SAcbisDBM$_3$●Z@AuNP50** as measured by TEM. n=24. **d** Intensity (light grey), volume (dark grey) and number (black) distributions of hydrodynamic diameter of **Eu_2SAcbisDBM$_3$●Z@AuNP50** (DLS). **Table 4.15** – Sizes (as measured by TEM and DLS) of **Eu_2SAcbisDBM$_3$●Z@AuNP50**.



Instrument	Size/nm	PDI
TEM	111±8	0.03
DLS	*Intensity:* 105 ± 28 *Volume:* 96 ± 30 *Number:* 79 ± 21	0.07

Figure 4.48 – **a, b** TEM images of **Eu_2SAcbisDBM$_3$●Z@AuNP100**. **c** Size distribution of **Eu_2SAcbisDBM$_3$●Z@AuNP100** as measured by TEM. n=23. **d** Intensity (light grey), volume (dark grey) and number (black) distributions of hydrodynamic diameter of **Eu_2SAcbisDBM$_3$●Z@AuNP100** (DLS). **Table 4.16** – Sizes (as measured by TEM and DLS) of **Eu_2SAcbisDBM$_3$●Z@AuNP100**.



d

Instrument	Size/nm	PDI
TEM	15±1	0.06

Figure 4.49 – **a, b** TEM images of **Yb_2SAcbisDBM$_3$●Z@AuNP14**. The images were acquired by Sarah Akponasa at the University of Birmingham. **c** Size distribution of **Yb_2SAcbisDBM$_3$●Z@AuNP14** as measured by TEM. n=22.
Table 4.17 – Sizes (as measured by TEM and DLS) of **Yb_2SAcbisDBM$_3$●Z@AuNP14**.

4.5.9 UV-Vis data

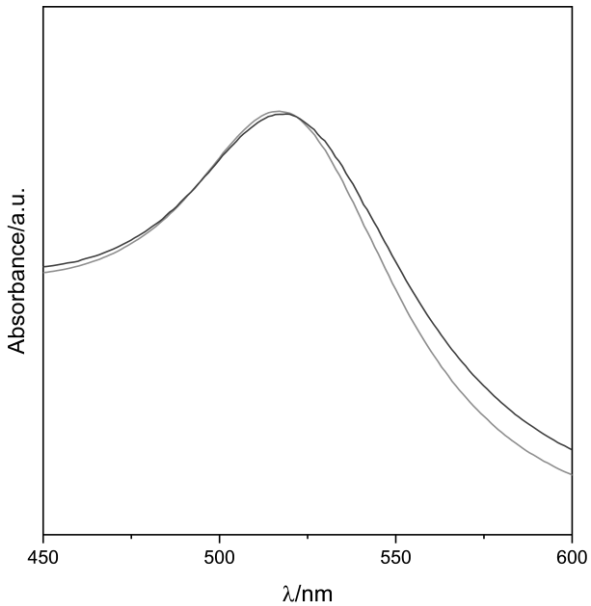


Figure 4.50 – Overlaid extinction spectra displaying the LSPR bands of synthesized AuNP14 (light grey) and of Z@AuNP14 (dark grey). For clarity, the spectra have been scaled at the LSPR.

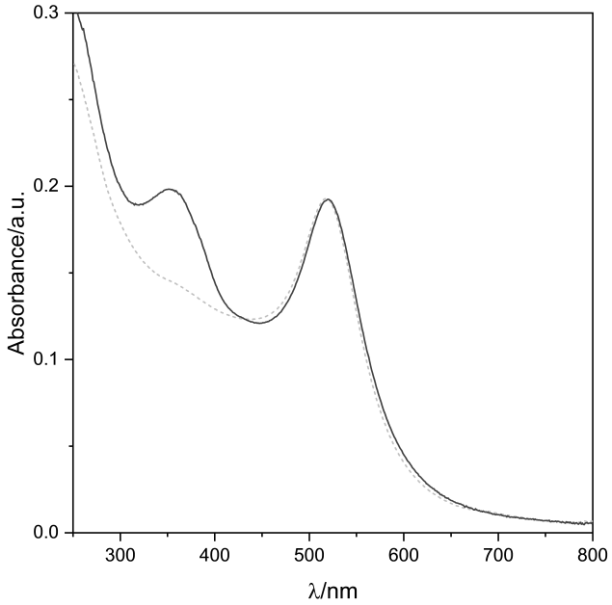
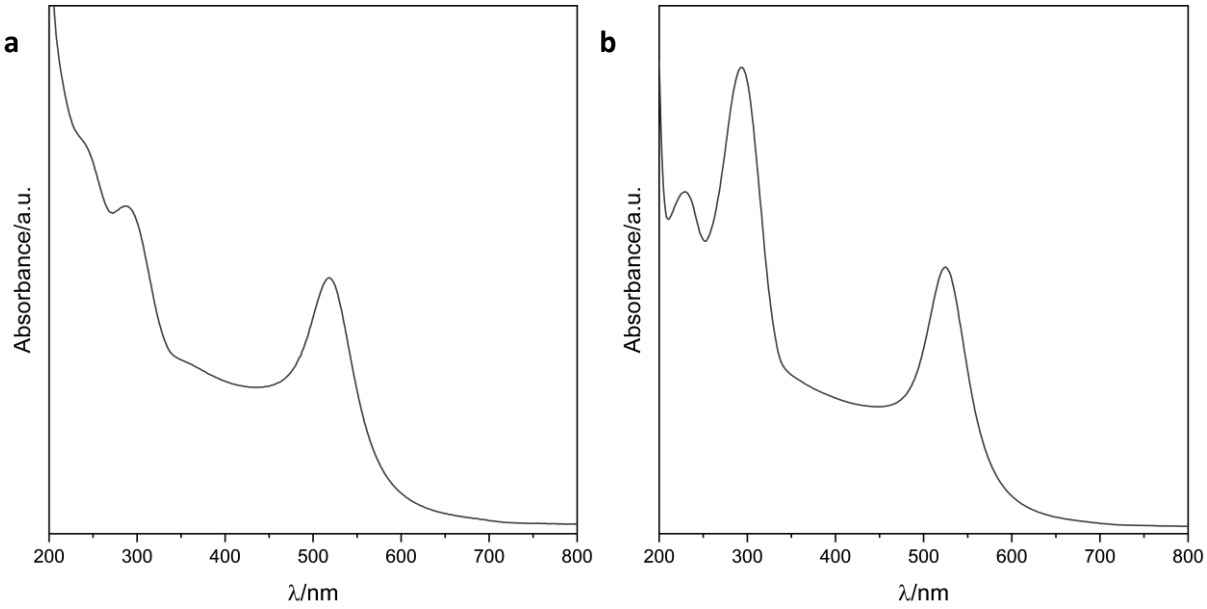


Figure 4.51 – Overlaid absorption spectra of Z@AuNP14 (dashed, light grey) and **Eu_2SAcbisDBM$_3$●Z@AuNP14** (solid, black). The concentration of **Eu_2SAcbisDBM$_3$●Z@AuNP14** is 0.5 nM.



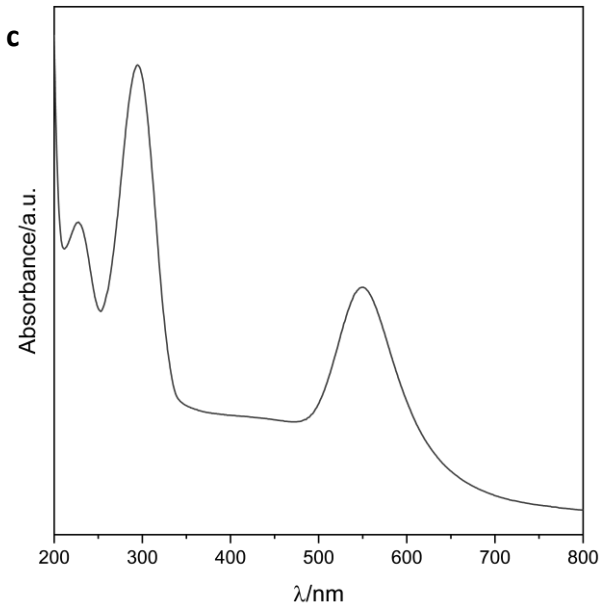


Figure 4.52 – Absorption spectra of AuNP25 (**a**), AuNP50 (**b**) and AuNP100 (**c**).

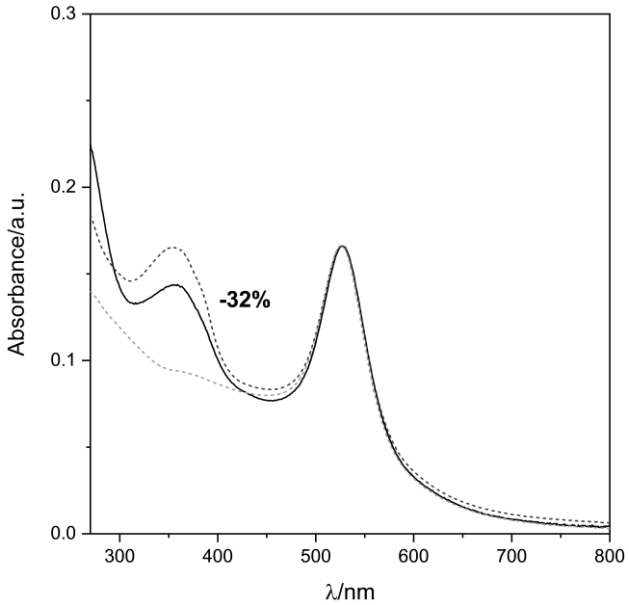


Figure 4.53 – Overlaid absorption spectra of Z@AuNP50 (dashed, light grey), **Eu_2SAcbisDBM$_3$●Z@AuNP50** before purification (dashed, dark grey) and **Eu_2SAcbisDBM$_3$●Z@AuNP50** after purification (solid, black). For clarity, the spectra of **Eu_2SAcbisDBM$_3$●Z@AuNP50** before purification and Z@AuNP50 were scaled to the LSPR band of **Eu_2SAcbisDBM$_3$●Z@AuNP50** after purification. The percentage decrease of **Eu_2SAcbisDBM$_3$** absorbance is calculated to be 32%. The concentration of **Eu_2SAcbisDBM$_3$●Z@AuNP50** is 6 pM.

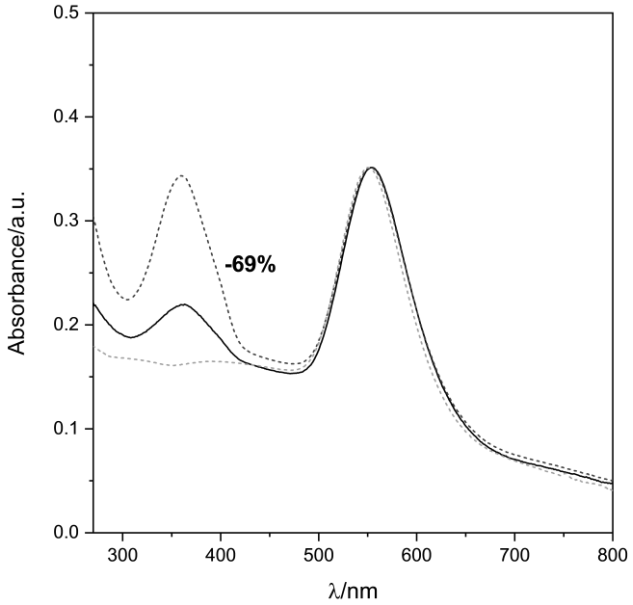


Figure 4.54 – Overlaid absorption spectra of Z@AuNP100 (dashed, light grey), **Eu_2SAcbisDBM$_3$●Z@AuNP100** before purification (dashed, dark grey) and **Eu_2SAcbisDBM$_3$●Z@AuNP100** after purification (solid, black). For clarity, the spectra of **Eu_2SAcbisDBM$_3$●Z@AuNP100** before purification and Z@AuNP100 were scaled to the LSPR band of **Eu_2SAcbisDBM$_3$●Z@AuNP100** after purification. The percentage decrease of **Eu_2SAcbisDBM$_3$** absorbance is calculated to be 69%. The concentration of **Eu_2SAcbisDBM$_3$●Z@AuNP50** is 2 pM.

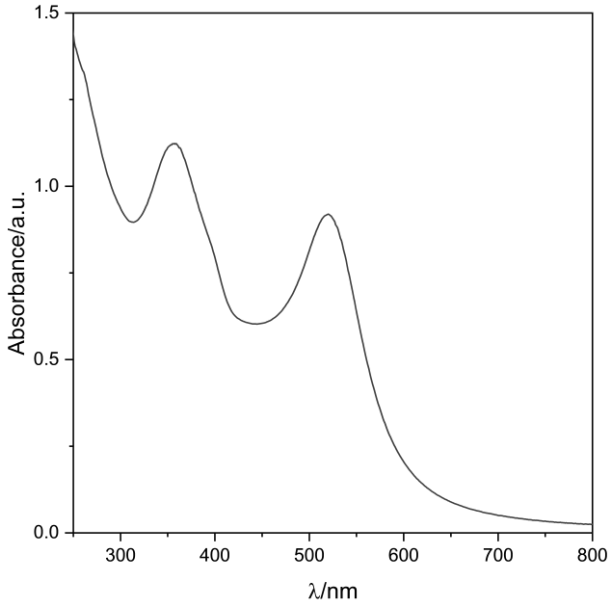


Figure 4.55 – Absorption spectrum of **Yb_2SAcbisDBM$_3$●Z@AuNP14** after purification by size exclusion chromatography. The LSPR band displays a 1.5 nm shift from Z@AuNP14 after coating with up to 4 μM of **Yb_2SAcbisDBM$_3$**. The concentration of **Yb_2SAcbisDBM$_3$●Z@AuNP14** after purification is 3 nM.

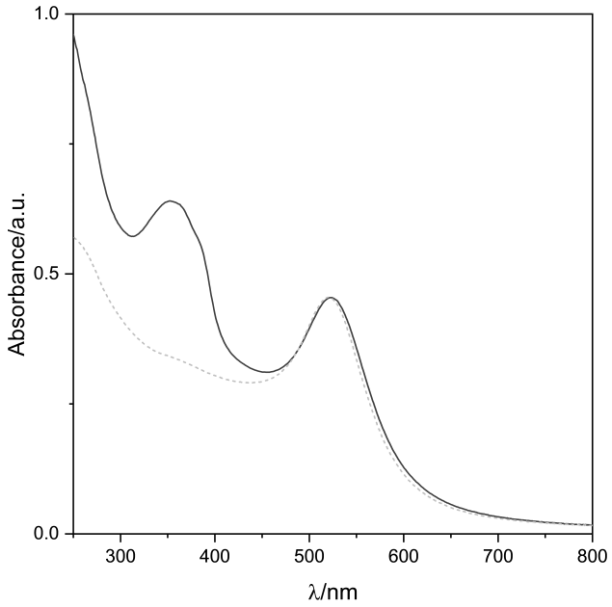


Figure 4.56 – Overlaid absorption spectra of **Nd_2SAcbisDBM$_3$●Z@AuNP14** after purification by size exclusion chromatography (solid, dark grey) and Z@AuNP14 (dashed, light grey). The LSPR band displays a 1.9 nm shift from Z@AuNP14 after coating with up to 4 μM of **Nd_2SAcbisDBM$_3$**. The concentration of **Nd_2SAcbisDBM$_3$●Z@AuNP14** after purification is 1 nM. The absorbance of **Nd_2SAcbisDBM$_3$** after subtraction of the Z@AuNP14 baseline is 0.3.

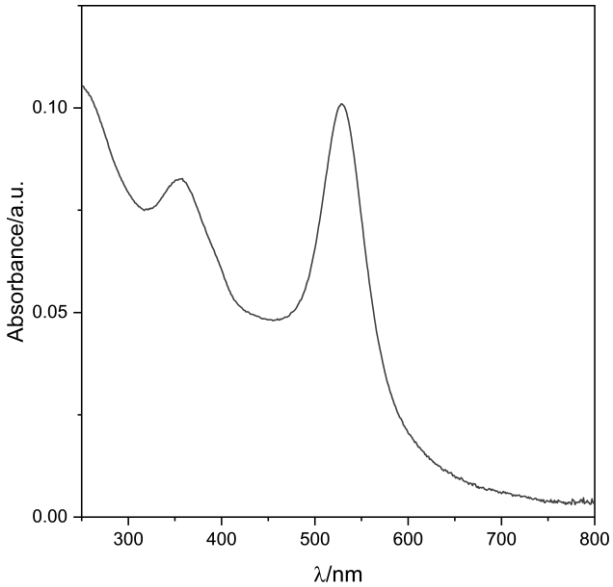


Figure 4.57 – Absorption spectra of **Yb_2SAcbisDBM$_3$●Z@AuNP50** after purification by size exclusion chromatography. The LSPR band displays a 2 nm shift from Z@AuNP50 after coating with up to 4 μM of **Yb_2SAcbisDBM$_3$** and purification. The concentration of **Yb_2SAcbisDBM$_3$●Z@AuNP50** after purification is 4 pM.

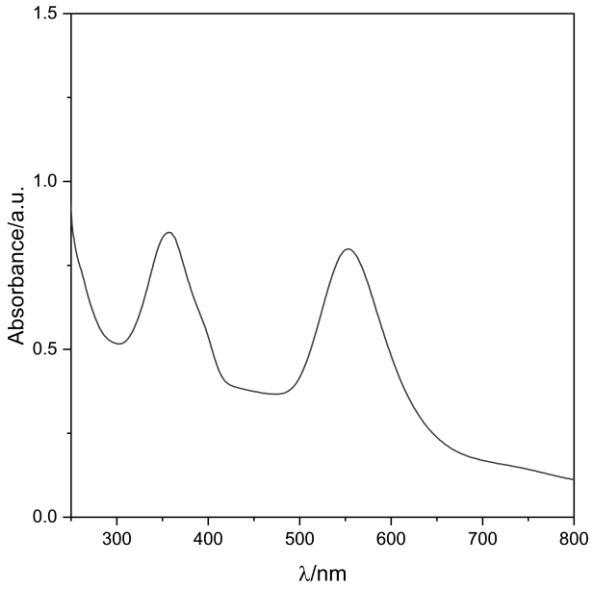


Figure 4.58 – Absorption spectra of **Yb_2SAcbisDBM$_3$●Z@AuNP100** after purification by size exclusion chromatography. The LSPR band displays a 2.6 nm shift from Z@AuNP100 after coating with up to 4 μM of **Yb_2SAcbisDBM$_3$** and purification. The concentration of **Yb_2SAcbisDBM$_3$●Z@AuNP100** after purification is 6 pM.

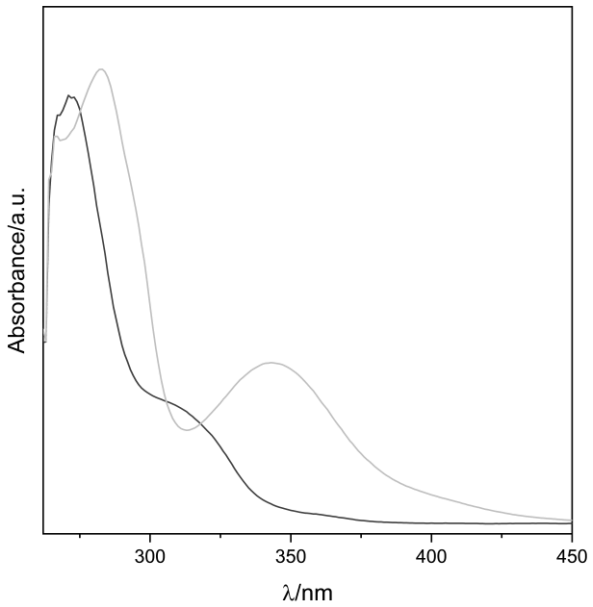


Figure 4.59 – Overlaid absorption spectra of compound **1** (light grey) and **PhenSS** (dark grey) in DMF.

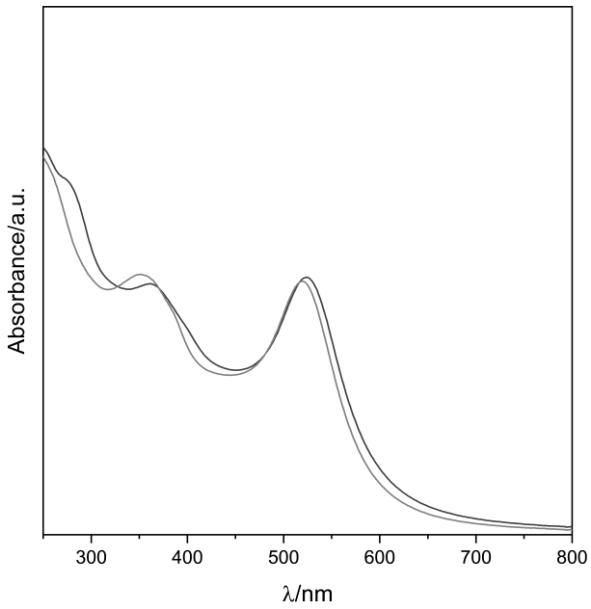


Figure 4.60 – Overlaid absorption spectra of **Eu₂bisDBM₃_PhenSS₂●Z@AuNP14** (dark grey) and **Eu₂SAcbisDBM₃●Z@AuNP14** (light grey) in H_2O after purification. The concentration of AuNPs is 2 nM.

4.5.10 Epsilon curves

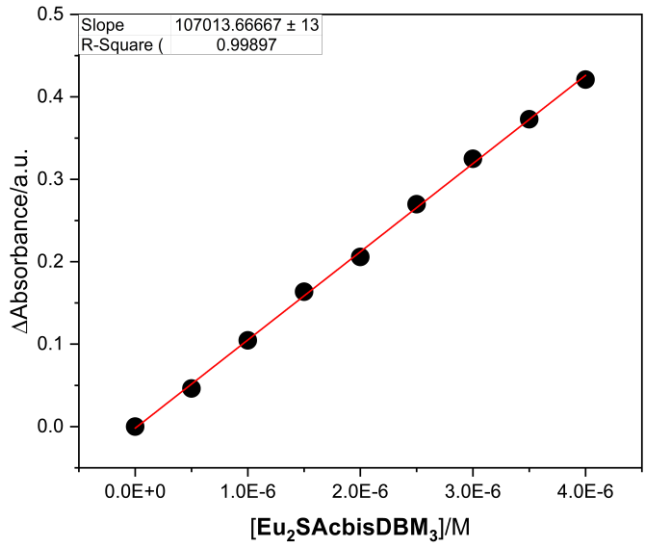


Figure 4.61 – Plot for the calculation of the ε (i.e. "Slope") at 350 nm for **Eu₂SAcbisDBM₃●Z@AuNP14** showing the linear fit. The ΔAbsorbance is calculated by subtracting the absorbance at 350 nm of Z@AuNP14 to the found values at 350 nm of **Eu₂SAcbisDBM₃●Z@AuNP14**.

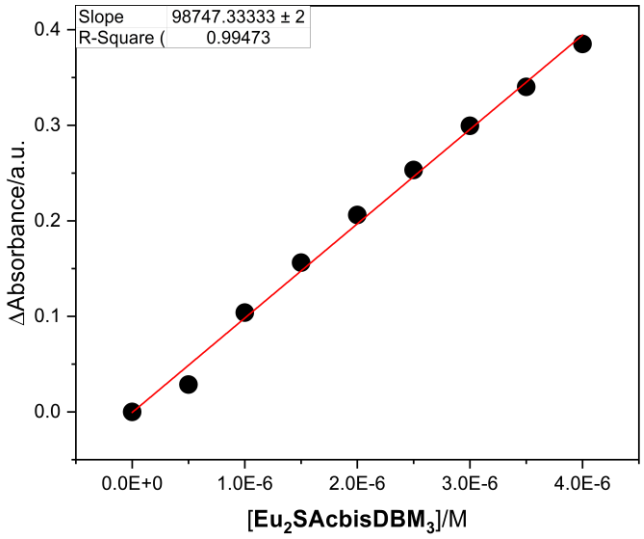


Figure 4.62 – Plot for the calculation of the ε (i.e. "Slope") at 350 nm for **Eu₂SAcbisDBM₃●Z@AuNP50** showing the linear fit. The ΔAbsorbance is calculated by subtracting the absorbance at 350 nm of Z@AuNP50 to the found values at 350 nm of **Eu₂SAcbisDBM₃●Z@AuNP50**.

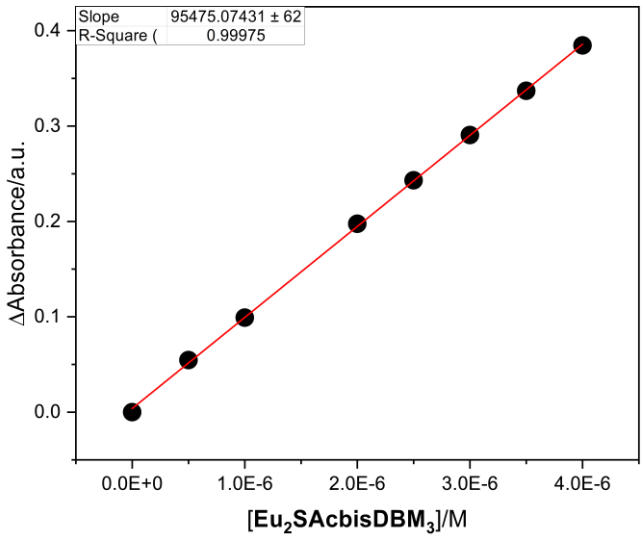


Figure 4.63 – Plot for the calculation of the ε (i.e. "Slope") at 350 nm for **Eu₂SAcbisDBM₃●Z@AuNP100** showing the linear fit. The ΔAbsorbance is calculated by subtracting the absorbance at 350 nm of Z@AuNP100 to the found values at 350 nm of **Eu₂SAcbisDBM₃●Z@AuNP100**.

4.5.11 Additional photophysical data

4.5.11.1 Steady state excitation and emission data

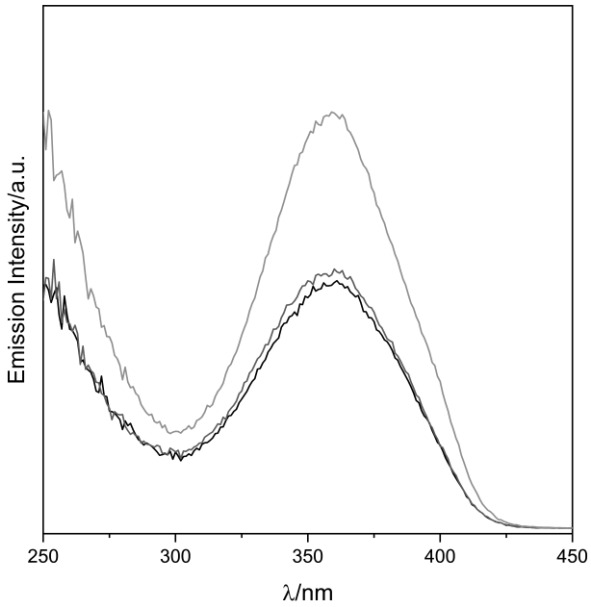


Figure 4.64 – Overlaid excitation spectra of **Eu_2SAcbisDBM$_3$●Z@AuNP14** (black), **Eu_2SAcbisDBM$_3$●Z@AuNP50** (dark grey) and **Eu_2SAcbisDBM$_3$●Z@AuNP100** (light grey). λ_{em}: 611 nm.

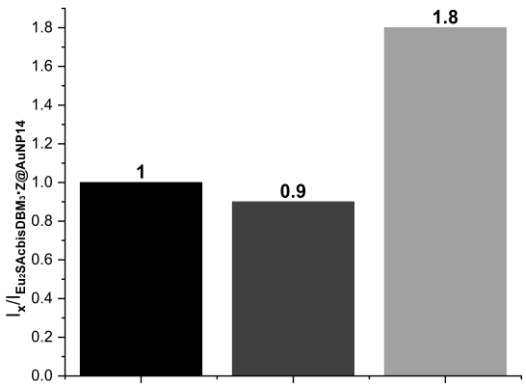


Figure 4.65 – Graph displaying the emission ratios of **Eu_2SAcbisDBM$_3$●Z@AuNP14** (black), **Eu_2SAcbisDBM$_3$●Z@AuNP50** (dark grey) and **Eu_2SAcbisDBM$_3$●Z@AuNP100** (light grey) in H_2O over **Eu_2SAcbisDBM$_3$●Z@AuNP14** corrected by the absorbance loss due to total AuNP absorption at 350 nm.

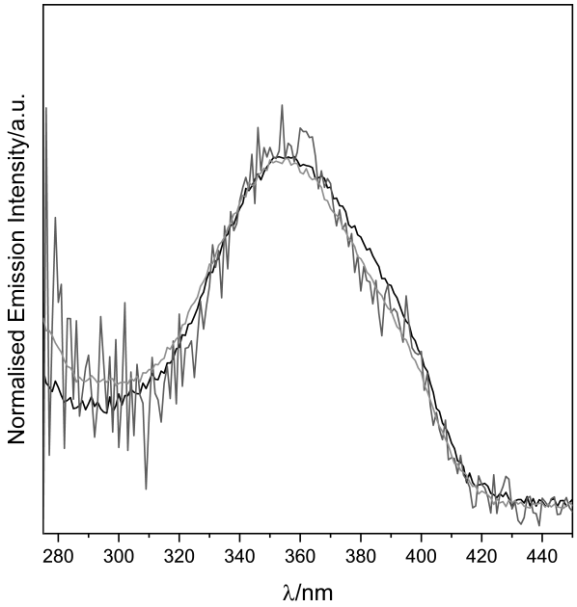


Figure 4.66 – Normalised and overlaid excitation spectra of **Yb_2SAcbisDBM$_3$●Z@AuNP14** (black), **Yb_2SAcbisDBM$_3$●Z@AuNP50** (dark grey) and **Yb_2SAcbisDBM$_3$●Z@AuNP100** (light grey). λ_{em}: 977 nm.

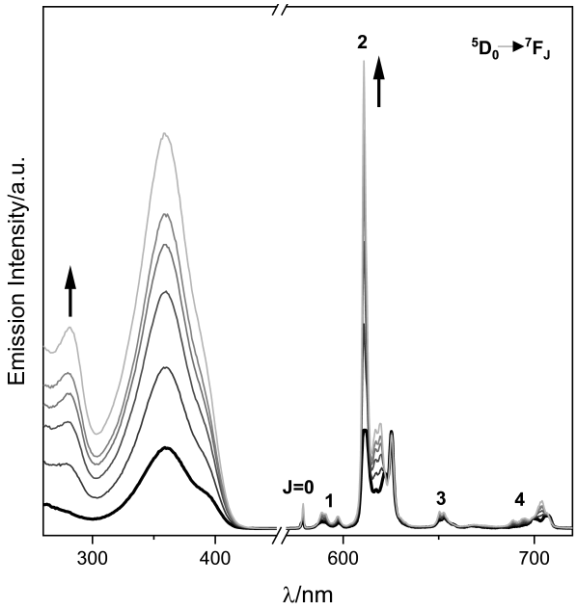


Figure 4.67 – Overlaid excitation (all scaled by 2) and emission spectra of **Eu_2bisDBM$_3$** upon addition of up to 3 equivalents of **PhenSS** in THF (0.2% DMF). λ_{exc}: 350 nm, λ_{em}: 611 nm.

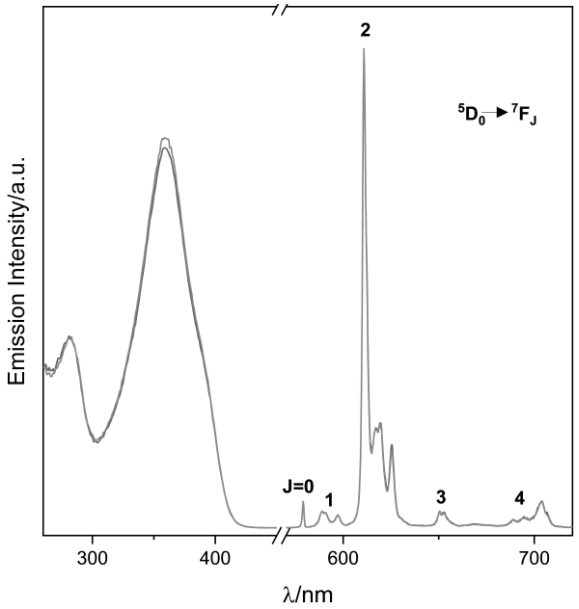


Figure 4.68 – Overlaid excitation (all scaled by 2) and emission spectra of **Eu_2bisDBM$_3$** upon addition of 5 and 7 equivalents of **PhenSS** in THF (0.2% DMF). λ_{exc}: 350 nm, λ_{em}: 611 nm.

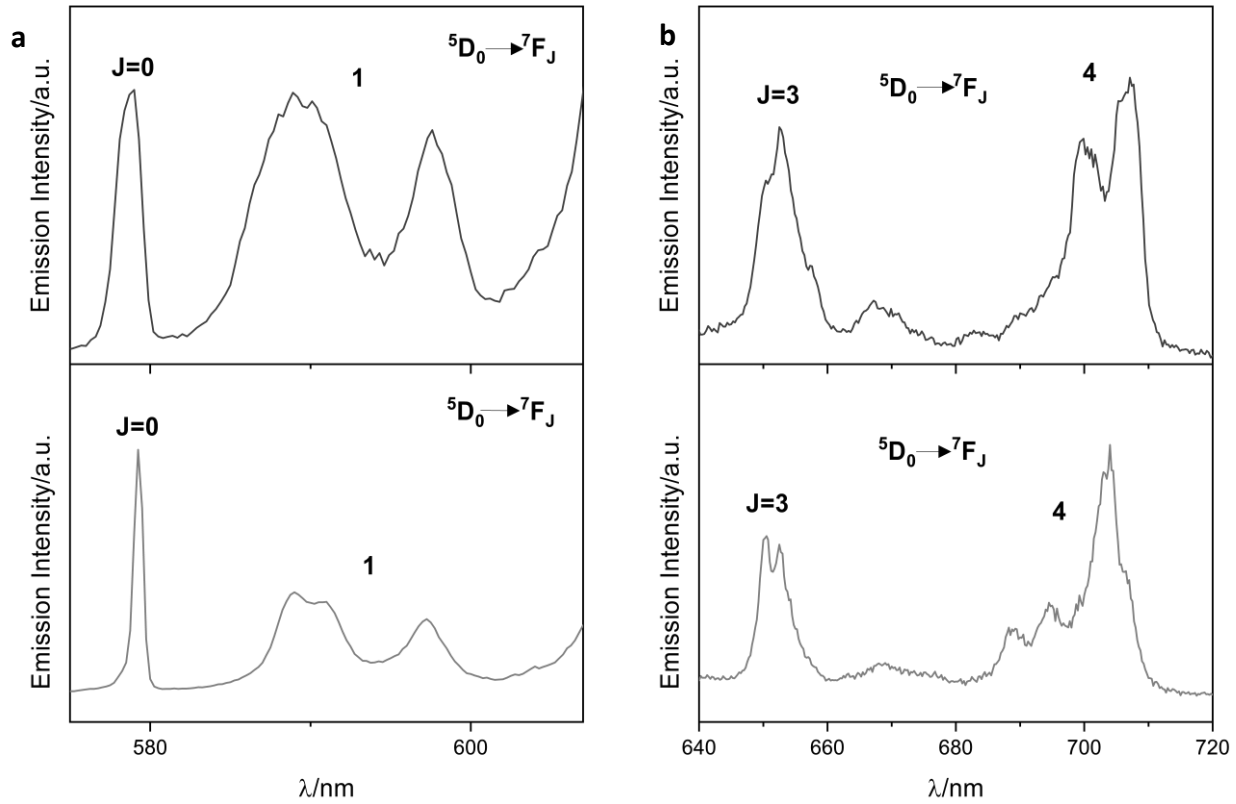


Figure 4.69 – Sections of the emission spectra of **Eu_2bisDBM$_3$** before (top, dark grey) and after (bottom, light grey) of 10 equivalents of **PhenSS** in THF (0.2% DMF) displaying the $^5D_0 \rightarrow ^7F_{0\text{-}1}$ (**a**) and $^5D_0 \rightarrow ^7F_{3\text{-}4}$ (**b**). λ_{exc}: 350 nm.

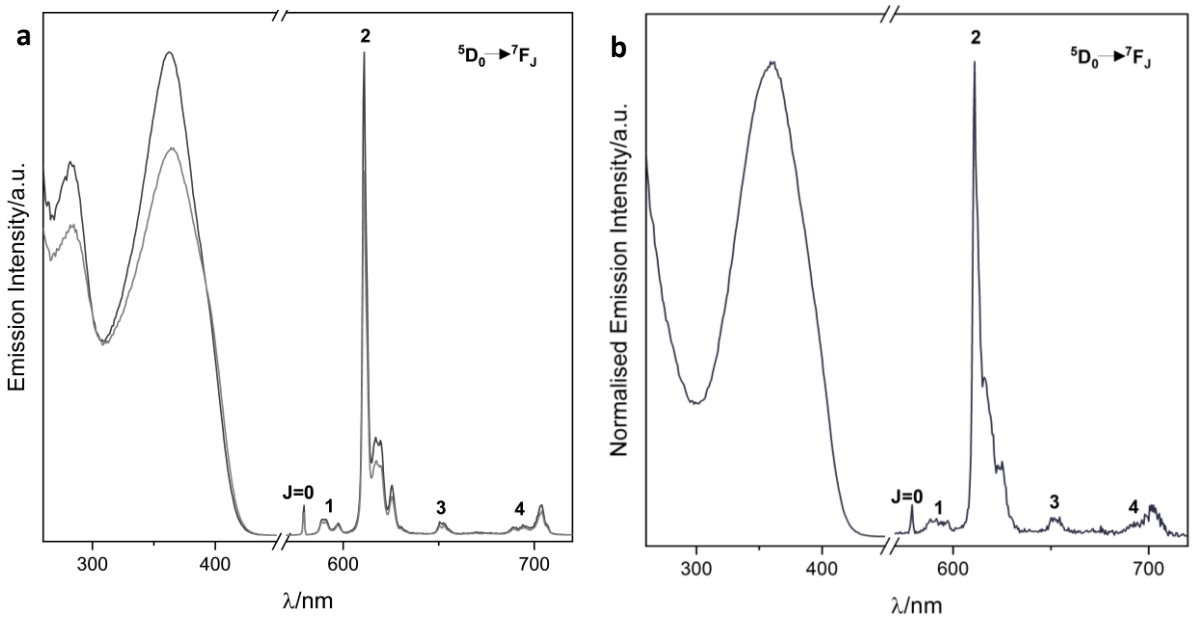


Figure 4.70 – **a** Overlaid emission (both scaled by 5.3) and excitation spectra of pre-formed **Eu_2bisDBM$_3$_PhenSS_2** diluted in H_2O (dark grey) and D_2O (light grey) (0.5% THF, < 0.05% DMF). λ_{exc}: 350 nm, λ_{em}: 611 nm. **b** Normalised emission and excitation spectra of **Eu_2SAcbisDBM$_3$** in H_2O (0.2% DMF). λ_{exc}: 350 nm, λ_{em}: 611 nm.

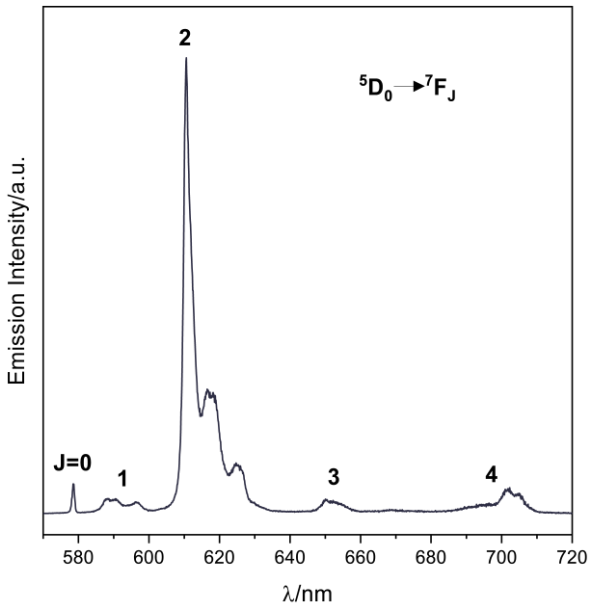


Figure 4.71 – Emission spectrum of **Eu_2bisDBM$_3$** in DMF. λ_{exc}: 350 nm, λ_{em}: 611 nm.

4.5.11.2 Time resolved data

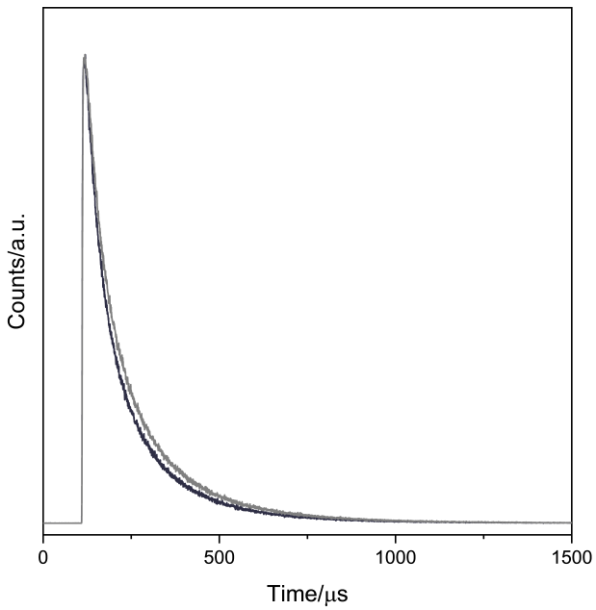


Figure 4.72 – Overlaid lifetime spectra of **Eu_2SAcbisDBM$_3$** in H_2O (0.2% DMF, grey) and **Eu_2SAcbisDBM$_3$●Z@AuNP14** (black). λ_{exc}: 350 nm, λ_{em}: 611 nm.

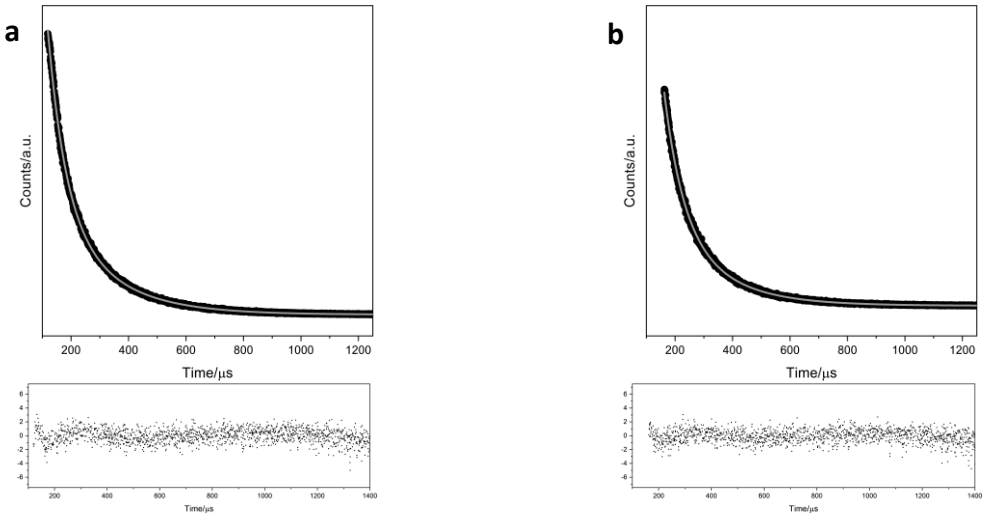


Figure 4.73 – Decay curve fittings of **Eu_2SAcbisDBM$_3$** in H_2O (0.2% DMF, **a**) and **Eu_2SAcbisDBM$_3$●Z@AuNP14** (**b**). Below are the respective residuals.

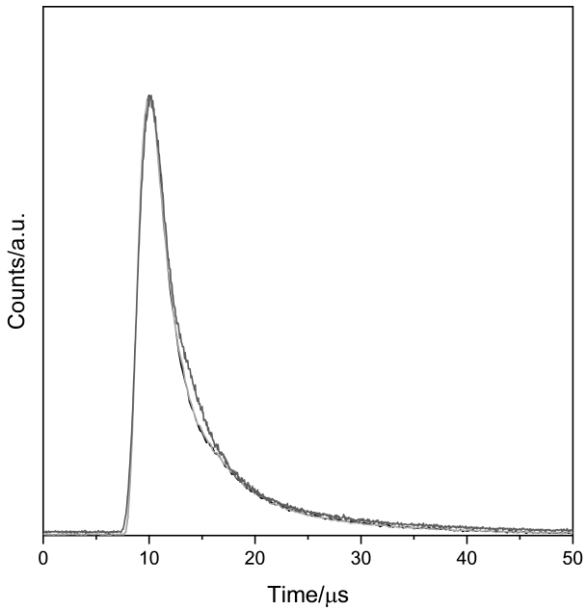


Figure 4.74 – Overlaid and normalised lifetime spectra of **Yb_2SAcbisDBM$_3$●Z@AuNP14** (black), **Yb_2SAcbisDBM$_3$●Z@AuNP50** (dark grey) and **Yb_2SAcbisDBM$_3$●Z@AuNP100** (light grey). λ_{exc}: 350 nm, λ_{em}: 977 nm.

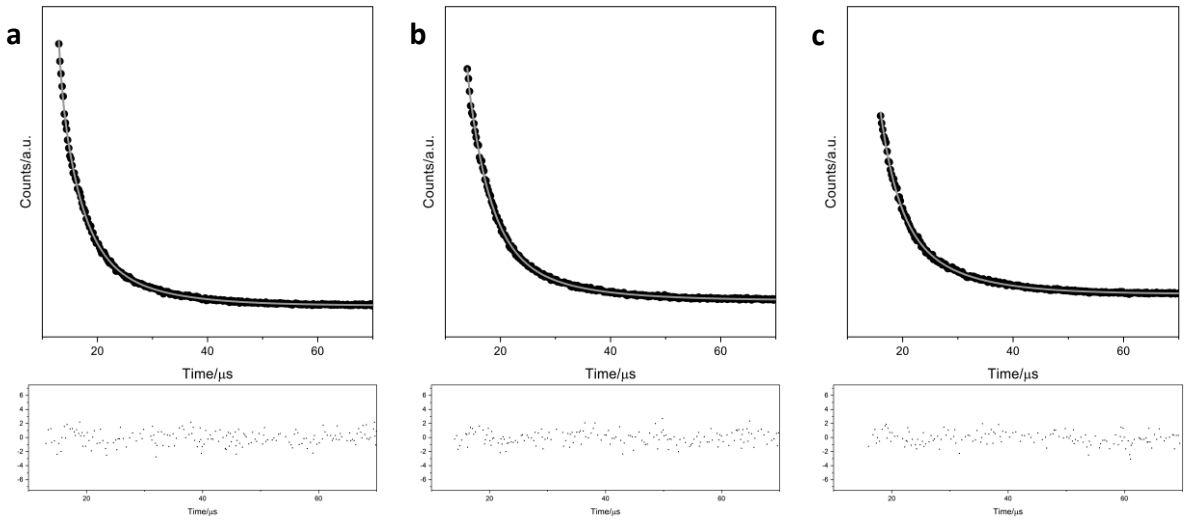


Figure 4.75 – Decay curve fittings of **Yb_2SAcbisDBM$_3$●Z@AuNP14** (**a**), **Yb_2SAcbisDBM$_3$●Z@AuNP100** (**b**) and **Yb_2SAcbisDBM$_3$** in H_2O (0.2% DMF, **c**). Below are the respective residuals.

Sample	**τ/μs (%)**
Yb_2SAcbisDBM$_3$ in H_2O	11 (70%), 3.3 (30%)
Yb_2SAcbisDBM$_3$●Z@AuNP14	10 (89%), 2.3 (10%)
Yb_2SAcbisDBM$_3$●Z@AuNP100	11 (86%), 2.9 (14%)

Table 4.17 – Exponential decay analysis of **Yb_2SAcbisDBM$_3$** in H_2O (0.2% DMF), **Yb_2SAcbisDBM$_3$●Z@AuNP14** and **Yb_2SAcbisDBM$_3$●Z@AuNP100**. Due to the low signal of **Yb_2SAcbisDBM$_3$●Z@AuNP50**, no reliable lifetime data could be obtained.

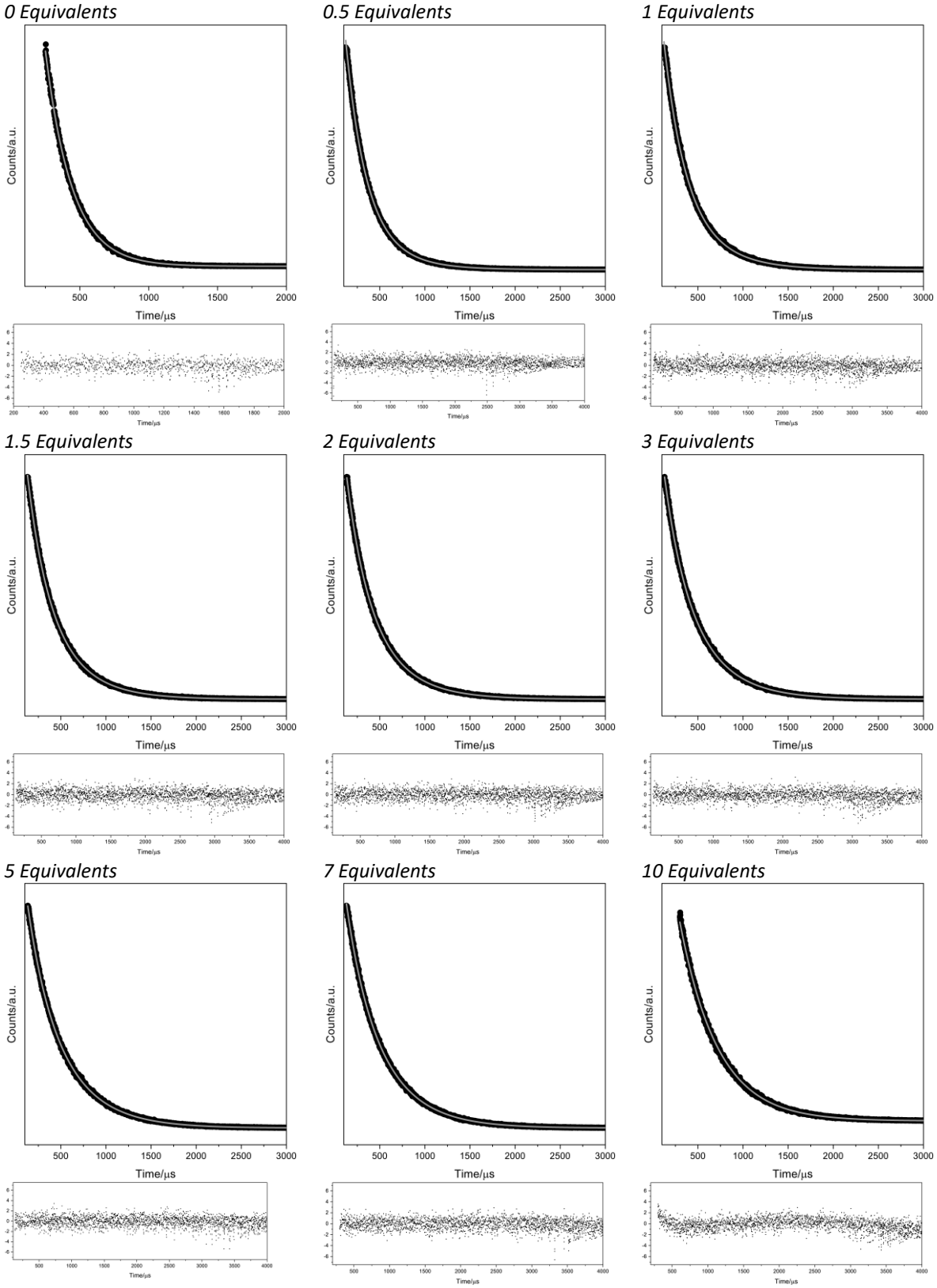


Figure 4.76 – Decay curve fittings of **Eu_2bisDBM$_3$** upon addition of **PhenSS** at the specified equivalents in THF (0.2% DMF). Below are the respective residuals.

Equivalents PhenSS	τ/μs (%)
0	190±20 (100%)
0.5	210±20 (58%), **390±40** (42%)
1	**410±40** (58%), 220±20 (42%)
1.5	**410±40** (69%), 220±20 (31%)
2	**420±40** (72%), 220±20 (28%)
3	**420±40** (72%), 210±20 (18%)
5	**440±40** (87%), 210±20 (13%)
7	**430±40** (91%), 190±20 (9%)
10	**400±40** (100%)

Table 4.18 – Exponential decay analysis of the lifetimes (**τ**) of **Eu_2bisDBM$_3$** upon addition of up to 10 equivalents of **PhenSS** in THF (0.2% DMF). Highlighted is the longest component. Included are the fitting errors (10%).

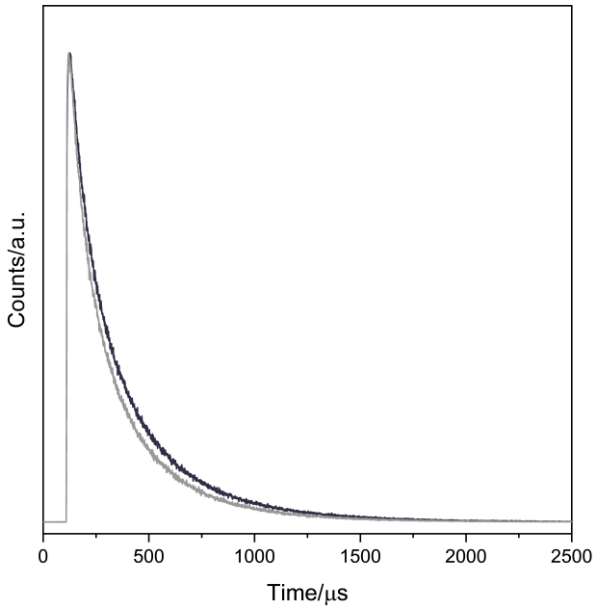


Figure 4.77 – Overlaid lifetime spectra of pre-formed **Eu_2bisDBM$_3$_PhenSS$_2$** and diluted in H_2O (dark grey) and D_2O (light grey) (0.5% THF, < 0.05% DMF). λ_{exc}: 350 nm, λ_{em}: 611 nm.

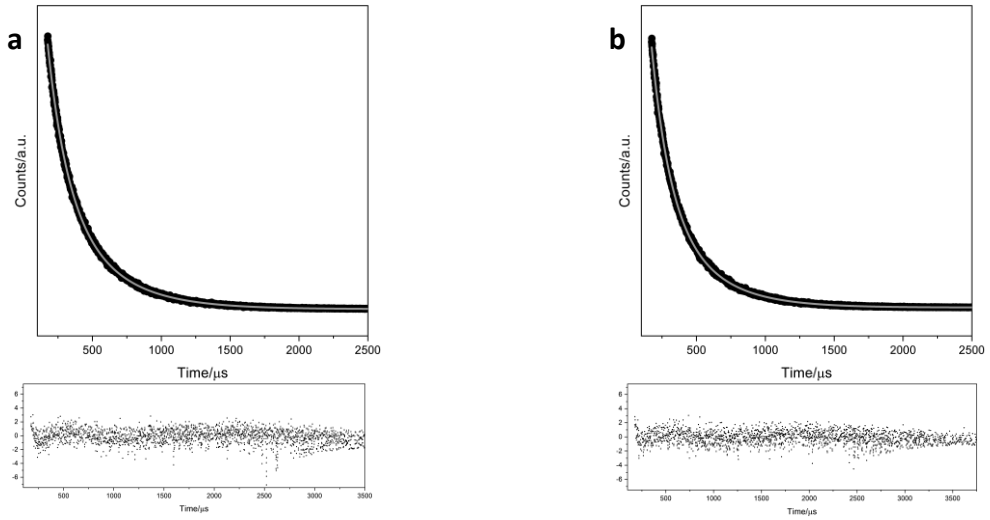


Figure 4.78 – Decay curve fittings of pre-formed **Eu_2bisDBM$_3$_PhenSS_2** and diluted in H_2O and D_2O (0.5% THF, < 0.05% DMF). Below are the respective residuals.

Solvent	**τ/μs (%)**
H_2O	360 (72%), 120 (28%)
D_2O	320 (71%), 110 (29%)

Table 4.19 – Exponential decay analysis of the lifetimes (**τ**) of pre-formed **Eu_2bisDBM$_3$_PhenSS_2** and diluted in H_2O and D_2O (0.5% THF, < 0.05% DMF).

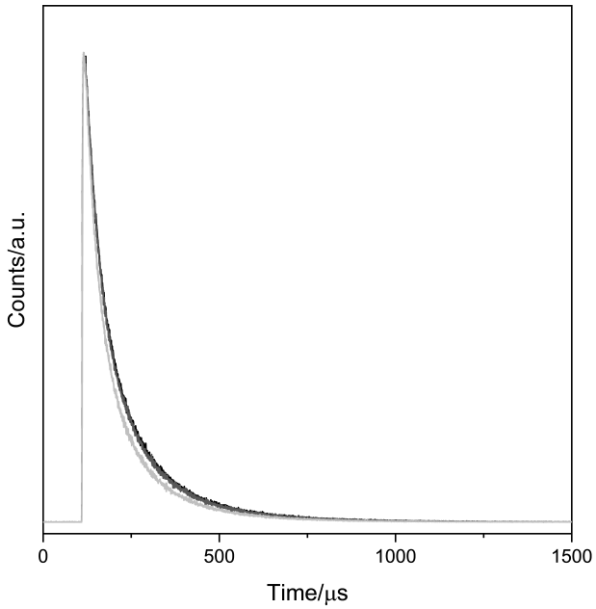


Figure 4.79 – Overlaid lifetime spectra of **Eu_2SAcbisDBM$_3$●Z@AuNP14** (black), **Eu_2SAcbisDBM$_3$●Z@AuNP50** (dark grey) and **Eu_2SAcbisDBM$_3$●Z@AuNP100** (light grey) isolated in H_2O. λ_{exc}: 350 nm, λ_{em}: 611 nm.

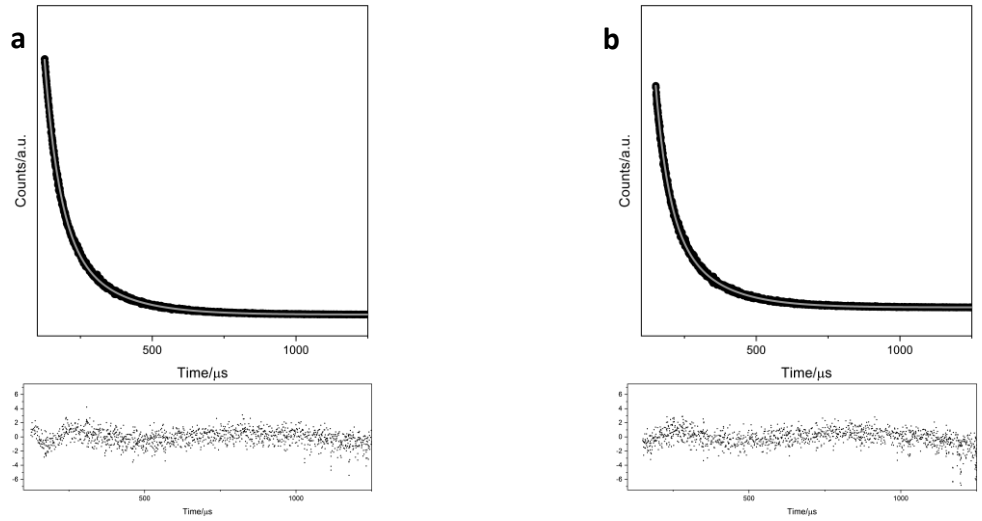


Figure 4.80 – Decay curve fittings of **Eu_2SAcbisDBM$_3$●Z@AuNP50** (**a**) and **Eu_2SAcbisDBM$_3$●Z@AuNP100** (**b**) isolated in H_2O. Below are the respective residuals.

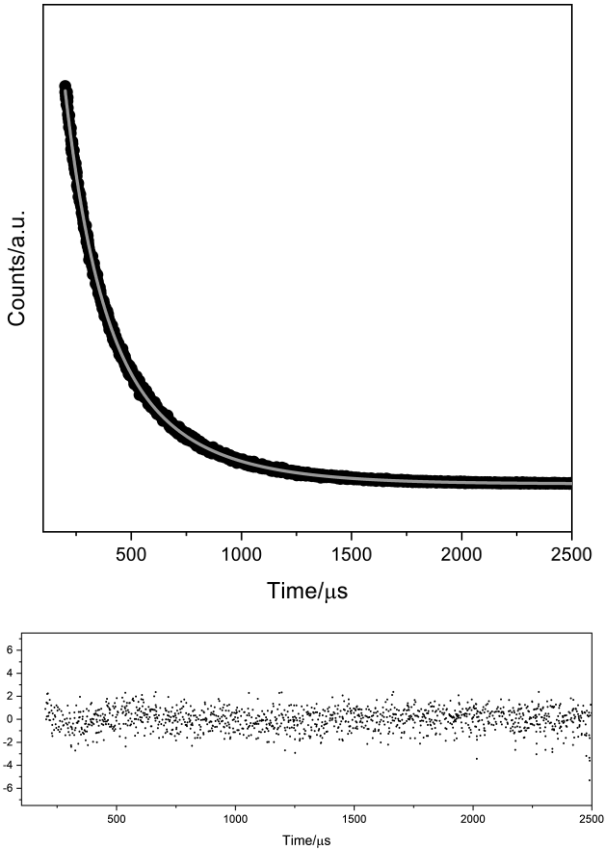


Figure 4.81 – Decay curve fittings of **Eu_2bisDBM$_3$_PhenSS$_2$_Z@AuNP14** isolated in H_2O. Below are the respective residuals.

4.5.12 Additional characterisation data of PhenSS

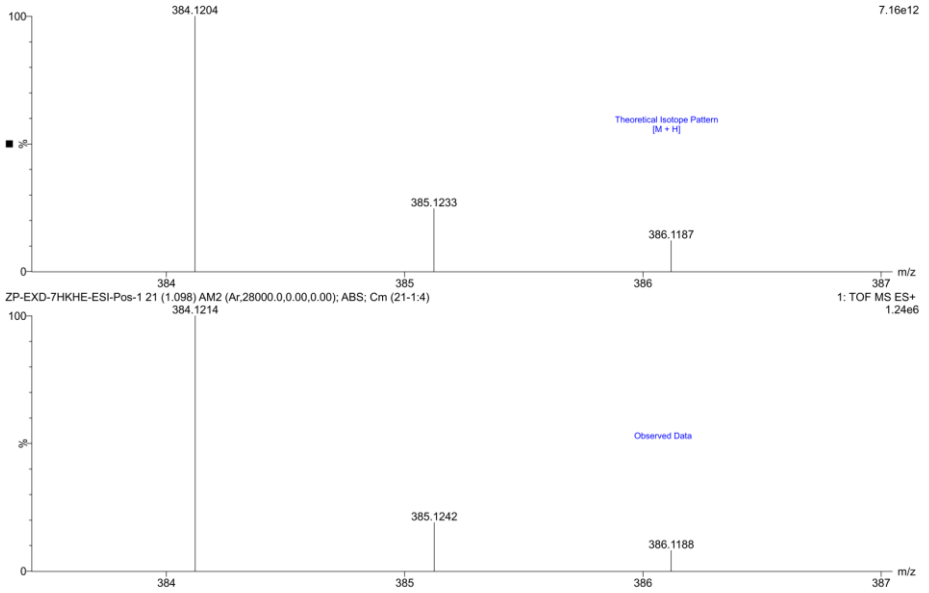


Figure 4.82 – ESI^{+}-MS calculated (top) and observed (bottom) spectra of **PhenSS**.

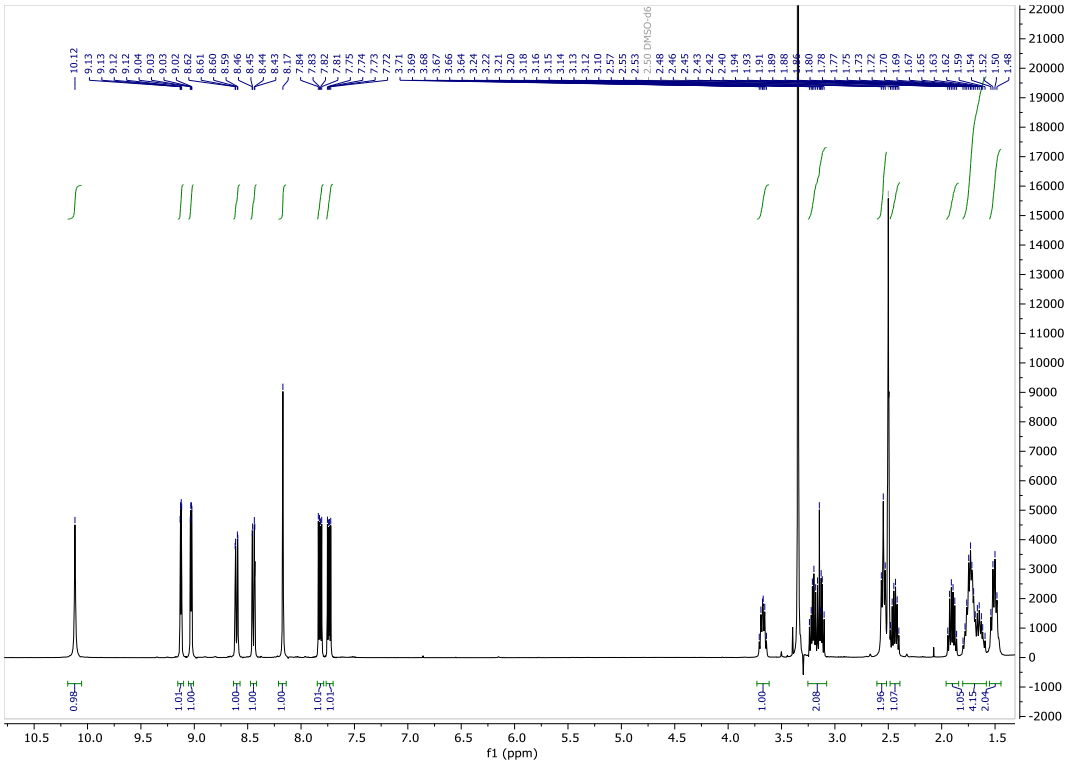


Figure 4.83 – ^{1}H-NMR spectrum (400 MHz, DMSOd_6) of **PhenSS**.

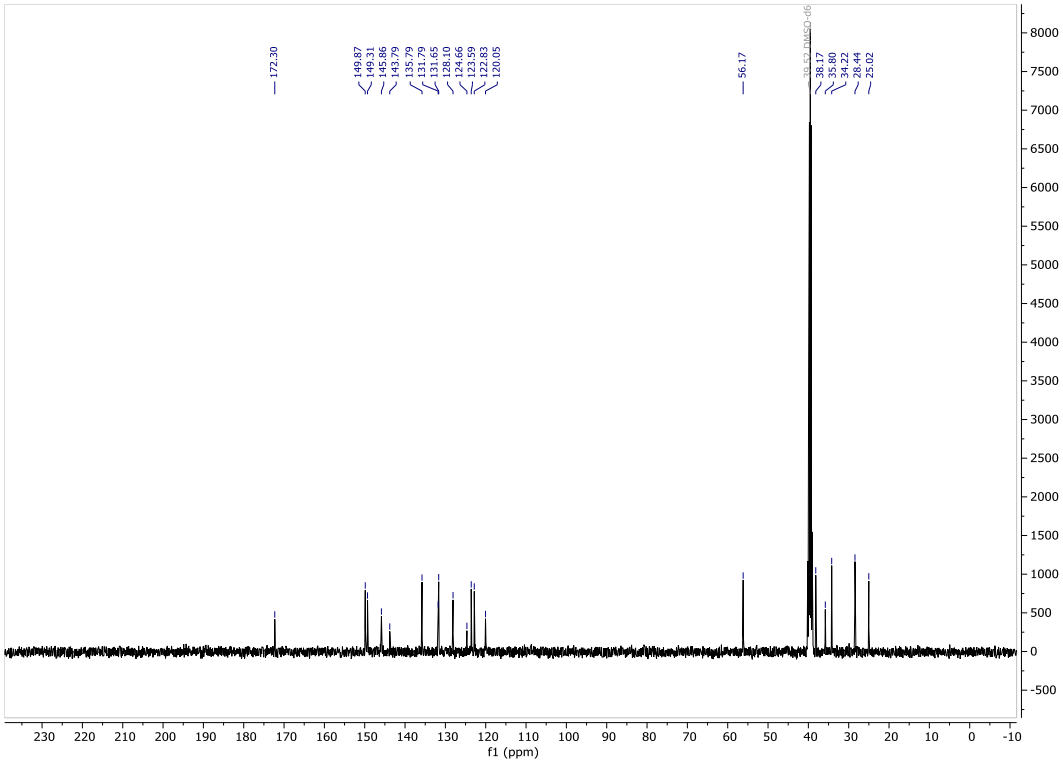


Figure 4.84 – ^{13}C-NMR spectrum (101 MHz, DMSOd_6) of **PhenSS**.

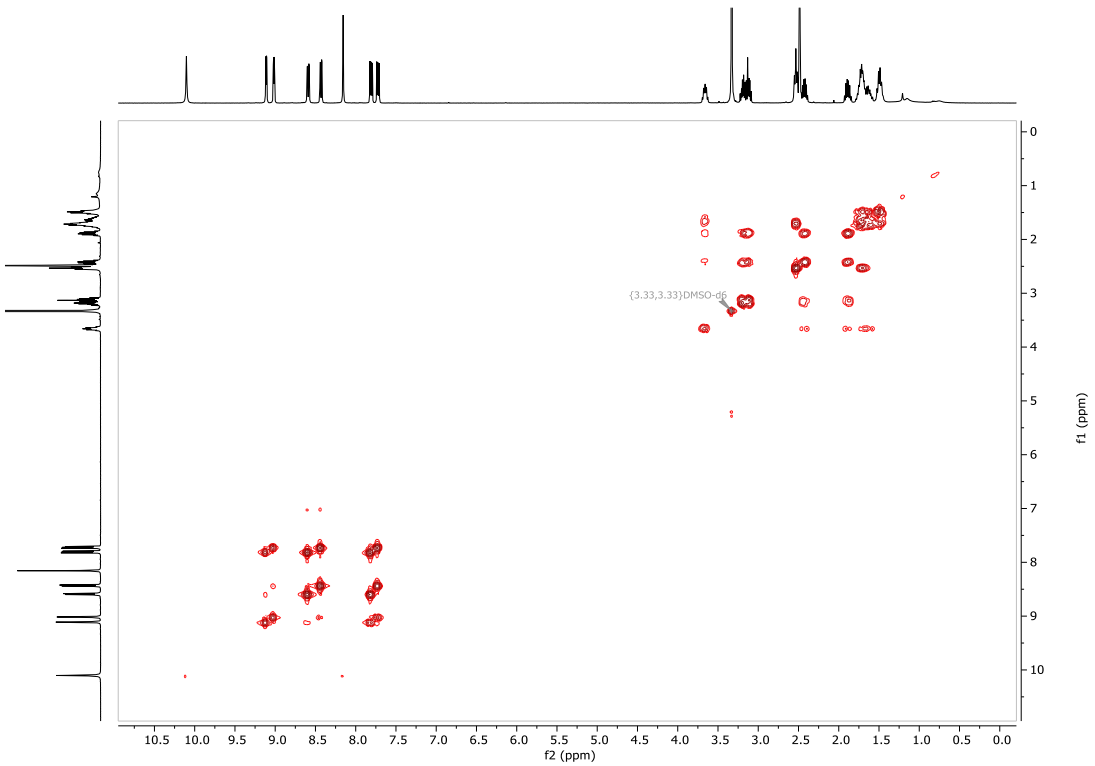


Figure 4.85 – 2D COSY spectrum (DMSOd_6) of **PhenSS**.

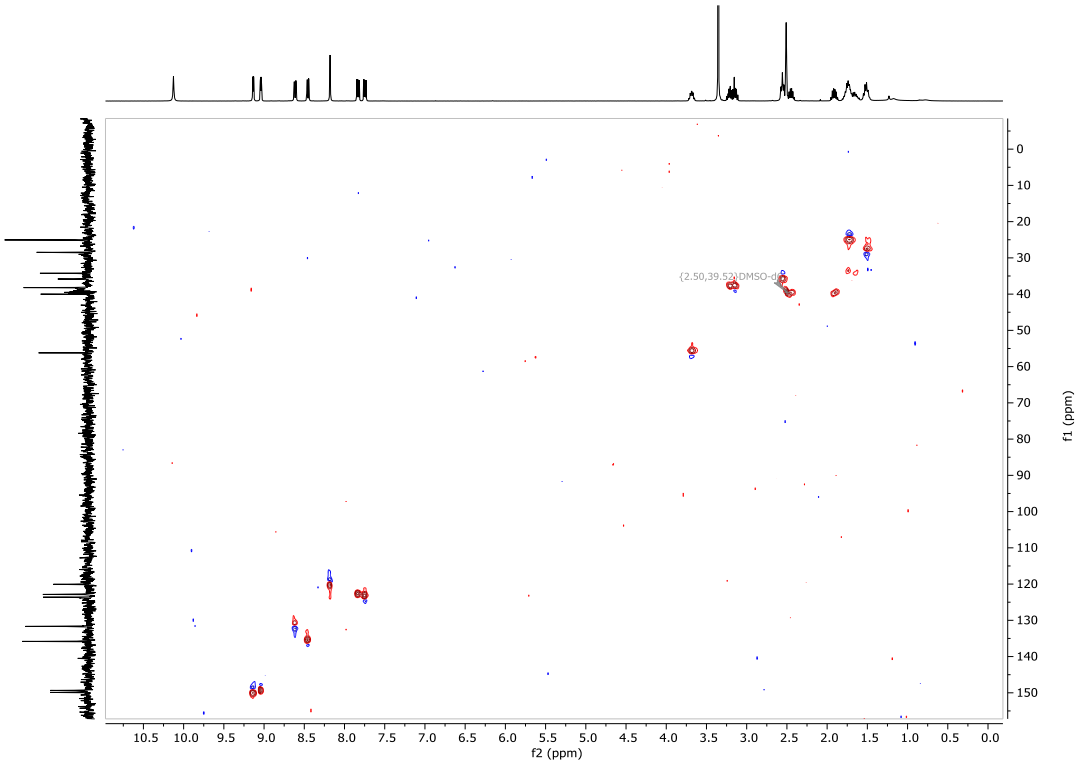


Figure 4.86 – 2D HSQC spectrum (DMSOd_6) of **PhenSS**.

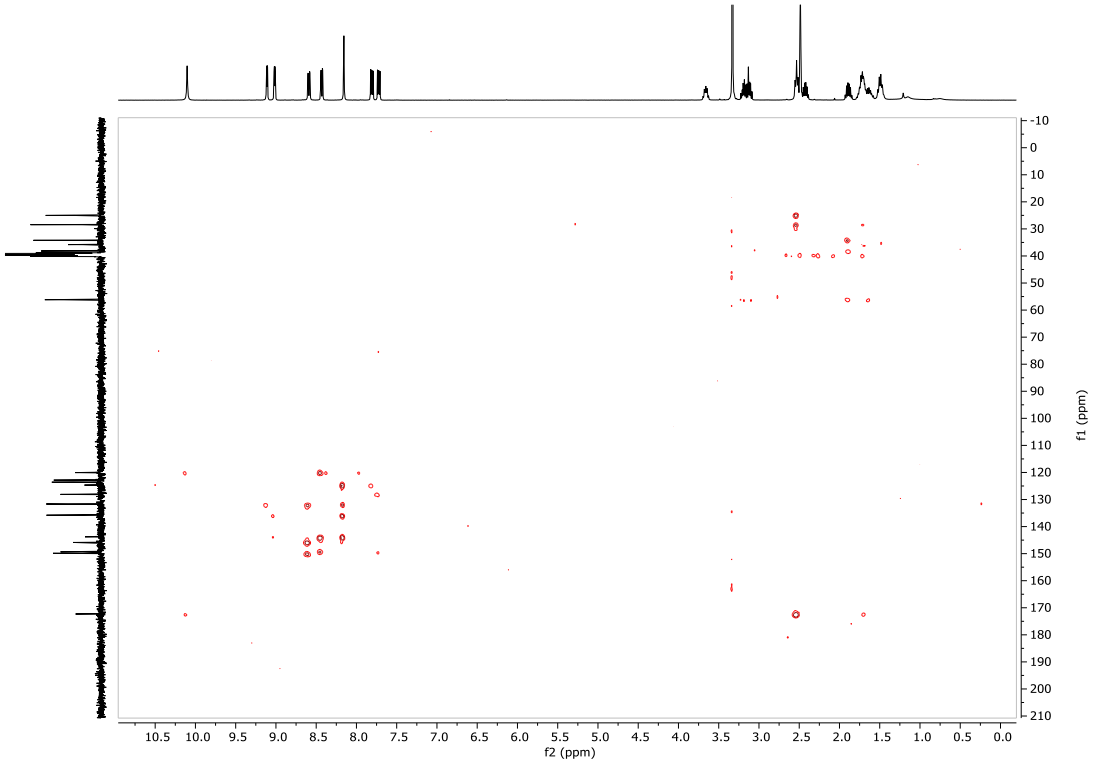


Figure 4.87 – 2D HMBC spectrum (DMSOd_6) of **PhenSS**.

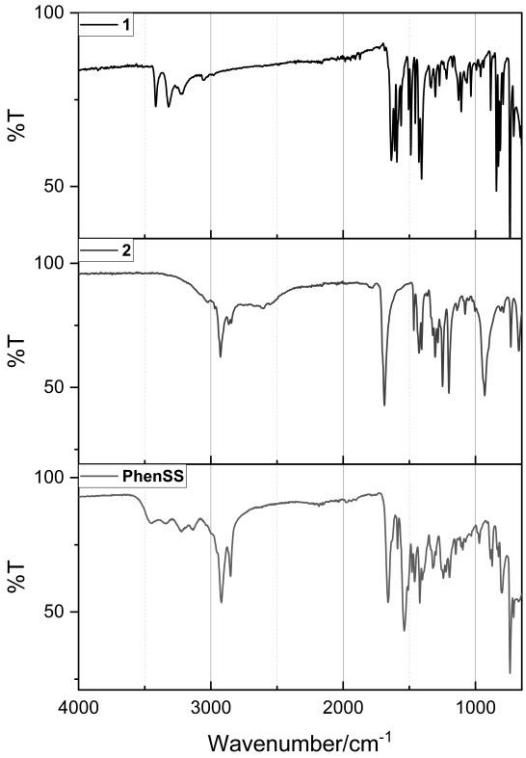


Figure 4.88 – Stacked IR spectra of 1,10-phenanthrolin-5-amine (**1**, top), α-lipoic acid (**2**, middle) and **PhenSS** (bottom).

4.5.13 ICP-MS data

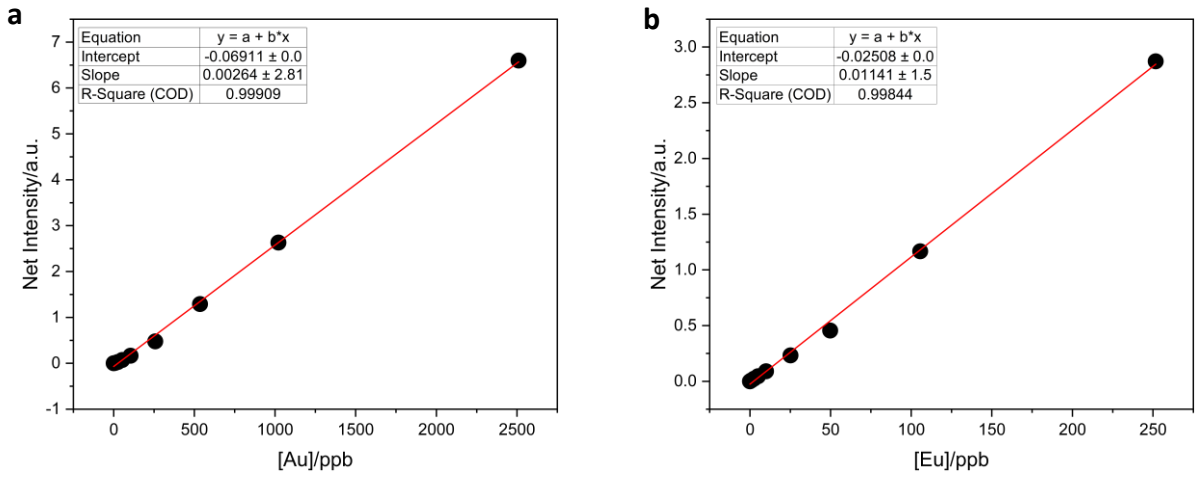


Figure 4.89 – ICP-MS calibration curves of Au (**a**) and Eu (**b**).

Sample	[Au]/ppb	[Eu]/ppb	[AuNP]/pM	[Eu]/µM	[Eu Complex]/µM
Eu_2bisDBM$_3$_PhenSS_2●Z@AuNP14	724.695	8.524	300	0.6	0.3
Eu_2SAcbisDBM$_3$●Z@AuNP14	864.572	9.495	400 (500)	0.6	0.3 (0.5)
Eu_2SAcbisDBM$_3$●Z@AuNP50	444.142	9.850	5 (6)	0.6	0.3 (0.5)
Eu_2SAcbisDBM$_3$●Z@AuNP100	1,418.194	10.445	2 (2)	0.6	0.3 (0.5)

Table 4.20 – Concentrations of Au and Eu in ppb as obtained by ICP-MS, concentrations of AuNPs, Eu and Eu complex (i.e. **Eu_2bisDBM$_3$_PhenSS_2** or **Eu_2SAcbisDBM$_3$**) in each **Eu_2bisDBM$_3$_PhenSS_2●Z@AuNP14** and **Eu_2SAcbisDBM$_3$●Z@AuNP14-50-100** system. As the complexes contain two Eu(III) atoms, the value is divided by two. In brackets and where relevant, the values estimated by UV-Vis absorption spectroscopy are reported.

Sample	Eu/AuNP	Complex/AuNP
Eu_2bisDBM$_3$_PhenSS_2●Z@AuNP14	1,144	613
Eu_2SAcbisDBM$_3$●Z@AuNP14	1,226	572
Eu_2SAcbisDBM$_3$●Z@AuNP50	107,900	53,950
Eu_2SAcbisDBM$_3$●Z@AuNP100	311,208	155,604

Table 4.21 – Number of Eu atoms and respective **Eu_2SAcbisDBM$_3$** and **Eu_2bisDBM$_3$_PhenSS_2** complexes per AuNP14, as calculated from ICP-MS. The method for the calculation of these values is reported in section 5.6.2.

Chapter 5 – General conclusions and future studies

In this thesis, a novel surface active bis β-diketone ligand has been presented, along with the synthesis and characterisation of the respective dinuclear **Ln_2SAcbisDBM$_3$** complexes and their incorporation to metallic substrates.

In the second chapter, the optical properties of the complexes were investigated and they were found to be comparable to the ones of the previously reported and unfunctionalized **Ln_2bisDBM$_3$** complexes. Furthermore, the crystal structures of both **Yb_2SAcbisDBM$_3$** and **Yb_2bisDBM$_3$** complexes were obtained for the first time. The complexes were found in a seven-coordinate state and displayed a distorted helical conformation. For **Yb_2bisDBM$_3$**, extensive hydrogen-bonding and π-π stacking networks were also observed and believed to contribute to the helical distortion.

Due to the unfilled coordination sphere of the prepared complexes, the visible emitting **Eu_2SAcbisDBM$_3$** derivative was assessed as a luminescent probe for the detection of anions. F^- coordination in THF was translated as both a significant increase in the luminescence lifetime (> 9-fold for longer component), as well as a modulation of the splitting pattern and relative intensities of the **Eu_2SAcbisDBM$_3$** emission spectrum. Importantly, we demonstrated how the more rigid structure of the **Eu_2SAcbisDBM$_3$** complex could withstand F^- coordination, while the mononuclear **EuDBM$_3$** counterpart was found to disassociate. The sensing of F^- in H_2O, however, is preferable. Our system did not display any response to F^- in aqueous media, a significant limitation caused by a combination of factors: namely, the high free hydration energies of F^-, the low solubility of the complex in solvents other than DMF and DMSO, and the lack of positive charge of the complex to increase the affinity with the F^- anion. In future

studies, a second generation of surface active bis β-diketonates could be designed to include e.g. -CF_3 groups to address solubility issues, while also potentially aiding the sensing of anions in aqueous media.

In the third chapter, we incorporated the **Ln_2SAcbisDBM$_3$** complexes to Au surfaces and presented the fabrication of a handheld sensing device by assessing the luminescence response of the **Eu_2SAcbisDBM$_3$@Au** surface to F^- in THF. Furthermore, two coating approaches were demonstrated: spin coating, for the reliable preparation of thin films, and dip coating, for the slow assembly of **Ln_2SAcbisDBM$_3$** complexes on the surface. Spin coating was selected for the comparison of the luminescence properties of either Au or plasmonic (pGold and AgNIs) **Ln_2SAcbisDBM$_3$** coated surfaces. Whereas the plasmonic enhancement of lanthanide(III) luminescence has been previously demonstrated, examples of the direct functionalisation with surface active complexes is scarce. The prepared **Ln_2SAcbisDBM$_3$@pGold** surfaces exhibited impressive luminescence enhancements by the Purcell effect, both in the visible (12-fold, Eu(III)) and, particularly, in the NIR (64-fold, Nd(III)). These results have enormous potential for the advancement of lanthanide(III) NIR emission in biomedical applications. Future studies should investigate the implementation of **Ln_2SAcbisDBM$_3$@pGold** as NIR emitting diagnostic platforms, thus benefitting from both the unique lanthanide(III) luminescence and low scattering in the NIR region, while also overcoming the poor signal to noise ratios and low quantum yields of the emitters.

In a brief last section of the chapter, we also proposed an alternative approach for the functionalisation of Au surfaces with **Ln_2bisDBM$_3$** complexes. Our aim was to assess the dispersion interactions between the complex and the selected polymer, PANI, to prepare

combined luminescent materials. The surfaces displayed well resolved luminescence in the visible and NIR, and the **Ln_2bisDBM$_3$** complex was found to drive the de-doping and conversion of PANI, from its ES to its EB form. Fascinating morphologies were observed on the surface, ascribed to the assembly of the complex and polymer. In future work, the mechanical and conductive properties of PANI should be investigated, thus offering a more complete view of the outcome of **Ln_2bisDBM$_3$** and polymer interaction. Furthermore, alternative polymers should be considered. Although energy transfer from the polymer to the lanthanide(III) was hypothesized here, the selection of polymers with well reported sensitisation of luminescence would allow for the fabrication of highly emissive and functional materials.

Finally, in the fourth and last chapter, the preparation of luminescent, H_2O dispersed AuNPs was presented. Here, the **Ln_2SAcbisDBM$_3$** complexes were anchored on AuNPs stabilised with a fluorinated surfactant (Zonyl FSA). For the Eu(III) and Yb(III) derivatives, the characteristic visible and NIR emission was retained in the **Ln_2SAcbisDBM$_3$●Z@AuNP** systems. Importantly, the luminescence lifetimes were found to be unaltered, indicating the efficacy of the spacer unit to prevent significant quenching on the AuNPs. **Eu_2SAcbisDBM$_3$●Z@AuNP14** were imaged by SuperSTEM-HAADF and the Eu(III) complexes were visually identified surrounding the AuNP core. This offered a unique perspective of the system, and the observed Eu-Au distances were correctly correlated to the Yb-S distances in the crystal structure of **Yb_2SAcbisDBM$_3$**. In the last section, we proposed the synthesis and coordination of the surface active **PhenSS** ligand to unfunctionalized **Eu_2bisDBM$_3$** complexes, with subsequent attachment to Zonyl FSA coated AuNP14. This approach afforded optimised quantum yields and luminescence lifetimes, compared to **Eu_2SAcbisDBM$_3$●Z@AuNP14**, while also representing a simple method for the preparation of surface active bis β-diketonate complexes. Future studies should impart further

functionality to the proposed AuNP systems. Anchoring of both visible and NIR emissive complexes to the same AuNP could be valuable for anticounterfeiting applications or as logic gate mimics, while addition of antibodies would produce targeting luminescent nanomaterials.